Title

Designing new fluorophore scaffolds for biological imaging

ISBN

9798270211653

Author

Wilson, Quintashia Dawnita

Publication Date

2025-12-12

Peer reviewed|Thesis/dissertation

UNIVERSITY OF CALIFORNIA

Los Angeles

Designing new fluorophore scaffolds for biological imaging

A dissertation submitted in partial satisfaction of the

requirements for the degree Doctor of Philosophy

in Chemistry

by

Quintashia Dawnita Wilson

2025

ABSTRACT OF THE DISSERTATION

Designing new fluorophore scaffolds for biological imaging

by

Quintashia Dawnita Wilson

Doctor of Philosophy in Chemistry

University of California, Los Angeles, 2025

Professor Ellen M. Sletten, Chair

Biological imaging has transformed our understanding of life at the molecular and cellular levels. By enabling real-time visualization of dynamic processes, it has driven major breakthroughs in both fundamental research and clinical practice. Among the available imaging modalities, fluorescence imaging stands at the forefront for its exceptional sensitivity in living systems. These advantages are amplified in the near-infrared (NIR, 700–1000 nm) and shortwave infrared (SWIR, 1000–2000 nm) regions of the electromagnetic spectrum, where reduced autofluorescence and minimal light scattering enable deeper, clearer imaging. Polymethine dyes have emerged as the leading fluorophore scaffold for NIR imaging due to their high brightness, low toxicity, and tunable optical properties. Many derivatives have advanced into applications involving environmental sensing and triggered payload release. However, translating these strengths into the SWIR region presents the significant challenge of increasing absorption wavelengths while preserving brightness. This dissertation focuses on the development of new

polymethine scaffolds for enhanced SWIR imaging, while also advancing the design of responsive NIR fluorophores for real-time detection in biological systems.

Chapter One is a perspective that outlines key strategies for advancing SWIR polymethine dye design, including chain extension, heterocycle modification and water solubility, and frames the central challenges and opportunities that motivate the work presented in subsequent chapters. Chapter Two builds directly on these design principles through the development of a new class of silicon-containing flavylium (SiliFlav) polymethine dyes. Incorporation of a silicon heteroatom into the flavylium scaffold yields bathochromic shifts of up to 200 nm while preserving respectable fluorescence quantum yields. A modular synthetic approach allows for fine-tuning of photophysical properties through functionalization at key positions on the heterocycle. The lead compound, SiliFlav5, formulated into oil-based nanoemulsions, demonstrates strong chemical stability, low cytotoxicity, and bright SWIR emission above 1300 nm. *In vivo* imaging in mice reveals high-resolution visualization of vasculature and spleen, establishing SiliFlav dyes as a robust new platform for deep-tissue SWIR imaging.

Chapter Three is a perspective that explores the transformation of polymethine dyes from traditional NIR fluorophores into dynamic, responsive tools for biological imaging and intervention. This includes the development of fluorogenic probes activated by specific cellular conditions and photocages capable of controlled release of bioactive molecules. These advances highlight the shift toward chemically responsive dye platforms for real-time sensing and targeted therapeutic applications. Building on this theme of responsive NIR fluorophores, Chapter Four introduces a new class of far-red to NIR flavylium merocyanine dyes that favor the fluorescent cyanine state under biologically relevant conditions. Unlike traditional scaffolds, these dyes are responsive to solvent viscosity and hydrogen bonding rather than polarity. Their unique photophysical properties enable intrinsic labeling of the endoplasmic reticulum and lipid droplets in live cells with minimal spectral crosstalk, offering a red-shifted, structurally simple alternative to conventional ER stains.

Chapter Five focuses on small molecule photocages for light-triggered drug release in photoactivated chemotherapy (PACT). To meet the demands of clinical translation, this work targets photocages that are aqueous-soluble, biologically stable, oxygen-independent, and NIR-activated. A π-extended silicon coumarin scaffold incorporating a flavylium donor is proposed to overcome the limited tissue penetration of traditional coumarin systems. Synthetic efforts toward this platform reveal key structure–reactivity relationships, including the role of a 7-dimethylamino substituent in promoting non-canonical oxidation pathways. These insights inform the future design of clinically viable photocages for targeted therapeutic applications.

The dissertation of Quintashia Dawnita Wilson is approved.

Justin R. Caram

Alexander M. Spokoyny

Robert Michael van Dam

Ellen M. Sletten, Committee Chair

University of California, Los Angeles

2025

This dissertation is dedicated to my niece, Camila.

TABLE OF CONTENTS

LIST OF FIGURES

CHAPTER ONE

CHAPTER TWO

LIST OF SCHEMES

LIST OF TABLES

CHAPTER TWO

CHAPTER FOUR

ACKNOWLEDGEMENTS

First, thank you to my dissertation committee. I appreciate the time and assistance each of you has contributed throughout my graduate career. I would also like to thank my colleagues whose skills and expertise meaningfully contributed to this research. Your input helped shape this work, and I am glad to share the final result.

Thank you to the friends I made during this journey. I would do redo this entire PhD just to meet you all again. I hope that I have impacted your lives as much as you all have impacted mine, and I am so excited to see you each of you embark on the next stage of your lives. Thank you as well to my longtime friends and extended family for the encouragement that has kept me grounded these past five years.

Lastly, but above all, thank you to my parents, Jacqulyn and Quincy, my siblings, Quinton and Trayle, and my life partner, Nick. Words cannot fully express the love and gratitude I feel for each of you, but I hope this dissertation stands as a small reflection of the unwavering love and support you have given me.

Chapter One is an unpublished perspective written by Wilson.

Chapter Two is an unpublished version of a manuscript, Wilson, Q.D.; Mobley, E. B.; Lin, E. Y.; Li, B. Y.; Hua, A. S.; Caram, J. R.; Sletten, E. M. Wilson, Mobley, Lin, Li and Hua contributed to experimental work. Wilson is responsible for writing.

Chapter Three is an unpublished perspective written by Wilson.

Chapter Four is a version of Wilson, Q.D.; Lin, H.H.; Lin, E.Y.; Chen, L.-J.; Sletten, E.M. "Exploiting Flavylium Merocyanine Dyes for Intrinsic, Multiplexed Labeling of the Endoplasmic Reticulum." *Anal. Chem.* **2025**, *97, 10,* 5595-5604. Wilson, Lin, Lin and Chen contributed to experimental work. Wilson is responsible for writing.

Chapter Five is unpublished studies with Wilson, Q. D. and Chen, L.-J. Both authors contributed to experimental work. Wilson is responsible for writing.

I would like to thank the Eugene V. Cota-Robles Fellowship, UCLA and the Chan Zuckerberg Initiative for support throughout these studies.

BIOGRAPHICAL SKETCH

EDUCATION

University of California, Los Angeles — **Los Angeles, California**
Master of Science, Chemistry — 2022

Boston University — **Boston, Massachusetts**
Bachelor of Arts, Biochemistry and Molecular Biology — 2020

CERTIFICATIONS

Registered Patent Agent, United States Patent & Trademark Office — 2025

RESEARCH EXPERIENCE

University of California, Los Angeles — **Los Angeles, California**
Graduate Student Researcher — *2020 – 2025*
Advisor: Dr. Ellen M. Sletten

- Designed and led two interdisciplinary research projects involving the synthesis of novel flavylium-based fluorophores and their application in live-cell and whole-animal molecular imaging
- Presented research progress and technical analyses at biweekly meetings and quarterly internal seminars
- Mentored a Master's student for one year; their work contributed to a published manuscript

SERVICE & LEADERSHIP

Graduate Admissions Committee, UCLA — *2024*

- Reviewed 200+ Ph.D. applications with faculty, assessing academic preparation and fit

Peer Reviewer (with Dr. Sletten) — *2022 – 2024*

- Assessed novelty, clarity, and impact of chemistry manuscripts for premier scientific journals

Undergraduate Recruitment Leader, Sletten Lab — *2021 – 2024*

- Designed equitable application process, hosted open houses, and built outreach pipelines for prospective students

HONORS & AWARDS

Herbert Newby McCoy Dissertation Award — *2025*
Evelyn Pan Excellence in Research Award, UCLA Graduate Division — *2024*
Eugene V. Cota-Robles Fellowship, UCLA Graduate Division — *2020 – 2024*

PUBLICATIONS

1. **Wilson, Q. D.**, Lin, H. H., Lin, E. Y., Chen, L-J., Sletten, E. M. "Exploiting flavylium merocyanine dyes for intrinsic, multiplexed labeling of the endoplasmic reticulum". *Anal. Chem.* **2025***, 97,* 10, 5595–5604.
2. **Wilson, Q. D.**, Sletten, E. M. "Engineering cyanine cyclizations for new fluorogenic probes". *Nat. Chem.* **2024**, *16*, 3-5.

CHAPTER ONE

Designing shortwave infrared polymethine dyes for *in vivo* imaging

Quintashia D. Wilson and Ellen M. Sletten

1.1 Abstract

Fluorescence imaging is a foundational technique in biomedical research and clinical diagnostics, offering high spatial resolution, real-time visualization, and molecular specificity. While visible (VIS, 400–700 nm) and near-infrared (NIR, 700–1000 nm) imaging have become well-established, the shortwave infrared (SWIR, 1000–2000 nm) region is emerging as a powerful platform for deep-tissue imaging due to its reduced light scattering, low background autofluorescence, and improved signal-to-noise ratio. However, a key limitation to widespread adoption of SWIR imaging remains the limited availability of bright, stable, and water-soluble small-molecule contrast agents. This chapter explores recent advances in the design and synthesis of polymethine dyes as SWIR fluorophores, highlighting three core strategies: chain elongation, heterocycle engineering, and water solubilization.

1.2 Introduction

Fluorescence imaging is a powerful technique used to visualize biological structures and processes with exceptional sensitivity and spatial resolution.[1–3] It works by tagging specific molecules with contrast agents that absorb and emit light, which can be detected using sensitive optical equipment that allows researchers to localize and quantify biomolecules in cells and organisms. Additionally, these fluorescent labels can be targeted to specific biomolecules, cellular compartments or tissues, providing unparalleled specificity. Accordingly, fluorescence imaging is widely used in research and clinical settings due to its ability to track biological processes in real time with minimal invasiveness.[4–6] A distinguishing feature of fluorescence imaging is the ability

to excite across different regions of the electromagnetic spectrum, with each region exhibiting unique capabilities. The visible (VIS, 400–700 nm) region is ideal for cell imaging applications, but limited by tissue penetration and background autofluorescence from endogenous chromophores, hindering its capacity in nontransparent systems like organs and whole animals. In contrast, the near-infrared (NIR, 700–1000 nm) region offers deeper light penetration and significantly reduced background autofluorescence compared to the VIS region, making it highly effective for applications in both cells and animals.[8–12,7,8] The shortwave infrared (SWIR, 1000–2000 nm) region represents the frontier of fluorescence imaging, providing the deepest tissue penetration and highest signal-to-noise ratio due to minimal scattering and negligible autofluorescence.[8–12] Accordingly, the SWIR region is a prime area of development for noninvasive whole-body imaging and diagnostics. Together, these spectral regions allow researchers to employ fluorescence imaging for a variety of applications, from subcellular resolution in fixed and living cells, to dynamic deep-tissue imaging in live animals.[13–16]

A notable bottleneck in expanding the capabilities of fluorescence imaging is the limited availability of effective contrast agents, particularly in the SWIR region. While the VIS and NIR regions benefit from a robust catalog of optimized fluorescent probes, the SWIR region remains relatively underserved. Therefore, expanding the toolbox of SWIR contrast agents remains a vital area of development for enhanced *in vivo* imaging. For many fluorescence imaging applications, small molecule fluorophores are often preferred because they offer a good balance between size, brightness, stability and spectral versatility.[5,10–12] Among these, polymethine dyes are the most prolific scaffold for *in vivo* imaging.[12,17–20] Consisting of two conjugated heterocycles connected by a polymethine chain, polymethine dyes exhibit narrow absorption (λ_{abs}) and emission (λ_{em}) bands, large absorption coefficients (ϵ_{max}) and moderate fluorescence quantum yields (ϕ_F), enabling precise excitation and high molecular brightness ($\epsilon_{max} \times \phi_F$).[21] Additionally, their modular heterocycles and extendable chain are readily fine-tuned to increase λ_{max}, brightness and

solubility.[22–24] Due to this unique architecture, polymethine dyes have emerged as the benchmark scaffold for NIR imaging, with noteworthy advancements in solubility,[25–27] targeted delivery,[28–31] environmental sensing[32–35,35–37] and triggered release[38–41] (see Chapter 3). However, extending these properties into the SWIR region poses unique photophysical and synthetic challenges, including the need for enhanced brightness and solubility. This chapter explores how innovative techniques in chain elongation, heterocycle engineering, and late-stage solubilization have been harnessed to push polymethine dyes deeper into the SWIR region for high resolution *in vivo* imaging.

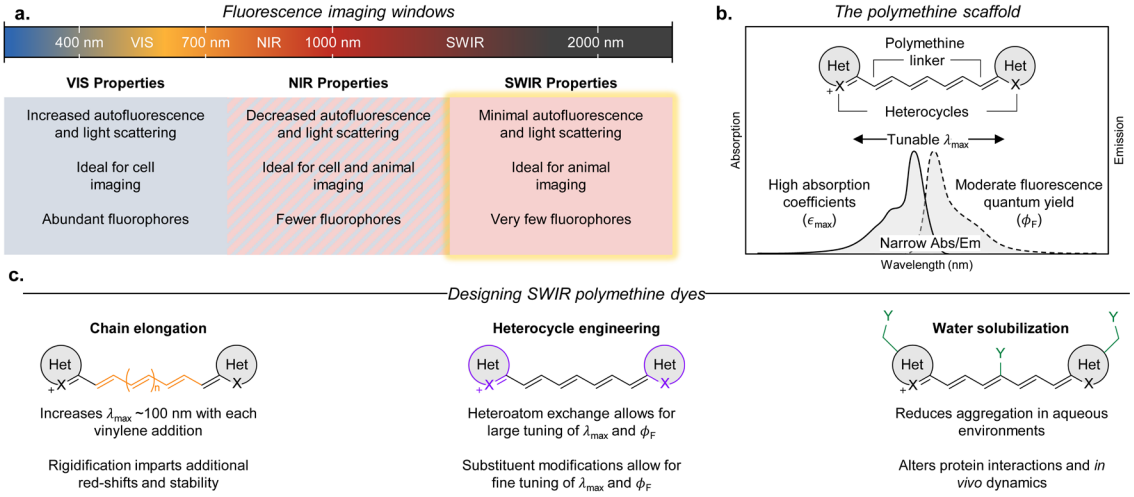

Figure 1.1. Overview of fluorescence imaging and polymethine dye design for SWIR imaging. A) Regions of fluorescence imaging and their properties. B) General structure and properties of polymethine dyes. C) Strategies to design optimized SWIR polymethine dyes for *in vivo* imaging.

1.3 Chain elongation

One of the earliest contrast agents used for *in vivo* imaging was **indocyanine green (ICG)**, a water-soluble heptamethine dye introduced by Eastman Kodak in the 1950s.[42–45] Initially designed as a photographic agent, **ICG** was rapidly repurposed due to its aqueous solubility and strong NIR emission, becoming a valuable clinical contrast agent for applications like vascular imaging, lymphatic mapping and image-guided surgery.[42,43,46,47] Therefore, it was a natural point of interest for SWIR fluorophore development. One of the earliest demonstrations of the potential

of **ICG** for SWIR imaging came from Bawendi and coworkers, who showed that the tail emission could be captured in the SWIR region, enabling through-skull brain imaging in mice.[48] Tail imaging of **ICG** is a promising avenue for translating the properties of the SWIR into clinical settings,[49] but misses out on the enhanced resolution and spectral real estate obtained by fluorophores with full SWIR absorption and emission. Therefore, significant efforts have focused on designing SWIR variants of ICG and related cyanine scaffolds. The most ubiquitous approach to increase λ_{max} is extension of the polymethine chain, where each vinylene addition imparts ~100 nm red-shift.[21] Jin and coworkers recently employed this strategy, generating nonamethine and undecamethine analogs of **ICG**, coined **ICG-C9** and **ICG-C11**. [50,51] The lead scaffold, **ICG-C11**, exhibits SWIR emission at 1030 nm in water, illustrating the reliability of chain elongation. That being said, this approach also increases the risk of ground state desymmetrization. In polar solvents, the fluorophore shifts away from the ideal polymethine ground state, wherein the positive charge is fully delocalized, towards the localized polyene ground state. Spectrally, this manifests as broad, blue-shifted absorption with decreased fluorophore brightness and stability.[52–54] Compared to **ICG**, there is noticeable ground state desymmetrization in the absorption spectra of **ICG-C9** and **ICG-C11**, although both scaffolds were highly effective for *in vivo* imaging. In 2022, Schnermann and coworkers adapted an alternative elongation strategy featuring a rigidified nonamthine backbone.[55] The lead derivative, **FNIR-1072**, exhibits narrow absorption, high brightness and excellent stability, with $\lambda_{max,abs}$ at 1072 nm and $\lambda_{max,em}$ at 1103 nm. Using a combination of FNIR dyes and **ICG**, the researchers achieved multicolor imaging and image-guided surgery in mouse tumor models, exemplifying the extended spectral real estate and enhanced tissue penetration of the SWIR region. In 2025, Zhang and coworkers pushed chain extension to its current limit by synthesizing rigidified pentadecamethine cyanine dyes (Cy15s).[56] The researchers generated a diverse panel of ultralong cyanine dyes with absorption up to 1233 nm and emission up to 1287 nm. Like the rigidified FNIR series, these Cy15 fluorophores maintained high brightness and

stability despite their extended conjugation, enabling high-contrast SWIR imaging of tumors and vasculature with excellent signal-to-noise ratios. Collectively, these findings confirm that chain elongation remains a powerful strategy for pushing polymethine fluorophores into the SWIR region, but success increasingly depends on structural stabilization to preserve brightness and stability. Additionally, these advances build upon the clinical familiarity and safety profile of ICG, highlighting how structurally enhanced derivatives can bridge the gap between established NIR contrast agents and the next generation of clinic-ready SWIR fluorophores.

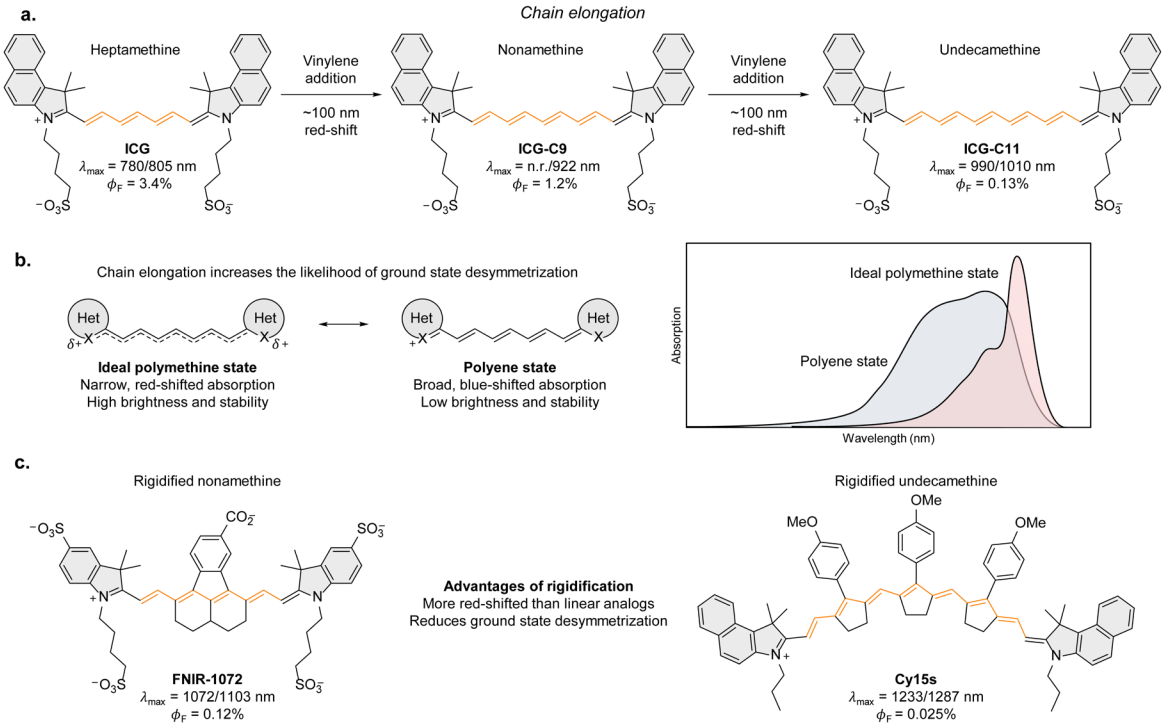

Figure 1.2. Representative examples of chain elongation. A) Chain elongation of **ICG**[51] to generate **ICG-C9**[51] and **ICG-C11**[50]. B) Properties of ground state desymmetrization caused by overextension of the polymethine chain. C) Structures of rigidified extended polymethine dyes **FNIR-1072**[55] and **SJ-1287**[56], which exhibit minimal ground state desymmetrization. Fluorophore counterions are omitted. Photophysical data was obtained from the listed references.

1.4 Heterocycle engineering

While chain elongation has proven to be a robust strategy for pushing cyanine dyes into the SWIR region, many of the earliest and most successful small molecule SWIR fluorophores utilize alternative heterocyclic motifs. In 2013, Dai and coworkers employed IR-1061, a

thiopyrylium-based heptamethine dye with emission at 1081 nm, marking the first small molecule used for SWIR imaging.[57] Around the same time, a more conjugated derivative featuring a thioflavylium heterocycle, **IR-26**, emerged as a benchmark standard for SWIR quantum yield measurements due to its emission at 1129 nm.[58,59] These heterocycles are advantageous for generating SWIR polymethine dyes due to their extended conjugation and electron-donating sulfur heteroatom, which enable shorter polymethine chains, improving stability and synthetic accessibility. While thiopyrylium and thioflavylium polymethine dyes have transformed the SWIR imaging space, there is still room for improvement in the quantum yields of these scaffolds.[20,60–63] SWIR fluorophores are inherently limited by low quantum yields due to energy gap law constraints.[64] This effect is worsened by the sulfur heteroatom, which can promote intersystem crossing resulting in even lower quantum yields.[64,64–66] To overcome these limitations, we and others have replaced the sulfur heteroatom with oxygen to suppress nonradiative decay and enhance quantum yield, as seen with **IR-27**.[65] Although this substitution causes a blue-shift in emission, we found that installing an electron-donating dimethylamino substituent at the 7-position of the heterocycle increased the emission wavelength, leading to the development of a new class of flavylium (Flav) polymethine dyes.[65] The leading heptamethine fluorophore in this series, coined **Flav7**, exhibits SWIR emission at 1045 nm with brightness values 13-fold higher than **IR-26**. Capitalizing on the high spatiotemporal resolution afforded by SWIR wavelengths, **Flav7** enabled imaging of hindlimb vasculature and non-invasive quantification of heart rate in anesthetized mice. We later expanded this platform to include various amines at the 5-, 6-, 7-, and 8-positions, as well as *tert*-butyl and adamantyl substituents at the 2-position, resulting in the chromenylium (Chrom) scaffold.[67–69] These modifications allowed fine-tuning of the λ_{max} and ϕ_F, resulting in bright, laser-matched fluorophores for three- and four-color *in vivo* imaging. Altogether, these advances demonstrate how heterocycle engineering serves as a powerful design principle for tailoring λ_{max} while improving quantum yields. By expanding beyond traditional indolenium

cores to include sulfur- and oxygen-based heterocycles, researchers have broadened the structural landscape of polymethine dyes and unlocked new opportunities for high-resolution, multicolor SWIR imaging in complex biological systems.

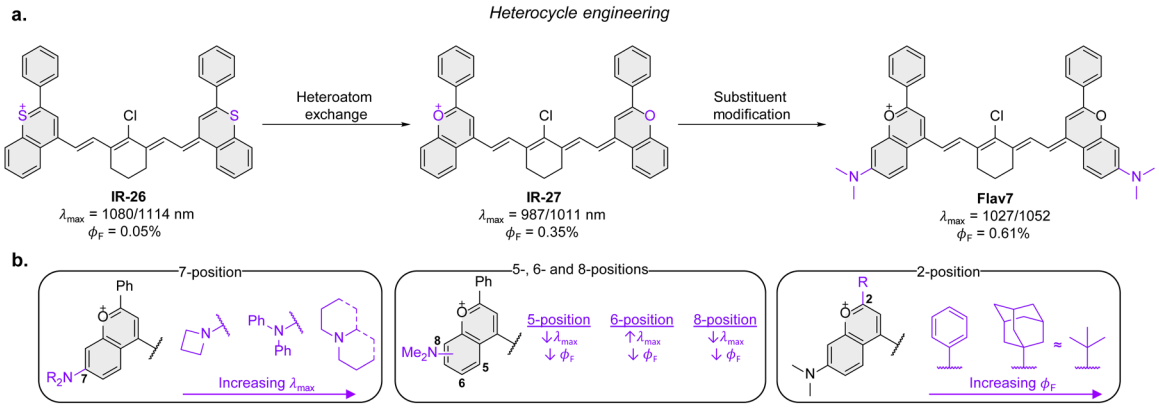

Figure 1.3. Representative examples of heterocycle engineering. A) Heteroatom exchange from **IR-26**[58] (sulfur) to **IR-27**[68] (oxygen), and substituent modification to **Flav7**[65]. B) Additional examples of substituent modifications of the flavylium scaffold that affect λ_{max} and ϕ_F.[67–69]

1.5 Water solubilization

While chain elongation and heterocycle engineering have increased the emission wavelength, brightness and stability of polymethine dyes in the SWIR region, translating these properties into biological systems introduces new challenges in aqueous solubility. Both strategies increase the overall hydrophobicity of the scaffold, resulting in the formation of non-emissive H-aggregates in aqueous solutions.[21,70] In the case of SWIR cyanine dyes such as **ICG-11** and **FNIR**, the pendant alkyl sulfonate groups attached to the heterocycle are sufficient solubilizing handles.[50,51,55] However, other heterocycles like (thio)pyrylium and (thio)flavylium-based scaffolds lack obvious linkages to append solubilizing groups, and simple alkyl sulfonates are often insufficient to improve solubility of these hydrophobic cores. To overcome these limitations, researchers have developed late-stage functionalization strategies that install water solubilization handles without compromising photophysical properties. Central to this strategy is the incorporation of terminal alkyne handles for copper(I)-catalyzed azide-alkyne chemistry (CuAAC) with various solubilizing groups.[60,61,71,72] Hong and coworkers appended terminal alkynes to

thiopyrylium dye **5H5**, enabling CuAAC with polyethylene glycol (PEG)-cyclic RGD conjugates (**5H5-PEG$_8$-cRGD$_{fk}$**). This not only enhanced aqueous solubility through PEG chains, but also allowed targeted integrin receptor labeling *in vivo*. Capitalizing on the modularity of the Chrom scaffold, we introduced propargyl groups at the 7-position amine to act as a clickable intermediate for diverse modifications.[71] With this core scaffold, we were able to append various water-solubilizing groups, including sulfonates, quaternary amines and phosphonates, all of which exhibit minimal aggregation and high brightness in biological settings. The sulfonated derivative, **SulfoChrom7**, exhibited strong albumin association and clearance patterns comparable to **ICG**,[73] effectively serving as a SWIR-emissive analog. The phosphonated derivative, **PhosphoChrom7**, demonstrated strong bone localization, acting as a pseudo-targeting group *in vivo*.

In 2025, we expanded this methodology to include CuAAC with poly(2-methyl-2-oxazoline) (POx) polymers to generate star-shaped fluorophore-polymer conjugates, coined CStars.[72] The leading conjugate, **CStar30**, which contains 30 POx repeat units, exhibits exceptionally narrow absorption in water and serum with high brightness and negligible protein binding. Unlike **SulfoChrom7** and **ICG**, **CStar30** clears rapidly via the kidneys. This enables two-color, video-rate multiplexed imaging alongside **ICG**, providing a powerful platform for real-time clinical diagnostics and surgical guidance. Altogether, these developments illustrate the importance of late-stage functionalization in bridging synthetic design and biological utility. By providing versatile, modular handles for solubilizing and targeting groups, this strategy enables SWIR fluorophores with improved solubility, tunable biodistribution, and robust *in vivo* performance essential for advanced imaging techniques.

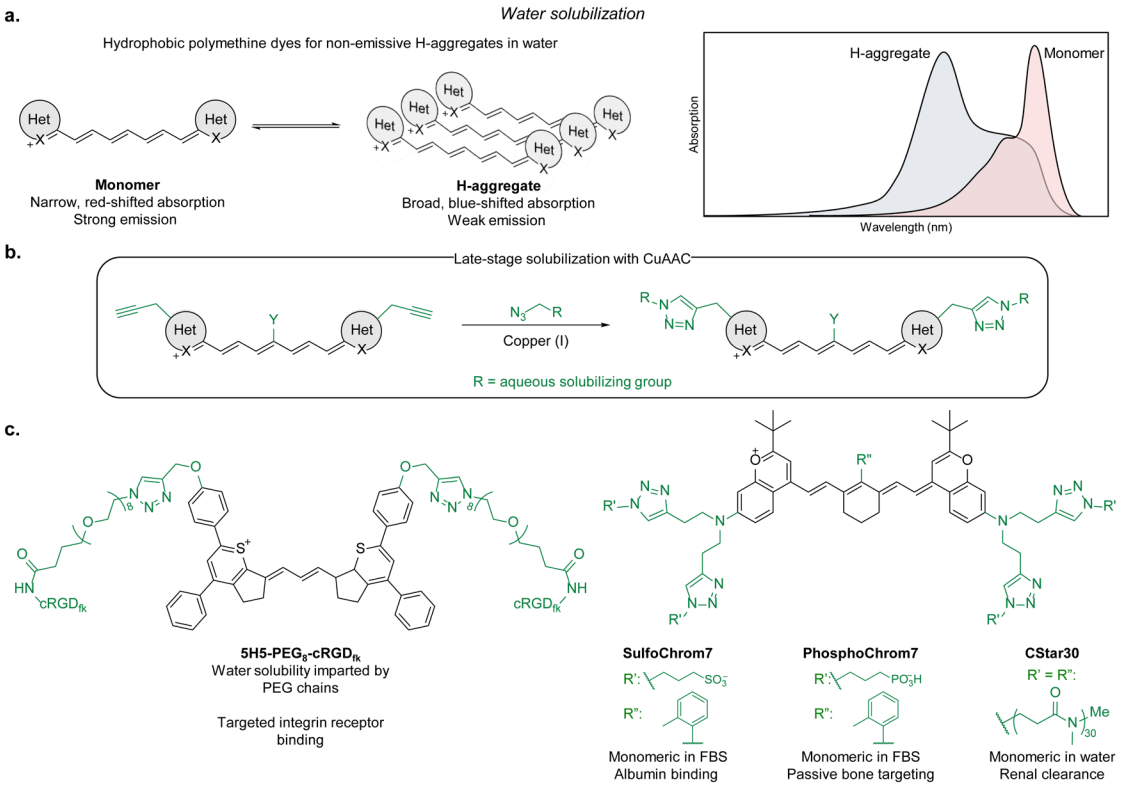

Figure 1.4. Representative examples of water solubilization. A) Overview of non-emissive H-aggregates. B) Overview of CuAAC employed for late-stage solubilization of polymethine dyes. C) Chemical structures of water soluble **5H5-PEG$_8$-cRGD$_{fk}$**[60], **SulfoChrom7**[71], **PhosphoChrom7**[71] and **CStar30**[72] fluorophores used for *in vivo* imaging.

1.6 Conclusion

In summary, the development of polymethine-based fluorophores for SWIR imaging has advanced significantly through three key strategies: chain elongation, heterocycle engineering, and late-stage water solubilization. Chain elongation effectively red-shifts absorption and emission into the SWIR region, while rigidification helps preserve brightness and stability. Heterocycle engineering introduces new electronic properties that improve quantum yields and spectral tunability. Finally, late-stage functionalization enables the installation of water-solubilizing and targeting groups, facilitating biological compatibility without compromising photophysical performance. Together, these innovations have expanded the capabilities of SWIR fluorophores,

establishing a robust foundation for high-resolution, noninvasive imaging in complex biological systems.

1.7 References

(1) Owens, E. A.; Henary, M.; El Fakhri, G.; Choi, H. S. Tissue-Specific Near-Infrared Fluorescence Imaging. *Acc. Chem. Res.* **2016**, *49* (9), 1731–1740. https://doi.org/10.1021/acs.accounts.6b00239.

(2) Ma, K.; Jiang, Q.; Yang, Y.; Zhang, F. Recent Advances of Versatile Fluorophores for Multifunctional Biomedical Imaging in the NIR-II Region. *J. Mater. Chem. B* **2024**, *13* (1), 15–36. https://doi.org/10.1039/D4TB01957A.

(3) Renz, M. Fluorescence Microscopy—A Historical and Technical Perspective. *Cytometry Part A* **2013**, *83* (9), 767–779. https://doi.org/10.1002/cyto.a.22295.

(4) Studwell, A. J.; Kotton, D. N. A Shift From Cell Cultures to Creatures: In Vivo Imaging of Small Animals in Experimental Regenerative Medicine. *Molecular Therapy* **2011**, *19* (11), 1933–1941. https://doi.org/10.1038/mt.2011.194.

(5) Wang, F.; Zhong, Y.; Bruns, O.; Liang, Y.; Dai, H. In Vivo NIR-II Fluorescence Imaging for Biology and Medicine. *Nat. Photon.* **2024**, *18* (6), 535–547. https://doi.org/10.1038/s41566-024-01391-5.

(6) Zhang, X.; Bloch, S.; Akers, W.; Achilefu, S. Near-Infrared Molecular Probes for In Vivo Imaging. *Curr Protoc Cytom* **2012**, *CHAPTER*, Unit12.27. https://doi.org/10.1002/0471142956.cy1227s60.

(7) Kenry; Duan, Y.; Liu, B. Recent Advances of Optical Imaging in the Second Near-Infrared Window. *Advanced Materials* **2018**, *30* (47), 1802394. https://doi.org/10.1002/adma.201802394.

(8) Bashkatov, A. N.; Genina, E. A.; Kochubey, V. I.; Tuchin, V. V. Optical Properties of Human Skin, Subcutaneous and Mucous Tissues in the Wavelength Range from 400 to 2000 Nm. *J. Phys. D: Appl. Phys.* **2005**, *38* (15), 2543–2555. https://doi.org/10.1088/0022-3727/38/15/004.

(9) Xu, L.; Zhang, Q.; Wang, X.; Lin, W. Biomedical Applications of NIR-II Organic Small Molecule Fluorescent Probes in Different Organs. *Coordination Chemistry Reviews* **2024**, *519*, 216122. https://doi.org/10.1016/j.ccr.2024.216122.

(10) Jiang, Z.; Ding, Y.; Lovell, J. F.; Zhang, Y. Design and Application of Organic Contrast Agents for Molecular Imaging in the Second near Infrared (NIR-II) Window. *Photoacoustics* **2022**, *28*, 100426. https://doi.org/10.1016/j.pacs.2022.100426.

(11) Zhang, X.; Lin, J.; Huang, P. Design Strategies and Biomedical Applications of Organic NIR-IIb Fluorophores. *Chem. Commun.* **2025**. https://doi.org/10.1039/D4CC04532G.

(12) Chen, X.; Li, J.; Roy, S.; Ullah, Z.; Gu, J.; Huang, H.; Yu, C.; Wang, X.; Wang, H.; Zhang, Y.; Guo, B. Development of Polymethine Dyes for NIR-II Fluorescence Imaging and Therapy. *Advanced Healthcare Materials* **2024**, *13* (16), 2304506. https://doi.org/10.1002/adhm.202304506.

(13) Grimm, J. B.; Muthusamy, A. K.; Liang, Y.; Brown, T. A.; Lemon, W. C.; Patel, R.; Lu, R.; Macklin, J. J.; Keller, P. J.; Ji, N.; Lavis, L. D. A General Method to Fine-Tune Fluorophores for Live-Cell and in Vivo Imaging. *Nat Methods* **2017**, *14* (10), 987–994. https://doi.org/10.1038/nmeth.4403.

(14) Chen, Y.; Wang, S.; Zhang, F. Near-Infrared Luminescence High-Contrast in Vivo Biomedical Imaging. *Nat Rev Bioeng* **2023**, *1* (1), 60–78. https://doi.org/10.1038/s44222-022-00002-8.

(15) Min, W.; Lu, S.; Chong, S.; Roy, R.; Holtom, G. R.; Xie, X. S. Imaging Chromophores with Undetectable Fluorescence by Stimulated Emission Microscopy. *Nature* **2009**, *461* (7267), 1105–1109. https://doi.org/10.1038/nature08438.

(16) Chen, F.; Liu, W.; Li, H.; Deng, T.; Xing, B.; Liu, F. Rhodamine Fluorophores for STED Super-Resolution Biological Imaging. *Analysis & Sensing* **2022**, *2* (3), e202100066. https://doi.org/10.1002/anse.202100066.

(17) Antaris, A. L.; Chen, H.; Cheng, K.; Sun, Y.; Hong, G.; Qu, C.; Diao, S.; Deng, Z.; Hu, X.; Zhang, B.; Zhang, X.; Yaghi, O. K.; Alamparambil, Z. R.; Hong, X.; Cheng, Z.; Dai, H. A Small-Molecule Dye for NIR-II Imaging. *Nature Mater* **2016**, *15* (2), 235–242. https://doi.org/10.1038/nmat4476.

(18) Li, B.; Lu, L.; Zhao, M.; Lei, Z.; Zhang, F. An Efficient 1064 Nm NIR-II Excitation Fluorescent Molecular Dye for Deep-Tissue High-Resolution Dynamic Bioimaging. *Angewandte Chemie* **2018**, *130* (25), 7605–7609. https://doi.org/10.1002/ange.201801226.

(19) Lei, Z.; Li, X.; Luo, X.; He, H.; Zheng, J.; Qian, X.; Yang, Y. Bright, Stable, and Biocompatible Organic Fluorophores Absorbing/Emitting in the Deep Near-Infrared Spectral Region. *Angewandte Chemie International Edition* **2017**, *56* (11), 2979–2983. https://doi.org/10.1002/anie.201612301.

(20) Yang, Y.; Sun, C.; Wang, S.; Yan, K.; Zhao, M.; Wu, B.; Zhang, F. Counterion-Paired Bright Heptamethine Fluorophores with NIR-II Excitation and Emission Enable

Multiplexed Biomedical Imaging. *Angewandte Chemie International Edition* **2022**, *61* (24), e202117436. https://doi.org/10.1002/anie.202117436.

(21) Bricks, J. L.; Kachkovskii, A. D.; Slominskii, Y. L.; Gerasov, A. O.; Popov, S. V. Molecular Design of near Infrared Polymethine Dyes: A Review. *Dyes and Pigments* **2015**, *121*, 238–255. https://doi.org/10.1016/j.dyepig.2015.05.016.

(22) Zhao, X.; Zhang, F.; Lei, Z. The Pursuit of Polymethine Fluorophores with NIR-II Emission and High Brightness for *in Vivo* Applications. *Chem. Sci.* **2022**, *13* (38), 11280–11293. https://doi.org/10.1039/D2SC03136A.

(23) Chen, X.; Li, J.; Roy, S.; Ullah, Z.; Gu, J.; Huang, H.; Yu, C.; Wang, X.; Wang, H.; Zhang, Y.; Guo, B. Development of Polymethine Dyes for NIR-II Fluorescence Imaging and Therapy. *Advanced Healthcare Materials n/a* (n/a), 2304506. https://doi.org/10.1002/adhm.202304506.

(24) Pascal, S.; Haefele, A.; Monnereau, C.; Charaf-Eddin, A.; Jacquemin, D.; Le Guennic, B.; Maury, O.; Andraud, C. On the Versatility of Electronic Structures in Polymethine Dyes; Burgess, D., Owen, G., Rana, H., Zamboni, R., Kajzar, F., Szep, A. A., Eds.; Amsterdam, Netherlands, 2014; p 92531A. https://doi.org/10.1117/12.2072624.

(25) Li, D.-H.; Gamage, R. S.; Smith, B. D. Sterically Shielded Hydrophilic Analogs of Indocyanine Green. *J. Org. Chem.* **2022**, *87* (17), 11593–11601. https://doi.org/10.1021/acs.joc.2c01229.

(26) Li, D.-H.; Schreiber, C. L.; Smith, B. D. Sterically Shielded Heptamethine Cyanine Dyes for Bioconjugation and High Performance Near-Infrared Fluorescence Imaging.

Angewandte Chemie International Edition **2020**, *59* (29), 12154–12161. https://doi.org/10.1002/anie.202004449.

(27) Lim, I.; Vian, A.; van de Wouw, H. L.; Day, R. A.; Gomez, C.; Liu, Y.; Rheingold, A. L.; Campàs, O.; Sletten, E. M. Fluorous Soluble Cyanine Dyes for Visualizing Perfluorocarbons in Living Systems. *J. Am. Chem. Soc.* **2020**, *142* (37), 16072–16081. https://doi.org/10.1021/jacs.0c07761.

(28) Eiring, P.; McLaughlin, R.; Matikonda, S. S.; Han, Z.; Grabenhorst, L.; Helmerich, D. A.; Meub, M.; Beliu, G.; Luciano, M.; Bandi, V.; Zijlstra, N.; Shi, Z.-D.; Tarasov, S. G.; Swenson, R.; Tinnefeld, P.; Glembockyte, V.; Cordes, T.; Sauer, M.; Schnermann, M. J. Targetable Conformationally Restricted Cyanines Enable Photon-Count-Limited Applications. *Angewandte Chemie International Edition* **2021**, *60* (51), 26685–26693. https://doi.org/10.1002/anie.202109749.

(29) König, S. G.; Krämer, R. Accessing Structurally Diverse Near-Infrared Cyanine Dyes for Folate Receptor-Targeted Cancer Cell Staining. *Chemistry – A European Journal* **2017**, *23* (39), 9306–9312. https://doi.org/10.1002/chem.201700026.

(30) Jiang, Y.; Wang, L.; Hu, B.; Nong, C.; Shen, X.-C.; Chen, H. Engineering of Kidney-Targeting Fluorophores with Tunable Emission from NIR-I to NIR-II for Early Diagnosis of Kidney Disease. *Advanced Healthcare Materials n/a* (n/a), 2402828. https://doi.org/10.1002/adhm.202402828.

(31) Kelderhouse, L. E.; Chelvam, V.; Wayua, C.; Mahalingam, S.; Poh, S.; Kularatne, S. A.; Low, P. S. Development of Tumor-Targeted Near Infrared Probes for Fluorescence Guided Surgery. *Bioconjugate Chem.* **2013**, *24* (6), 1075–1080. https://doi.org/10.1021/bc400131a.

(32) Usama, S. M.; Marker, S. C.; Li, D.-H.; Caldwell, D. R.; Stroet, M.; Patel, N. L.; Tebo, A. G.; Hernot, S.; Kalen, J. D.; Schnermann, M. Method To Diversify Cyanine Chromophore Functionality Enables Improved Biomolecule Tracking and Intracellular Imaging. *J. Am. Chem. Soc.* **2023**, *145* (27), 14647–14659. https://doi.org/10.1021/jacs.3c01765.

(33) Martin, A.; Rivera-Fuentes, P. Fluorogenic Polymethine Dyes by Intramolecular Cyclization. *Current Opinion in Chemical Biology* **2024**, *80*, 102444. https://doi.org/10.1016/j.cbpa.2024.102444.

(34) Martin, A.; Rivera-Fuentes, P. A General Strategy to Develop Fluorogenic Polymethine Dyes for Bioimaging. *Nat. Chem.* **2024**, *16* (1), 28–35. https://doi.org/10.1038/s41557-023-01367-y.

(35) Miki, K.; Kojima, K.; Oride, K.; Harada, H.; Morinibu, A.; Ohe, K. pH-Responsive near-Infrared Fluorescent Cyanine Dyes for Molecular Imaging Based on pH Sensing. *Chem. Commun.* **2017**, *53* (55), 7792–7795. https://doi.org/10.1039/C7CC03035E.

(36) Mu, H.; Miki, K.; Harada, H.; Tanaka, K.; Nogita, K.; Ohe, K. pH-Activatable Cyanine Dyes for Selective Tumor Imaging Using Near-Infrared Fluorescence and Photoacoustic Modalities. *ACS Sens.* **2021**, *6* (1), 123–129. https://doi.org/10.1021/acssensors.0c01926.

(37) Oe, M.; Miki, K.; Mu, H.; Harada, H.; Morinibu, A.; Ohe, K. pH-Responsive Cy5 Dyes Having Nucleophilic Substituents for Molecular Imaging. *Tetrahedron Letters* **2018**, *59* (35), 3317–3321. https://doi.org/10.1016/j.tetlet.2018.07.044.

(38) Janeková, H.; Fisher, S.; Šolomek, T.; Štacko, P. Surfing the Limits of Cyanine Photocages One Step at a Time. *Chem. Sci.* **2025**, *16* (4), 1677–1683. https://doi.org/10.1039/D4SC07165D.

(39) Nani, R. R.; Gorka, A. P.; Nagaya, T.; Kobayashi, H.; Schnermann, M. J. Near-IR Light-Mediated Cleavage of Antibody–Drug Conjugates Using Cyanine Photocages. *Angewandte Chemie International Edition* **2015**, *54* (46), 13635–13638. https://doi.org/10.1002/anie.201507391.

(40) Russo, M.; Zielinska, D.; Hanc, K.; Ramundo, A.; Meier, D.; Szabo, A.; Štacko, P. Near-Infrared-Activated Photocages Made to Order: Late-Stage Caging Protocol. *JACS Au* **2025**, *5* (6), 2632–2640. https://doi.org/10.1021/jacsau.5c00223.

(41) Zhang, Y.; Yan, C.; Zheng, Q.; Jia, Q.; Wang, Z.; Shi, P.; Guo, Z. Harnessing Hypoxia-Dependent Cyanine Photocages for In Vivo Precision Drug Release. *Angewandte Chemie* **2021**, *133* (17), 9639–9647. https://doi.org/10.1002/ange.202017349.

(42) Boni, L.; David, G.; Mangano, A.; Dionigi, G.; Rausei, S.; Spampatti, S.; Cassinotti, E.; Fingerhut, A. Clinical Applications of Indocyanine Green (ICG) Enhanced Fluorescence in Laparoscopic Surgery. *Surg Endosc* **2015**, *29* (7), 2046–2055. https://doi.org/10.1007/s00464-014-3895-x.

(43) Lim, C.; Vibert, E.; Azoulay, D.; Salloum, C.; Ishizawa, T.; Yoshioka, R.; Mise, Y.; Sakamoto, Y.; Aoki, T.; Sugawara, Y.; Hasegawa, K.; Kokudo, N. Indocyanine Green Fluorescence Imaging in the Surgical Management of Liver Cancers: Current Facts and Future Implications. *Journal of Visceral Surgery* **2014**, *151* (2), 117–124. https://doi.org/10.1016/j.jviscsurg.2013.11.003.

(44) Cosco, E. D.; Lim, I.; Sletten, E. M. Photophysical Properties of Indocyanine Green in the Shortwave Infrared Region. *ChemPhotoChem* **2021**, *5* (8), 727–734. https://doi.org/10.1002/cptc.202100045.

(45) Lingg, J. G. P.; Bischof, T. S.; Arús, B. A.; Cosco, E. D.; Sletten, E. M.; Rowlands, C. J.; Bruns, O. T.; Chmyrov, A. Shortwave-Infrared Line-Scan Confocal Microscope for Deep Tissue Imaging in Intact Organs. *Laser & Photonics Reviews* **2023**, *17* (11), 2300292. https://doi.org/10.1002/lpor.202300292.

(46) Alander, J. T.; Kaartinen, I.; Laakso, A.; Pätilä, T.; Spillmann, T.; Tuchin, V. V.; Venermo, M.; Välisuo, P. *A Review of Indocyanine Green Fluorescent Imaging in Surgery*. International Journal of Biomedical Imaging. https://doi.org/10.1155/2012/940585.

(47) Schaafsma, B. E.; Mieog, J. S. D.; Hutteman, M.; van der Vorst, J. R.; Kuppen, P. J. K.; Löwik, C. W. G. M.; Frangioni, J. V.; van de Velde, C. J. H.; Vahrmeijer, A. L. The Clinical Use of Indocyanine Green as a Near-Infrared Fluorescent Contrast Agent for Image-Guided Oncologic Surgery. *Journal of Surgical Oncology* **2011**, *104* (3), 323–332. https://doi.org/10.1002/jso.21943.

(48) Carr, J. A.; Aellen, M.; Franke, D.; So, P. T. C.; Bruns, O. T.; Bawendi, M. G. Absorption by Water Increases Fluorescence Image Contrast of Biological Tissue in the Shortwave Infrared. *Proceedings of the National Academy of Sciences* **2018**, *115* (37), 9080–9085. https://doi.org/10.1073/pnas.1803210115.

(49) Arena, F.; La Cava, F.; Faletto, D.; Roberto, M.; Crivellin, F.; Stummo, F.; Adamo, A.; Boccalon, M.; Napolitano, R.; Blasi, F.; Koch, M.; Taruttis, A.; Reitano, E. Short-Wave Infrared Fluorescence Imaging of near-Infrared Dyes with Robust End-Tail

Emission Using a Small-Animal Imaging Device. *PNAS Nexus* **2023**, *2* (8), pgad250. https://doi.org/10.1093/pnasnexus/pgad250.

(50) Swamy, M. M. M.; Murai, Y.; Monde, K.; Tsuboi, S.; Jin, T. Shortwave-Infrared Fluorescent Molecular Imaging Probes Based on π-Conjugation Extended Indocyanine Green. *Bioconjugate Chem.* **2021**, *32* (8), 1541–1547. https://doi.org/10.1021/acs.bioconjchem.1c00253.

(51) Swamy, M. M. M.; Murai, Y.; Monde, K.; Tsuboi, S.; Swamy, A. K.; Jin, T. Biocompatible and Water-Soluble Shortwave-Infrared (SWIR)-Emitting Cyanine-Based Fluorescent Probes for In Vivo Multiplexed Molecular Imaging. *ACS Appl. Mater. Interfaces* **2024**, *16* (14), 17253–17266. https://doi.org/10.1021/acsami.4c01000.

(52) Tolbert, L. M.; Zhao, X. Beyond the Cyanine Limit: Peierls Distortion and Symmetry Collapse in a Polymethine Dye. *J. Am. Chem. Soc.* **1997**, *119* (14), 3253–3258. https://doi.org/10.1021/ja9626953.

(53) Ryabitsky, A. B.; Kachkovski, A. D.; Przhonska, O. V. Symmetry Breaking in Cationic and Anionic Polymethine Dyes. *Journal of Molecular Structure: THEOCHEM* **2007**, *802* (1–3), 75–83. https://doi.org/10.1016/j.theochem.2006.09.004.

(54) Bondarev, S. L.; Raichenok, T. F.; Tikhomirov, S. A.; Kozlov, N. G.; Mikhailova, T. V.; Ivanov, A. I. Symmetry Breaking in an Excited Quadrupolar Acridine-Dione Derivative Driven by Hydrogen Bonding. *J. Phys. Chem. B* **2021**. https://doi.org/10.1021/acs.jpcb.1c03745.

(55) Bandi, V. G.; Luciano, M. P.; Saccomano, M.; Patel, N. L.; Bischof, T. S.; Lingg, J. G. P.; Tsrunchev, P. T.; Nix, M. N.; Ruehle, B.; Sanders, C.; Riffle, L.; Robinson, C. M.;

Difilippantonio, S.; Kalen, J. D.; Resch-Genger, U.; Ivanic, J.; Bruns, O. T.; Schnermann, M. J. Targeted Multicolor in Vivo Imaging over 1,000 Nm Enabled by Nonamethine Cyanines. *Nat Methods* **2022**, *19* (3), 353–358. https://doi.org/10.1038/s41592-022-01394-6.

(56) Ge, R.-T.; Xiong, F.; Chen, Z.-B.; Wang, Y.; Zheng, L.; Zhou, J.; Wu, D.; Zhang, S.-Y. Indocyanine Polymethine Fluorophores with Extended π-Conjugation Emitting beyond 1,200 Nm for Enhanced NIR-II Imaging. *Chem* **2025**, *0* (0). https://doi.org/10.1016/j.chempr.2025.102489.

(57) Tao, Z.; Hong, G.; Shinji, C.; Chen, C.; Diao, S.; Antaris, A. L.; Zhang, B.; Zou, Y.; Dai, H. Biological Imaging Using Nanoparticles of Small Organic Molecules with Fluorescence Emission at Wavelengths Longer than 1000 Nm. *Angewandte Chemie* **2013**, *125* (49), 13240–13244. https://doi.org/10.1002/ange.201307346.

(58) Hatami, S.; Würth, C.; Kaiser, M.; Leubner, S.; Gabriel, S.; Bahrig, L.; Lesnyak, V.; Pauli, J.; Gaponik, N.; Eychmüller, A.; Resch-Genger, U. Absolute Photoluminescence Quantum Yields of IR26 and IR-Emissive Cd1−xHgxTe and PbS Quantum Dots – Method- and Material-Inherent Challenges. *Nanoscale* **2014**, *7* (1), 133–143. https://doi.org/10.1039/C4NR04608K.

(59) Semonin, O. E.; Johnson, J. C.; Luther, J. M.; Midgett, A. G.; Nozik, A. J.; Beard, M. C. Absolute Photoluminescence Quantum Yields of IR-26 Dye, PbS, and PbSe Quantum Dots. *J. Phys. Chem. Lett.* **2010**, *1* (16), 2445–2450. https://doi.org/10.1021/jz100830r.

(60) Ding, B.; Xiao, Y.; Zhou, H.; Zhang, X.; Qu, C.; Xu, F.; Deng, Z.; Cheng, Z.; Hong, X. Polymethine Thiopyrylium Fluorophores with Absorption beyond 1000 Nm for

Biological Imaging in the Second Near-Infrared Subwindow. *J. Med. Chem.* **2019**, *62* (4), 2049–2059. https://doi.org/10.1021/acs.jmedchem.8b01682.

(61) Wang, S.; Fan, Y.; Li, D.; Sun, C.; Lei, Z.; Lu, L.; Wang, T.; Zhang, F. Anti-Quenching NIR-II Molecular Fluorophores for in Vivo High-Contrast Imaging and pH Sensing. *Nat Commun* **2019**, *10* (1), 1058. https://doi.org/10.1038/s41467-019-09043-x.

(62) Pan, H.-M.; Wu, C.-C.; Lin, C.-Y.; Hsu, C.-S.; Tsai, Y.-C.; Chowdhury, P.; Wang, C.-H.; Chang, K.-H.; Yang, C.-H.; Liu, M.-H.; Chen, Y.-C.; Su, S.-P.; Lee, Y.-J.; Chiang, H. K.; Chan, Y.-H.; Chou, P.-T. Rational Design of Asymmetric Polymethines to Attain NIR(II) Bioimaging at >1100 Nm. *J. Am. Chem. Soc.* **2023**, *145* (1), 516–526. https://doi.org/10.1021/jacs.2c10860.

(63) Ou, Y.-F.; Xiang, H.-Y.; Yang, X.; Wang, R.-X.; Huan, S.-Y.; Yuan, L.; Ren, T.-B.; Zhang, X.-B. Constructing Stable and Wavelength-Extended Heptamethine Cyanines via Donor Ectopic Substitution for NIR-IIa/b Bioimaging. *Angewandte Chemie International Edition n/a* (n/a), e202423978. https://doi.org/10.1002/anie.202423978.

(64) Friedman, H. C.; Cosco, E. D.; Atallah, T. L.; Jia, S.; Sletten, E. M.; Caram, J. R. Establishing Design Principles for Emissive Organic SWIR Chromophores from Energy Gap Laws. *Chem* **2021**, *7* (12), 3359–3376. https://doi.org/10.1016/j.chempr.2021.09.001.

(65) Cosco, E. D.; Caram, J. R.; Bruns, O. T.; Franke, D.; Day, R. A.; Farr, E. P.; Bawendi, M. G.; Sletten, E. M. Flavylium Polymethine Fluorophores for Near- and Shortwave Infrared Imaging. *Angewandte Chemie International Edition* **2017**, *56* (42), 13126–13129. https://doi.org/10.1002/anie.201706974.

(66) Janeková, H.; Friedman, H. C.; Russo, M.; Zyberaj, M.; Ahmed, T.; Hua, A. S.; Sica, A. V.; Caram, J. R.; Štacko, P. Deuteration of Heptamethine Cyanine Dyes Enhances Their Emission Efficacy. *Chem. Commun.* **2024**, *60* (8), 1000–1003. https://doi.org/10.1039/D3CC05153F.

(67) Cosco, E. D.; Arús, B. A.; Spearman, A. L.; Atallah, T. L.; Lim, I.; Leland, O. S.; Caram, J. R.; Bischof, T. S.; Bruns, O. T.; Sletten, E. M. Bright Chromenylium Polymethine Dyes Enable Fast, Four-Color In Vivo Imaging with Shortwave Infrared Detection. *J. Am. Chem. Soc.* **2021**, *143* (18), 6836–6846. https://doi.org/10.1021/jacs.0c11599.

(68) Cosco, E. D.; Spearman, A. L.; Ramakrishnan, S.; Lingg, J. G. P.; Saccomano, M.; Pengshung, M.; Arús, B. A.; Wong, K. C. Y.; Glasl, S.; Ntziachristos, V.; Warmer, M.; McLaughlin, R. R.; Bruns, O. T.; Sletten, E. M. Shortwave Infrared Polymethine Fluorophores Matched to Excitation Lasers Enable Non-Invasive, Multicolour in Vivo Imaging in Real Time. *Nat. Chem.* **2020**, *12* (12), 1123–1130. https://doi.org/10.1038/s41557-020-00554-5.

(69) Pengshung, M.; Li, J.; Mukadum, F.; Lopez, S. A.; Sletten, E. M. Photophysical Tuning of Shortwave Infrared Flavylium Heptamethine Dyes via Substituent Placement. *Org. Lett.* **2020**, *22* (15), 6150–6154. https://doi.org/10.1021/acs.orglett.0c02213.

(70) Egorov, V. V. Quantum-Classical Mechanics: Luminescence Spectra in Polymethine Dyes and J-Aggregates. Nature of the Small Stokes Shift. *Results in Physics* **2019**, *13*, 102252. https://doi.org/10.1016/j.rinp.2019.102252.

(71) Jia, S.; Lin, E. Y.; Mobley, E. B.; Lim, I.; Guo, L.; Kallepu, S.; Low, P. S.; Sletten, E. M. Water-Soluble Chromenylium Dyes for Shortwave Infrared Imaging in Mice. *Chem* **2023**, *9* (12), 3648–3665. https://doi.org/10.1016/j.chempr.2023.08.021.

(72) Mobley, E. B.; Lin, E. Y.; Sletten, E. M. Chromenylium Star Polymers: Merging Water Solubility and Stealth Properties with Shortwave Infrared Emissive Fluorophores. *ACS Cent. Sci.* **2025**, *11* (2), 208–218. https://doi.org/10.1021/acscentsci.4c01570.

(73) Jiang, G.; Hu, Z.; Bai, L.; Zhong, C.; Lu, S.; Han, B.; Sun, Z.; Zhu, S.; Liang, Y.; Sun, H. Origins of Near-Infrared-II Emission Tail and Fluorescence Enhancement of Albumin-Chaperoned Cyanine Dyes from a Multiscale Computational Study. *J. Mater. Chem. C* **2023**, *11* (22), 7243–7251. https://doi.org/10.1039/D3TC00452J.

CHAPTER TWO

Silicon flavylium polymethine dyes for shortwave infrared imaging

Quintashia D. Wilson, Emily B. Mobley, Eric Y. Lin, Barry Y. Li, Ash S. Hua, Justin R. Caram and Ellen M. Sletten

2.1 Abstract

The shortwave infrared (SWIR, 1000–2000 nm) region offers significant advantages for *in vivo* fluorescence imaging, including reduced scattering, minimal autofluorescence, and deep tissue penetration. However, the development of small molecule fluorophores with high brightness and maximum emission above 1100 nm remains a key challenge. Here, we report a new class of silicon-containing flavylium (SiliFlav) polymethine dyes that address this limitation. By incorporating a silicon heteroatom into the established Flav scaffold, we achieve unprecedented bathochromic shifts in emission up to 200 nm, while maintaining respectable fluorescence quantum yields (up to 0.30%). A modular synthetic route enables diverse functionalization at the 1-, 2-, and 7-positions of the heterocycle, allowing for systematic tuning of photophysical properties and improved dye performance. The lead fluorophore, SiliFlav5, formulated into canola oil nanoemulsions, exhibits excellent chemical stability, low cytotoxicity, and bright SWIR emission above 1300 nm. *In vivo* imaging in mice demonstrates high-resolution visualization of vasculature and spleen, confirming the utility of SiliFlav polymethine dyes as a robust new platform for deep-tissue SWIR imaging.

2.2 Introduction

The shortwave infrared (SWIR, 1000–2000 nm) region of the electromagnetic spectrum has emerged as the premier region for fluorescence imaging in mammals (Figure 2.1A).[1–6] Compared to the visible (VIS, 400–700 nm) and near-infrared (NIR, 700–1000 nm) regions, the

SWIR region offers reduced photon scattering, minimal autofluorescence and deeper tissue penetration, enabling enhanced contrast and resolution *in vivo*.[2–11] Since the initial reports of SWIR imaging, significant progress has been made toward contrast agents that have maximum emission ($\lambda_{max,em}$) in this region, with small molecule fluorophores distinguished for their low toxicity and favorable pharmokinetics.[6–8,10,12–19] Among these, polymethine dyes are one of the few scaffolds that readily achieve SWIR wavelengths due to their conjugated heterocycles and extendable polymethine chain (Figure 2.1B, center).[6,13,18,20–23] Additionally, their large absorption coefficients (ϵ_{max}) and moderate fluorescence quantum yields (ϕ_F) produce high brightness values ($\epsilon_{max} \times \phi_F$), necessary for *in vivo* imaging. We showcased these advantages in 2017 with the report of Flav7, a dimethylamino flavylium heptamethine dye with $\lambda_{max,em}$ = 1045 nm and ϕ_F = 0.53%.[24] As the brightest SWIR fluorophore of its time, we detected strong signal from Flav7 micelles in the vasculature of mice, and were able to quantify the heart rate of an anesthetized mouse, exemplifying the enhanced spatiotemporal resolution obtained in the SWIR region.

Since Flav7, the number of SWIR polymethine dyes (and SWIR small molecule fluorophores, in general) has increased considerably. We have incorporated modifications at the 2- and 7-positions of the Flav heterocycle as well as the polymethine chain to achieve bright, multicolor SWIR imaging across organic, aqueous and fluorous phases (Figure 2.1B). [24–31] Others have designed SWIR fluorophores based on FDA-approved indocyanine green (ICG),[32,33] other *N*-containing polymethine dyes,[8,34–39] and various xanthene architectures,[40–46] increasing both the structural diversity and clinical aptitude of this region. Despite this tremendous growth, very few small molecule fluorophores reach $\lambda_{max,em}$ above 1100 nm, limiting their capacity for enhanced imaging in deeper SWIR windows (*e.g.,* 1300–1450 nm) where opportunistic water absorption increases contrast.[11,14,47–50] As such, the development of small molecule fluorophores with $\lambda_{max,em}$ above 1100 nm provides the opportunity for improved SWIR imaging.

Design strategies to red-shift polymethine dyes can be divided into two general categories: extending the polymethine chain and modifying the heterocycle. Between these, lengthening the polymethine chain is the most straightforward approach, yielding ~100 nm red-shift in λ_{max} with each vinylene addition.[51] We recently adapted this methodology to the Flav scaffold, obtaining linear nonamthine derivatives with $\lambda_{max,em}$ spanning 1088–1188 nm and respectable ϕ_F (0.15–0.50%).[52] Lengthening the polymethine chain even further will impart larger bathochromic shifts, but also poses the risk of ground state desymmetrization, leading to decreased brightness and decreased fluorophore stability.[53–56] Therefore, chain extension is often paired with heterocycle modifications to increase λ_{max} without compromising brightness and stability. Of the various heterocycle modifications known to red-shift λ_{max}, heteroatom exchange typically provides the greatest increase. In the Flav scaffold, exchanging the oxygen heteroatom to sulfur can induce bathochromic shifts in emission up to ~90 nm, comparable to chain extension.[13,24,57,58] However, sulfur incorporation also promotes intersystem crossing and nonradiative decay, causing up to a 6-fold decrease in ϕ_F.[57,58] Another common heteroatom, typically employed in xanthene scaffolds, is silicon. Compared to their oxygen analogs, silicon xanthene dyes exhibit red-shifted emission (~70–100 nm) maintaining high ϕ_F.[59–61] This is an attractive quality for designing SWIR fluorophores, which inherently possess lower ϕ_F due to energy gap law constraints.[62] To evaluate these effects on the polymethine scaffold, we designed the first class of silicon polymethine dyes featuring two silicon xanthene (SiXan) heterocycles.[59] SiXan polymethine dyes exhibit ~100 nm red-shift in $\lambda_{max,em}$ and ~2-fold decrease in ϕ_F compared to the oxygen derivatives, demonstrating that silicon incorporation is a viable strategy in polymethine dyes. However, their broad absorption bands containing significant xanthene character and overall low brightness preclude the use of this scaffold *in vivo*.

Given the imaging success with flavylium polymethine dyes, we believe that silicon incorporation in the Flav scaffold has the potential to readily generate SWIR fluorophores with

$\lambda_{max,em}$ above 1100 nm while retaining high ϕ_F. However, the current synthetic route for Flav fluorophores is not amenable to silicon incorporation. Notably, all of the Flav derivatives arise from one modular synthesis featuring a Mentzer pyrone condensation of commercially available (or synthetically accessible) aniline analogs with various β-keto esters.[25,27] Herein, we report a general synthetic method to achieve a new class of silicon flavylium ("SiliFlav") polymethine dyes (Figure 2.1B). We prepared a panel of SiliFlav derivatives featuring modifications at the 1-, 2- and 7-positions of the heterocycle—which are deemed the most influential in tuning photophysical properties—as well as the polymethine chain. We used these derivatives to evaluate the effects of silicon incorporation in the Flav scaffold. Finally, we performed *in vivo* imaging with this new class of dyes, achieving strong detection of the vasculature and spleen above 1300 nm (Figure 2.1C).

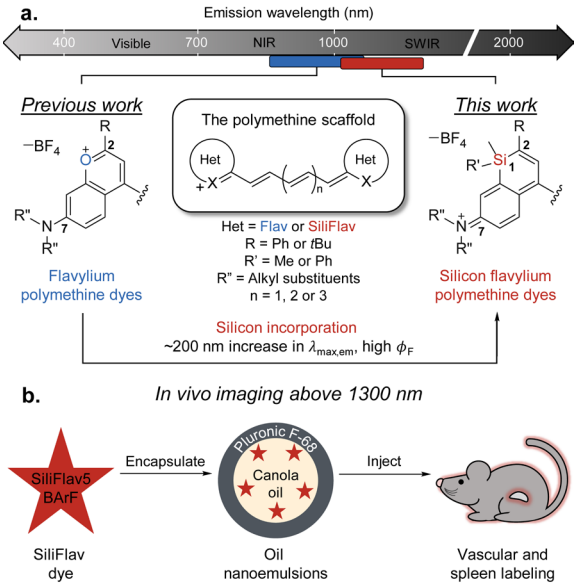

Figure 2.1. Overview of this work. A) Fluorescent region of the electromagnetic spectrum. A generic structure of polymethine dyes. Structural modifications and emission wavelengths of flavylium polymethine dyes (previous works) and silicon polymethine dyes (this work).

2.3 Results and discussion

2.3.1 Designing functionalized silicon flavones

Generating SiliFlav fluorophores requires the synthesis of a silicon flavone precursor that can undergo methylation and subsequent condensation with a polymethine linker (Scheme 2.1A). Importantly, a phenyl group (or any bulky, non-acidic substituent) is required at the 2-position for steric protection, and an electron-donating group is required at the 7-position to impart the positive charge. Literature examples of silicon flavones are exceedingly sparse, with only two reports of relevant benzosilinone precursors (Scheme 2.1B,C). In one report, benzosilinone derivatives functionalized at the 2-position were synthesized via palladium (Pd)-catalyzed carbonylation of hydrosilanes with various terminal alkynes.[63] While this approach enabled the synthesis of several functionalized benzosilinones, the severe reaction conditions limit its practicality. In another report, benzosilinones were synthesized via lithium exchange of a dihalogenated precursor followed by intramolecular cyclization with dimethyldichlorosilane (DMDCS) and subsequent oxidation.[64] However, the benzosilinones in this work do not possess the required functionalities at the 2- and 7-positions. To address this, we designed a modular synthetic route featuring a key propargylation step to install 2-position functionality, an intramolecular cyclization to install the 1-position silicon heteroatom, and a strategic fluorine handle to enable late-stage nucleophilic aromatic substitution (S_NAr) at the 7-position with various amines (Scheme 2.1D). Additionally, this work addresses the long-awaited need for synthetically accessible silicon flavone derivatives, permitting the opportunity for fundamental investigations on this class of compounds.

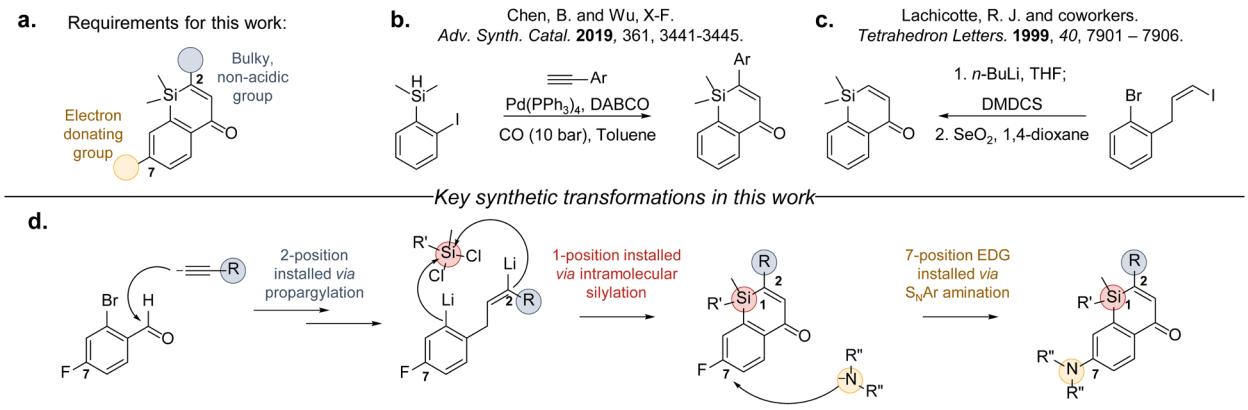

Scheme 2.1. Synthetic overview of this work. A) Structural requirements for silicon flavones in this work. B and C) Previous reports of relevant benzosilinone precursors. D) Key synthetic transformations in this work to access a panel of functionalized silicon flavones.

2.3.2 Synthesizing and investigating SiliFlav vinylogs

We initiated the synthesis of a functionalized silicon flavone precursor with *n*-BuLi-promoted propargylation of 2-bromo-4-fluorobenzaldehyde using phenylacetylene. Starting with this commercially available aldehyde afforded **2.1a** in 82% yield at multigram scale (Scheme 2.2A). With the 2-position phenyl group installed, **2.1a** was then subjected to deoxygenation conditions with Et_3SiH and trifluoroacetic acid (TFA), yielding **2.2a**, which readily underwent regioselective hydroiodination using Et_3SiH and iodine to produce **2.3a** in a 1:3 mixture of *E*- and *Z*-isomers. Lithium-halogen exchange of isomeric **2.3a** followed by treatment with DMDCS formed cyclized precursor **2.4a**, which was rapidly oxidized with SeO_2 to form fluorinated silicon flavone **2.5a**.

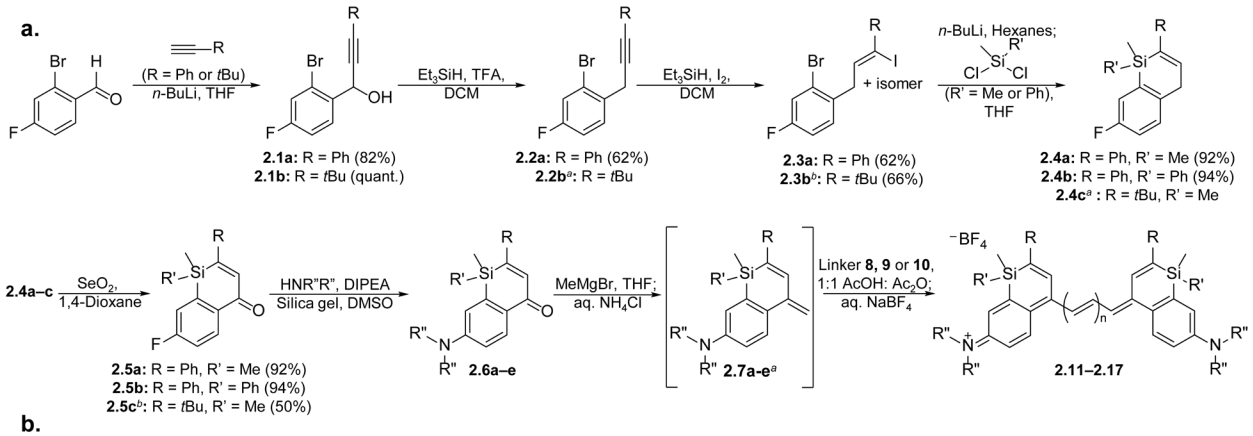

b.

S_NAr precursor	HNR"R"	Silicon flavone	R	R'	NR"R"	Yield 2.6a– e		Linker	Dye	Yield[b] 2.11–2.17
2.5a	$NHMe_2$	**2.6a**	Ph	Me		92%	*SiliFlav vinylogs*	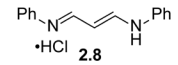 **2.8**	**2.11** (SiliFlav5, n = 2)	31%
								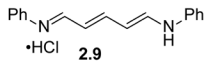 **2.9**	**2.12** (SiliFlav7, n = 3)	12%
								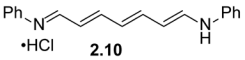 **2.10**	**2.13** (SiliFlav9, n = 4)	16%
2.5a	$NHMe_2$-d_6	**2.6b**	Ph	Me	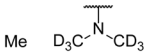	62%	*SiliFlav5 derivatives*		**2.14** (SiliFlav5-d_{12}, n = 2)	9%
2.5a	Pyrrolidine	**2.6c**	Ph	Me		85%		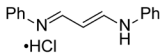 **2.8**	**2.15** (Py-SiliFlav5, n = 2)	37%
2.5b	$NHMe_2$	**2.6d**	Ph	Ph		59%			**2.16** (Sili(MePh)Flav5, n = 2)	18%
2.5c	$NHMe_2$	**2.6e**	*t*Bu	Me		44%			**2.17** (SiliChrom5, n = 2)	26%

[a]Compound not isolated. [b]Isolated yield over two steps.

Scheme 2.1. Synthesis of silicon flavones and silicon flavylium fluorophores in this work. A) Synthetic scheme of compounds **2.1-2.17**. B) R" groups, polymethine linkers and reaction yields for compounds **2.6**–**2.17**. See "Synthetic procedures" for details.

With the 1-position silicon heteroatom installed, we then turned our attention to the advantageous fluorine handle at the 7-position of **2.5a**. We expected this site to be sufficiently electrophilic due to the electron-withdrawing ketone, allowing for late-stage S_NAr with different amines. Aromatic substitution of **2.5a** in the presence of dimethylamine and diisopropylethylamine (DIPEA) produced trace amounts of aminated silicon flavone **2.6a**, with the major product being desilylated enone, **2.18** (Figure 2.2). We suspected that **2.18** is formed upon reaction of **2.6a** with the fluoride anion generated *in situ*, causing desilylation and subsequent ring opening. To counteract this, we used silica gel as an additive to scavenge the reactive fluoride anion.

Remarkably, this completely suppressed the fluoride-promoted desilylation, exclusively generating **2.6a** in 92% yield (Scheme 2.2B).

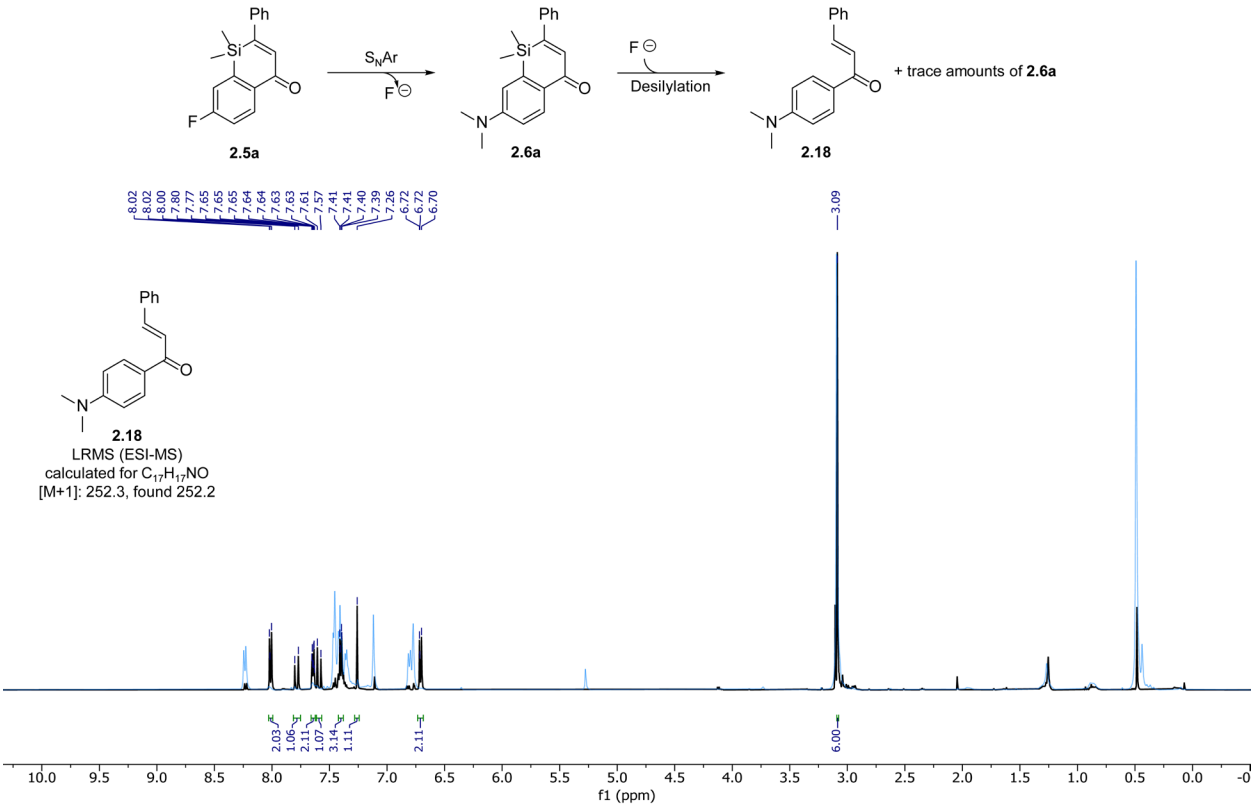

Figure 2.2. Side product **2.18** formed during the S_NAr amination of **2.5a**. Overlay of the ^1H NMR of **2.6a** (blue) and the crude ^1H NMR of **2.18** (black) with trace amounts of **2.6a**. The mass and chemical shifts for the proposed structure of **2.18** are consistent with previous literature reports of this compound.[65]

Achieving an appropriate functionalized silicon flavone, we set out to prepare silicon-containing polymethine dyes. We treated **2.6a** with MeMgBr followed by an aqueous quench with 50% fluoroboric acid (HBF_4), producing heterocycle **2.7a**, but in very low yields due to poor stability (Figure 2.3). Based on the broad NMR spectrum and general insolubility of the resulting compound, we suspect that HBF_4 promotes polymerization.[66] Quenching with saturated NH_4Cl improved solubility, but did not improve the overall stability of the resulting heterocycle. Thus, we pursued *in situ* formation of **2.7a** followed by immediate subjection to dye condensation conditions. Gratifyingly, this was a successful approach, wherein acid-promoted condensation of **2.7a** with electrophilic linkers **2.8**–**2.10** readily afforded pentamethine **2.11** (SiliFlav5),

heptamethine **2.12** (SiliFlav7) and nonamethine **2.13** (SiliFlav9) in 12—31% yield after purification (Scheme 2.2B).

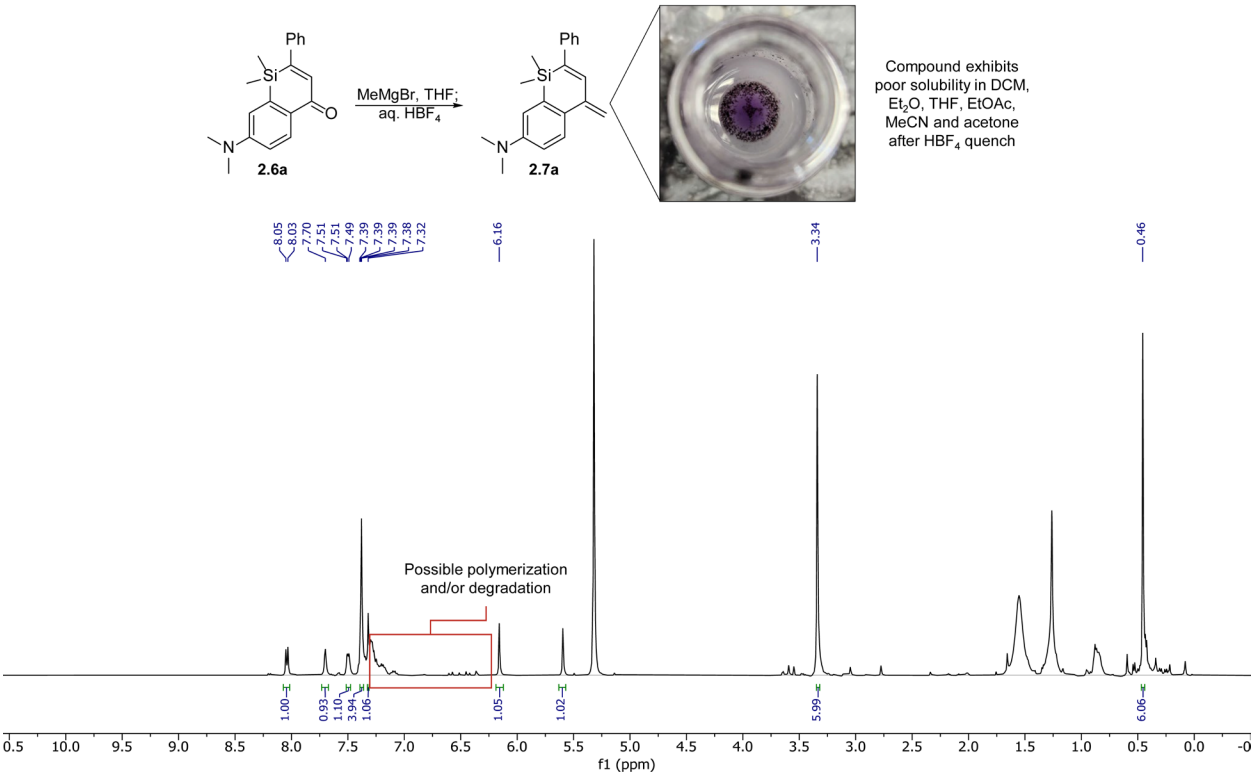

Figure 2.3. Synthesis and crude ^{1}H NMR of **2.7a** after quenching with 5% tetrafluoroboric acid.

Having synthesized a panel of SiliFlav vinylogs, we measured their photophysical properties in dichloromethane (DCM) to evaluate the effects of silicon substitution in the Flav scaffold (Figures 2.4A,B, 2.5 and 2.6) (Tables 2.1 and 2.2).

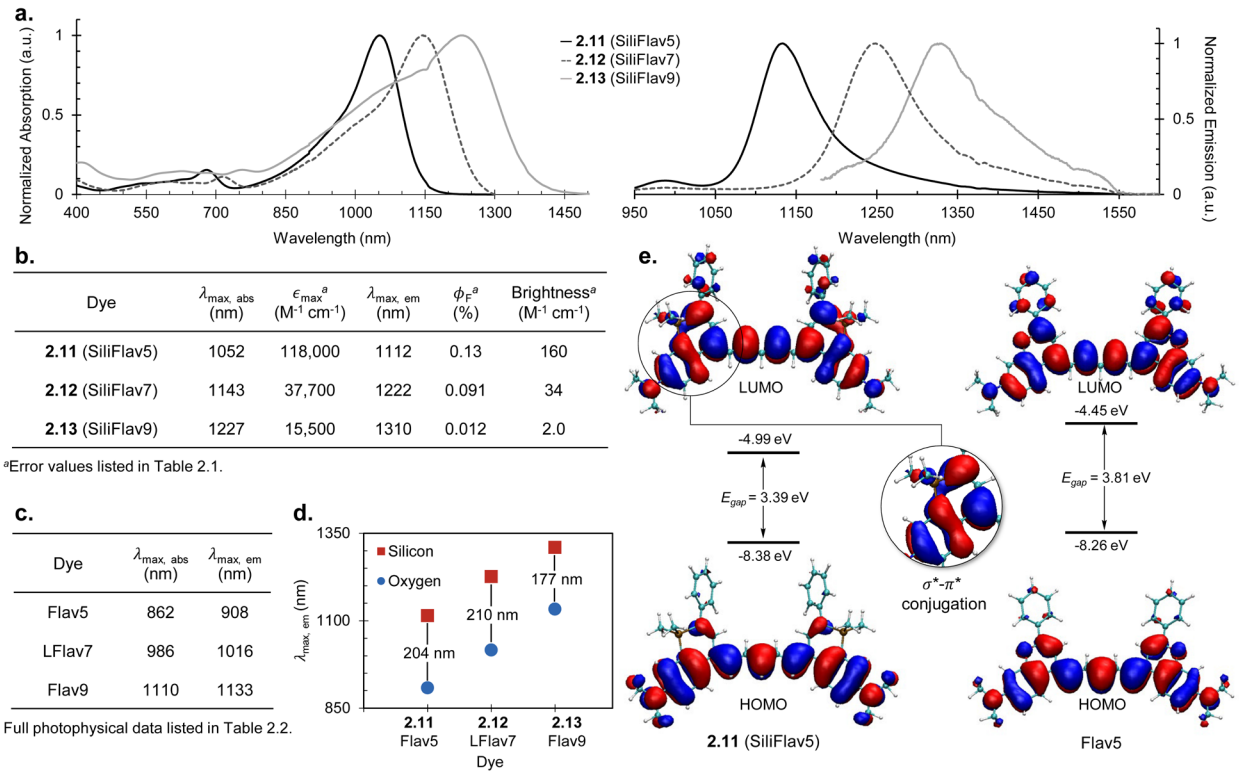

Dye	$\lambda_{max,\ abs}$ (nm)	ϵ_{max}[a] ($M^{-1}\ cm^{-1}$)	$\lambda_{max,\ em}$ (nm)	ϕ_F[a] (%)	Brightness[a] ($M^{-1}\ cm^{-1}$)
2.11 (SiliFlav5)	1052	118,000	1112	0.13	160
2.12 (SiliFlav7)	1143	37,700	1222	0.091	34
2.13 (SiliFlav9)	1227	15,500	1310	0.012	2.0

[a]Error values listed in Table 2.1.

Dye	$\lambda_{max,\ abs}$ (nm)	$\lambda_{max,\ em}$ (nm)
Flav5	862	908
LFlav7	986	1016
Flav9	1110	1133

Full photophysical data listed in Table 2.2.

Figure 2.4. Photophysical characterization of SiliFlav vinylogs and comparisons to their Flav analogs. A) Normalized absorption spectra of **2.11**–**2.13** (5 μM) in DCM and normalized emission spectra (5 μM, ex. 885 nm, collect 930-1600 nm) in deuterated DCM. B) Photophysical characterization of **2.11**–**2.13** in DCM. See "Photophysical procedures" for details. C) Absorption and emission data of Flav analogs in DCM. D) $\lambda_{max,em}$ comparisons of SiliFlav and Flav fluorophores in DCM. E) Molecular orbital diagrams of **2.11** and Flav5. See "Computation procedures" for details.

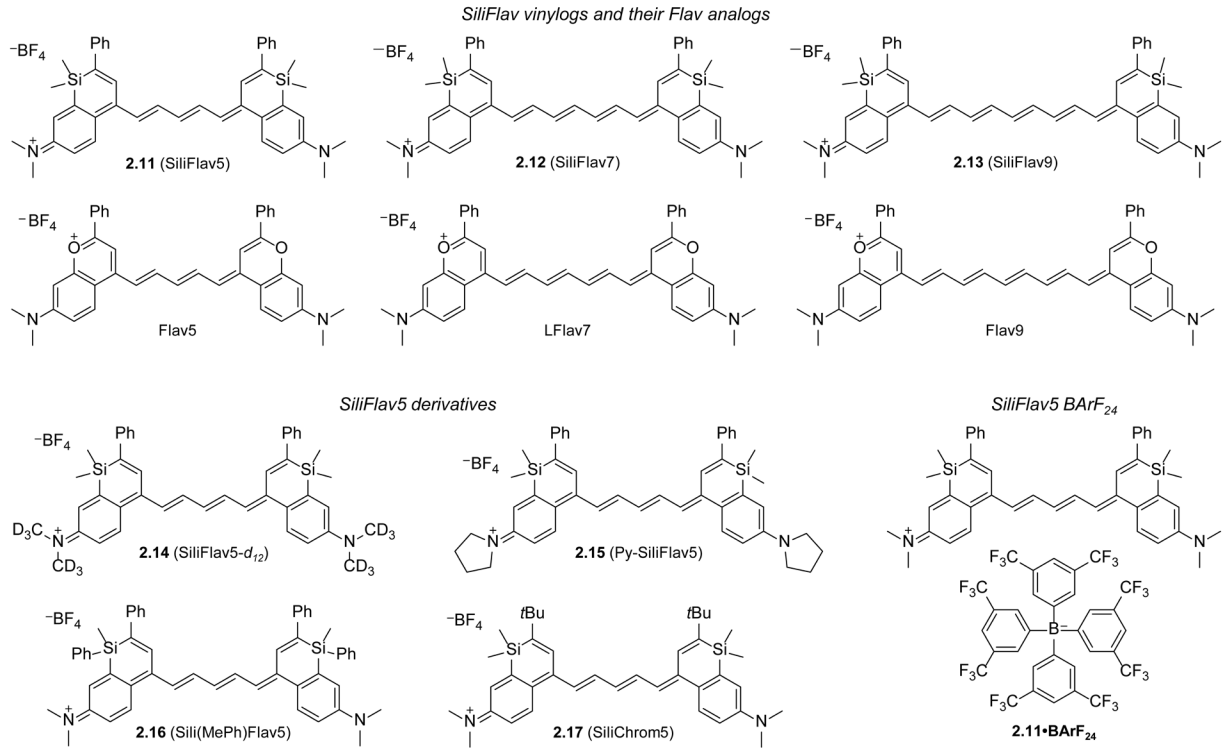

Figure 2.5. Chemical structures of SiliFlav fluorophores and their oxygen analogs, Flav5, LFlav7 and Flav9.[52]

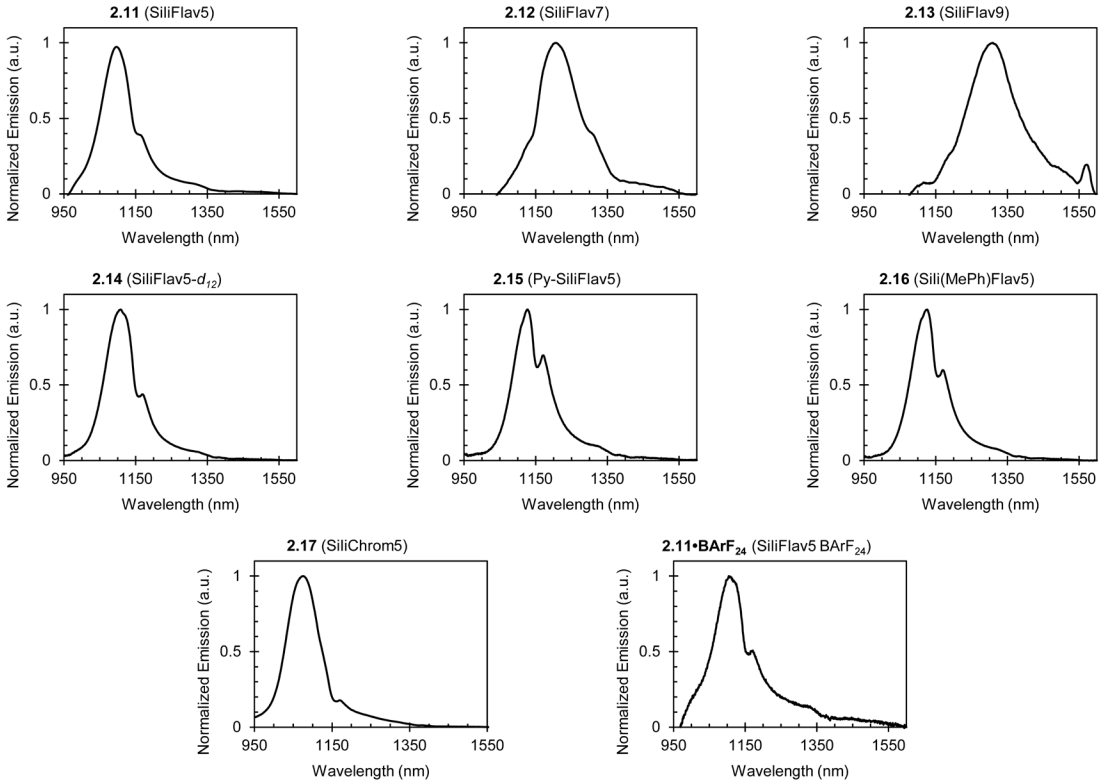

Figure 2.6. Normalized emission spectra of SiliFlav fluorophores (5 μM, ex. 885 nm, collect 930-1600 nm) in DCM. See "Photophysical procedures" for details.

Table 2.1. Photophysical properties of SiliFlav fluorophores in DCM with error.

Dye	$\lambda_{max,\ abs}$ (nm)	ϵ_{max} (M^{-1} cm^{-1})	$\lambda_{max,\ em}$ (nm)	ϕ_F (%)	Brightness (M^{-1} cm^{-1})
2.11 (SiliFlav5)	1052	118,000 ± 2,000	1112	0.13 ± 0.02	160 ± 30
2.12 (SiliFlav7)	1143	37,700 ± 700	1222	0.091 ± 0.003	34 ± 2
2.13 (SiliFlav9)	1227	15,500 ± 200	1310	0.012 ± 0.001	2.0 ± 0.2
2.14 (SiliFlav5-d_{12})	1051	99,700 ± 600	1112	0.17 ± 0.02	170 ± 20
2.15 (Py-SiliFlav5)	1077	79,000 ± 400	1129	0.10 ± 0.01	80 ± 8
2.16 (Sili(MePh)Flav5)	1067	98,700 ± 400	1127	0.12 ± 0.02	120 ± 5
2.17 (SiliChrom5)	1019	34,690 ± 40	1073	0.30 ± 0.01	100 ± 3
2.11•BArF$_{24}$	1051	42,900 ± 500	1114	0.17 ± 0.01	73 ± 5

Table 2.2 Photophysical properties of Flav fluorophores in DCM with error.[52]

Dye	$\lambda_{max,\ abs}$ (nm)	ϵ_{max} ($M^{-1}\ cm^{-1}$)	$\lambda_{max,\ em}$ (nm)	ϕ_F (%)	Brightness ($M^{-1}\ cm^{-1}$)
Flav5	862	327,000 ± 7,000	883	28 ± 2	19,900 ± 500
LFlav7	986	149,000 ± 2,000	1016	1.5 ± 0.3	2,300 ± 400
Flav9	1110	159,000 ± 1000	1133	0.19 ± 0.02	310 ± 30

The biggest advantage of silicon incorporation is its red-shifting properties, with silicon xanthene derivatives exhibiting $\lambda_{max,em}$ increases up to 100 nm. Interestingly, we observed an unprecedented 200 nm increase in $\lambda_{max,em}$ for the SiliFlav scaffold (Figure 2.4C,D), placing **2.11** (SiliFlav5), **2.12** (SiliFlav7) and **2.13** (SiliFlav9) among the most red-shifted vinylogs in the polymethine family (Figures 2.7 and 2.8).[8,12,13,34,38,57,67–69]

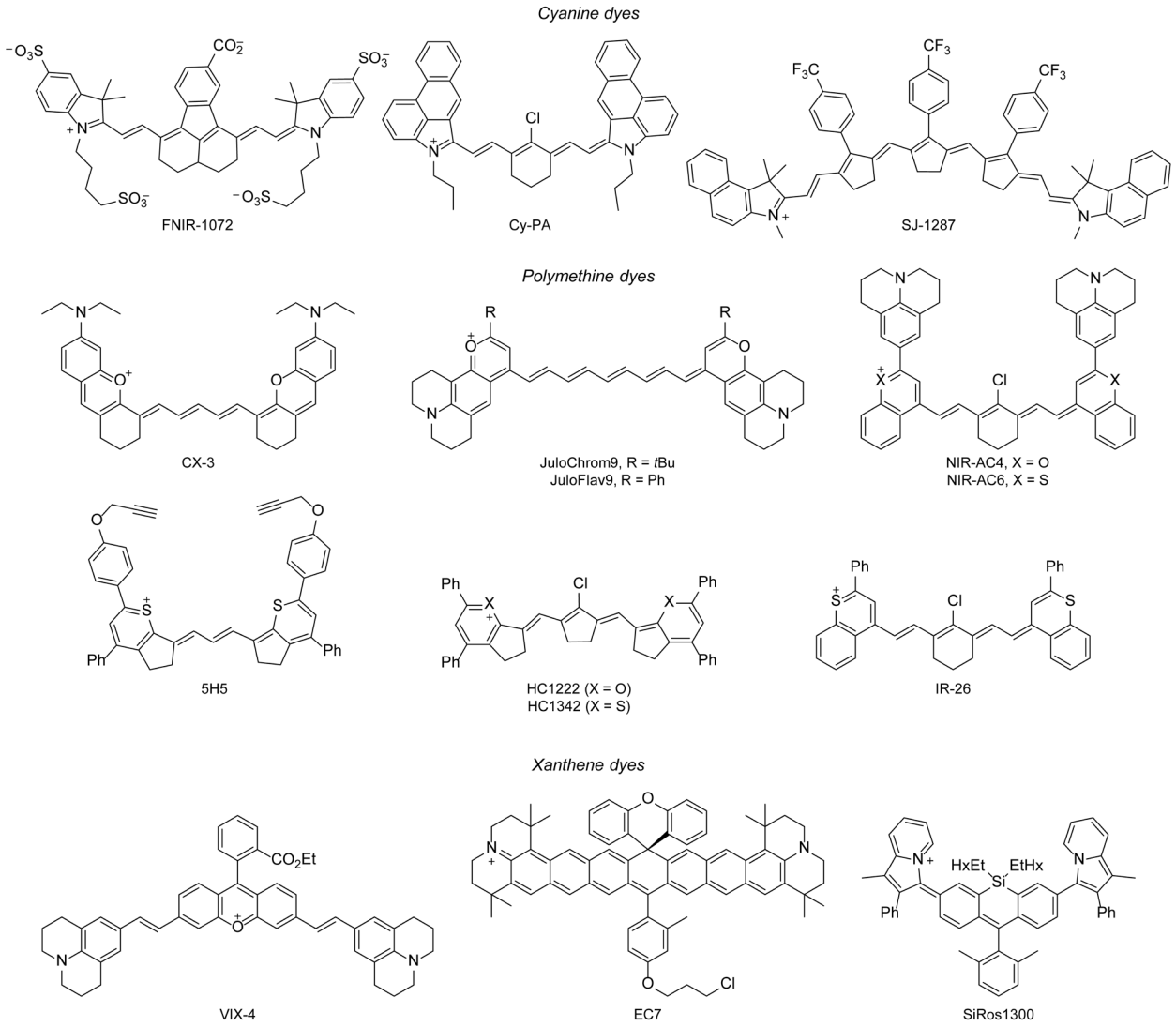

Figure 2.7. Chemical structures of representative small molecule fluorophores with $\lambda_{max,em}$ above 1100 nm. Counterions are omitted. Full photophysical data can be found in following references: FNIR-1072,[34] Cy-PA,[67] SJ-1287,[70] CX-3,[71] JuloChrom9 and JuloFlav9,[52] NIR-AC4 and NIR-AC6,[57] 5H5,[68] HC1222 and HC1342,[69] IR-26,[72] VIX-4,[73] EC7,[46] SiRos1300.[43]

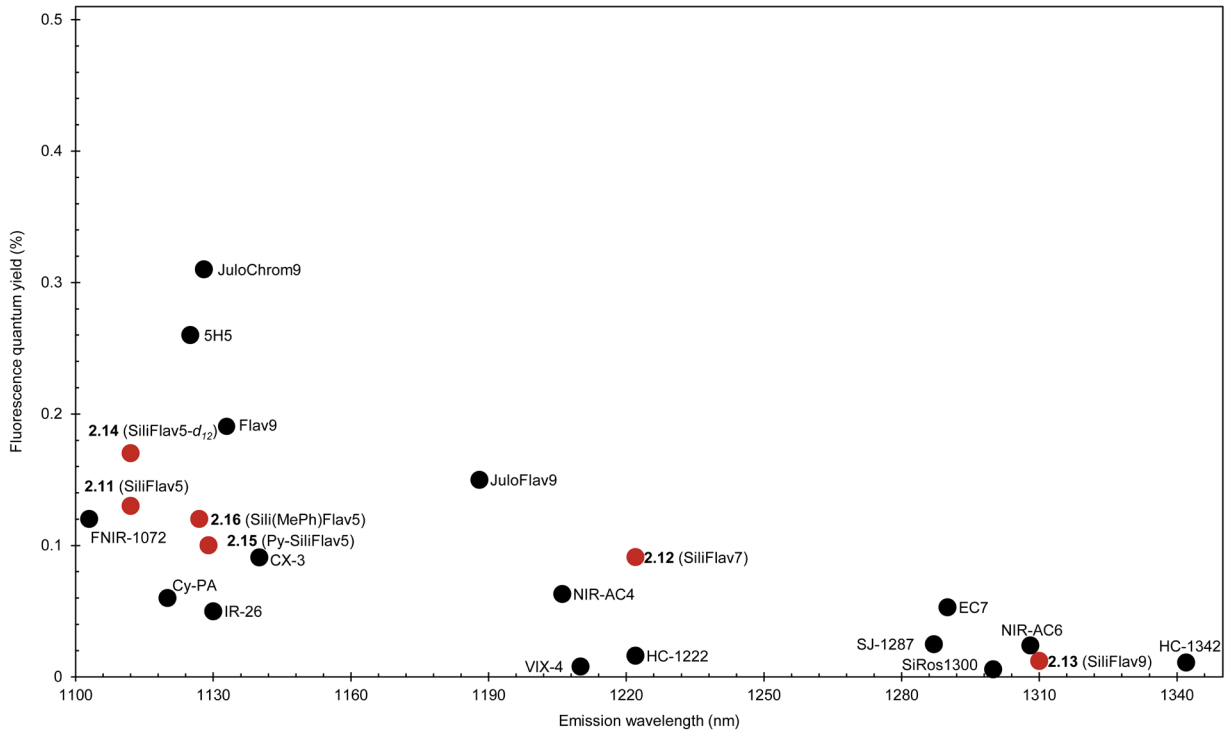

Figure 2.8. Scatter plot of the $\lambda_{max,em}$ and ϕ_F of small molecule fluorophores listed in **Figure 2.7**.

To further understand this substantial bathochromic shift, we performed time-dependent Hartree-Fock (TDHF) calculations using a CAM-B3LYP basis set (Figures 2.4E and 2.9). Comparing the HOMOs of **2.11**–**2.13** to their Flav analogs, there is a noticeable increase in electron density along the polymethine chain with silicon incorporation. Since the silicon atom does not participate in π-delocalization, the electron density is shifted between the terminal nitrogen atoms, increasing the effective length of conjugation. Additionally, there is favorable σ^*–π^* conjugation in the LUMOs of **2.11**–**2.13** resulting in a smaller energy gap (E_{gap}) compared to their Flav analogs. While σ^*–π^* conjugation is often cited as the crucial orbital interaction in silicon fluorophores,[74,75] we did not observe this interaction in the SiXan polymethine dyes, suggesting that the orbital effects of silicon are not uniform across small molecule scaffolds.

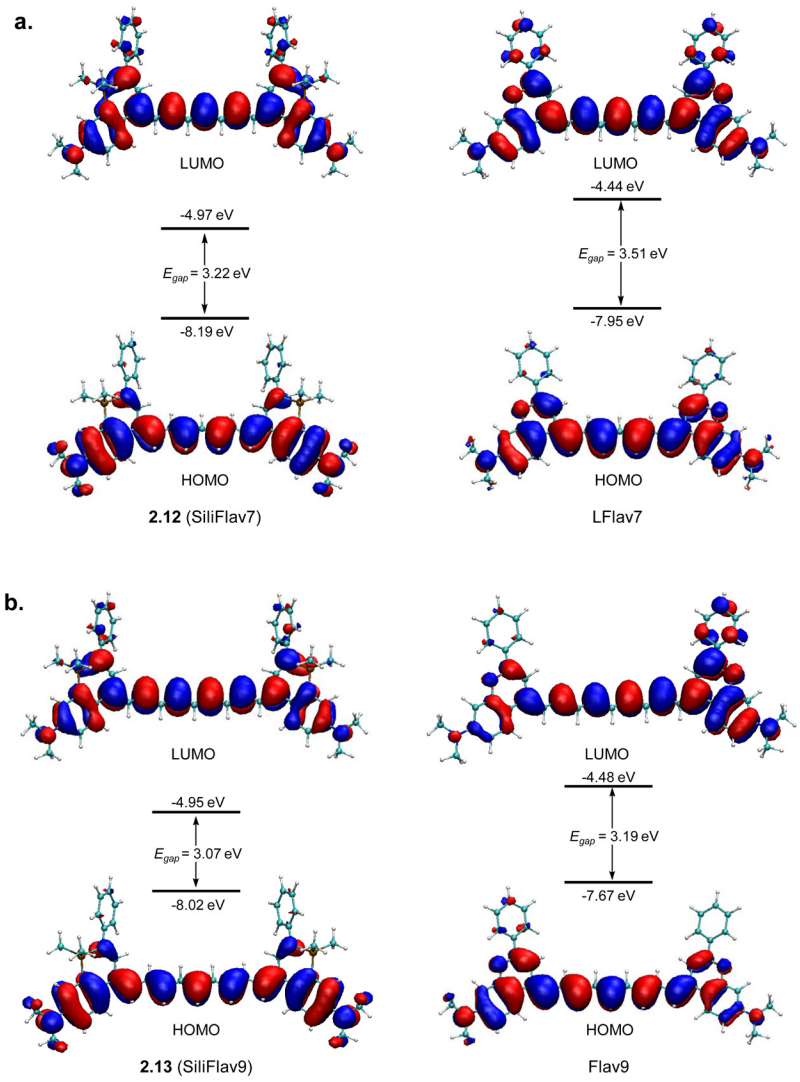

Figure 2.9. Molecular orbital diagrams of SiliFlav vinylogs **2.12** and **2.13** alongside their corresponding Flav analogs. See "Computation procedures" for details.

Another benefit of silicon incorporation is the ability to achieve long wavelengths while maintaining high brightness. The ϕ_F for **2.11** (0.13%), **2.12** (0.091%) and **2.13** 0.012%) are higher than most small molecule scaffolds that emit above 1100 nm (Figures 2.7 and 2.8), with noteworthy exceptions being flavylium nonamethine derivatives.[12,13,34,38,42,43,46,52,57,67,69] We believe that advantageous electron donation from the oxygen heteroatom and reduced vibronic coupling in the excited state (evidenced by the small Stokes shift) result in the uncharacteristically high ϕ_F of flavylium nonamethine dyes.[62] Considering **2.11**–**2.13** do not have favorable heteroatom donation, and they exhibit relatively large Stokes shifts for polymethine dyes (~60–80 nm), the ϕ_F

are quite respectable for this region of the SWIR. The biggest downside to these dyes is their low ϵ (16,000–118,000 M^{-1} cm^{-1}). We observed similarly low ϵ for the SiXan dyes, suggesting that silicon incorporation may weaken the transition dipole moment in the polymethine dyes. Fortunately, the overcompensation in ϕ_F produces brightness values for **2.11**–**2.13** (2.0–160 M^{-1} cm^{-1}) that are on par with small molecule fluorophores with similar $\lambda_{max,em}$. Importantly, we achieved these brightness values with less structural complexity than the extended xanthene dyes and rigidified polymethine dyes in this region, allowing us to investigate additional structure-property relationships that affect the ϕ_F of this scaffold.

2.3.3 Achieving enhanced SiliFlav5 derivatives

To access enhanced SiliFlav fluorophores, we returned our attention to fluorinated precursor **2.5a** to expand the scope of the S_NAr reaction (Scheme 2.2A). Modulating the 7-position of Flav fluorophores has enabled brighter, red-shifted probes with enhanced solubility. By leveraging the S_NAr reaction, these advantageous functionalities can be installed late-stage, increasing the utility of this synthetic route. We found that S_NAr substitution of **2.5a** with small amines readily occurred, affording dimethylamine-d_6 **2.6b**, pyrrolidine **2.6c** and azetidine **2.19** using the same conditions as **2.6a** (Figure 2.10). For bulkier amines, we found that S_NAr substitution of **2.5a** with allylamine to **2.20**, followed by deprotection to **2.21** and substitution with heptadecafluoro-10-iododecane yielded fluorous silicon flavone **2.22** in 75% yield (Figure 2.10). All of the modified silicon flavones were stable to methylation, generating heterocycles **2.7b**, **2.7c**, **2.23** and **2.25**, but the condensation with **2.8** proved to be variable. In the case of **2.24** (Azet-SiliFlav5), we suspect that the 4-membered ring is too strained to stabilize the positive charge, leading to fluorophore degradation (Figure 2.10). In the case of **2.26** (F_{104}-SiliFlav5), the condensation proceeded smoothly, but the fluorophore began to degrade during purification (Figure 2.10). Fortunately, **2.7b** and **2.7c** were stable to condensation with **2.8**, readily affording pentamethine dyes **2.14** (SiliFlav5-d_{12}) and **2.15** (Py-SiliFlav5) (Scheme 2.2B).

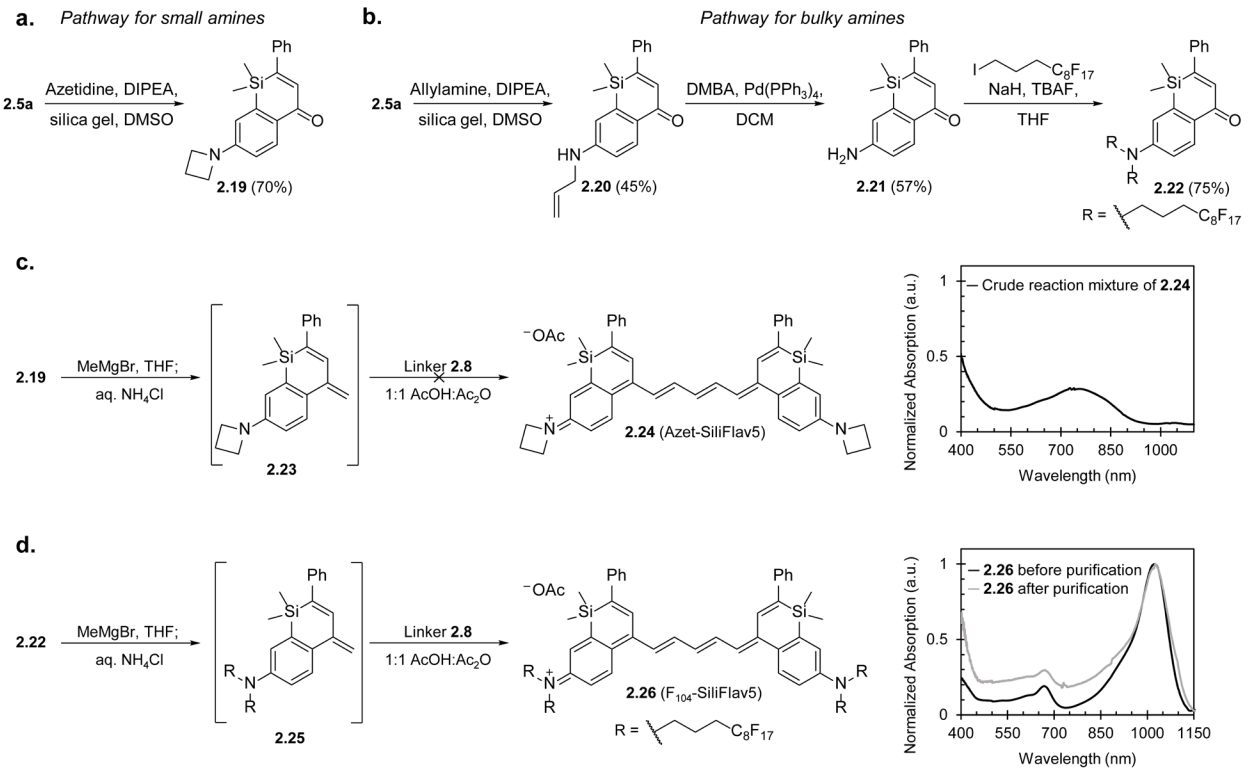

Figure 2.10. Expanded S_NAr substrate scope and dye synthesis of SiliFlav fluorophores featuring azetidine and a fluorous amine. A and B) Synthesis of **2.19** and **2.22**. C) and D) Attempted synthesis of **2.24** (Azet-SiliFlav5) and **2.26** (F_{104}-SiliFlav5).

Beyond the 7-position, the 1- and 2-positions are also synthetically accessible sites that permit fine-tuning of λ_{max} and brightness. Starting with the Li-halogen exchanged intermediate of **2.3a**, we found that cyclization with methylphenyl dichlorosilane to yield **2.4b**, followed by oxidation to **2.5b** and S_NAr substitution to **2.6e** occurred with comparable efficiency to the dimethylsilane analogs. Methylation of **2.6d** to **2.7d** followed by condensation with **2.8** also proceeded smoothly, yielding silicon functionalized pentamethine **2.16** (Sili(MePh)Flav5). Unlike the previous modifications, substituting the 2-position required us to return to the beginning of the synthetic route. Fortunately, we found that the *tert*-butyl substituent was well-tolerated throughout the entire synthesis, affording compounds **2.1b**–**2.6e** with negligible changes to the reaction conditions, purification methods or obtained yields. Methylation of **2.6e** to **2.7e** followed by condensation with **2.8** afforded the final pentamethine of the lineup, silicon chromenylium **2.17**

(SiliChrom5). In total, we prepared seven silicon flavylium fluorophores modified at the 1-, 2- and 7-positions using this modular synthetic route.

To determine the effects of substituent modification on ϕ_F, we measured the photophysical properties of **2.14**–**2.17** in DCM (Figure 2.11A,B). Additionally, their fluorescence lifetimes (τ) were obtained using time-correlated single-photon counting (TCSPC), and the rates of radiative (k_r) and nonradiative (k_{nr}) decay were used to determine their contributions to the change in ϕ_F relative to **2.11** (Figure 2.11B,C and Table 2.3). Based on previous work with deuterated Flav dyes, we expected **2.14** (SiliFlav5-d_{12}) to have a higher ϕ_F due to the suppression of nonradiative C–H vibrational frequencies.[76,77] Gratifyingly, **2.14** has a higher ϕ_F (0.17%) compared to **2.11**, with the largest contribution coming from an increase in k_r. Another strategy to increase ϕ_F is to inhibit twisted intramolecular charge-transfer (TICT) in the excited state through rigidification. Interestingly, we found that **2.15** (Py-SiliFlav5) has a lower ϕ_F (0.10%), despite having a longer τ (43 ps). Since the λ_{max} of **2.15** is longer than **2.11**, it is possible that the advantages of rigidification and TICT suppression are counteracted by the effects of the energy gap law, producing an overall lower ϕ_F. Moving to other sites of the SiliFlav scaffold, we found that the 1-position phenyl substituent in **2.16** (Sili(MePh)Flav5) caused a ~30 nm red-shift in $\lambda_{max,em}$, but a small decrease in ϕ_F (0.12%) compared to **2.11**. These results indicate that the 1-position could be useful for installing functional handles without disrupting the properties of the fluorophore core. In contrast, the 2-position *t*ert-butyl substituent in **2.17** (SiliChrom5) produced a ~40 nm blue-shift in $\lambda_{max,em}$ and a two-fold increase in ϕ_F (0.30%) compared to **2.11**. This is consistent with the trends observed for the Flav versus Chrom heterocycles, where the bulky *tert*-butyl group suppresses internal conversion, leading to a decrease in k_{nr}. Overall, the structure-property relationships observed for Flav fluorophores generally translate to the SiliFlav scaffold, making the design and optimization of future SiliFlav derivatives a promising endeavor.

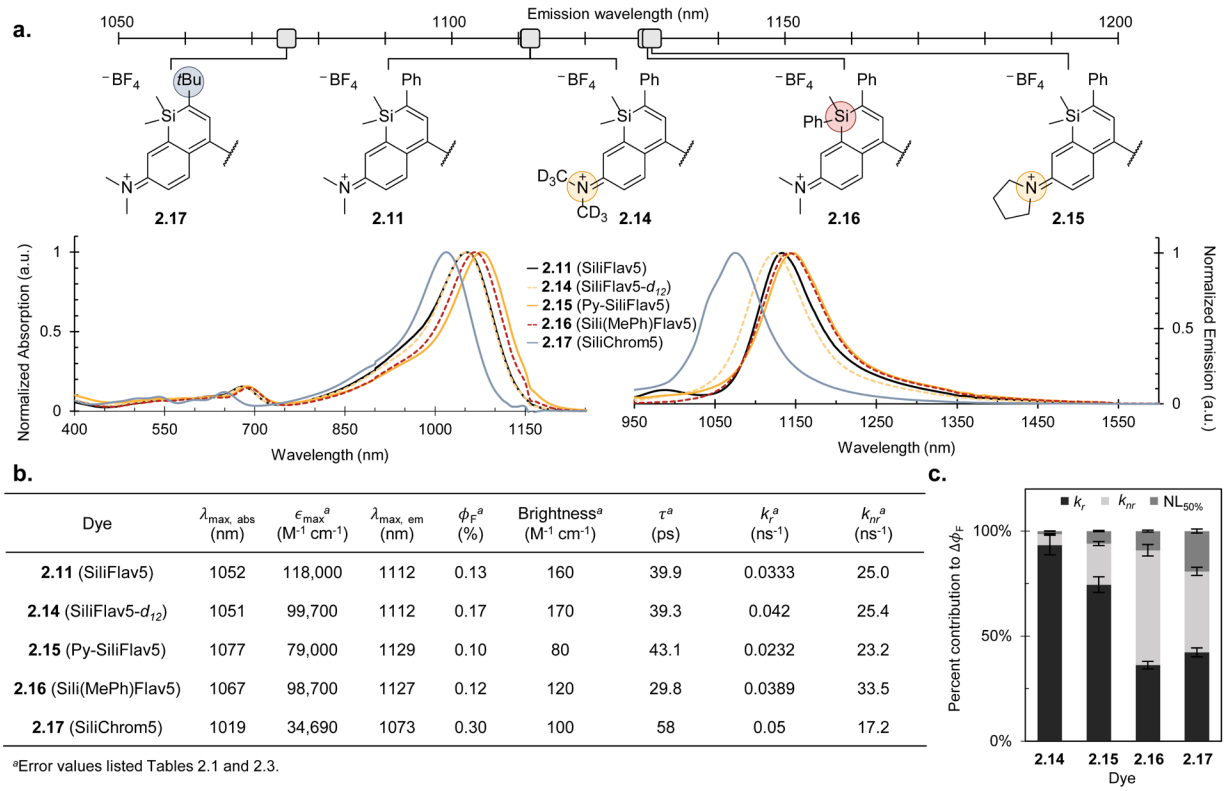

Dye	$\lambda_{max,\ abs}$ (nm)	ϵ_{max}[a] ($M^{-1}\ cm^{-1}$)	$\lambda_{max,\ em}$ (nm)	ϕ_F[a] (%)	Brightness[a] ($M^{-1}\ cm^{-1}$)	τ[a] (ps)	k_r[a] (ns^{-1})	k_{nr}[a] (ns^{-1})
2.11 (SiliFlav5)	1052	118,000	1112	0.13	160	39.9	0.0333	25.0
2.14 (SiliFlav5-d_{12})	1051	99,700	1112	0.17	170	39.3	0.042	25.4
2.15 (Py-SiliFlav5)	1077	79,000	1129	0.10	80	43.1	0.0232	23.2
2.16 (Sili(MePh)Flav5)	1067	98,700	1127	0.12	120	29.8	0.0389	33.5
2.17 (SiliChrom5)	1019	34,690	1073	0.30	100	58	0.05	17.2

[a]Error values listed Tables 2.1 and 2.3.

Figure 2.11. Photophysical properties of SiliFlav5 derivatives. Full structures are listed in Figure 2.5. A) $\lambda_{max,em}$ comparisons of SiliFlav5 derivatives in DCM. Normalized absorption spectra of **2,11-2.17** (5 μM) in DCM and normalized emission spectra (5 μM, ex. 885 nm, collect 930-1600 nm) in deuterated DCM. Emission spectra in nondeuterated DCM are listed in Figure 2.6. B) Photophysical characterization and excited state lifetime measurements of **2.11-2.17** in DCM. Error values are listed in Tables 2.1 and 2.3. See "Photophysical procedures" and "Excited state lifetime procedures" in the supporting information for details. C) Contributions of k_r, k_{nr} and nonlinear mixing to the change in ϕ_F of **2.14-17** relative to **2.11**.

Table 2.3. Lifetime measurements of SiliFlav pentamethine dyes with error.

Dye	τ (ps)	k_r (ns^{-1})	k_{nr} (ns^{-1})
2.11 (SiliFlav5)	39.9 ± 0.3	0.0333 ± 0.0001	25.0 ± 0.1
2.14 (SiliFlav5-d_{12})	39.3 ± 0.3	0.042 ± 0.002	25.4 ± 0.1
2.15 (Py-SiliFlav5)	43.1 ± 0.5	0.0232 ± 0.0002	23.2 ± 0.2
2.16 (Sili(MePh)Flav5)	29.8 ± 0.4	0.0389 ± 0.0003	33.5 ± 0.2
2.17 (SiliChrom5)	58 ± 0.2	0.05 ± 0.001	17.2 ± 0.4

2.3.4 In vivo investigations with SiliFlav5

After elucidating the photophysical properties of SiliFlav fluorophores, we assessed the utility of this scaffold for *in vivo* imaging. We employed **2.11** for imaging studies as it could be readily excited with a standard 1060 nm laser, an exceptionally low-energy excitation for a pentamethine dye. Previous work with SWIR-emissive silicon xanthene dyes suggests that canola oil nanoemulsions are required for prolonged stability of silicon fluorophores *in vivo*.[43] Considering the general hydrophobicity of **2.11** alongside its concerning stability in the presence of methanol and biological nucleophiles (Figure 2.12), a nanoemulsion formulation seemed necessary for imaging.

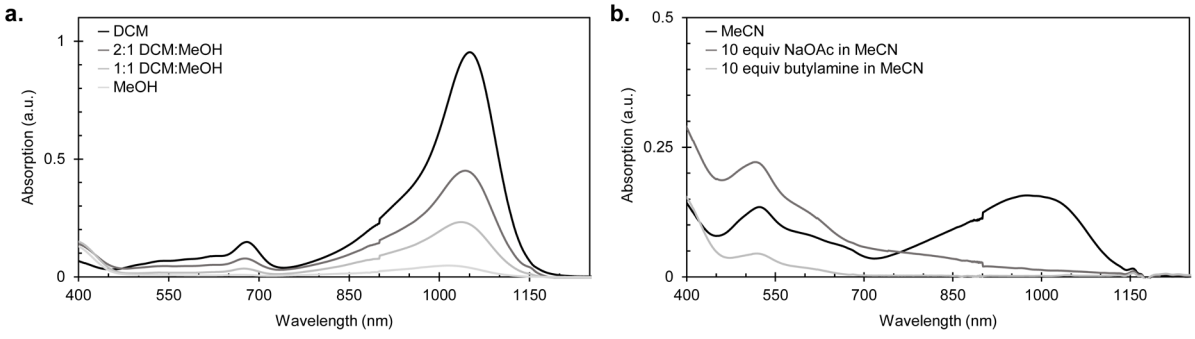

Figure 2.12. Chemical stability of **2.11**. A) Normalized absorption spectra of **2.11** (5 μM) in mixtures of DCM and MeOH. B) Normalized absorption spectra of **2.11** (5 μM) in MeCN, 10 equiv of NaOAc in MeCN and 10 equiv of butylamine in MeCN.

First, to increase the solubility and stability of **2.11** in canola oil, we exchanged the small, hard tetrafluoroborate counterion to the soft, bulky tetrakis[3,5-bis(perfluorohexyl)phenyl]borate ($BArF_{24}$) ion. Sonicating **2.11** in a biphasic solution of DCM and aqueous $NaBArF_{24}$ followed by column chromatography afforded counterion exchanged **2.11•BArF$_{24}$** in 87% yield (Figure 2.13A).

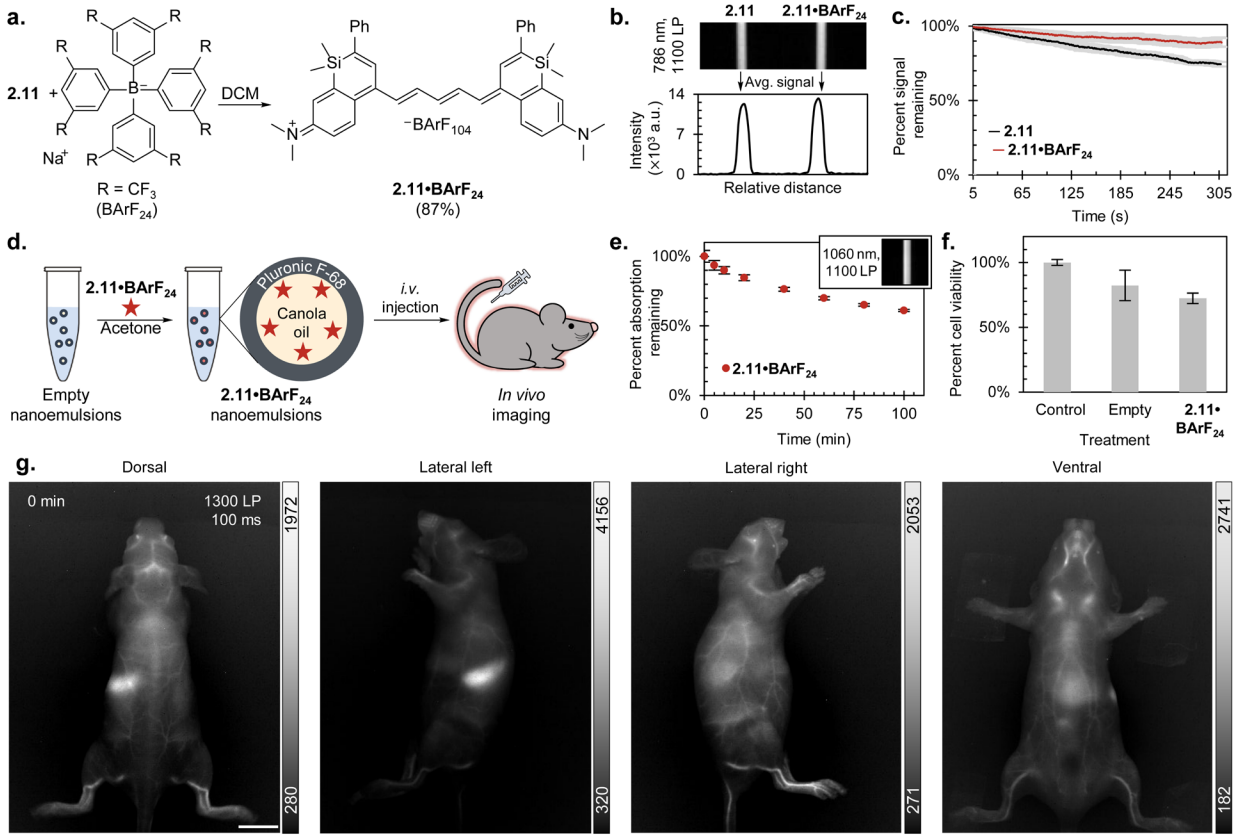

Figure 2.13. Synthesis, stability assessment, formulation procedure, cell viability assessment and *in vivo* imaging of **2.11•BArF$_{24}$**. A) Synthesis of **2.11•BArF$_{24}$**. Full structure is listed in Figure 2.5. B) Capillary images of **2.11** (330 nmol) and **2.11•BArF$_{104}$** (330 nmol) in DCM (786 nm excitation, 1100 nm LP, 8 ms ET, 100 mW/cm^2). C) Photobleaching curves of **2.11** and **2.11•BArF$_{24}$** in DCM with continuous irradiation for 5 min (786 nm excitation, 1100 nm LP filter, 100 fps, 100 mW/cm^2). See "Photobleaching procedures" for details. D) Formulation of **2.11•BArF$_{24}$** in Pluronic-F68 stabilized canola oil nanoemulsions. See "Formulation procedures" for details. E) Chemical stability of **2.11•BArF$_{24}$** (330 nmol) nanoemulsions in FBS. Inset: Capillary image of **2.11•BArF$_{24}$** nanoemulsions in FBS (1060 nm excitation, 1100 nm LP, 0.5 ms ET, 160 mW/cm^2). F) MTT viability assay on A375 cells with empty and **2.11•BArF$_{24}$** nanoemulsions at 0.75x the projected *in vivo* imaging concentration (330 nmol). See "Cell viability procedures" for details. G) *In vivo* imaging with **2.11•BArF$_{24}$** nanoemulsions immediately after *i.v.* injection (1060 nm excitation, 1300 nm LP, 100 ms, 160 mW/cm^2). See "Animal imaging procedures" for details. Scale bars represent 10 mm. Approximately 290 nmol of **2.11•BArF$_{24}$** was loaded into the nanoemulsions. See "Formulation procedures" for calculation details.

We then measured the photophysical properties of **2.11•BArF$_{24}$** and were pleased to find that the λ_{max} remained unaffected by the bulky counterion while the ϕ_F increased to 0.17% (Figures 2.13B and 2.14).

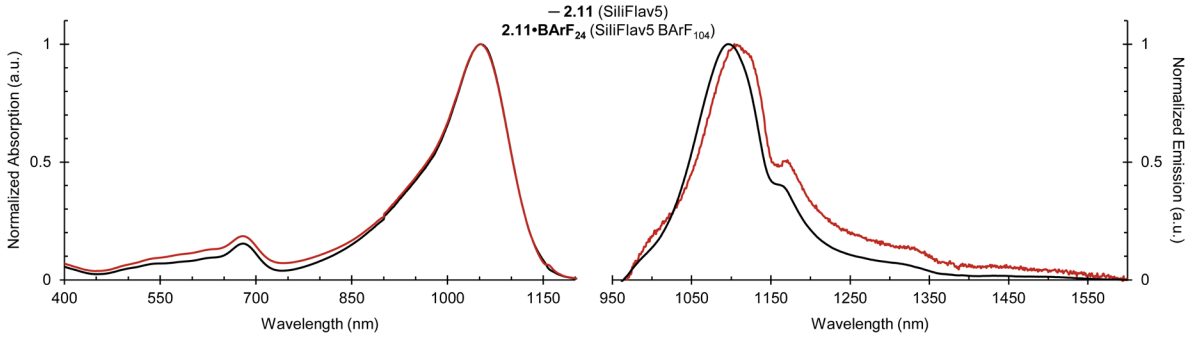

Dye	$\lambda_{max,\ abs}$ (nm)	ϵ_{max}[a] (M^{-1} cm^{-1})	$\lambda_{max,\ em}$ (nm)	ϕ_F[a] (%)	Brightness[a] (M^{-1} cm^{-1})
2.11	1052	118,000	1112	0.13	160
2.11•BArF$_{24}$	1051	42,900	1114	0.17	73

Figure 2.14. Normalized absorption and emission spectra (ex. 885 nm, collect 930-1600 nm) of **2.11** and **2.11•BArF$_{24}$** (5 μM) and their photophysical properties in DCM. [a]Error values listed in Table 2.1.

In our previous investigation of a fluorous pentamethine dye, we observed an increase in photostability with counterion exchange.[78] To determine if the effects were similar for the SiliFlav5 scaffold, we continuously irradiated **2.11** and **2.11•BArF$_{24}$** at 786 nm for 5 minutes and measured the loss in emission over time (Figures 2.13C and 2.15). We observed a 25% decrease in signal intensity for **2.11** and a 10% decrease for **2.11•BArF$_{24}$**, representing a 2-fold increase in relative photostability after counterion exchange. Comparing their photostability to Flav5, both **2.11** exhibits comparable stability while **2.11•BArF$_{24}$** is ~2-fold more stable (Figure 2.15). Overall, these results showcase that the photostability of the SiliFlav scaffold is more than sufficient for *in vivo* imaging, with **2.11•BArF$_{24}$** boasting enhanced stability.

a.

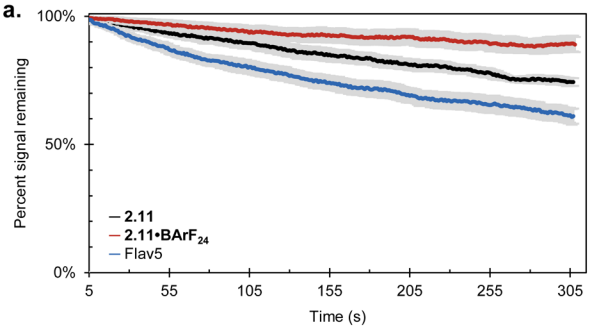

b.

Dye	k_{raw} (s^{-1})	k_{rel} (s^{-1})	Relative Stability
2.11	0.00095	1.25×10^{-29}	1.00
2.11•BArF$_{24}$	0.00037	5.84×10^{-30}	2.15
Flav5	0.0015	1.03×10^{-29}	1.22

Figure 2.15. Photobleaching curves and the raw (k_{raw}) and relative (k_{rel}) photobleaching rates of pentamethines **2.11**, **2.11•BArF$_{24}$** and Flav5 in DCM with continuous irradiation for 5 min (786 nm excitation, 1100 nm LP filter, 100 fps, 100 mW/cm^2). See "Photobleaching procedures" for details. Error bars represent the standard deviation of three replicates.

To formulate **2.11•BArF$_{24}$** into canola nanoemulsions, we first prepared empty nanoemulsions by sonicating canola oil in a solution of Pluronic F-68 surfactant and phosphate-buffered saline (PBS) (Figures 2.13D and 2.16). The empty nanoemulsions were then rocked with a solution of dye in acetone for 1 h and concentrated to afford **2.11•BArF$_{24}$** nanoemulsions with an average size of ~210 nm and a polydispersity of ~0.026. Notably, this approach was not successful with unexchanged **2.11**, further illustrating the effects of counterion exchange of fluorophore utility (Figure 2.16). To assess the chemical stability of **2.11•BArF$_{24}$** emulsions in biological settings, we incubated the emulsions in fetal bovine serum (FBS) at 37 °C and monitored the decrease in monomer absorption over time (Figure 2.13E). Gratifyingly, **2.11•BArF$_{24}$** exhibits excellent chemical stability under these conditions, retaining over 60% monomer absorption after 90 minutes. Additionally, **2.11•BArF$_{24}$** nanoemulsions showed strong SWIR emission in FBS, with detectable signal up to 1600 nm (Figure 2.16).

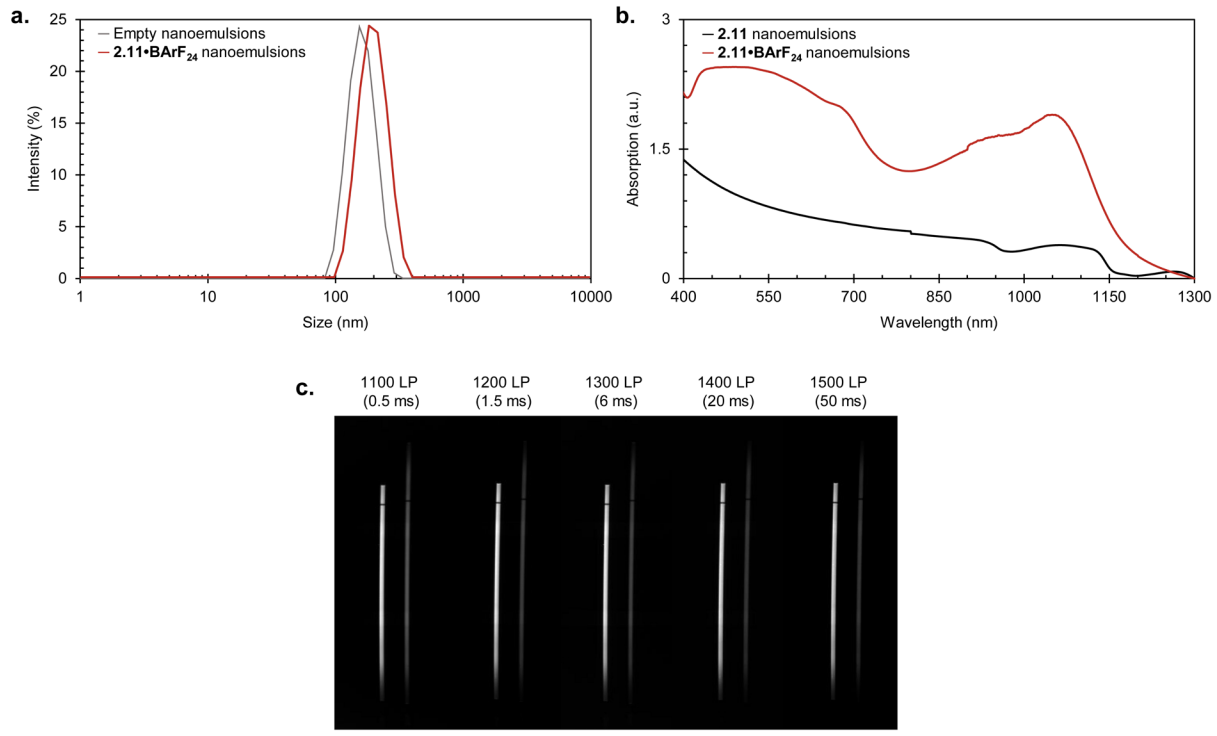

Figure 2.16. Synthesis and characterization of SiliFlav5 formulations. A) DLS of empty and **2.11•BArF$_{24}$** (330 nmol) nanoemulsions with an average size of ~200 nm. See "Formulation procedures" for details. B) Absorption spectra of **2.11** and **2.11•BArF$_{24}$** nanoemulsions in FBS. C) Capillary images of **2.11•BArF$_{24}$** nanoemulsions undiluted (left) and 1:10 diluted (right) in FBS (1060 nm excitation, 1100-1500 nm LP, 0.5-50 ms ET, 160 mW/cm^2).

After evaluating the stability of the SiliFlav scaffold *in vitro*, we assessed its toxicity *in cellulo*. A375 cells were incubated with empty nanoemulsions and **2.11•BArF$_{24}$** nanoemulsions at varying concentrations, and their viability was assessed after 24 h using the MTT assay (Figures 2.13F and 2.17). The cells exhibited good viability (75–95%) for both the empty and loaded nanoemulsions at relevant *in vivo* concentrations. The **2.11•BArF$_{24}$** nanoemulsions exhibited comparable viability to empty nanoemulsions, suggesting negligible toxicity from the dye itself.

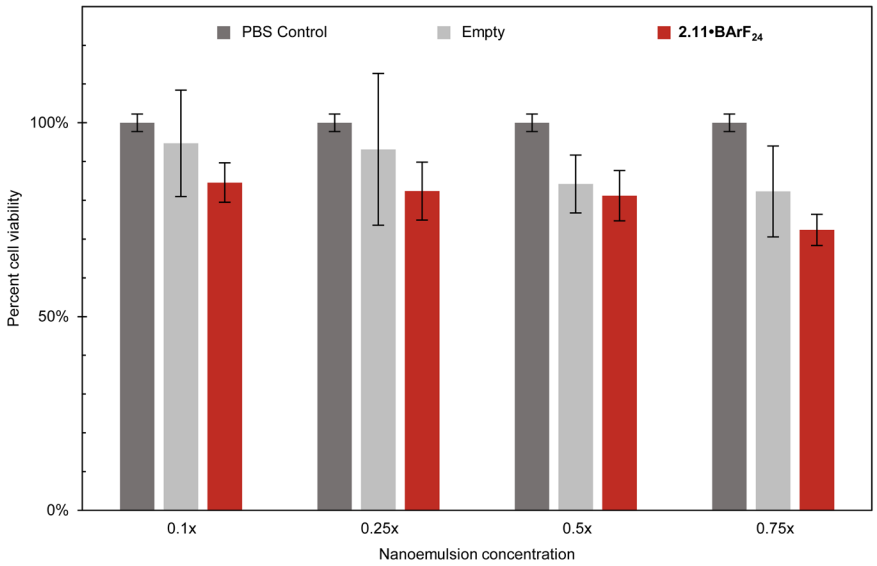

Figure 2.17. MTT viability assay on A375 cells with empty and **2.11•BArF$_{24}$** nanoemulsions at 0.1, 0.25, 0.5 and 0.75x the projected *in vivo* imaging concentration (330 nmol). See "Cell viability procedures" for details.

With these promising results, **2.11•BArF$_{24}$** nanoemulsions were intravenously injected into 7-week-old nude mice and immediately imaged using 1060 nm excitation (Figure 2.13G). We imaged the mice using both 1200 nm long-pass (LP) and 1300 nm LP filters. While more signal was obtained in 1200 nm LP images (Figure 2.18), the hallmark high resolution of the SWIR region is evident in the 1300 nm LP images. From the dorsal view, we detected excellent labeling of subcutaneous veins in the head and back, as well as strong signal in the spleen. The spleen is also very apparent in the lateral left view. The later right and ventral views showcase additional vasculature labeling as well as the liver. With time, the vasculature signal diminishes and strong emission from the spleen is apparent, characteristic of the biodistribution of ~200 nm nanoemulsions (Figure 2.18). After two days, *ex vivo* analysis confirms near exclusive localization spleen (Figure 2.19). Taken together, these imaging results show that SiliFlav formulations are capable of serving as bright, stable, red-shifted probes for longwave, high-resolution SWIR imaging above 1300 nm.

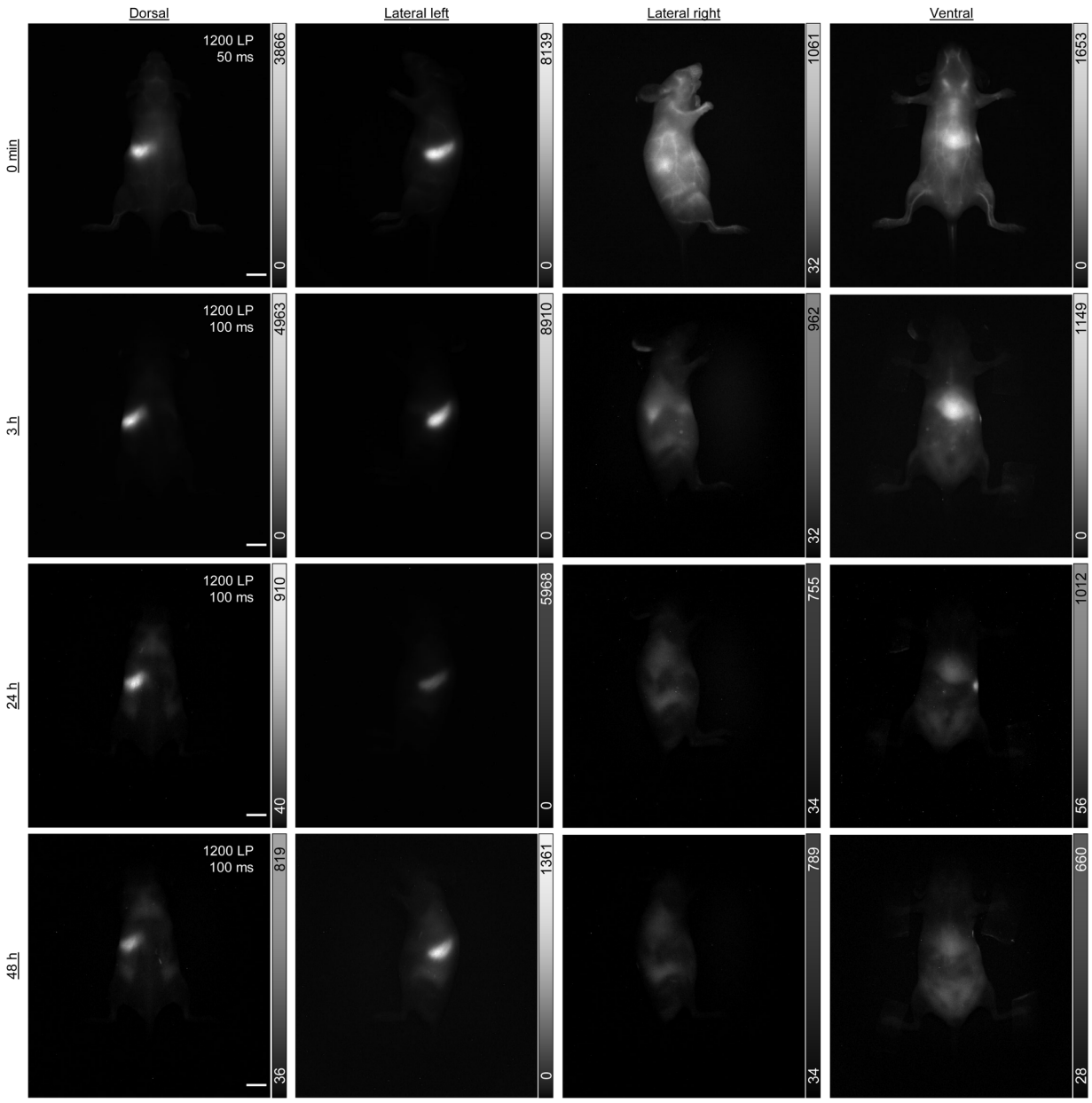

Figure 2.18. Longitudinal in vivo imaging with **2.11•BArF$_{24}$** nanoemulsions up to 48 h (1060 nm excitation, 1200 nm LP, 100 ms ET, 160 mW/cm2). Scale bars represent 10 mm. See “Animal imaging procedures” for details. Approximately 290 nmol of **2.11•BArF$_{24}$** was loaded into the nanoemulsions. See “Formulation procedures” for calculation details.

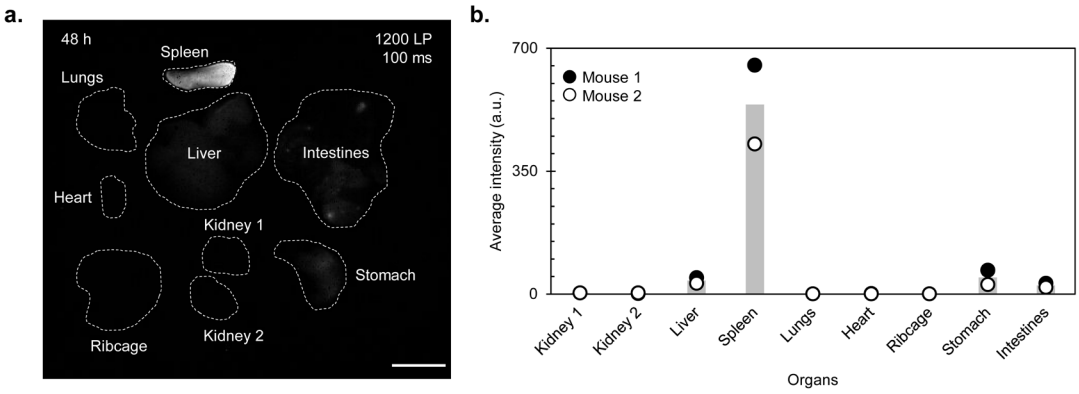

Figure 2.19. Biodistribution and quantification of **2.11•BArF$_{24}$** nanoemulsions. A) *Ex vivo* imaging of different organs 48 h after injection (1060 nm excitation, 1200 LP, 100 ms, 160 mW/cm^2). B) Mean signal intensity across the ROI for each organ plotted (points) and averaged (bar) for 2 mice. Scale bars represent 10 mm.

2.4 Conclusion

In this work, we report the development of a new class of SWIR polymethine fluorophores based on a silicon flavylium (SiliFlav) scaffold. Through the incorporation of a silicon heteroatom into the established Flav framework, we achieved unprecedented red-shifts in emission up to 200 nm, placing the SiliFlav scaffold among the most red-shifted small molecule fluorophores to date. Importantly, these fluorophores retain respectable ϕ_F, demonstrating that silicon substitution can effectively tune optical properties without fully compromising brightness, even in the challenging SWIR region. We developed a modular and scalable synthetic route that enables diversification at the 1-, 2-, and 7-positions of the SiliFlav core. This strategy not only allowed us to explore structure–property relationships in detail, but also led to several enhanced derivatives with improved photophysical performance. Notably, the 2-*tert*-butyl derivative (**2.17**, SiliChrom5) exhibited a 2-fold increase in ϕ_F, while deuteration at the 7-position (**2.14**, SiliFlav5-d_{12}) improved radiative decay rates. These findings suggest that many of the design principles established for flavylium dyes are transferrable to the silicon scaffold, offering a clear roadmap for future optimization. We also demonstrated the practical utility of this scaffold for *in vivo* imaging. A nanoemulsion formulation of counterion-exchanged SiliFlav5 (**2.11•BArF$_{24}$**) provided excellent

chemical stability, low toxicity, and good signal using a 1300 nm LP filter. Following intravenous injection in mice, this fluorophore formulation enabled high-resolution imaging of the vasculature and spleen, with *ex vivo* analysis confirming organ-specific accumulation consistent with the expected biodistribution of nanoemulsions. Overall, this work establishes silicon flavylium dyes as a promising new platform for bright, red-shifted SWIR imaging. The modular synthetic approach, combined with the favorable photophysical and biological performance, opens the door to a new generation of functional small-molecule probes for deep-tissue, high-resolution imaging in the SWIR window.

2.5 Experimental procedures

2.5.1 Abbreviations

DCM = dichloromethane; DLS = dynamic light scattering; DMSO = dimethyl sulfoxide; ET = exposure time; LP = longpass filter; PBS = phosphate-buffered saline; O.D. = optical density;

2.5.2 Photophysical procedures

Absorption spectra were obtained on a JASCO V-770 UV-Visible/NIR spectrophotometer after blanking with the appropriate solvent. Absorption spectra were collected between 350-1600 nm with a step size of 1 nm and a scan rate of 2000 nm/min. Emission spectra were obtained on a Horiba PTI QuantaMaster400 fluorimeter equipped with a liquid N_2 cooled InGaAs detector (Horiba Edison DSS IGA 020L). Emission spectra were obtained using 885 nm excitation (15 nm × 15 nm slit widths) and 930-1600 collection (30 nm × 30 nm slit widths), with a step size of 1 nm and integration time of 0.1 s.

The absorption coefficients (ϵ) of **2.11**–**2.17** were determined in DCM according to the Beer-Lambert law in the equation below:

$$A = \epsilon\, l\, c \quad (1)$$

In this equation, A is the absorbance in O.D., l is the path length in cm and c is the concentration in molarity. Analytical masses were obtained using a Sartorius MSE6.6S-000-DM S13 Cubis Micro Balance, and serial dilutions were performed with volumetric glassware and Hamilton syringes. Error was calculated using the standard deviation of measurements performed in triplicate, with $R^2 > 0.99$ for all traces.

Relative quantum yields (ϕ_F) of **2.11**–**2.17** (x) were determined according to the equation below, using IR-26 ($\phi_F = 0.05\%$) in DCM as the reference (r)[72]:

$$\phi_{F,x} = \phi_{F,r} \left(\frac{m_x}{m_f}\right)\left(\frac{\eta_x^2}{\eta_r^2}\right) \quad (2)$$

In this equation, m is the slope of the line ($y = mx + b$) obtained from the integrated fluorescence values versus the absorption of a series of samples and η is the refractive index of DCM. To obtain a plot integrated fluorescence intensity versus absorption, five solutions and a solvent blank were prepared and the absorption and emission spectra were acquired. IR-26 and each SiliFlav dye were diluted to concentrations less than 0.1 O.D. to minimize reabsorption. The emission spectrum of each solution was baseline corrected to 1600 nm, and integrated and background corrected using the integrated emission of the solvent blank. The integrated fluorescence intensity values were then plotted against the baseline corrected O.D. at 885 nm, and the slope and error in slope were calculated. All R^2 values were > 0.99.

2.5.3 Excited state lifetime procedures

Excited state lifetime measurements were obtained for SiliFlav pentamethine derivatives **2.11** and **2.14**–**2.17** using a home-built, all-reflective epifluorescence setup.[27] Samples were

diluted to ~1.0 O.D. in DCM and excited using a 780 nm picosecond pulsed diode laser (Picoquant, LDH-D-C-780). The emission was separated from the excitation using an 805 nm long pass dichroic mirror (Thorlabs, DMLP805R) and filtered using three 800 nm and one 850 nm dielectric longpass filters (Thorlabs, FEL0800 and Thorlabs, FGL850M). All reflective optics (unprotected silver) were used to direct and fiber couple emission into a reflective collimator where it was detected using broadband optimized super conducting nanowire single photon detectors (SNSPDS) (Quantum Opus, Opus One). Time correlated single photon counting (TCSPC) traces were histogrammed using a HydraHarp400 and corresponding software [Picoquant]. All measurements were carried out at room temperature. Curve fitting was performed with Igor Pro.

The TCSPC decay curves (listed below) were fit to a single exponential using the convolution integral of the instrument response function (IRF) and the impulse response function:

$$I(t) = \left(\frac{a}{2}\right)\left(e^{-k\left((t-t_0)-\frac{\sigma^2 k}{2}\right)}\right)\left(1 + \operatorname{erf}\left[(t-t_0) - \frac{\sigma^2 k}{\sqrt{2}\sigma}\right]\right) + c$$

where I = intensity, a = amplitude, k = total excited state decay rate, t = time, t_0 = initial time, σ = IRF width and c = constant.

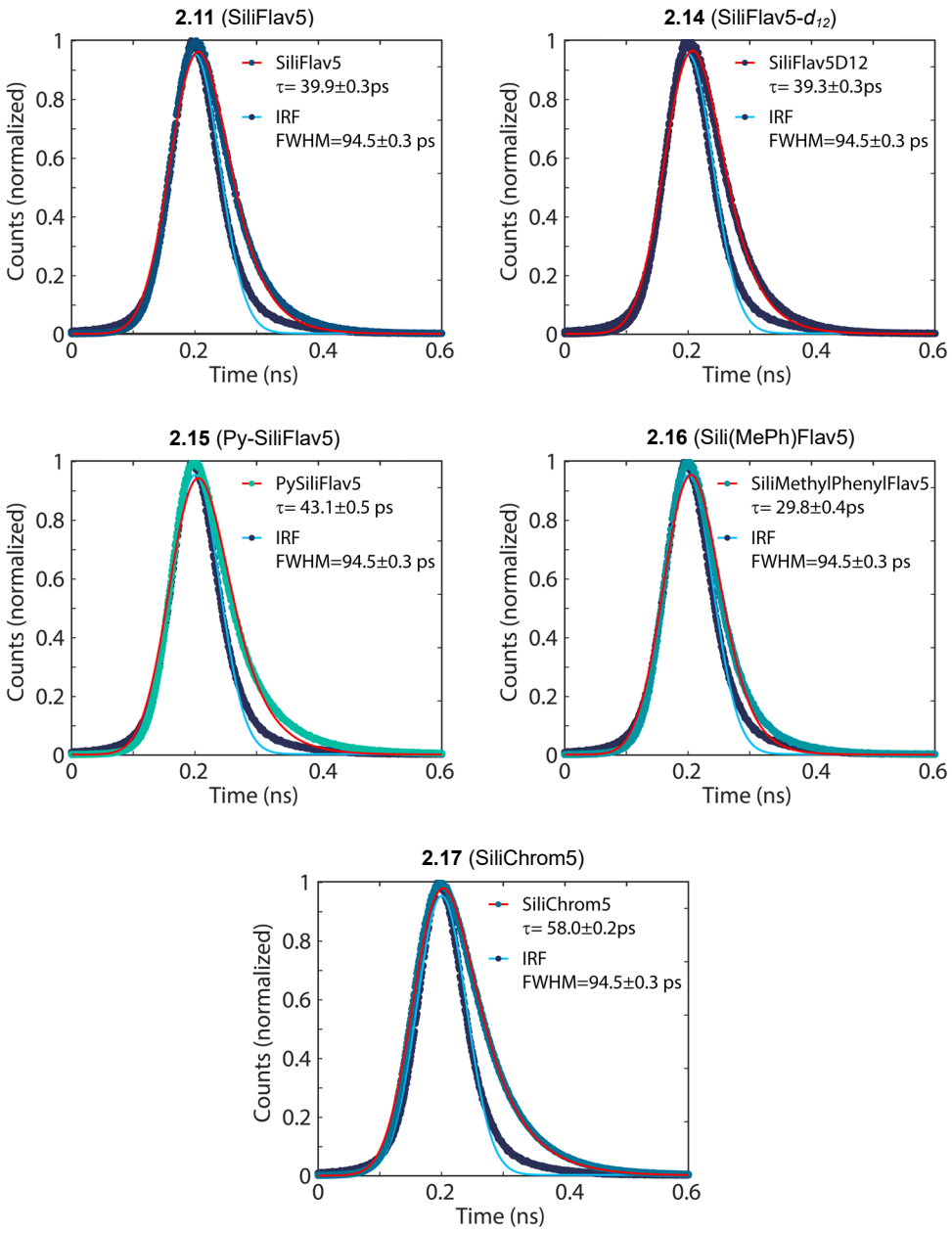

The excited state lifetime is defined as the inverse of total excited state decay rate:

$$\tau = \frac{1}{k}$$

Errors in τ were calculated as ± 1 ps, the value of the detector resolution. Errors in fitting parameters were sufficiently small such that they are negligible when considering the detector resolution.

The radiative (k_r) and nonradiative (k_{nr}) rates were calculated according to the following equations:

$$k_r = \frac{\Phi_F}{\tau}$$

$$k_{n.r.} = \frac{1 - \Phi_F}{\tau}$$

The errors for k_r and k_{nr} were determined by propagating the error of τ and Φ_F .

2.5.4 Photobleaching procedures

Solutions of **2.11** (SiliFlav5), **2.11•BArF$_{24}$** (SiliFlav5•BArF$_{24}$) and Flav5 were prepared in DCM at ~1 O.D. at the maximum intensity absorption wavelength. Each solution was placed in capillary tubes (Disposable Micro Capillary Pipets, 50 μL, DWK Life Sciences Kimble, #71900-50), sealed, and positioned onto a holder under an InGaAs camera and 786 nm laser (see "SWIR imaging setup"). Samples were irradiated with the 786 nm laser (100 mW/cm^2) continuously for 5 min at 100 fps and SWIR emission was detected beyond 1100 nm using a 1100 LP. Raw imaging files were processed according to "Image processing" to generate a plot of exposure time normalized emission intensity over time. The data was fit to a mono-exponential decay curve and the rate of photobleaching (k_{raw}) was determined via the following relationship:

$$\ln[A] = -kt + \ln[A]_0$$

where A and A_0 represent collection at time t and initial emission collected, respectively. All R^2 values were > 0.99. Photobleaching rate is reported as the mean of three replicate measurements, with standard deviation as the error.

To compare photobleaching rates across each fluorophore of interest, a relative rate of photobleaching (k_{rel}) was then determined. The raw photobleaching rate was first corrected according to the photon flux absorbed by the sample (N_{abs}):

$$N_p = fluence \div \frac{hc}{\lambda}$$

$$N_{abs} = N_p \times (1 - 10^{-Abs})$$

$$k_{rel} = \frac{k_{raw}}{N_{abs}}$$

N_{abs} is dependent on the density of irradiated photons (N_p) and the optical density of the sample at the wavelength of irradiation (Abs). Fluence was measured according to the procedure listed in "SWIR imaging setup", h is Planck's constant, and c is the speed of light, and λ is the irradiation wavelength. Each k_{rel} was then normalized to the rate of **2.11**:

$$Relative\ stability = \frac{k_{rel(\mathbf{11})}}{k_{rel,dye}}$$

2.5.5 Formulation procedures

To prepare empty nanoemulsions, a fresh solution of Pluronic-F-68 surfactant in PBS (28 mg/mL, 200 μL) was added to the bottom of a 1.5 mL Eppendorf tube, and canola oil (20 μL) was layered on top. Using a QSonica (Q125) probe sonicator, the tip of the probe was fully submerged into the mixture. To ensure that the probe did not come into contact with the sides or bottom of the Eppendorf, the tube was clamped into place. The mixture was cooled with an ice bath and sonicated for 90 s at 35% amplitude to produce nanomulsions with a hydrodynamic diameter of

190 nm. The empty nanoemulsions were layered with a solution of **2.11•BArF$_{24}$** (500 μg) in acetone (25 μL) and the sealed Eppendorf tube was placed on an orbital shaker at 60 rotations/min for 1 h. After rocking, the nanoemulsions were transferred to a dram vial and the residual acetone was removed via rotary evaporation. After evaporation, the bottom layer of the nanoemulsions (200 μL) were transferred to a new 1.5 mL Eppendorf tube, and the top layer consisting of unformulated dye and canola oil was discarded. The resulting **2.11•BArF$_{24}$** nanoemulsions were resuspended in 150 μL of PBS and filtered through a 1.0 μm syringe filter for *in vivo* use.

To determine the size, a 20 μL aliquot of the nanoemulsions was diluted in 2 mL of MilliQ water and transferred to a plastic 1 cm cuvette for characterization. Size was determined using Coulter Beckman N4 PLUS Particle Size Analyzer with the following SOP parameters: 10 runs, 10 seconds/run, three measurements, no delay between measurements, 25 °C with 120 second equilibration time. Collection parameters: Lower limit = 0.6, Upper limit = 1000, Resolution = High, Number of size classes = 70, Lower size limit = 0.4, Upper size limit = 1000, Lower threshold = 0.05, Upper threshold = 0.01. Data are representative of three replicate measurements.

To approximate the amount of **2.11•BArF$_{24}$** loaded into the canola oil nanoemulsions, a 20 μL aliquot of the emulsions was added to a 1.5 mL Eppendorf tube containing 800 μL of DCM. The mixture was centrifuged for at 1610 g for 20 min to destroy the nanoemulsions, producing a thin layer of oil and surfactant and a bottom layer of **2.11•BArF$_{24}$** in DCM. The absorption spectrum of the bottom layer was acquired, and Beer's law was used to back-calculate the concentration and moles of **2.11•BArF$_{24}$** per batch of nanoemulsions.

2.5.6 Cell viability procedures

A375 cells were purchased from ATCC (Catalog number: CRL-1619). They were cultured in Dulbecco's Modified Eagle Media (DMEM, Life Technologies, Catalog number: 11995073) supplemented with 10% fetal bovine serum (FBS, Corning), sodium pyruvate (Thermo Fisher,

Catalog number: 11360070) and 1% penicillin-streptomycin (Life Technologies, Catalog number: 15070063) at 37 °C and 5% CO_2 in Heracell 150i CO_2 incubators. Cells were pelleted using a Sorvall ST 40R series centrifuge. All cell work was executed in a sterile 1300 Series A2 biosafety cabinet.

A375 cells were seeded onto 96-well plates with average density 50,000 cells per well. On the first day, cells were treated with **2.11•BArF$_{24}$** nanoemulsions or empty nanoemulsions at 0.1x, 0.25x, 0.5x and 0.75x the *in vivo* concentrations to prevent surfactant-related toxicity. Each treatment condition was performed in sextuplicate. On the third day, MTT reagent (Millipore Sigma, Catalog Number: M2128) was diluted in media to a working concentration of 1.2 mg/mL, and a 20 μL aliquot of this solution was added to each well. Cells were incubated at 37 °C for 30 min, followed by aspiration of the media and addition of DMSO (100 μL) to solubilize the formazan product. The cells were then incubated for an additional 10 minutes at 37 °C, and the absorbance was measured at 560 nm using the Varioskan Lux Multimode Microplate Reader.

2.5.7 Animal imaging procedures

Animal procedures were performed in accordance with the guidelines of the University of California, Los Angeles International Animal Care and Use Committee (IACUC), with specific protocols approved by the Animal Research Committee (ARC, protocol number ARC-2018-047). Noninvasive, whole mouse imaging was performed on athymic female mice (NU/J) purchased from The Jackson Laboratories. Mice were 7 weeks of age at the start of imaging experiments. For all animal procedures, mice were anesthetized by inhalation of isoflurane (2–4% isoflurane/oxygen) and placed on a heating pad to maintain normal body temperature while under anesthesia. The heating pad was affixed with a nose cone to deliver anesthetic to the imaging stage (see “SWIR imaging setup”). Artificial tears were added to each eye to prevent corneas from drying out during imaging procedures. Intravenous (*i.v.*) injections were performed through the tail vein. Briefly, a catheter was assembled from a 29-gauge needle (VetriJec^{TM}) connected

through plastic tubing (0.8 mm x 0.3 mm tygon catheter tubing, Braintree Scientific, Inc) prefilled with a sterile isotonic saline solution. The bevel of the needle was inserted into the tail vein and secured with a tissue adhesive. The catheter was then connected to a syringe (29-gauge, VetriJec™) prefilled with fluorophore-containing emulsions sterilized with a 1 μm syringe filter. Finally, the solution was injected to the tail vein followed by a sterile saline flush to ensure full dosage was achieved. The total volume of *i.v.* injections never exceeded 200 μL. Mice were briefly imaged post-injection at defined timepoints up to 2 days, followed by humane euthanasia at the endpoint. Individual organs were then dissected and imaged.

2.5.8 SWIR imaging setup

For photobleaching (see “Photobleaching procedures”) and whole mouse imaging (see “Animal procedures”) a custom-built SWIR imaging setup was used. The setup was partially enclosed to avoid excess light pollution, while still allowing for physical manipulation of the field of view during operation. Lumics laser unit LU0785D250-U70AN (25 W) "785 nm” was used for photobleaching experiments, and LU1064D350- U30AN (35 W) “1064 nm” was used for whole mouse imaging experiments. Excitation wavelengths are reported as “786 nm” and “1060 nm”, respectively, corresponding to the peak wavelength intensity recorded via spectrometer measurement. All lasers were coupled in a fan-out fiber optic bundle with a 600 µm core diameter (Thorlabs BF46LS01) for each optical path. The fiber bundle output was affixed to an excitation cube (ThorLabs KCB1E), reflected off a mirror (Thorlabs BBE-E03), and passed through a positive achromat (Thorlabs AC254-050-AB-ML), SP filters (1100 nm, 2X 25 mm #64-339, Edmund Optics) and an engineered 20˚ square diffuser (Thorlabs ED1-S20-MD) to provide uniform illumination over the imaging stage. This area was covered by a heating pad affixed with a nose cone and non-reflective blackout fabric (Thorlabs BK5) and/or foil (BKF12). The excitation flux at the imaging stage was measured with a digital optical power and energy meter (Thorlabs PM1000D) coupled to a photodiode sensor (S130C). For photobleaching experiments, the power

density was set to 100 mW/cm^2. For whole mouse imaging, the power density was set to 160 mW/cm^2, in accordance with the ICNIRP guidelines for whole mouse imaging.[79] An InGaAs camera (Allied Vision Goldeye G-032 Cool TEC2) was mounted vertically above the imaging stage to detect emitted SWIR light. The camera used a SWIR C-mount lens (Kowz LM35HC-SW) and a set of longpass (LP) filters. For “1100 nm LP” filtering, 1X 25 mm FELH1100 (Thorlabs) was affixed to the camera lens, followed by 1X 50 mm #84-768 (Edmund Optics) mounted by a filter holder (LCFH2-F, Thorlabs) and 1X 50 mm #84-768 (Edmund Optics) mounted to a lens tube (SM2L05, ThorLabs). For “1200 nm LP” filtering, 1X 25 mm FELH1200 (Thorlabs) was mounted to a lens tube (SM1L03, Thorlabs) followed by another lens tube (SM1L10) and a 5 mm silicon window (WG81050, Thorlabs) mounted to a lens tube (SM1L03, Thorlabs) and affixed to the camera lens; additionally, 3X lens tubes (SM2L03), followed by 1X 50 mm #89-666 (Edmund Optics) mounted to a lens tube (SM2L05, ThorLabs), a lens tube (SM2L20), and 1X 50 mm #89-666 (Edmund Optics) mounted to a lens tube (SM2L05, ThorLabs) were placed in series below the camera lens filters. For “1300 nm LP” filtering, 1X 25 mm FELH1300 (Thorlabs) was affixed to the camera lens, followed by 1X 50 mm #89-669 (Edmund Optics) mounted by a filter holder (LCFH2-F, Thorlabs), a lens tube (SM2L20), and 1X 50 mm #89-669 (Edmund Optics) mounted to a lens tube (SM2L05, ThorLabs). The camera was set to -30 ˚C and was set to gain = 1. The exposure time property was set for each image. Both the camera and lasers were externally controlled. For image acquisition, the toolbox of MATLAB programming environment was used in combination with a MATLAB script (CCDA V3, https://gitlab.com/brunslab/ccda) to preview and collect image data in 14-bit depth.

2.5.9 Image processing

Raw image files were processed using the FIJI distribution of ImageJ.[80,81] All image stacks were first subtracted with a no-laser background (100–200 frames taken at the beginning of each acquisition) to correct for non-linearities in the detector. For still fluorescence images, frames of

interest were then averaged using the “Z-project” function (50–100 frames, unless otherwise stated). Still images underwent no further processing. Brightness values obtained from the 14-bit images are displayed with the grey LUT scale. All images were then compressed to an 8-bit depth for display.

For *ex vivo* organ quantification, regions of interest were highlighted around individual organs using the hand-drawn ROI tool. The mean intensities were calculated with the “Measure” function and reported as the mean of three hand-drawn measurements, after subtracting image background (measured within the blank region between organs in the same manner). For each animal, these values were normalized to the exposure time property for comparison of fluorescence remaining in each organ 2 days post-injection. Normalized fluorescence intensity values for replicate animals were then averaged to generate quantitative bar graphs, with individual values displayed accordingly.

For capillary image quantification, regions of interest were highlighted via the line ROI tool, drawing a line horizontally across a set of capillary tubes. Fluorescence intensity across this ROI was plotted using the “Plot profile” feature.

For photobleaching quantification, the background subtracted stack was used. The stack was imported at a step size of 100, corresponding to the frame rate of the acquisition (100 fps), such that each sequential frame corresponds to 1 second of illumination time. A line ROI was drawn vertically across each individual capillary tube, and mean fluorescence intensity over time across the ROI was plotted using the “Plot Z-axis profile” feature.

All raw and processed files can be found on BioImage Archive, accession number: S-BIAD2235.

2.6 Synthetic procedures

2.6.1 Abbreviations

AcOH = acetic acid; Ac_2O = acetic anhydride; DCM = dichlormethane; DMDCS = dimethyldichlorosilane; EtOAc = ethyl acetate; HRMS = high resolution mass spectrometry; MeOH = methanol; *n*-BuLi = *n*-butyllithium; NMR = nuclear magnetic resonance; TBAB = tetrabutylammonium bromide; TFE = trifluoroethanol; THF = tetrahydrofuran; TLC = thin layer chromatography

2.6.2 Materials and instrumentation

Chemical reagents were purchased from Acros Organics, Alfa Aesar, Fisher Scientific, Sigma-Aldrich, Spectrum Chemicals or TCI and used without purification. Anhydrous and deoxygenated DCM or THF was dispensed from a Grubb's-type Phoenix Solvent Drying System. Flash chromatography was performed with technical grade silica gel containing 60 Å pores and 40-63 μm mesh particle sizes (Sorbtech Technologies). Solvent was removed under reduced pressure using a Büchi Rotovapor with a Welch self-cleaning dry vacuum pump, and a Welch DuoSeal pump for additional evaporation. Nuclear magnetic resonance (^{1}H NMR, ^{13}C NMR and ^{19}F NMR) spectra were taken on a Bruker AV500 or Bruker NEO600 spectrometer and processed with MestReNova software. All ^{1}H NMR and ^{13}C NMR peaks are referenced to their respective solvent peaks (CD_2Cl_2 δH = 5.32 ppm, δC = 53.84 ppm; $CDCl_3$ δH = 7.26 ppm, δC = 77.16 ppm). ^{19}F NMR peaks are referenced to trifluoroethanol (δF = -77.59 ppm). Low resolution liquid chromatography-mass spectrometry were obtained using a 1260 Infinity II, Agilent 6100 series quadrupole LC/MSD equipped with a Zorbax SB-C18 column (Agilent). High resolution mass spectrometry (HRMS) data were obtained on an Agilent 6545 Q-TOF mass spectrometer (ESI-MS) or a Thermo Exactive Plus Orbitrap with IonSense ID-CUBE DART source and Vapour Interace (DART-MS).

2.6.3 Synthetic procedures

Synthesis of 1-(2-bromo-4-fluorophenyl)-3-phenylprop-2-yn-1-ol (**2.1a**).

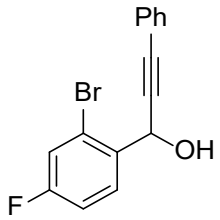

In a dry two-neck round-bottom flask charged with a stir bar under N_2 atmosphere, phenylacetylene (7.57 mL, 69.0 mmol, 1.40 equiv) was dissolved in anhydrous THF (98.5 mL) and cooled to 0 °C. *n*-BuLi (2.5 M solution in hexanes, 23.6 mL, 59.1 mmol, 1.20 equiv) was added dropwise and the mixture was stirred for 1 h before adding 2-bromo-4-fluorobenzaldehyde (10.0 g, 49.3 mmol, 1.00 equiv). The mixture was warmed to rt and stirred for 4 h, with full consumption of starting material by TLC (10:1 hexanes:EtOAc). The mixture was quenched with saturated NH_4Cl, extracted with DCM (150 mL × 3) and washed with water and brine. The crude product was dried with Na_2SO_4, evaporated and recrystallized in hexanes at 4 °C for two days to give **2.1a** as a white crystalline solid (12.3 g, 40.4 mmol, 82%). R_F = 0.46 in 10:1 hexanes:EtOAc. ^{1}H NMR (500 MHz, $CDCl_3$) δ 7.84 (dd, *J* = 8.7, 5.9 Hz, 1H), 7.49 – 7.42 (m, 2H), 7.36 – 7.28 (m, 4H), 7.11 (td, *J* = 8.3, 2.6 Hz, 1H), 5.98 (s, 1H). ^{13}C NMR (126 MHz, $CDCl_3$) δ 162.21 (d, *J* = 251.9 Hz), 135.66 (d, *J* = 3.4 Hz), 131.77, 129.86 (d, *J* = 8.7 Hz), 128.82, 128.36, 122.95 (d, *J* = 9.6 Hz), 122.10, 120.28 (d, *J* = 24.6 Hz), 115.01 (d, *J* = 21.1 Hz), 87.44, 86.99, 64.06. HRMS (DART-MS): calculated for $C_{15}H_{10}BrFO$ $[M-17]^+$, 288.9879; found 288.9851.

Synthesis of 1-(2-bromo-4-fluorophenyl)-4,4-dimethylpent-2-yn-1-ol (**2.1b**).

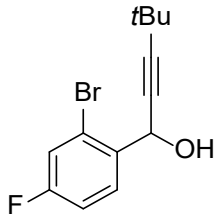

In a dry two-neck round-bottom flask charged with a stir bar under N_2 atmosphere, *tert*-butylacetylene (1.70 mL, 13.8 mmol, 1.40 equiv) was dissolved in anhydrous THF (19.7 mL) and cooled to 0 °C. *n*-BuLi (2.5 M solution in hexanes, 4.72 mL, 11.8 mmol, 1.20 equiv) was added dropwise and the mixture was stirred for 1 h before adding 2-bromo-4-fluorobenzaldehyde (2.00 g, 9.86 mmol, 1.00 equiv). The mixture was warmed to rt and stirred for 4 h, with full consumption of starting material by TLC (10:1 hexanes:EtOAc). The mixture was quenched with saturated NH_4Cl, extracted with DCM (50 mL × 3) and washed with water and brine. The crude product was dried with Na_2SO_4, evaporated to give **2.1b** as a tan oil, which was used without further purification (3.94 g, 13.8 mmol, Quantitative). R_F = 0.75 in 10:1 hexanes:EtOAc. ^{1}H NMR (500 MHz, $CDCl_3$) δ 7.73 (ddd, *J* = 8.9, 6.0, 2.9 Hz, 1H), 7.28 (d, *J* = 8.4, 4.2 Hz, 1H), 7.05 (td, *J* = 8.5, 2.7 Hz, 1H), 5.70 (s, 1H), 2.54 (s, 1H), 1.26 – 1.22 (m, 9H). ^{13}C NMR (126 MHz, $CDCl_3$) δ 162.03 (d, *J* = 251.3 Hz), 136.29 (d, *J* = 3.5 Hz), 129.76 (d, *J* = 8.6 Hz), 123.06 (d, *J* = 9.7 Hz), 120.09 (d, *J* = 24.6 Hz), 114.79 (d, *J* = 21.0 Hz), 96.19, 90.84, 83.37, 65.30, 63.58, 30.81, 27.53. HRMS (DART-MS): calculated for $C_{13}H_{14}BrFO$ $[M-17]^+$, 267.0212; found 267.0183.

Synthesis of 2-bromo-4-fluoro-1-(3-phenylprop-2-yn-1-yl)benzene (**2.2a**).

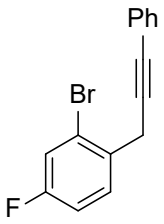

In a two-neck round-bottom flask charged with a stir bar, **2.1a** (4.00 g, 13.1 mmol, 1.00 equiv) was dissolved in DCM (131 mL) and triethylsilane (2.09 mL, 13.1 mmol, 1.00 equiv) was added. TFA (1.01 mL, 13.1 mmol, 1.00 equiv) was added dropwise and the mixture was stirred at rt for 4 h with full consumption of the starting material by TLC (10:1 hexanes:EtOAc). The mixture was quenched with saturated $NaHCO_3$, extracted with DCM (50 mL × 3) and washed with water and brine. The crude product was dried with Na_2SO_4, evaporated onto silica gel and purified via flash chromatography, eluting with hexanes to give **2.2a** as a yellow oil (2.35 g, 8.13 mmol, 62%). R_F = 0.26 in hexanes. ^{1}H NMR (500 MHz, $CDCl_3$) δ 7.71 (dd, J = 8.7, 6.0 Hz, 1H), 7.58 – 7.51 (m, 2H), 7.41 – 7.33 (m, 4H), 7.09 (td, J = 8.3, 2.7 Hz, 1H), 3.89 (s, 2H). ^{13}C NMR (126 MHz, $CDCl_3$) δ 161.40 (d, J = 249.5 Hz), 132.11 (d, J = 3.5 Hz), 131.78, 130.54 (d, J = 8.2 Hz), 128.40, 128.18, 123.74 (d, J = 9.5 Hz), 123.43, 119.81 (d, J = 24.7 Hz), 114.66 (d, J = 20.9 Hz), 86.16, 84.03, 26.15. HRMS (DART-MS): calculated for $C_{15}H_{10}BrF$ $[M+1]^+$, 288.9950; found, 288.9745.

Synthesis of 2-bromo-4-fluoro-1-(3-iodo-3-phenylallyl)benzene (**2.3a**).

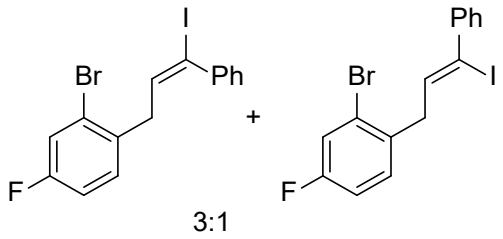

In a two-neck round-bottom flask charged with a stir bar, **2.2a** (2.35 g, 8.13 mmol, 1.00 equiv) was dissolved in DCM (81.3 mL) and idodine (2.06 g, 8.13 mmol, 1.00 equiv) was added. Triethylsilane (1.30 mL, 8.13 mmol, 1.00 equiv) was added dropwise and the mixture was stirred at rt for 4 h with full consumption of the starting material by TLC (hexanes) and GCMS. The mixture was quenched with saturated $Na_2S_2O_3$, extracted with DCM (50 mL × 3) and washed with water and brine. The crude product was dried with Na_2SO_4, evaporated onto silica and purified via flash chromatography, eluting with hexanes to give **2.3a** as a yellow oil in a 3:1 mixture of *Z:E* isomers (2.10 g, 5.04 mmol, 62%). R_F = 0.33 in hexanes. ^{1}H NMR (500 MHz, $CDCl_3$) *Z*-isomer: δ 7.50 – 7.44 (m, 2H), 7.39 – 7.23 (m, 5H), 7.03 – 6.94 (m, 1H), 6.04 (t, *J* = 6.7 Hz, 1H), 3.75 (d, *J* = 6.7 Hz, 2H), 3.38 (d, *J* = 7.5 Hz, 1H). *E*-isomer: δ 7.50 – 7.44 (m, 2H), 7.39 – 7.23 (m, 5H), 7.09 (dd, *J* = 8.5, 6.1 Hz, 1H), 6.59 (t, *J* = 7.6 Hz, 1H), 3.75 (d, *J* = 6.7 Hz, 2H), 3.38 (d, *J* = 7.5 Hz, 1H). ^{13}C NMR (126 MHz, $CDCl_3$) *Z*-isomer: δ 161.15 (dd, *J* = 249.4, 12.8 Hz), 142.84, 139.20, 135.53, 134.38 (d, *J* = 3.7 Hz), 131.11 (d, *J* = 8.4 Hz), 128.61, 128.27, 124.37 (d, *J* = 9.5 Hz), 120.03 (dd, *J* = 24.3, 4.8 Hz), 114.71 (d, *J* = 20.8 Hz), 107.07, 43.64.HRMS (DART-MS): calculated for $C_{15}H_{11}BrFI$ $[M+1]^+$, 416.9073; found, 416.9239.

Synthesis of 2-bromo-4-fluoro-1-(3-iodo-4,4-dimethylpent-2-en-1-yl)benzene (**2.3b**).

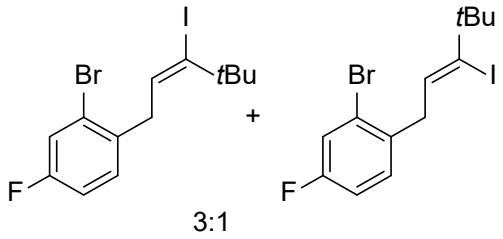

In a two-neck round-bottom flask charged with a stir bar, **2.1b** (2.00 g, 7.01 mmol, 1.00 equiv) was dissolved in DCM (70.1 mL) and triethylsilane (1.12 mL, 7.01 mmol, 1.00 equiv) was added. TFA (540 μL, 7.01 mmol, 1.00 equiv) was added dropwise and the mixture was stirred at rt for 4 h with full consumption of the starting material by TLC (10:1 hexanes:EtOAc). The mixture was quenched with saturated $NaHCO_3$, extracted with DCM (50 mL × 3) and washed with water and brine. The crude product was dried with Na_2SO_4 and evaporated to give a tan oil (labeled as **2.2b** in the manuscript). The crude oil was dissolved in DCM (70.1 mL) and idodine (1.77 g, 7.01 mmol, 1.00 equiv) was added. Triethylsilane (1.12 mL, 7.01 mmol, 1.00 equiv) was added dropwise and the mixture was stirred at rt for 4 h, with full consumption of the starting material by TLC (hexanes) and GCMS. The mixture was quenched with saturated $Na_2S_2O_3$, extracted with DCM (50 mL × 3) and washed with water and brine. The crude product was dried with Na_2SO_4, evaporated onto silica and purified via flash chromatography, eluting with hexanes to give **2.3b** as a yellow oil in a 3:1 mixture of *Z:E* isomers (1.25 g, 4.63 mmol, 66%). R_F = 0.36 in hexanes. ^{1}H NMR (500 MHz, $CDCl_3$) *Z*-isomer: δ 7.33 – 7.27 (m, 1H), 7.27 – 7.20 (m, 1H), 7.00 – 6.93 (m, 1H), 5.68 (t, *J* = 3.3 Hz, 1H), 3.64 – 3.57 (m, 2H), 1.25 (s, 9H). *E*-isomer: δ 7.63 (td, *J* = 6.4, 3.3 Hz, 1H), 7.27 – 7.20 (m, 1H), 7.08 – 7.01 (m, 1H), 5.28 (d, *J* = 3.0 Hz, 1H), 3.64 – 3.57 (m, 2H), 1.25 (s, 9H). ^{13}C NMR (126 MHz, $CDCl_3$) *Z*-isomer: δ 161.06 (d, *J* = 249.3 Hz), 134.95 (d, *J* = 3.4 Hz), 130.88 (d, *J* = 8.1 Hz), 130.22 (d, *J* = 8.1 Hz), 128.54, 124.47 (d, *J* = 9.4 Hz), 119.96 (d, *J* = 24.3 Hz), 114.58 (d, *J* = 20.7 Hz), 43.51, 31.35, 30.74. HRMS (DART-MS): calculated for $C_{13}H_{15}BrFI$ $[M+1]^+$, 396.9386; found 396.9041.

Synthesis of 7-fluoro-1,1-dimethyl-2-phenyl-1,4-dihydrobenzo[*b*]siline (**2.4a**).

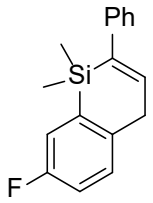

In a dry two-neck round-bottom flask charged with a stir bar under N_2 atmosphere, **2.3a** (2.00 g, 4.80 mmol, 1.00 equiv) was dissolved in anhydrous hexanes (48.0 mL) and cooled to 0 °C. *n*-BuLi (2.5 M solution in hexanes, 42.2 mL, 10.6 mmol, 2.20 equiv) was added dropwise and the mixture was stirred for 30 minutes, with full consumption of the starting material by TLC (hexanes). Anhydrous THF (48.0 mL) was added, followed by addition of DMDCS (13.9 mL, 11.5 mmol, 2.40 equiv) and the mixture was warmed to rt and stirred for 16 h. The mixture was quenched with saturated NH_4Cl, extracted with DCM (100 mL × 3) and washed with water and brine. The crude product was dried with Na_2SO_4, evaporated onto silica and purified via flash chromatography, eluting with hexanes to give **2.4a** as a yellow oil (1.18 g, 4.41 mmol, 92%). R_F = 0.24 in hexanes. ^{1}H NMR (500 MHz, $CDCl_3$) δ 7.40 – 7.36 (m, 2H), 7.32 – 7.23 (m, 5H), 7.08 – 7.03 (m, 1H), 6.87 (t, *J* = 4.4 Hz, 1H), 3.83 (d, *J* = 4.4 Hz, 2H), 0.42 (s, 6H). ^{13}C NMR (126 MHz, $CDCl_3$) δ 161.22 (d, *J* = 246.5 Hz), 143.94, 141.77, 139.34 (d, *J* = 3.0 Hz), 137.12 (d, *J* = 3.8 Hz), 129.87 (d, *J* = 6.6 Hz), 128.49, 126.76, 126.29, 118.88 (d, *J* = 17.8 Hz), 115.99 (d, *J* = 21.5 Hz), 35.83, -1.17. HRMS (DART-MS): calculated for $C_{17}H_{17}FSi$ $[M+1]^+$, 269.1084; found, 269.0938.

Synthesis of 7-fluoro-1-methyl-1,2-diphenyl-1,4-dihydrobenzo[*b*]siline (**2.4b**).

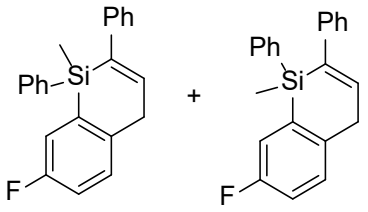

In a dry two-neck round-bottom flask charged with a stir bar under N_2 atmosphere, **2.3a** (200 mg, 0.480 mmol, 1.00 equiv) was dissolved in anhydrous hexanes (4.80 mL) and cooled to 0 °C. *n*-BuLi (2.5 M solution in hexanes, 424 μL, 1.06 mol, 2.20 equiv) was added dropwise and the mixture was stirred for 30 minutes, with full consumption of the starting material by TLC (hexanes). Anhydrous THF (4.80 mL) was added, followed by addition of dichloro(methyl)phenylsilane (187 μL, 1.15 mol, 2.40 equiv) and the mixture was warmed to rt and stirred for 18 h. The mixture was quenched with saturated NH_4Cl, extracted with DCM (25 mL × 3) and washed with water and brine. The crude product was dried with Na_2SO_4, evaporated onto silica and purified via flash chromatography, eluting with hexanes to give **2.4b** as an inseparable mixture of isomers (yellow oil, 149 mg, 0.452 mmol, 94%). R_F = 0.26 in hexanes. ^{1}H NMR (500 MHz, $CDCl_3$) δ 7.56 (ddt, *J* = 12.4, 5.3, 2.3 Hz, 4H), 7.38 (dd, *J* = 6.5, 3.2 Hz, 4H), 7.28 (dd, *J* = 7.2, 5.7 Hz, 2H), 7.23 – 7.21 (m, 2H), 7.12 – 7.06 (m, 1H), 7.06 – 6.99 (m, 1H), 4.01 – 3.88 (m, 2H), 0.71 (s, 3H). ^{13}C NMR (126 MHz, $CDCl_3$) Major isomer: δ 161.18 (d, *J* = 247.0 Hz), 143.40, 143.16, 139.46 (d, *J* = 2.9 Hz), 137.25, 135.64 (d, *J* = 3.9 Hz), 134.54, 133.89, 129.94 (d, *J* = 6.7 Hz), 129.53, 128.72, 128.43, 128.11, 127.70, 126.88, 119.51 (d, *J* = 18.4 Hz), 116.30 (d, *J* = 21.5 Hz), 36.09, -4.17. Major isomer: δ 161.18 (d, *J* = 247.0 Hz), 143.40, 143.16, 139.03 (d, *J* = 2.9 Hz), 136.83, 135.64 (d, *J* = 3.9 Hz), 134.54, 133.89, 129.94 (d, *J* = 6.7 Hz), 129.53, 128.72, 128.43, 128.11, 127.70, 126.37, 119.51 (d, *J* = 18.4 Hz), 116.30 (d, *J* = 21.5 Hz), 36.09, -5.07. HRMS (DART-MS): calculated for $C_{22}H_{19}FSi$ $[M+15]^+$, 345.1240; found, 345.1107.

Synthesis of 7-fluoro-1,1-dimethyl-2-phenylbenzo[*b*]silin-4(*1H*)-one (**2.5a**).

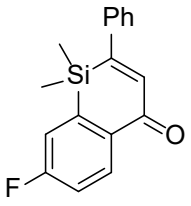

In a two-neck round-bottom flask charged with a stir bar and fitted with a reflux condenser, **2.4a** (1.00 g, 3.73 mmol, 1.00 equiv) and SeO_2 (455 mg, 4.10 mmol, 1.10 equiv) were dissolved in 1,4-dioxane (37.3 mL) and the mixture stirred at 100 °C for 1 h, with full consumption of the starting material by TLC (hexanes). The mixture was cooled to rt, evaporated onto silica and purified via flash chromatography, eluting with 50:1 hexanes:EtOAc to give **2.5a** as a yellow solid (968 mg, 3.43 mmol, 92%). R_F = 0.36 in 40:1 hexanes:EtOAc. ^{1}H NMR (500 MHz, $CDCl_3$) δ 8.36 (dd, *J* = 8.8, 5.3 Hz, 1H), 7.49 – 7.42 (m, 4H), 7.42 – 7.36 (m, 1H), 7.30 (dd, *J* = 7.9, 2.7 Hz, 1H), 7.21 (td, *J* = 8.7, 2.7 Hz, 1H), 7.16 (s, 1H), 0.51 (s, 4H). ^{13}C NMR (126 MHz, $CDCl_3$) δ 186.96, 165.05 (d, *J* = 257.4 Hz), 158.67, 142.77 (d, *J* = 5.7 Hz), 141.44, 140.63, 135.72 (d, *J* = 2.9 Hz), 131.96 (d, *J* = 8.5 Hz), 129.01, 128.98 (d, *J* = 8.1 Hz), 126.79, 119.05 (d, *J* = 19.4 Hz), 117.37 (d, *J* = 21.6 Hz), -1.57. HRMS (DART-MS): calculated for $C_{17}H_{15}FOSi$ $[M+1]^+$, 283.0876; found, 283.0932.

Synthesis of 7-fluoro-1-methyl-1,2-diphenylbenzo[*b*]silin-4(*1H*)-one (**2.5b**).

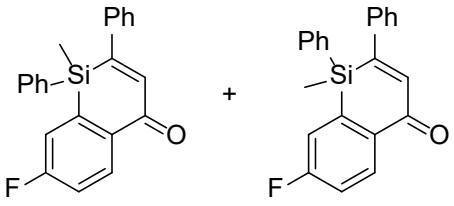

In a scintillation vial charged with a stir bar and fitted with a PTFE-lined cap, **2.4b** (100 mg, 303 μmol, 1.00 equiv) and SeO_2 (36.9 mg, 333 μmol, 1.10 equiv) were dissolved in 1,4-dioxane (3.03 mL) and the mixture was stirred at 100 °C for 1 h, with full consumption of the starting material by TLC (hexanes). The mixture was cooled to rt, evaporated onto silica and purified via flash chromatography, eluting with 50:1 hexanes:EtOAc to give **2.5b** as a mixture of isomers (yellow solid, 82.7 mg, 0.285 mmol, 94%). R_F = 0.37 in 40:1 hexanes:EtOAc. ^{1}H NMR (600 MHz, $CDCl_3$) δ 8.40 (dd, *J* = 8.7, 5.3 Hz, 1H), 7.55 (dt, *J* = 6.8, 1.4 Hz, 2H), 7.52 – 7.48 (m, 1H), 7.45 – 7.41 (m, 1H), 7.38 (dd, *J* = 7.5, 1.3 Hz, 2H), 7.36 – 7.34 (m, 3H), 7.32 (dd, *J* = 5.0, 1.8 Hz, 2H), 7.23 – 7.17 (m, 2H), 0.79 (s, 3H). ^{13}C NMR (151 MHz, $CDCl_3$) Major isomer: δ 187.10, 165.04 (d, *J* = 257.7 Hz), 156.55, 142.25, 141.41 (d, *J* = 5.8 Hz), 140.19, 139.01, 135.87 (d, *J* = 2.7 Hz), 134.59, 133.86, 131.96 (d, *J* = 8.5 Hz), 130.48, 129.07, 128.90, 128.57, 127.67, 127.11, 119.88 (d, *J* = 19.5 Hz), 117.64 (d, *J* = 21.7 Hz), -4.67 (d, *J* = 64.5 Hz). Minor isomer: δ 187.10, 165.04 (d, *J* = 257.7 Hz), 156.55, 142.25, 141.41 (d, *J* = 5.8 Hz), 140.19, 139.01, 135.87 (d, *J* = 2.7 Hz), 134.59, 133.22, 131.96 (d, *J* = 8.5 Hz), 130.48, 129.07, 128.68, 128.57, 127.67, 127.11, 119.88 (d, *J* = 19.5 Hz), 117.64 (d, *J* = 21.7 Hz), -5.10 (d, *J* = 64.5 Hz).HRMS (DART-MS): calculated for $C_{22}H_{17}FOSi$, 345.1033; found 345.1108.

Synthesis of 2-(*tert*-butyl)-7-fluoro-1,1-dimethylbenzo[*b*]silin-4(*1H*)-one (**2.5c**).

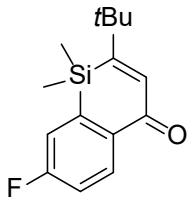

In a dry two-neck round-bottom flask charged with a stir bar under N_2 atmosphere, **2.3b** (200 mg, 762 μmol, 1.00 equiv) was dissolved in anhydrous hexanes (7.62 mL) and cooled to 0 °C. *n*-BuLi (2.5 M solution in hexanes, 672 μL, 1.68 mmol, 2.20 equiv) was added dropwise and the mixture was stirred for 30 minutes, with full consumption of the starting material by TLC (hexanes). Anhydrous THF (7.62 mL) was added, followed by addition of DMDCS (165 μL, 1.83 mmol, 2.40 equiv) and the mixture was warmed to rt and stirred for 16 h. The mixture was quenched with saturated NH_4Cl, extracted with DCM (25 mL × 3) and washed with water and brine. The crude product was dried with Na_2SO_4, evaporated to give a yellow oil (labeled as **2.4c** in the manuscript). The crude oil was dissolved in 1,4-dioxane (7.62 mL) and transferred to a scintillation vial charged with a stir bar and fitted with a PTFE-lined cap. SeO_2 (93.0 mg, 838 μmol, 1.10 equiv) was added and the mixture was heated at 100 °C for 1 h, with full consumption of the starting material by TLC (hexanes). The mixture was cooled to rt, evaporated onto silica and purified via flash chromatography, eluting with 50:1 hexanes:EtOAc to give **2.5c** as a yellow solid (100 mg, 381 μmol, 50%). R_F = 0.41 in 40:1 hexanes:EtOAc. ^{1}H NMR (500 MHz, $CDCl_3$) δ 8.24 (dd, *J* = 8.8, 5.4 Hz, 1H), 7.21 (dd, *J* = 8.1, 2.7 Hz, 1H), 7.13 (td, *J* = 8.7, 2.7 Hz, 1H), 6.92 (s, 1H), 1.24 (s, 9H), 0.48 (s, 6H). ^{13}C NMR (126 MHz, $CDCl_3$) δ 206.64, 187.34, 169.84, 164.75 (d, *J* = 256.9 Hz), 143.63 (d, *J* = 5.5 Hz), 139.84, 135.11 (d, *J* = 2.8 Hz), 131.14 (d, *J* = 8.2 Hz), 118.30 (d, *J* = 19.3 Hz), 116.68 (d, *J* = 21.9 Hz), 38.29, 30.35, -0.00. HRMS (DART-MS): calculated for $C_{15}H_{19}FOSi$ $[M+1]^+$, 263.1189; found 263.1255.

Synthesis of 7-(dimethylamino)-1,1-dimethyl-2-phenylbenzo[*b*]silin-4(*1H*)-one (**2.6a**).

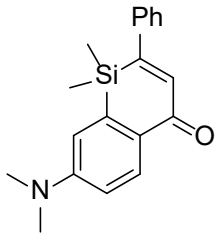

In a two-neck round-bottom flask charged with a stir bar and fitted with a reflux condenser, **2.5a** (400 mg, 1.42 mmol, 1.00 equiv) and silica gel (80.0 mg, 20 wt%) were dissolved in DMSO (14.2 mL). Dimethylamine (40 wt% in water, 1.08 mL, 8.52 mmol, 6.00 equiv) and DIPEA (989 μL, 5.68 mmol, 4.00 equiv) were added and the mixture was stirred at 70 °C for 16 h, with full consumption of the starting material by TLC (40:1 hexanes:EtOAc). The mixture was cooled to rt, quenched with saturated NH_4Cl, extracted with DCM (50 mL × 3) and washed with water and brine. The crude product was dried with Na_2SO_4, evaporated onto silica and purified via flash chromatography, eluting with 10:1 hexanes:EtOAc to give **2.6a** as a yellow solid (403 mg, 1.31 mmol, 92%). R_F = 0.41 in 4:1 hexanes:EtOAc. HRMS (ESI-MS): calculated for $C_{19}H_{21}NOSi$ $[M+1]^+$, 308.1392; found, 308.1487. ^{1}H NMR (500 MHz, $CDCl_3$) δ 8.29 – 8.17 (m, 1H), 7.41 (ddd, J = 28.4, 22.0, 7.1 Hz, 5H), 7.15 – 7.07 (m, 1H), 6.84 – 6.74 (m, 2H), 3.09 (s, 6H), 0.49 (s, 6H). ^{13}C NMR (126 MHz, $CDCl_3$) δ 188.53, 158.32, 158.30, 151.94, 143.61, 135.52, 132.38, 130.50, 130.16, 129.76, 128.12, 118.32, 116.77, 115.26, 47.13, 0.00. HRMS (ESI-MS): calculated for $C_{19}H_{21}NOSi$ $[M+1]^+$, 308.1392; found, 308.1487.

Synthesis of 7-(bis(methyl-d_3)amino)-1,1-dimethyl-2-phenylbenzo[*b*]silin-4(*1H*)-one (**2.6b**).

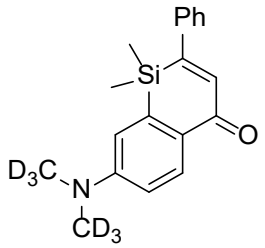

In a scintillation vial charged with a stir bar and fitted with a PTFE-lined cap, **2.5a** (100 mg, 0.355 mmol, 1.00 equiv) and silica gel (20.0 mg, 20 wt%) were dissolved in DMSO (3.55 mL). Dimethyl-d_6-amine hydrochloride (187 mg, 2.13 mmol, 6.00 equiv) and DIPEA (494 μL, 2.84 mmol, 8.00 equiv) were added and the mixture was stirred at 70 °C for 16 h, with full consumption of the starting material by TLC (40:1 hexanes:EtOAc). The mixture was cooled to rt, quenched with saturated NH_4Cl, extracted with DCM (10 mL × 3) and washed with water and brine. The crude product was dried with Na_2SO_4, evaporated onto silica and purified via flash chromatography, eluting with 10:1 hexanes:EtOAc to give **2.6b** as a yellow solid (69.0 mg, 0.220 mmol, 62%). R_F = 0.41 in 4:1 hexanes:EtOAc. ^{1}H NMR (600 MHz, $CDCl_3$) δ 8.23 (d, *J* = 9.0 Hz, 1H), 7.48 – 7.44 (m, 2H), 7.41 (td, *J* = 7.0, 1.2 Hz, 2H), 7.36 (d, *J* = 7.3 Hz, 1H), 7.11 (s, 1H), 6.81 (dd, *J* = 9.0, 2.8 Hz, 1H), 6.76 (d, *J* = 2.8 Hz, 1H), 0.49 (s, 6H). ^{13}C NMR (151 MHz, $CDCl_3$) δ 188.32, 157.87, 153.23, 143.62, 142.50, 142.25, 131.94, 129.96, 129.49, 128.88, 127.95, 115.22, 114.11, 40.58 – 40.03 (q, *J* = 17.6 Hz), -0.00. HRMS (ESI-MS): calculated for $C_{19}H_{15}D_6NOSi$ $[M+1]^+$, 314.1769; found, 314.1855.

Synthesis of 1,1-dimethyl-2-phenyl-7-(pyrrolidin-1-yl)benzo[*b*]silin-4(*1H*)-one (**2.6c**).

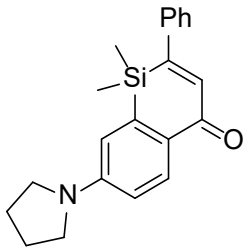

In a scintillation vial charged with a stir bar and fitted with a PTFE-lined cap, **2.5a** (100 mg, 0.355 mmol, 1.00 equiv) and silica gel (20.0 mg, 20 wt%) were dissolved in DMSO (3.55 mL). Pyrrolidine (175 μL, 2.13 mmol, 6.00 equiv) and DIPEA (247 μL, 1.42 mmol, 4.00 equiv) were added and the mixture was stirred at 70 °C for 5 h, with full consumption of the starting material by TLC (40:1 hexanes:EtOAc). The mixture was cooled to rt, quenched with saturated NH_4Cl, extracted with DCM (10 mL × 3) and washed with water and brine. The crude product was dried with Na_2SO_4, evaporated onto silica and purified via flash chromatography, eluting with 10:1 hexanes:EtOAc to give **2.6c** as a yellow solid (100 mg, 0.302 mmol, 62%). R_F = 0.44 in 4:1 hexanes:EtOAc. ^{1}H NMR (500 MHz, $CDCl_3$) δ 8.23 (dd, *J* = 8.8, 2.8 Hz, 1H), 7.49 – 7.35 (m, 5H), 7.11 (dd, *J* = 7.9, 2.6 Hz, 1H), 6.72 – 6.61 (m, 2H), 3.43 (qd, *J* = 6.7, 4.2 Hz, 4H), 2.13 – 2.04 (m, 4H), 0.48 (d, *J* = 3.0 Hz, 6H). ^{13}C NMR (126 MHz, $CDCl_3$) δ 187.16, 149.65, 142.64, 141.40, 130.99, 128.80, 128.30, 127.33, 126.83, 114.21, 113.14, 47.56, 25.48, -1.13. HRMS (ESI-MS): calculated for $C_{21}H_{23}NOSi$ $[M+1]^+$, 334.1549; found, 334.1736.

Synthesis of 7-(dimethylamino)-1-methyl-1,2-diphenylbenzo[*b*]silin-4(*1H*)-one (**2.6d**).

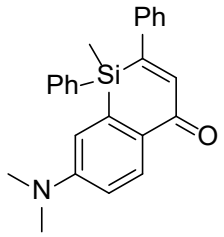

In a scintillation vial charged with a stir bar and fitted with a PTFE-lined cap, **2.5b** (80 mg, 0.23 mmol, 1.0 equiv) and silica gel (16 mg, 20 wt%) were dissolved in DMSO (2.3 mL). Dimethylamine (40 wt% in water, 180 μL, 1.4 mmol, 6.0 equiv) and DIPEA (160 μL, 0.92 mmol, 4.0 equiv) were added and the mixture was stirred at 70 °C for 16 h, with full consumption of the starting material by TLC (40:1 hexanes:EtOAc). The mixture was cooled to rt, quenched with saturated NH_4Cl, extracted with DCM (10 mL × 3) and washed with water and brine. The crude product was dried with Na_2SO_4, evaporated onto silica and purified via flash chromatography, eluting with 10:1 hexanes:EtOAc to give **2.6d** as a mixture of isomers (yellow solid, 52 mg, 0.14 mmol, 59%). R_F = 0.43 in 4:1 hexanes:EtOAc. ^{1}H NMR (500 MHz, $CDCl_3$) δ 8.29 – 8.21 (m, 1H), 7.58 – 7.45 (m, 3H), 7.36 – 7.27 (m, 8H), 6.80 (dd, *J* = 9.6, 3.5 Hz, 1H), 6.66 (t, *J* = 3.0 Hz, 1H), 3.02 – 2.96 (m, 6H), 0.76 (s, 3H). ^{13}C NMR (126 MHz, $CDCl_3$) Major isomer δ: 187.33, 154.73, 152.00, 144.64, 143.30, 140.93, 134.64, 133.85, 133.28, 130.82, 129.95, 128.68, 128.47, 128.41, 128.08, 127.66, 126.20, 115.02, 113.17, 110.86, 40.04, -4.08. Minor isomer δ: 187.33, 154.73, 152.00, 144.64, 143.30, 140.93, 134.64, 133.85, 133.28, 130.82, 129.95, 128.68, 128.47, 128.29, 127.94, 127.08, 126.20, 115.02, 113.17, 110.86, 40.04, -4.30. HRMS (ESI-MS): calculated for $C_{24}H_{23}NOSi$ $[M+1]^+$, 370.1549; found, 370.1631.

Synthesis of 2-(*tert*-butyl)-7-(dimethylamino)-1,1-dimethylbenzo[*b*]silin-4(*1H*)-one (**2.6e**).

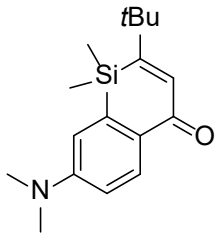

In a scintillation vial charged with a stir bar and fitted with a PTFE-lined cap, **2.5c** (80 mg, 0.30 mmol, 1.0 equiv) and silica gel (16 mg, 20 wt%) were dissolved in DMSO (3.0 mL). Dimethylamine (40 wt% in water, 240 μL, 1.8 mmol, 6.0 equiv) and DIPEA (200 μL, 1.2 mmol, 4.0 equiv) were added and the mixture was stirred at 70 °C for 16 h, with full consumption of the starting material by TLC (40:1 hexanes:EtOAc). The mixture was cooled to rt, quenched with saturated NH_4Cl, extracted with DCM (10 mL × 3) and washed with water and brine. The crude product was dried with Na_2SO_4, evaporated onto silica and purified via flash chromatography, eluting with 10:1 hexanes:EtOAc to give **2.6e** as a yellow solid (37 mg, 0.13 mmol, 44%). R_F = 0.46 in 4:1 hexanes:EtOAc. ^{1}H NMR (500 MHz, $CDCl_3$) δ 8.14 (d, J = 8.9 Hz, 1H), 6.89 (s, 1H), 6.78 (dd, J = 8.9, 2.7 Hz, 1H), 6.71 (d, J = 2.7 Hz, 1H), 3.08 (s, 6H), 1.24 (s, 9H), 0.47 (s, 6H). ^{13}C NMR (126 MHz, $CDCl_3$) δ 187.13, 167.09, 151.21, 141.40, 140.06, 129.51, 126.83, 112.97, 112.00, 39.25, 37.56, 30.00, 0.00. HRMS (ESI-MS): calculated for $C_{17}H_{25}NOSi$, 288.1705; found, 288.1795.

Synthesis of *N*-(4-((1*E*,3*E*,5*E*)-5-(7-(dimethylamino)-1,1-dimethyl-2-phenylbenzo[*b*]silin-4(*1H*)-ylidene)penta-1,3-dien-1-yl)-1,1-dimethyl-2-phenylbenzo[*b*]silin-7(*1H*)-ylidene)-*N*-methylmethanaminium tetrafluoroborate (**2.11**, SiliFlav5).

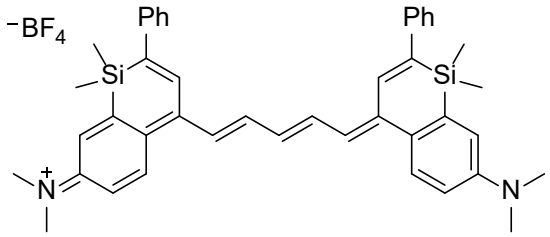

In a dry round-bottom flask charged with a stir bar under N_2 atmosphere, **2.6a** (30 mg, 98 μmol, 1.0 equiv) was dissolved in anhydrous THF (0.98 mL) and cooled to 0 °C. MeMgBr (1.5 M solution in THF, 0.26 mL, 0.39 mmol, 4.0 equiv) was added dropwise and the mixture was warmed to rt and stirred for 1 h, with full consumption of the starting material by TLC (4:1 hexanes:EtOAc). The mixture was quenched with saturated NH_4Cl, extracted with DCM (5 mL × 3) and washed with water and brine, then dried with Na_2SO_4 and evaporated to afford the crude product (referenced as **2.7a** in the manuscript) as a tan solid. The crude material was transferred to a scintillation vial charged with a stir bar and fitted with a PTFE-lined cap and linker **2.8** (13 mg, 49 μmol, 0.50 equiv) was added. The solids were dissolved in 1:1 AcOH:Ac_2O (vol:vol, 9.8 mL) and stirred at 110 °C for 30 min. The mixture was cooled to rt, filtered through a silica plug to remove the AcOH:Ac_2O, then flushed with 10:1 DCM:MeOH to elute the crude product. The crude product was evaporated and purified using reverse-phase preparatory HPLC, eluting with a gradient of 80% to 100% MeCN in H_2O to afford **2.11** as a dark blue solid (11 mg, 15 μmol, 31%). R_F = 0.23 in 50:1 DCM:MeOH. ^{1}H NMR (500 MHz, CD_2Cl_2) δ 8.15 (d, J = 9.4 Hz, 2H), 8.05 – 7.84 (m, 4H), 7.44 (ddd, J = 31.3, 22.0, 7.6 Hz, 12H), 7.15 – 7.00 (m, 5H), 3.28 (s, 12H), 0.49 (d, J = 3.0 Hz, 12H). HRMS (ESI-MS): calculated for $C_{43}H_{47}N_2Si_2^+$, 647.3272; found, 647.3580.

Synthesis of *N*-(4-((1*E*,3*E*,5*E*,7*E*)-7-(7-(dimethylamino)-1,1-dimethyl-2-phenylbenzo[*b*]silin-4(1*H*)-ylidene)hepta-1,3,5-trien-1-yl)-1,1-dimethyl-2-phenylbenzo[*b*]silin-7(1*H*)-ylidene)-*N*-methylmethanaminium tetrafluoroborate (**2.12**, SiliFlav7).

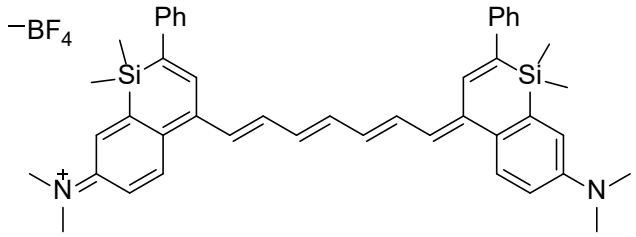

In a dry round-bottom flask charged with a stir bar under N_2 atmosphere, **2.6a** (30 mg, 98 μmol, 1.0 equiv) was dissolved in anhydrous THF (0.98 mL) and cooled to 0 °C. MeMgBr (1.5 M solution in THF, 0.26 mL, 0.39 mmol, 4.0 equiv) was added dropwise and the mixture was warmed to rt and stirred for 1 h, with full consumption of the starting material by TLC (4:1 hexanes:EtOAc). The mixture was quenched with saturated NH_4Cl, extracted with DCM (5 mL × 3) and washed with water and brine, then dried with Na_2SO_4 and evaporated to afford the crude product (referenced as **2.7a** in the manuscript) as a tan solid. The crude material was transferred to a scintillation vial charged with a stir bar and fitted with a PTFE-lined cap and linker **2.9** (14 mg, 49 μmol, 0.50 equiv) was added. The solids were dissolved in 1:1 AcOH:Ac_2O (vol:vol, 9.8 mL) and stirred at 110 °C for 30 min. The mixture was cooled to rt, filtered through a silica plug to remove the AcOH:Ac_2O, then flushed with 10:1 DCM:MeOH to elute the crude product. The crude product was evaporated and purified using reverse-phase preparatory HPLC, eluting with a gradient of 80% to 100% MeCN in H_2O to afford **2.12** as a dark blue solid (4.5 mg, 5.9 μmol, 12%). R_F = 0.21 in 50:1 DCM:MeOH. ^{1}H NMR (600 MHz, CD_2Cl_2) δ 8.00 (d, *J* = 9.6 Hz, 2H), 7.81 (s, 2H), 7.72 (t, *J* = 12.9 Hz, 2H), 7.49 – 7.27 (m, 14H), 7.24 (s, 1H), 6.94 (s, 2H), 6.85 (d, *J* = 12.2 Hz, 4H), 3.17 (s, 12H), 0.41 (d, *J* = 2.2 Hz, 12H). ^{19}F NMR (565 MHz, CD_2Cl_2) δ -153.25. HRMS (ESI-MS): calculated for $C_{45}H_{49}N_2Si_2^+$, 673.3429; found, 673.3744.

Synthesis of *N*-(4-((1*E*,3*E*,5*E*,7*E*,9*E*)-9-(7-(dimethylamino)-1,1-dimethyl-2-phenylbenzo[*b*]silin-4(1*H*)-ylidene)nona-1,3,5,7-tetraen-1-yl)-1,1-dimethyl-2-phenylbenzo[*b*]silin-7(1*H*)-ylidene)-*N*-methylmethanaminium tetrafluoroborate (**2.13,** SiliFlav9).

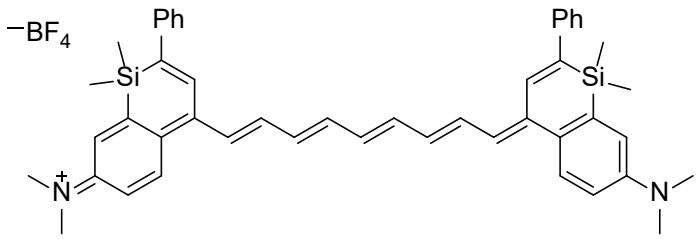

In a dry round-bottom flask charged with a stir bar under N_2 atmosphere, **2.6a** (30 mg, 98 μmol, 1.0 equiv) was dissolved in anhydrous THF (0.98 mL) and cooled to 0 °C. MeMgBr (1.5 M solution in THF, 0.26 mL, 0.39 mmol, 4.0 equiv) was added dropwise and the mixture was warmed to rt and stirred for 1 h, with full consumption of the starting material by TLC (4:1 hexanes:EtOAc). The mixture was quenched with saturated NH_4Cl, extracted with DCM (5 mL × 3) and washed with water and brine, then dried with Na_2SO_4 and evaporated to afford the crude product (referenced as **2.7a** in the manuscript) as a tan solid. The crude material was transferred to a scintillation vial charged with a stir bar and fitted with a PTFE-lined cap and linker **2.10** (15 mg, 49 μmol, 0.50 equiv) was added. The solids were dissolved in 1:1 AcOH:Ac_2O (vol:vol, 9.8 mL) and stirred at 110 °C for 30 min. The mixture was cooled to rt, filtered through a silica plug to remove the AcOH:Ac_2O, then flushed with 10:1 DCM:MeOH to elute the crude product. The crude product was evaporated and purified using reverse-phase preparatory HPLC, eluting with a gradient of 80% to 100% MeCN in H_2O to afford **13** as a dark green solid (5.8 mg, 7.4 μmol, 16%). R_F = 0.21 50:1 DCM:MeOH. ^{1}H NMR (600 MHz, CD_2Cl_2) δ 8.04 (s, 2H), 7.87 (s, 2H), 7.72 (s, 2H), 7.48 (dd, *J* = 14.2, 7.5 Hz, 10H), 7.40 (s, 3H), 7.17 (s, 2H), 7.01 (d, *J* = 2.8 Hz, 2H), 6.90 (d, *J* = 9.2 Hz, 2H), 6.84 (s, 2H), 3.24 (s, 12H), 0.48 (s, 12H). ^{19}F NMR (565 MHz, CD_2Cl_2) δ -153.26. HRMS (ESI-MS): calculated for $C_{47}H_{51}N_2Si_2^+$, 699.3585; found, 699.3825.

Synthesis of *N*-(4-((1*E*,3*E*,5*E*)-5-(7-(bis(methyl-d_3)amino)-1,1-dimethyl-2-phenylbenzo[*b*]silin-4(*1H*)-ylidene)penta-1,3-dien-1-yl)-1,1-dimethyl-2-phenylbenzo[*b*]silin-7(*1H*)-ylidene)-N-(methyl-d_3)methanaminium-d_3 tetrafluoroborate (**2.14**, SiliFlav5-d_{12}).

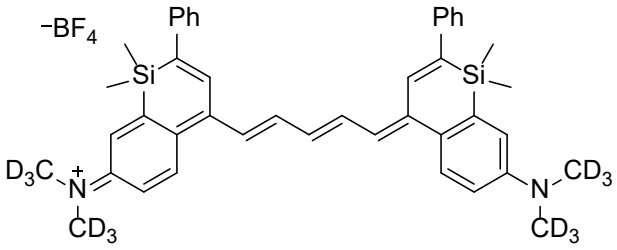

In a dry round-bottom flask charged with a stir bar under N_2 atmosphere, **2.6b** (30 mg, 96 μmol, 1.0 equiv) was dissolved in anhydrous THF (0.96 mL) and cooled to 0 °C. MeMgBr (1.5 M solution in THF, 0.25 mL, 0.38 mmol, 4.0 equiv) was added dropwise and the mixture was warmed to rt and stirred for 1 h, with full consumption of the starting material by TLC (4:1 hexanes:EtOAc). The mixture was quenched with saturated NH_4Cl, extracted with DCM (5 mL × 3) and washed with water and brine, then dried with Na_2SO_4 and evaporated to afford the crude product (referenced as **2.7b** in the manuscript) as a tan solid. The crude material was transferred to a scintillation vial charged with a stir bar and fitted with a PTFE-lined cap and linker **2.8** (13 mg, 48 μmol, 0.50 equiv) was added. The solids were dissolved in 1:1 AcOH:Ac_2O (vol:vol, 9.6 mL) and stirred at 110 °C for 30 min. The mixture was cooled to rt, filtered through a silica plug to remove the AcOH:Ac_2O, then flushed with 10:1 DCM:MeOH to elute the crude product. The crude product was evaporated and purified using reverse-phase preparatory HPLC, eluting with a gradient of 80% to 100% MeCN in H_2O to afford **2.14** as a dark blue solid (3.2 mg, 4.3 μmol, 9%). R_F = 0.23 in 50:1 DCM:MeOH. ^{1}H NMR (600 MHz, CD_2Cl_2) δ 8.04 (d, J = 9.2 Hz, 2H), 7.91 (s, 2H), 7.85 (s, 2H), 7.39 (dd, J = 18.6, 11.3 Hz, 10H), 7.33 (d, J = 7.6 Hz, 2H), 6.99 (d, J = 12.1 Hz, 1H), 6.92 (d, J = 2.7 Hz, 2H), 6.82 (d, J = 9.4 Hz, 2H), 0.42 (d, J = 1.5 Hz, 12H). ^{19}F NMR (565 MHz, CD_2Cl_2) δ -153.26. HRMS (ESI-MS): calculated for $C_{43}H_{35}D_{12}N_2Si_2^+$, 659.4025; found, 659.4264.

Synthesis of 1-(4-((1*E*,3*E*,5*E*)-5-(1,1-dimethyl-2-phenyl-7-(pyrrolidin-1-yl)benzo[*b*]silin-4(*1H*)-ylidene)penta-1,3-dien-1-yl)-1,1-dimethyl-2-phenylbenzo[*b*]silin-7(*1H*)-ylidene)pyrrolidin-1-ium tetrafluoroborate (**2.15**, Py-SiliFlav5).

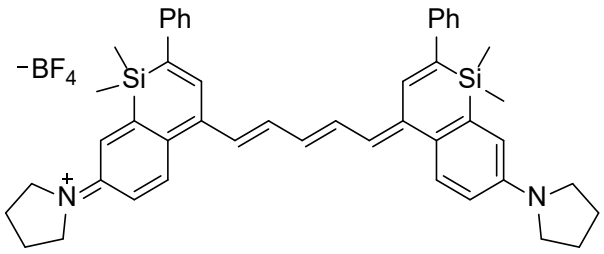

In a dry round-bottom flask charged with a stir bar under N_2 atmosphere, **2.6c** (30 mg, 72 μmol, 1.0 equiv) was dissolved in anhydrous THF (0.72 mL) and cooled to 0 °C. MeMgBr (1.5 M solution in THF, 0.23 mL, 0.17 mmol, 4.0 equiv) was added dropwise and the mixture was warmed to rt and stirred for 1 h, with full consumption of the starting material by TLC (4:1 hexanes:EtOAc). The mixture was quenched with saturated NH_4Cl, extracted with DCM (5 mL × 3) and washed with water and brine, then dried with Na_2SO_4 and evaporated to afford the crude product (referenced as **2.7c** in the manuscript) as a tan solid. The crude material was transferred to a scintillation vial charged with a stir bar and fitted with a PTFE-lined cap and linker **2.8** (9.6 mg, 36 μmol, 0.50 equiv) was added. The solids were dissolved in 1:1 AcOH:Ac_2O (vol:vol, 7.2 mL) and stirred at 110 °C for 30 min. The mixture was cooled to rt, filtered through a silica plug to remove the AcOH:Ac_2O, then flushed with 10:1 DCM:MeOH to elute the crude product. The crude product was evaporated and purified using reverse-phase preparatory HPLC, eluting with a gradient of 80% to 100% MeCN in H_2O to afford **2.15** as a dark blue solid (6.0 mg, 13 μmol, 37%). R_F = 0.26 in 50:1 DCM:MeOH. ^{1}H NMR (500 MHz, CD_2Cl_2) δ 8.12 (d, *J* = 9.0 Hz, 2H), 7.95 (d, *J* = 21.9 Hz, 4H), 7.52 – 7.45 (m, 10H), 7.41 (d, *J* = 7.2 Hz, 2H), 7.10 – 6.98 (m, 1H), 6.90 (d, *J* = 2.4 Hz, 2H), 6.83 – 6.76 (m, 2H), 3.59 (d, *J* = 6.9 Hz, 8H), 2.15 – 2.12 (m, 8H), 0.50 (s, 12H). ^{19}F NMR (565 MHz, CD_2Cl_2) δ -153.26. HRMS (ESI-MS): calculated for $C_{47}H_{51}N_2Si_2^+$, 699.3585; found, 699.3834.

Synthesis of *N*-(4-((1*E*,3*E*,5*E*)-5-(7-(dimethylamino)-1-methyl-1,2-diphenylbenzo[*b*]silin-4(1*H*)-ylidene)penta-1,3-dien-1-yl)-1-methyl-1,2-diphenylbenzo[*b*]silin-7(1*H*)-ylidene)-*N*-methylmethanaminium tetrafluoroborate (**2.16**, Sili(MePh)Flav5).

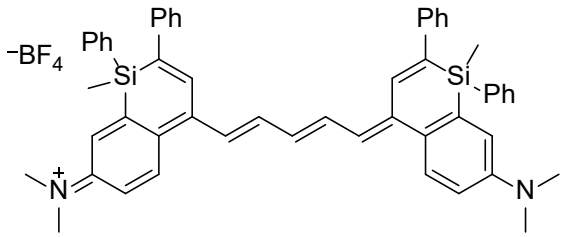

In a dry round-bottom flask charged with a stir bar under N_2 atmosphere, **2.6d** (30 mg, 81 μmol, 1.0 equiv) was dissolved in anhydrous THF (0.81 mL) and cooled to 0 °C. MeMgBr (1.5 M solution in THF, 0.26 mL, 0.19 mmol, 4.0 equiv) was added dropwise and the mixture was warmed to rt and stirred for 1 h, with full consumption of the starting material by TLC (4:1 hexanes:EtOAc). The mixture was quenched with saturated NH_4Cl, extracted with DCM (5 mL × 3) and washed with water and brine, then dried with Na_2SO_4 and evaporated to afford the crude product (referenced as **2.7d** in the manuscript) as a tan solid. The crude material was transferred to a scintillation vial charged with a stir bar and fitted with a PTFE-lined cap and linker **2.8** (11 mg, 41 μmol, 0.50 equiv) was added. The solids were dissolved in 1:1 AcOH:Ac_2O (vol:vol, 8.1 mL) and stirred at 110 °C for 30 min. The mixture was cooled to rt, filtered through a silica plug to remove the AcOH:Ac_2O, then flushed with 10:1 DCM:MeOH to elute the crude product. The crude product was evaporated and purified using reverse-phase preparatory HPLC, eluting with a gradient of 80% to 100% MeCN in H_2O to afford **2.16** as a dark blue solid (6.4 mg, 7.4 μmol, 18%). R_F = 0.24 in 50:1 DCM:MeOH. ^{1}H NMR (500 MHz, CD_2Cl_2) δ 8.22 – 8.02 (m, 6H), 7.59 (d, *J* = 13.4 Hz, 2H), 7.55 – 7.52 (m, 4H), 7.42 (dddd, *J* = 6.2, 4.6, 3.2, 1.5 Hz, 6H), 7.36 (qdd, *J* = 6.8, 3.4, 2.0 Hz, 10H), 7.15 (t, *J* = 12.5 Hz, 1H), 6.98 – 6.87 (m, 4H), 3.19 (s, 12H), 0.82 (d, *J* = 2.4 Hz, 6H). ^{19}F NMR (565 MHz, CD_2Cl_2) δ -153.19. HRMS (ESI-MS): calculated for $C_{53}H_{51}N_2Si_2^+$, 771.3585; found, 771.3872.

Synthesis of *N*-(2-(*tert*-butyl)-4-((1*E*,3*E*,5*E*)-5-(2-(*tert*-butyl)-7-(dimethylamino)-1,1-dimethylbenzo[*b*]silin-4(*1H*)-ylidene)penta-1,3-dien-1-yl)-1,1-dimethylbenzo[*b*]silin-7(*1H*)-ylidene)-*N*-methylmethanaminium tetrafluoroborate (**2.17**, SiliChrom5).

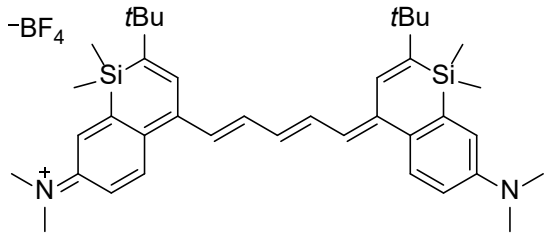

In a dry round-bottom flask charged with a stir bar under N_2 atmosphere, **2.6e** (30 mg, 0.11 mmol, 1.0 equiv) was dissolved in anhydrous THF (1.1 mL) and cooled to 0 °C. MeMgBr (1.5 M solution in THF, 0.35 mL, 0.26 mmol, 4.0 equiv) was added dropwise and the mixture was warmed to rt and stirred for 1 h, with full consumption of the starting material by TLC (4:1 hexanes:EtOAc). The mixture was quenched with saturated NH_4Cl, extracted with DCM (5 mL × 3) and washed with water and brine, then dried with Na_2SO_4 and evaporated to afford the crude product (referenced as **2.7e** in the manuscript) as a tan solid. The crude material was transferred to a scintillation vial charged with a stir bar and fitted with a PTFE-lined cap and linker **2.8** (15 mg, 55 μmol, 0.50 equiv) was added. The solids were dissolved in 1:1 AcOH:Ac_2O (vol:vol, 11 mL) and stirred at 110 °C for 30 min. The mixture was cooled to rt, filtered through a silica plug to remove the AcOH:Ac_2O, then flushed with 10:1 DCM:MeOH to elute the crude product. The crude product was evaporated and purified using reverse-phase preparatory HPLC, eluting with a gradient of 80% to 100% MeCN in H_2O to afford **2.17** as a dark purple solid (9.7 mg, 14 μmol, 18%). R_F = 0.30 in 50:1 DCM:MeOH. ^{1}H NMR (500 MHz, CD_2Cl_2) δ 8.04 (d, *J* = 9.4 Hz, 2H), 7.90 (t, *J* = 12.9 Hz, 2H), 7.71 (s, 2H), 7.38 – 7.34 (m, 2H), 6.99 (d, *J* = 12.6 Hz, 1H), 6.95 (d, *J* = 2.9 Hz, 2H), 6.87 (dd, *J* = 9.3, 2.9 Hz, 2H), 3.24 (s, 12H), 1.33 (s, 18H), 0.49 (s, 12H). ^{19}F NMR (565 MHz, CD_2Cl_2) δ -153.19. HRMS (ESI-MS): calculated for $C_{53}H_{51}N_2Si_2^+$, 607.3898; found, 607.4137.

Synthesis of *N*-(4-((1*E*,3*E*,5*E*)-5-(7-(dimethylamino)-1,1-dimethyl-2-phenylbenzo[*b*]silin-4(*1H*)-ylidene)penta-1,3-dien-1-yl)-1,1-dimethyl-2-phenylbenzo[*b*]silin-7(*1H*)-ylidene)-*N*-methylmethanaminium tetrakis[3,5-bis(perfluorohexyl)phenyl]borate (**2.11•BArF$_{24}$**).

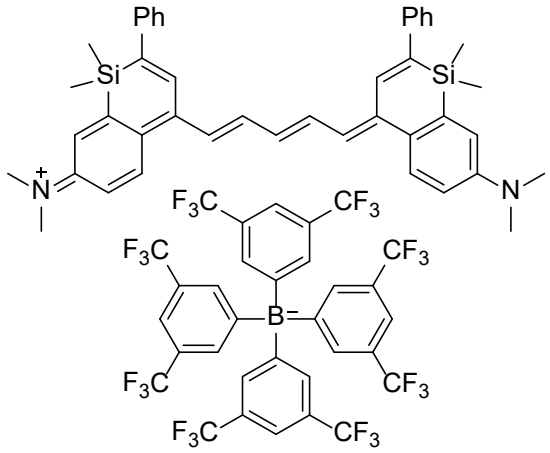

In a scintillation vial containing **2.11** (5.0 mg, 7.0 μmol, 1.0 equiv) and sodium tetrakis(3,5-bis(trifluoromethyl)phenyl)borate (22 mg, 7.5 μmol, 1.1 equiv), DCM (1.4 mL) and water (1.4 mL) were added and the mixture was sonicated for 1 min. The DCM layer was collected, dried with Na_2SO_4 and concentrated. The crude product was purified via column chromatography, eluting with DCM to yield **2.11•BArF$_{24}$** as a dark blue solid (21 mg, 6.1 μmol, 87%). R_F = 0.61 in 50:1 DCM:MeOH. ^{1}H NMR (600 MHz, CD_2Cl_2) δ 8.07 (d, *J* = 9.4 Hz, 2H), 7.97 (t, *J* = 12.9 Hz, 2H), 7.90 (s, 2H), 7.68 (dd, *J* = 5.2, 2.6 Hz, 8H), 7.52 (s, 4H), 7.48 – 7.42 (m, 10H), 7.40 – 7.36 (m, 2H), 7.03 – 6.96 (m, 3H), 6.86 (dd, *J* = 9.4, 2.8 Hz, 2H), 3.22 (s, 12H), 0.46 (s, 12H). ^{19}F NMR (151 MHz, CD_2Cl_2) δ 152.13, 138.10, 136.82, 133.84, 131.07, 128.87, 120.55, 119.48, 116.09, 42.38, 31.73, 0.90.

Synthesis of 7-(azetidin-1-yl)-1,1-dimethyl-2-phenylbenzo[*b*]silin-4(1*H*)-one (**2.19**).

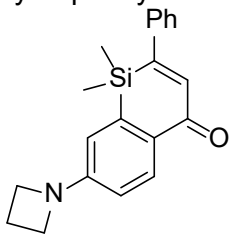

In a scintillation vial charged with a stir bar and fitted with a PTFE-lined cap, **2.5a** (50 mg, 0.18 mmol, 1.0 equiv) and silica gel (10 mg, 20 wt%) were dissolved in DMSO (1.8 mL). Azetidine (74 μL, 1.1 mmol, 6.00 equiv) and DIPEA (0.12 mL, 0.71 mmol, 4.0 equiv) were added and the mixture was stirred at 70 °C for 16 h, with full consumption of the starting material by TLC (40:1 hexanes:EtOAc). The mixture was cooled to rt, quenched with saturated NH_4Cl, extracted with DCM (5 mL × 3) and washed with water and brine. The crude product was dried with Na_2SO_4, evaporated onto silica and purified via flash chromatography, eluting with 10:1 hexanes:EtOAc to give **2.19** as a yellow solid (42 mg, 0.13 mmol, 70%). R_F = 0.43 in 4:1 hexanes:EtOAc. ^{1}H NMR (500 MHz, $CDCl_3$) δ 8.20 (dd, *J* = 8.7, 1.9 Hz, 1H), 7.49 – 7.30 (m, 5H), 7.10 (t, *J* = 2.5 Hz, 1H), 6.58 – 6.41 (m, 2H), 4.11 – 3.98 (m, 4H), 2.45 (qd, *J* = 8.2, 3.6 Hz, 2H), 0.47 (d, *J* = 2.0 Hz, 6H). ^{13}C NMR (126 MHz, $CDCl_3$) δ 187.19, 156.65, 152.97, 142.43, 141.29, 141.05, 130.64, 128.81, 128.43, 128.36, 126.79, 112.95, 111.85, 51.63, 16.62, -1.23. HRMS (ESI-MS): calculated for $C_{20}H_{21}NOSi$ $[M+1]^+$, 320.1392; found, 320.1627.

Synthesis of 7-(allylamino)-1,1-dimethyl-2-phenylbenzo[*b*]silin-4(1*H*)-one (**2.20**).

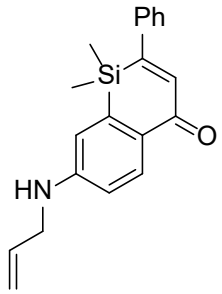

In a scintillation vial charged with a stir bar and fitted with a PTFE-lined cap, **2.5a** (100 mg, 0.355 mmol, 1.00 equiv) and silica gel (20.0 mg, 20 wt%) were dissolved in DMSO (3.55 mL). Allylamine (159 μL, 2.13 mmol, 6.00 equiv) and DIPEA (247 μL, 1.42 mmol, 4.00 equiv) were added and the mixture was stirred at 70 °C for 4 h, with full consumption of the starting material by TLC (40:1 hexanes:EtOAc). The mixture was cooled to rt, quenched with saturated NH_4Cl, extracted with DCM (10 mL × 3) and washed with water and brine. The crude product was dried with Na_2SO_4, evaporated onto silica gel and purified via flash chromatography, eluting with 10:1 hexanes:EtOAc to give **2.20** as a yellow solid (51 mg, 160 μmol, 45%). R_F = 0.47 in 4:1 hexanes:EtOAc. ^{1}H NMR (500 MHz, $CDCl_3$) δ 8.22 – 8.15 (m, 1H), 7.46 – 7.39 (m, 4H), 7.36 (d, *J* = 7.2 Hz, 1H), 7.10 (s, 1H), 6.73 (s, 2H), 5.95 (ddt, *J* = 17.2, 10.5, 5.3 Hz, 1H), 5.31 (dt, *J* = 17.2, 1.6 Hz, 1H), 5.23 (dd, *J* = 10.4, 1.5 Hz, 1H), 4.41 (s, 1H), 3.89 (t, *J* = 5.2 Hz, 2H), 0.46 (s, 6H). ^{13}C NMR (126 MHz, $CDCl_3$) δ 188.53, 158.30, 151.94, 143.61, 142.81, 142.56, 135.52, 132.38, 130.28, 130.16, 129.76, 128.11, 118.32, 116.77, 115.26, 47.13, 0.00. HRMS (ESI-MS): calculated for $C_{20}H_{21}NOSi$ $[M+1]^+$, 320.1392; found, 320.1584.

Synthesis of 7-amino-1,1-dimethyl-2-phenylbenzo[*b*]silin-4(1*H*)-one (**2.21**).

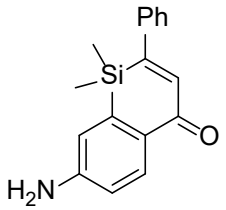

In a two-neck round-bottom flask charged with a stir bar under N_2 atmosphere, **2.20** (50.0 mg, 157 μmol, 1.00 equiv), *N,N*-dimethylbarbituric acid (244 mg, 1.57 mmol, 10.0 equiv) and tetrakis(triphenylphosphine)palladium(0) (18.1 mg, 15.7 μmol, 10 mol%) were dissolved in anhydrous, deoxygenated DCM (1.57 mL) and the mixture was stirred for 24 h, with full consumption of the starting material by TLC (10:1 hexanes:EtOAc). The mixture was evaporated onto silica and purified via flash chromatography, eluting with 4:1 hexanes:EtOAc to give **2.21** as a bright yellow solid (24.9 mg, 89.2 μmol, 57%). R_F = 0.37 in 4:1 hexanes:EtOAc. ^{1}H NMR (600 MHz, $CDCl_3$) δ 8.09 (d, *J* = 8.5 Hz, 1H), 7.37 – 7.34 (m, 2H), 7.32 (ddd, *J* = 7.8, 6.7, 1.2 Hz, 2H), 7.29 – 7.25 (m, 1H), 7.01 (s, 1H), 6.73 (d, *J* = 2.5 Hz, 1H), 6.69 (dd, *J* = 8.5, 2.5 Hz, 1H), 4.08 (s, 2H), 0.38 (s, 6H). ^{13}C NMR (151 MHz, $CDCl_3$) δ 187.16, 157.14, 149.77, 142.17, 141.61, 141.17, 131.11, 130.20, 128.84, 128.46, 126.78, 117.46, 116.08, -1.41. HRMS (ESI-MS): calculated for $C_{17}H_{17}NOSi$ $[M+1]^+$, 280.1079; found, 280.1294.

Synthesis of 7-(bis(4,4,5,5,6,6,7,7,8,8,9,9,10,10,11,11,11-heptadecafluoroundecyl)amino)-1,1-dimethyl-2-phenylbenzo[*b*]silin-4(1*H*)-one (**2.22**).

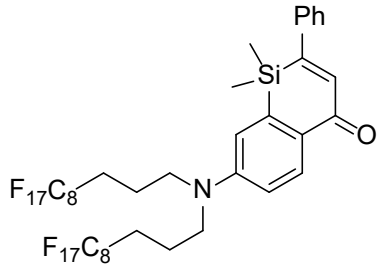

In a two-neck round-bottom flask charged with a stir bar under N_2 atmosphere, **2.21** (24.9 mg, 89.2 μmol, 1.00 equiv), 1,1,1,1,1,1,1,1,1,1,1,1,1,1,1,1,1-heptadecafluoro-11-iodo-1λ^{20}-undeca-1,3,5,7-tetrayne (158 mg, 0.268 mmol, 3.00 equiv), NaH (60% dispersion in mineral oil, 17.8 mg, 0.446 mmol, 5.00 equiv) and TBAB (144 mg,0.446 mmol, 5.00 equiv) were dissolved in anhydrous THF (2.68 mL) and the mixture was stirred at rt for 24 h, with full consumption of the starting material by TLC (10:1 hexanes:EtOAc). The mixture was quenched with MeOH and water, extracted with DCM (5 mL × 3) and washed with water and brine. The crude product was dried with Na_2SO_4, evaporated onto silica gel and purified via flash chromatography, eluting with 10:1 hexanes:EtOAc to give **2.22** as a bright yellow solid (80.3 mg, 66.9 μmol, 78%). R_F = 0.50 in 10:1 hexanes:EtOAc. ^{1}H NMR (500 MHz, $CDCl_3$) δ 8.24 (d, *J* = 8.8 Hz, 1H), 7.47 – 7.34 (m, 5H), 7.11 (s, 1H), 6.82 – 6.76 (m, 2H), 3.57 – 3.49 (m, 4H), 2.25 – 2.11 (m, 4H), 1.99 (qd, *J* = 8.7, 6.3 Hz, 4H), 0.47 (s, 6H). ^{13}C NMR (126 MHz, $CDCl_3$) δ 187.12, 157.04, 149.43, 142.43, 141.80, 141.30, 131.31, 128.99, 128.72 (d, *J* = 24.4 Hz), 126.93, 120.77 – 120.27 (m), 118.74 – 118.15 (m), 116.72 – 115.85 (m), 114.48, 113.22, 111.42 – 110.10 (m), 109.25 – 108.19 (m), 50.17, 29.86, 28.33, 18.55, -1.36. ^{19}F NMR (565 MHz, $CDCl_3$) δ -80.77 (t, *J* = 9.8 Hz), -113.98 (dt, *J* = 344.4, 16.5 Hz), -121.53 – -122.03 (m), -122.60 – -122.79 (m), -123.38 (dt, *J* = 112.3, 14.4 Hz), -126.10 (td, *J* = 13.8, 6.5 Hz).

2.6.4 ^{1}H NMR Spectra

^{1}H NMR of **2.1a** (500 MHz, $CDCl_3$).

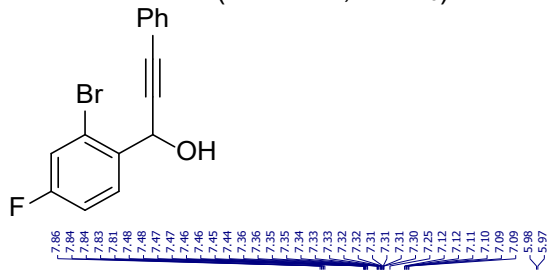

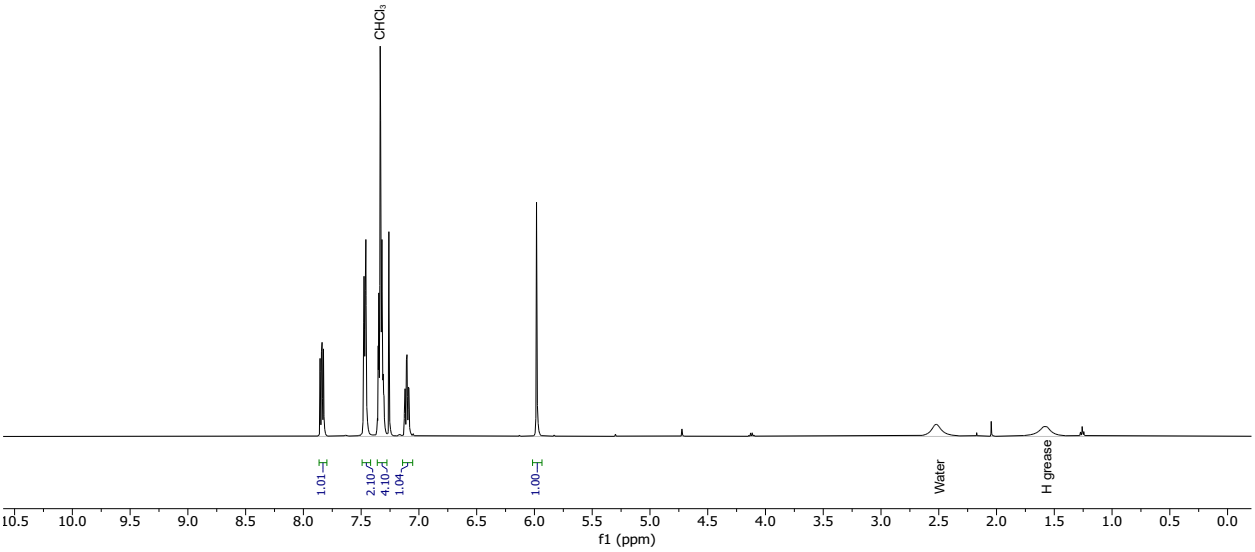

^{1}H NMR of **2.1b** (500 MHz, $CDCl_3$).

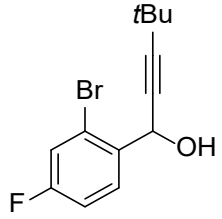

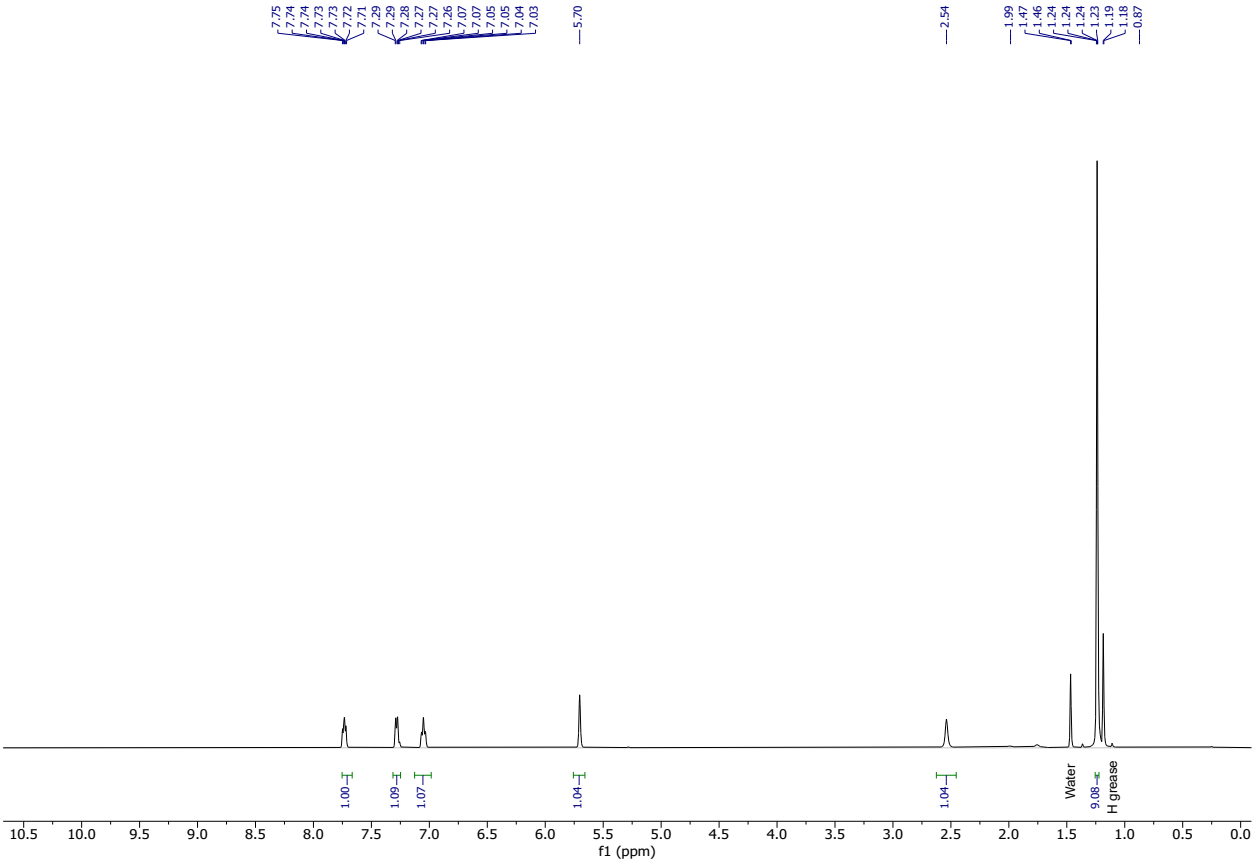

^{1}H NMR of **2.2a** (500 MHz, $CDCl_3$).

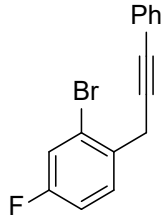

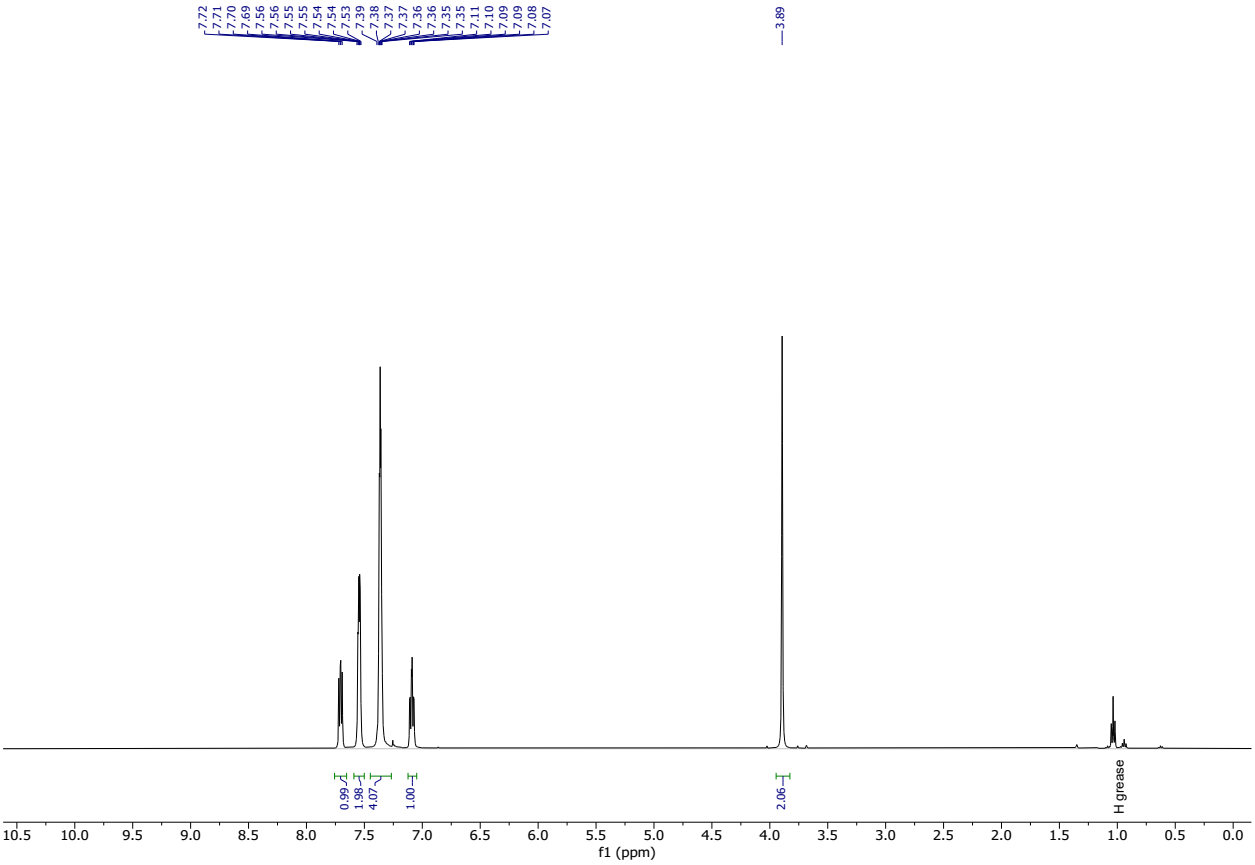

^{1}H NMR of **2.3a** (500 MHz, $CDCl_3$).

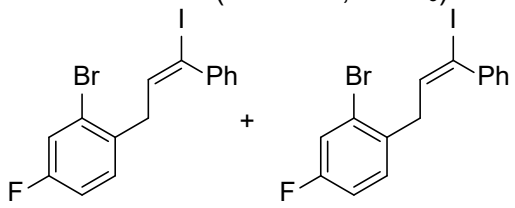

3:1

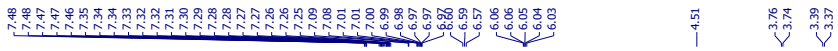

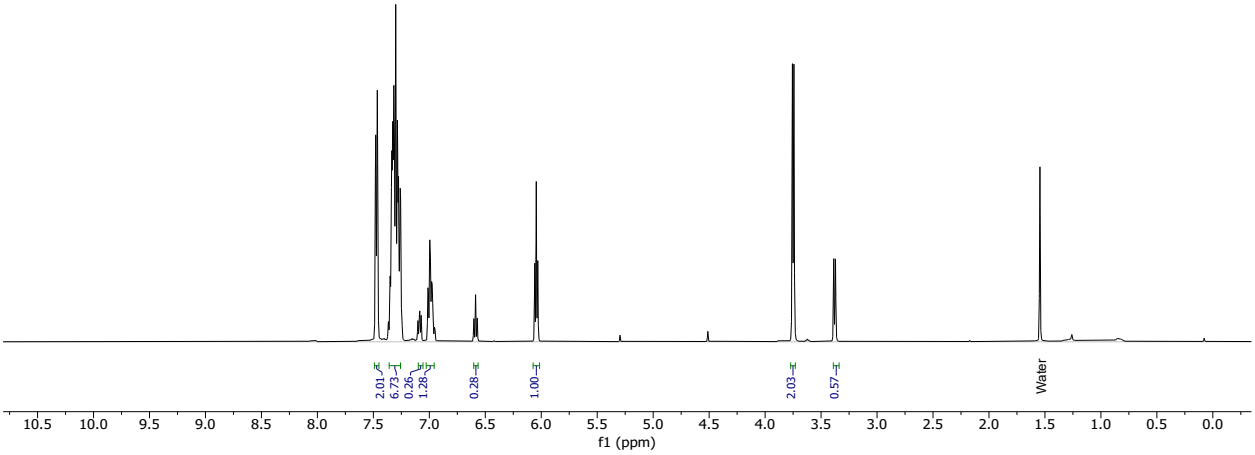

^{1}H NMR of **2.3b** (500 MHz, $CDCl_3$).

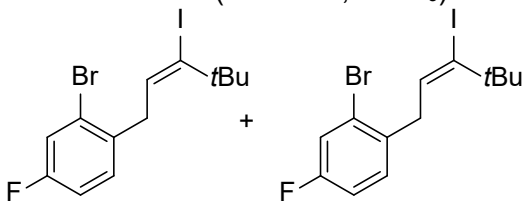

3:1

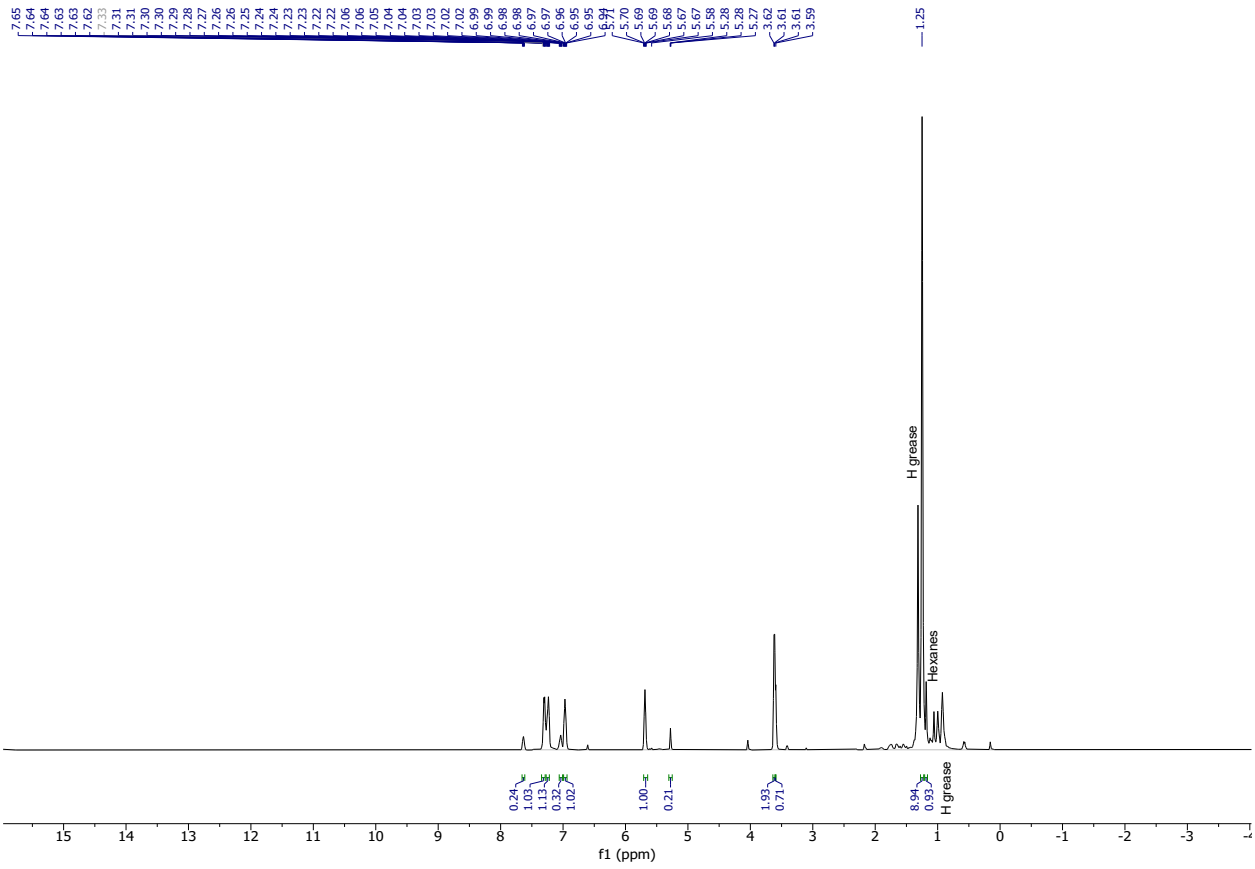

^{1}H NMR of **2.4a** (500 MHz, $CDCl_3$).

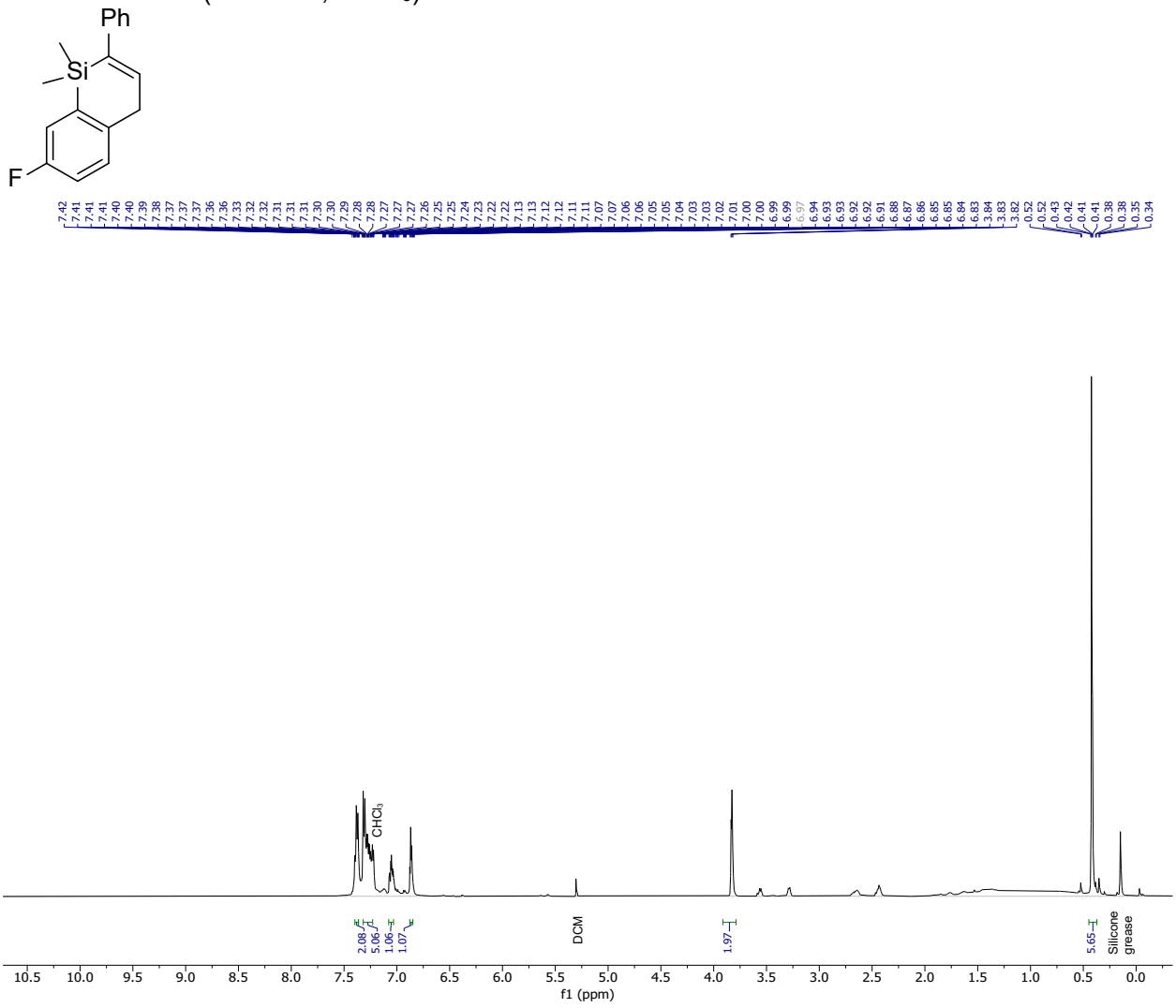

^{1}H NMR of **2.4b** (500 MHz, $CDCl_3$).

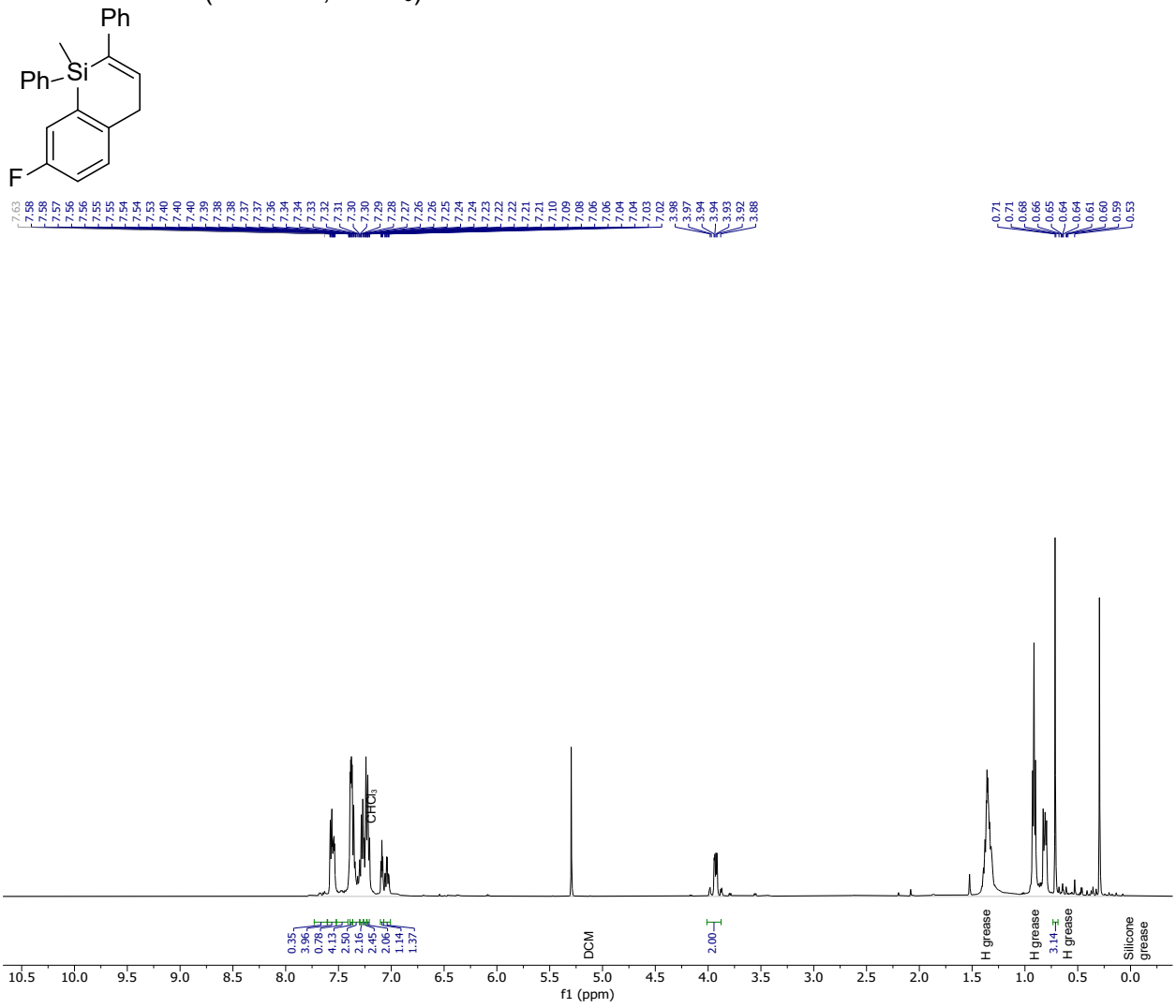

^{1}H NMR of **2.5a** (500 MHz, $CDCl_3$).

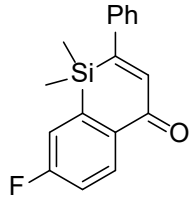

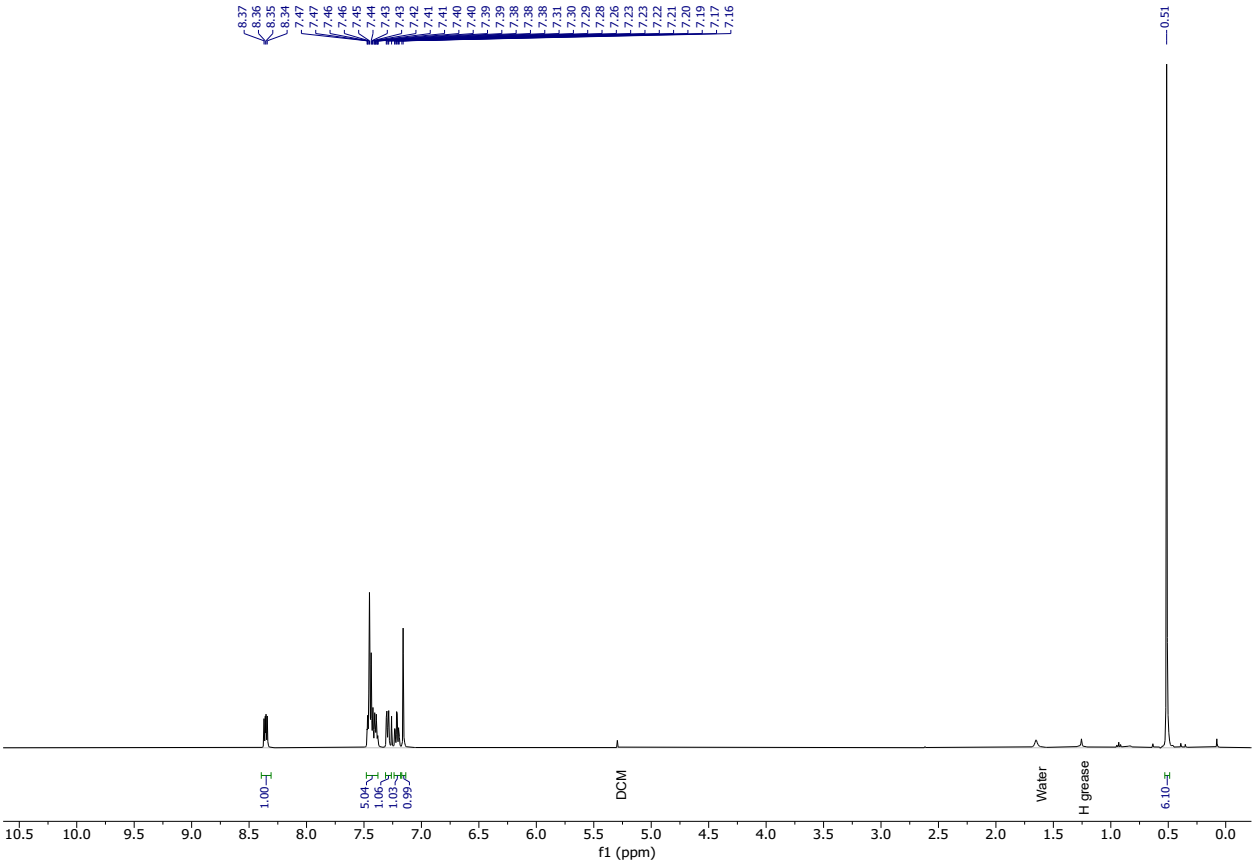

^{1}H NMR of **2.5b** (500 MHz, $CDCl_3$).

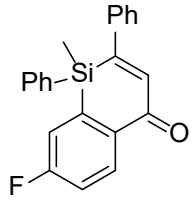

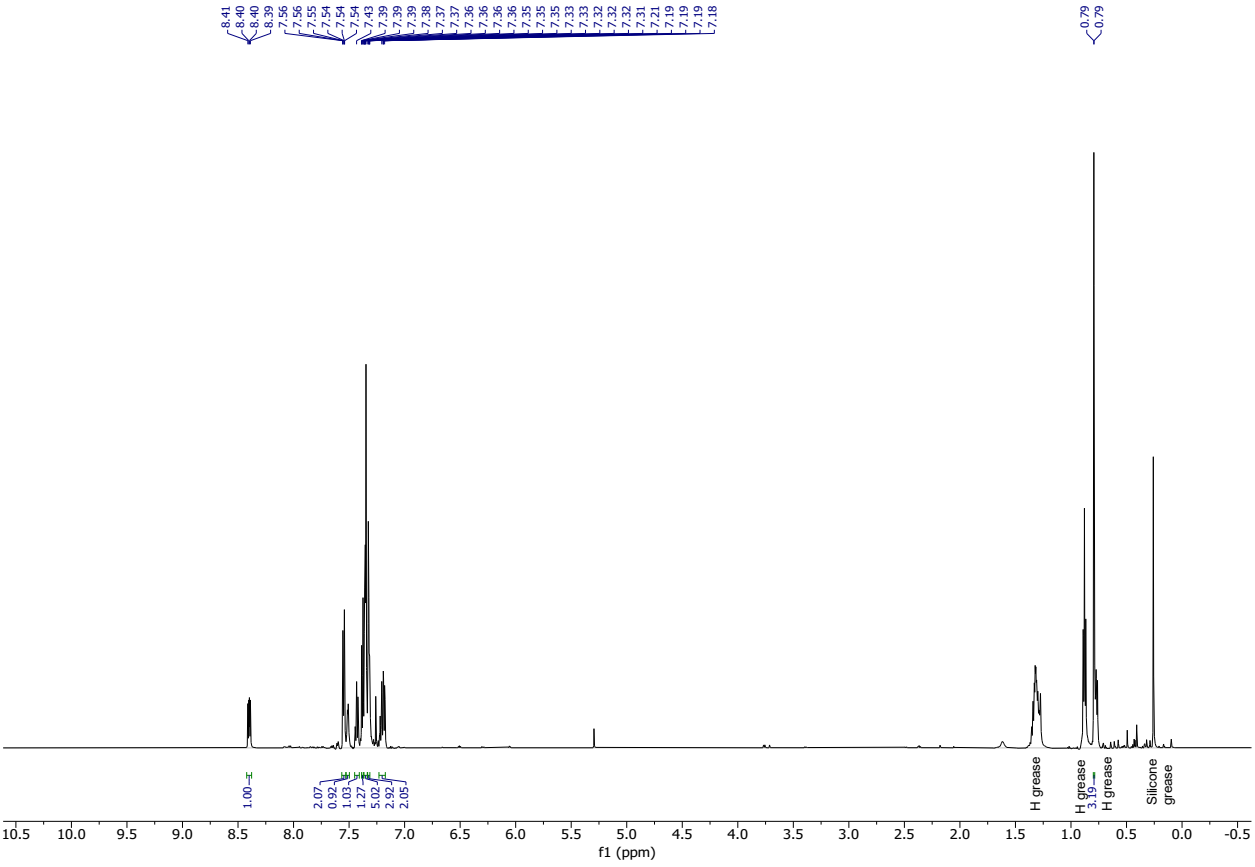

^{1}H NMR of **2.5c** (500 MHz, $CDCl_3$).

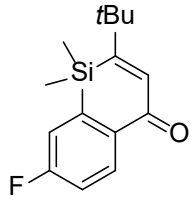

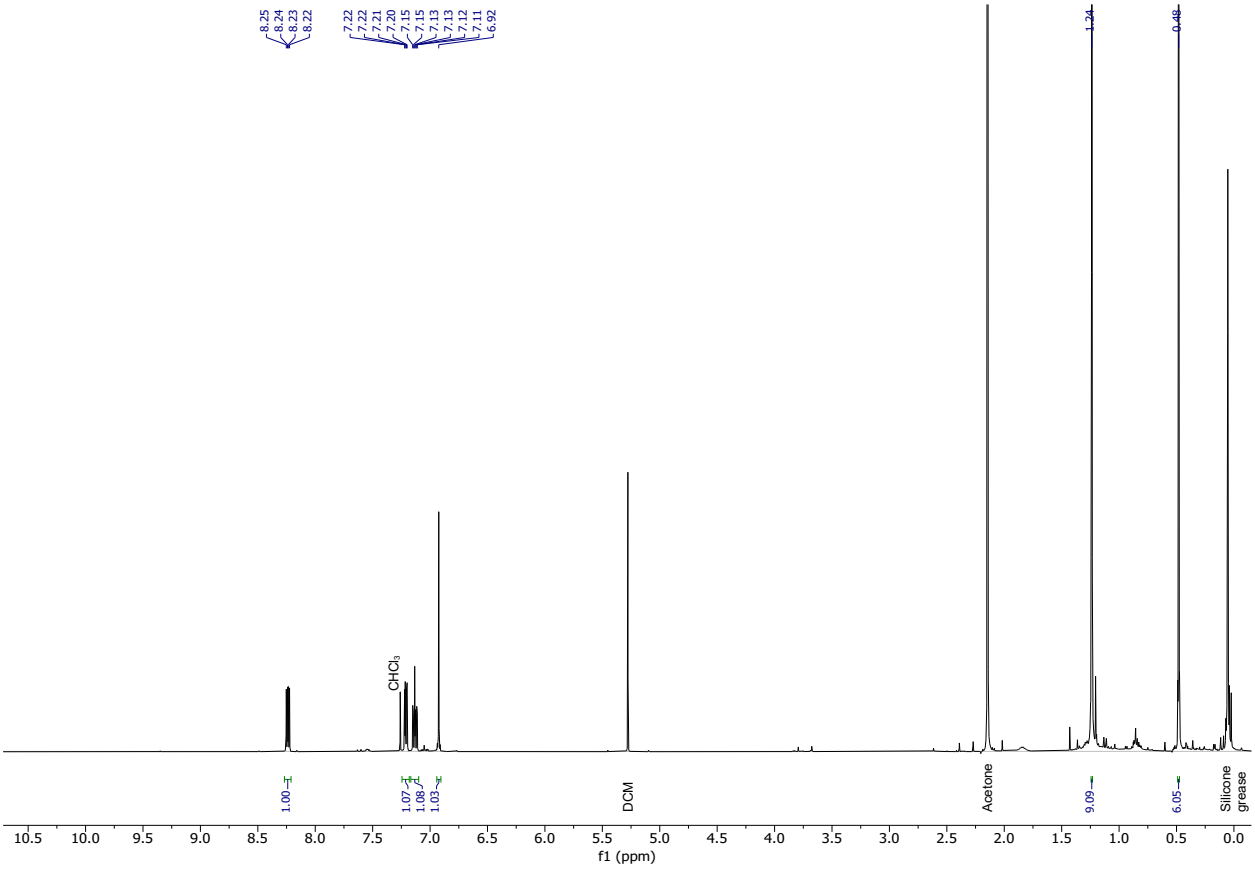

^{1}H NMR of **2.6a** (500 MHz, $CDCl_3$).

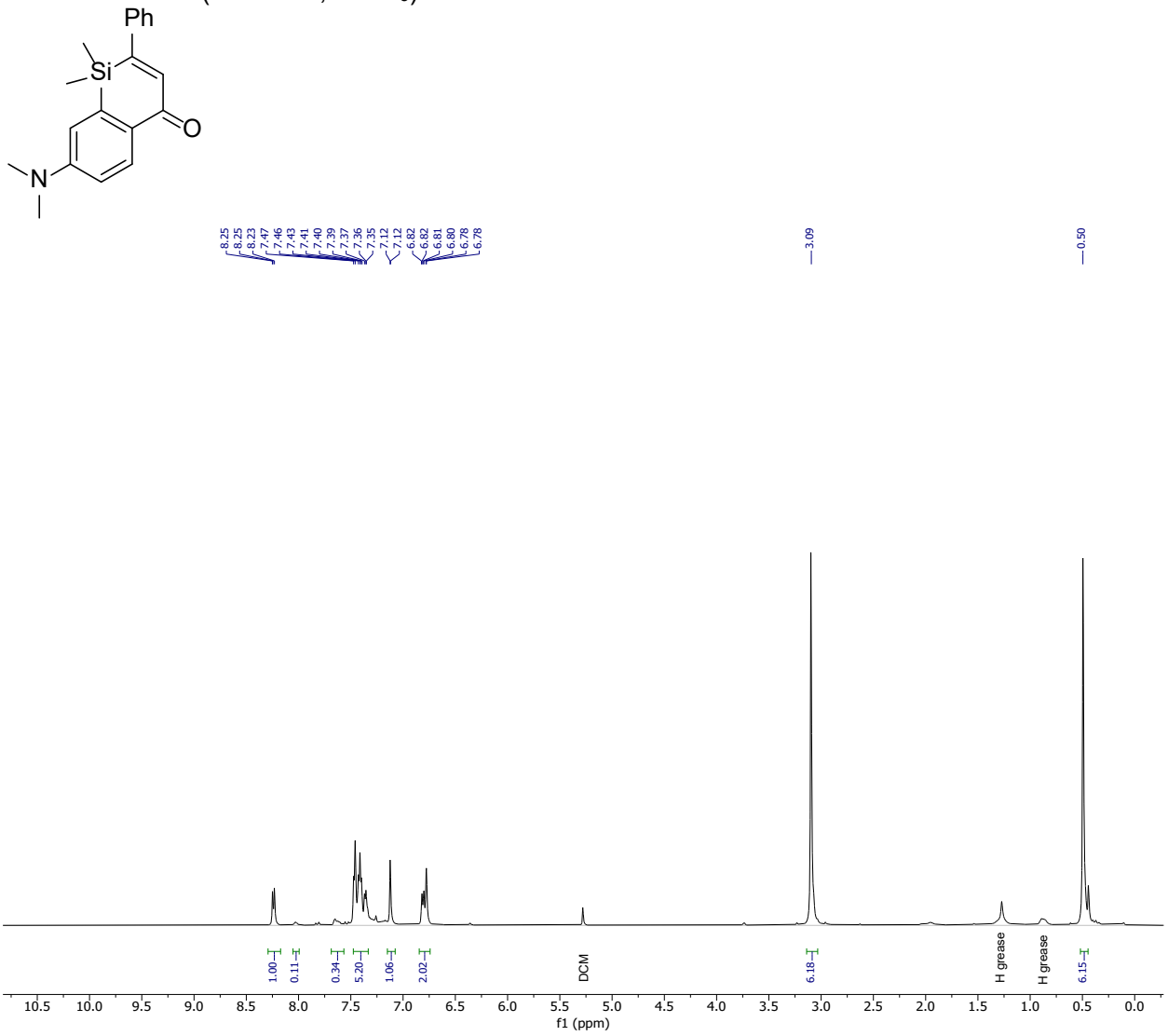

^{1}H NMR of **2.6b** (500 MHz, $CDCl_3$).

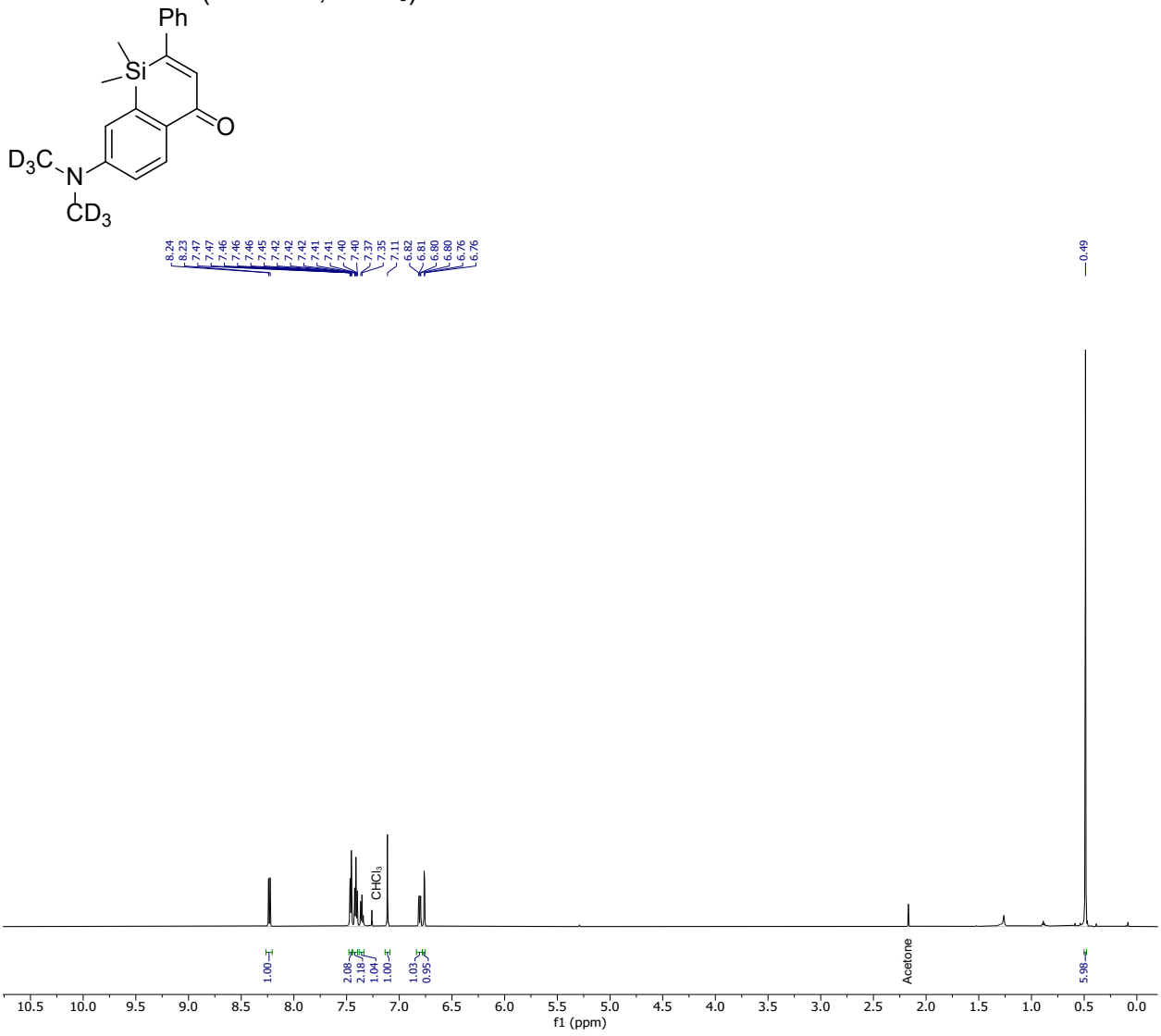

^{1}H NMR of **2.6c** (500 MHz, $CDCl_3$).

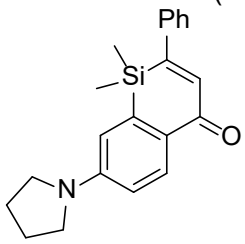

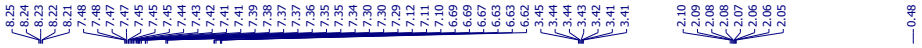

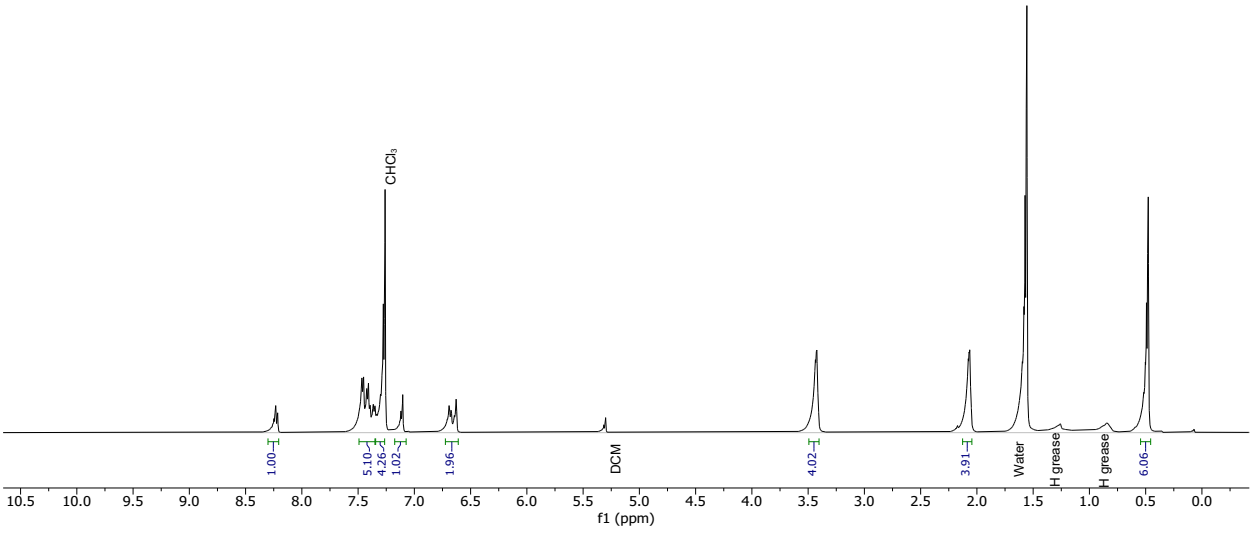

^{1}H NMR of **2.6d** (500 MHz, $CDCl_3$).

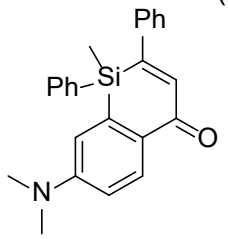

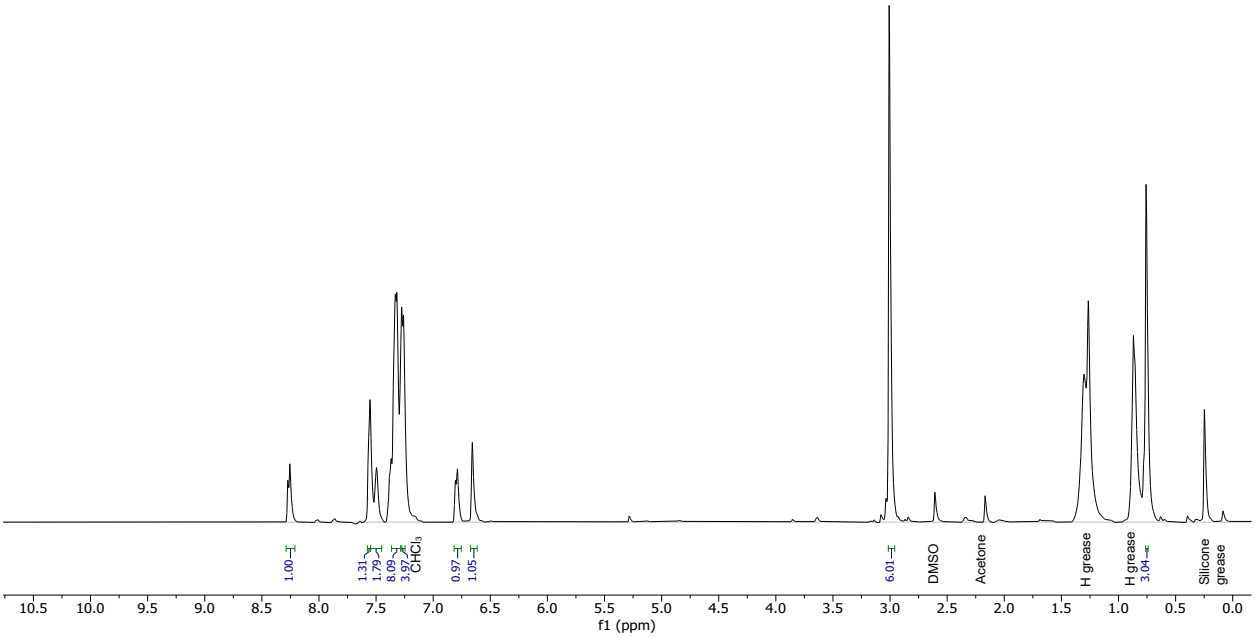

^{1}H NMR of **2.6e** (500 MHz, $CDCl_3$).

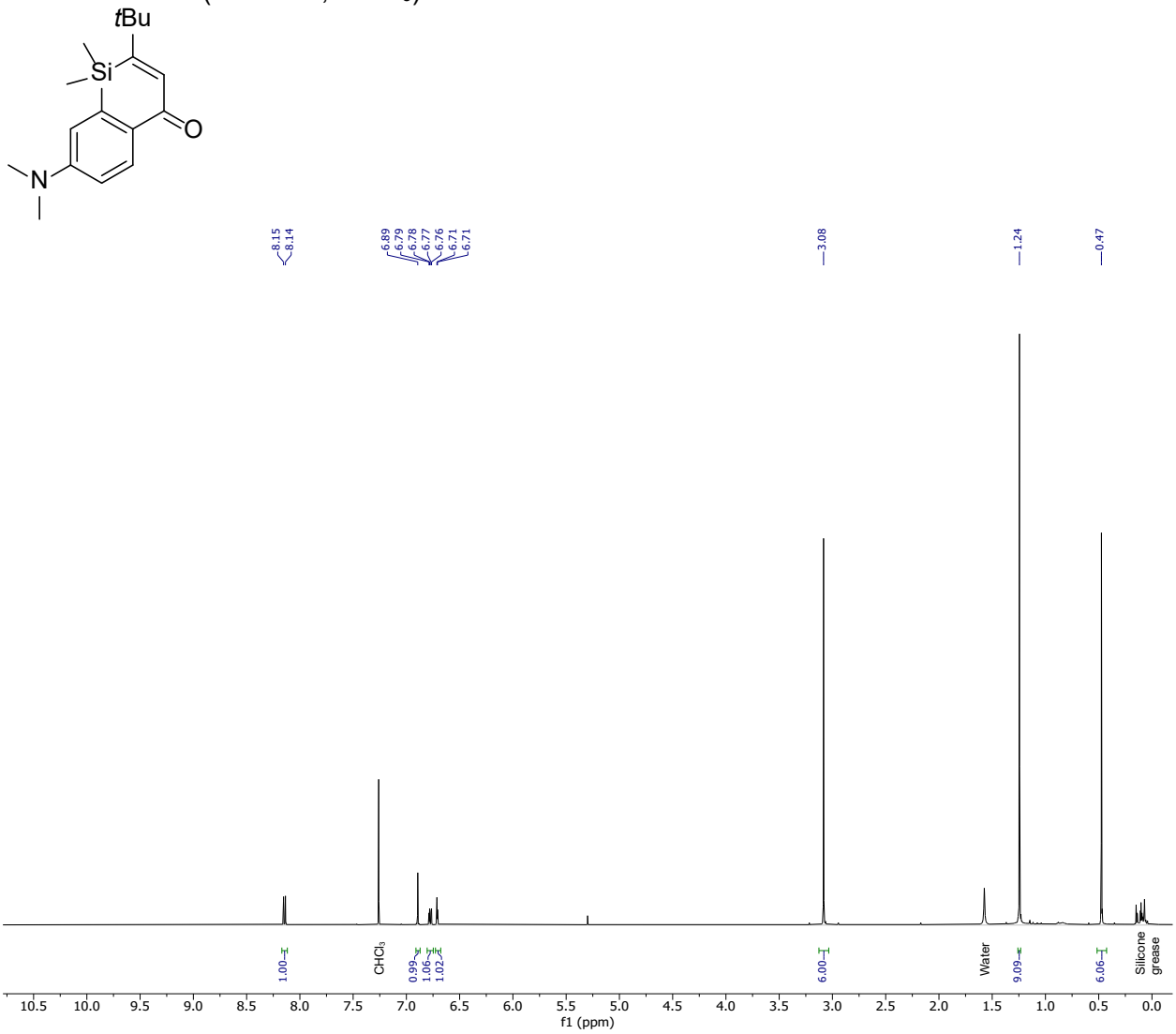

^{1}H NMR of **2.11** (SiliFlav5, 500 MHz, CD_2Cl_2 in 10% MeOD).

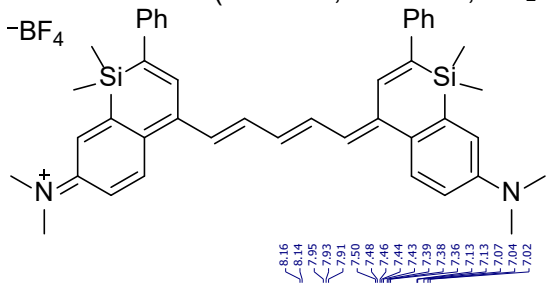

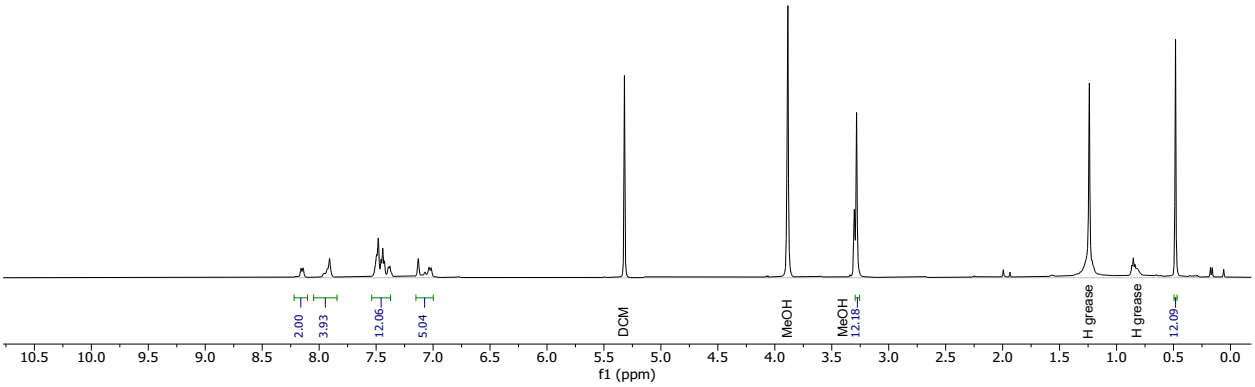

^{1}H NMR of **2.12**, SiliFlav7 (600 MHz, CD_2Cl_2).

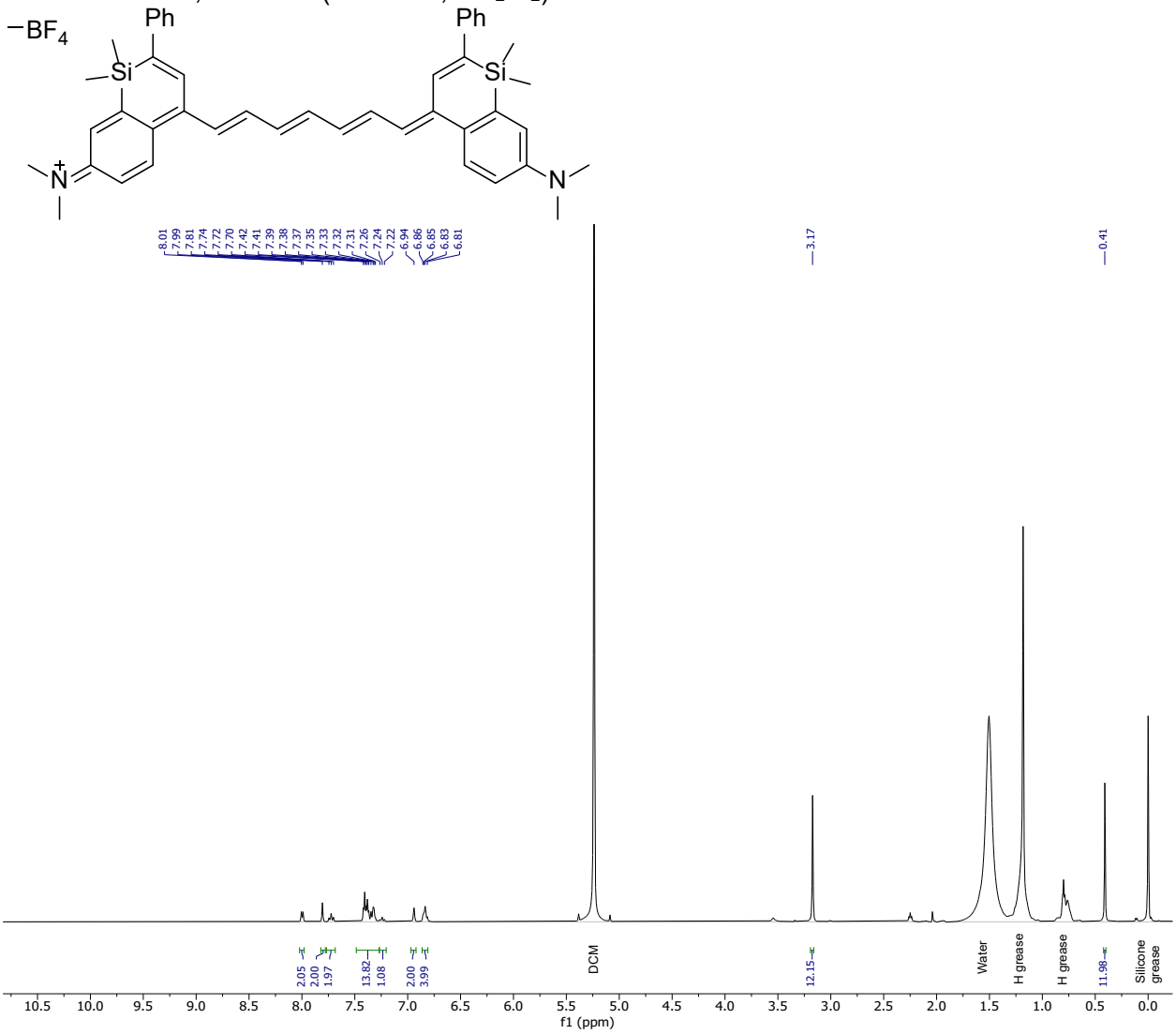

^{1}H NMR of **2.13**, SiliFlav9 (600 MHz, CD_2Cl_2).

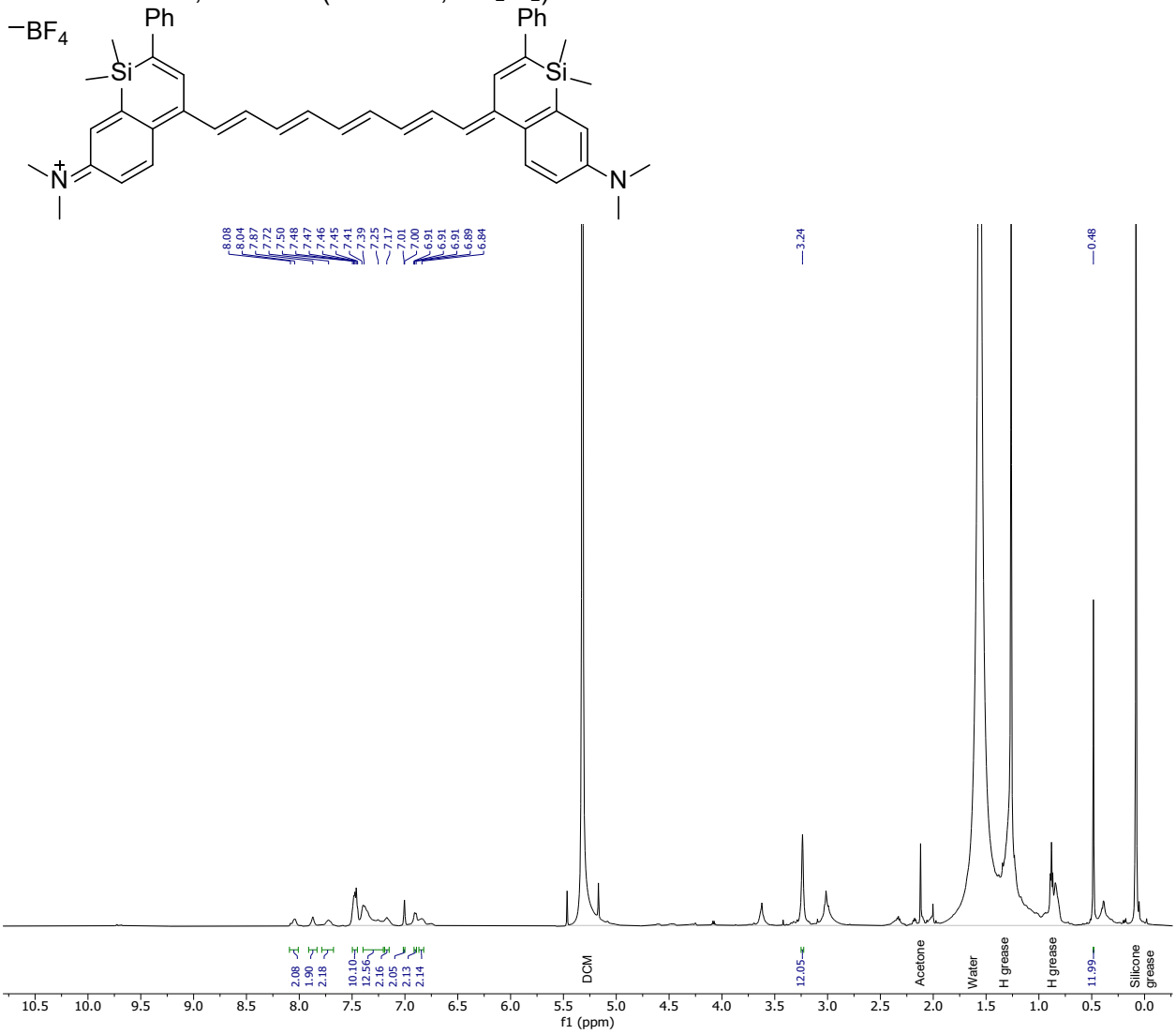

^{1}H NMR of **2.14,** SiliFlav5-d_{12} (600 MHz, CD_2Cl_2).

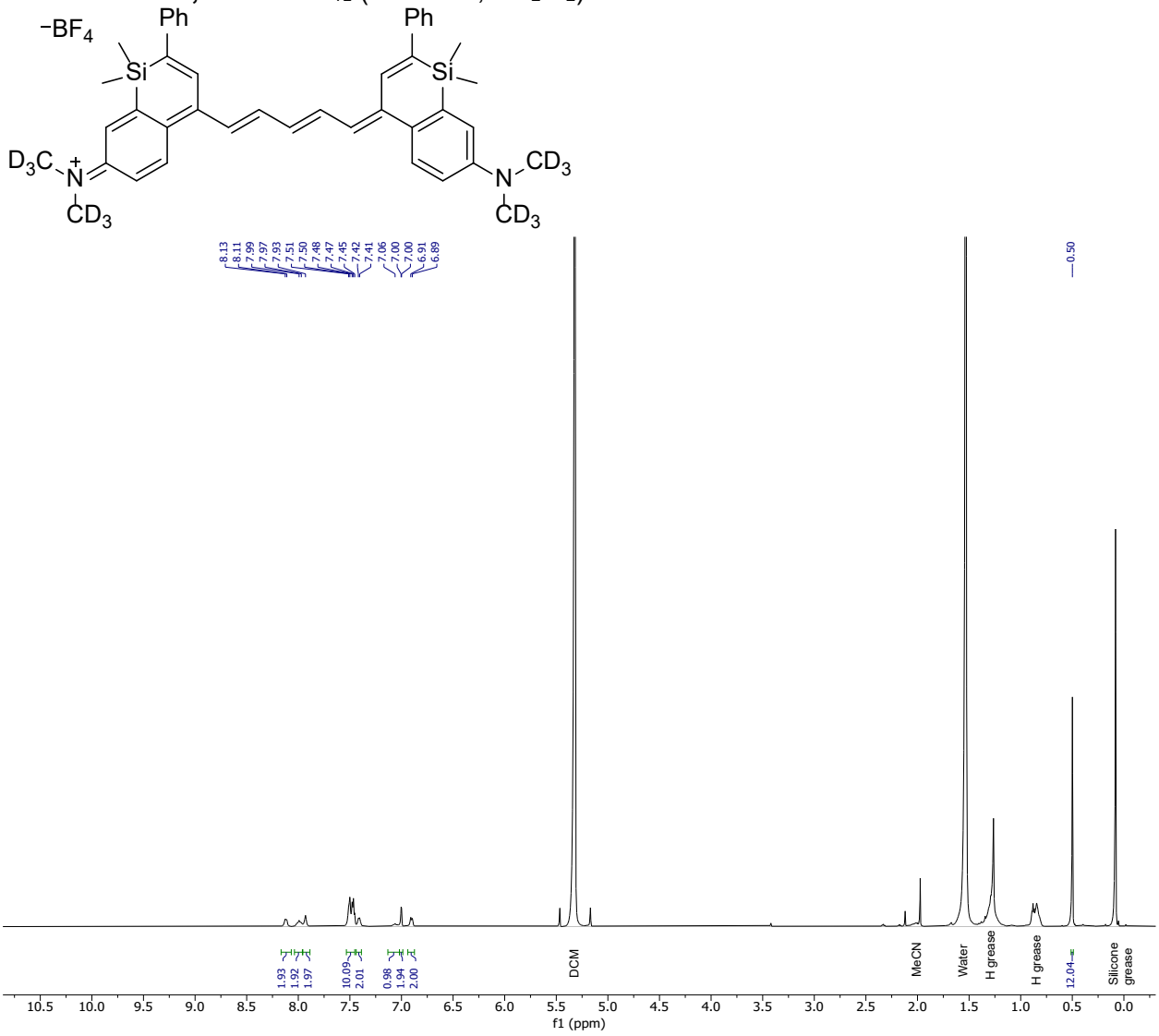

^{1}H NMR of **2.15**, Py-SiliFlav5 (500 MHz, CD_2Cl_2).

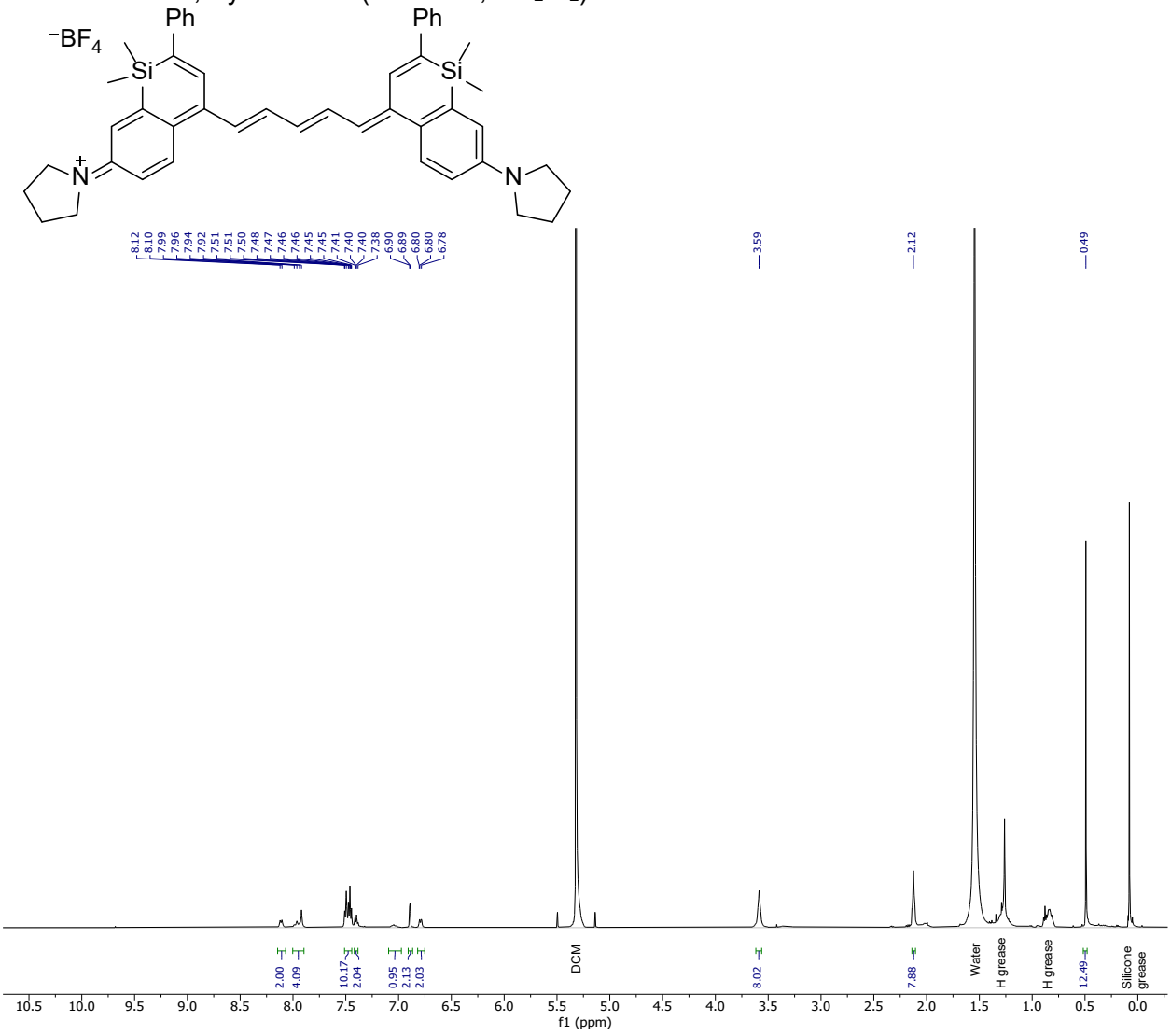

^{1}H NMR of **2.16**, Sili(MePh)Flav5 (500 MHz, CD_2Cl_2).

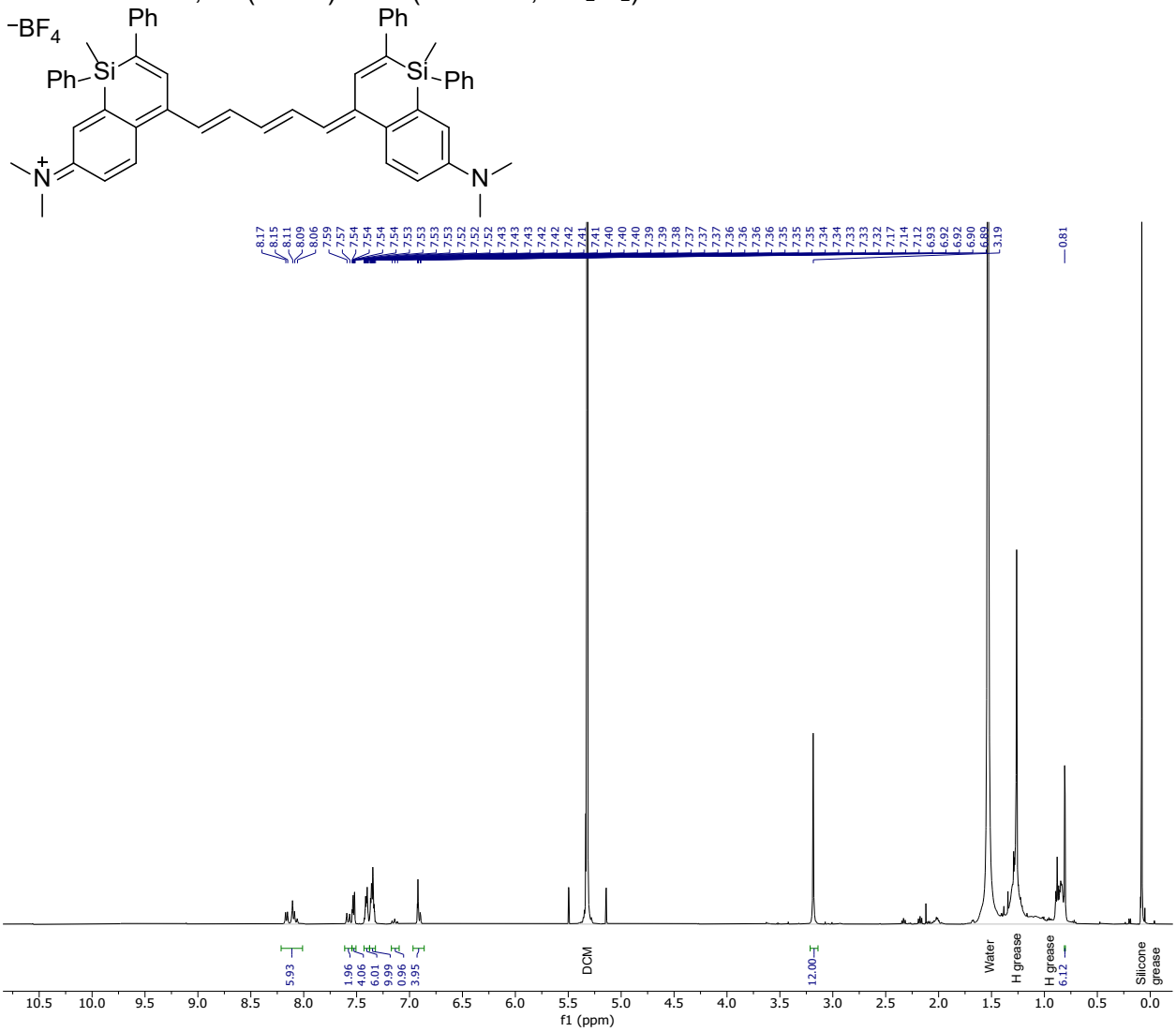

^{1}H NMR of **2.17**, SiliChrom5 (500 MHz, CD_2Cl_2).

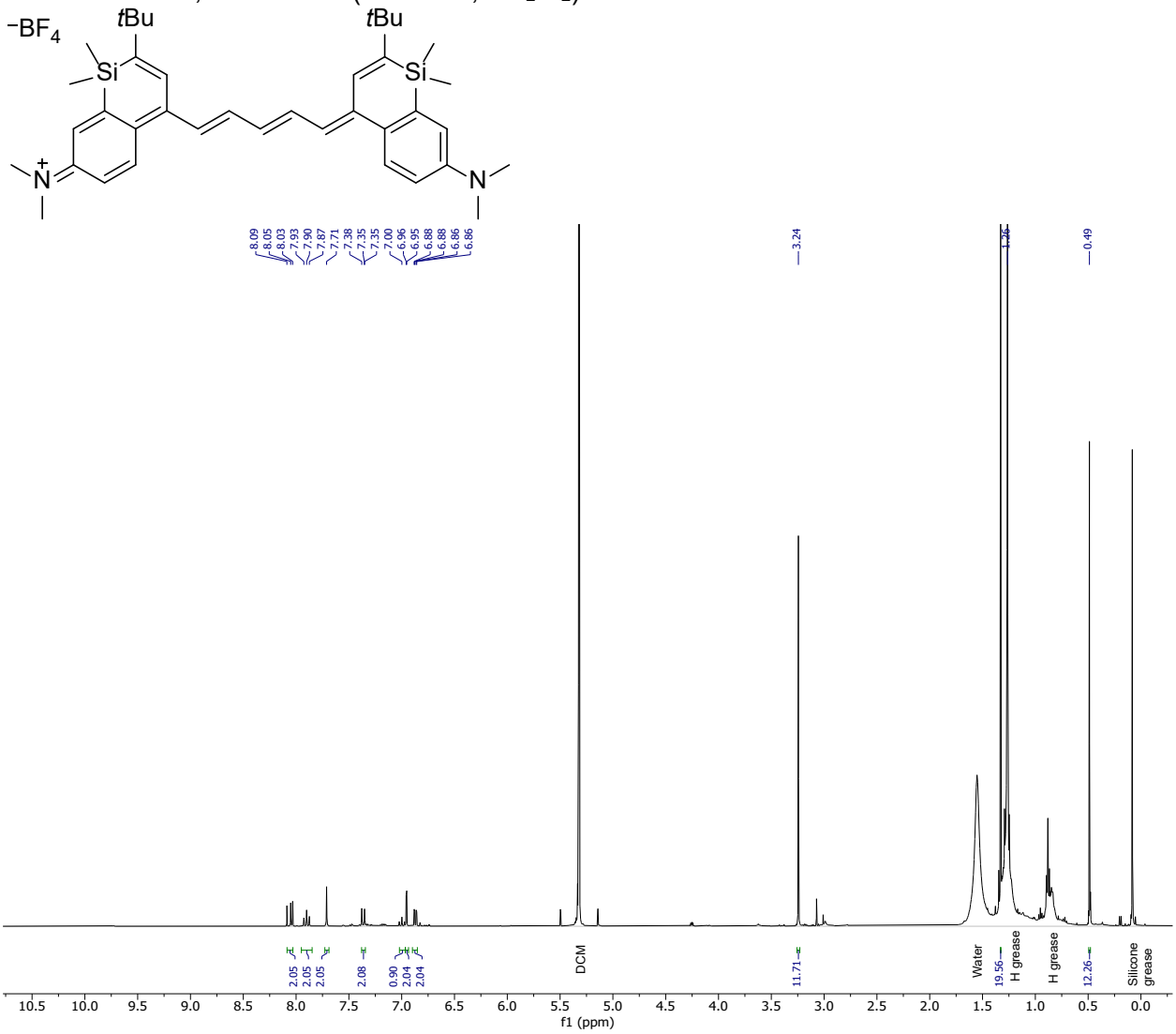

^{1}H NMR **2.11•BArF$_{24}$**, SiliFlav5 BArF$_{24}$ (600 MHz, CD_2Cl_2).

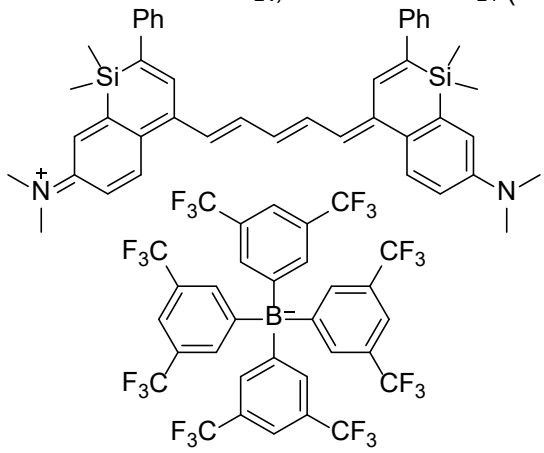

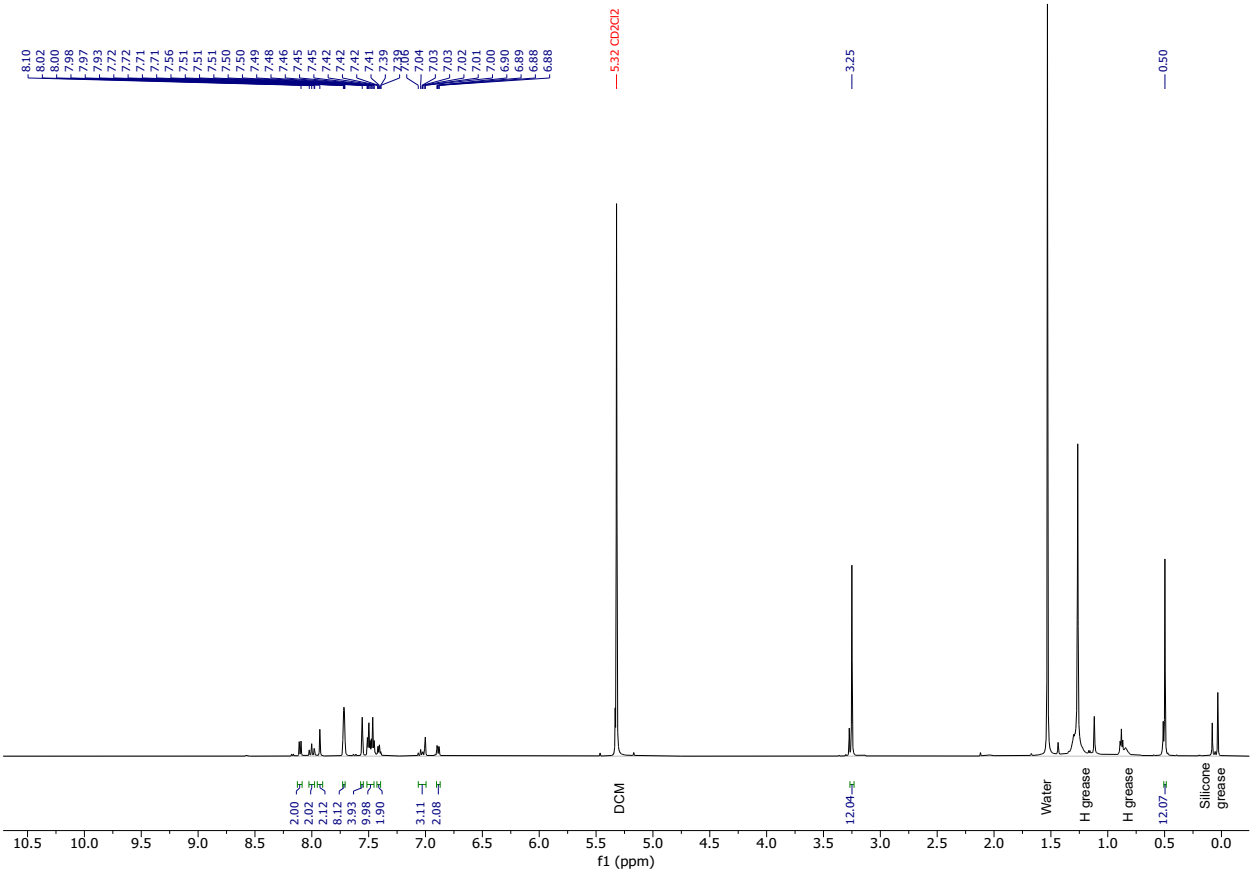

^{1}H NMR of **2.19** (500 MHz, $CDCl_3$).

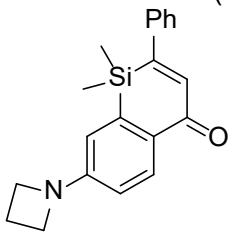

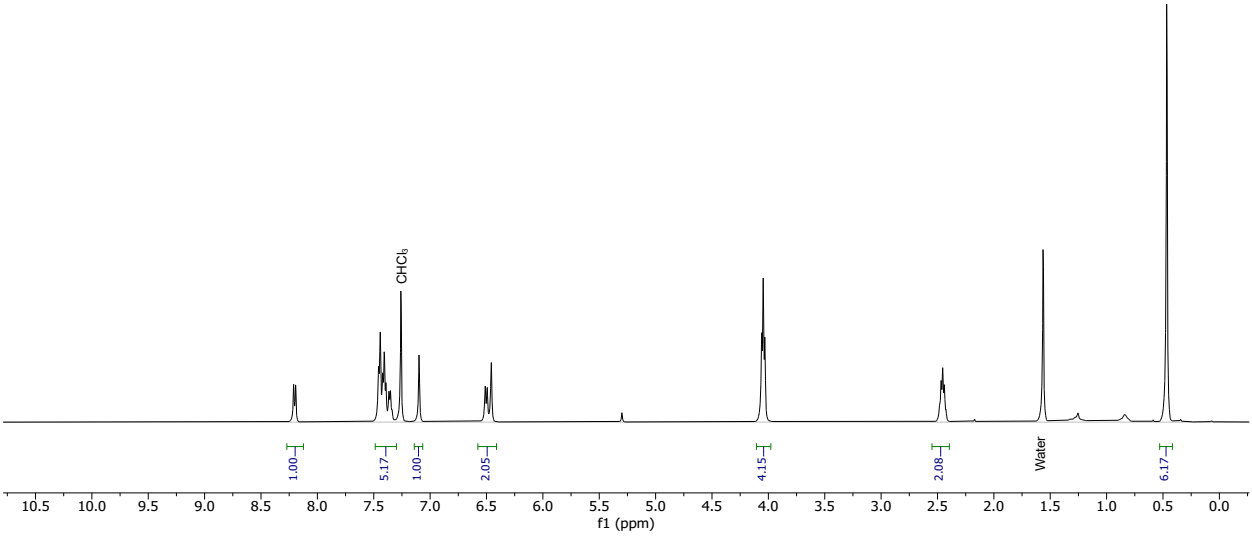

^{1}H NMR of **2.20** (500 MHz, $CDCl_3$).

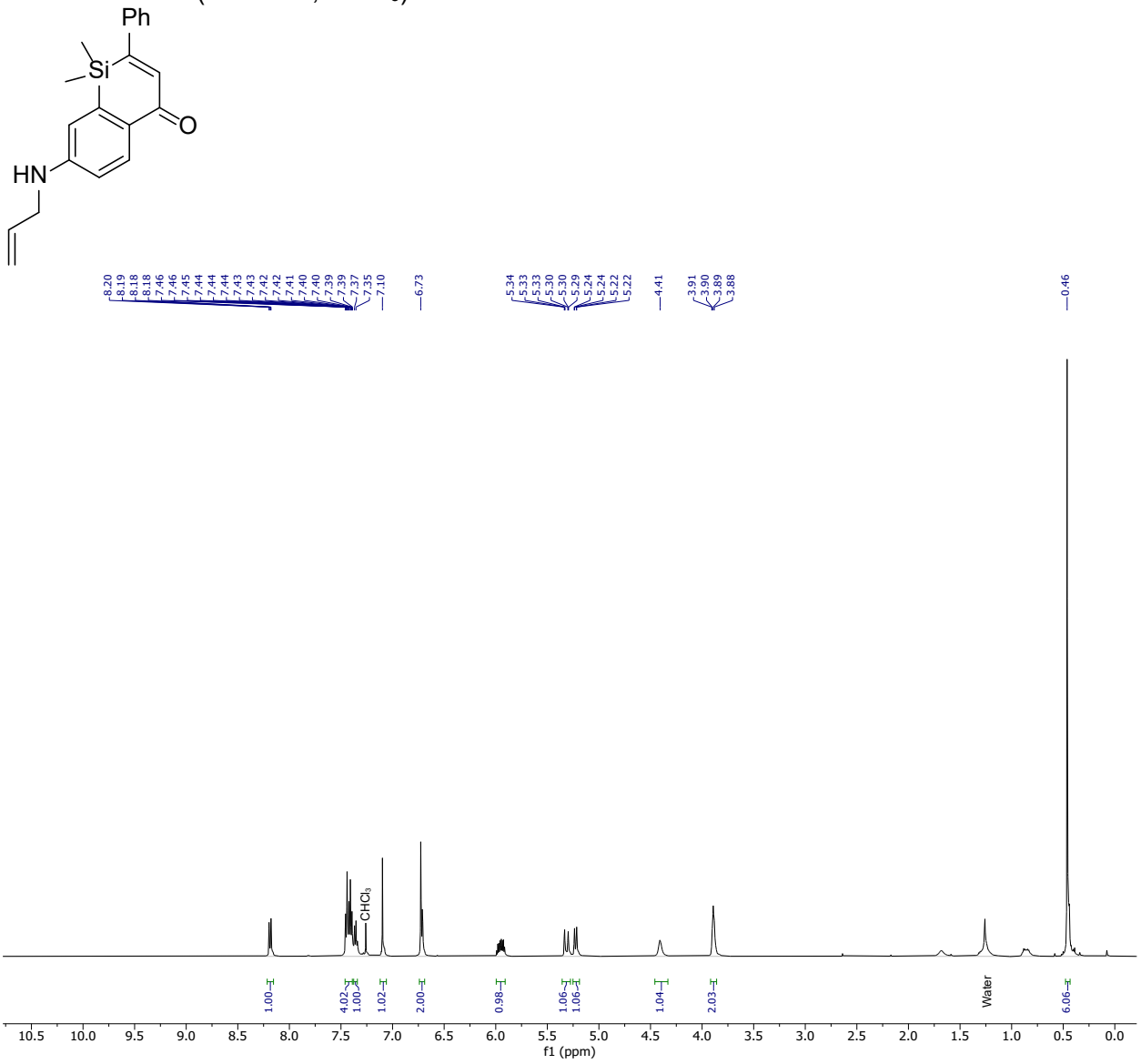

^{1}H NMR of **2.1** (600 MHz, $CDCl_3$).

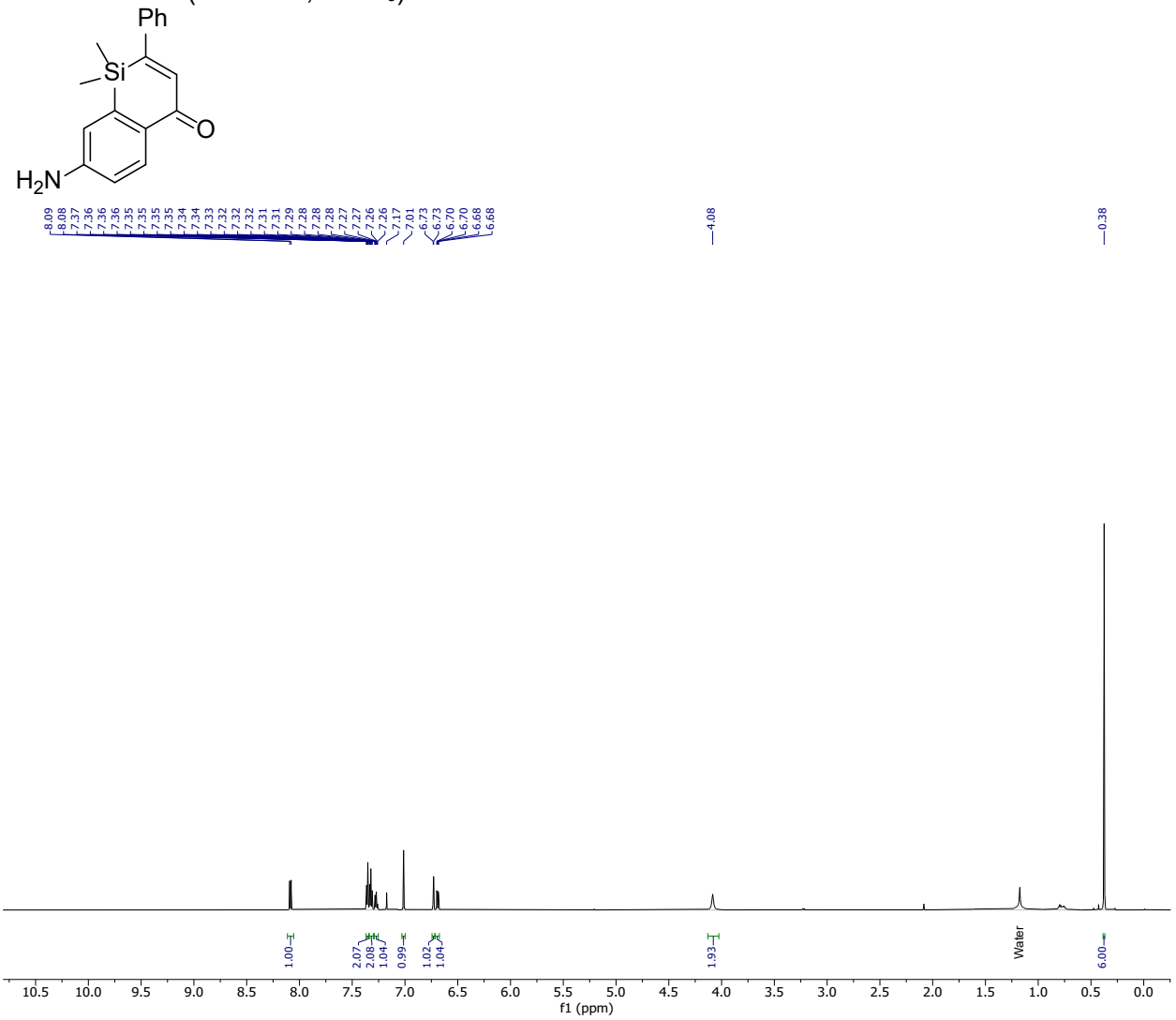

^{1}H NMR of **2.22** (500 MHz, $CDCl_3$).

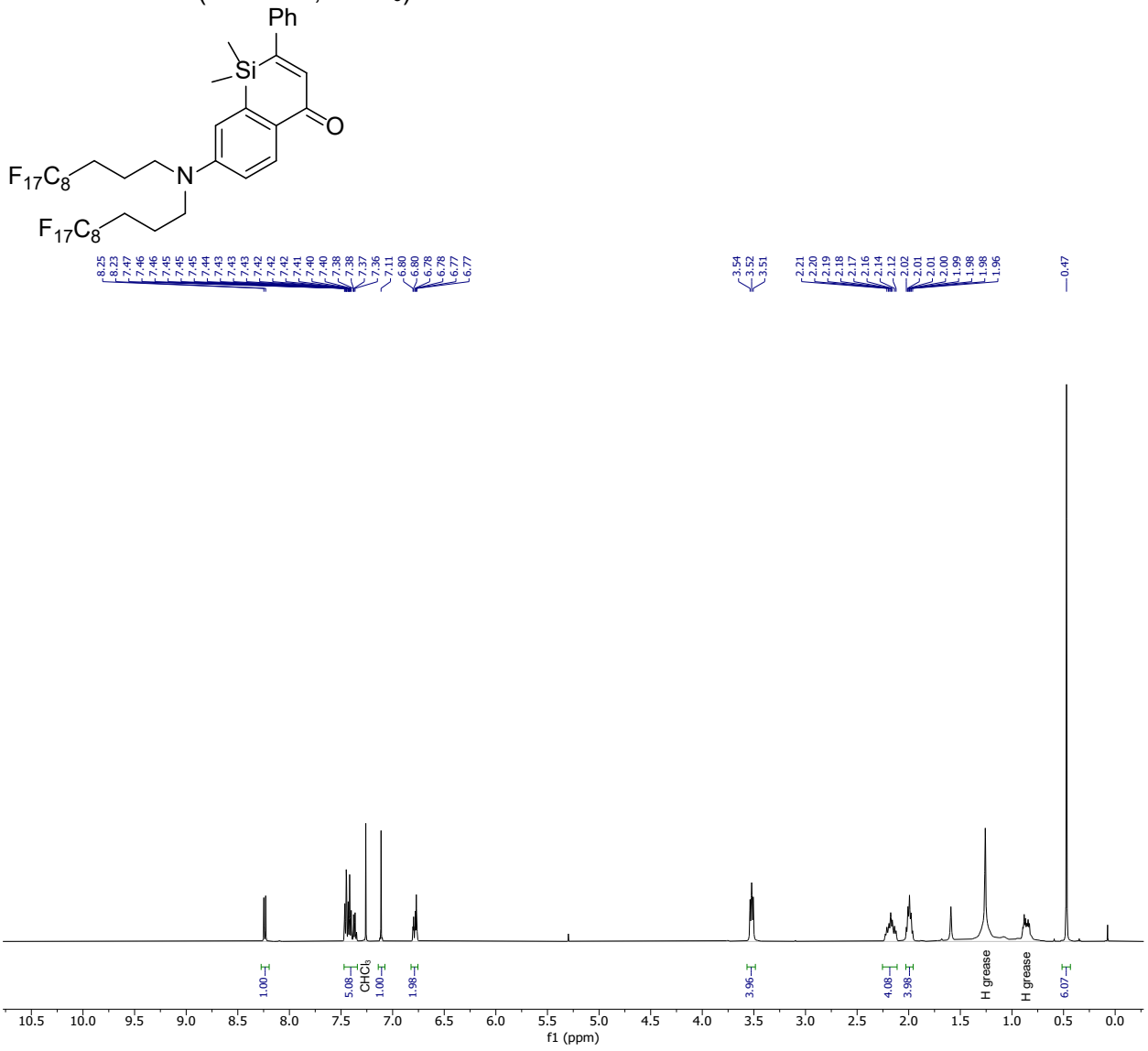

2.6.5 ^{13}C NMR Spectra

^{13}C NMR of **2.1a** (126 MHz, $CDCl_3$).

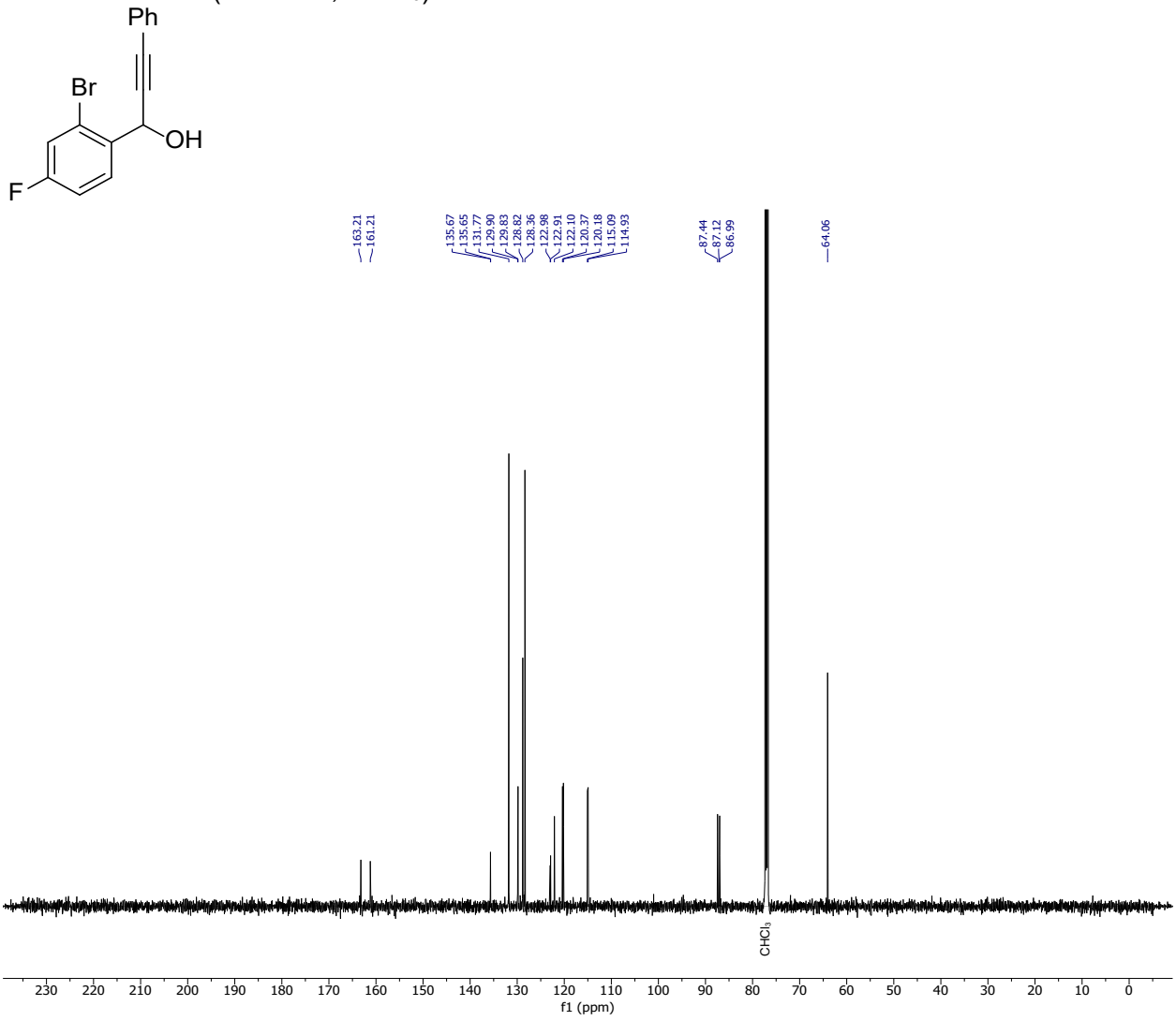

^{13}C NMR of **2.1b** (126 MHz, $CDCl_3$).

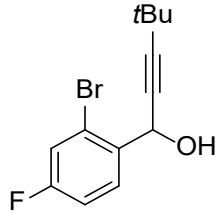

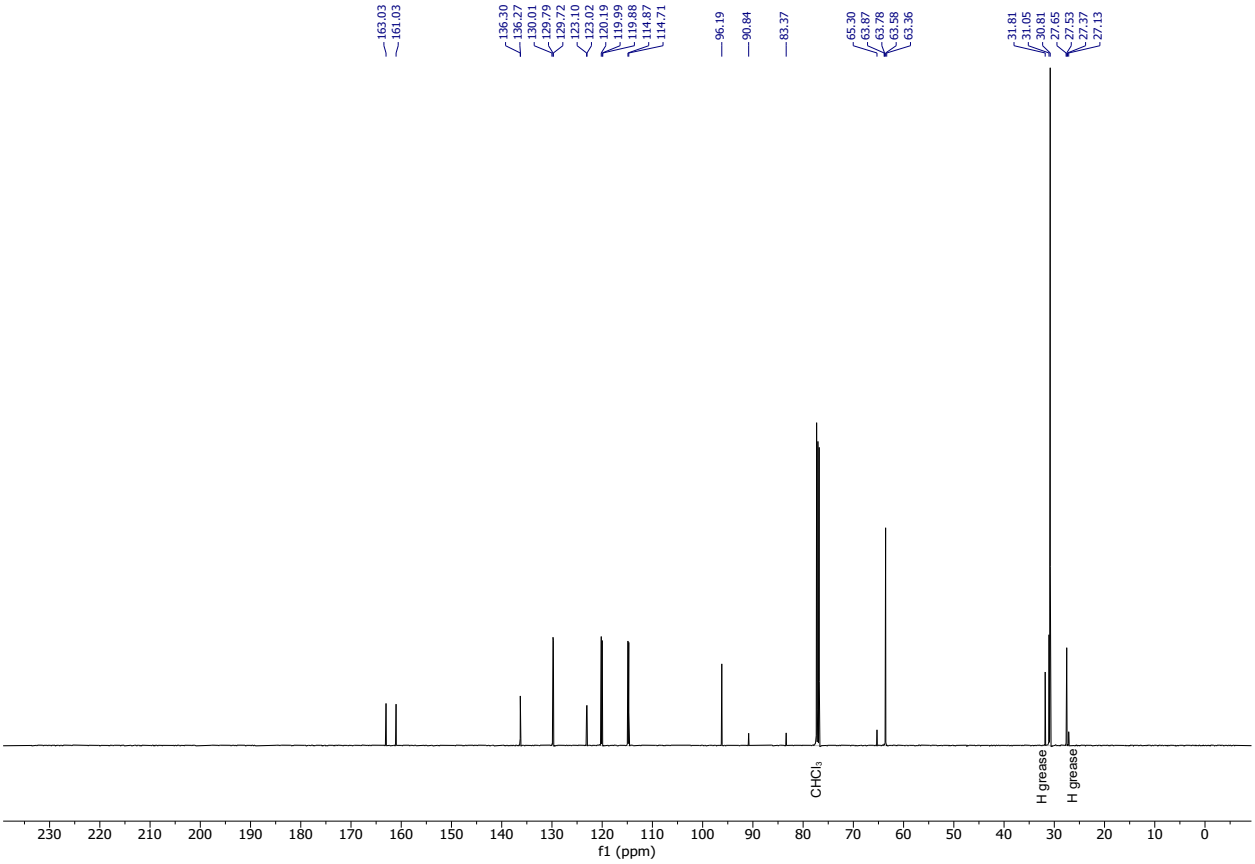

^{13}C NMR of **2.2a** (126 MHz, $CDCl_3$).

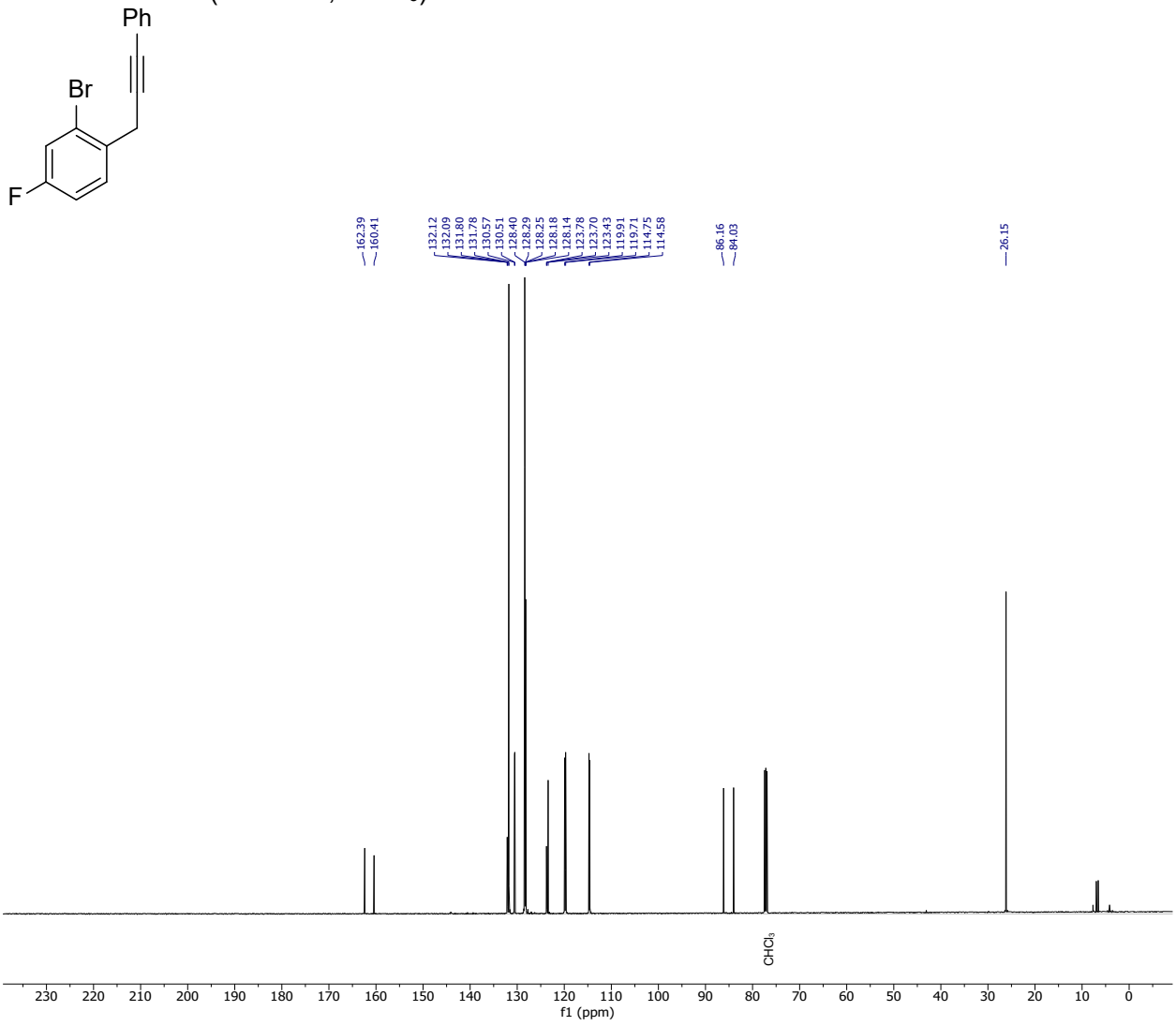

^{13}C NMR of **2.3a** (126 MHz, $CDCl_3$).

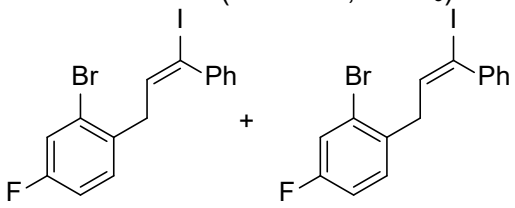

3:2

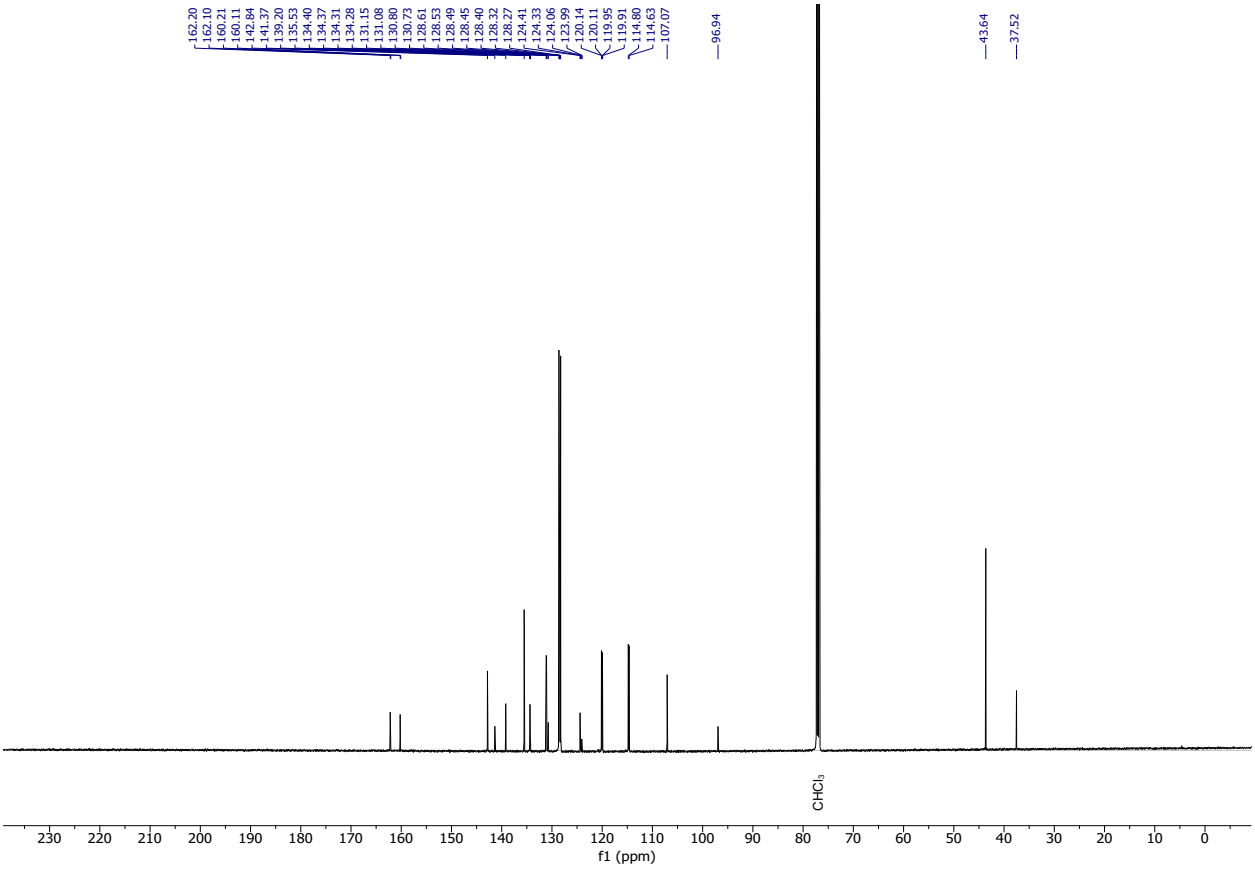

^{13}C NMR of **2.3b** (126 MHz, $CDCl_3$).

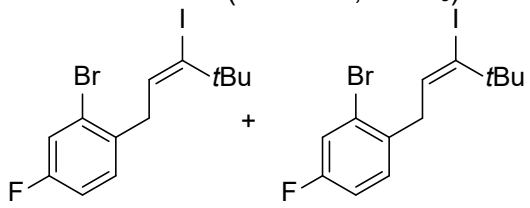

3:1

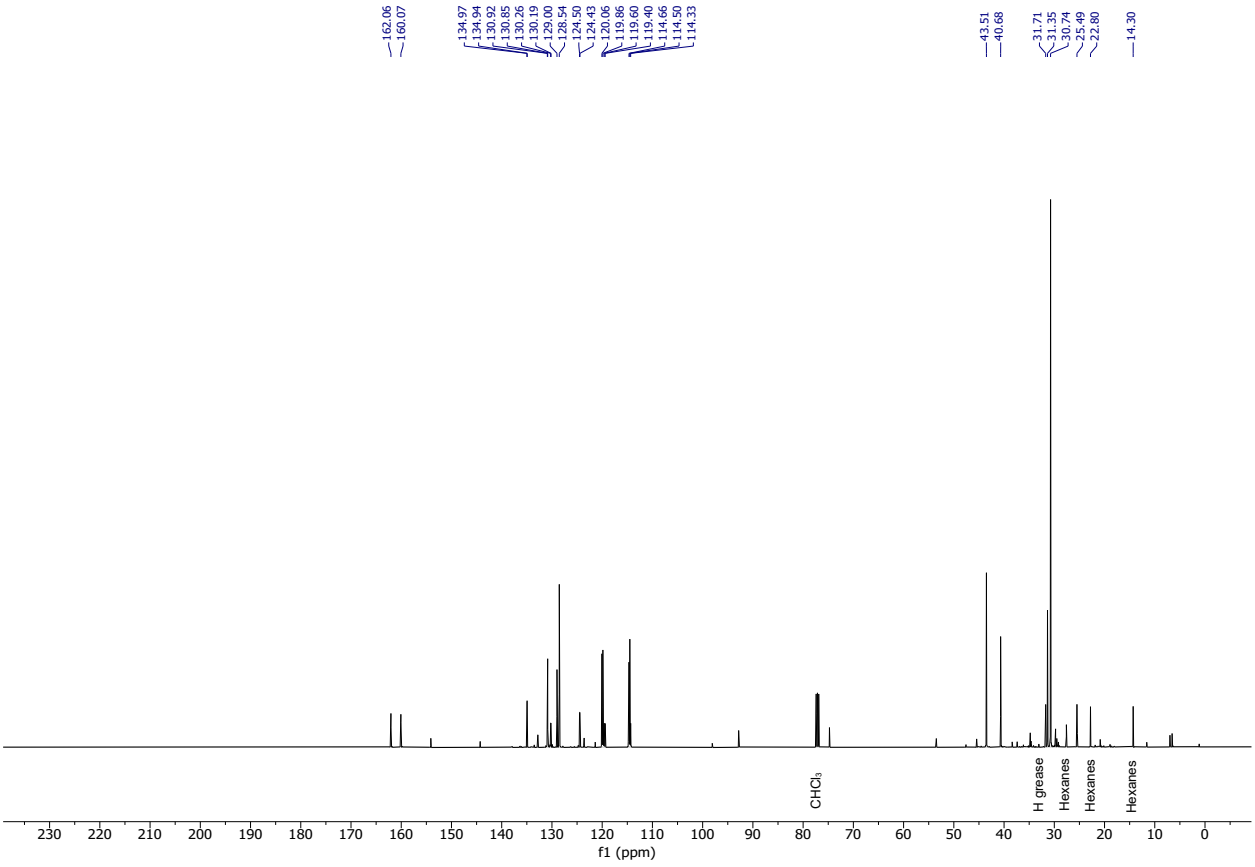

^{13}C NMR of **2.4a** (126 MHz, $CDCl_3$).

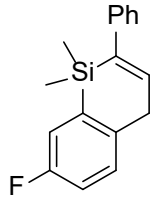

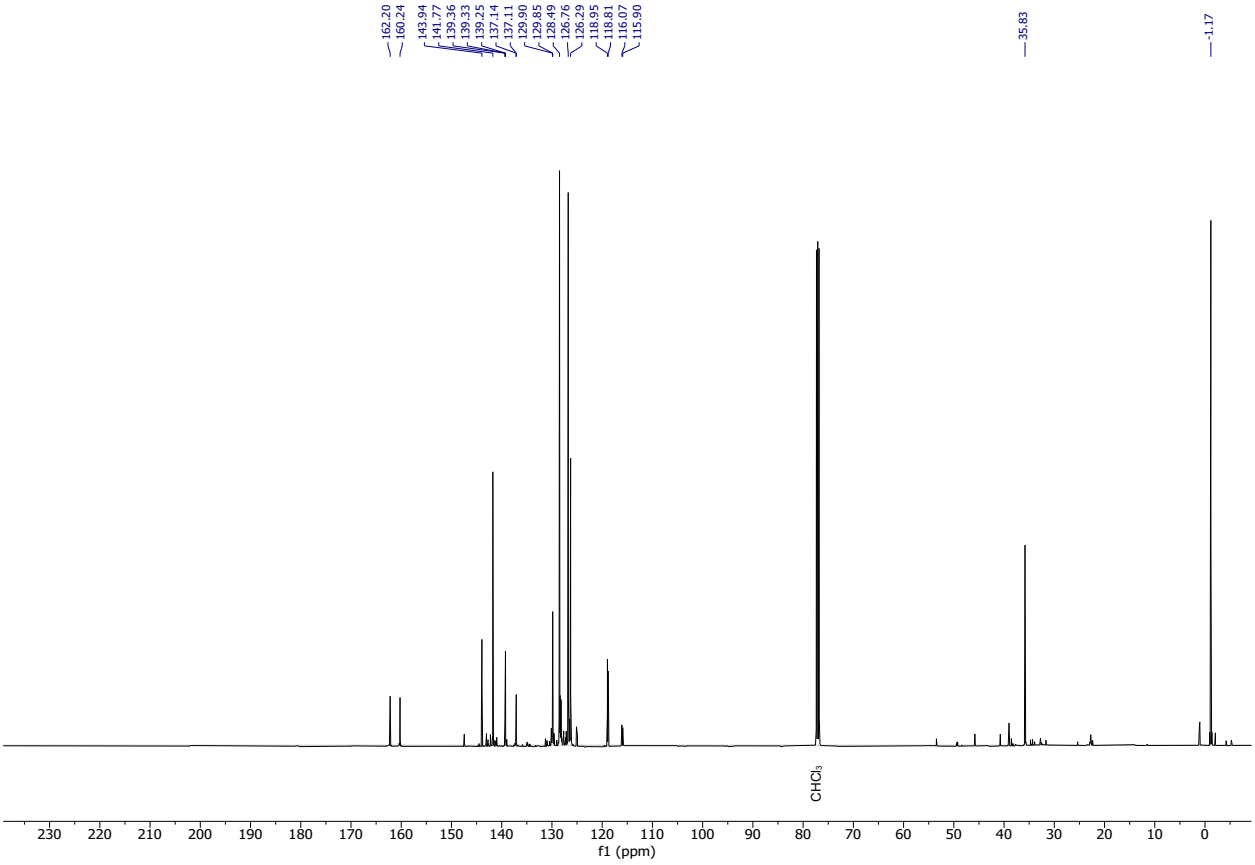

^{13}C NMR of **2.4b** (126 MHz, $CDCl_3$).

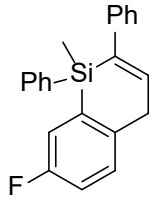

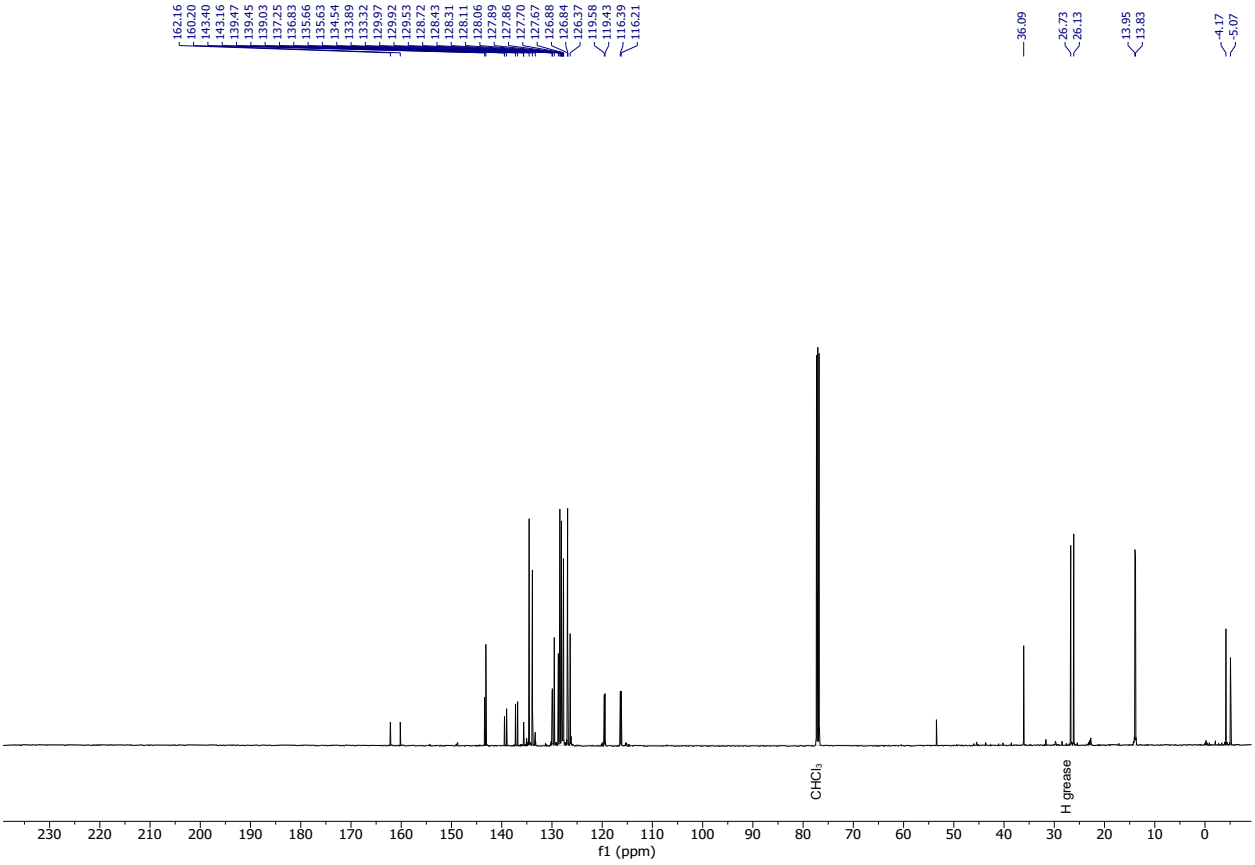

^{13}C NMR of **2.5a** (126 MHz, $CDCl_3$).

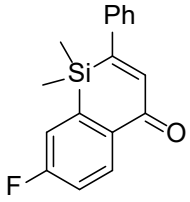

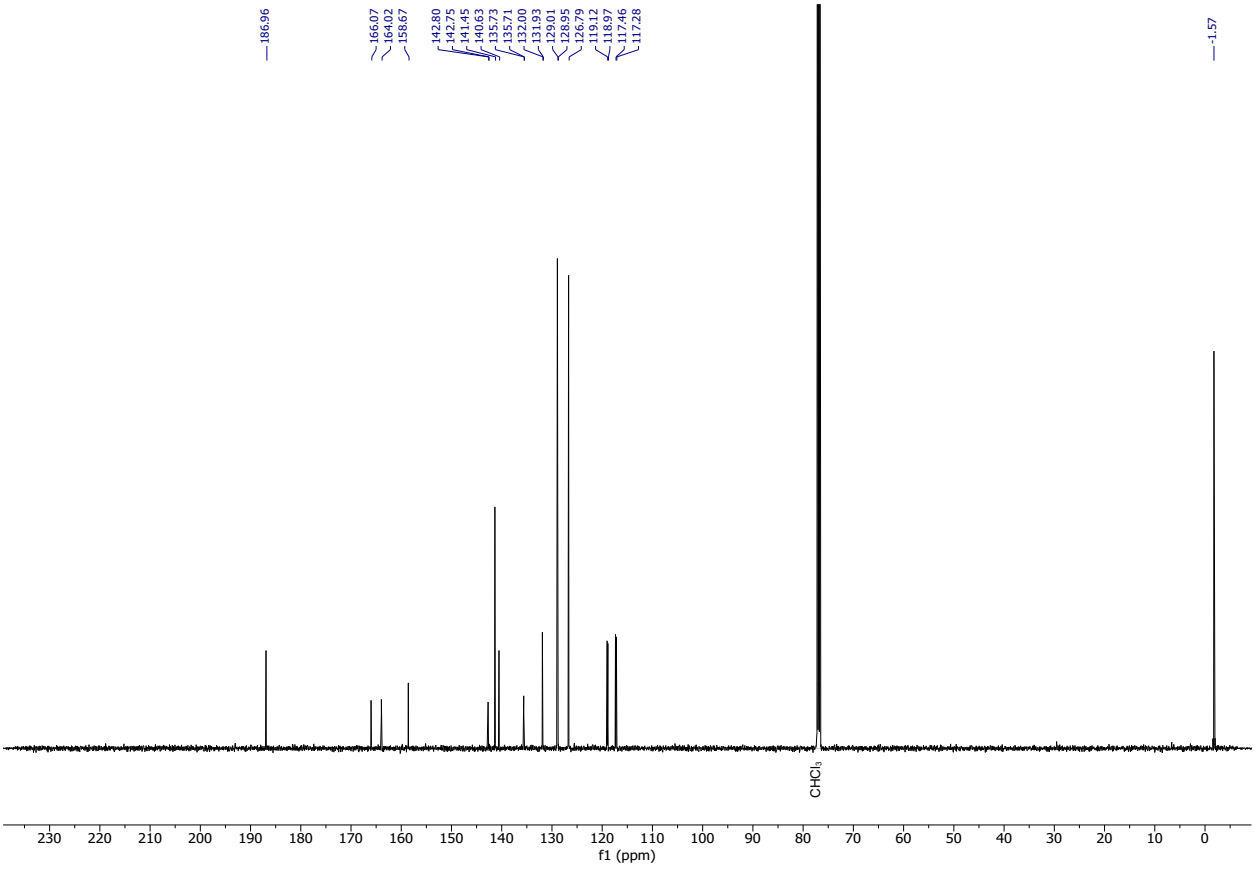

^{13}C NMR of **2.5b** (126 MHz, $CDCl_3$).

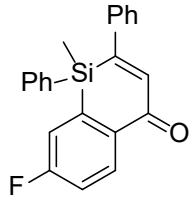

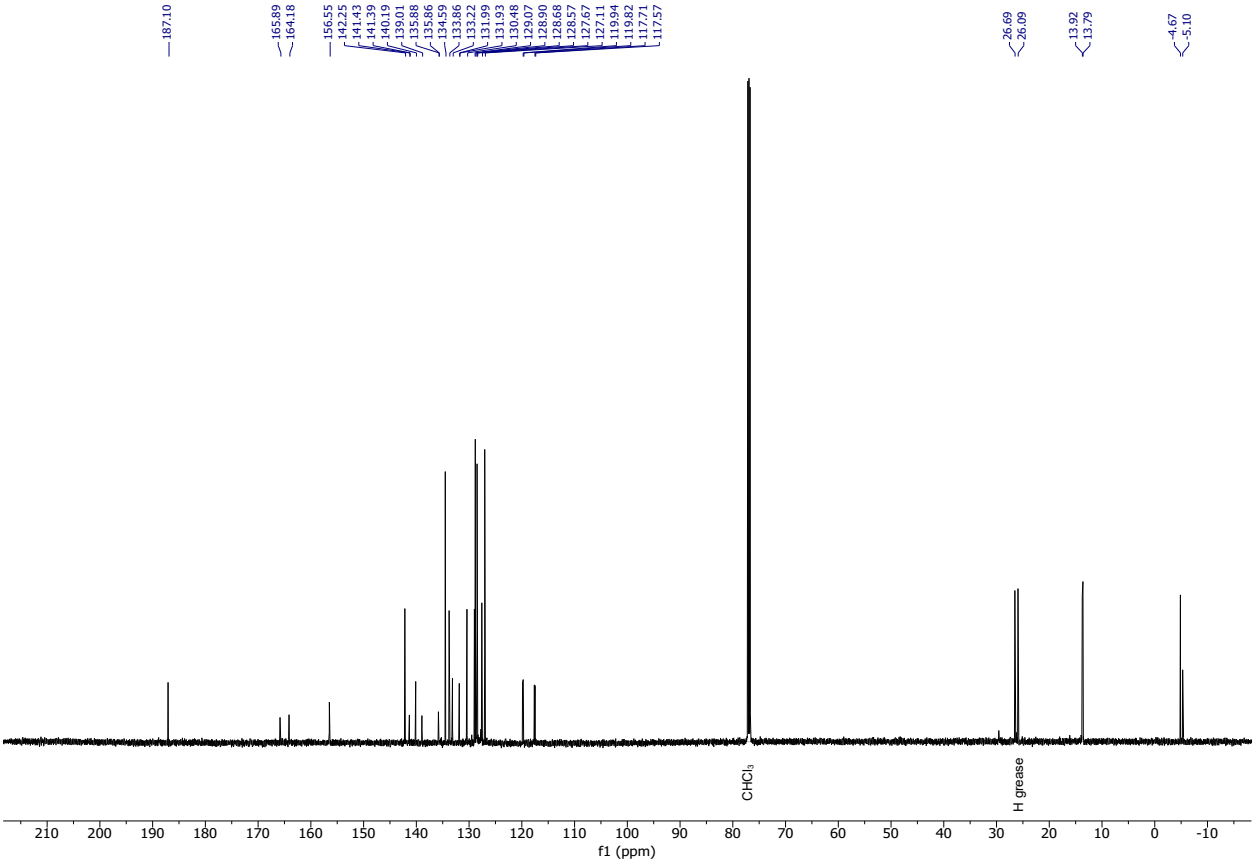

^{13}C NMR of **2.5c** (126 MHz, $CDCl_3$).

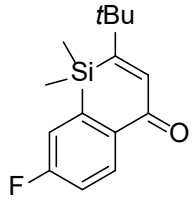

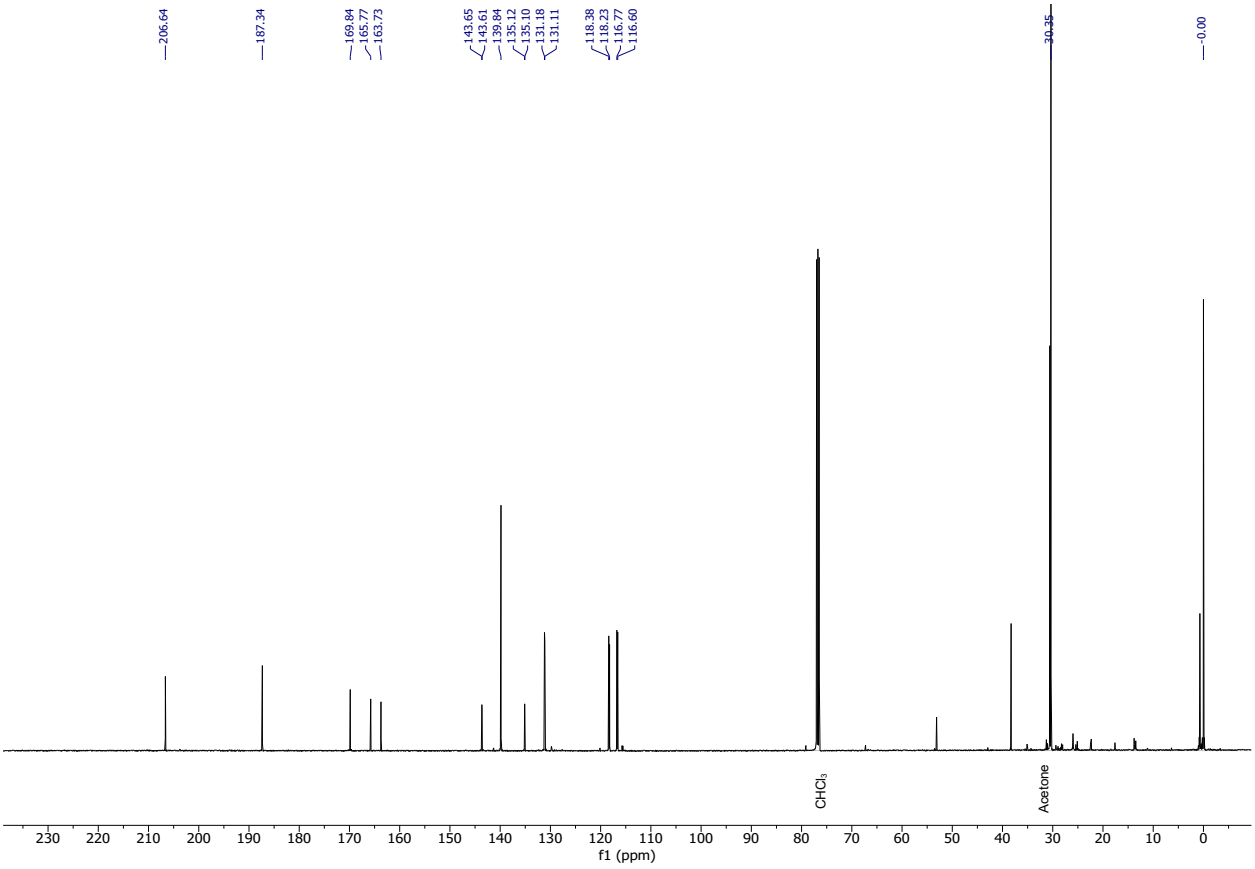

^{13}C NMR of **2.6a** (126 MHz, $CDCl_3$).

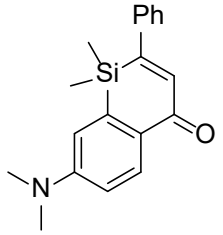

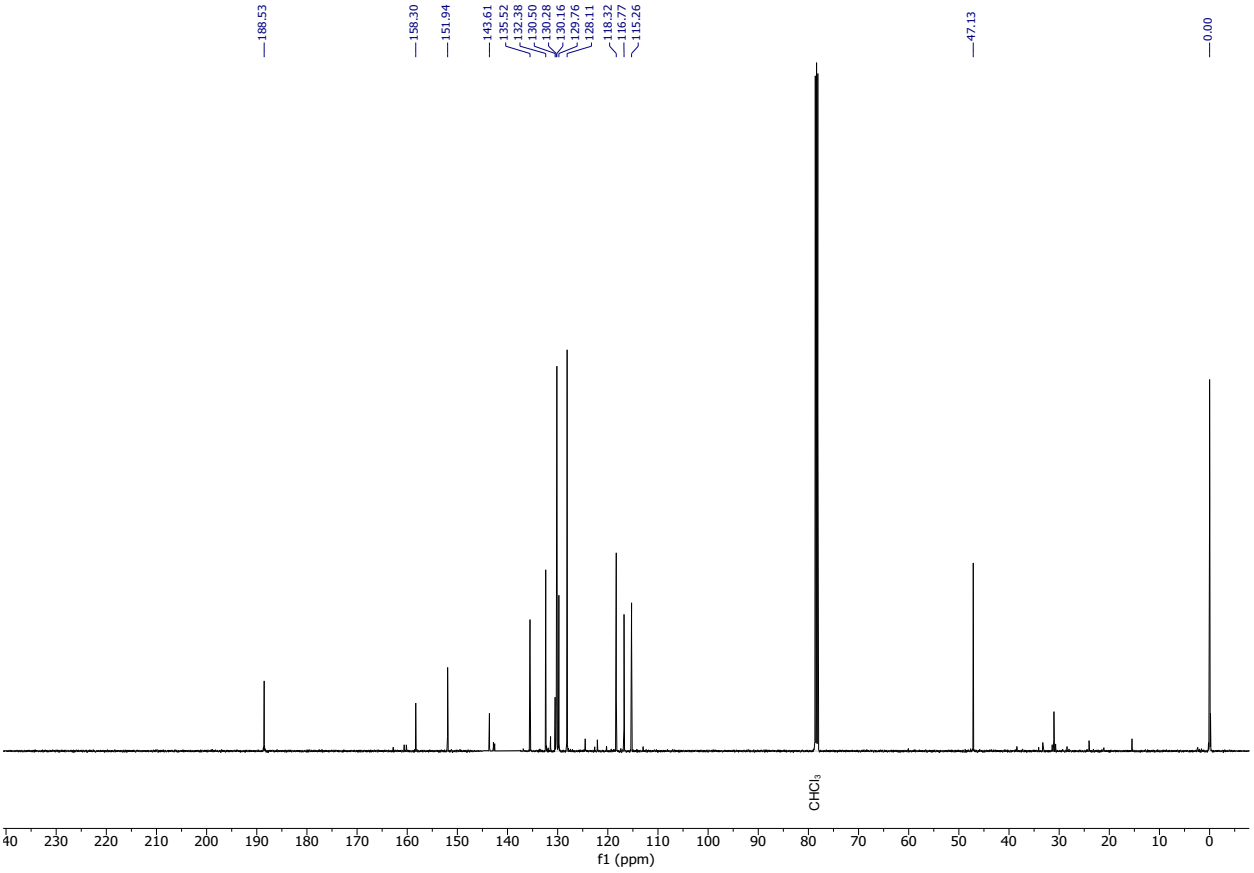

^{13}C NMR of **2.6b** (126 MHz, $CDCl_3$).

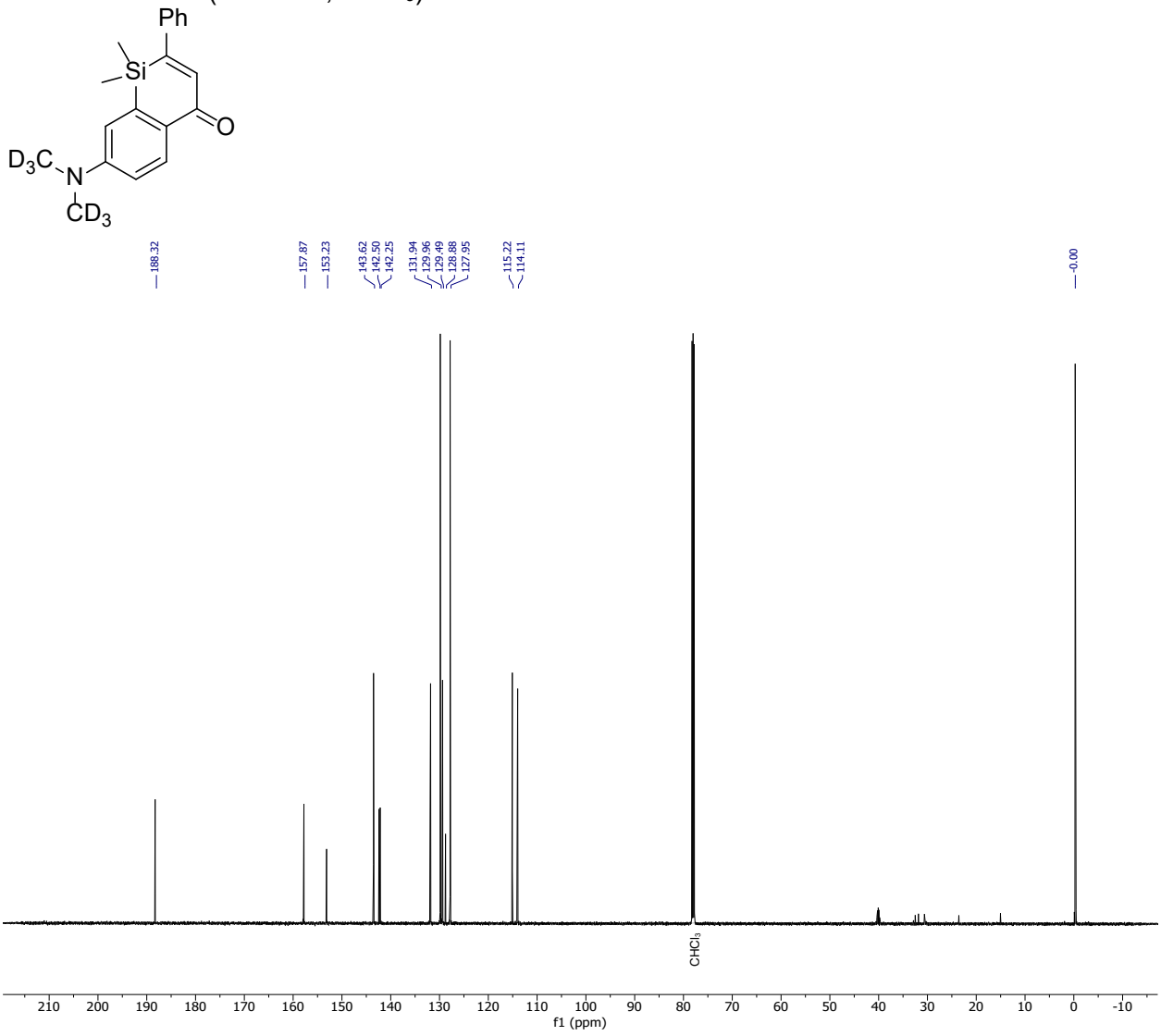

^{13}C NMR of **2.6c** (126 MHz, $CDCl_3$).

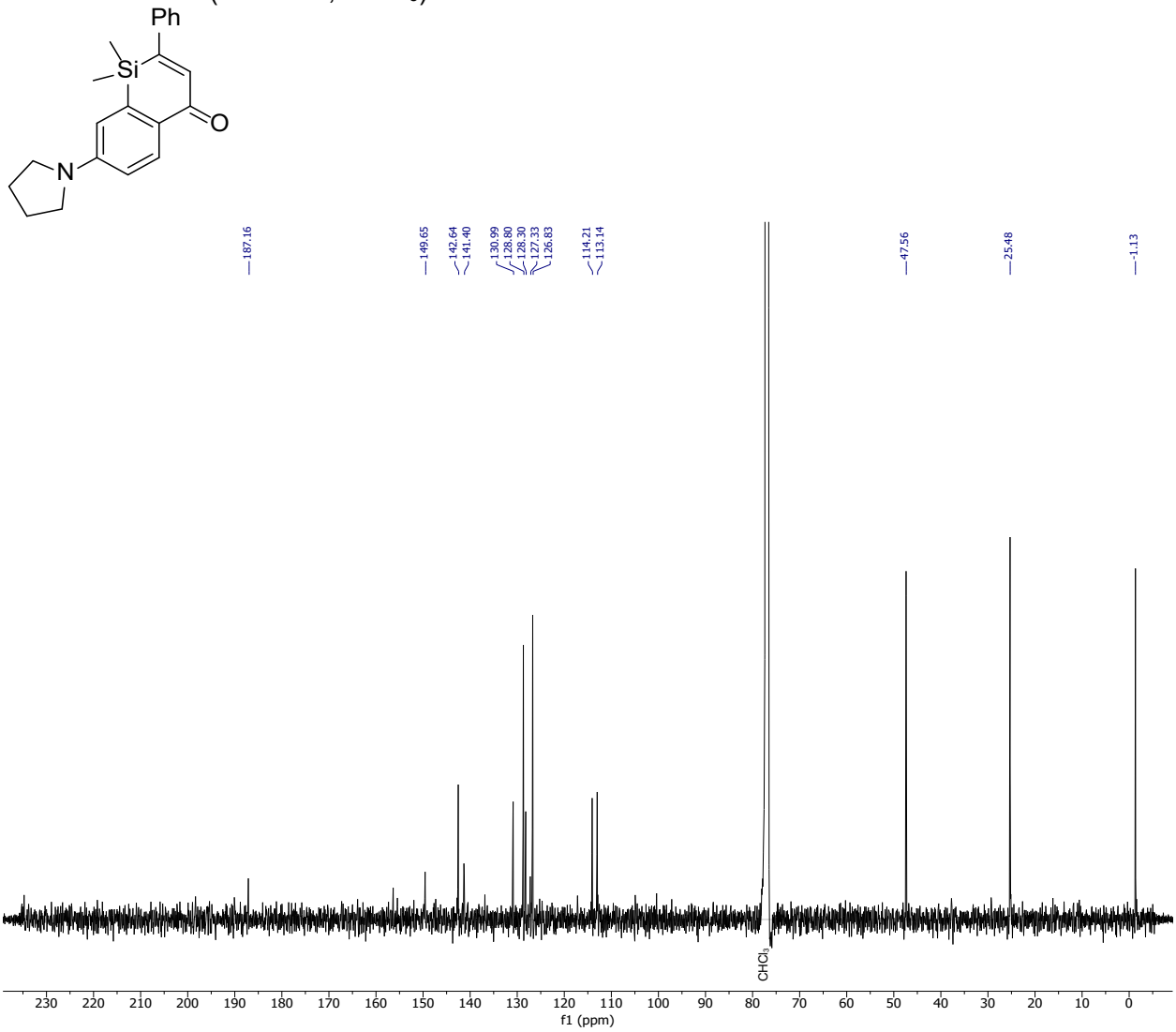

^{13}C NMR of **2.6d** (126 MHz, $CDCl_3$).

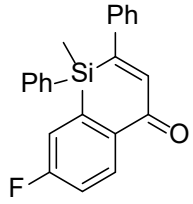

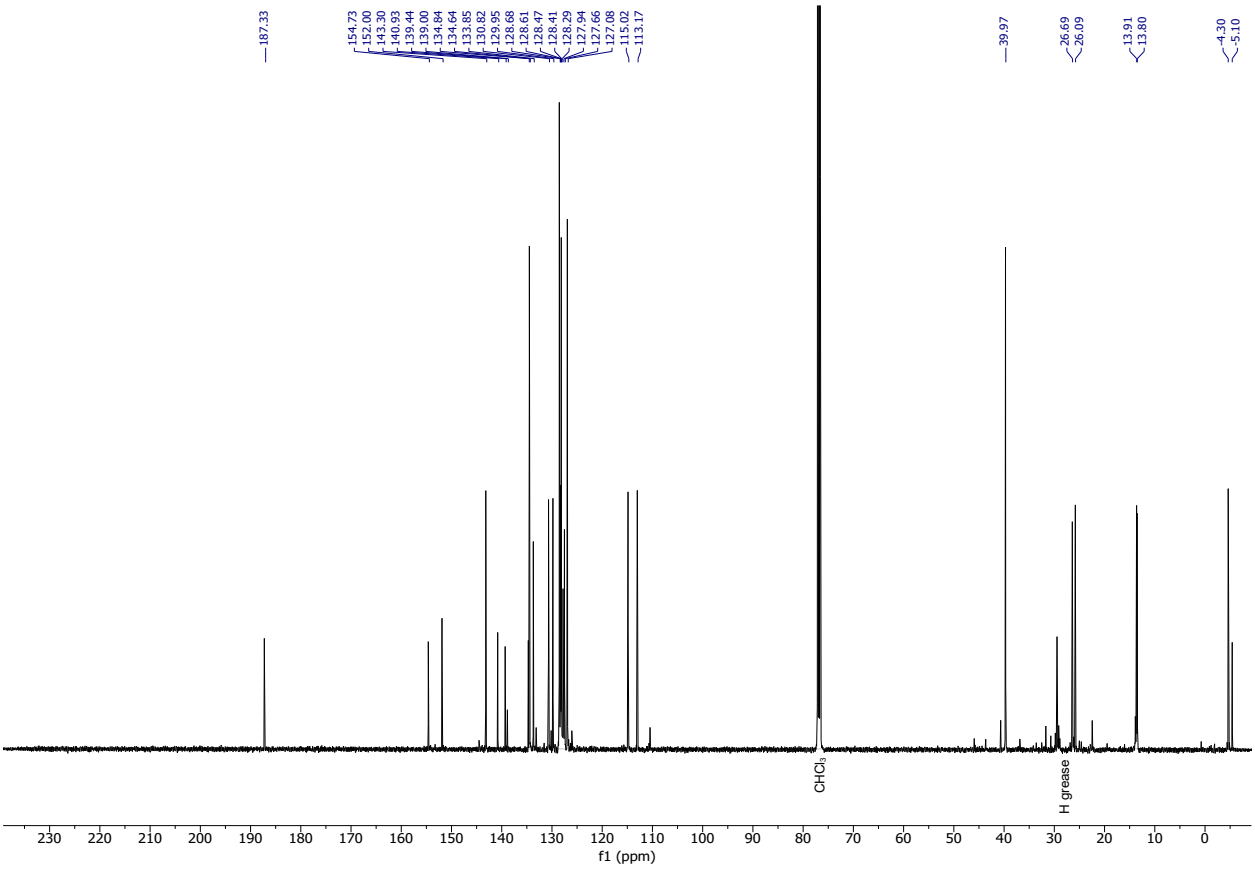

^{13}C NMR of **2.6e** (500 MHz, $CDCl_3$).

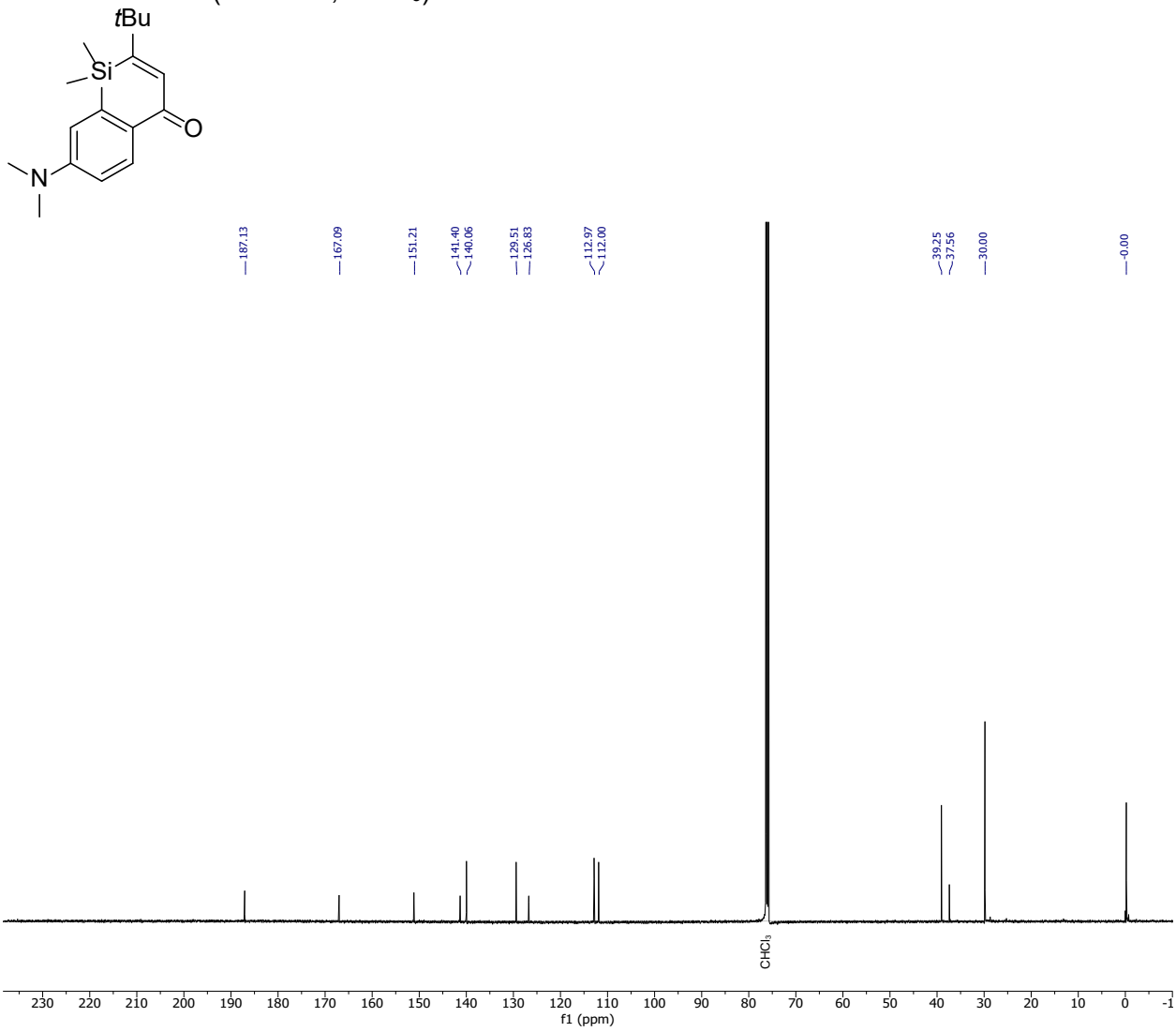

^{13}C NMR of **2.19** (126 MHz, $CDCl_3$).

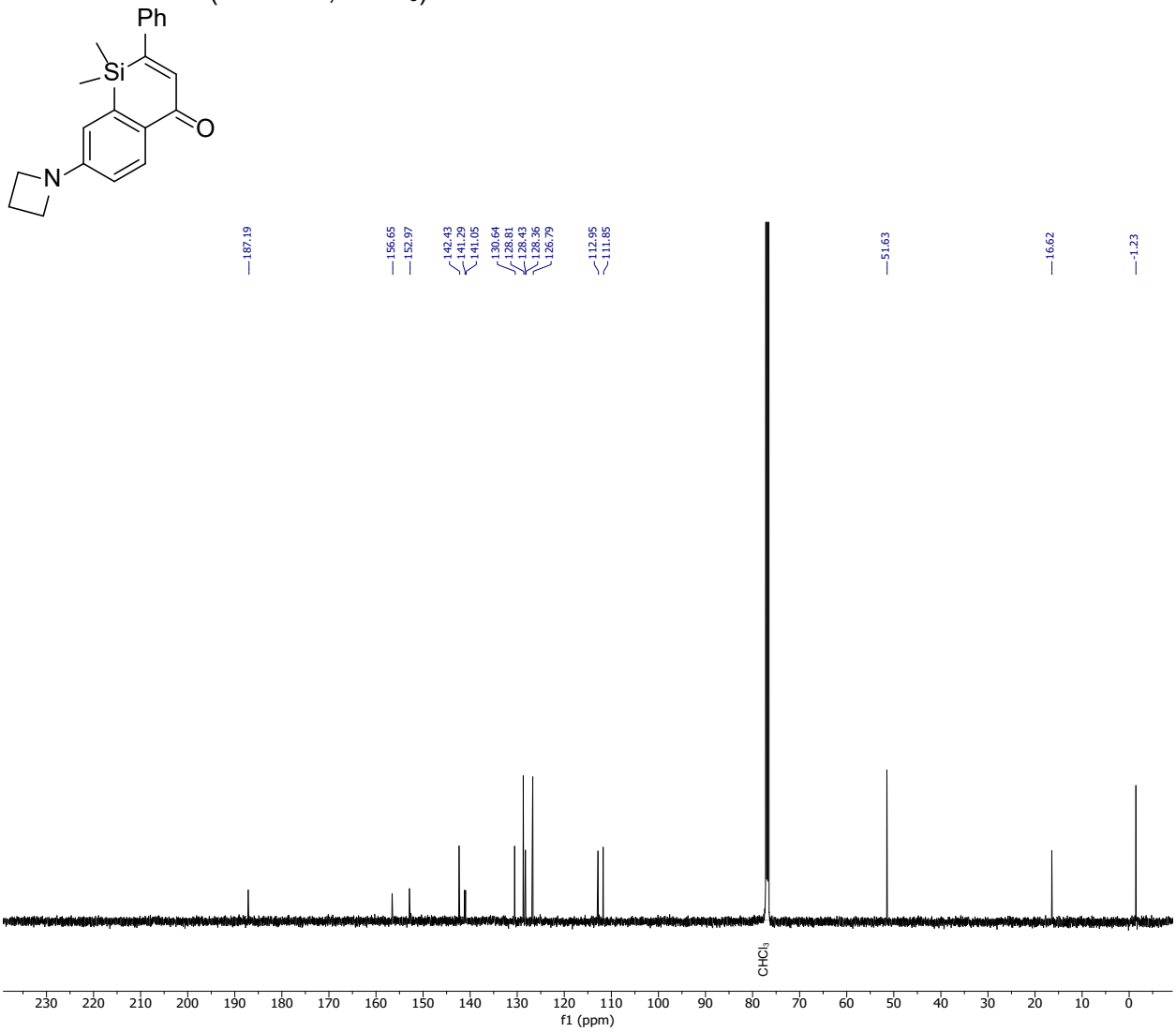

^{13}C NMR of **2.20** (126 MHz, $CDCl_3$).

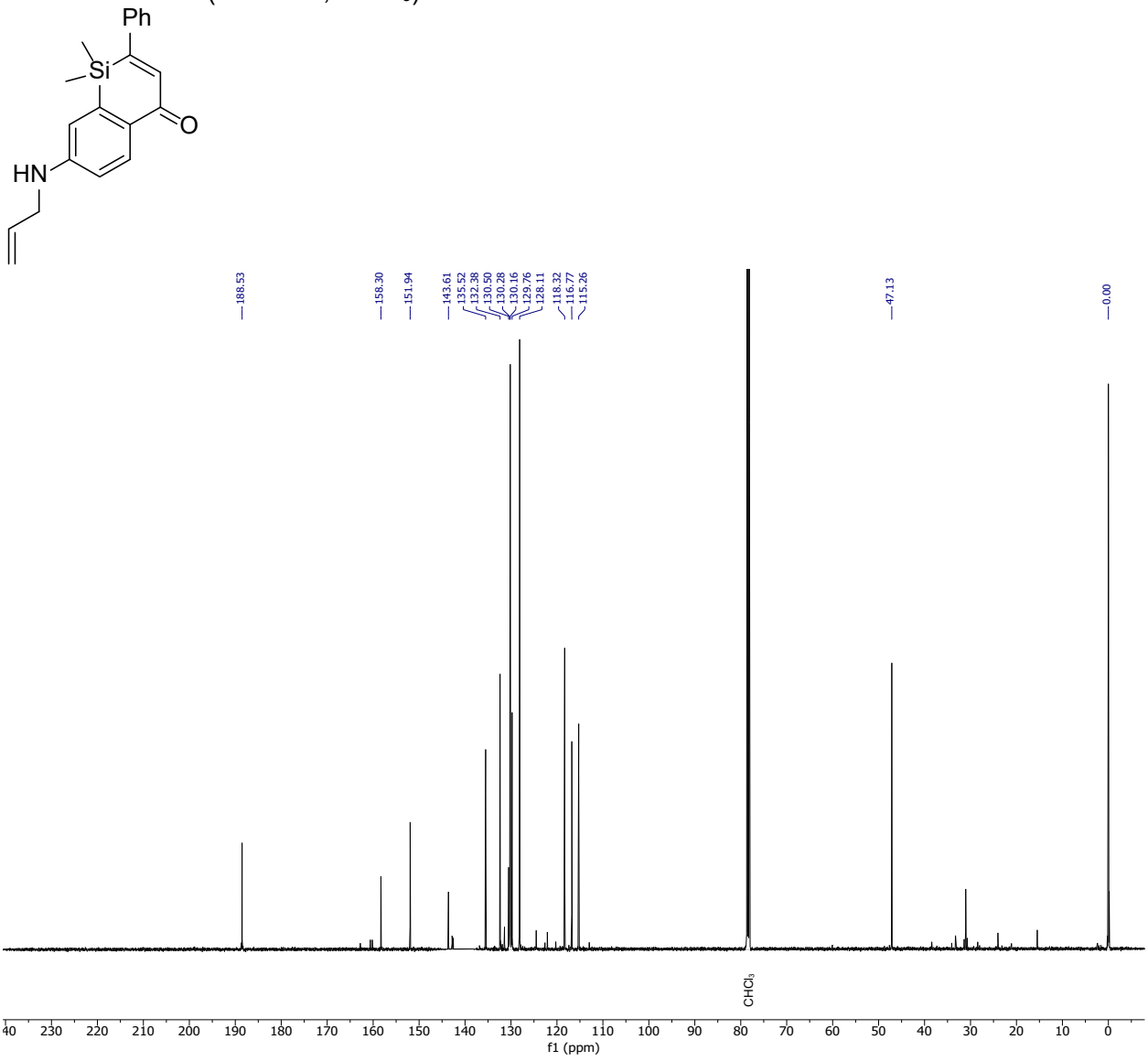

^{13}C NMR of **2.21** (151 MHz, $CDCl_3$).

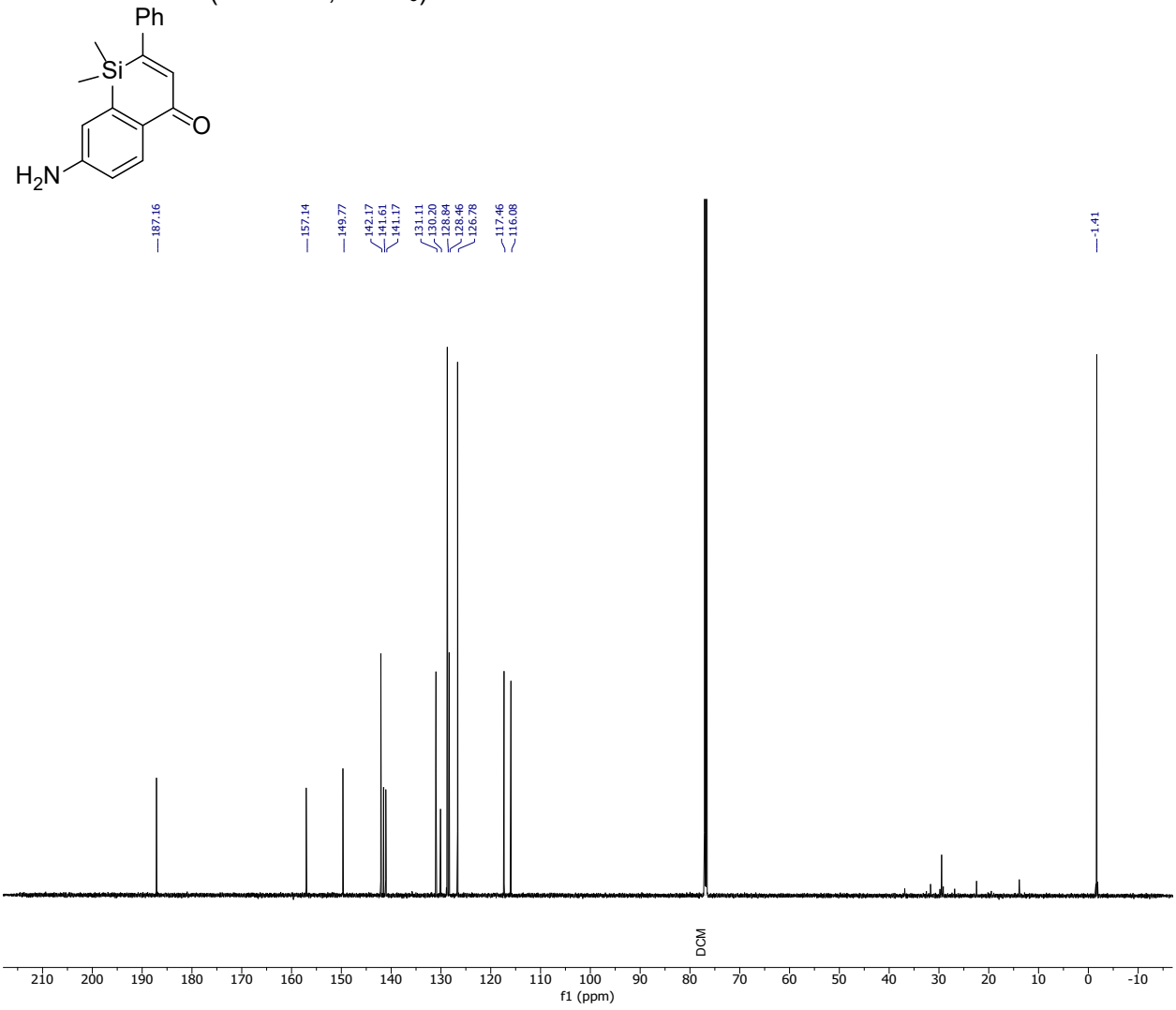

^{13}C NMR of **2.22** (126 MHz, $CDCl_3$).

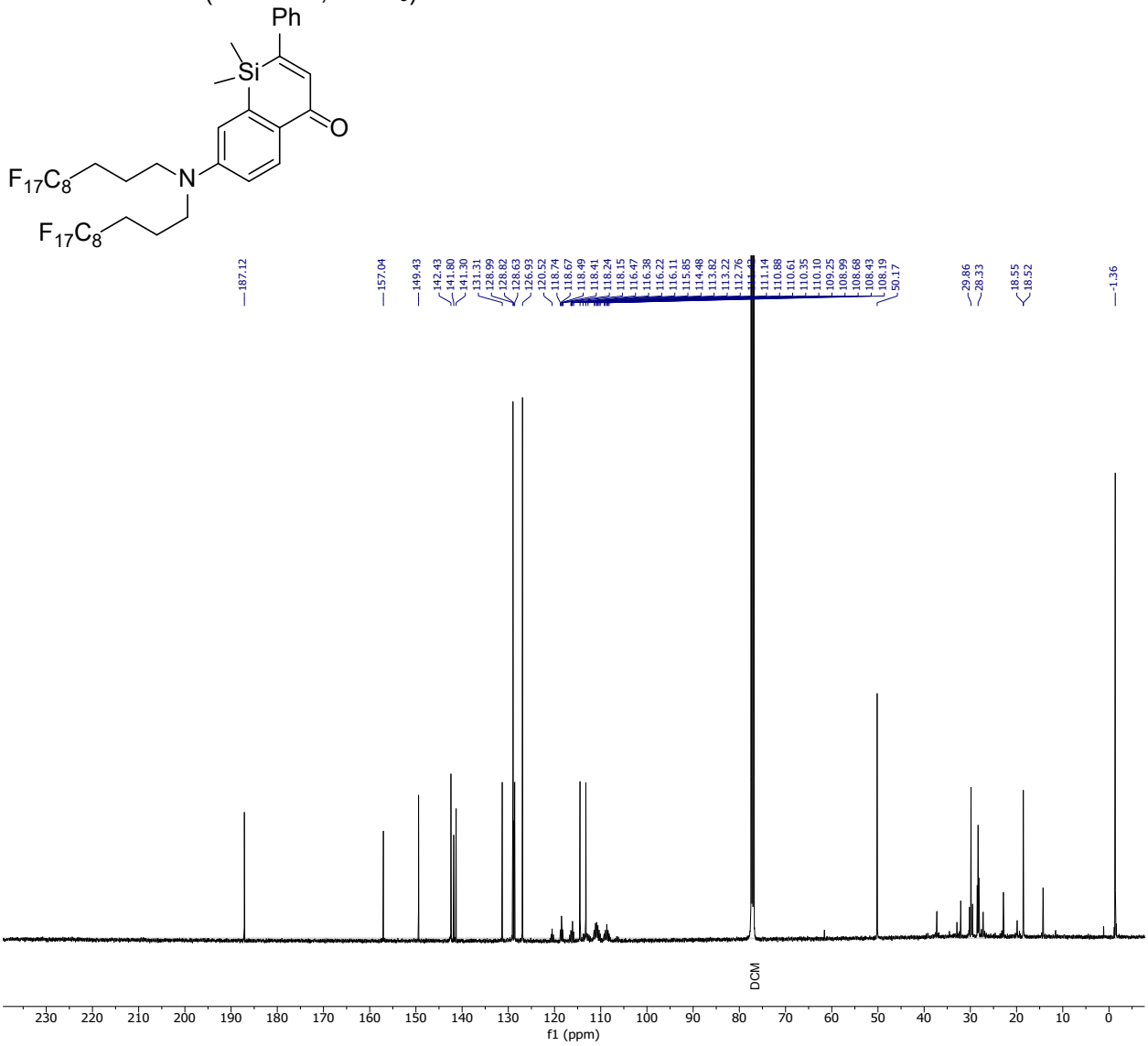

2.6.6 ^{19}F NMR Spectra

^{19}F NMR of **2.11**, SiliFlav5 (500 MHz, CD_2Cl_2 in 10% MeOD).

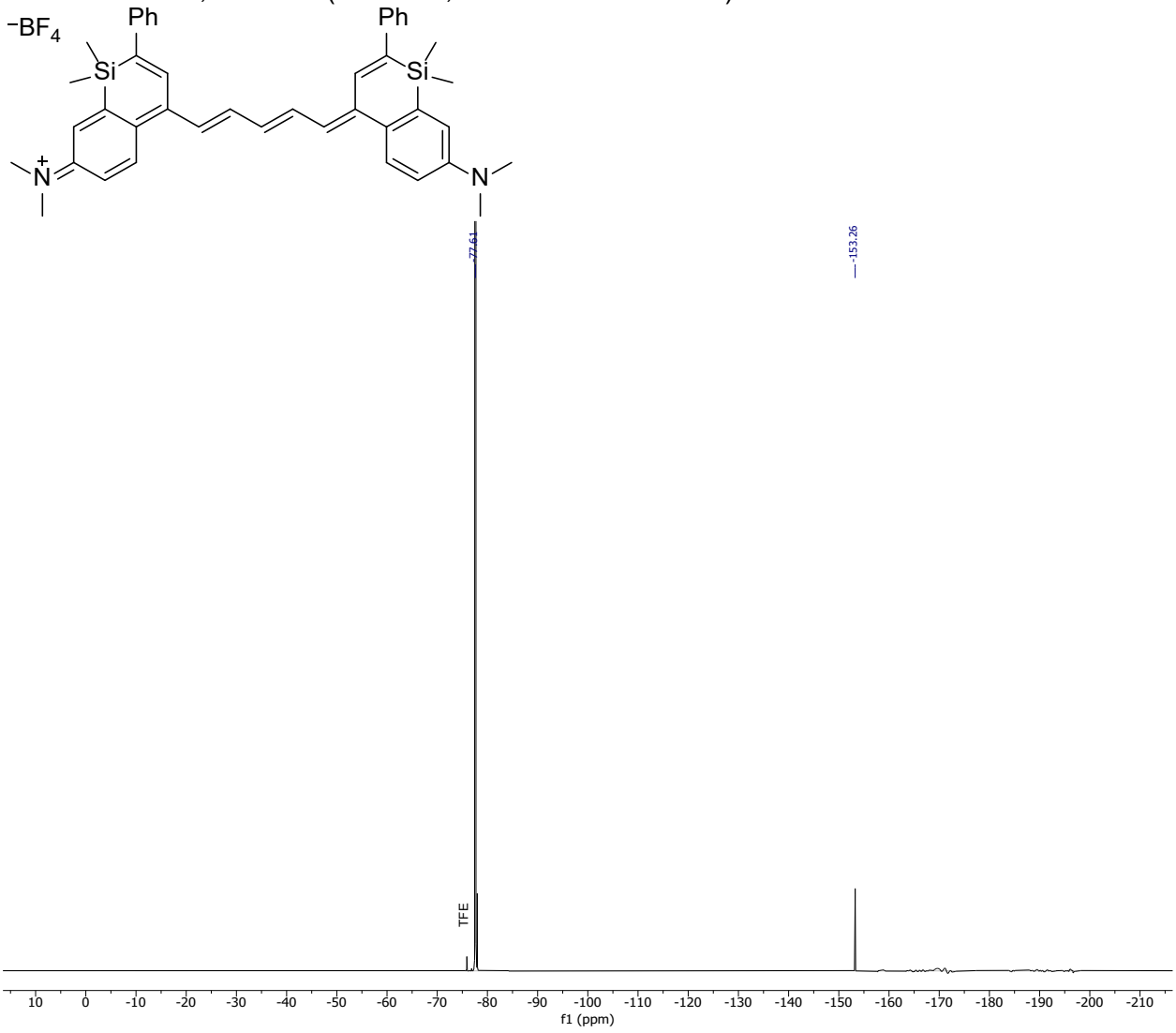

^{19}F NMR of **2.12**, SiliFlav7 (565 MHz, CD_2Cl_2).

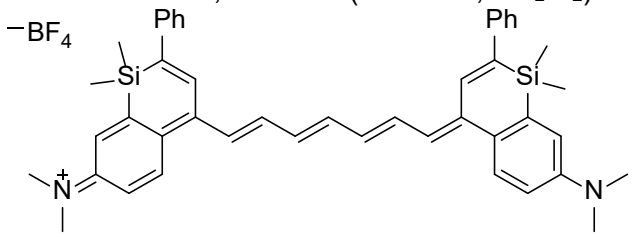

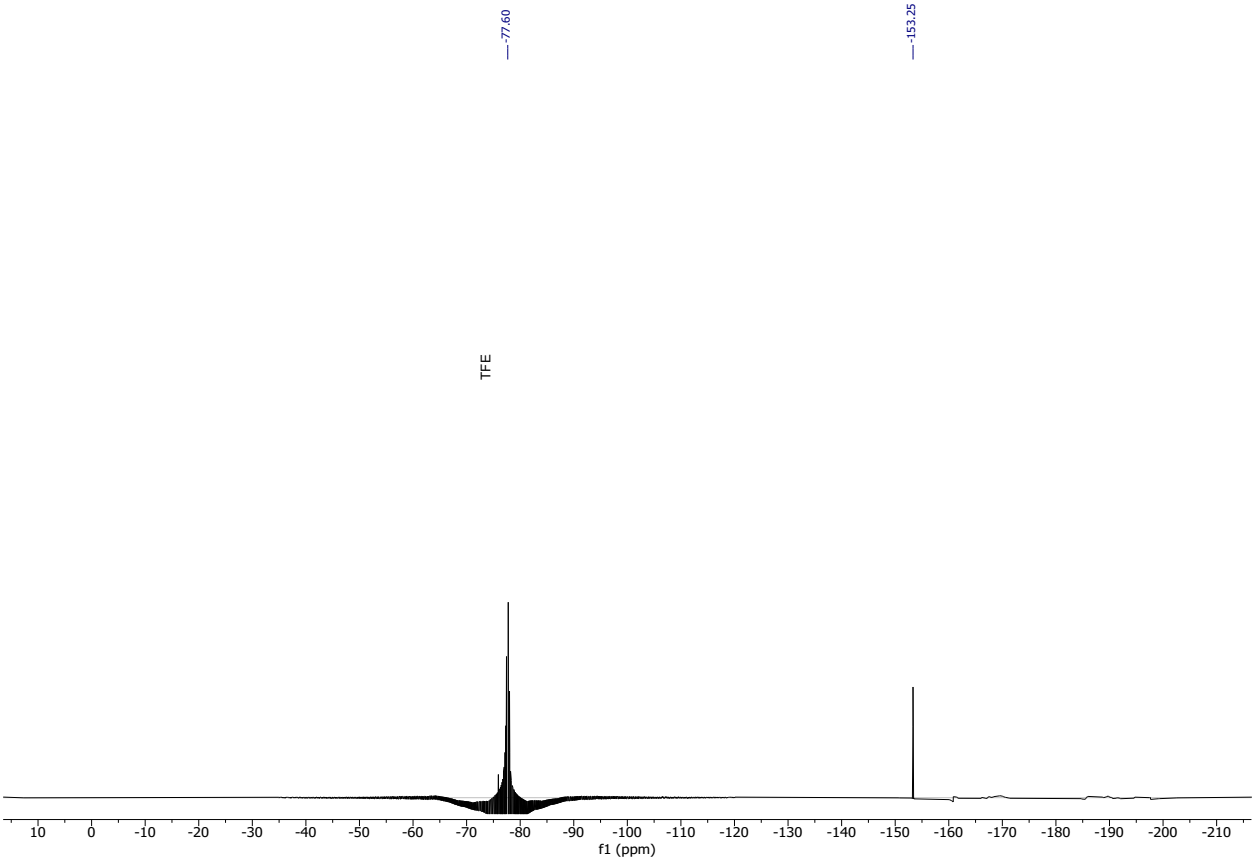

^{19}F NMR of **2.13**, SiliFlav9 (565 MHz, CD_2Cl_2).

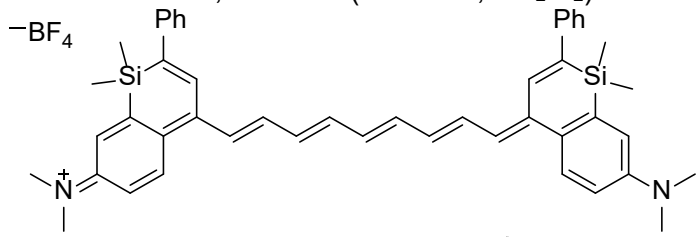

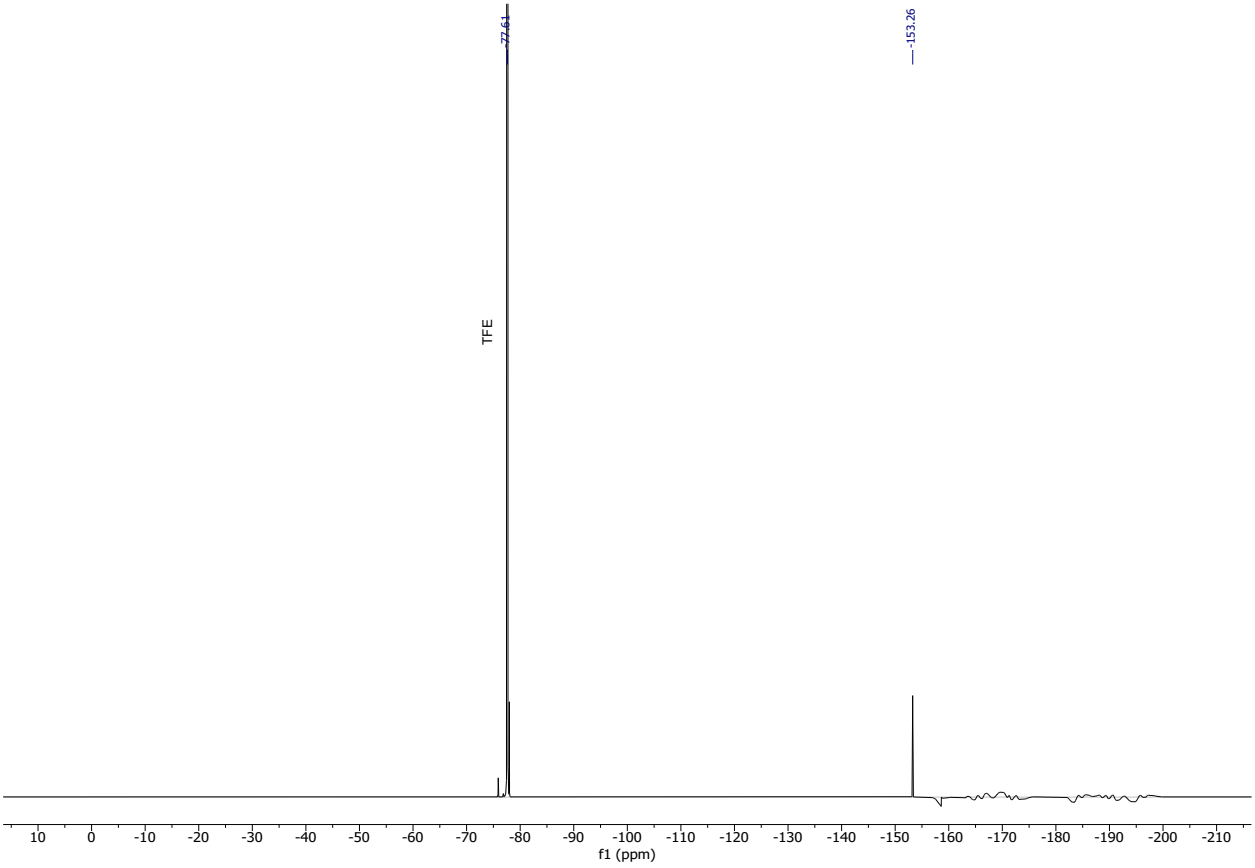

^{19}F NMR of **2.14,** SiliFlav5-*d*$_{12}$ (565 MHz, CD_2Cl_2).

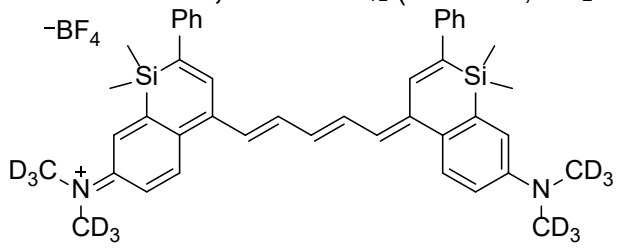

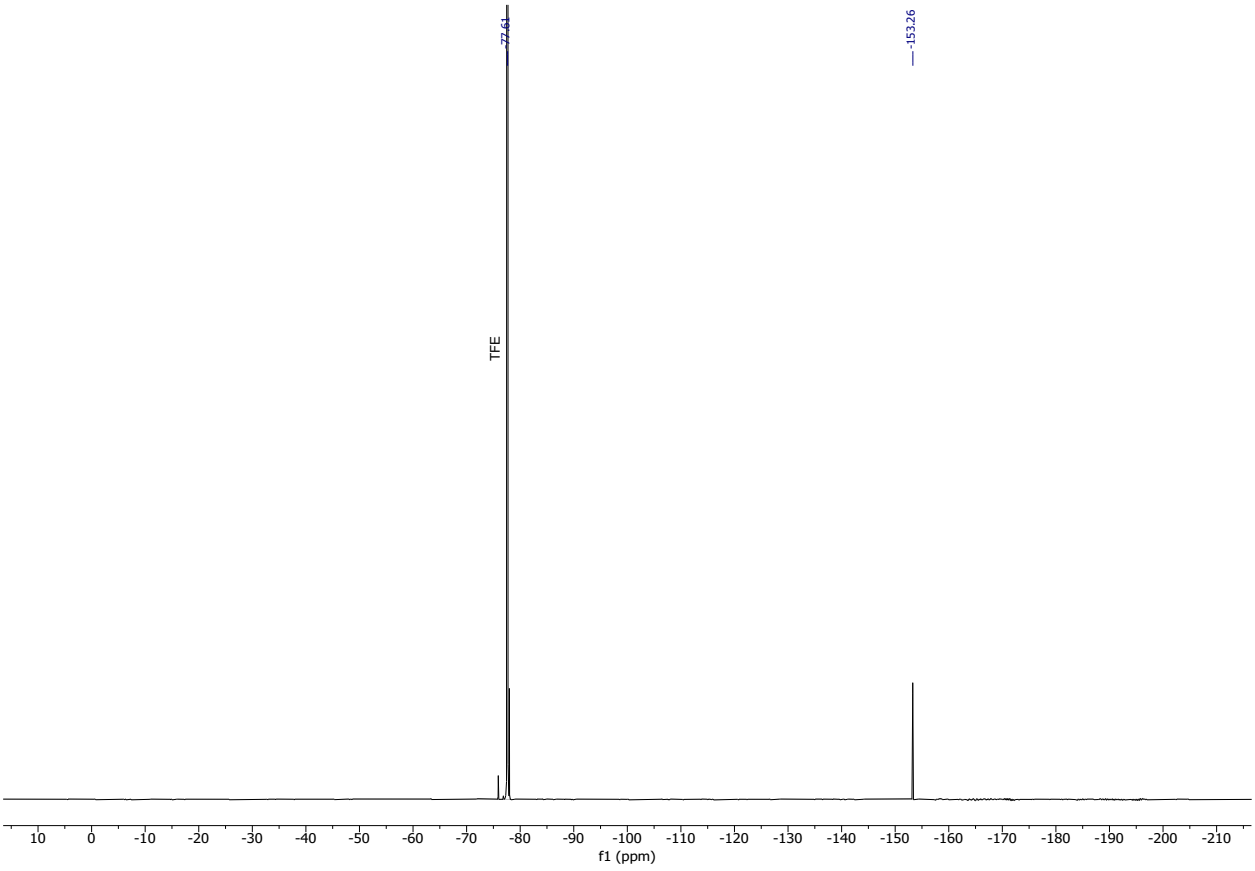

^{19}F NMR of **2.15**, Py-SiliFlav5 (565 MHz, CD_2Cl_2).

^{19}F NMR of **2.16**, Sili(MePh)Flav5 (565 MHz, CD_2Cl_2).

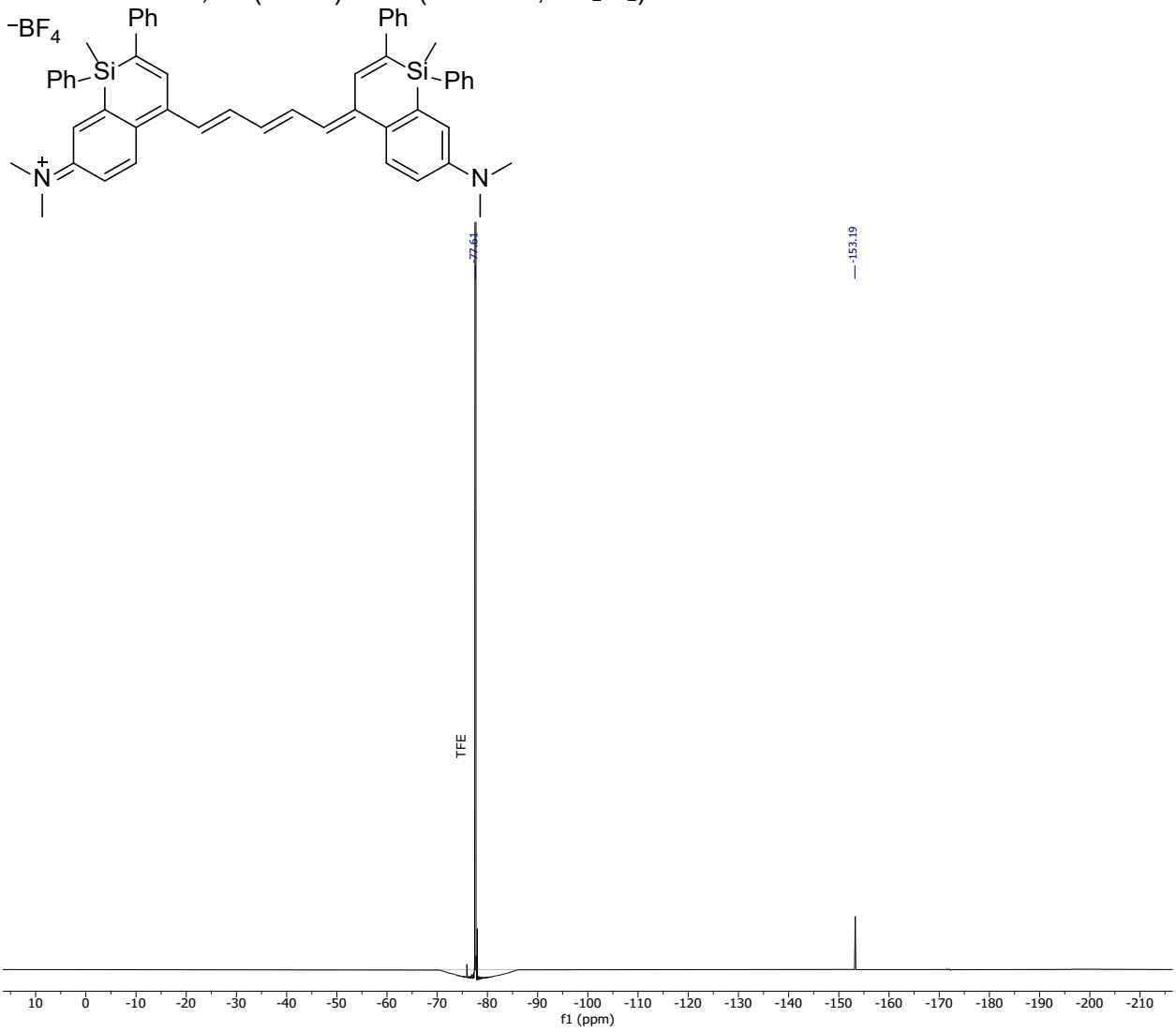

^{19}F NMR of **2.17**, SiliChrom5 (565 MHz, CD_2Cl_2).

^{19}F NMR **2.11•BArF$_{104}$**, SiliFlav5 BArF$_{104}$ (565 MHz, CD_2Cl_2).

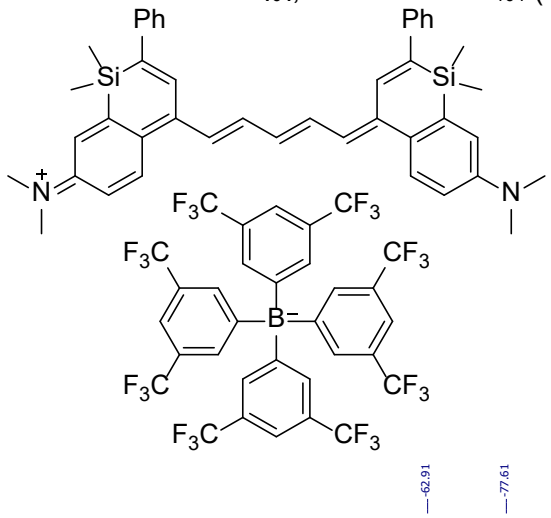

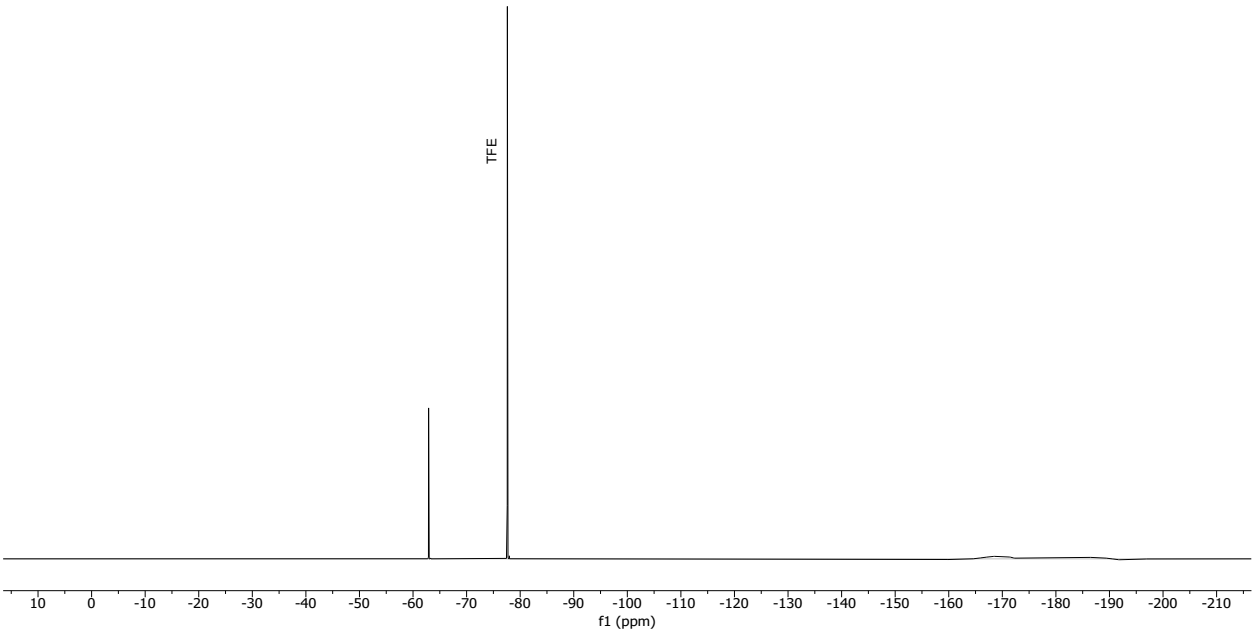

^{19}F NMR of **2.22** (565 MHz, $CDCl_3$).

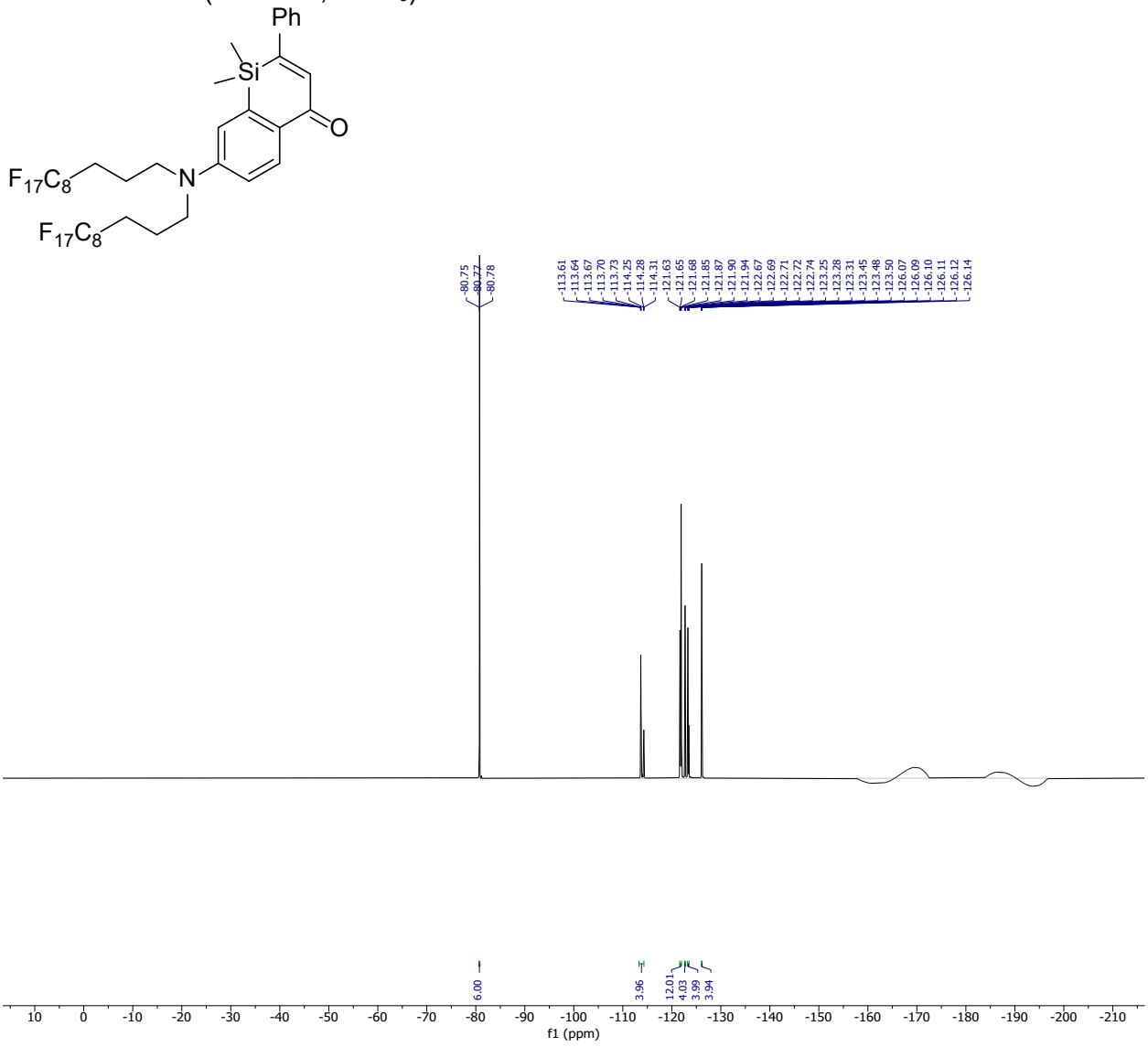

2.6.7 HRMS Spectra

HRMS of **2.1a**.

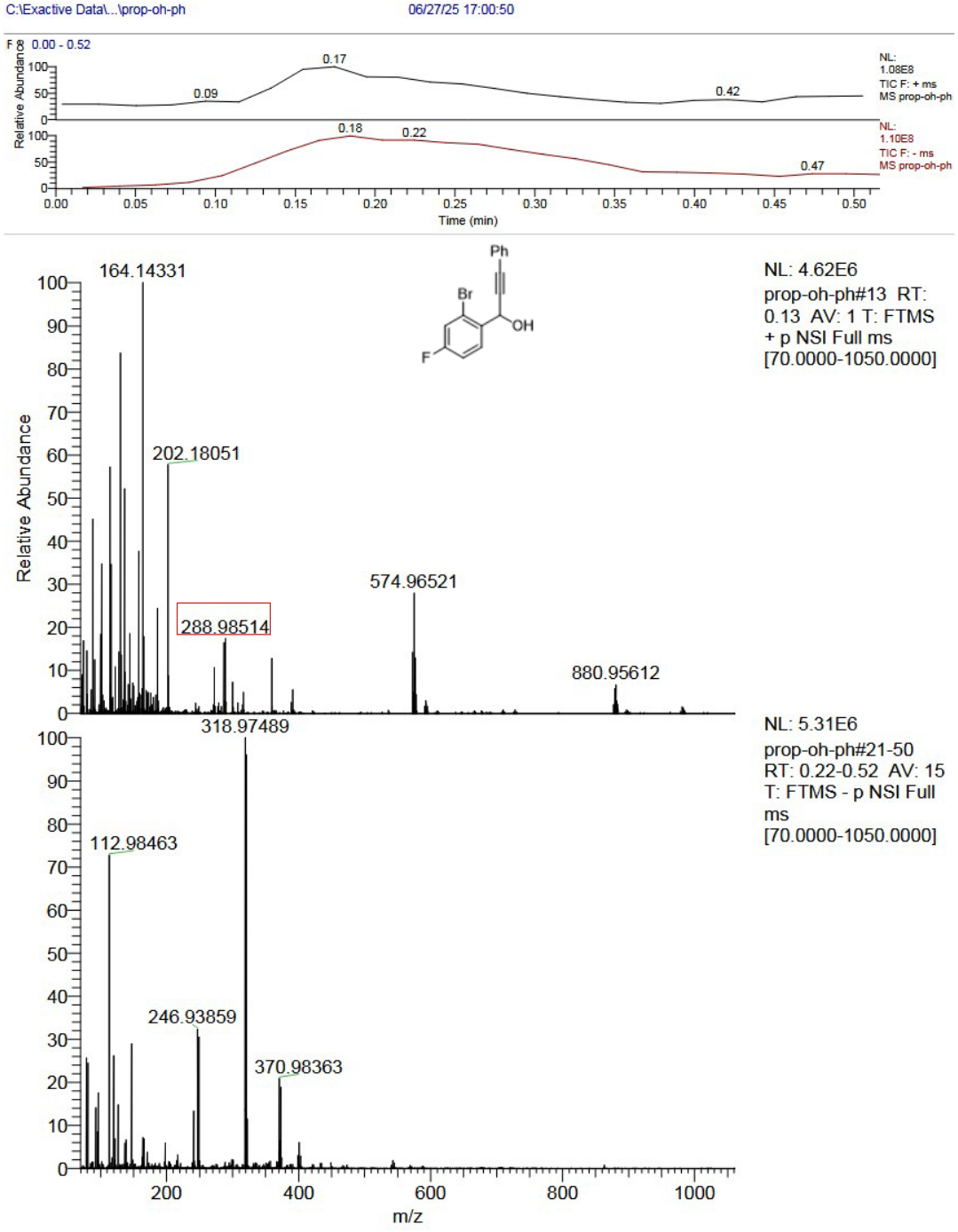

HRMS of **2.1b**.

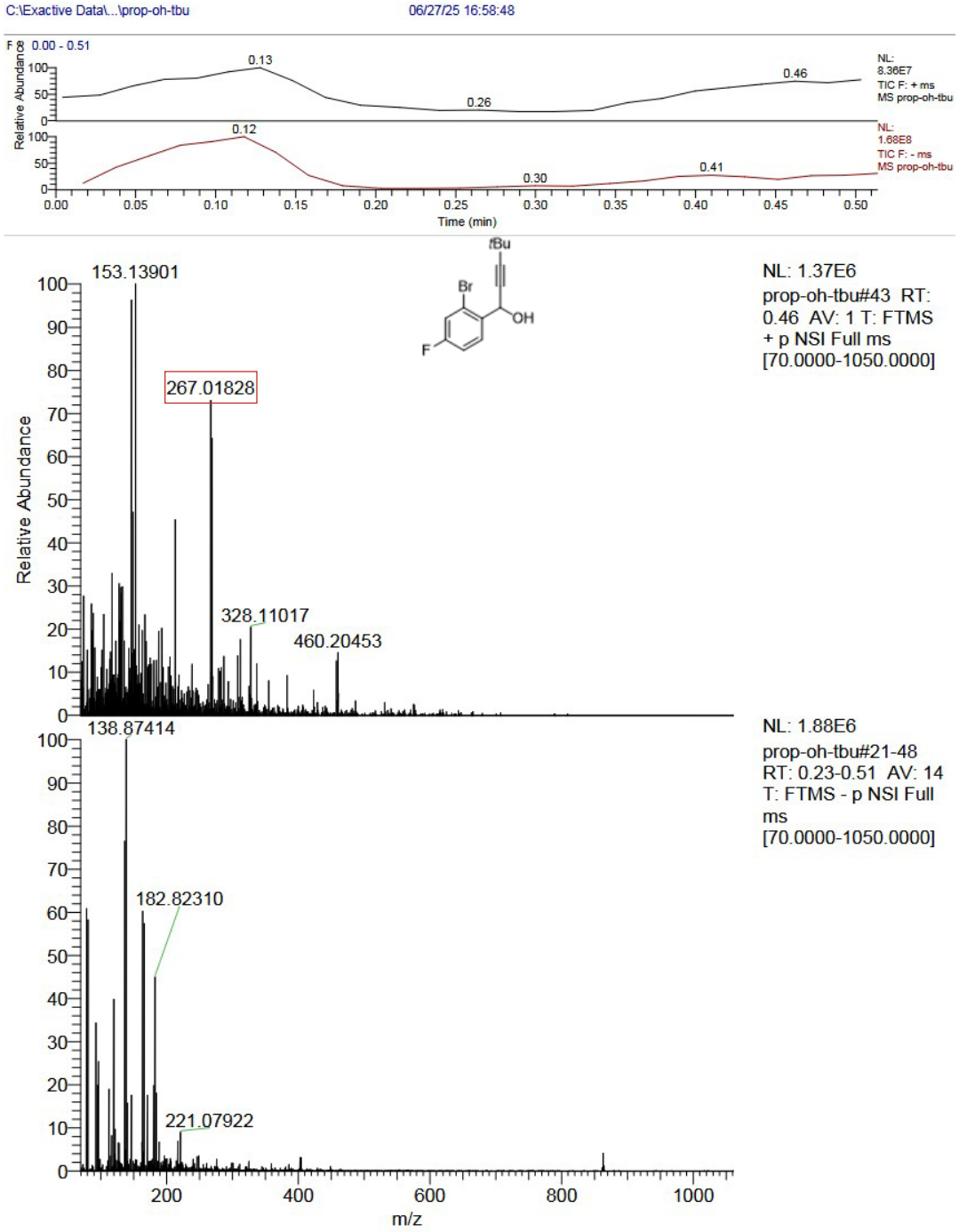
C:\Exactive Data\...\prop-oh-tbu
06/27/25 16:58:48
F: 0.00 - 0.51
Relative Abundance
0.13
0.26
0.46
NL: 8.36E7 TIC F: + ms MS prop-oh-tbu
0.12
0.30
0.41
NL: 1.68E8 TIC F: - ms MS prop-oh-tbu
Time (min)
tBu
Br
OH
F
153.13901
267.01828
328.11017
460.20453
NL: 1.37E6 prop-oh-tbu#43 RT: 0.46 AV: 1 T: FTMS + p NSI Full ms [70.0000-1050.0000]
138.87414
182.82310
221.07922
NL: 1.88E6 prop-oh-tbu#21-48 RT: 0.23-0.51 AV: 14 T: FTMS - p NSI Full ms [70.0000-1050.0000]
Relative Abundance
m/z

HRMS of **2.2a**.

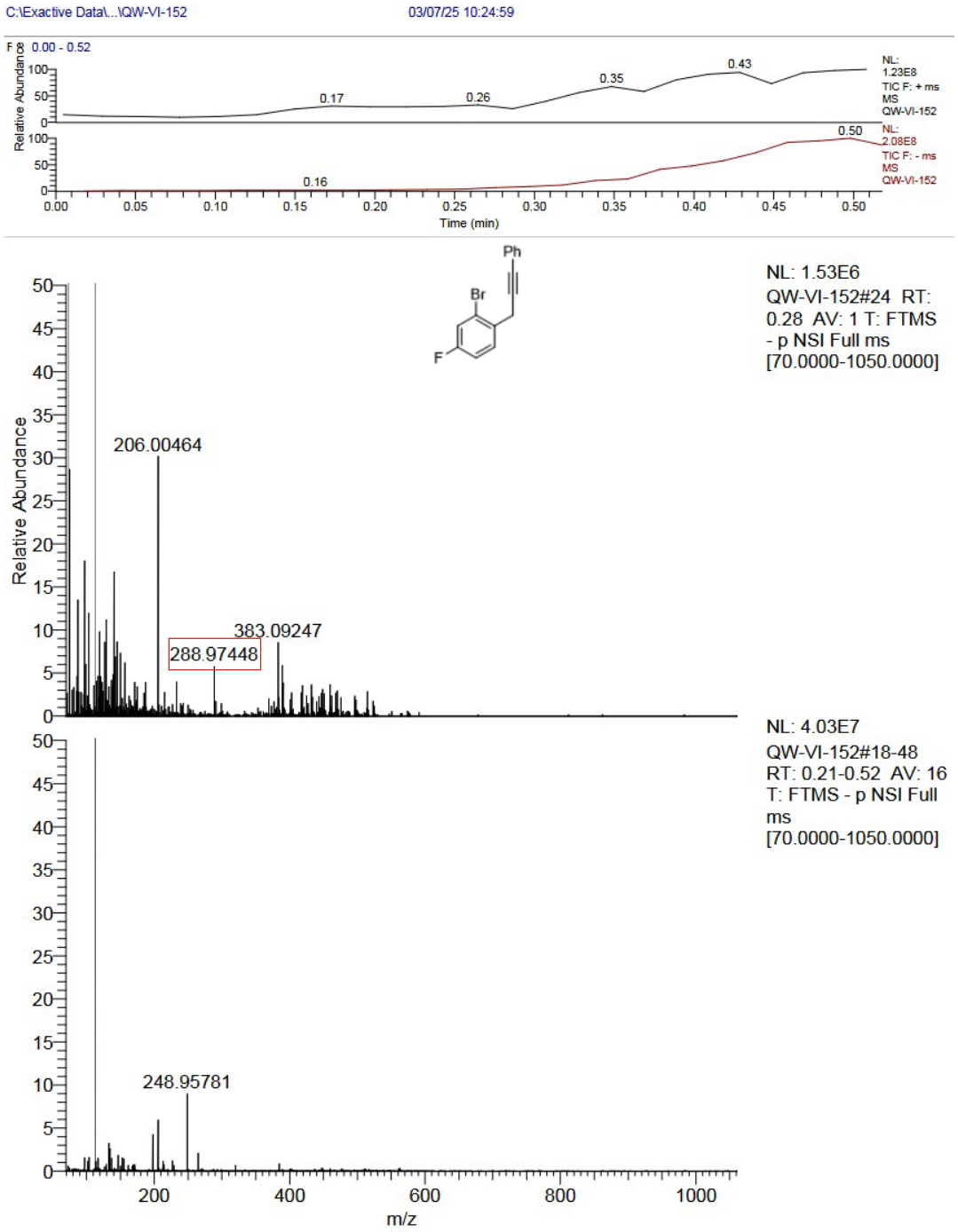
C:\Exactive Data\...\QW-VI-152
03/07/25 10:24:59
F 0.00 - 0.52
Relative Abundance
0.17
0.26
0.35
0.43
NL: 1.23E8 TIC F: + ms MS QW-VI-152
0.16
0.50
NL: 2.08E8 TIC F: - ms MS QW-VI-152
Time (min)
Ph
Br
F
NL: 1.53E6 QW-VI-152#24 RT: 0.28 AV: 1 T: FTMS - p NSI Full ms [70.0000-1050.0000]
206.00464
383.09247
288.97448
NL: 4.03E7 QW-VI-152#18-48 RT: 0.21-0.52 AV: 16 T: FTMS - p NSI Full ms [70.0000-1050.0000]
248.95781
m/z

HRMS of **2.3a**.

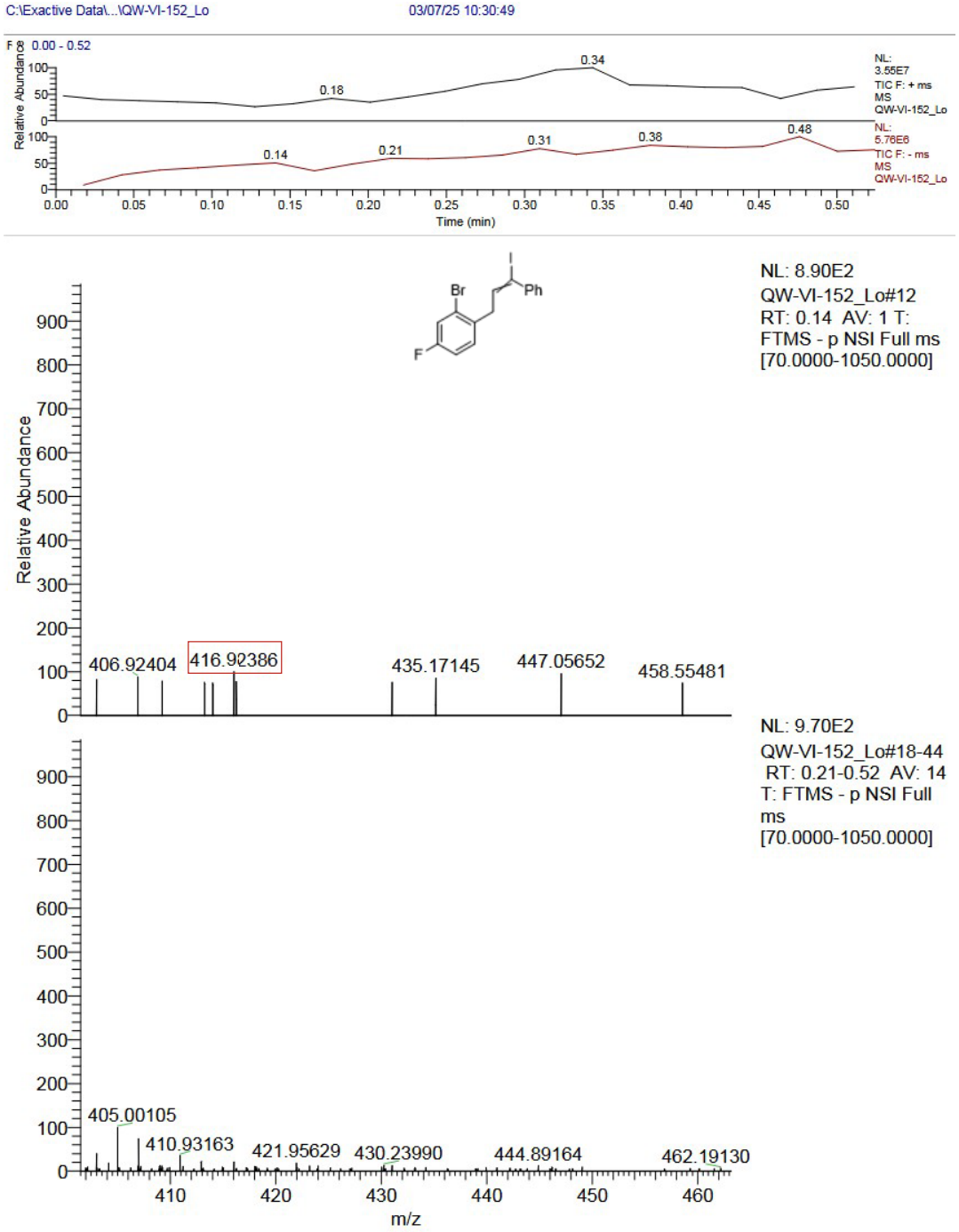
C:\Exactive Data\...\QW-VI-152_Lo
03/07/25 10:30:49
F 0.00 - 0.52
Relative Abundance
0.18
0.34
NL: 3.55E7 TIC F: + ms MS QW-VI-152_Lo
0.14
0.21
0.31
0.38
0.48
NL: 5.76E6 TIC F: - ms MS QW-VI-152_Lo
Time (min)
Br
I
Ph
F
NL: 8.90E2
QW-VI-152_Lo#12
RT: 0.14 AV: 1 T:
FTMS - p NSI Full ms
[70.0000-1050.0000]
406.92404
416.92386
435.17145
447.05652
458.55481
NL: 9.70E2
QW-VI-152_Lo#18-44
RT: 0.21-0.52 AV: 14
T: FTMS - p NSI Full
ms
[70.0000-1050.0000]
405.00105
410.93163
421.95629
430.23990
444.89164
462.19130
m/z

HRMS of **2.3b**.

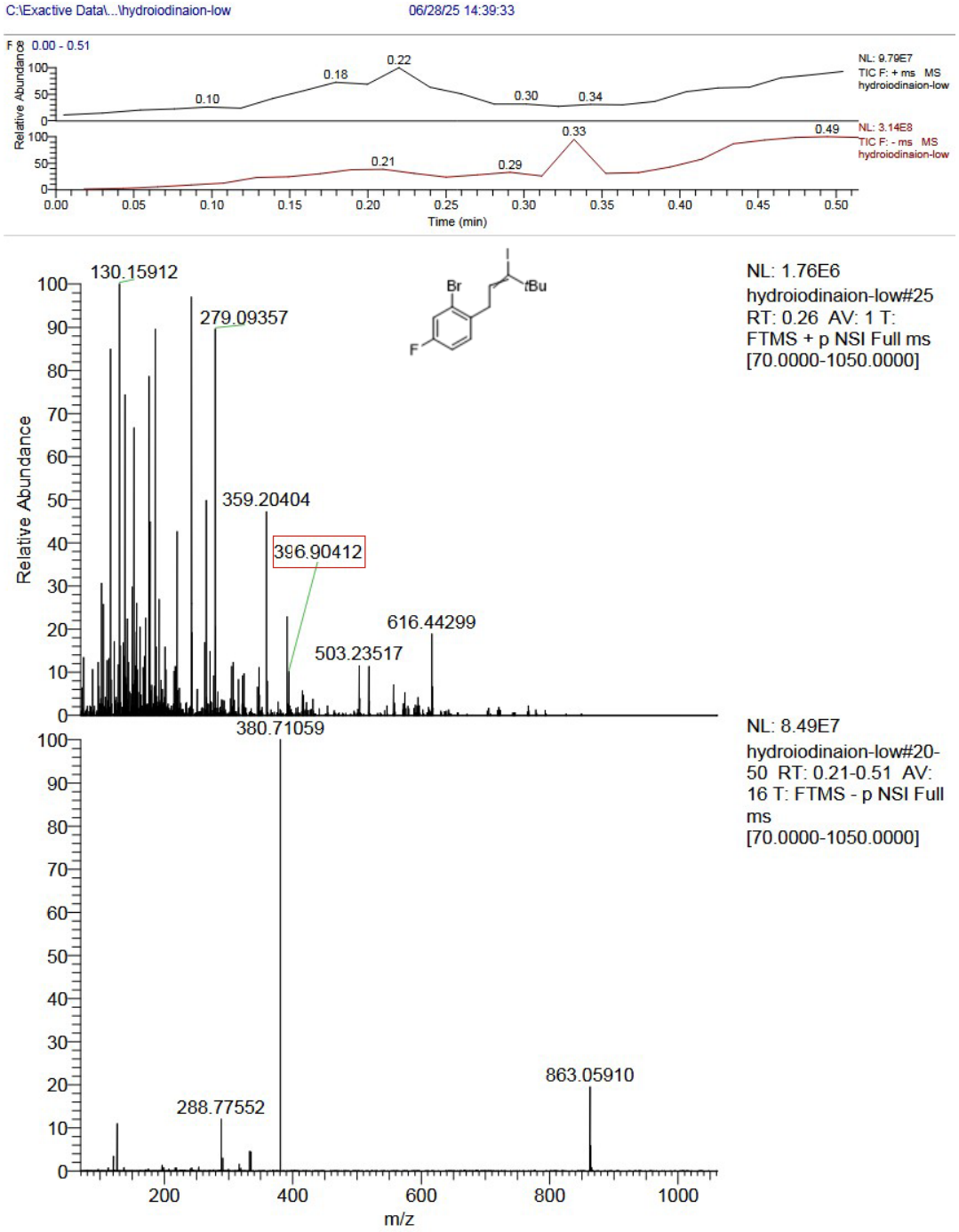
C:\Exactive Data\...\hydroiodinaion-low
06/28/25 14:39:33
F 0.00 - 0.51
Relative Abundance
0.10
0.18
0.22
0.30
0.34
NL: 9.79E7
TIC F: + ms MS
hydroiodinaion-low
0.21
0.29
0.33
0.49
NL: 3.14E8
TIC F: - ms MS
hydroiodinaion-low
Time (min)
130.15912
279.09357
359.20404
396.90412
616.44299
503.23517
Br
tBu
F
NL: 1.76E6
hydroiodinaion-low#25
RT: 0.26 AV: 1 T:
FTMS + p NSI Full ms
[70.0000-1050.0000]
380.71059
863.05910
288.77552
NL: 8.49E7
hydroiodinaion-low#20-
50 RT: 0.21-0.51 AV:
16 T: FTMS - p NSI Full
ms
[70.0000-1050.0000]
m/z

HRMS of **2.4a**.

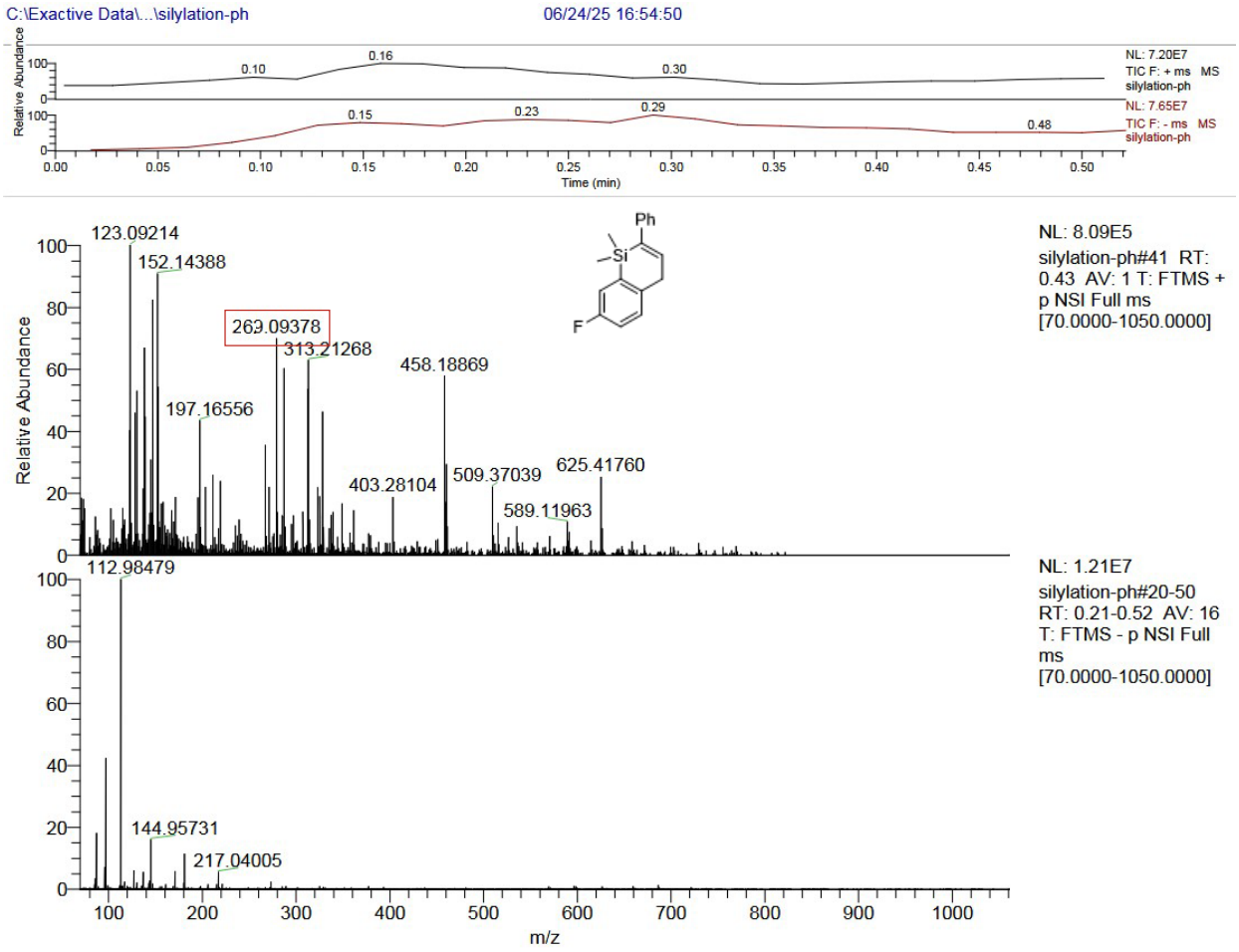
C:\Exactive Data\...\silylation-ph
06/24/25 16:54:50
Relative Abundance
0.10
0.16
0.30
NL: 7.20E7
TIC F: + ms MS
silylation-ph
0.15
0.23
0.29
0.48
NL: 7.65E7
TIC F: - ms MS
silylation-ph
Time (min)
123.09214
152.14388
263.09378
313.21268
458.18869
197.16556
403.28104
509.37039
625.41760
589.11963
Ph
Si
F
NL: 8.09E5
silylation-ph#41 RT: 0.43 AV: 1 T: FTMS + p NSI Full ms [70.0000-1050.0000]
112.98479
144.95731
217.04005
NL: 1.21E7
silylation-ph#20-50 RT: 0.21-0.52 AV: 16 T: FTMS - p NSI Full ms [70.0000-1050.0000]
m/z

HRMS of **2.4b**.

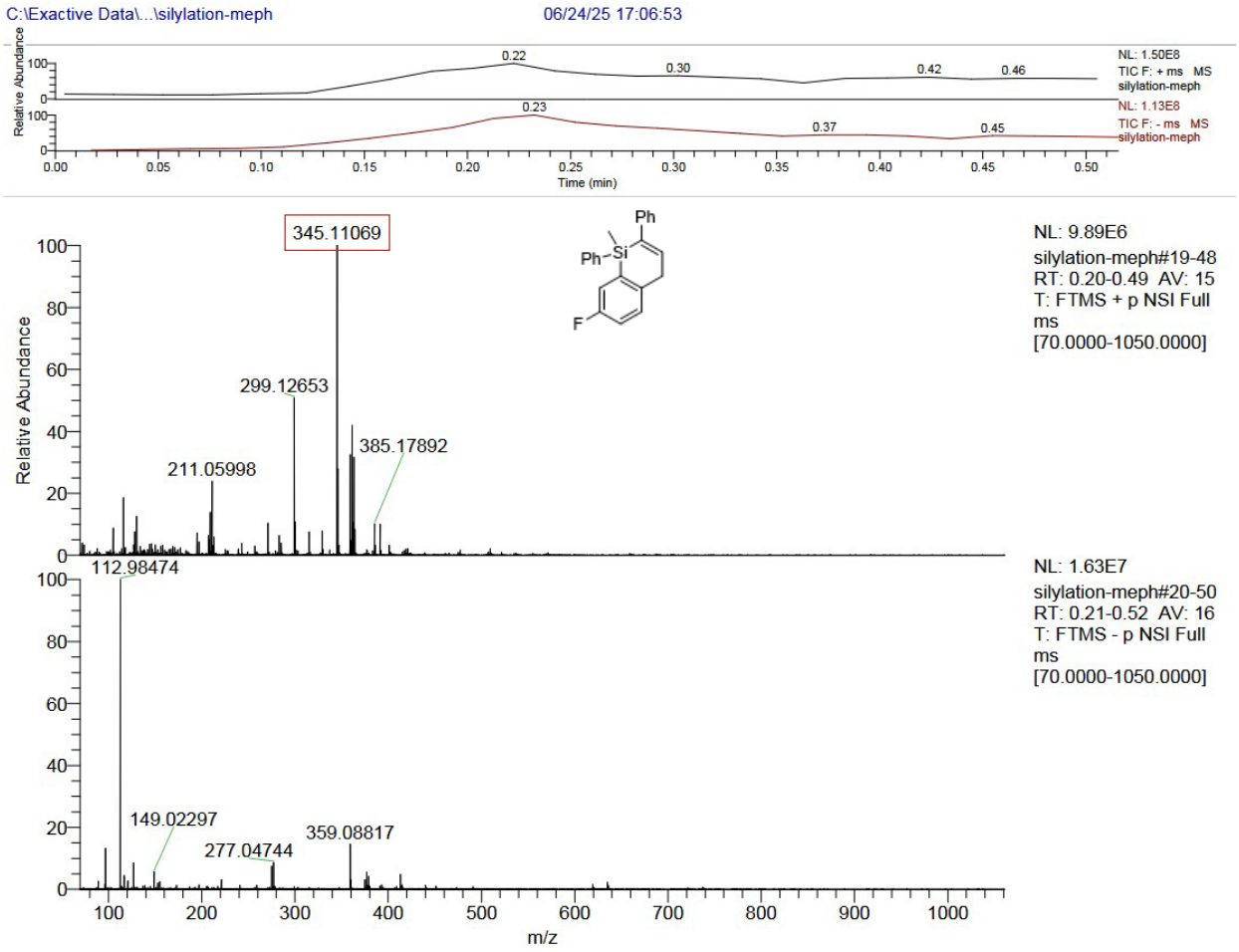
C:\Exactive Data\...\silylation-meph
06/24/25 17:06:53
Relative Abundance
0.22
0.30
0.42
0.46
NL: 1.50E8
TIC F: + ms MS
silylation-meph
0.23
0.37
0.45
NL: 1.13E8
TIC F: - ms MS
silylation-meph
Time (min)
345.11069
299.12653
385.17892
211.05998
Ph
Ph
Si
F
NL: 9.89E6
silylation-meph#19-48
RT: 0.20-0.49 AV: 15
T: FTMS + p NSI Full
ms
[70.0000-1050.0000]
112.98474
149.02297
277.04744
359.08817
NL: 1.63E7
silylation-meph#20-50
RT: 0.21-0.52 AV: 16
T: FTMS - p NSI Full
ms
[70.0000-1050.0000]
m/z

HRMS of **2.5a**.

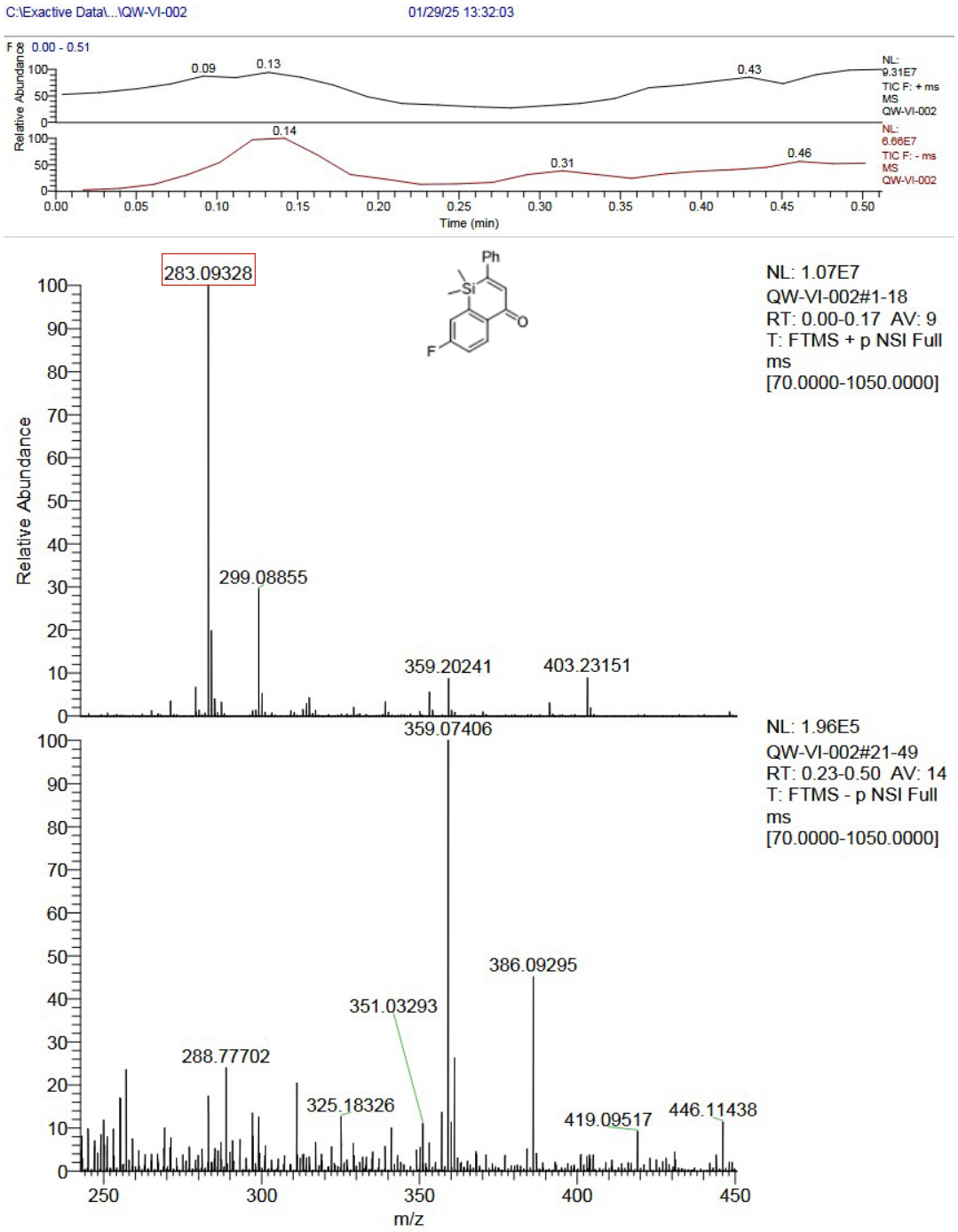
C:\Exactive Data\...\QW-VI-002
01/29/25 13:32:03
F 0.00 - 0.51
Relative Abundance
0.09
0.13
0.43
NL: 9.31E7 TIC F: + ms MS QW-VI-002
0.14
0.31
0.46
NL: 6.66E7 TIC F: - ms MS QW-VI-002
Time (min)
283.09328
Ph
Si
O
F
NL: 1.07E7
QW-VI-002#1-18
RT: 0.00-0.17 AV: 9
T: FTMS + p NSI Full ms
[70.0000-1050.0000]
299.08855
359.20241
403.23151
359.07406
NL: 1.96E5
QW-VI-002#21-49
RT: 0.23-0.50 AV: 14
T: FTMS - p NSI Full ms
[70.0000-1050.0000]
386.09295
351.03293
288.77702
325.18326
419.09517
446.11438
m/z

HRMS of **2.5b**.

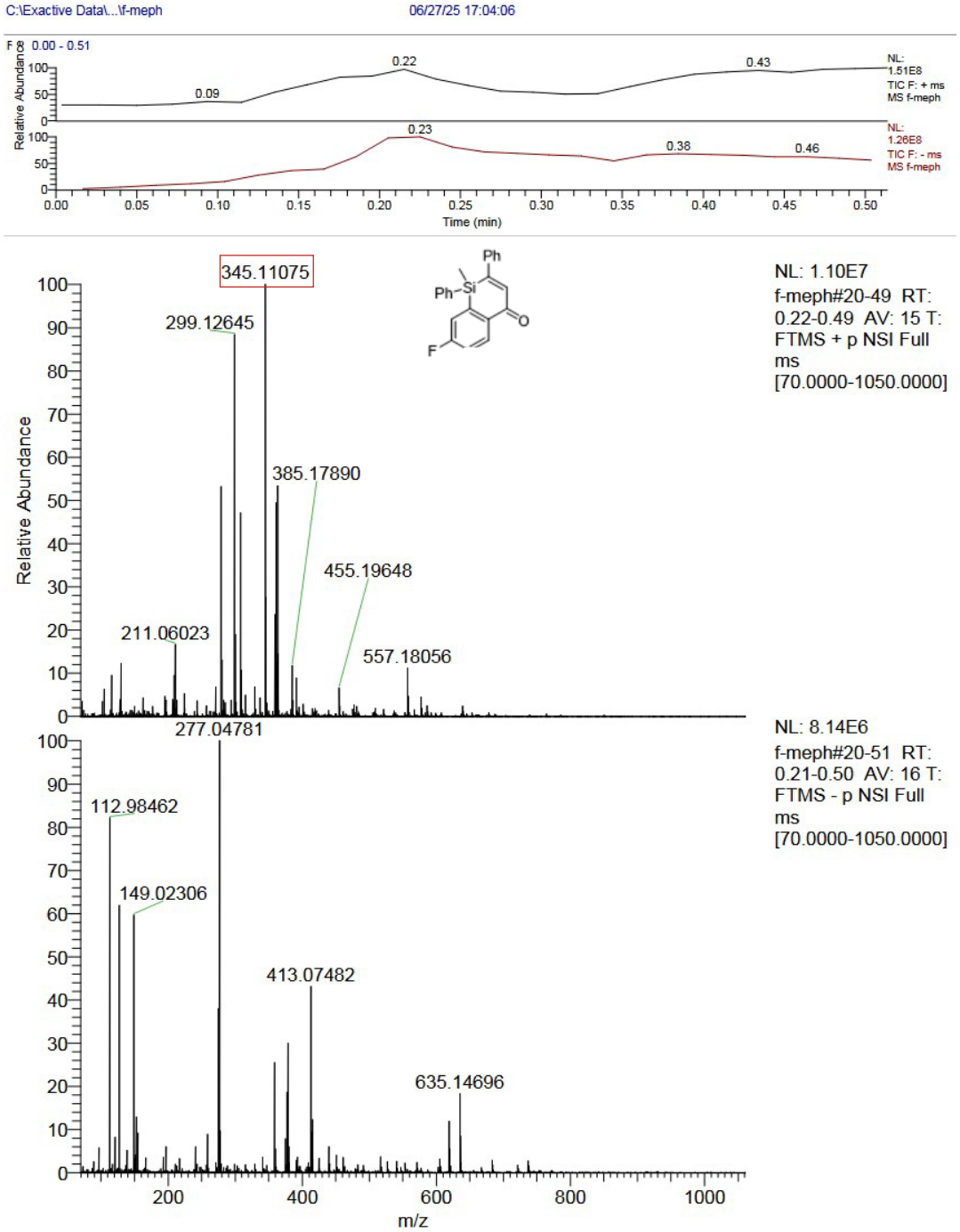
C:\Exactive Data\...\f-meph
06/27/25 17:04:06
F 0.00 - 0.51
Relative Abundance
0.09
0.22
0.43
NL: 1.51E8 TIC F: + ms MS f-meph
0.23
0.38
0.46
NL: 1.26E8 TIC F: - ms MS f-meph
Time (min)
345.11075
299.12645
385.17890
455.19648
211.06023
557.18056
277.04781
NL: 1.10E7 f-meph#20-49 RT: 0.22-0.49 AV: 15 T: FTMS + p NSI Full ms [70.0000-1050.0000]
112.98462
149.02306
413.07482
635.14696
NL: 8.14E6 f-meph#20-51 RT: 0.21-0.50 AV: 16 T: FTMS - p NSI Full ms [70.0000-1050.0000]
m/z

HRMS of **2.5c**.

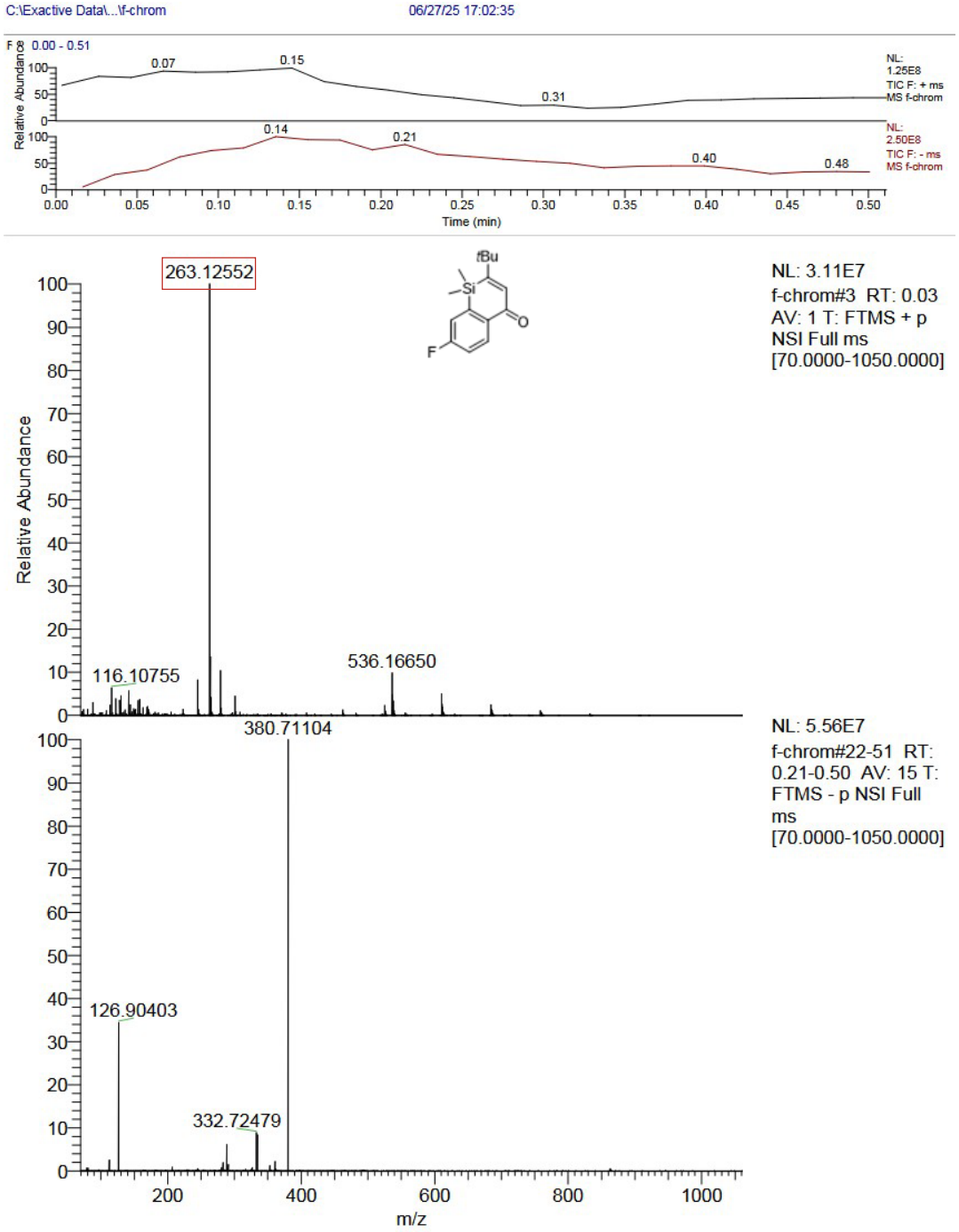
C:\Exactive Data\...\f-chrom
06/27/25 17:02:35
F 0.00 - 0.51
Relative Abundance
0.07
0.15
0.31
NL:
1.25E8
TIC F: + ms
MS f-chrom
0.14
0.21
0.40
0.48
NL:
2.50E8
TIC F: - ms
MS f-chrom
Time (min)
263.12552
tBu
Si
O
F
NL: 3.11E7
f-chrom#3 RT: 0.03
AV: 1 T: FTMS + p
NSI Full ms
[70.0000-1050.0000]
116.10755
536.16650
380.71104
NL: 5.56E7
f-chrom#22-51 RT:
0.21-0.50 AV: 15 T:
FTMS - p NSI Full
ms
[70.0000-1050.0000]
126.90403
332.72479
m/z

HRMS of **2.6a**.

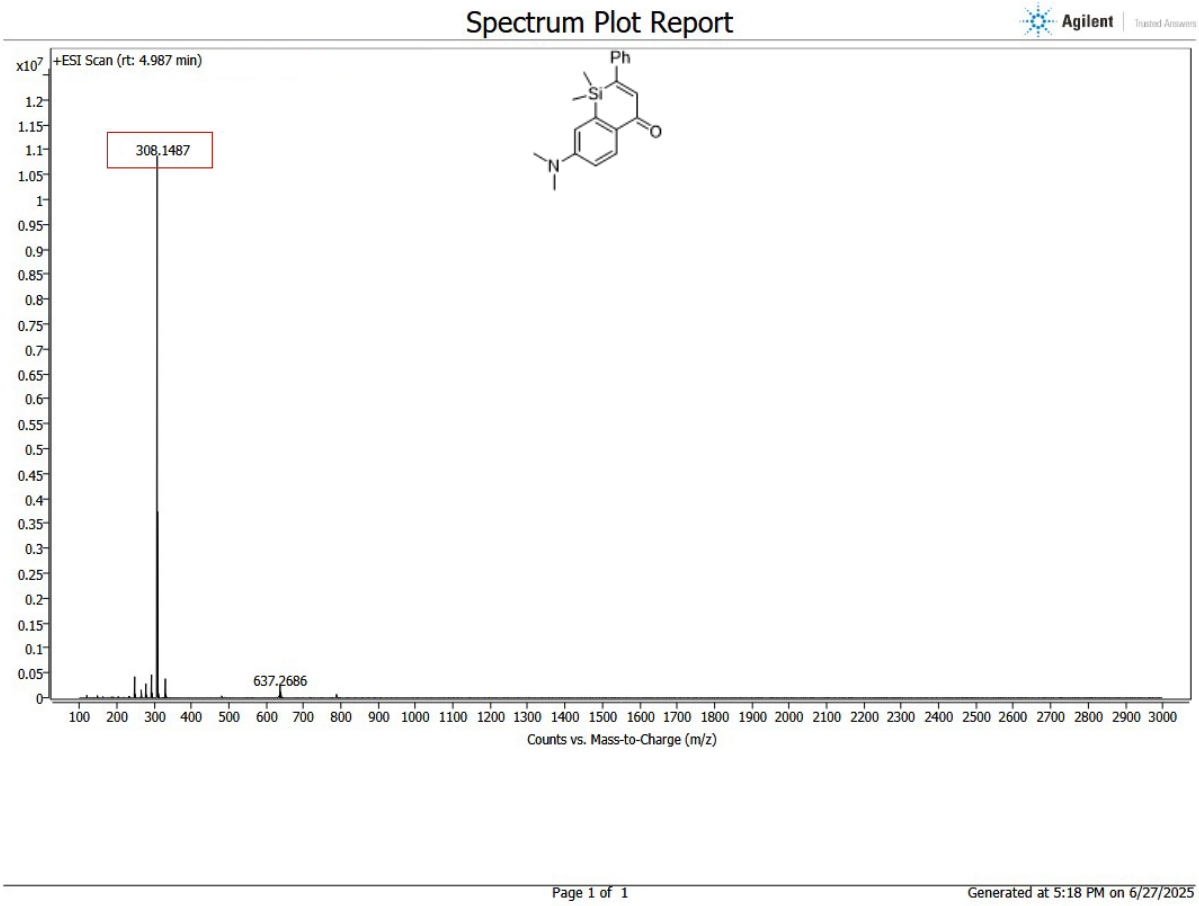
Spectrum Plot Report
Agilent
+ESI Scan (rt: 4.987 min)
x10^7
308.1487
637.2686
Ph
Si
O
N
Counts vs. Mass-to-Charge (m/z)
Page 1 of 1
Generated at 5:18 PM on 6/27/2025

HRMS of **2.6b**.

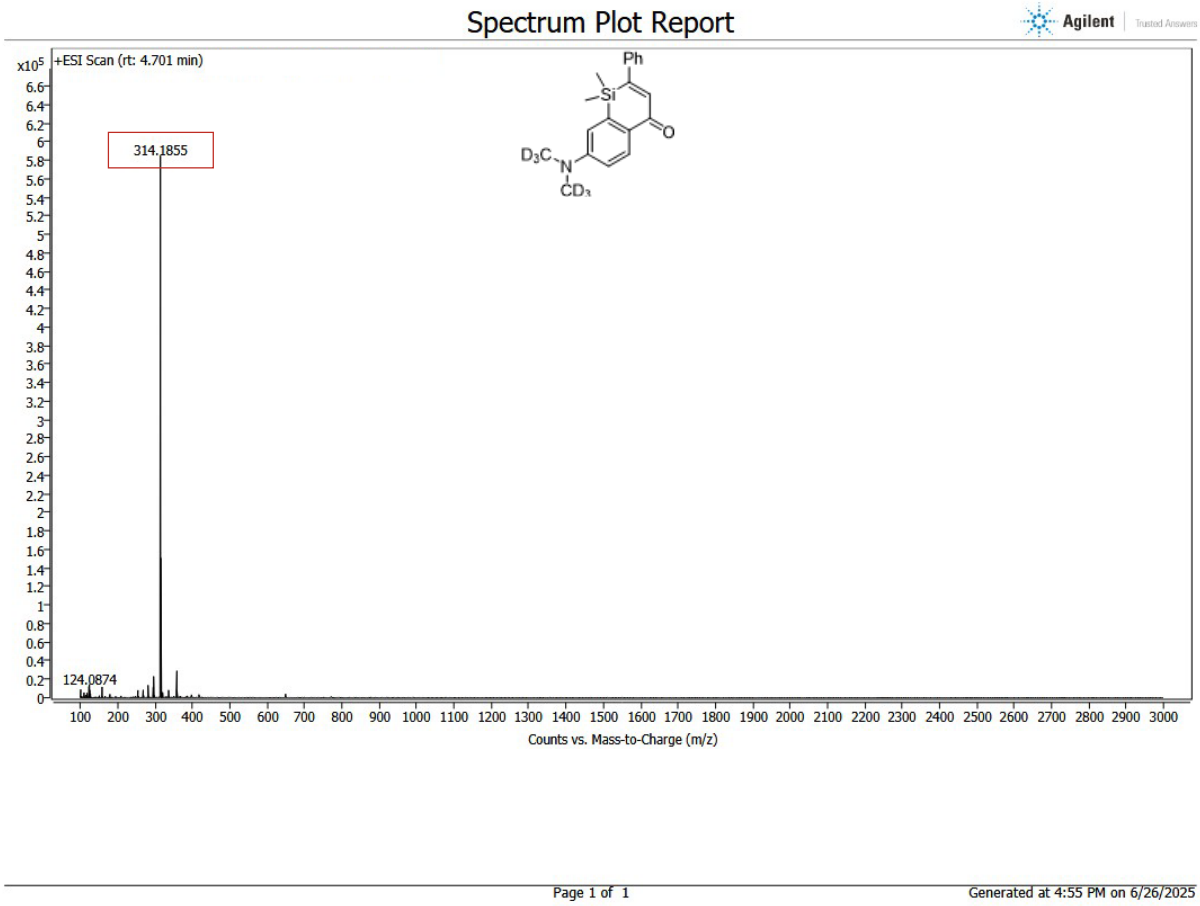
Spectrum Plot Report
Agilent
+ESI Scan (rt: 4.701 min)
x10^5
314.1855
124.0874
Ph
Si
O
D3C
N
CD3
Counts vs. Mass-to-Charge (m/z)
Page 1 of 1
Generated at 4:55 PM on 6/26/2025

HRMS of **2.6c**.

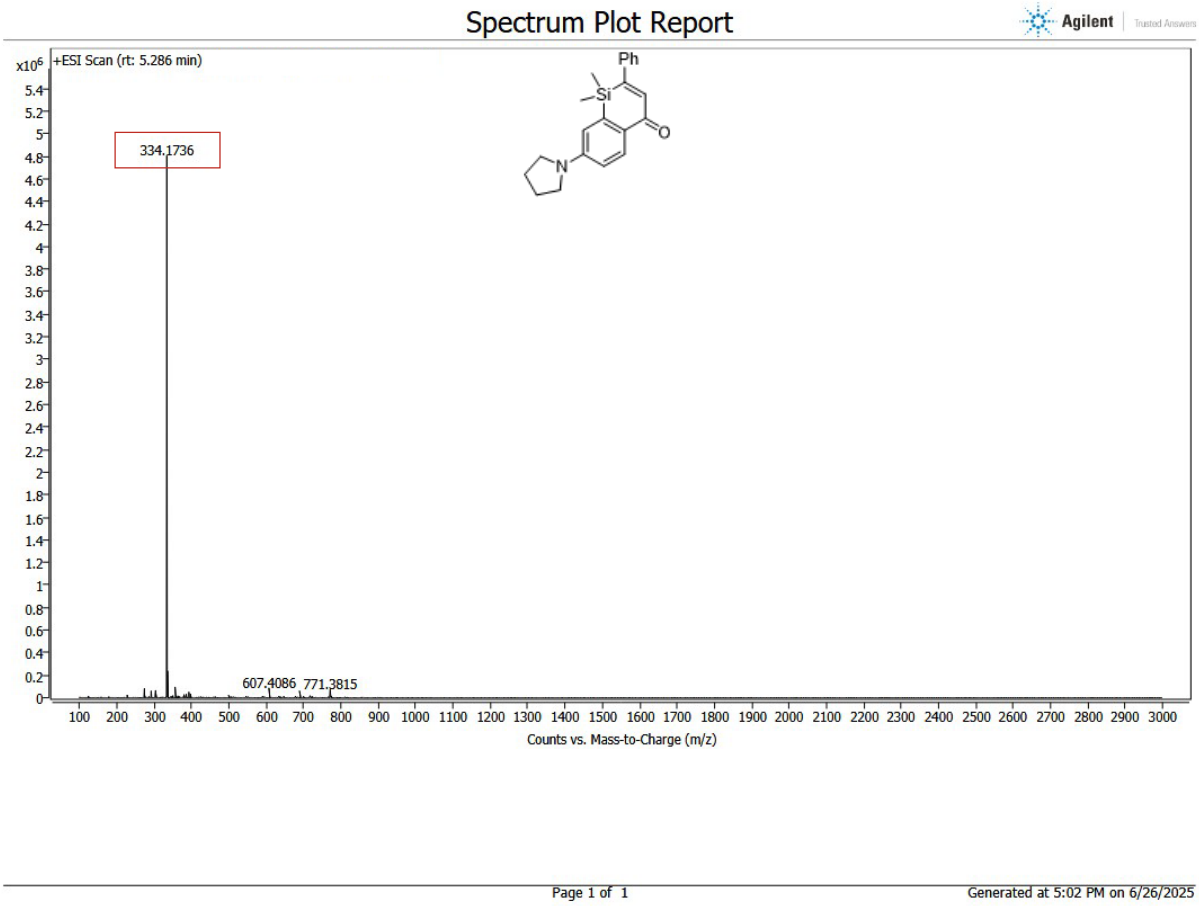
Spectrum Plot Report
Agilent
+ESI Scan (rt: 5.286 min)
x10^6
334.1736
607.4086
771.3815
Ph
Si
O
N
Counts vs. Mass-to-Charge (m/z)
Page 1 of 1
Generated at 5:02 PM on 6/26/2025

HRMS of **2.6d**.

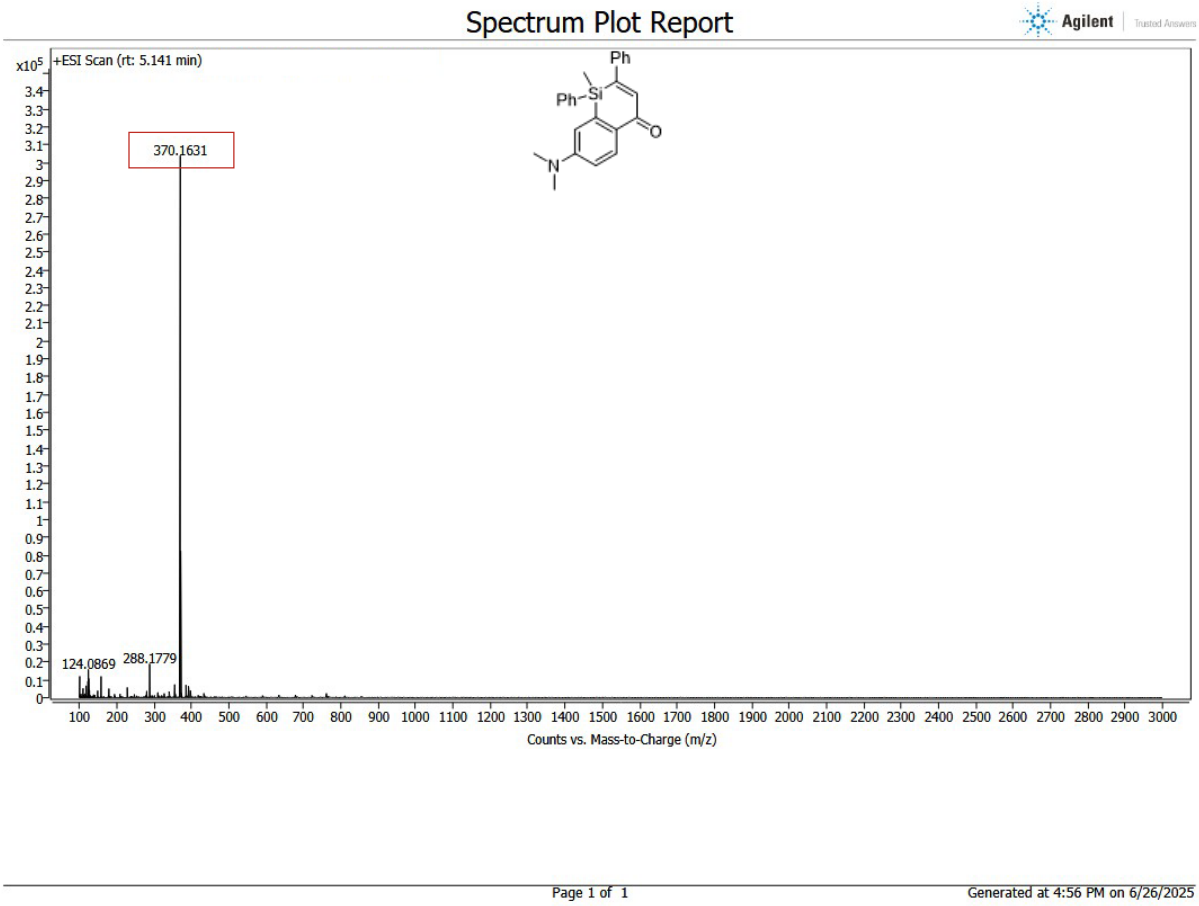
Spectrum Plot Report
Agilent
+ESI Scan (rt: 5.141 min)
x10^5
370.1631
124.0869
288.1779
Ph
Ph
Si
O
N
Counts vs. Mass-to-Charge (m/z)
Page 1 of 1
Generated at 4:56 PM on 6/26/2025

HRMS of **2.6e**.

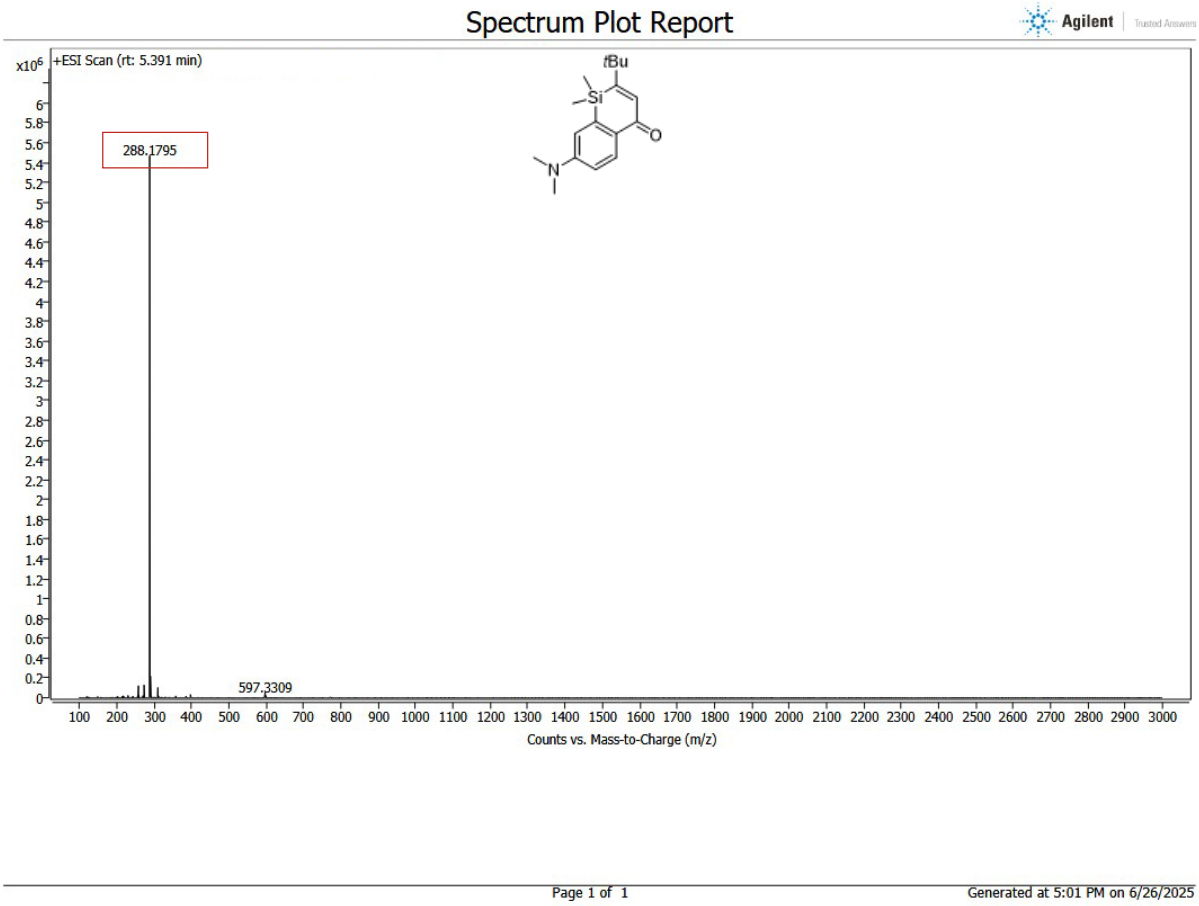
Spectrum Plot Report
Agilent
+ESI Scan (rt: 5.391 min)
x10^6
tBu
Si
O
N
288.1795
597.3309
Counts vs. Mass-to-Charge (m/z)
Page 1 of 1
Generated at 5:01 PM on 6/26/2025

HRMS of **2.11** (SiliFlav5).

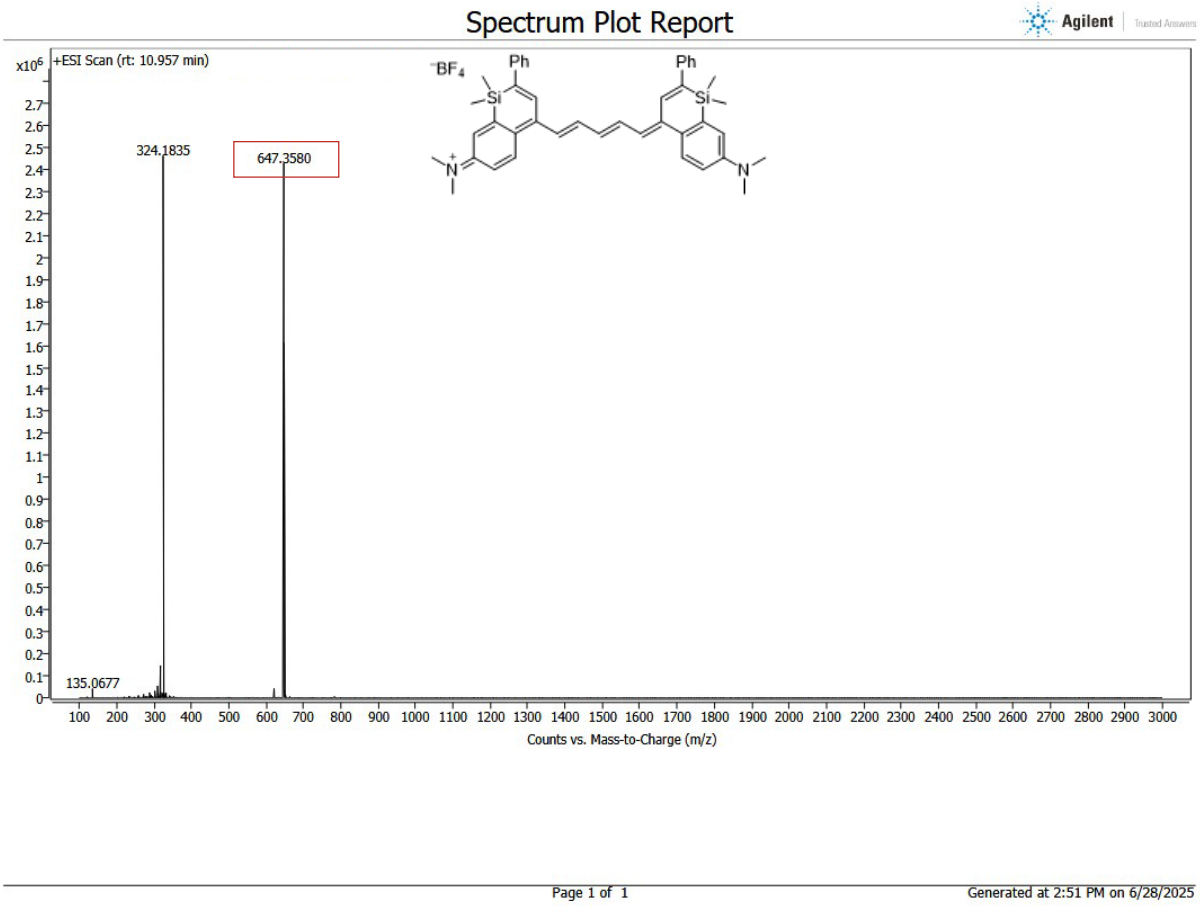

HRMS of **2.12** (SiliFlav7).

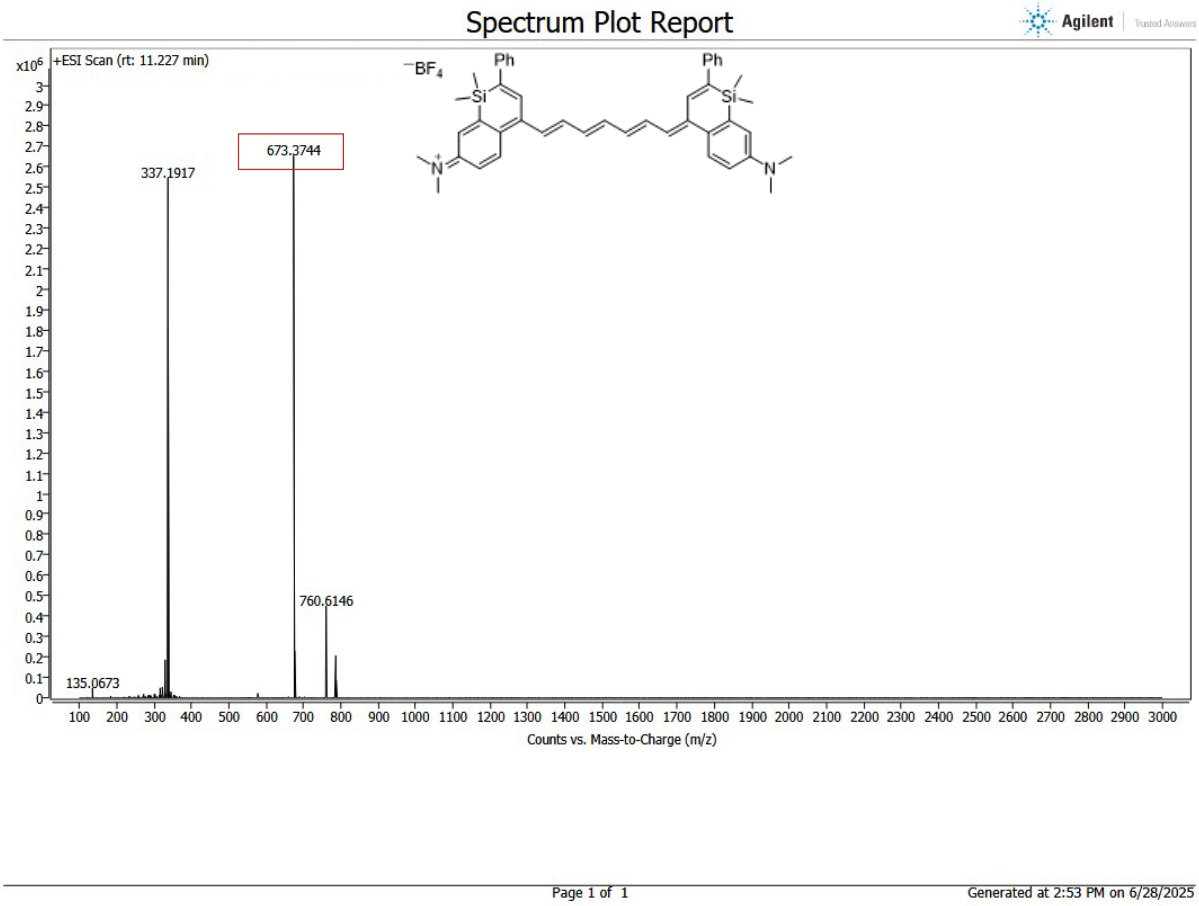

HRMS of **2.13** (SiliFlav9).

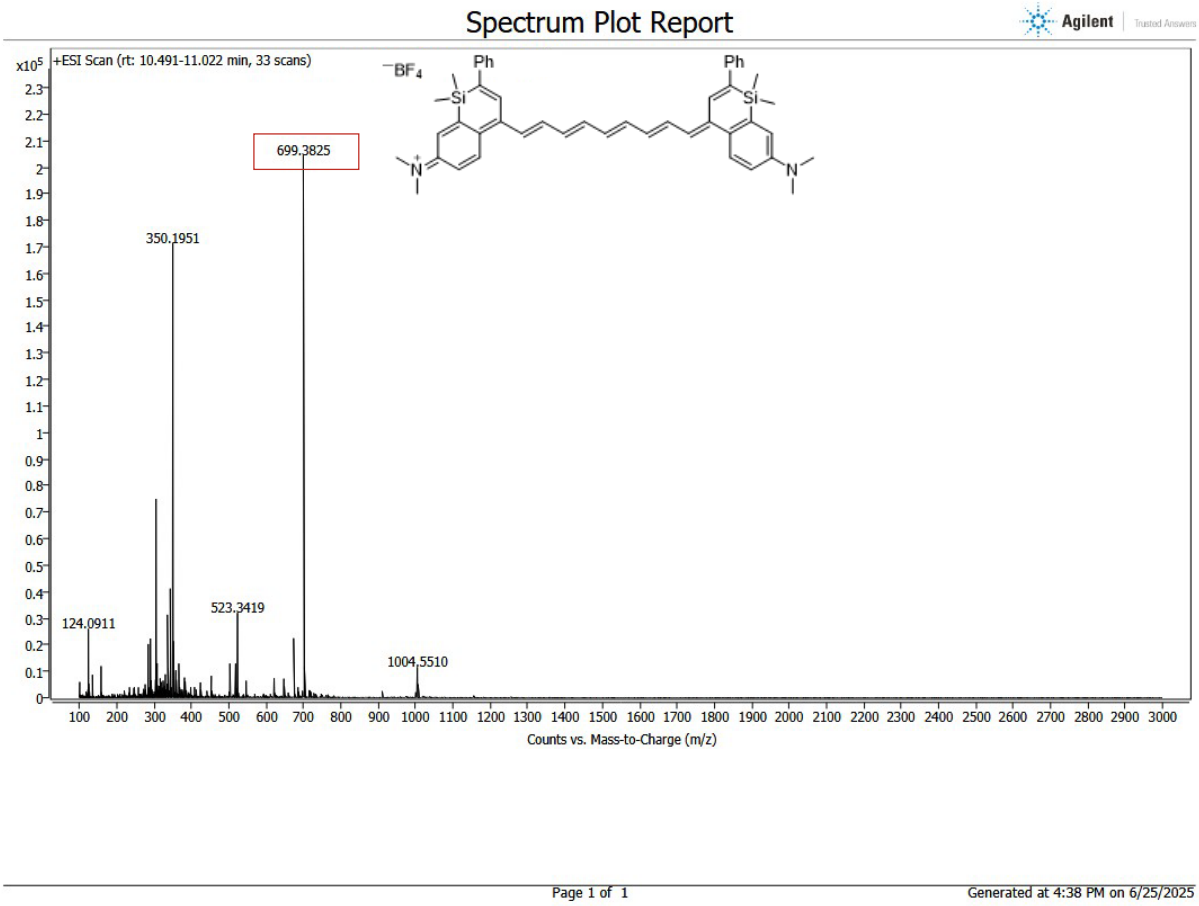

HRMS of **2.14** (SiliFlav-d_{12}).

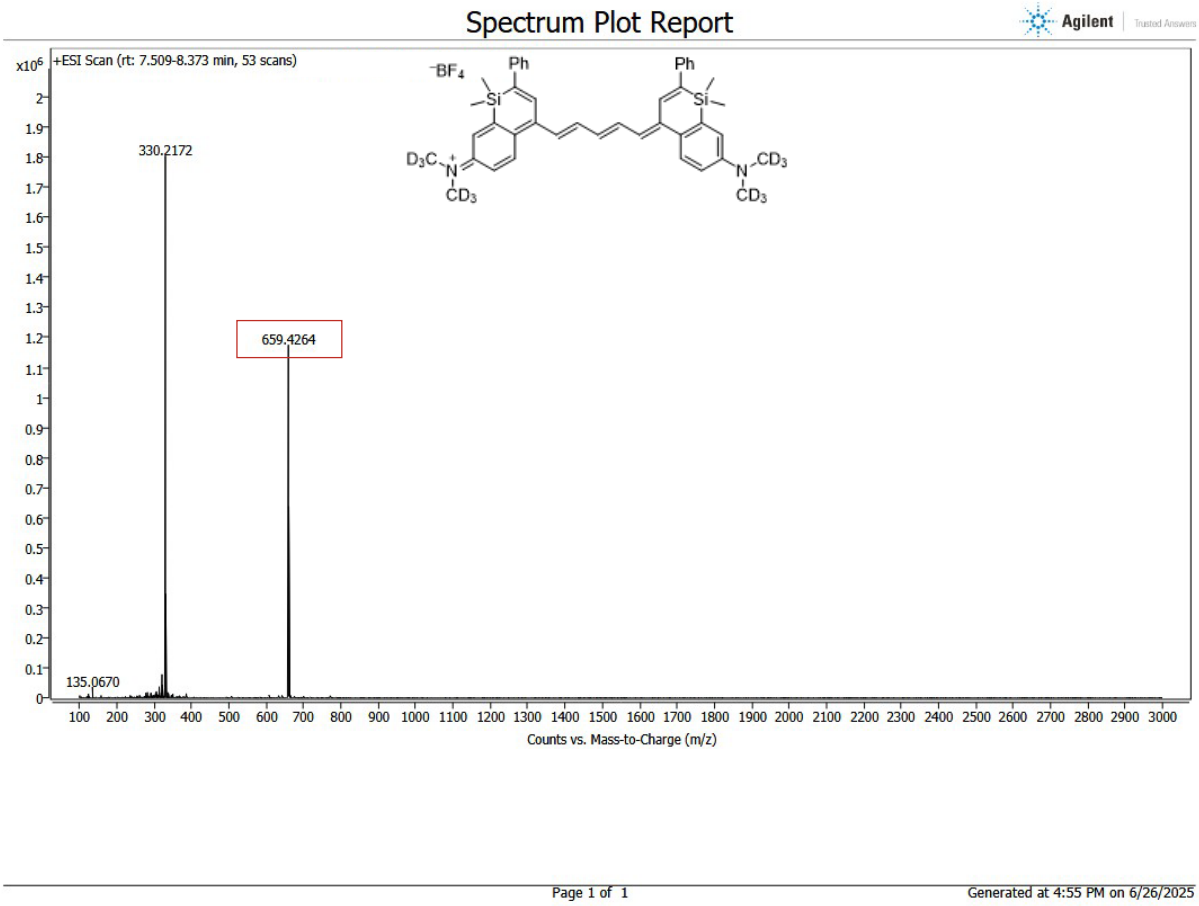

HRMS of **2.15**.

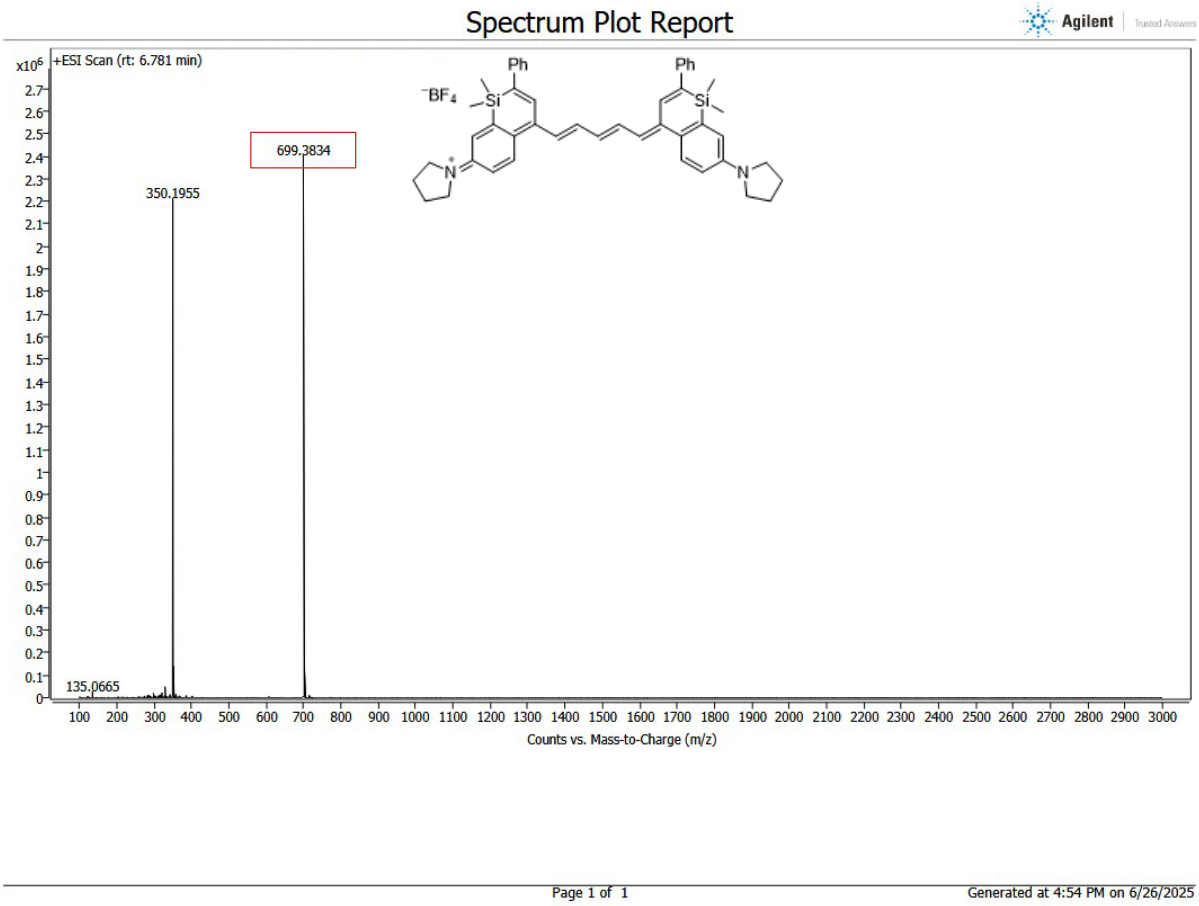
Spectrum Plot Report
Agilent
+ESI Scan (rt: 6.781 min)
x10^6
699.3834
350.1955
135.0665
Counts vs. Mass-to-Charge (m/z)
Page 1 of 1
Generated at 4:54 PM on 6/26/2025

HRMS of **2.16**.

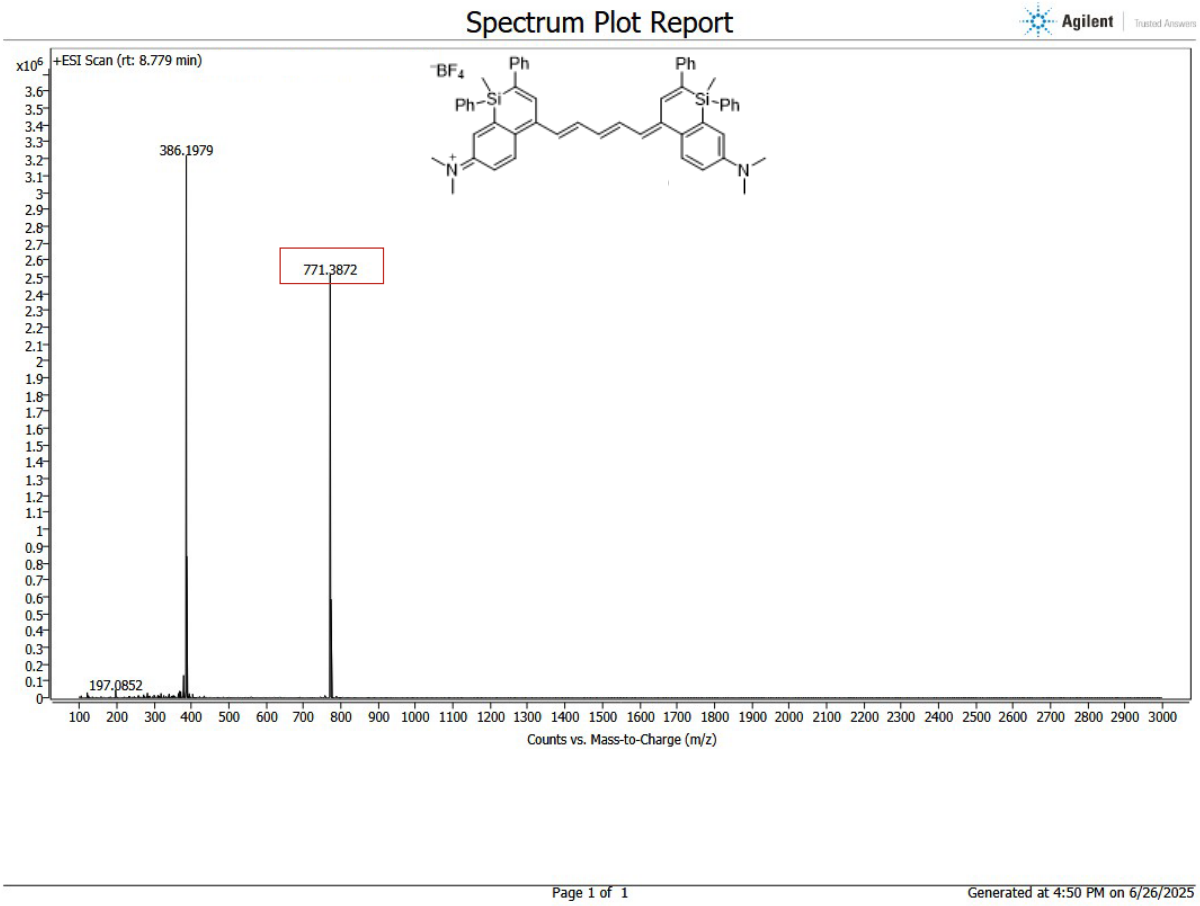
Spectrum Plot Report
Agilent
+ESI Scan (rt: 8.779 min)
x10^6
386.1979
771.3872
197.0852
Counts vs. Mass-to-Charge (m/z)
Page 1 of 1
Generated at 4:50 PM on 6/26/2025

HRMS of **2.17**.

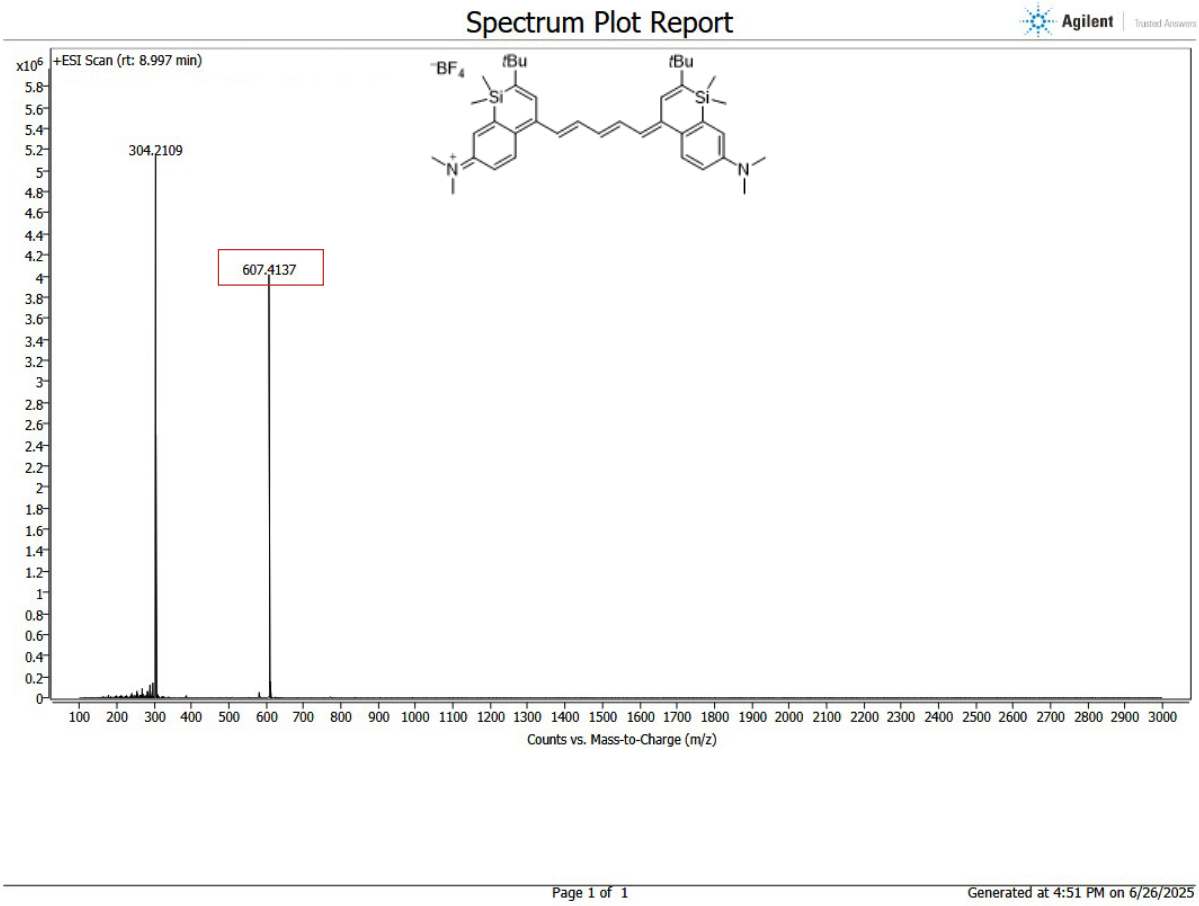
Spectrum Plot Report
Agilent
+ESI Scan (rt: 8.997 min)
x10^6
304.2109
607.4137
BF4
tBu
tBu
Si
Si
N
N
Counts vs. Mass-to-Charge (m/z)
Page 1 of 1
Generated at 4:51 PM on 6/26/2025

HRMS of **2.19**.

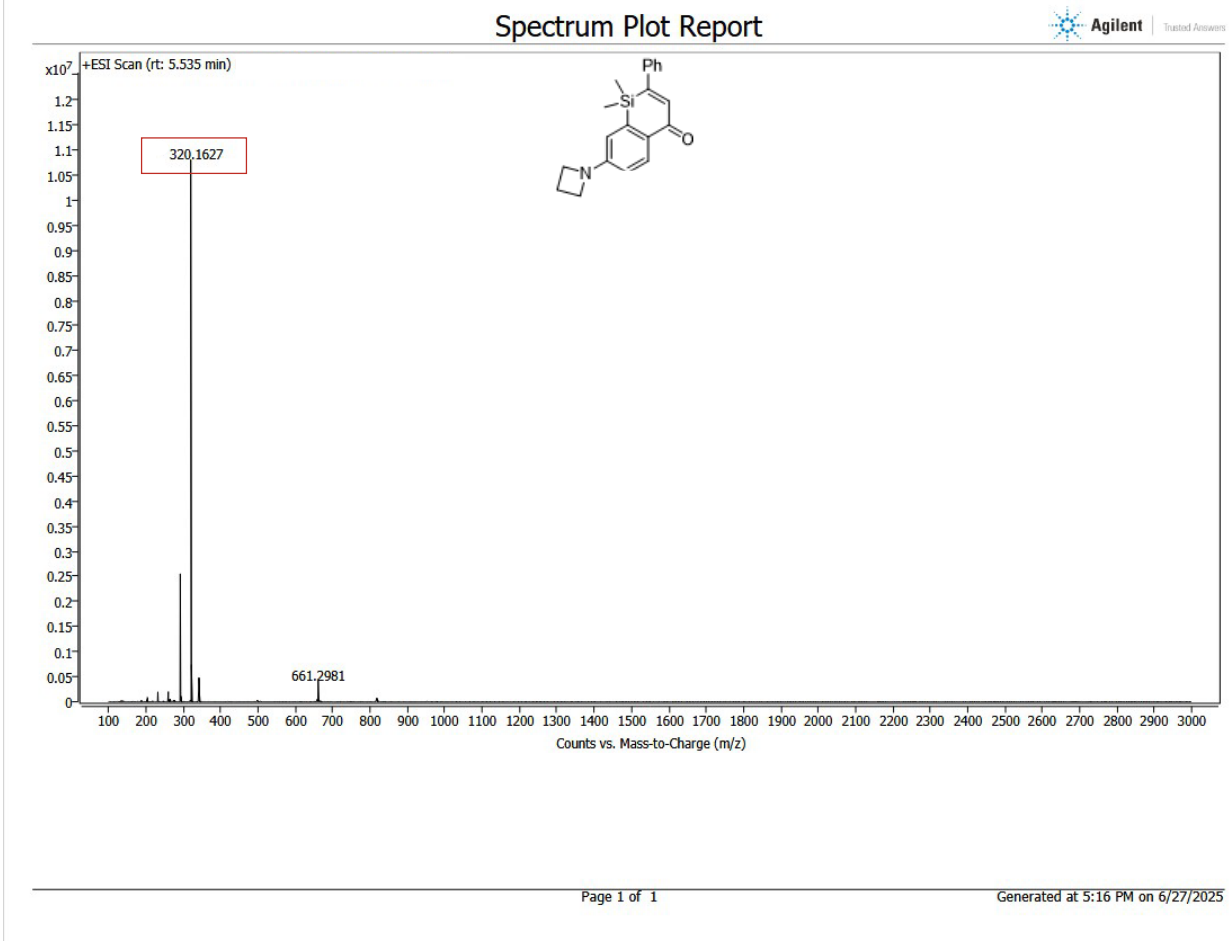
Spectrum Plot Report
Agilent
+ESI Scan (rt: 5.535 min)
x10^7
320.1627
661.2981
Ph
Si
O
N
Counts vs. Mass-to-Charge (m/z)
Page 1 of 1
Generated at 5:16 PM on 6/27/2025

HRMS of **2.20**.

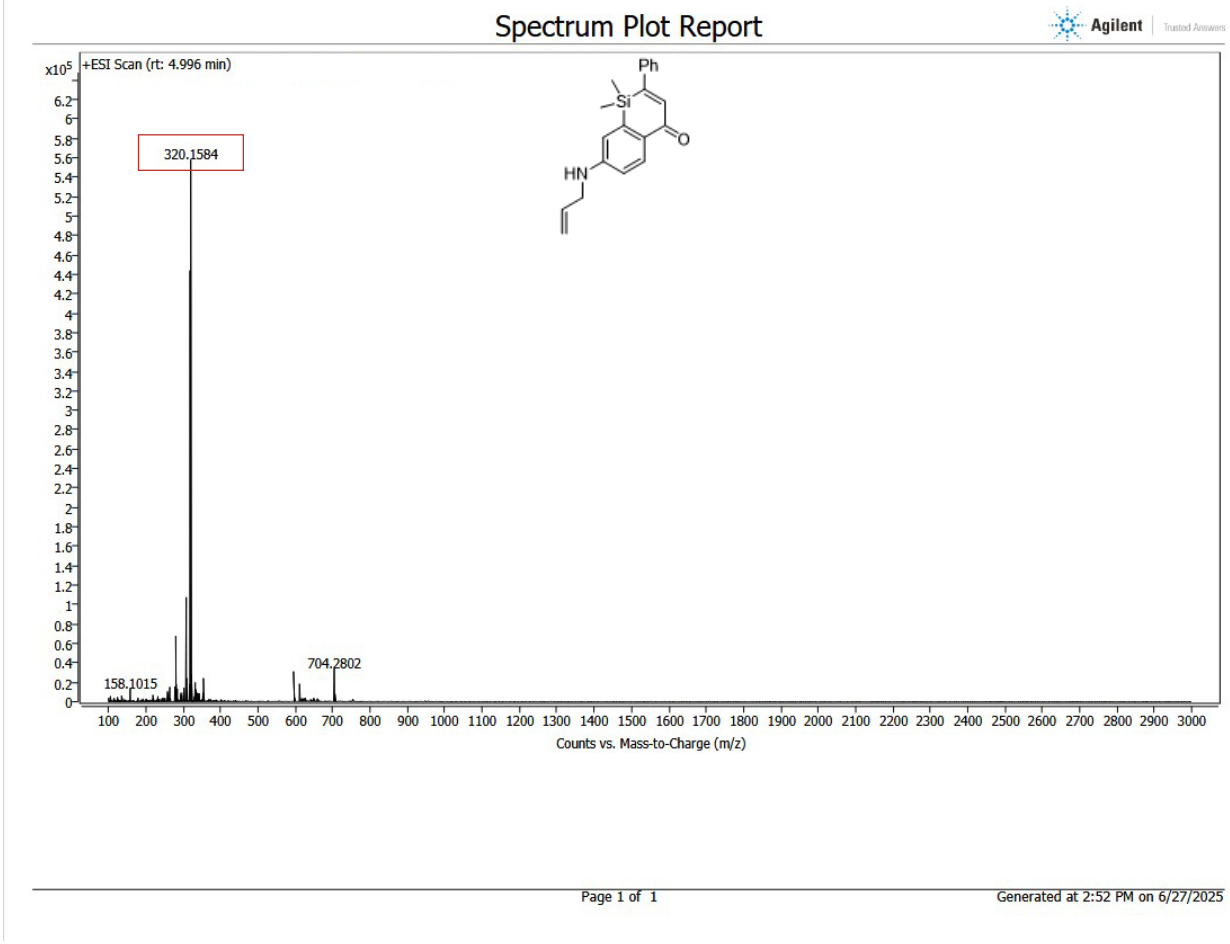
Spectrum Plot Report
Agilent
+ESI Scan (rt: 4.996 min)
x10^5
320.1584
704.2802
158.1015
Ph
Si
O
HN
Counts vs. Mass-to-Charge (m/z)
Page 1 of 1
Generated at 2:52 PM on 6/27/2025

HRMS of **2.21**.

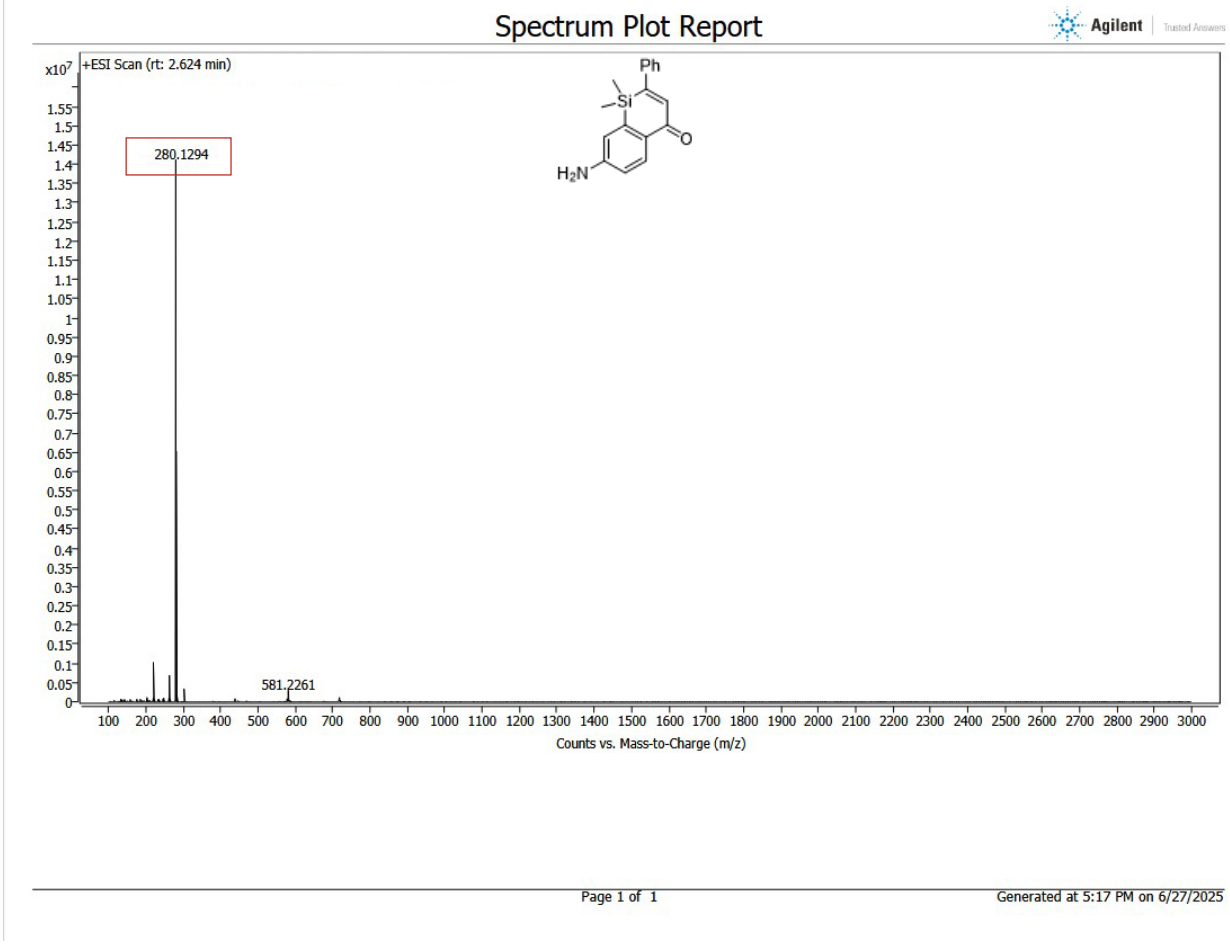
Spectrum Plot Report
Agilent
+ESI Scan (rt: 2.624 min)
x10^7
280.1294
581.2261
Ph
Si
O
H2N
Counts vs. Mass-to-Charge (m/z)
Page 1 of 1
Generated at 5:17 PM on 6/27/2025

2.7 Computation procedures

2.7.1 Geometry Optimization Scheme Using ORCA 6.0

All molecular geometries are optimized using density functional theory (DFT) under the CPCM-SMD solvation model of CH_2Cl_2 using ORCA 6.0 at the B3LYP/def2-TZVPPD level.[82–84] All geometries are optimized with ORCA's B3LYP (distinct from Gaussian's B3LYP/G). No counterion is included in geometry optimization, therefore, the net charge for each dye molecule is $+1e$. The general geometry optimization input file is included:

```
! CPCM RIJCOSX B3LYP def2-TZVPPD def2/J Opt NoTrah NoPop SOSCF
* xyzfile +1 1 dye_ini.xyz
%pal nprocs  32 end
%maxcore  6000

%cpcm
smd true
SMDsolvent "CH2Cl2"
end

%scf
MaxIter 3000
DIISMaxEq 35
end

%geom
```

MaxIter 300

MaxStep 0.2

end

2.7.2 TDHF@v_W Spectral Calculation

The TDHF@v_W method is a simplified approach to time-dependent Hartree-Fock (TDHF) theory in which the full screened electron-hole interaction kernel $W(r, r')$ is replaced by an approximate, translationally invariant, and computationally efficient potential, $v_W(|r - r'|)$.[85–87] This approximation retains the essential physics of screened exchange while significantly reducing computational cost, making it suitable for modeling excited-state properties in large systems. The computational protocol begins with a grid-based (uniform real-space grids are used for all the calculations, where $dx = dy = dz = 0.4$ Bohr with verified convergence in previous publication.) planewave pseudopotential local density approximation (LDA) DFT calculation under vacuum, followed by a near-gap hybrid treatment (with CAM-LDA0 range-separated hybrid, $N_v = N_{\text{occ.}}$ and $N_c = 400$ among all molecules) to include explicit exchange.[88] As CAM functional has been verified that it is able to reproduce the similar-quality electronic structure as *GW* correction for π-conjugated polymethines, the CAM-LDA0 energy gap between the lowest-unoccupied and highest occupied molecular orbitals are assumed as the fundamental gap ($E_{\text{fundamental}}$).[89] Next, a small number of stochastic actions, W_β, yield the static random phase approximation response, where v_W is then individually fitted by averaging over W_β.[87] Finally, the v_W is used as an attenuated exchange kernel in the TDHF calculations for optical spectra.[85,86] The lowest peak position on the spectrum is the optical gap (E_{optical}), therefore, the exciton binding energy is derived as $E_{\text{bind}} = E_{\text{fundamental}} - E_{\text{optical}}$.

2.7.3 Optimized Geometries

Geometries are listed in *xyz* format in Å.

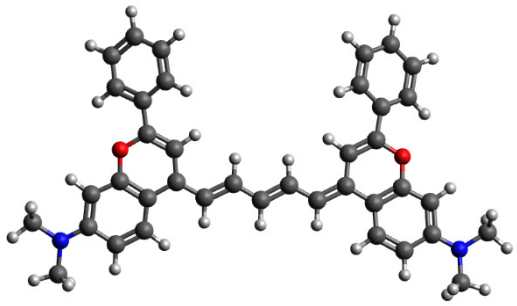

Flav5

78

C	-1.31478461285138	-2.73474883914008	-0.52806906639475
C	-0.17891105204316	-1.94224643868990	-0.52823033994872
C	1.08437737143464	-2.38426292105911	-0.89182511973342
C	-2.56011832859307	-2.23455469488911	-0.17666469566699
C	-3.73578774213251	-2.96385394233731	-0.23327345348551
C	2.23128462036199	-1.59248461127625	-0.95484430881283
C	2.20960988466103	-0.19104665406334	-0.68229885482928
C	3.51209027319613	-2.12799411686371	-1.32673311120781
C	3.31706856176578	0.57267883361729	-0.76971887450991
C	4.61949362100675	-1.27386935518430	-1.40453543114298
O	4.50479861145767	0.05165809366730	-1.12197922410889
H	1.28488412433404	0.29698481009938	-0.42922043482459
C	3.76662089390525	-3.47907354072888	-1.63433817736277
C	5.88243541077992	-1.69267631658748	-1.76066941870545

C	5.00338589659573	-3.92617450551470	-1.99143357523120
C	6.11232048772963	-3.03912185233474	-2.07208720704197
H	2.96151720649676	-4.19653740092744	-1.58809702170061
H	5.13378020984451	-4.97247002605548	-2.21484090840219
H	5.25621499098218	4.72458045488589	-1.32883738694114
C	4.45628618622038	4.14680814804895	-0.88670129747175
C	3.48343668327245	4.77433741447681	-0.12573769721671
H	3.52316993323396	5.84343740631558	0.03181902327206
C	2.46145874911248	4.02580345615047	0.43808349278976
H	1.70561850448359	4.50744506424704	1.04281255705827
C	2.40852954572390	2.65933337239592	0.23807226075343
H	1.61742259821607	2.08610734818817	0.69915935258543
C	3.37902490184635	2.02150531254391	-0.53297676192922
C	4.40914144918299	2.77880813923057	-1.08763518855369
H	5.16815220964798	2.29808521632990	-1.68657000010728
C	-5.00688474437547	-2.48236600758096	0.08750225940907
C	-5.22047243520885	-1.17163433180679	0.61092668569956
C	-6.19042822827984	-3.27270565399019	-0.10210910720578
C	-7.44013327089087	-2.73411929456013	0.23104582066921
C	-6.45133949935997	-0.72321495528858	0.93153855385233
O	-7.54573841148773	-1.48314547861407	0.75399071366777
H	-4.38984052929225	-0.50265984974856	0.75410244972136
C	-8.63034967634694	-3.40669902208795	0.06184127824183
C	-6.21550727575257	-4.57533442210127	-0.63912958399500
C	-8.63293898593967	-4.70100732759309	-0.47538205027457

C	-7.37449738924490	-5.26682059066758	-0.82229340466787
H	-7.32766331238816	-6.25943230379966	-1.23940167723372
H	-5.29053477451259	-5.05260979861203	-0.92411280103823
H	-7.59159300977348	4.12640637984424	2.84113018980521
C	-7.36111749721480	3.14143849471206	2.45886483329086
C	-8.31790339001711	2.42577319925670	1.75725206914489
H	-9.29656114575720	2.85189034134865	1.58452972477459
C	-8.02625203318924	1.16367837152597	1.27194229441605
C	-6.76509930135679	0.60566539388632	1.47476341373861
C	-5.81039759138718	1.32875534942270	2.18782549993986
H	-4.83757289657220	0.90093860253934	2.38263616426901
C	-6.10848488626196	2.58762599351930	2.67474792382150
H	-5.36160577206369	3.13529181543774	3.23262853069858
H	-3.65232051992950	-3.98289208878623	-0.58256081558090
H	6.67079764642962	-0.95861314744952	-1.79026017295662
H	-8.77562616365581	0.61392340979571	0.72198968758613
H	-9.54132214189436	-2.90671929907997	0.34732877498144
N	7.33597322442678	-3.48149591214293	-2.43349240173955
N	-9.78014278131248	-5.38766715623828	-0.66175522402303
C	-9.76274474457102	-6.71532536768378	-1.24739469069919
C	-11.05079401820599	-4.78898207049640	-0.30503781170179
C	7.55320920293639	-4.87865678596110	-2.75776311241146
C	8.45134043309186	-2.55902014363244	-2.49730367448127
H	-11.08578944171518	-4.52904918433649	0.75475459414721
H	-11.84663214341650	-5.49780088963755	-0.50594269454912

H -11.24453146890988 -3.88356491263605 -0.88485466764412

H -9.20083872684721 -7.41982214833801 -0.63160432170540

H -9.32636821549523 -6.70835263552805 -2.24778179939257

H -10.78215732928339 -7.07643459188132 -1.32804724570691

H 6.93927420186294 -5.19615479631925 -3.60254345249320

H 7.33281101450731 -5.52894767069156 -1.90913855438479

H 8.59437655884632 -5.01836279084285 -3.02781145253717

H 8.26840592663276 -1.75864387861310 -3.21729194084029

H 9.33989767886887 -3.09763106056824 -2.80773674353103

H 8.65052151411702 -2.10371649356510 -1.52469343514165

H 1.17076995850414 -3.42818808166795 -1.15723172095831

H -0.31638420036919 -0.90952465877749 -0.22924049035051

H -2.59030063756606 -1.19774034269289 0.13800905485250

H -1.23340996025054 -3.77170006181645 -0.83554460061271

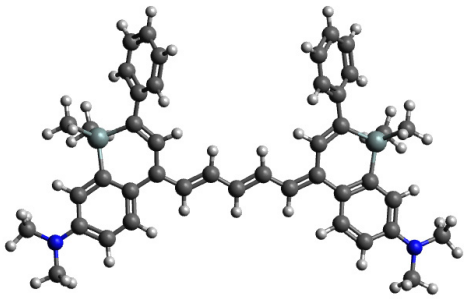

11 (SiliFlav5)

94

C	-1.31433723518958	-2.60874990230223	-0.43624590707241
C	-0.17785588480652	-1.82034251112961	-0.35392967550727
C	1.08276979532945	-2.25307717840637	-0.75355343029733
C	-2.55016955736766	-2.13015096559796	-0.03877223616519
C	-3.72783747067970	-2.86856980560645	-0.13268500874790
C	2.26263697935638	-1.51178085936168	-0.77000670386214
C	2.19426599903665	-0.11845956118337	-0.34420204851549
C	3.49757337605918	-2.13509215067824	-1.20966385527887
C	3.10272080444443	0.86199964521114	-0.49118458963350
C	4.65853280352249	-1.38599367452970	-1.51499492648382
Si	4.72490844631025	0.47777024771448	-1.34743416751555
H	1.26375281398795	0.15300046661101	0.13279833801527
C	3.59202197806224	-3.53503877391239	-1.34691999780789
C	5.79283783310305	-2.01879519969232	-1.97856633280929
C	4.72224511757072	-4.16209439859283	-1.79125997186689
C	5.86652976470977	-3.41769621908357	-2.15461184970216
H	2.76180757651367	-4.16650942936040	-1.07190232721307

H	4.72891072179593	-5.23829538821094	-1.85731483985067
H	3.21229280057728	5.49502152779581	-0.65445215299619
C	2.91334444766494	4.61366122595507	-0.10332133365813
C	2.25408834521579	4.74113964192099	1.10826244371974
H	2.04042137312764	5.72127991299222	1.51221418800777
C	1.88033421338566	3.60190254545404	1.80454813160552
H	1.37941540873187	3.69044163640588	2.75921756444341
C	2.15449506146965	2.34773501454389	1.28921419981422
H	1.87684257459101	1.46860629449782	1.85427341749036
C	2.81060034651068	2.20135480617393	0.06461091605330
C	3.19579583940124	3.35837515588204	-0.61383463424014
H	3.70348404491267	3.28101463396955	-1.56449108195171
C	-5.00896753300375	-2.44176844027750	0.19975239949366
C	-5.16281017200406	-1.09116832088117	0.73409025596955
C	-6.13877840897950	-3.33879013181761	0.02374929294243
C	-7.47818022744803	-2.88485110953538	0.05460153785520
C	-6.27950784741776	-0.35310741736939	0.85282799076592
Si	-7.90804831558110	-1.07515036414172	0.27076620924671
H	-4.23891332523617	-0.62933728464015	1.05254291322429
C	-8.51860555957955	-3.77183849038293	-0.12853440897106
C	-5.94074950261422	-4.72033645892279	-0.16932834536330
C	-8.31300754682610	-5.15296959626200	-0.33702744471337
C	-6.97369409943174	-5.60036979093896	-0.33824026382905
H	-6.74930401625525	-6.64770269919429	-0.46200591865005
H	-4.94502992868507	-5.13544530033783	-0.15704839882017

H	-5.94040805079533	4.51613133314882	3.07112481278082
C	-6.00969003568513	3.53398742176792	2.62374139969794
C	-6.81848577485663	3.32540172466039	1.51818140762117
H	-7.37986941619269	4.14691701594985	1.09405678447580
C	-6.91578678916390	2.06558693463680	0.95267384051272
C	-6.18979914070700	0.99016739900083	1.46580898124950
C	-5.38455143418723	1.21523020024505	2.58431951130051
H	-4.83849033741518	0.39049881991393	3.02133004676569
C	-5.29696186105674	2.47159838590861	3.15745904808030
H	-4.67412806116910	2.61997752925563	4.02937039639131
H	-3.61244351618697	-3.85653808249850	-0.55260203621879
H	6.66246319787885	-1.42403223487532	-2.21607114148603
H	-7.54785239502488	1.92473192548038	0.08730306841290
H	-9.53200519118912	-3.39922096711713	-0.10955526406171
N	6.97605281754816	-4.01600372975394	-2.63571797005281
N	-9.34387216363618	-6.00672794187031	-0.51490806177592
C	-9.09778089424715	-7.42095007029905	-0.72083607943997
C	-10.71191786506366	-5.52774274257620	-0.48528987746456
C	7.02236957344808	-5.45621457048256	-2.79944996204189
C	8.13768036419899	-3.22872817021148	-3.00154621842245
H	-10.95689994137988	-5.07083911785266	0.47563427139980
H	-11.38253962129539	-6.36565200561562	-0.64160838281758
H	-10.89675367430759	-4.79264025928674	-1.27090494602017
H	-8.60397521206028	-7.87399951469575	0.14142837729819
H	-8.47610092798249	-7.59430516755847	-1.60090348470004

H	-10.04558941072757	-7.92587794220338	-0.87196376149315
H	6.23929684636180	-5.80719837718551	-3.47393904465789
H	6.90921325037786	-5.97378211784629	-1.84469877933959
H	7.98193851837039	-5.73222039114051	-3.22268097563367
H	7.89476198723300	-2.49371590808798	-3.77097854688704
H	8.90236266891313	-3.88980974896274	-3.39478661011465
H	8.55372865384107	-2.69973003779190	-2.14176051575048
H	1.11420117294127	-3.26639505912329	-1.12387820535582
H	-0.31967092298512	-0.82139999890029	0.03700214807061
H	-2.56768696207994	-1.12019878178831	0.34802896624190
H	-1.23547438858325	-3.61543261794929	-0.83116433196209
C	-9.23046066984067	-0.85502609416592	1.56565550160757
C	-8.45809175337596	-0.37611500019813	-1.37241941757904
C	4.86924771015326	1.23600458262683	-3.04897741410902
C	6.15734044534430	0.99302731403771	-0.27017464856558
H	-8.92310032186540	-1.27798756472374	2.52272357221547
H	-10.15603794302459	-1.34703939091388	1.26270377427703
H	-9.45550224496408	0.20124270074477	1.71955218102194
H	6.10373223271083	0.52512888904189	0.71333897223086
H	6.16850150843563	2.07471028083089	-0.12860423825066
H	7.10767510249596	0.71118496317131	-0.72636763655476
H	-7.65529735358147	-0.41684549135019	-2.10955856594284
H	-8.79265570800965	0.65789436241048	-1.29018550819015
H	-9.29483807911425	-0.96294774232409	-1.75641853850182
H	3.96461300309042	1.07667576232911	-3.63647938592242

H	5.69922496606745	0.76717921890380	-3.58119756272202
H	5.06883220805943	2.30660874250639	-3.01076789674205

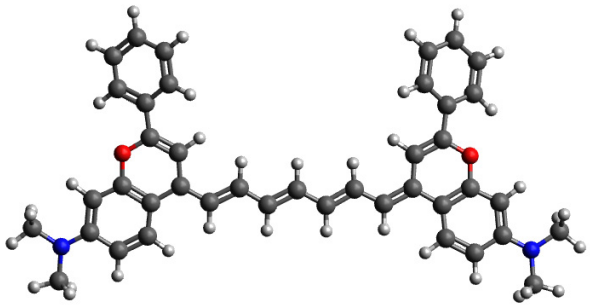

LFlav7

82

C	-0.09113141354244	-2.10761371688138	-0.48352779466172
C	-1.25702801786328	-2.85312417208101	-0.50621078517466
C	1.16233149696820	-2.57868618832050	-0.85204983730226
H	-1.20930304805221	-3.88593665417527	-0.83425524135195
H	1.26108953048561	-3.61548902778955	-1.15521820530586
H	-0.16371067289700	-1.06977333153871	-0.17023794280908
C	2.27988351207052	-1.76505275467743	-0.87341582758999
C	3.54689962615352	-2.18838052467464	-1.25560477139784
C	-2.48946426615669	-2.32146839399170	-0.15659289983618
C	-3.68223941970293	-3.02039423645199	-0.24186221137353
H	2.12928878919846	-0.73380886613581	-0.57560637653437
C	4.67825534619613	-1.38191028384760	-1.34491896044250
C	4.64088672416777	0.02356484747520	-1.09033015572930
C	5.96298304342837	-1.90352429110470	-1.72957265731016
C	5.73574891067655	0.80115196849929	-1.20244530274035
C	7.05605580956126	-1.03508905836579	-1.83360825430529
O	6.92751991288817	0.29245950711675	-1.56368376419880

H	3.71218525074983	0.50175988346579	-0.83268316662845
C	6.23215257718638	-3.25381862155288	-2.02422936338915
C	8.31944099694176	-1.44048686693452	-2.20459925787351
C	7.46982647668019	-3.68832236900964	-2.39553343584073
C	8.56374187792835	-2.78686979664148	-2.50469990247797
H	5.43829362776055	-3.98199393963916	-1.95591876402943
H	7.61172631811457	-4.73548092365636	-2.60750471490970
H	7.61943179961154	4.96964681264576	-1.82658177568617
C	6.82896183835965	4.38792870684536	-1.37273718741993
C	5.85234416534714	5.01348448133316	-0.61512669293124
H	5.87947218477674	6.08498872506459	-0.47189807297113
C	4.84276642134995	4.25961627431076	-0.03612364600067
H	4.08388531764837	4.73971621176316	0.56603585582689
C	4.80609633891215	2.89005773337715	-0.21759132856692
H	4.02463926232400	2.31339929498345	0.25545909667768
C	5.78039467899111	2.25375206392544	-0.98535548089814
C	6.79779275457515	3.01683222764067	-1.55550967005645
H	7.55965723434424	2.53786338406633	-2.15211305977937
C	-4.94639199061411	-2.52103647448882	0.07634936371972
C	-5.14048107349471	-1.21635635710480	0.62189474280088
C	-6.14252888569190	-3.28657492697438	-0.13796647474782
C	-7.38520979197266	-2.72990298594046	0.19085059562188
C	-6.36625071118344	-0.74896007212985	0.93451754959985
O	-7.47330900146040	-1.48407685523261	0.72952042710027
H	-4.29818676327440	-0.56724288912883	0.78714192493498

C	-8.58587062164202	-3.37858258387456	0.00254742965250
C	-6.18642902542499	-4.58119057168100	-0.69256256099010
C	-8.60679767622582	-4.66636295113888	-0.54971389701962
C	-7.35602515764299	-5.24963370386794	-0.89426837361141
H	-7.32323635022291	-6.23703250165724	-1.32482088914927
H	-5.26805141237179	-5.07175389429063	-0.97621100157299
H	-7.43599193023902	4.08891638977342	2.91301697931073
C	-7.21985185305544	3.10630942677131	2.51654122612694
C	-8.18285801821977	2.41997838675478	1.79448280250110
H	-9.15188915597005	2.86687815250136	1.62000673740731
C	-7.90968131807839	1.16086512245776	1.29083918317074
C	-6.66099766201405	0.57635106311119	1.49617589468662
C	-5.69998203057901	1.27013602003984	2.22977255050604
H	-4.73690610364504	0.82156457654636	2.42617757570084
C	-5.97966036458914	2.52601597351058	2.73479642554202
H	-5.22823791411287	3.05049064578092	3.30863046585395
H	-2.49424076826939	-1.29119878560647	0.18038565231806
H	-3.61633839729213	-4.03295687074549	-0.61306081585958
H	3.64509753088502	-3.23335115426281	-1.51300845216853
H	9.09686357911857	-0.69591526971287	-2.25473556086974
H	-8.66369016495106	0.63425285475063	0.72488364771380
H	-9.49025701448282	-2.86603238077043	0.28673733615410
N	9.78830034735553	-3.21608529690692	-2.88158328686022
N	-9.76428417173764	-5.33142881234966	-0.75193946204168
C	-9.76460376593305	-6.65369140388916	-1.34969447708427

C	-11.02751648647988	-4.71248605067666	-0.40400162684729
C	10.01923163520422	-4.61322547644740	-3.19484908324650
C	10.88962911516647	-2.27930759939466	-2.97012483796838
H	-11.07152255589783	-4.46497277660806	0.65848076868511
H	-11.83431359174162	-5.40292234484683	-0.62424236134643
H	-11.19602954143187	-3.79635918435715	-0.97472975881618
H	-9.20673032301420	-7.36920738371012	-0.74321009455892
H	-9.33400724042922	-6.64313496470768	-2.35271458786951
H	-10.78823712110360	-7.00357978448828	-1.42639512715619
H	9.39109878885003	-4.94944913911913	-4.02176582212320
H	9.82771872707934	-5.25731994750372	-2.33443444135745
H	11.05587488849045	-4.74073807362573	-3.48749889016016
H	10.68646281051611	-1.48966091012121	-3.69663502645171
H	11.78176695256373	-2.80898559210750	-3.28576173168489
H	11.09496659407822	-1.80998074757269	-2.00545908252709

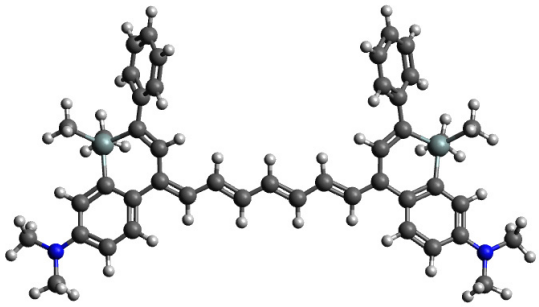

12 (SiliFlav7)

98

C	-0.05900178294242	-2.10015453232427	-0.24716599955173
C	-1.23308583605744	-2.83662372998930	-0.32419264847232
C	1.18703420538922	-2.54751071029011	-0.66086904028085
H	-1.19794560308815	-3.84160731904625	-0.72954350435091
H	1.28121115117139	-3.55077216957764	-1.06099162648365
H	-0.12309396779586	-1.09288303474329	0.15335866554070
C	2.30049174872202	-1.73448847758251	-0.59943792305251
C	3.56491676713470	-2.13163356295957	-1.03958202576346
C	-2.44328454161330	-2.31211398707145	0.07834777889820
C	-3.65199491349307	-3.00491602381793	-0.03144054036352
H	2.14566092906414	-0.73972008956537	-0.20258631386246
C	4.71059508838872	-1.35166700065485	-1.09797631989833
C	4.62522332629728	0.03313912623421	-0.64419249996696
C	5.95007421092023	-1.92742756481619	-1.59902452608510
C	5.46558556775439	1.05339567160507	-0.88932506683534
C	7.03927744726236	-1.12893071508280	-2.01232956495143
Si	6.96091736895783	0.74098340236247	-1.97797878769221

H	3.74611038680636	0.25250767285017	-0.05502926397018
C	6.11689674175322	-3.32283219630341	-1.67554046172326
C	8.18658969615240	-1.71820693502170	-2.50462284210363
C	7.26065521834401	-3.90606683358720	-2.14911447475051
C	8.33939361771206	-3.11735028676033	-2.60408813296450
H	5.33905809204452	-3.98343260393334	-1.32407179835918
H	7.32847084624089	-4.98209831485717	-2.16261324515632
H	5.41474247827737	5.68875219104468	-0.99936682866943
C	5.19948016201797	4.79262418999670	-0.43320523712525
C	4.66016376001920	4.88660327059331	0.83935078639644
H	4.45584170731747	5.85515101814160	1.27490992994308
C	4.39597060291819	3.72890287773513	1.55492775519553
H	3.99132976401802	3.79120326848746	2.55619365566855
C	4.65885537680538	2.48970432513765	0.99893137741572
H	4.46935958990739	1.59692680068369	1.57876572081042
C	5.19098226863795	2.37643652819850	-0.28796201714434
C	5.46883889168543	3.55235761742620	-0.98609046786879
H	5.88118759079003	3.50285337160135	-1.98389558397640
C	-4.91433616936038	-2.53060961751013	0.28559950459281
C	-5.03242193195295	-1.18529201426689	0.84245955660120
C	-6.07761803215768	-3.38073386105180	0.07051308725701
C	-7.38923105047454	-2.86178042503164	0.00431580789606
C	-6.12054636471318	-0.39894075097923	0.90774797300080
Si	-7.72529800171719	-1.02693380813041	0.16584876484923
H	-4.10717408495894	-0.78040889849030	1.22910379573965

C	-8.45879770307952	-3.70255398805403	-0.23389265273992
C	-5.93293242889717	-4.77261848504769	-0.07258198912096
C	-8.30669446247663	-5.09568187894105	-0.39755723643569
C	-6.99558608482595	-5.60693507691579	-0.29096281829006
H	-6.81621336734028	-6.66710343241645	-0.37051954652137
H	-4.96022604555118	-5.23069790016963	0.02192508519265
H	-5.72414887945083	4.40433364083242	3.25840621178207
C	-5.80528429901141	3.43536674214833	2.78506390572035
C	-6.58506323747370	3.27481832405254	1.65121218027400
H	-7.11222569029613	4.12068422560432	1.23111163710997
C	-6.69707880976129	2.03191357036194	1.05188957113416
C	-6.01585894550473	0.92465879127055	1.55927194129854
C	-5.24151002790285	1.10179210773212	2.70816622872633
H	-4.73194837933280	0.25313122007119	3.14321928202716
C	-5.13790027430807	2.34138167617661	3.31383268964411
H	-4.53883485598978	2.45196642732308	4.20774636667779
H	-2.42550515491538	-1.30555596285144	0.47519757988808
H	-3.57337713780337	-3.99144652987974	-0.46427647339030
H	3.61685285670383	-3.14113757602816	-1.41949781393785
H	9.00171531843923	-1.08597609027179	-2.82400738190383
H	-7.30737437606046	1.93009465911782	0.16550755411385
H	-9.45104888714135	-3.28054752719716	-0.29331062801297
N	9.46562788162301	-3.67700305908998	-3.10022787715236
N	-9.36372797310438	-5.90666345738836	-0.63122887069216
C	-9.17044106140578	-7.33520819536553	-0.78179174532551

C	-10.70429345426051	-5.36302586342436	-0.71657674558241
C	9.60330200780577	-5.11873355836829	-3.16121497446424
C	10.56433933123874	-2.84482563844411	-3.54894103422904
H	-11.00258068050770	-4.87689882989958	0.21483689452085
H	-11.40140745133354	-6.16999214888590	-0.91517103505393
H	-10.79111316973385	-4.63395895359670	-1.52474777628376
H	-8.76210594187136	-7.78595395631632	0.12551497100282
H	-8.49560588706109	-7.56305968811911	-1.60897641458885
H	-10.12752380348624	-7.80128533447871	-0.98939642050941
H	8.81853840314485	-5.57046387225752	-3.77077099424150
H	9.56691065809898	-5.57063435503134	-2.16748716112506
H	10.56062364779468	-5.36365877982958	-3.60849420103534
H	10.24956186262689	-2.15856522594557	-4.33711638471169
H	11.34813225670217	-3.47915756950887	-3.94876293978108
H	10.98598807054735	-2.25547415016505	-2.73148045591465
C	-9.16974586523908	-0.71108226785556	1.30043675318775
C	-8.04007282334920	-0.30897600880728	-1.53111505216048
C	6.72441114420377	1.37286771135496	-3.72155188970406
C	8.50438288576563	1.45616423251125	-1.21699264850418
H	-9.00009222838769	-1.14024961575206	2.28855383508092
H	-10.08306290432982	-1.14958038157318	0.89546304193730
H	-9.34641621919197	0.35811552641577	1.42383002346321
H	8.64469517547265	1.10392185590775	-0.19450803160344
H	8.46029610061284	2.54576875954893	-1.19582957245848
H	9.38775147434623	1.17553748599224	-1.79265054204529

H	-7.16657975625301	-0.41957702955182	-2.17471109341855
H	-8.29998016995566	0.74888911180195	-1.49048772988001
H	-8.87199738212677	-0.83442636103564	-2.00440144693297
H	5.76797494692058	1.04999277574905	-4.13417551872924
H	7.51401823997898	0.97692306216543	-4.36310012920775
H	6.77049123450935	2.46041097367232	-3.77894794547620

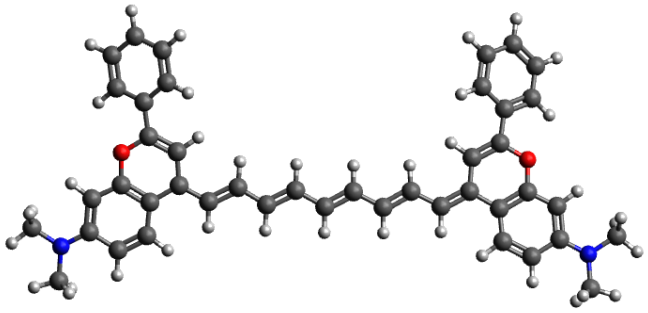

Flav9

86

C	2.09819547603895	-1.89805352164759	-0.74054164953156
C	-1.45438841380376	-2.88579572370278	-0.42367069761218
C	3.38059435722289	-2.35455027911969	-1.11453119988988
C	4.47162190482025	-1.53770063480371	-1.16008381816031
C	5.76099339369405	-1.96215737935328	-1.54482687295816
C	-2.70528054006080	-2.34184088832157	-0.08229272789822
C	-3.88021369534045	-3.03374952961827	-0.18752826616947
C	6.87349903235098	-1.16398270003533	-1.65972673389269
C	6.84240567774710	0.25434550678190	-1.42554326417646
C	8.17119790354091	-1.68292687121268	-2.05371537409566
C	7.93084240128125	1.02994019170096	-1.55761541381542
C	9.25473277322802	-0.81143198094223	-2.17777614630771
O	9.12903560116512	0.52290644138559	-1.92346902395228
H	5.91564643918988	0.73494219152476	-1.16396233854454
C	8.44523480207758	-3.03054432395581	-2.33498605227263
C	10.51831557955767	-1.21696293993122	-2.55659255969217
C	9.68418089039172	-3.46716349725225	-2.71434495910171

C	10.76934900472933	-2.56403358575621	-2.84305916388015
H	7.65496076934218	-3.76168201046985	-2.25101512537221
H	9.82734575863734	-4.51654315876196	-2.91488770332467
H	9.80117416744342	5.19529454796227	-2.25591587117267
C	9.01472514374871	4.61948284856723	-1.78751367576499
C	8.04324997522691	5.25531057182488	-1.03226340924067
H	8.06937604941109	6.32888743817500	-0.90502934238348
C	7.04023296135793	4.50718893296297	-0.43436477657531
H	6.28489572536692	4.99429802266978	0.16684926969349
C	7.00573818673033	3.13473613219392	-0.59446629177123
H	6.22973410725339	2.56349346239291	-0.10590643574459
C	7.97387935794619	2.48736952920876	-1.36099789777861
C	8.98438107044639	3.24523949675311	-1.94967769553985
H	9.74293661716304	2.75862360075132	-2.54425050089793
C	-5.16542718074687	-2.53141862043055	0.12256303032999
C	-5.35528435668979	-1.24210150183149	0.68501052870695
C	-6.34386004457995	-3.29306958043445	-0.12351779475973
C	-7.59653864886271	-2.73934745737699	0.19008640852810
C	-6.58865386415437	-0.77204620517262	0.98158223458507
O	-7.68619181617172	-1.50184147935633	0.73968397754618
H	-4.51138978111323	-0.60313033373346	0.87776503321241
C	-8.79219802007771	-3.38394076026448	-0.02429005402209
C	-6.37671921057395	-4.58580222066109	-0.69346028813268
C	-8.80073307191639	-4.66807231389484	-0.58826769922879
C	-7.54109243894918	-5.24853069812366	-0.91953742609415

H	-7.50301004521112	-6.23159720335088	-1.35920971362969
H	-5.45420699420489	-5.07418076399271	-0.96584262551405
H	-7.68930783020184	4.02361772878388	3.03522747651136
C	-7.46670085336678	3.04920188879179	2.62252233419185
C	-8.42397342744236	2.37105718458340	1.88499708530676
H	-9.39449126928761	2.81618574080639	1.71487308330501
C	-8.14277874302883	1.12269038848723	1.36068888912568
C	-6.89129297075209	0.54168718739909	1.56104788608412
C	-5.93534567316063	1.22748705357944	2.30896276464782
H	-4.97003014534662	0.78214960748152	2.50121390577748
C	-6.22394803857388	2.47232741499072	2.83512673675388
H	-5.47745013127284	2.99099785471556	3.42038291188474
H	-2.70600094466167	-1.31410440309821	0.26182030538792
H	-3.81394050051506	-4.04475335265953	-0.56166151188054
H	11.29076483615621	-0.46820301606098	-2.62292668003570
H	-8.89216268691429	0.60274175904271	0.78262030519693
H	-9.70199934263747	-2.87550264454749	0.24912512940910
N	11.99858592528260	-2.99025869053404	-3.22630181593621
N	-9.94906415964048	-5.33263314715183	-0.81311763577769
C	-9.93946509502276	-6.65047396274772	-1.42435056368265
C	-11.22104790383273	-4.71886089250667	-0.48263081034691
C	12.23239075741317	-4.38756362139084	-3.52819852742796
C	13.09338516406119	-2.04914408883233	-3.32450827847957
H	-11.27877438646269	-4.47272804548987	0.57902519297712
H	-12.02099316037121	-5.41331154280817	-0.71381850522244

H	-11.38392162370223	-3.80396971064907	-1.05625711814460
H	-9.37870384135588	-7.36622526271120	-0.82187875256285
H	-9.50665693652038	-6.62608782605186	-2.42580068827601
H	-10.96070287479518	-7.00549917266903	-1.50590840060627
H	11.59267135714020	-4.73768216516748	-4.34090480563642
H	12.05886378504694	-5.02605609621685	-2.65899194416998
H	13.26467496942355	-4.51308847952048	-3.83764157161289
H	12.88970709894929	-1.26875111703274	-4.06162000398584
H	13.98989101638094	-2.57749623696064	-3.63078160618331
H	13.29543242402984	-1.56493477801920	-2.36608408314011
C	-0.29657252080645	-2.16272596226493	-0.38045183527626
C	0.97097244364601	-2.66515374931563	-0.73689696950960
H	-1.41824481696340	-3.91873399501606	-0.75273563020031
H	-0.35032661109858	-1.12507759748704	-0.06350034929014
H	1.04000304465364	-3.70521308380278	-1.03786364646210
H	3.48860441520259	-3.39819784126488	-1.39155035557703
H	5.85962848860767	-3.01422245499381	-1.77449581218165
H	4.31791035231695	-0.50046095196460	-0.88501911014733
H	2.00884340477039	-0.85532067107277	-0.44865688851083

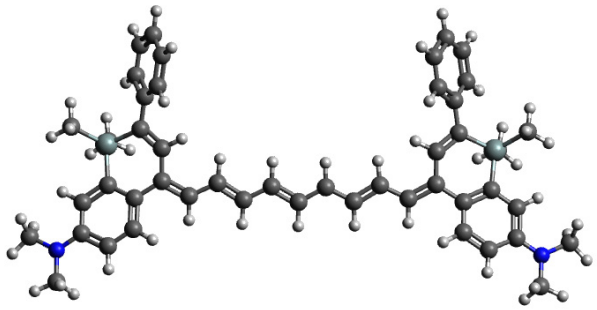

13 (SiliFlav9)

102

C	2.14184493826762	-1.96928449557488	-0.54340788924841
C	-1.43783218707487	-2.94134610300405	-0.30729510048479
C	3.40310674757445	-2.39078291877302	-0.95468742777034
C	4.49570881761462	-1.55688499072550	-0.89890814575603
C	5.77243490132017	-1.93606095862930	-1.33502325107661
C	-2.63338567780371	-2.38736236270839	0.08402772323759
C	-3.86004066072265	-3.05690606595091	-0.03497278042879
C	6.90289962851561	-1.14219769902843	-1.39736893806916
C	6.79895921055304	0.24796129608299	-0.96102424447719
C	8.15671162328322	-1.70692015663772	-1.88641021105158
C	7.62501118303366	1.27578509258700	-1.22170942401598
C	9.23097644411291	-0.89823807206301	-2.31375419681203
Si	9.12142768792340	0.96979059207711	-2.30969714963129
H	5.91744838050084	0.46272431654182	-0.37294787839644
C	8.34780306645535	-3.09929681924275	-1.93452488227390
C	10.39109150120324	-1.47727794230184	-2.79215781522534
C	9.50337806768263	-3.67192617678088	-2.39529652611216

C	10.56906528907295	-2.87413555001651	-2.86292863148479
H	7.58063990859187	-3.76646567604180	-1.57153744825635
H	9.58945589979827	-4.74682097515404	-2.38765282345685
H	7.50429075420109	5.90840993211274	-1.39714635530487
C	7.30608426925583	5.01741437690853	-0.81673212504588
C	6.77513269064376	5.12172265495398	0.45869848365010
H	6.56028858551082	6.09330021910734	0.88238220935341
C	6.53328380200423	3.97039853467371	1.19230419865062
H	6.13531364092838	4.04085920537691	2.19576934626875
C	6.81072508131687	2.72719857528259	0.65185645836557
H	6.63877076737502	1.83989899292114	1.24554250650258
C	7.33420353075795	2.60345826140435	-0.63753694565978
C	7.58899343098534	3.77329005701234	-1.35439487246732
H	7.99475288388544	3.71560720464091	-2.35460439698425
C	-5.11180230844421	-2.56514797713903	0.27845654948346
C	-5.21343621701659	-1.21897664712274	0.83821364108654
C	-6.29083074616931	-3.39894621043074	0.05867407477599
C	-7.59223638479859	-2.85944764542972	-0.01587637357056
C	-6.29048620538652	-0.41754903906555	0.90038628528641
Si	-7.90076293115699	-1.02082167409928	0.15097103460432
H	-4.28362058209038	-0.82894383343241	1.23019360007035
C	-8.67484326256323	-3.68397425025586	-0.26132650613982
C	-6.16768539612667	-4.79209894142248	-0.08110646695625
C	-8.54416970389113	-5.07829136342349	-0.42453822370012
C	-7.24275563354026	-5.60981355411048	-0.30772242971550

H	-7.07927685716464	-6.67277693714939	-0.38563693902472
H	-5.20310942511536	-5.26598881565689	0.02068291123622
H	-5.83931835204200	4.37170342503267	3.27207449647529
C	-5.93133305230809	3.40582549941888	2.79432979794730
C	-6.70428721443625	3.26119794788100	1.65357443828292
H	-7.21524730788155	4.11646082345049	1.23234324275275
C	-6.83020994163853	2.02226853218283	1.04845327442378
C	-6.17040652020559	0.90262790378515	1.55708052991594
C	-5.40289683992563	1.06389821131895	2.71285372595426
H	-4.90990578458817	0.20602776769838	3.14907221846601
C	-5.28485582190016	2.29972815609379	3.32397579380658
H	-4.69115668385991	2.39770470347411	4.22300577388994
H	-2.59742728948263	-1.38128622212874	0.48140459572728
H	-3.79542651367796	-4.04401580346112	-0.46936270768819
H	11.19537120300288	-0.83648719563137	-3.12214081225188
H	-7.43507433113711	1.93333774332977	0.15689000037453
H	-9.65968574289707	-3.24538552842278	-0.32636186915712
N	11.70810408944744	-3.42464617697861	-3.34511369500416
N	-9.61313799794883	-5.87414082988825	-0.66709185924407
C	-9.43994933565049	-7.30496869862983	-0.81491313576431
C	-10.94367004902099	-5.30948489901573	-0.76229547974308
C	11.86894323000509	-4.86431334715546	-3.37926804562687
C	12.79140239467579	-2.58213529551792	-3.80977522047580
H	-11.24341768097084	-4.82095768368114	0.16773151985904
H	-11.65198882023257	-6.10460937795119	-0.96961414482086

H	-11.01267002410105	-4.57650326943301	-1.56895597857572
H	-9.04316172477861	-7.76148865875752	0.09489338681187
H	-8.76399586378937	-7.54466443816097	-1.63817022856579
H	-10.40258539334491	-7.75765741673519	-1.02721616245294
H	11.09470939351029	-5.34060801240591	-3.98409652283293
H	11.83513616787003	-5.29956081536250	-2.37783714715793
H	12.83235523124045	-5.10224319899050	-3.81749573868369
H	12.46685364604681	-1.92001691594688	-4.61488200126680
H	13.58919727633253	-3.20991062493064	-4.19219144261237
H	13.19925600021520	-1.96544773663602	-3.00528632722965
C	-0.23676301031057	-2.24090564633374	-0.21895304473707
C	0.99174132860872	-2.73459395548089	-0.61590478139025
H	-1.42592997840751	-3.94731711118200	-0.71196709450857
H	-0.27110035477411	-1.23114684921195	0.17904656247470
H	1.05254734355088	-3.74223893363394	-1.01146807730184
H	3.51814808124604	-3.39531235886063	-1.34641586756688
H	5.84081909603416	-2.94918916003963	-1.70338106676848
H	4.32296619476118	-0.56182204731220	-0.51007655418174
H	2.05326841459826	-0.96103032504548	-0.14997539521761
C	-9.34548412179534	-0.68773138612457	1.28071482056806
C	-8.20201494537926	-0.29269842982723	-1.54429396689270
C	8.87053605084311	1.57138472897605	-4.06213796423398
C	10.65608669123661	1.72195104614698	-1.56652976442560
H	-9.18760704187290	-1.12515935745119	2.26724747769448
H	-10.26353566026964	-1.10979285024519	0.86881790379492

H	-9.50669668235494	0.38331427374585	1.40977691525998
H	10.80767919840802	1.38522658416173	-0.54033222991269
H	10.59417194598868	2.81093150049876	-1.55890787333793
H	11.54133033161433	1.44876658667581	-2.14302497701666
H	7.91722011267212	1.22896205253136	-4.46636781184190
H	9.66324248394518	1.17570179759997	-4.70018168822963
H	8.90144410915546	2.65845526933363	-4.13755960193976
H	-7.32865279048177	-0.41385814889796	-2.18629914369286
H	-8.44748139874810	0.76861255093885	-1.50243800538701
H	-9.03990429810054	-0.80551385911919	-2.02118567071695

2.8 References

(1) Welsher, K.; Liu, Z.; Sherlock, S. P.; Robinson, J. T.; Chen, Z.; Daranciang, D.; Dai, H. A Route to Brightly Fluorescent Carbon Nanotubes for Near-Infrared Imaging in Mice. *Nature Nanotech* **2009**, *4* (11), 773–780. https://doi.org/10.1038/nnano.2009.294.

(2) Naczynski, D. J.; Tan, M. C.; Zevon, M.; Wall, B.; Kohl, J.; Kulesa, A.; Chen, S.; Roth, C. M.; Riman, R. E.; Moghe, P. V. Rare-Earth-Doped Biological Composites as in Vivo Shortwave Infrared Reporters. *Nat Commun* **2013**, *4* (1), 2199. https://doi.org/10.1038/ncomms3199.

(3) Salo, D.; Zhang, H.; Kim, D. M.; Berezin, M. Y. Multispectral Measurement of Contrast in Tissue-Mimicking Phantoms in near-Infrared Spectral Range of 650 to 1600 Nm. *JBO* **2014**, *19* (8), 086008. https://doi.org/10.1117/1.JBO.19.8.086008.

(4) Hong, G.; Diao, S.; Chang, J.; Antaris, A. L.; Chen, C.; Zhang, B.; Zhao, S.; Atochin, D. N.; Huang, P. L.; Andreasson, K. I.; Kuo, C. J.; Dai, H. Through-Skull Fluorescence Imaging of the Brain in a New near-Infrared Window. *Nature Photon* **2014**, *8* (9), 723–730. https://doi.org/10.1038/nphoton.2014.166.

(5) Diao, S.; Blackburn, J. L.; Hong, G.; Antaris, A. L.; Chang, J.; Wu, J. Z.; Zhang, B.; Cheng, K.; Kuo, C. J.; Dai, H. Fluorescence Imaging In Vivo at Wavelengths beyond 1500 Nm. *Angewandte Chemie International Edition* **2015**, *54* (49), 14758–14762. https://doi.org/10.1002/anie.201507473.

(6) Antaris, A. L.; Chen, H.; Cheng, K.; Sun, Y.; Hong, G.; Qu, C.; Diao, S.; Deng, Z.; Hu, X.; Zhang, B.; Zhang, X.; Yaghi, O. K.; Alamparambil, Z. R.; Hong, X.; Cheng, Z.; Dai, H. A Small-Molecule Dye for NIR-II Imaging. *Nature Mater* **2016**, *15* (2), 235–242. https://doi.org/10.1038/nmat4476.

(7) Starosolski, Z.; Bhavane, R.; Ghaghada, K. B.; Vasudevan, S. A.; Kaay, A.; Annapragada, A. Indocyanine Green Fluorescence in Second Near-Infrared (NIR-II) Window. *PLOS ONE* **2017**, *12* (11), e0187563. https://doi.org/10.1371/journal.pone.0187563.

(8) Li, B.; Lu, L.; Zhao, M.; Lei, Z.; Zhang, F. An Efficient 1064 Nm NIR-II Excitation Fluorescent Molecular Dye for Deep-Tissue High-Resolution Dynamic Bioimaging. *Angewandte Chemie* **2018**, *130* (25), 7605–7609. https://doi.org/10.1002/ange.201801226.

(9) Ma, Z.; Zhang, M.; Yue, J.; Alcazar, C.; Zhong, Y.; Doyle, T. C.; Dai, H.; Huang, N. F. Near-Infrared IIb Fluorescence Imaging of Vascular Regeneration with Dynamic Tissue Perfusion Measurement and High Spatial Resolution. *Advanced Functional Materials* **2018**, *28* (36), 1803417. https://doi.org/10.1002/adfm.201803417.

(10) Carr, J. A.; Franke, D.; Caram, J. R.; Perkinson, C. F.; Saif, M.; Askoxylakis, V.; Datta, M.; Fukumura, D.; Jain, R. K.; Bawendi, M. G.; Bruns, O. T. Shortwave Infrared Fluorescence Imaging with the Clinically Approved Near-Infrared Dye Indocyanine Green. *Proceedings of the National Academy of Sciences* **2018**, *115* (17), 4465–4470. https://doi.org/10.1073/pnas.1718917115.

(11) Carr, J. A.; Aellen, M.; Franke, D.; So, P. T. C.; Bruns, O. T.; Bawendi, M. G. Absorption by Water Increases Fluorescence Image Contrast of Biological Tissue in the Shortwave Infrared. *Proceedings of the National Academy of Sciences* **2018**, *115* (37), 9080–9085. https://doi.org/10.1073/pnas.1803210115.

(12) Lei, Z.; Sun, C.; Pei, P.; Wang, S.; Li, D.; Zhang, X.; Zhang, F. Stable, Wavelength-Tunable Fluorescent Dyes in the NIR-II Region for In Vivo High-Contrast Bioimaging and Multiplexed Biosensing. *Angewandte Chemie* **2019**, *131* (24), 8250–8255. https://doi.org/10.1002/ange.201904182.

(13) Wang, S.; Fan, Y.; Li, D.; Sun, C.; Lei, Z.; Lu, L.; Wang, T.; Zhang, F. Anti-Quenching NIR-II Molecular Fluorophores for in Vivo High-Contrast Imaging and pH Sensing. *Nat Commun* **2019**, *10* (1), 1058. https://doi.org/10.1038/s41467-019-09043-x.

(14) Li, Y.; Liu, Y.; Li, Q.; Zeng, X.; Tian, T.; Zhou, W.; Cui, Y.; Wang, X.; Cheng, X.; Ding, Q.; Wang, X.; Wu, J.; Deng, H.; Li, Y.; Meng, X.; Deng, Z.; Hong, X.; Xiao, Y. Novel NIR-II Organic Fluorophores for Bioimaging beyond 1550 Nm. *Chem. Sci.* **2020**, *11* (10), 2621–2626. https://doi.org/10.1039/C9SC06567A.

(15) Shao, W.; Wei, Q.; Wang, S.; Li, F.; Wu, J.; Ren, J.; Cao, F.; Liao, H.; Gao, J.; Zhou, M.; Ling, D. Molecular Engineering of D–A–D Conjugated Small Molecule Nanoparticles for High Performance NIR-II Photothermal Therapy. *Mater. Horiz.* **2020**, *7* (5), 1379–1386. https://doi.org/10.1039/C9MH00660E.

(16) Lei, Z.; Zhang, F. Molecular Engineering of NIR-II Fluorophores for Improved Biomedical Detection. *Angewandte Chemie International Edition* **2021**, *60* (30), 16294–16308. https://doi.org/10.1002/anie.202007040.

(17) Liu, Y.; Li, Y.; Koo, S.; Sun, Y.; Liu, Y.; Liu, X.; Pan, Y.; Zhang, Z.; Du, M.; Lu, S.; Qiao, X.; Gao, J.; Wang, X.; Deng, Z.; Meng, X.; Xiao, Y.; Kim, J. S.; Hong, X. Versatile Types of Inorganic/Organic NIR-IIa/IIb Fluorophores: From Strategic Design toward Molecular Imaging and Theranostics. *Chem. Rev.* **2022**, *122* (1), 209–268. https://doi.org/10.1021/acs.chemrev.1c00553.

(18) Xu, L.; Zhang, Q.; Wang, X.; Lin, W. Biomedical Applications of NIR-II Organic Small Molecule Fluorescent Probes in Different Organs. *Coordination Chemistry Reviews* **2024**, *519*, 216122. https://doi.org/10.1016/j.ccr.2024.216122.

(19) Ma, K.; Jiang, Q.; Yang, Y.; Zhang, F. Recent Advances of Versatile Fluorophores for Multifunctional Biomedical Imaging in the NIR-II Region. *J. Mater. Chem. B* **2024**. https://doi.org/10.1039/D4TB01957A.

(20) Chen, X.; Li, J.; Roy, S.; Ullah, Z.; Gu, J.; Huang, H.; Yu, C.; Wang, X.; Wang, H.; Zhang, Y.; Guo, B. Development of Polymethine Dyes for NIR-II Fluorescence Imaging and Therapy. *Advanced Healthcare Materials n/a* (n/a), 2304506. https://doi.org/10.1002/adhm.202304506.

(21) Yang, Z.; Sun, Q.; Ji, L.; Meng, C.; Heng, H.; Feng, F. Recent Advances for Synthesis and Bioapplications of Polymethine Cyanines. *Asian Journal of Organic Chemistry n/a* (n/a), e202500109. https://doi.org/10.1002/ajoc.202500109.

(22) Feng, X.; Wei, L.; Liu, Y.; Chen, X.; Tian, R. Orchestrated Strategies for Developing Fluorophores for NIR-II Imaging. *Advanced Healthcare Materials* **2023**, *12* (24), 2300537. https://doi.org/10.1002/adhm.202300537.

(23) Jiang, Z.; Ding, Y.; Lovell, J. F.; Zhang, Y. Design and Application of Organic Contrast Agents for Molecular Imaging in the Second near Infrared (NIR-II) Window. *Photoacoustics* **2022**, *28*, 100426. https://doi.org/10.1016/j.pacs.2022.100426.

(24) Cosco, E. D.; Caram, J. R.; Bruns, O. T.; Franke, D.; Day, R. A.; Farr, E. P.; Bawendi, M. G.; Sletten, E. M. Flavylium Polymethine Fluorophores for Near- and Shortwave Infrared Imaging. *Angewandte Chemie International Edition* **2017**, *56* (42), 13126–13129. https://doi.org/10.1002/anie.201706974.

(25) Cosco, E. D.; Spearman, A. L.; Ramakrishnan, S.; Lingg, J. G. P.; Saccomano, M.; Pengshung, M.; Arús, B. A.; Wong, K. C. Y.; Glasl, S.; Ntziachristos, V.; Warmer, M.; McLaughlin, R. R.; Bruns, O. T.; Sletten, E. M. Shortwave Infrared Polymethine Fluorophores Matched to Excitation Lasers Enable Non-Invasive, Multicolour in Vivo Imaging in Real Time. *Nat. Chem.* **2020**, *12* (12), 1123–1130. https://doi.org/10.1038/s41557-020-00554-5.

(26) Pengshung, M.; Li, J.; Mukadum, F.; Lopez, S. A.; Sletten, E. M. Photophysical Tuning of Shortwave Infrared Flavylium Heptamethine Dyes via Substituent Placement. *Org. Lett.* **2020**, *22* (15), 6150–6154. https://doi.org/10.1021/acs.orglett.0c02213.

(27) Cosco, E. D.; Arús, B. A.; Spearman, A. L.; Atallah, T. L.; Lim, I.; Leland, O. S.; Caram, J. R.; Bischof, T. S.; Bruns, O. T.; Sletten, E. M. Bright Chromenylium Polymethine Dyes Enable Fast, Four-Color In Vivo Imaging with Shortwave Infrared Detection. *J. Am. Chem. Soc.* **2021**, *143* (18), 6836–6846. https://doi.org/10.1021/jacs.0c11599.

(28) Garcia, C. A.; Mobley, E. B.; Lin, E. Y.; Bui, K.; Sletten, E. M. Palladium-Catalyzed Functionalization of Shortwave Infrared Heptamethine Fluorophores Expands Their In Vivo Utility. *JACS Au* **2025**. https://doi.org/10.1021/jacsau.4c01279.

(29) Lim, I.; Vian, A.; van de Wouw, H. L.; Day, R. A.; Gomez, C.; Liu, Y.; Rheingold, A. L.; Campàs, O.; Sletten, E. M. Fluorous Soluble Cyanine Dyes for Visualizing Perfluorocarbons in Living Systems. *J. Am. Chem. Soc.* **2020**, *142* (37), 16072–16081. https://doi.org/10.1021/jacs.0c07761.

(30) Jia, S.; Lin, E. Y.; Mobley, E. B.; Lim, I.; Guo, L.; Kallepu, S.; Low, P. S.; Sletten, E. M. Water-Soluble Chromenylium Dyes for Shortwave Infrared Imaging in Mice. *Chem* **2023**, *9* (12), 3648–3665. https://doi.org/10.1016/j.chempr.2023.08.021.

(31) Mobley, E. B.; Lin, E. Y.; Sletten, E. M. Chromenylium Star Polymers: Merging Water Solubility and Stealth Properties with Shortwave Infrared Emissive Fluorophores. *ACS Cent. Sci.* **2024**. https://doi.org/10.1021/acscentsci.4c01570.

(32) Swamy, M. M. M.; Murai, Y.; Monde, K.; Tsuboi, S.; Jin, T. Shortwave-Infrared Fluorescent Molecular Imaging Probes Based on π-Conjugation Extended Indocyanine Green. *Bioconjugate Chem.* **2021**, *32* (8), 1541–1547. https://doi.org/10.1021/acs.bioconjchem.1c00253.

(33) Swamy, M. M. M.; Murai, Y.; Monde, K.; Tsuboi, S.; Swamy, A. K.; Jin, T. Biocompatible and Water-Soluble Shortwave-Infrared (SWIR)-Emitting Cyanine-Based Fluorescent Probes for In Vivo Multiplexed Molecular Imaging. *ACS Appl. Mater. Interfaces* **2024**, *16* (14), 17253–17266. https://doi.org/10.1021/acsami.4c01000.

(34) Bandi, V. G.; Luciano, M. P.; Saccomano, M.; Patel, N. L.; Bischof, T. S.; Lingg, J. G. P.; Tsrunchev, P. T.; Nix, M. N.; Ruehle, B.; Sanders, C.; Riffle, L.; Robinson, C. M.; Difilippantonio, S.; Kalen, J. D.; Resch-Genger, U.; Ivanic, J.; Bruns, O. T.; Schnermann, M. J. Targeted Multicolor in Vivo Imaging over 1,000 Nm Enabled by Nonamethine Cyanines. *Nat Methods* **2022**, *19* (3), 353–358. https://doi.org/10.1038/s41592-022-01394-6.

(35) Wan, Y.; Chen, W.; Liu, Y.; Lee, K.-W.; Gao, Y.; Zhang, D.; Li, Y.; Huang, Z.; Luo, J.; Lee, C.-S.; Li, S. Neutral Cyanine: Ultra-Stable NIR-II Merocyanines for Highly Efficient Bioimaging and Tumor-Targeted Phototheranostics. *Advanced Materials* **2024**, *36* (31), 2405966. https://doi.org/10.1002/adma.202405966.

(36) Zhao, L.; Zhu, H.; Duo, Y.-Y.; Wang, Z.-G.; Pang, D.-W.; Liu, S.-L. A Cyanine with 83.2% Photothermal Conversion Efficiency and Absorption Wavelengths over 1200 Nm for Photothermal Therapy. *Advanced Healthcare Materials* **2024**, *13* (20), 2304421. https://doi.org/10.1002/adhm.202304421.

(37) Guo, J.; Zhu, Y.; Qu, Y.; Zhang, L.; Fang, M.; Xu, Z.; Wang, T.; Qin, Y.; Xu, Y.; Li, Y.; Chen, Y.; Fu, H.; Liu, X.; Liu, Y.; Liu, C.; Gao, Y.; Cui, M.; Zhou, K. Structure Tailoring of Hemicyanine Dyes for In Vivo Shortwave Infrared Imaging. *J. Med. Chem.* **2024**, *67* (18), 16820–16834. https://doi.org/10.1021/acs.jmedchem.4c01662.

(38) Ge, R.-T.; Xiong, F.; Chen, Z.-B.; Wang, Y.; Zheng, L.; Zhou, J.; Wu, D.; Zhang, S.-Y. Indocyanine Polymethine Fluorophores with Extended π-Conjugation Emitting beyond 1,200 Nm for Enhanced NIR-II Imaging. *Chem* **2025**, 102489. https://doi.org/10.1016/j.chempr.2025.102489.

(39) Bin, Y.; Huang, L.; Qin, J.; Zhao, S.; Tian, J.; Zhang, L. Exceptional Near-Infrared II Organic Small Molecule Nanoagent for Photoacoustic/Photothermal Imaging-Guided Highly Efficient Therapy in Cancer. *Bioconjugate Chem.* **2025**, *36* (4), 803–814. https://doi.org/10.1021/acs.bioconjchem.5c00058.

(40) Brøndsted, F.; Stains, C. I. Heteroatom-Substituted Xanthene Fluorophores Enter the Shortwave-Infrared Region. *Photochem Photobiol* **2022**, *98* (2), 400–403. https://doi.org/10.1111/php.13578.

(41) Gao, X.; Wang, J.; Qin, Y.; Zhu, Y.; Liu, Y.; Zhou, K.; Cui, M. Design, Synthesis, and In Vivo Imaging of a Stable Xanthene-Based Dye with NIR-II Emission up to 1450 Nm. *Anal. Chem.* **2025**, *97* (3), 1827–1836. https://doi.org/10.1021/acs.analchem.4c05794.

(42) Liu, D.; He, Z.; Zhao, Y.; Yang, Y.; Shi, W.; Li, X.; Ma, H. Xanthene-Based NIR-II Dyes for In Vivo Dynamic Imaging of Blood Circulation. *J. Am. Chem. Soc.* **2021**, *143* (41), 17136–17143. https://doi.org/10.1021/jacs.1c07711.

(43) Meador, W. E.; Lin, E. Y.; Lim, I.; Friedman, H. C.; Ndaleh, D.; Shaik, A. K.; Hammer, N. I.; Yang, B.; Caram, J. R.; Sletten, E. M.; Delcamp, J. H. Silicon-RosIndolizine Fluorophores with Shortwave Infrared Absorption and Emission Profiles Enable in Vivo Fluorescence Imaging. *Nat. Chem.* **2024**, *16* (6), 970–978. https://doi.org/10.1038/s41557-024-01464-6.

(44) Chatterjee, S.; E. Meador, W.; Smith, C.; Chandrasiri, I.; Farid Zia, M.; Nguyen, J.; Dorris, A.; Flynt, A.; L. Watkins, D.; I. Hammer, N.; H. Delcamp, J. SWIR Emissive RosIndolizine Dyes with Nanoencapsulation in Water Soluble Dendrimers. *RSC Advances* **2021**, *11* (45), 27832–27836. https://doi.org/10.1039/D1RA05479A.

(45) Saucier, M. A.; Kruse, N. A.; Seidel, B. E.; Hammer, N. I.; Tschumper, G. S.; Delcamp, J. H. Phospha-RosIndolizine Dye with Shortwave Infrared (SWIR) Absorption and Emission. *J. Org. Chem.* **2024**, *89* (12), 9092–9097. https://doi.org/10.1021/acs.joc.4c00741.

(46) Wei, R.; Dong, Y.; Wang, X.; Li, J.; Lei, Z.; Hu, Z.; Chen, J.; Sun, H.; Chen, H.; Luo, X.; Qian, X.; Yang, Y. Rigid and Photostable Shortwave Infrared Dye Absorbing/Emitting beyond 1200 Nm for High-Contrast Multiplexed Imaging. *J. Am. Chem. Soc.* **2023**, *145* (22), 12013–12022. https://doi.org/10.1021/jacs.3c00594.

(47) Kenry; Duan, Y.; Liu, B. Recent Advances of Optical Imaging in the Second Near-Infrared Window. *Advanced Materials* **2018**, *30* (47), 1802394. https://doi.org/10.1002/adma.201802394.

(48) Abdelhameed, M.; Martir, D. R.; Chen, S.; Xu, W. Z.; Oyeneye, O. O.; Chakrabarti, S.; Zysman-Colman, E.; Charpentier, P. A. Tuning the Optical Properties of Silicon Quantum Dots via Surface Functionalization with Conjugated Aromatic Fluorophores. *Sci Rep* **2018**, *8* (1), 3050. https://doi.org/10.1038/s41598-018-21181-8.

(49) Feng, Z.; Tang, T.; Wu, T.; Yu, X.; Zhang, Y.; Wang, M.; Zheng, J.; Ying, Y.; Chen, S.; Zhou, J.; Fan, X.; Zhang, D.; Li, S.; Zhang, M.; Qian, J. Perfecting and Extending the Near-Infrared Imaging Window. *Light Sci Appl* **2021**, *10* (1), 197. https://doi.org/10.1038/s41377-021-00628-0.

(50) Chen, Z.-H.; Wang, X.; Yang, M.; Ming, J.; Yun, B.; Zhang, L.; Wang, X.; Yu, P.; Xu, J.; Zhang, H.; Zhang, F. An Extended NIR-II Superior Imaging Window from 1500 to 1900 Nm for High-Resolution In Vivo Multiplexed Imaging Based on Lanthanide Nanocrystals. *Angewandte Chemie International Edition* **2023**, *62* (49), e202311883. https://doi.org/10.1002/anie.202311883.

(51) Bricks, J. L.; Kachkovskii, A. D.; Slominskii, Y. L.; Gerasov, A. O.; Popov, S. V. Molecular Design of near Infrared Polymethine Dyes: A Review. *Dyes and Pigments* **2015**, *121*, 238–255. https://doi.org/10.1016/j.dyepig.2015.05.016.

(52) Spearman, A. L.; Lin, E. Y.; Mobley, E. B.; Chmyrov, A.; Arús, B. A.; Turner, D. W.; Garcia, C. A.; Bui, K.; Rowlands, C.; Bruns, O. T.; Sletten, E. M. High-Resolution Multicolor Shortwave Infrared Dynamic In Vivo Imaging with Chromenylium Nonamethine Dyes. *J. Am. Chem. Soc.* **2025**, *147* (20), 17384–17393. https://doi.org/10.1021/jacs.5c03673.

(53) Iordanov, T. D.; Davis, J. L.; Masunov, A. E.; Levenson, A.; Przhonska, O. V.; Kachkovski, A. D. Symmetry Breaking in Cationic Polymethine Dyes, Part 1: Ground State Potential Energy Surfaces and Solvent Effects on Electronic Spectra of Streptocyanines. *International Journal of Quantum Chemistry* **2009**, *109* (15), 3592–3601. https://doi.org/10.1002/qua.22403.

(54) Masunov, A. E.; Anderson, D.; Freidzon, A. Ya.; Bagaturyants, A. A. Symmetry-Breaking in Cationic Polymethine Dyes: Part 2. Shape of Electronic Absorption Bands Explained by the Thermal Fluctuations of the Solvent Reaction Field. *J. Phys. Chem. A* **2015**, *119* (26), 6807–6815. https://doi.org/10.1021/acs.jpca.5b03877.

(55) Tolbert, L. M.; Zhao, X. Beyond the Cyanine Limit: Peierls Distortion and Symmetry Collapse in a Polymethine Dye. *J. Am. Chem. Soc.* **1997**, *119* (14), 3253–3258. https://doi.org/10.1021/ja9626953.

(56) *Continuous Symmetry Breaking Induced by Ion Pairing Effect in Heptamethine Cyanine Dyes: Beyond the Cyanine Limit | Journal of the American Chemical Society*. https://pubs.acs.org/doi/10.1021/ja9100886 (accessed 2020-08-16).

(57) Ou, Y.-F.; Xiang, H.-Y.; Yang, X.; Wang, R.-X.; Huan, S.-Y.; Yuan, L.; Ren, T.-B.; Zhang, X.-B. Constructing Stable and Wavelength-Extended Heptamethine Cyanines via Donor Ectopic Substitution for NIR-IIa/b Bioimaging. *Angewandte Chemie International Edition n/a* (n/a), e202423978. https://doi.org/10.1002/anie.202423978.

(58) Garcia, C. A. Structural Modifications of Polymethine Fluorophores to Improve Their In Vivo Utility. **2024**.

(59) Pengshung, M.; Neal, P.; Atallah, T.; Kwon, J.; Caram, J.; Lopez, S.; Sletten, E. Silicon Incorporation in Polymethine Dyes. **2020**. https://doi.org/10.26434/chemrxiv.11320064.v2.

(60) Ikeno, T.; Nagano, T.; Hanaoka, K. Silicon-Substituted Xanthene Dyes and Their Unique Photophysical Properties for Fluorescent Probes. *Chemistry – An Asian Journal* **2017**, *12* (13), 1435–1446. https://doi.org/10.1002/asia.201700385.

(61) Kushida, Y.; Nagano, T.; Hanaoka, K. Silicon-Substituted Xanthene Dyes and Their Applications in Bioimaging. *Analyst* **2015**, *140* (3), 685–695. https://doi.org/10.1039/C4AN01172D.

(62) Friedman, H. C.; Cosco, E. D.; Atallah, T. L.; Jia, S.; Sletten, E. M.; Caram, J. R. Establishing Design Principles for Emissive Organic SWIR Chromophores from Energy Gap Laws. *Chem* **2021**, *7* (12), 3359–3376. https://doi.org/10.1016/j.chempr.2021.09.001.

(63) Chen, B.; Wu, X.-F. Palladium-Catalyzed Carbonylative Synthesis of Benzosilinones from (2-Iodophenyl)Hydrosilanes and Terminal Alkynes. *Advanced Synthesis & Catalysis* **2019**, *361* (14), 3441–3445. https://doi.org/10.1002/adsc.201900432.

(64) Kende, A. S.; Mineur, C. M.; Lachicotte, R. J. Benzosilacyclohexadienones: Synthesis and Reactivity. *Tetrahedron Letters* **1999**, *40* (45), 7901–7906. https://doi.org/10.1016/S0040-4039(99)01494-X.

(65) Yatabe, T.; Mizuno, N.; Yamaguchi, K. Transition-Metal-Free Catalytic Formal Hydroacylation of Terminal Alkynes. *ACS Catal.* **2018**, *8* (12), 11564–11569. https://doi.org/10.1021/acscatal.8b02832.

(66) Choi, A.; Miller, S. C. Silicon Substitution in Oxazine Dyes Yields Near-Infrared Azasiline Fluorophores That Absorb and Emit beyond 700 Nm. *Org. Lett.* **2018**, *20* (15), 4482–4485. https://doi.org/10.1021/acs.orglett.8b01786.

(67) Ma, X.; Huang, Y.; Abedi, S. A. A.; Kim, H.; Davin, T. T. B.; Liu, X.; Yang, W.-C.; Sun, Y.; Liu, S. H.; Yin, J.; Yoon, J.; Yang, G.-F. Rational Design and Application of an Indolium-Derived Heptamethine Cyanine with Record-Long Second Near-Infrared Emission. *CCS Chemistry* **2022**, *4* (6), 1961–1976. https://doi.org/10.31635/ccschem.021.202101630.

(68) Ding, B.; Xiao, Y.; Zhou, H.; Zhang, X.; Qu, C.; Xu, F.; Deng, Z.; Cheng, Z.; Hong, X. Polymethine Thiopyrylium Fluorophores with Absorption beyond 1000 Nm for Biological Imaging in the Second Near-Infrared Subwindow. *J. Med. Chem.* **2019**, *62* (4), 2049–2059. https://doi.org/10.1021/acs.jmedchem.8b01682.

(69) Yang, Y.; Sun, C.; Wang, S.; Yan, K.; Zhao, M.; Wu, B.; Zhang, F. Counterion-Paired Bright Heptamethine Fluorophores with NIR-II Excitation and Emission Enable Multiplexed Biomedical Imaging. *Angewandte Chemie International Edition* **2022**, *61* (24), e202117436. https://doi.org/10.1002/anie.202117436.

(70) Ge, R.-T.; Xiong, F.; Chen, Z.-B.; Wang, Y.; Zheng, L.; Zhou, J.; Wu, D.; Zhang, S.-Y. Indocyanine Polymethine Fluorophores with Extended π-Conjugation Emitting beyond 1,200 Nm for Enhanced NIR-II Imaging. *Chem* **2025**, *0* (0). https://doi.org/10.1016/j.chempr.2025.102489.

(71) Lei, Z.; Sun, C.; Pei, P.; Wang, S.; Li, D.; Zhang, X.; Zhang, F. Stable, Wavelength-Tunable Fluorescent Dyes in the NIR-II Region for In Vivo High-Contrast Bioimaging and Multiplexed Biosensing. *Angewandte Chemie International Edition* **2019**, *58* (24), 8166–8171. https://doi.org/10.1002/anie.201904182.

(72) Semonin, O. E.; Johnson, J. C.; Luther, J. M.; Midgett, A. G.; Nozik, A. J.; Beard, M. C. Absolute Photoluminescence Quantum Yields of IR-26 Dye, PbS, and PbSe Quantum Dots. *J. Phys. Chem. Lett.* **2010**, *1* (16), 2445–2450. https://doi.org/10.1021/jz100830r.

(73) Liu, D.; He, Z.; Zhao, Y.; Yang, Y.; Shi, W.; Li, X.; Ma, H. Xanthene-Based NIR-II Dyes for In Vivo Dynamic Imaging of Blood Circulation. *J. Am. Chem. Soc.* **2021**, *143* (41), 17136–17143. https://doi.org/10.1021/jacs.1c07711.

(74) Yamaguchi, S.; Tamao, K. Silole-Containing σ- and π-Conjugated Compounds. *J. Chem. Soc., Dalton Trans.* **1998**, No. 22, 3693–3702. https://doi.org/10.1039/A804491K.

(75) Fu, M.; Xiao, Y.; Qian, X.; Zhao, D.; Xu, Y. A Design Concept of Long-Wavelength Fluorescent Analogs of Rhodamine Dyes: Replacement of Oxygen with Silicon Atom. *Chem. Commun.* **2008**, No. 15, 1780–1782. https://doi.org/10.1039/B718544H.

(76) Janeková, H.; Friedman, H. C.; Russo, M.; Zyberaj, M.; Ahmed, T.; Hua, A. S.; Sica, A. V.; Caram, J. R.; Štacko, P. Deuteration of Heptamethine Cyanine Dyes Enhances Their Emission Efficacy. *Chem. Commun.* **2024**, *60* (8), 1000–1003. https://doi.org/10.1039/D3CC05153F.

(77) Ramos, P.; Friedman, H.; Li, B. Y.; Garcia, C.; Sletten, E.; Caram, J. R.; Jang, S. J. Nonadiabatic Derivative Couplings through Multiple Franck–Condon Modes Dictate the Energy Gap Law for Near and Short-Wave Infrared Dye Molecules. *J. Phys. Chem. Lett.* **2024**, *15* (7), 1802–1810. https://doi.org/10.1021/acs.jpclett.3c02629.

(78) Lin, H. H.; Lim, I.; Sletten, E. M. Counterion Exchange Enhances the Brightness and Photostability of a Fluorous Cyanine Dye. *Chemistry – A European Journal* **2024**, *30* (64), e202402514. https://doi.org/10.1002/chem.202402514.

(79) Protection, I. C. on N.-I. R. ICNIRP Guidelines on Limits of Exposure to Laser Radiation of Wavelengths between 180 Nm and 1,000 Mm. *Health Physics* **2013**, *105* (3), 271. https://doi.org/10.1097/HP.0b013e3182983fd4.

(80) Schneider, C. A.; Rasband, W. S.; Eliceiri, K. W. NIH Image to ImageJ: 25 Years of Image Analysis. *Nat Methods* **2012**, *9* (7), 671–675. https://doi.org/10.1038/nmeth.2089.

(81) Schindelin, J.; Arganda-Carreras, I.; Frise, E.; Kaynig, V.; Longair, M.; Pietzsch, T.; Preibisch, S.; Rueden, C.; Saalfeld, S.; Schmid, B.; Tinevez, J.-Y.; White, D. J.; Hartenstein, V.; Eliceiri, K.; Tomancak, P.; Cardona, A. Fiji: An Open-Source Platform for Biological-Image Analysis. *Nat Methods* **2012**, *9* (7), 676–682. https://doi.org/10.1038/nmeth.2019.

(82) Universal Solvation Model Based on Solute Electron Density and on a Continuum Model of the Solvent Defined by the Bulk Dielectric Constant and Atomic Surface Tensions | The Journal of Physical Chemistry B. https://pubs.acs.org/doi/10.1021/jp810292n (accessed 2025-09-01).

(83) Neese, F.; Wennmohs, F.; Becker, U.; Riplinger, C. The ORCA Quantum Chemistry Program Package. *J. Chem. Phys.* **2020**, *152* (22), 224108. https://doi.org/10.1063/5.0004608.

(84) Neese, F. Software Update: The ORCA Program System—Version 5.0. *WIREs Computational Molecular Science* **2022**, *12* (5), e1606. https://doi.org/10.1002/wcms.1606.

(85) Bradbury, N. C.; Allen, T.; Nguyen, M.; Ibrahim, K. Z.; Neuhauser, D. Optimized Attenuated Interaction: Enabling Stochastic Bethe–Salpeter Spectra for Large Systems. *J. Chem. Phys.* **2023**, *158* (15), 154104. https://doi.org/10.1063/5.0146555.

(86) Bradbury, N. C.; Li, B. Y.; Allen, T.; Caram, J. R.; Neuhauser, D. No More Gap-Shifting: Stochastic Many-Body-Theory Based TDHF for Accurate Theory of Polymethine Cyanine Dyes. *The Journal of Chemical Physics* **2024**, *161* (14), 141101. https://doi.org/10.1063/5.0223783.

(87) Bradbury, N. C.; Nguyen, M.; Caram, J. R.; Neuhauser, D. Bethe–Salpeter Equation Spectra for Very Large Systems. *J. Chem. Phys.* **2022**, *157* (3), 031104. https://doi.org/10.1063/5.0100213.

(88) Bradbury, N. C.; Allen, T.; Nguyen, M.; Neuhauser, D. Deterministic/Fragmented-Stochastic Exchange for Large-Scale Hybrid DFT Calculations. *J. Chem. Theory Comput.* **2023**, *19* (24), 9239–9247. https://doi.org/10.1021/acs.jctc.3c00987.

(89) Yanai, T.; Tew, D. P.; Handy, N. C. A New Hybrid Exchange–Correlation Functional Using the Coulomb-Attenuating Method (CAM-B3LYP). *Chemical Physics Letters* **2004**, *393* (1), 51–57. https://doi.org/10.1016/j.cplett.2004.06.011.

CHAPTER THREE

Designing near-infrared polymethine dyes for responsive imaging

Quintashia Wilson and Ellen M. Sletten

3.1 Abstract

Polymethine dyes are foundational fluorophores in the near-infrared (NIR) spectral range, offering tunable photophysical properties and high compatibility with biological systems. While traditionally used for passive imaging, recent developments have transformed these scaffolds into dynamic, responsive platforms. This chapter explores the evolution of polymethine dyes into two emerging classes: fluorogenic probes and photocages. Fluorogenic polymethine dyes leverage mechanisms such as enzymatic cleavage, pH-triggered cyclization, and reversible addition to enable fluorescence activation under specific biological conditions, allowing for high-contrast, multicolor imaging in live cells. In parallel, polymethine-based photocages employ light-induced bond cleavage to release bioactive molecules with precise spatial and temporal control, including under hypoxic conditions where traditional phototherapies falter. These advances reveal a broader shift in dye design from static reporters to chemically responsive tools that enable real-time sensing and therapeutic intervention in complex biological environments.

3.2 Introduction

Polymethine dyes are a foundational class of fluorophores in the near-infrared (NIR, 700–1000 nm) region valued for their tunable photophysical properties and compatibility with biological systems.[1–3] For these reasons, NIR polymethine dyes are widely used in cell and animal applications where optical transparency and minimal phototoxicity are essential.[4–7] With the basic framework of NIR polymethine dyes well-established, recent advancements have focused on expanding their capabilities to create responsive systems that react to biological processes in real

time.[8–11] These responsive polymethine dyes are designed to undergo significant changes in their fluorescence or chemical reactivity in response to specific external stimuli, providing dynamic control and new functionalities in complex biological environments.

NIR fluorogenic polymethine dyes represent a noteworthy example of this shift, wherein established polymethine architectures are equipped with stimulus-responsive motifs that allow for fluorescence activation under defined conditions.[8,11] These changes are commonly driven by mechanisms such as photoinduced electron transfer (PET), fluorescence resonance energy transfer (FRET) and intramolecular charge transfer (ICT), where binding to an analyte or changes in the local environment alter the electronic structure of the dye, resulting in a change in fluorescence.[12–15] Other systems leverage reversible structural changes, including protonation[16] and cyclization,[11] that modulate the conjugation or molecular flexibility to control fluorescence. These strategies extend classic approaches that optimize brightness and stability to introduce selective, conditional activation, and a much higher degree of biological specificity. Alongside fluorogenic probes, polymethine dyes have also been increasingly adapted for use as photocages, which release biologically relevant payloads upon irradiation.[17–22] These systems utilize the strong NIR absorption and favorable excited-state properties of the polymethine core, coupling them with reactive linkers or therapeutic cargos that are cleaved upon exposure to light. By carefully tuning these properties, photocages enable precise, spatiotemporal control over biological processes, such as drug delivery, enzyme activation, and signaling modulation, all using minimally invasive NIR light.[21,23] Both fluorogenic probes and photocages rely on intricate design principles to balance photophysical performance with biological compatibility, integrating classic structure–property relationships while incorporating new considerations of reactivity and efficiency. These advances further illustrate the shift from using NIR dyes solely for passive imaging to leveraging their full potential in responsive sensing. In this chapter, we will explore the mechanisms and design principles driving the development of responsive polymethine scaffolds,

focusing on fluorogenic probes and light-activated photocages as emerging platforms for dynamic bioimaging and molecular manipulation.

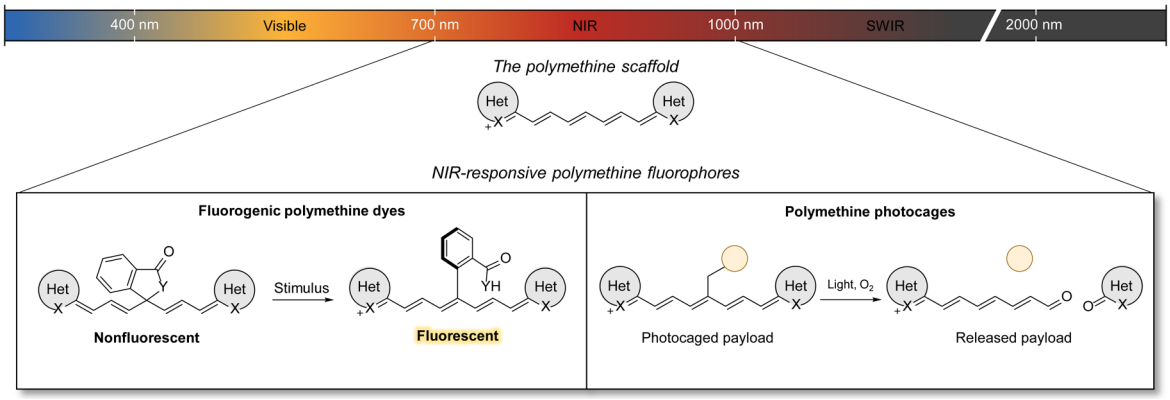

Figure 3.1. Overview of responsive NIR polymethine dyes.

3.3 Fluorogenic polymethine dyes

One of the most straightforward ways to achieve polymethine dyes with turn on fluorescence is to alter the local environment of the fluorophore. In crowded[24,25] or viscous[8,26,27] environments, there is less torsional rotation, increasing fluorescence output. Additionally, many polymethine scaffolds, especially merocyanine dyes (see Chapter 4), are sensitive environmental polarity and pH that affect fluorescence output.[28–30] Beyond tuning the local environment of the fluorophore, another common strategy to generate fluorogenic polymethine dyes involves the use of fluorescent quenchers which inhibit fluorescence through various energy transfer processes.[14,31–33] Although these approaches have been successful in converting polymethine dyes into a responsive scaffold, there is a growing push to design true fluorogenic probes wherein the fluorescence response is the result of a chemical transformation in the fluorophore itself, as seen with coumarin, xanthene and BODIPY fluorogens.[16] A notable advance in this area was the development of cyanine carbamate heptamethine dyes by Schnermann and coworkers.[16] Enzymatic cleavage of the carbamate linkage yields a pH-sensitive norcyanine fluorophore that exhibits a strong increase in fluorescence when protonated. The researchers later expanded this

methodology to include lysosome-targeting moieties, which facilitated superior fluorescence activation in cells and animals.[34]

Another strategy to generate fluorogenic polymethine dyes an involves incorporating an intramolecular cyclization mechanism similar to rhodamine fluorogens. Early studies demonstrated the feasibility of cyanine intramolecular cyclization for pH sensing.[11,35–39] However, these designs generally offered limited sensitivity, modest signal contrast, and few opportunities for spectral and environmental tuning. In response, Schnermann and coworkers introduced a class of fluorogenic heptamethine dyes featuring a nucleophilic aryl sulfamide moiety at the C4′ position.[40] By precisely modulating the electrophilicity of the polymethine chain and the nucleophilicity of pendant amides, the researchers were able to fine-tune the cyclization equilibrium between the fluorescent zwitterion and nonfluorescent lactam, affording NIR heptamethine dyes with enhanced cellular uptake and robust fluorogenic response. In particular, the researchers achieved no-wash live cell imaging using organelle-targeted HaloTag self-labeling proteins, a feat that was primarily limited to fluorogenic rhodamine dyes. Concurrent work by Rivera-Fuentes and Martin introduced an alternative strategy based on reversible addition into the indolenium heterocycle.[41] Early versions of this method showed limited turn-on responses and suffered from high background fluorescence due to unfavorable cyclization pathways.[36–38] To overcome this, the researchers adopted a more favorable 5-*exo-trig* cyclization,[42] which produced robust fluorogenic activation with minimal background signal. Additionally, because cyclization occurs at the C1 position of the heterocycle rather than the polymethine chain, they were able to develop a series of Cy3-, Cy5-, and Cy7-based fluorogens spanning the VIS-NIR regions. This spectral flexibility enabled multicolor cell imaging using a visible rhodamine-HaloTag system in tandem with the far-red Cy5-SNAPTag pair. By shifting the site of reactivity to the indolenium core and leveraging favorable cyclization geometry, this approach showcases how precise control over

reaction topology can overcome key limitations in fluorogenic probe design while maintaining the tunability of the cyanine scaffold.

These recent advances in fluorogenic polymethine dye design highlight a clear shift from passive environmental sensitivity to active, chemically driven fluorescence activation. By leveraging mechanisms such as enzymatic cleavage, pH-triggered cyclization, and targeted intramolecular reactivity, researchers have expanded the functional diversity and biological applicability of these scaffolds. Improved control over fluorescence contrast, cellular uptake and spectral range has enabled no-wash, multicolor imaging in live cells, capabilities previously limited to other dye classes. Collectively, these strategies underscore the growing potential of polymethine dyes as versatile and responsive tools for real-time biological sensing and imaging.

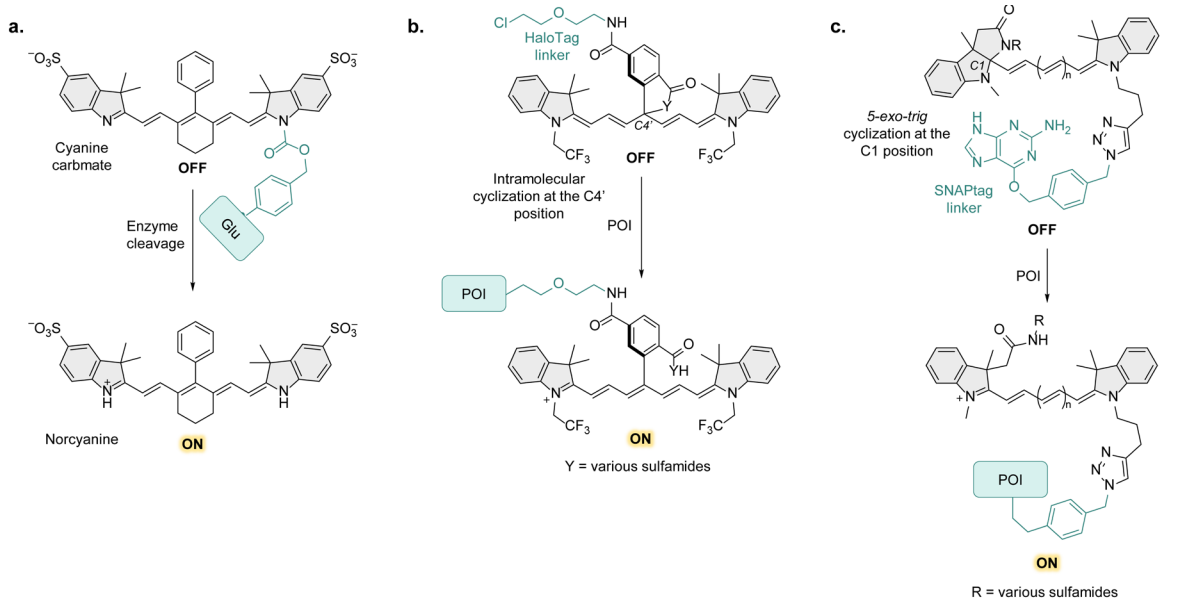

Figure 3.2. Representative fluorogenic polymethine dyes. A) Cyanine carbmate (CyBam) probes that fluoresce after enzymatic cleavage. B) HaloTag-labeled heptamethine probes that fluoresce after protein conjugation. C) SNAPtag-labeled cyanine probes that fluoresce after protein conjugation.

3.4 Polymethine photocages

While fluorogenic polymethine dyes respond to biological events through fluorescence, photocages are the opposite; they use light to induce biological events. Upon irradiation light, photocages undergo covalent bond cleavage to release payloads with precise spatiotemporal

control. In an early demonstration, Schnermann and coworkers showed that Cy7 derivatives could function as viable NIR photocages. Using a dialkylamine linker, small-molecule payloads were conjugated to the C4′ position of the polymethine chain via a carbamate linkage. Upon irradiation, photooxidative cleavage of the polymethine backbone generates two carbonyl-containing fragments. This initiates hydrolysis of the C4′–N bond, followed by intramolecular cyclization, ultimately cleaving the carbamate and releasing the payload. Although effective, this method is primarily limited to phenol-containing compounds, restricting its applicability to a broader range of biologically relevant cargos.[43] To overcome these limitations, more recent have focused on expanding both the scope of releasable functional groups and the mechanistic flexibility of the uncaging process. A notable advance came Štacko and coworkers with the development of cyanine photocages that release carboxylic acids[44] and, later, a wide array of biologically relevant functionalities including alcohols, thiols, and amines. [45] These expanded systems eliminate the need for specialized linkers and provide access to a much broader chemical space for biological applications. Newer platforms have introduced orthogonal uncaging mechanisms that enable photocage activation under oxygen-rich and oxygen-poor conditions. While traditional cyanine photocages rely on photooxidative cleavage, the incorporation of photoheterolytic pathways allows for efficient payload release even in hypoxic environments, such as the tumor microenvironment. [17,45] This oxygen-independence is a major step forward, enabling photocage function where conventional phototherapies often fail. These innovations have translated into clinical utility, where light-controlled release of FDA-approved therapeutics, such as palbociclib, was readily achieved in live cells, resulting in modulation of tumor cell proliferation pathways under NIR light. [46] This work highlights not only the biochemical specificity of polymethine photocages but also their therapeutic potential—especially in contexts where precise spatial and temporal control is critical.

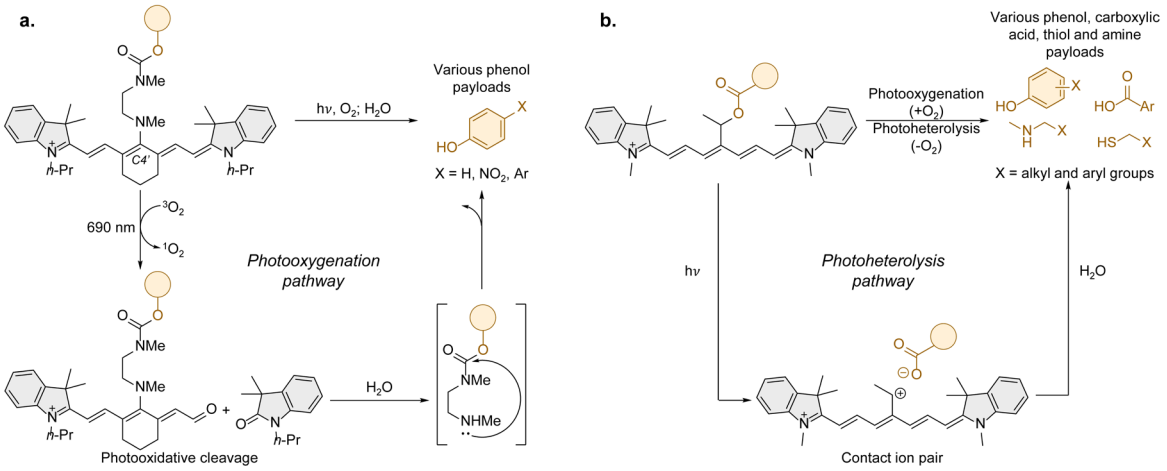

Figure 3.3. Cleavage pathways of cyanine photocages. A) Photooxidative cleavage pathway of heptamethine photocages featuring a dialkylamine linker. B) Photoheterolysis pathway of heptamethine photocages featuring payloads directly conjugated to the linker.

3.5 Conclusion

The landscape of NIR polymethine dyes has expanded significantly beyond traditional imaging, evolving into a versatile platform for responsive molecular tools. Fluorogenic polymethine dyes now offer precise, chemically triggered fluorescence activation with improved contrast, tunability, and cellular specificity, making them invaluable for live-cell and no-wash imaging. Simultaneously, polymethine photocages have opened new avenues for light-controlled molecular manipulation, enabling payload release with unprecedented control, even in challenging environments such as hypoxic tissues. Together, these innovations illustrate the growing potential of polymethine scaffolds in dynamic biological applications. As design principles continue to be developed, these systems are poised to play a central role in next-generation bioimaging and targeted therapeutic interventions.

3.6 References

(1) Ishchenko, A. A. Structure and Spectral-Luminescent Properties of Polymethine Dyes. *Russ. Chem. Rev.* **1991**, *60* (8), 865–884. https://doi.org/10.1070/RC1991v060n08ABEH001116.

(2) Tatikolov, A. S. Polymethine Dyes as Spectral-Fluorescent Probes for Biomacromolecules. *Journal of Photochemistry and Photobiology C: Photochemistry Reviews* **2012**, *13* (1), 55–90. https://doi.org/10.1016/j.jphotochemrev.2011.11.001.

(3) Bricks, J. L.; Kachkovskii, A. D.; Slominskii, Y. L.; Gerasov, A. O.; Popov, S. V. Molecular Design of near Infrared Polymethine Dyes: A Review. *Dyes and Pigments* **2015**, *121*, 238–255. https://doi.org/10.1016/j.dyepig.2015.05.016.

(4) Owens, E. A.; Henary, M.; El Fakhri, G.; Choi, H. S. Tissue-Specific Near-Infrared Fluorescence Imaging. *Acc. Chem. Res.* **2016**, *49* (9), 1731–1740. https://doi.org/10.1021/acs.accounts.6b00239.

(5) Klymchenko, A. S. Fluorescent Probes for Lipid Membranes: From the Cell Surface to Organelles. *Acc. Chem. Res.* **2023**, *56* (1), 1–12. https://doi.org/10.1021/acs.accounts.2c00586.

(6) Collot, M.; Fam, T. K.; Ashokkumar, P.; Faklaris, O.; Galli, T.; Danglot, L.; Klymchenko, A. S. Ultrabright and Fluorogenic Probes for Multicolor Imaging and Tracking of Lipid Droplets in Cells and Tissues. *J. Am. Chem. Soc.* **2018**, *140* (16), 5401–5411. https://doi.org/10.1021/jacs.7b12817.

(7) Wu, X.; Wang, X.; Li, Y.; Kong, F.; Xu, K.; Li, L.; Tang, B. A Near-Infrared Probe for Specific Imaging of Lipid Droplets in Living Cells. *Anal. Chem.* **2022**, *94* (11), 4881–4888. https://doi.org/10.1021/acs.analchem.2c00651.

(8) Chen, C.; Tian, R.; Zeng, Y.; Chu, C.; Liu, G. Activatable Fluorescence Probes for “Turn-On” and Ratiometric Biosensing and Bioimaging: From NIR-I to NIR-II. *Bioconjugate Chem.* **2020**, *31* (2), 276–292. https://doi.org/10.1021/acs.bioconjchem.9b00734.

(9) Lin, P.-H.; Clotworthy, M. R.; Dawson, J. J. M.; Fleming, C. L. Shining Light on Photo-Responsive Molecular Tools: Advances in Visible-to-NIR Activatable Photolabile Protecting Groups. *Org. Biomol. Chem.* **2025**. https://doi.org/10.1039/D5OB00542F.

(10) Welleman, I. M.; Hoorens, M. W. H.; Feringa, B. L.; Boersma, H. H.; Szymański, W. Photoresponsive Molecular Tools for Emerging Applications of Light in Medicine. *Chem. Sci.* **2020**, *11* (43), 11672–11691. https://doi.org/10.1039/D0SC04187D.

(11) Martin, A.; Rivera-Fuentes, P. Fluorogenic Polymethine Dyes by Intramolecular Cyclization. *Current Opinion in Chemical Biology* **2024**, *80*, 102444. https://doi.org/10.1016/j.cbpa.2024.102444.

(12) Abeywickrama, C. S. Large Stokes Shift Benzothiazolium Cyanine Dyes with Improved Intramolecular Charge Transfer (ICT) for Cell Imaging Applications. *Chem. Commun.* **2022**, *58* (71), 9855–9869. https://doi.org/10.1039/D2CC03880C.

(13) Moreira, B. G.; You, Y.; Owczarzy, R. Cy3 and Cy5 Dyes Attached to Oligonucleotide Terminus Stabilize DNA Duplexes: Predictive Thermodynamic Model. *Biophysical Chemistry* **2015**, *198*, 36–44. https://doi.org/10.1016/j.bpc.2015.01.001.

(14) Wu, L.; Huang, C.; Emery, B. P.; Sedgwick, A. C.; Bull, S. D.; He, X.-P.; Tian, H.; Yoon, J.; Sessler, J. L.; James, T. D. Förster Resonance Energy Transfer (FRET)-Based Small-Molecule Sensors and Imaging Agents. *Chem. Soc. Rev.* **2020**, *49* (15), 5110–5139. https://doi.org/10.1039/C9CS00318E.

(15) Ishikawa-Ankerhold, H. C.; Ankerhold, R.; Drummen, G. P. C. Advanced Fluorescence Microscopy Techniques—FRAP, FLIP, FLAP, FRET and FLIM. *Molecules* **2012**, *17* (4), 4047–4132. https://doi.org/10.3390/molecules17044047.

(16) Usama, S. M.; Inagaki, F.; Kobayashi, H.; Schnermann, M. J. Norcyanine-Carbamates Are Versatile Near-Infrared Fluorogenic Probes. *J. Am. Chem. Soc.* **2021**, *143* (15), 5674–5679. https://doi.org/10.1021/jacs.1c02112.

(17) Janeková, H.; Fisher, S.; Šolomek, T.; Štacko, P. Surfing the Limits of Cyanine Photocages One Step at a Time. *Chem. Sci.* **2025**, *16* (4), 1677–1683. https://doi.org/10.1039/D4SC07165D.

(18) Janeková, H.; Fisher, S.; Šolomek, T.; Štacko, P. Surfing the Limits of Cyanine Photocages One Step at a Time. *Chemical Science* **2025**, *16* (4), 1677–1683. https://doi.org/10.1039/D4SC07165D.

(19) Josa-Culleré, L.; Llebaria, A. In the Search for Photocages Cleavable with Visible Light: An Overview of Recent Advances and Chemical Strategies. *ChemPhotoChem* **2021**, *5* (4), 296–314. https://doi.org/10.1002/cptc.202000253.

(20) Nani, R. R.; Gorka, A. P.; Nagaya, T.; Kobayashi, H.; Schnermann, M. J. Near-IR Light-Mediated Cleavage of Antibody–Drug Conjugates Using Cyanine Photocages. *Angewandte Chemie International Edition* **2015**, *54* (46), 13635–13638. https://doi.org/10.1002/anie.201507391.

(21) Xiong, H.; Xu, Y.; Kim, B.; Rha, H.; Zhang, B.; Li, M.; Yang, G.-F.; Kim, J. S. Photo-Controllable Biochemistry: Exploiting the Photocages in Phototherapeutic Window. *Chem* **2023**, *9* (1), 29–64. https://doi.org/10.1016/j.chempr.2022.11.007.

(22) Zhang, Y.; Yan, C.; Zheng, Q.; Jia, Q.; Wang, Z.; Shi, P.; Guo, Z. Harnessing Hypoxia-Dependent Cyanine Photocages for In Vivo Precision Drug Release. *Angewandte Chemie* **2021**, *133* (17), 9639–9647. https://doi.org/10.1002/ange.202017349.

(23) Mangubat-Medina, A. E.; Ball, Z. T. Triggering Biological Processes: Methods and Applications of Photocaged Peptides and Proteins. *Chem. Soc. Rev.* **2021**, *50* (18), 10403–10421. https://doi.org/10.1039/D0CS01434F.

(24) Suss, O.; Motiei, L.; Margulies, D. Broad Applications of Thiazole Orange in Fluorescent Sensing of Biomolecules and Ions. *Molecules* **2021**, *26* (9), 2828. https://doi.org/10.3390/molecules26092828.

(25) Constantin, T. P.; Silva, G. L.; Robertson, K. L.; Hamilton, T. P.; Fague, K.; Waggoner, A. S.; Armitage, B. A. Synthesis of New Fluorogenic Cyanine Dyes and Incorporation into RNA Fluoromodules. *Org. Lett.* **2008**, *10* (8), 1561–1564. https://doi.org/10.1021/ol702920e.

(26) Bai, Y.; Huang, Y.; Wan, W.; Jin, W.; Shen, D.; Lyu, H.; Zeng, L.; Liu, Y. Derivatizing Merocyanine Dyes to Balance Their Polarity and Viscosity Sensitivities for Protein Aggregation Detection. *Chem. Commun.* **2021**, *57* (98), 13313–13316. https://doi.org/10.1039/D1CC05200D.

(27) Xiao, H.; Li, P.; Tang, B. Small Molecular Fluorescent Probes for Imaging of Viscosity in Living Biosystems. *Chemistry – A European Journal* **2021**, *27* (23), 6880–6898. https://doi.org/10.1002/chem.202004888.

(28) Mukherjee, T.; Martinez-Sanchez, R. J.; Fam, K. T.; Bou, S.; Richert, L.; Garnier, D.; Mély, Y.; Kanvah, S.; Klymchenko, A. S.; Collot, M. Near Infrared Emitting Molecular Rotor Based on Merocyanine for Probing the Viscosity of Cellular Lipid Environments. *Mater. Chem. Front.* **2021**, *5* (5), 2459–2469. https://doi.org/10.1039/D0QM00872A.

(29) Nishihara, H.; Watanabe, M.; Kawakami, R.; Murakami, M.; Seki, H.; Osaki, K.; Tsuda, T.; Imamura, T.; Hadano, S.; Watanabe, S.; Niko, Y. Pyrene-Fused Dioxaborine-Based Merocyanines with High Brightness, Photostability, and Fluorogenic Function for Deep-Skin Tissue Imaging of a Living Mouse. *Bulletin of the Chemical Society of Japan* **2024**, *97* (3), uoad027. https://doi.org/10.1093/bulcsj/uoad027.

(30) Chen, Y.; Wei, X.-R.; Sun, R.; Xu, Y.-J.; Ge, J.-J. Synthesis of Azonia Cyanine Derivatives as NIR Fluorescent Probes for Nucleic Acid Detection and Cell Imaging. *Anal. Methods* **2019**, *11* (28), 3523–3531. https://doi.org/10.1039/C9AY00982E.

(31) Xue, C.; Lei, Y.; Zhang, S.; Sha, Y. A Cyanine-Derived “Turn-on” Fluorescent Probe for Imaging Nitroreductase in Hypoxic Tumor Cells. *Anal. Methods* **2015**, *7* (24), 10125–10128. https://doi.org/10.1039/C5AY02312B.

(32) Grimm, J. B.; Xie, L.; Casler, J. C.; Patel, R.; Tkachuk, A. N.; Falco, N.; Choi, H.; Lippincott-Schwartz, J.; Brown, T. A.; Glick, B. S.; Liu, Z.; Lavis, L. D. A General Method to Improve Fluorophores Using Deuterated Auxochromes. *JACS Au* **2021**, *1* (5), 690–696. https://doi.org/10.1021/jacsau.1c00006.

(33) Kiyose, K.; Kojima, H.; Nagano, T. Functional Near-Infrared Fluorescent Probes. *Chemistry – An Asian Journal* **2008**, *3* (3), 506–515. https://doi.org/10.1002/asia.200700267.

(34) Usama, S. M.; Marker, S. C.; Caldwell, D. R.; Patel, N. L.; Feng, Y.; Kalen, J. D.; St. Croix, B.; Schnermann, M. J. Targeted Fluorogenic Cyanine Carbamates Enable In Vivo Analysis of Antibody–Drug Conjugate Linker Chemistry. *J. Am. Chem. Soc.* **2021**, *143* (51), 21667–21675. https://doi.org/10.1021/jacs.1c10482.

(35) He, L.; Lin, W.; Xu, Q.; Ren, M.; Wei, H.; Wang, J.-Y. A Simple and Effective “Capping” Approach to Readily Tune the Fluorescence of near-Infrared Cyanines. *Chem. Sci.* **2015**, *6* (8), 4530–4536. https://doi.org/10.1039/C5SC00348B.

(36) Miki, K.; Kojima, K.; Oride, K.; Harada, H.; Morinibu, A.; Ohe, K. pH-Responsive near-Infrared Fluorescent Cyanine Dyes for Molecular Imaging Based on pH Sensing. *Chem. Commun.* **2017**, *53* (55), 7792–7795. https://doi.org/10.1039/C7CC03035E.

(37) Oe, M.; Miki, K.; Mu, H.; Harada, H.; Morinibu, A.; Ohe, K. pH-Responsive Cy5 Dyes Having Nucleophilic Substituents for Molecular Imaging. *Tetrahedron Letters* **2018**, *59* (35), 3317–3321. https://doi.org/10.1016/j.tetlet.2018.07.044.

(38) Mu, H.; Miki, K.; Harada, H.; Tanaka, K.; Nogita, K.; Ohe, K. pH-Activatable Cyanine Dyes for Selective Tumor Imaging Using Near-Infrared Fluorescence and Photoacoustic Modalities. *ACS Sens.* **2021**, *6* (1), 123–129. https://doi.org/10.1021/acssensors.0c01926.

(39) Wilson, Q. D.; Sletten, E. M. Engineering Cyanine Cyclizations for New Fluorogenic Probes. *Nat. Chem.* **2024**, *16* (1), 3–5. https://doi.org/10.1038/s41557-023-01408-6.

(40) Usama, S. M.; Marker, S. C.; Li, D.-H.; Caldwell, D. R.; Stroet, M.; Patel, N. L.; Tebo, A. G.; Hernot, S.; Kalen, J. D.; Schnermann, M. Method To Diversify Cyanine Chromophore Functionality Enables Improved Biomolecule Tracking and Intracellular Imaging. *J. Am. Chem. Soc.* **2023**, *145* (27), 14647–14659. https://doi.org/10.1021/jacs.3c01765.

(41) Martin, A.; Rivera-Fuentes, P. A General Strategy to Develop Fluorogenic Polymethine Dyes for Bioimaging. *Nat. Chem.* **2024**, *16* (1), 28–35. https://doi.org/10.1038/s41557-023-01367-y.

(42) Baldwin, J. E. Rules for Ring Closure. *J. Chem. Soc., Chem. Commun.* **1976**, No. 18, 734–736. https://doi.org/10.1039/C39760000734.

(43) Gorka, A. P.; Nani, R. R.; Zhu, J.; Mackem, S.; Schnermann, M. J. A Near-IR Uncaging Strategy Based on Cyanine Photochemistry. *J. Am. Chem. Soc.* **2014**, *136* (40), 14153–14159. https://doi.org/10.1021/ja5065203.

(44) Janeková, H.; Russo, M.; Ziegler, U.; Štacko, P. Photouncaging of Carboxylic Acids from Cyanine Dyes with Near-Infrared Light**. *Angewandte Chemie International Edition* **2022**, *61* (33), e202204391. https://doi.org/10.1002/anie.202204391.

(45) Russo, M.; Janeková, H.; Meier, D.; Generali, M.; Štacko, P. Light in a Heartbeat: Bond Scission by a Single Photon above 800 Nm. *J. Am. Chem. Soc.* **2024**, *146* (12), 8417–8424. https://doi.org/10.1021/jacs.3c14197.

(46) Russo, M.; Zielinska, D.; Hanc, K.; Ramundo, A.; Meier, D.; Szabo, A.; Štacko, P. Near-Infrared-Activated Photocages Made to Order: Late-Stage Caging Protocol. *JACS Au* **2025**, *5* (6), 2632–2640. https://doi.org/10.1021/jacsau.5c00223.

CHAPTER FOUR

Exploiting Flavylium Merocyanine Dyes for Intrinsic, Multiplexed Labeling of the Endoplasmic Reticulum

Adapted from: Wilson, Q.D.; Lin, H.H.; Lin, E.Y.; Chen, L.; Sletten, E.M. "Exploiting Flavylium Merocyanine Dyes for Intrinsic, Multiplexed Labeling of the Endoplasmic Reticulum." *Anal. Chem.* **2025**, *97, 10,* 5595-5604. DOI: 10.1021/acs.analchem.4c06185.

4.1 Abstract

Merocyanine dyes are a versatile class of donor–acceptor polymethine dyes that exhibit unique properties depending on their structural makeup and surrounding environment. Scaffolds that favor the cyanine state (*i.e.*, narrow, red-shifted absorption and high fluorescence quantum yields) in biologically relevant settings are highly advantageous for multiplexed labeling experiments, but remain limited by their visible absorption. Herein, we synthesize a new class of far-red (650–700 nm) to near-infrared (NIR, 700–1000 nm) flavylium merocyanine dyes and demonstrate that, unlike conventional scaffolds, they favor the cyanine state with increasing solvent viscosity and hydrogen bond donation, rather than polarity. We leverage these advantageous properties for live cell labeling, where we observed intrinsic targeting to the endoplasmic reticulum (ER) and lipid droplets, and minimal crosstalk with commercial stains. We reveal that intrinsic ER labeling is achieved by the dipolarity in the cyanine state and lipophilicity (Clog*P*) of the merocyanine architecture, making this class of dyes a simple, red-shifted alternative to the more structurally complex ER stains currently available.

4.2 Introduction

A hallmark of optical imaging is the ease of multiplexing, which enables the simultaneous observation of distinct biological structures and processes in living cells.[1] Key to these

experiments is the selection of fluorophores with good spectral separation to minimize crosstalk. The landscape of commercial cell stains is extensive, but primarily skewed to absorption wavelengths ($\lambda_{max,abs}$) between 400 and 650 nm, increasing the likelihood of spectral overlap. Furthermore, these wavelengths are not amenable to complex biological settings (*e.g.*, organoids and whole animals) due to poor tissue penetration and high background fluorescence.[2] As such, the development of fluorophores that absorb beyond 650 nm is crucial to the optimization and translation of these technologies.

Among the different classes of small molecule fluorophores, polymethine dyes are an ideal scaffold for far-red (650–700 nm) and near-infrared (NIR, 700–1000 nm) imaging, as their structural makeup (an extendable polymethine chain flanked by two end groups) permits easy access to these advantageous wavelengths.[3-9] The most ubiquitous polymethine scaffolds for cell labeling are cationic dyes (*e.g.*, Cy5 and its derivatives), which feature a positive charge distributed between two electron-donating end groups.[10] In low polarity solvents, the "cyanine" ground state is favored, where the positive charge is fully delocalized across the entire molecule, and there is minimal bond-length alternation (BLA) in the polymethine chain (Figure 4.1A).[11-13] This results in a red-shifted absorption band with a small full-width half-maximum (FWHM) and good fluorescence quantum yield (ϕ_F).[14,15] These properties are highly advantageous for multiplexed imaging, but harder to achieve in biological settings due to H-aggregation and ground state desymmetrization.[16-19] Most cationic dyes are insoluble in biological media, forming broad, blue-shifted H-aggregates that are nonemissive.[16-20] Even when soluble, aqueous environments preferentially stabilize the asymmetric "polyene" ground state, where the charge is localized on either end group and there is considerable BLA in the polymethine chain.[21-23] As a result, cationic polymethine dyes often exhibit broad, blue-shifted absorption bands and diminished ϕ_F in biological settings. Many clever strategies have emerged to alleviate this problem, but require

additional functionalization steps and/or formulations that could affect cell labeling properties.[13,17-25]

To avoid these limitations, we are interested in exploring the neutral merocyanine scaffold. Like cationic polymethine dyes, merocyanine dyes also exist between a polyene and cyanine ground state (Figure 4.1A).[12-14] However, because they contain one electron-donating and one electron-accepting end group, merocyanine dyes exhibit two distinct polyene states that heavily depend on the strength of the donor–acceptor pair and solvent polarity.[26-31] We believe that merocyanine dyes between the nonpolar polyene (A1) and cyanine (A2) ground states have remarkable potential for biological imaging, as they exhibit increasing cyanine character with increasing environmental polarity.[32-37] Additionally, the inherent dipolarity of merocyanine dyes may impart unique cell localization properties from cationic dyes that are advantageous for cell labeling. Unfortunately, existing merocyanine scaffolds between the A1─A2 ground states (*e.g.*, dyes with indolenium and benzo[*cd*]indolium donors, Figure 4.1B) all absorb below 650 nm, stifling their capacity for multiplexing with commercial stains. Therefore, the goal of this work was to design a new class of red-shifted merocyanine dyes that favor the cyanine state under biologically relevant conditions, and examine their utility for cell labeling.

Toward this end, we selected the dimethylamino-substituted flavylium heterocycle as the donor end group, based on our previous success with red-shifted cationic polymethine dyes.[38.39] Furthermore, we hypothesized that its weak electron-donating properties would favor the desired A1─A2 ground states, leading to enhanced properties in biological conditions. Herein, we report a new class of flavylium merocyanine dyes that exist between the A1─A2 ground states, with absorption near or above 650 nm (Figure 4.1B). We evaluate their electronic ground states across a range of solvents to demonstrate that these dyes favor the cyanine state with increasing solvent viscosity and hydrogen bond donation, rather than polarity, which is canonically thought to determine the ground states of merocyanine dyes. We also examine their fluorescent properties

to reveal that the ϕ_F of flavylium merocyanine dyes increases with both solvent polarity and viscosity, making them well-suited for biological investigations. Finally, we exploit these properties for live cell multiplexed labeling experiments, observing excellent localization in the endoplasmic reticulum (ER) and lipid droplets, and negligible crosstalk with commercial stains for the nucleus, cell membrane, lysosomes and mitochondria (Figure 4.1C). We attribute the intrinsic ER labeling to the dipolarity and lipophilicity (Clog*P*) of the merocyanine architecture, substantially expanding the utility of this scaffold for cell imaging.

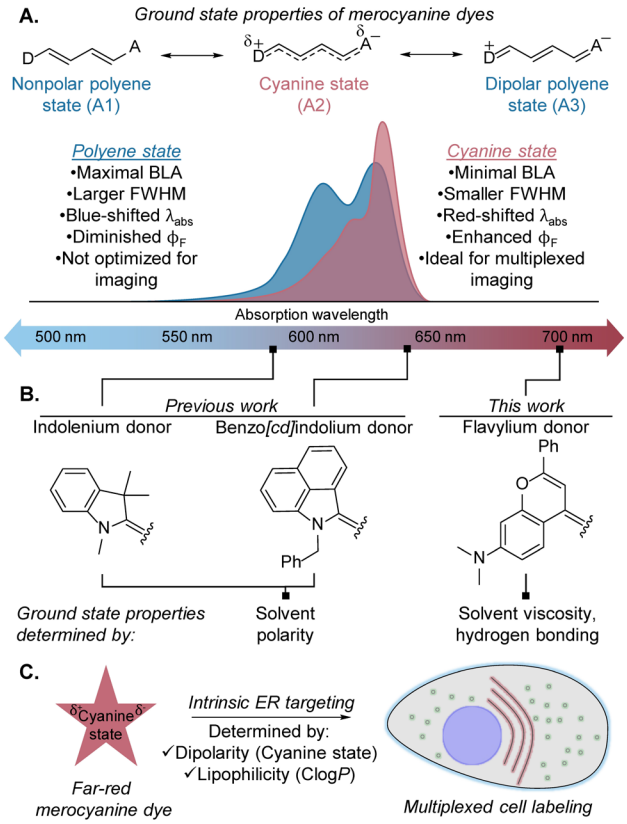

Figure 4.1. A) Characteristics of merocyanine ground states, including bond-length alternation (BLA), full-width half maximum (FWHM), absorption wavelength (λ_{abs}) and fluorescence quantum yield (ϕ_F) properties. B) Absorption wavelengths and ground state properties of merocyanine dyes with different donors and the same acceptor. C) Requirements for intrinsic labeling of the endoplasmic reticulum of merocyanine dyes developed in this work.

4.3 Results and Discussion

4.3.1 Design and Synthesis

We approached the design of red-shifted merocyanine dyes with the impression that the flavylium heterocycle (**4.1**) is a weak electron donor that would lie between the A1─A2 ground states with a well-matched acceptor (Scheme 4.1A). We selected malononitrile (**4.2**), 1,3-indandione (**4.3**) and *N*,*N*-1,3-dimethyl barbituric acid (**4.4**) as respectively weak, moderate and strong electron acceptors due to their commercial availability and prevalence in other merocyanine scaffolds (Scheme 4.1A).[26,40,41] Furthermore, we selected the tetramethine length, containing four methine units, for a balance of synthetic ease and red-shifted absorption. Synthesizing merocyanine dyes typically begins with the generation of an activated donor or acceptor hemicyanine dye that can undergo Knoevenagel condensation with a respective acceptor or donor group.[28] We envisioned that a donor hemicyanine dye based on **4.1** would be the most efficient way to access a panel of flavylium merocyanine dyes with varied acceptors (Scheme 4.1B). Refluxing **4.1** with malonaldehyde bis(phenylimine) (**4.5**) in a mixture of acetic acid and acetic anhydride readily afforded the desired donor hemicyanine dye **4.6** in 59% yield. Condensation of **4.6** with acceptor **4.2** occurred rapidly in the presence of base and heated acetic anhydride, generating the first merocyanine dye, named **MalonoFlav4**, in 70% yield. When we extended this procedure to acceptor **4.3**, a number of side products were observed, making the purification difficult. Instead, we decided to pursue acceptor hemicyanine dye **4.7**, which was synthesized by heating **4.3** with malonaldehyde linker **4.5** in acetic anhydride. Treatment of **4.7** with **4.1** in the presence of base and *n*-butanol afforded the second merocyanine dye, **IndaFlav4**, in 85% yield. We extended this methodology to barbituric acid acceptor **4.4** to generate hemicyanine dye **8**, which readily afforded the final merocyanine dye, **BarbiFlav4**, in 72% yield. We could also access **BarbiFlav4** from donor hemicyanine dye **4.6** (see experimental procedures), demonstrating the versatility of merocyanine synthesis.

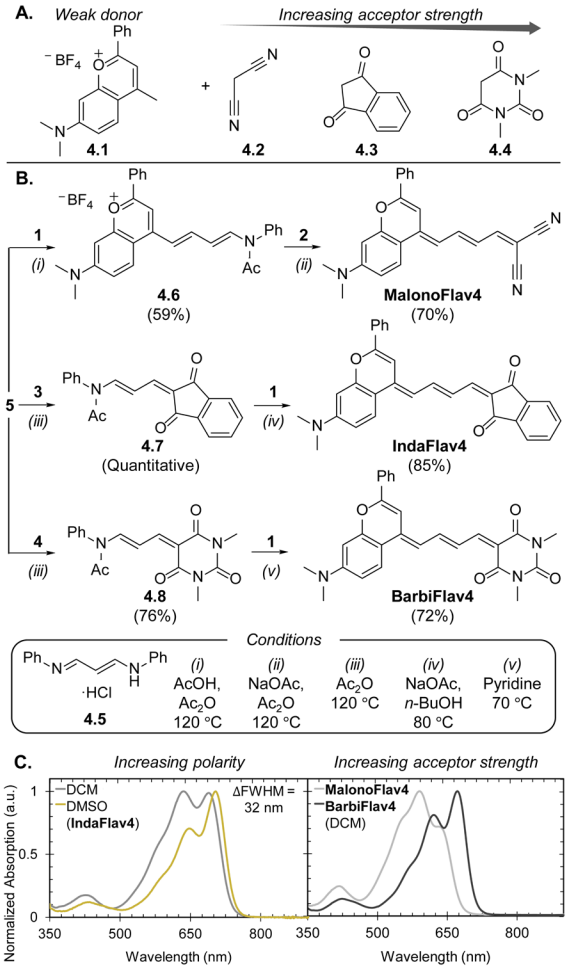

Scheme 4.1. A, B) Design and synthesis of flavylium merocyanine dyes developed in this work. C) Normalized absorption spectra showing the ground state properties of flavylium merocyanine dyes with increasing polarity (**IndaFlav4,** 12 μM, in DCM vs. DMSO) and increasing acceptor strength (**MalonoFlav4**, 5.0 μM, vs. **BarbiFlav4**, 12 μM, in DCM).

With access to a panel of flavylium merocyanine dyes, we conducted a preliminary assessment of our design approach by evaluating the ground state properties of each dye in less polar dichloromethane (DCM) and more polar dimethyl sulfoxide (DMSO) (Scheme 4.1C and Figure 4.2A). Based on the large difference in their dielectric constants (ϵ_R = 9.08 vs 46.02) (Table 4.1), we expected to see stronger cyanine character in DMSO if the dyes exist between the A1─A2 states. For all three dyes, we observed a decrease in the FWHM (11–32 nm) and an increase in the red-shifted cyanine shoulder in DMSO, suggesting that they exist between the desired A1─A2 states.

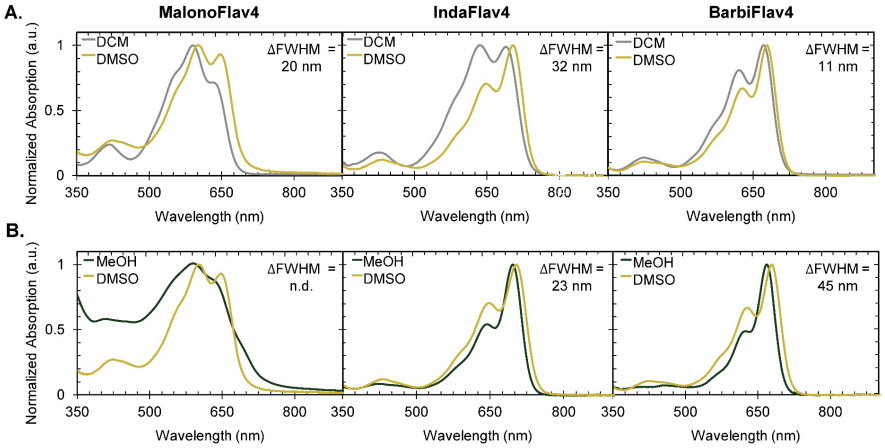

Figure 4.2. A, B) Normalized absorption spectra and change in full-width half-maximum (ΔFWHM) of **MalonoFlav4** (5.0 μM), **IndaFlav4** (12 μM) and **BarbiFlav4** (12 μM) in DCM vs. DMSO and MeOH vs. DMSO.

Table 4.1. Solvent parameters considered in this work.[43]

Solvent	Dielectric Constant (ϵ_R)	Viscosity (cP)	Hydrogen Bond Donor
DCM	9.08 [43a]	0.43 [43f]	No
1-Octanol	10.34 [43a]	7.36 [43g]	Yes
MeOH	32.63 [43a]	0.545 [43g]	Yes
MeCN	37.5 [43a]	0.34 [43h]	No
DMF	37.5 [43b]	0.92 [43i]	No
DMSO	46.02 [43c]	1.99 [43j]	No
25% Water/MeCN	56.92 [43d]	0.92 [43h]	Yes
25% Water/DMSO	64.67 [43e]	3.68 [43j]	Yes

To verify that these results are not due to differences in solubility/H-aggregation, we collected absorption spectra in each solvent over a range of concentrations, and observed no spectral changes upon normalization (Figure 4.3A). Furthermore, we collected excitation spectra

at the higher end of these concentrations (Figure 4.3B). In each case, the excitation spectra resemble their corresponding absorption spectra, supporting that the differences between DCM and DMSO reflect changes in the ground state, not aggregation.

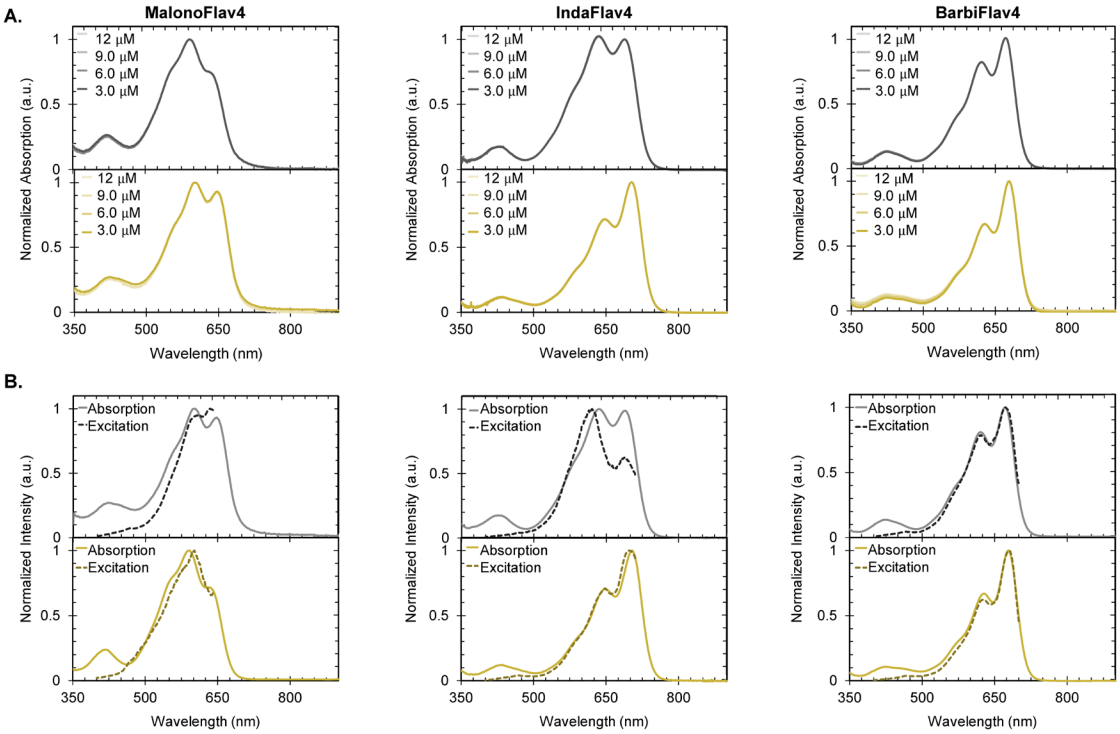

Figure 4.3. A) Concentration-varied (3.0-12 μM) normalized absorption spectra of **MalonoFlav4**, **IndaFlav4** and **BarbiFlav4** in DCM (top) and DMSO (bottom). B) Normalized absorption (solid line) and excitation (dashed line) spectra of **MalonoFlav4** (ex. 400-640 nm; collect 660 nm), **IndaFlav4** (ex. 400-720 nm; collect 720 nm) and **BarbiFlav4** (ex. 400-710 nm; collect 710 nm) in DCM (top) and DMSO (bottom). The concentration of **MalonoFlav4** is 12 μM in DCM and 12 μM in DMSO, **IndaFlav4** is 28 μM in DCM and 18 μM in DMSO and **BarbiFlav4** is 19 μM in DCM and 8.3 μM in DMSO.

In addition to solvent polarity, there is also a noticeable correlation between cyanine character and acceptor strength (Scheme 4.1C), with **MalonoFlav4** favoring the polyene state and **BarbiFlav4** favoring the cyanine state. Beyond their ground state properties, all three merocyanine dyes possess remarkably red-shifted absorption (*ca*. 50–100 nm) compared to indolenium and benzo[*cd*]indolium tetramethine dyes with the same acceptors (Scheme 4.2). We were especially delighted to see that **IndaFlav4** and**BarbiFlav4** absorb well above 650 nm, with **IndaFlav4** reaching the NIR region in DMSO. Overall, these results substantiate our hypothesis

that the flavylium heterocycle is a weak electron donor capable of generating red-shifted merocyanine dyes that appear to favor the cyanine state with increasing solvent polarity.

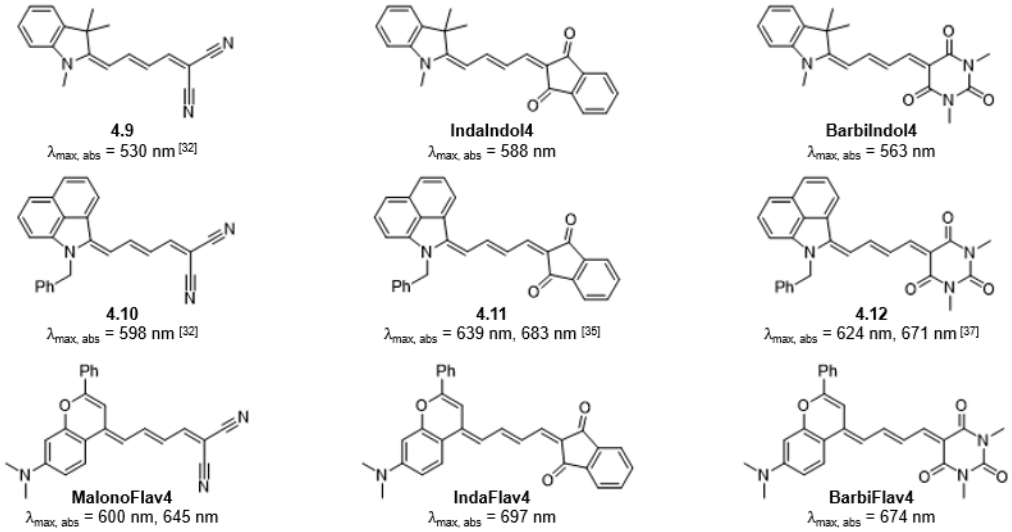

Scheme 4.2. Chemical structures and $\lambda_{max,\ abs}$ of previously synthesized indolenium and benzo[*cd*]indolium merocyanine dyes with chain lengths and acceptors reported in this work. Absorption wavelengths are reported in DMF to allow for consistency between scaffolds.

4.3.2 Ground State Properties

Having performed a cursory assessment in DCM and DMSO, we proceeded to evaluate the ground states of these flavylium merocyanine dyes in methanol (MeOH) to gage how they perform in polar protic conditions (Figure 4.2B). We were unable to fully solubilize **MalonoFlav4** in MeOH, resulting in strong H-aggregation. Although the solubility improved in ethanol, we ultimately decided not to proceed with **MalonoFlav4** due to its limited solubility and weak emission across various solvents (Figure 4.4).

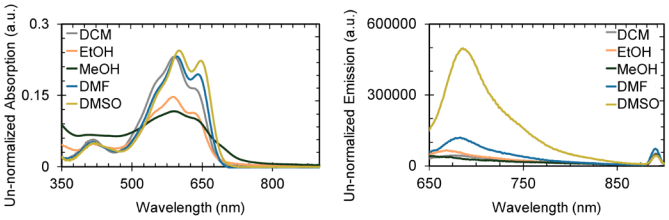

Figure 4.4. Un-normalized absorption and emission spectra (ex. 590 nm, collect 620-900 nm) of **MalonoFlav4** (5.0 μM) in various solvents.

In the case of **IndaFlav4** and **BarbiFlav4**, we were surprised to see that both dyes exhibit smaller FWHM in MeOH than DMSO, despite MeOH being a less polar solvent (ϵ_R = 32.63 vs 46.02) (Table 4.1). This prompted us to explore if other parameters (*e.g.*, hydrogen bond donation and viscosity) also play a role. These parameters are known to affect the ϕ_F of merocyanine dyes, but not necessarily by modulating their electronic ground states.[42, 44-47] Therefore, we conducted a systematic investigation of the photophysical (Figure 4.5 and 4.6) and spectral properties (Figure 4.7) of **IndaFlav4** and **BarbiFlav4** in protic and aprotic solvents across a range of polarities (ϵ_R = 9.08–64.67) and viscosities (η = 0.43–7.36 cP) (Table 4.1).

A.

Solvent	$\lambda_{max,\ abs}$ (nm)	FWHM (nm)	ϵ (M^{-1} cm^{-1})	$\lambda_{max,\ em}$ (nm)	ϕ_F (%)	$\epsilon \times \phi_F$ (M^{-1} cm^{-1})
DCM (*a*)	636, 689	145	31300 ± 200	737	1.8 ± 0.1	560 ± 30
1-Octanol (*b*)	701	105	44500 ± 400	723	10 ± 0.5	4500 ± 300
MeOH (*c*)	696	84	63000 ± 2000	732	4.9 ± 0.2	3100 ± 200
MeCN (*d*)	687	141	49000 ± 1000	720	3.3 ± 0.3	1600 ± 200
DMF (*e*)	697	122	37000 ± 500	738	5.7 ± 0.3	2100 ± 100
DMSO (*f*)	704	107	43000 ± 1000	731	16 ± 1	6900 ± 600
25% Water/MeCN (*g*)	697	89	37000 ± 1000	723	6.2 ± 0.4	2300 ± 200
25% Water/DMSO (*h*)	707	51	82000 ± 4000	731	15 ± 0.6	12000 ± 1000

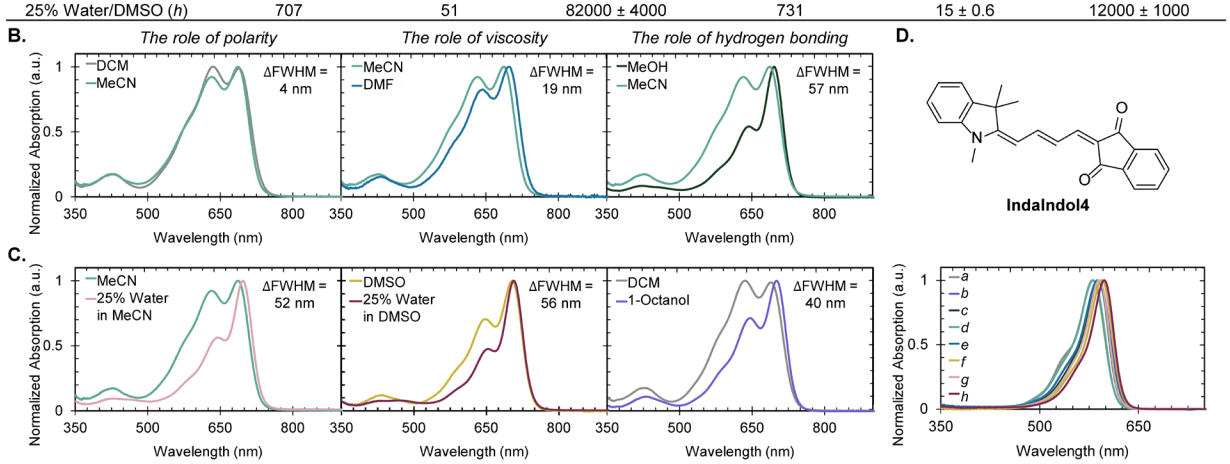

Figure 4.5. A) Photophysical properties of **IndaFlav4** in various solvents. Normalized absorption spectra showing the change in full-width half-maximum (ΔFWHM) of **IndaFlav4** (12 μM) with B) polarity (DCM vs. MeCN), viscosity (MeCN vs. DMF) and hydrogen bond donation (MeOH vs. MeCN) and C) solvent conditions with contributions from viscosity and hydrogen bond donation (MeCN vs. 25% water/MeCN, DMSO vs. 25% water/DMSO and DCM vs. 1-octanol). D) Structure and normalized absorption spectra of **IndaIndol4** (3.0 μM) in various solvents.

A. Solvent	$\lambda_{max,\ abs}$ (nm)	FWHM (nm)	ϵ (M^{-1} cm^{-1})	$\lambda_{max,\ em}$ (nm)	ϕ_F (%)	$\epsilon \times \phi_F$ (M^{-1} cm^{-1})
DCM (*a*)	672	105	47900 ± 200	715	2.1 ± 0.2	1000 ± 100
1-Octanol (*b*)	676	81	41000 ± 2000	695	17 ± 0.7	7000 ± 600
MeOH (*c*)	668	49	29000 ± 1000	690	3.1 ± 0.3	900 ± 100
MeCN (*d*)	665	112	66000 ± 1000	700	4 ± 0.6	2600 ± 400
DMF (*e*)	674	102	77800 ± 300	699	2.6 ± 0.1	2020 ± 90
DMSO (*f*)	677	94	77500 ± 600	706	5 ± 0.6	3900 ± 500
25% Water/MeCN (*g*)	669	69	67000 ± 1000	696	12 ± 2	8000 ± 1000
25% Water/DMSO (*h*)	679	50	65000 ± 1000	704	18.8 ± 0.8	12000 ± 1000

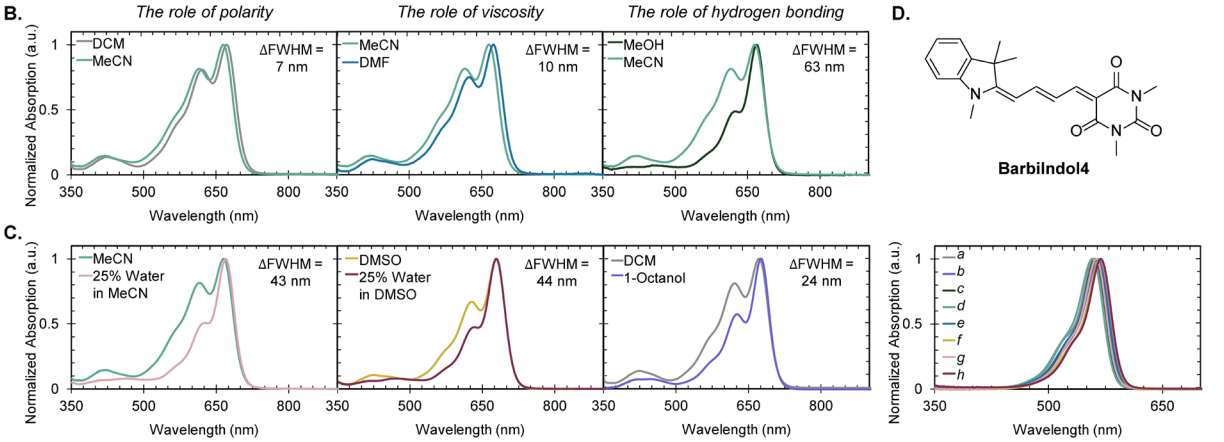

Figure 4.6. A) Photophysical properties of **BarbiFlav4** in various solvents. B, C) Normalized absorption spectra showing the changes in full-width half-maximum (ΔFWHM) of **BarbiFlav4** (12 μM) with polarity (DCM vs. MeCN), viscosity (MeCN vs. DMF) and hydrogen bond donation (MeOH vs. MeCN), and solvent contributions from viscosity and hydrogen bond donation (MeCN vs. 25% water/MeCN, DMSO vs. 25% water/DMSO and DCM vs. 1-octanol). D) Structure and normalized absorption spectra of **BarbiIndol4** (4.0 μM) in various solvents.

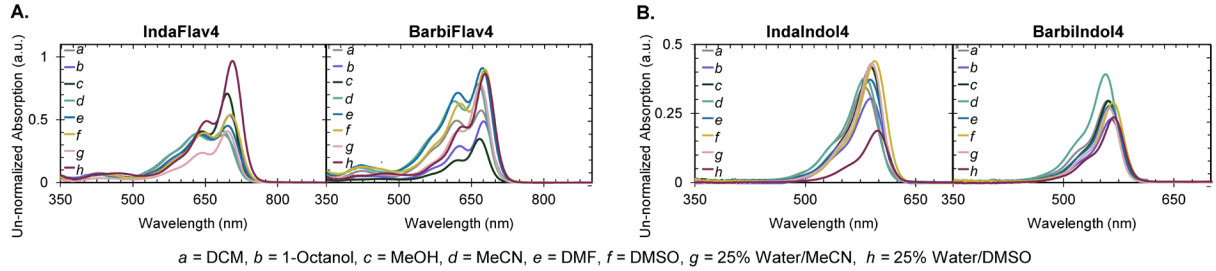

a = DCM, *b* = 1-Octanol, *c* = MeOH, *d* = MeCN, *e* = DMF, *f* = DMSO, *g* = 25% Water/MeCN, *h* = 25% Water/DMSO

Figure 4.7. A, B) Un-normalized absorption spectra of flavylium merocyanine dyes, **IndaFlav4** (12 μM) and **BarbiFlav4** (12 μM), and indolenium merocyanine dyes, **IndaIndol4** (3.0 μM) and **BarbiIndol4** (4.0 μM), in various solvents.

We began our investigation into the ground state sensitivity of **IndaFlav4** (Figure 4.5B) and **BarbiFlav4** (Figure 4.6B) with solvent polarity. To minimize the influence of hydrogen bond donation and viscosity, we selected DCM and acetonitrile (MeCN) as aprotic solvents with similar viscosities (η = 0.43 cP vs 0.34 cP), but different dielectric constants (ϵ_R = 9.08 vs 37.50). In the case of both **IndaFlav4** and **BarbiFlav4**, we observed minimal changes in their absorption spectra ($\Delta FWHM_{\textbf{IndaFlav4}}$ = 4 nm), suggesting that solvent polarity has a small impact on their ground states. Next, we determined the effects of viscosity using MeCN and *N*,*N*-dimethylformamide (DMF) as aprotic solvents with the same dielectric constant (ϵ_R = 37.50), but different viscosity values (η = 0.34 cP vs 0.92 cP). Both **IndaFlav4** and **BarbiFlav4** exhibit increasing cyanine character with increasing solvent viscosity ($\Delta FWHM_{\textbf{IndaFlav4}}$ = 19 nm). We observed a similar trend using the traditional glycerol titrations in MeOH[42,44-46] ($\Delta FWHM_{\textbf{IndaFlav4}}$ = 38 nm from 0 to 75% glycerol) (Figure 4.8), further supporting our hypothesis that viscosity is an influential parameter on the ground states of flavylium merocyanine dyes. Finally, to elucidate the role of hydrogen bonding, we selected MeOH and MeCN because they have similar dielectric constants (ϵ_R = 32.63 vs 37.50) and viscosity values (η = 0.55 cP vs 0.34 cP), but different hydrogen bonding abilities. In the case of both **IndaFlav4** and **BarbiFlav4**, we observed substantial increases in cyanine character ($\Delta FWHM_{\textbf{IndaFlav4}}$ = 57 nm), suggesting that hydrogen bond donation plays a very important role in stabilizing the cyanine ground state.

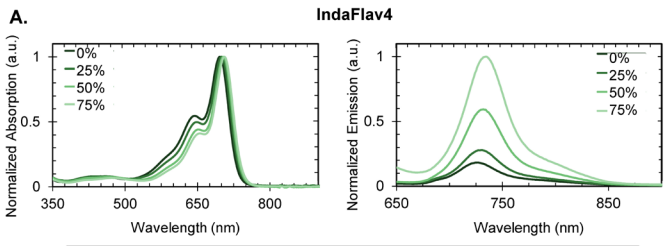

%Glycerol in MeOH	$\lambda_{max, abs}$ (nm)	FWHM (nm)	$\lambda_{max, em}$ (nm)
0%	696	84	727
25%	700	53	730
50%	703	48	732
75%	706	46	734

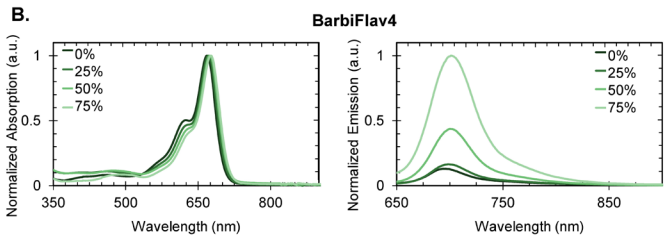

%Glycerol in MeOH	$\lambda_{max, abs}$ (nm)	FWHM (nm)	$\lambda_{max, em}$ (nm)
0%	668	49	696
25%	671	49	699
50%	674	49	700
75%	676	49	701

Figure 4.8. A, B) Normalized absorption spectra, emission (ex. 620 nm; collect 650-900 nm) spectra and photophysical properties of **IndaFlav4** (6.1 μM) and **BarbiFlav4** (6.1 μM) in varying percentages (0-75%) of glycerol/MeOH solutions.

Since **IndaFlav4** and **BarbiFlav4** are sensitive to both viscosity and hydrogen bonding, we hypothesized that they would exhibit even stronger cyanine character in solvents with high degrees of both properties (Figure 4.5C and 4.6C). To test this hypothesis, we prepared aqueous mixtures of 25% water/MeCN and 25% water/DMSO, which have higher viscosities (η = 0.92 cP and 3.68 cP) than MeCN and DMSO alone, and are able to act as hydrogen bond donors. Going from pure MeCN to a 25% water/MeCN, we observed a remarkable increase in cyanine character for both **IndaFlav4** ($\Delta FWHM_{\textbf{IndaFlav4}}$ = 52 nm) and **BarbiFlav4**, with FWHM values on par to those in MeOH. This increase is even stronger going from pure DMSO to 25% water/DMSO ($\Delta FWHM_{\textbf{IndaFlav4}}$ = 56 nm), with each dye exhibiting the smallest FWHM of all eight solvents in these conditions. These results are especially gratifying in the context of biological investigations, as the presence of water is capable of inducing dramatic shifts toward the cyanine state. However,

there are also many hydrophobic compartments within a biological setting (*e.g.*, organelle membranes, lipid droplets and protein cavities) where interactions with water are minimal. With this in mind, we examined the ground state properties of each dye in 1-octanol, a cell membrane mimic with low polarity (ϵ_R = 10.34), high viscosity (η = 7.36 cP), and the ability to hydrogen bond donate. On the basis of polarity, we would expect each dye to favor the polyene state, with absorption profiles similar to DCM. Instead, **IndaFlav4** and **BarbiFlav4** exhibit more cyanine character ($\Delta FWHM_{IndaFlav4}$ = 40 nm) which we attribute to contributions from viscosity and hydrogen bond donation. Although aqueous environments aid in favoring the cyanine state, these results demonstrate that hydrophobic environments with high viscosity and hydrogen bond donation can also favor the cyanine state of flavylium merocyanine dyes, increasing their utility across a range of biological settings.

Because we observed similar ground state properties for **IndaFlav4** and **BarbiFlav4**, we reasoned that the architecture of the flavylium donor (as opposed to the acceptor groups) is responsible for the pronounced solvent sensitivity. Based on previous work with cationic flavylium polymethine dyes,[48] we expect the decreased rotation of the phenyl substituent to increase the planarity of the fluorophore, leading to more efficient charge transfer and increased electron delocalization in viscous solvents. It remains unclear why there is increased cyanine character in protic solvents, but hydrogen bond donation presumably occurs with the acceptor end of the fluorophore, making this interaction applicable to other merocyanine dyes. To probe the contributions from the flavylium heterocycle, we prepared the previously reported indolenium analogs of each dye, which we named **IndaIndol4** (Figure 4.5D) and **BarbiIndol4** (Figure 4.6D). We expected the indolenium analogs to show less sensitivity to changes in viscosity because they do not contain the pendant aryl ring, but similar changes to hydrogen bonding, as that interaction is dependent on the acceptor. Surprisingly, both analogs exhibit minimal ground state changes across all eight solvents (Table 4.2 and 4.3), with the largest ΔFWHM totaling only 10 nm for

IndaIndol4. We attribute this to the fact that both dyes are very close to the cyanine state (indicated by their exceptionally narrow absorption spectra), making them less sensitive to solvent changes in general.[46] That being said, **IndaIndol4** exhibits slightly broader absorption in 1-octanol compared to other solvents, which is consistent with our hypothesis that contributions from solvent viscosity are less important for the indolenium scaffold. Additionally, the FWHM is smaller in solvents where strong hydrogen bond donation is possible, suggesting that this interaction is applicable to other merocyanine scaffolds. Overall, these data indicate that ground state sensitivity toward solvent viscosity is imparted by the structural makeup of the flavylium heterocycle.

Table 4.2. Photophysical properties of **IndaIndol4** in various solvents. Error represents the standard deviation.

Solvent	$\lambda_{max, abs}$ (nm)	FWHM (nm)	ϵ (M^{-1} cm^{-1})	$\lambda_{max, em}$ (nm)	ϕ_F (%)	$\epsilon \times \phi_F$ (M^{-1} cm^{-1})
DCM	580	49	123000 ± 5000	617	6.4 ± 0.5	8000 ± 1000
1-Octanol	589	50	92000 ± 5000	613	9.9 ± 0.9	9000 ± 1000
MeOH	589	51	133100 ± 500	613	0.54 ± 0.05	720 ± 70
MeCN	581	45	125000 ± 3000	612	7.1 ± 0.8	9000 ± 1000
DMF	588	48	129000 ± 3000	618	13 ± 1	17000 ± 2000
DMSO	594	43	152000 ± 5000	621	18 ± 2	27000 ± 4000
25% Water in MeCN	590	43	134000 ± 2000	613	0.9 ± 0.09	1200 ± 200
25% Water in DMSO	598	41	63000 ± 2000	621	7.7 ± 0.6	4900 ± 500

Table 4.3. Photophysical properties of **BarbiIndol4** in various solvents. Error represents the standard deviation.

Solvent	$\lambda_{max, abs}$ (nm)	FWHM (nm)	ϵ (M^{-1} cm^{-1})	$\lambda_{max, em}$ (nm)	ϕ_F (%)	$\epsilon \times \phi_F$ (M^{-1} cm^{-1})
DCM	560	42	79200 ± 800	589	3.3 ± 0.5	2600 ± 400
1-Octanol	565	42	59000 ± 2000	591	50 ± 5	30000 ± 3000
MeOH	561	39	74500 ± 400	587	5.1 ± 0.7	3800 ± 500
MeCN	557	42	72800 ± 500	585	5.3 ± 0.5	3900 ± 400
DMF	563	42	78000 ± 1000	592	6.8 ± 0.6	5300 ± 500
DMSO	567	39	77000 ± 4000	593	22 ± 3	17000 ± 2000
25% Water in MeCN	562	38	90000 ± 2000	587	4.7 ± 0.6	4200 ± 600
25% Water in DMSO	569	38	59000 ± 1000	593	11 ± 1	6500 ± 700

4.3.3 Fluorescent Properties

After investigating their ground state properties, we then measured the fluorescence and ϕ_F of **IndaFlav4** (Figure 4.9A) and **BarbiFlav4** (Figure 4.10A) across all eight solvents. In the case of **IndaFlav4**, we were delighted to see NIR fluorescence spanning 720–738 nm and ϕ_F up to 16% depending on the solvent. The emission for **BarbiFlav4** is *ca*. 30 nm blue-shifted (690–715 nm), but still reaches the NIR region in certain solvents, with ϕ_F up to 18.8%. Considering the ground state sensitivity of flavylium merocyanine dyes, we were interested to see if there are any solvent parameters that affect their ϕ_F. Scaffolds between the A1─A2 ground states typically exhibit higher ϕ_F with increasing solvent polarity because they are approaching the more-emissive cyanine state. It has also been demonstrated that high solvent polarity minimizes the competing pathway of photoisomerization, leading to higher ϕ_F in these conditions.[49] In the case of **IndaFlav4** and **BarbiFlav4**, we noticed a general increase in ϕ_F with increasing solvent polarity, but their relatively high ϕ_F in 1-octanol led us to consider viscosity as another important solvent parameter. Polymethine dyes typically show enhanced ϕ_F in viscous solvents due to the suppression of molecular rotation and photoisomerization, potentially explaining why both dyes have high ϕ_F in 1-octanol, despite its low polarity.[50,51] Contributions from both solvent parameters can be analyzed on a three-dimensional bar graph that shows ϕ_F with respect to the increasing polarity and viscosity (Figure 4.9B and 4.10B). For both **IndaFlav4** and **BarbiFlav4**, there is a pronounced ϕ_F enhancement with increasing polarity and viscosity, suggesting that the additive effect of each parameter is important for suppressing alternative pathways of nonradiative decay.

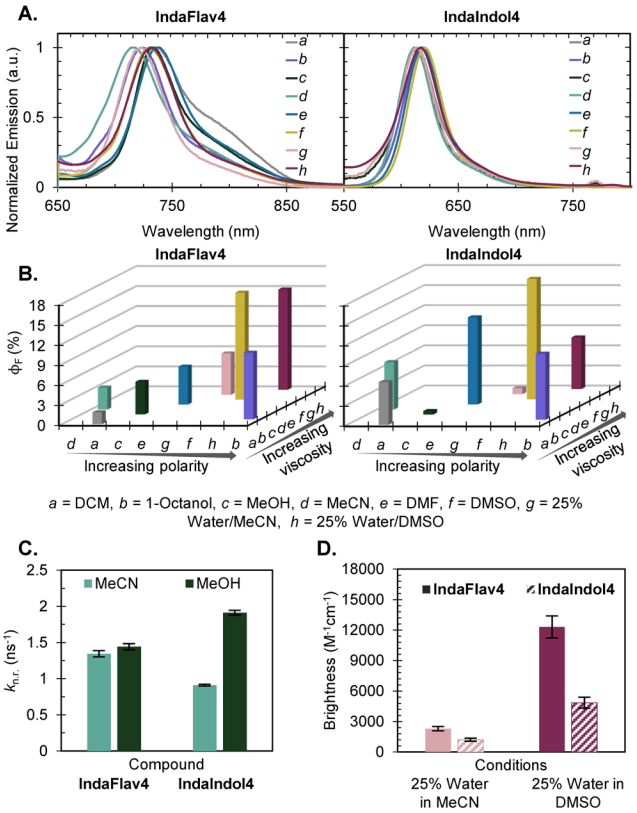

Figure 4.9. A) Normalized fluorescence spectra of **IndaFlav4** (12 μM, ex. 620 nm; collect 650-900 nm) and **IndaIndol4** (3.0 μM, ex. 510 nm; collect 550-900 nm) in various solvents. B) Three-dimensional bar graphs of the ϕ_F for **IndaFlav4** and **IndaIndol4** with increasing solvent viscosity and polarity. C) Bar graph of the calculated rates of nonradiative decay ($k_{n.r.}$) for **IndaFlav4** and **IndaIndol4** in MeCN and MeOH. Error bars represent the standard deviation of three replicates. D) Bar graphs of the calculated brightness ($\epsilon \times \phi_F$) for **IndaFlav4** and **IndaIndol4** in various solvents. Error bars represent the propagated error of ϵ and ϕ_F.

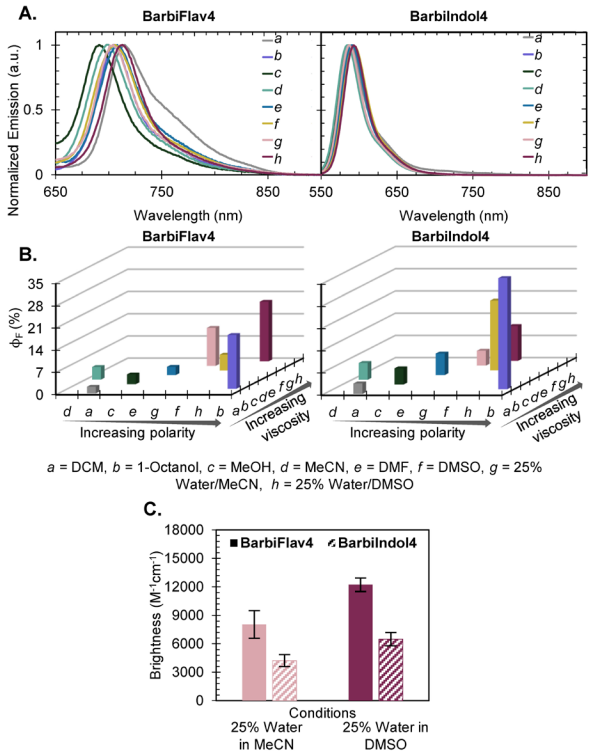

Figure 4.10. A) Normalized emission spectra of **BarbiFlav4** (12 μM, ex. 620 nm; collect 650-900 nm) and **BarbiIndol4** (4.0 μM, ex. 510 nm; collect 550-900 nm) in various solvents. B) Three-dimensional bar graphs of the ϕ_F for **BarbiFlav4** and **BarbiIndol4** with increasing solvent viscosity and polarity. C) Bar graphs of the calculated brightness ($\epsilon \times \phi_F$) for **BarbiFlav4** and **BarbiIndol4** in various solvents. Error bars represent the propagated error of ϵ and ϕ_F.

To determine if this behavior is unique to the flavylium scaffold, we investigated the emission and ϕ_F of the indolenium merocyanine dyes across all eight solvents. As expected, both dyes display blue-shifted emission spanning 612–621 nm for **IndaIndol4** (Figure 4.9A) and 585–593 nm for **BarbiIndol4** (Figure 4.10A). Furthermore, their ϕ_F values are generally higher ($\phi_F \leq$ 18% for **IndaIndol4** and ≤50% for **BarbiIndol4**) than the flavylium merocyanine dyes, likely due to the absence of the pendant aryl ring. Interestingly, the indolenium analogs show a stronger relationship between ϕ_F and solvent viscosity than polarity (Figure 4.9B and 4.10B). Again, the indolenium heterocycle does not have the pendant aryl ring, so molecular rotation should be less of a competing pathway for nonradiative decay. Instead, these results may derive from the propensity for indolenium polymethine dyes to undergo photoisomerization, which gets suppressed in viscous solvents like 1-octanol.[46,49]

Another notable comparison between the flavylium scaffold and the indolenium scaffold is their sensitivity to protic solvents, particularly in the case of the 1,3-indandione analogs. Quenched fluorescence in protic solvents has been reported for this class of acceptors, caused by hydrogen bond-induced stabilization of the charge-transfer excited state, which then rapidly relaxes via nonradiative decay.[52-54] Consequently, **IndaIndol4** is essentially nonfluorescent in MeOH (ϕ_F = 0.54%) and 25% water/MeCN (ϕ_F = 0.9%), and only recovers fluorescence in solvents with higher viscosity like 1-octanol (ϕ_F = 9.9%) and 25% water/DMSO (ϕ_F = 7.7%). We noticed similar behavior for **IndaFlav4**, but the ϕ_F in MeOH (4.9%) and 25% water/MeCN (6.2%) are much higher relative to the ϕ_F in 1-octanol (10%) and 25% water/DMSO (16%), suggesting that the flavylium scaffold is more resistant to hydrogen bond-induced quenching. To evaluate the effect of hydrogen bond donation on the excited states of **IndaFlav4** and **IndaIndol4**, we conducted time-correlated single photon counting lifetime measurements in MeCN and MeOH to determine their rates of nonradiative decay ($k_{n.r.}$) (Figure 4.9C). Again, we selected these solvents to normalize for contributions from polarity and viscosity. In the case of **IndaFlav4**, we observed a marginal increase in the rate of nonradiative decay going from MeCN ($k_{n.r.}$ = 1.34 ns^{-1}) to MeOH ($k_{n.r.}$ = 1.44 ns^{-1}), suggesting that hydrogen bond donation plays a minor role in excited state deactivation. In contrast, we observed a 2-fold increase in the rate of nonradiative decay for **IndaIndol4** ($k_{n.r.}$ = 0.91 ns^{-1} in MeCN vs 1.9 ns^{-1} in MeOH), supporting our hypothesis that the indolenium scaffold is more susceptible to hydrogen bond-induced quenching than the flavylium scaffold. This could be attributed to the fact that **IndaFlav4**, as a weaker donor–acceptor pair, has less charge-transfer character in the excited state and therefore less hydrogen bond-induced stabilization. Overall, it is gratifying to see that in aqueous mixtures, both **IndaFlav4** (Figure 4.9D) and **BarbiFlav4** (Figure 4.10C) actually outperform their indolenium analogs in terms of ϕ_F and overall brightness ($\epsilon \times \phi_F$).

4.3.4 Intrinsic Labeling of the Endoplasmic Reticulum

Having achieved far-red flavylium merocyanine dyes that favor the cyanine state in biologically relevant conditions, we were eager to evaluate the utility of the most red-shifted dye, **IndaFlav4**, for live cell labeling. First, we assessed its cytotoxicity in A375 cells using a trypan blue exclusion assay at concentrations spanning 0–50 μM. We observed excellent cell viability (>96%) at concentrations up to 50 μM (Figure 4.11). Next, we tested its stability in 10 μM mixtures of hydrogen peroxide (H_2O_2), peroxynitrite ($ONOO^-$) and hydrogen sulfide (H_2S) (Figure 4.12A) to determine if **IndaFlav4** can withstand reactive oxygen (ROS), nitrogen (RNS) and sulfur (RSS) species in cells. In all three conditions, characteristic absorption and emission of **IndaFlav4** is present after 2 h, suggesting adequate stability for use alongside the nanomolar concentrations of ROS, RNS, and RSS present in cells. We performed additional stability assessments in mixtures of citrate phosphate buffer at biologically relevant pHs 5.0, 6.0, and 7.4 (Figure 4.12B). We were pleased to find that **IndaFlav4** retains strong absorption and emission after 12 h, indicating it is applicable for imaging acidic environments like the endosome and lysosome. After analyzing the chemical stability of **IndaFlav4**, we examined its photostability in 1-octanol with continual LED irradiation at 660 nm for 8 h (Figure 4.13). Remarkably, **IndaFlav4** showed only ~15% absorption loss after 8 h, demonstrating its strong resistance toward photodegradation.

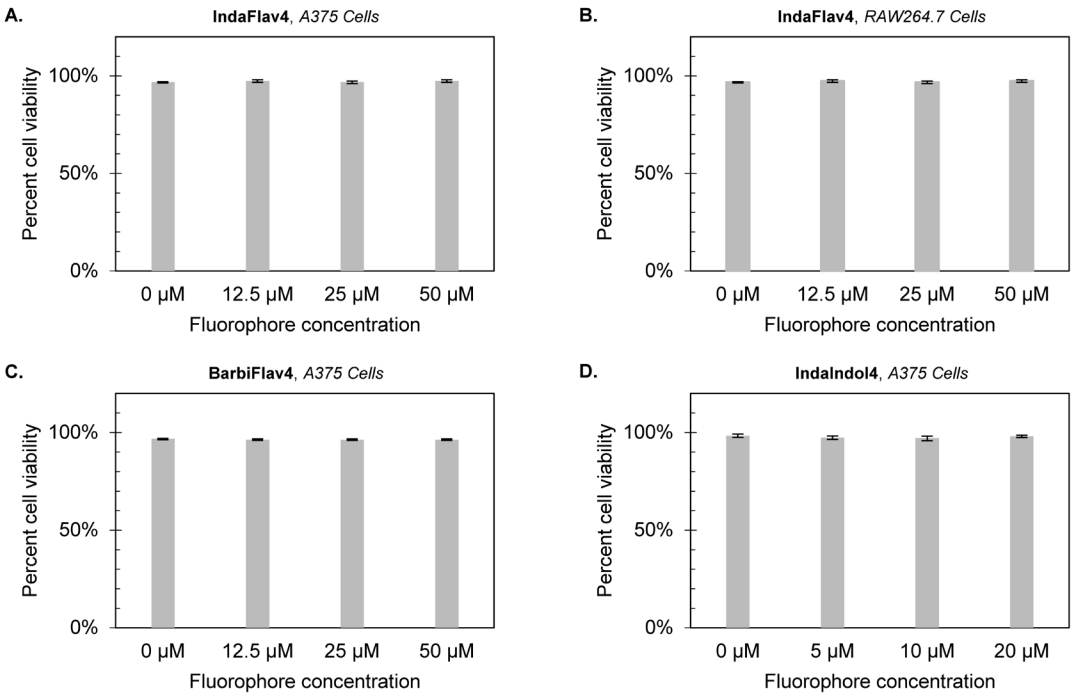

Figure 4.11. A-D) Dose-dependent cell viability using the trypan blue assay of **IndaFlav4** (0-50 μM) in A375 cells, **IndaFlav4** (0-50 μM) in RAW264.7 cells, **BarbiFlav4** (0-50 μM) in A375 cells and **IndaIndol4** (0-20 μM) in A375 cells. Error bars represent the standard deviation of three replicates.

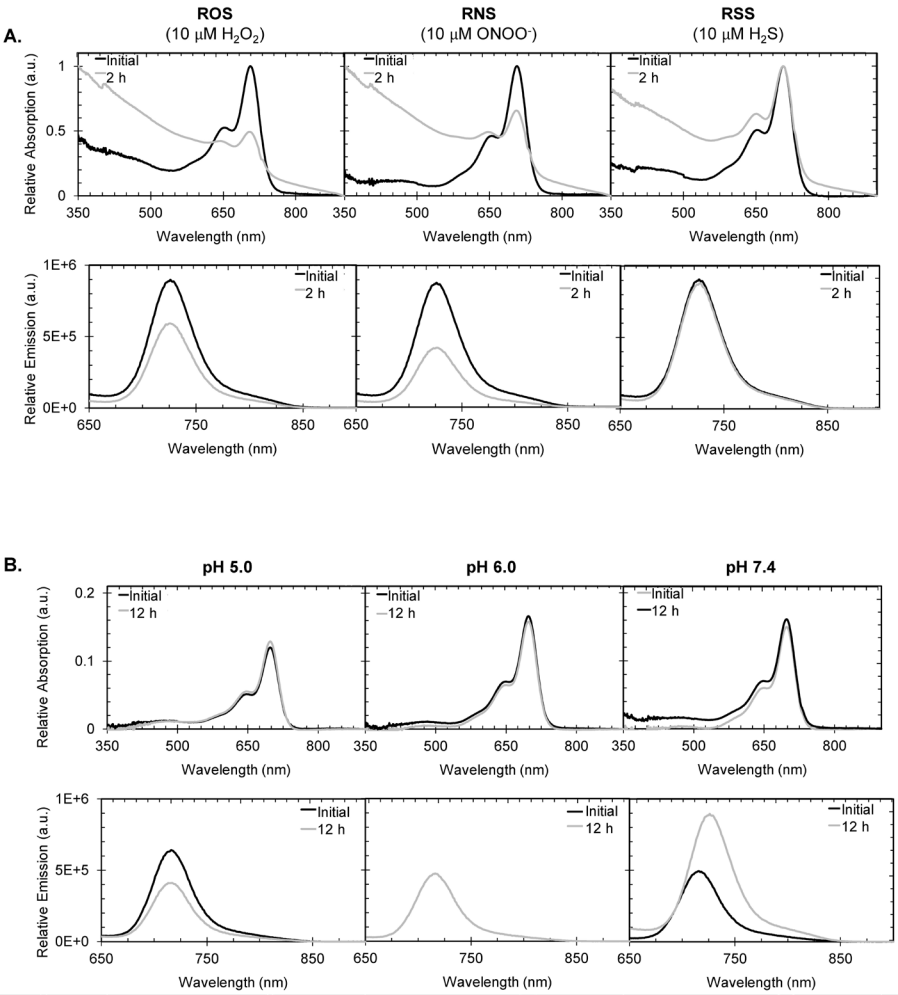

Figure 4.12. A) Normalized absorption and relative emission (ex. 620 nm; collect 650-900 nm) spectra of **IndaFlav4** (12 μM) in 10 μM mixtures of of H_2O_2, $ONOO^-$ and H_2S in 3:1 DMSO:PBS (pH 7.4). Peroxynitrite was generated *in situ* by combining equimolar amounts of H_2O_2 and $NaNO_2$. Hydrogen sulfide was generated *in situ* using Na_2S. B) Relative absorption and emission (ex. 620 nm; collect 650-900 nm) spectra of **IndaFlav4** (12 μM) in 3:1 mixtures of MeOH:citrate phosphate buffer at pH 5.0, 6.0 and 7.4.

A.

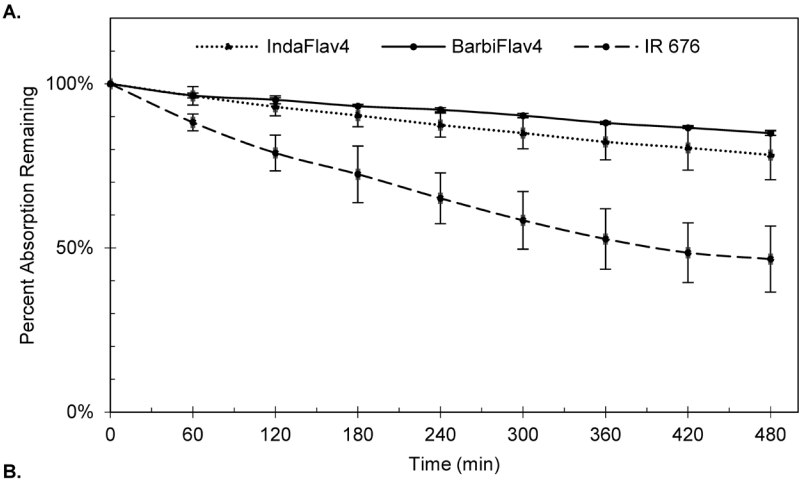

B.

Compound	k_{raw} ($\times 10^{-4}$, s^{-1})	ϵ ($\times 10^{4}$, M^{-1} cm^{-1})	k_{rel} ($\times 10^{-8}$, s^{-1})	Relative Stability
IndaFlav4	5.00 ± 0.08	2.94 ± 0.04	1.7 ± 0.1	1.00 ± 0.04
BarbiFlav4	3.06 ± 0.09	2.9 ± 0.2	1.043 ± 0.002	1.63 ± 0.06
IR 676	1.23 ± 0.04	8.6 ± 0.5	1.4 ± 0.1	1.18 ± 0.05

Figure 4.13. A) Photobleaching curves of **IndaFlav4**, **BarbiFlav4** and IR 676 in 1-octanol with continuous irradiation at 660 nm (36 mW/cm^2) over 8 hours (see photobleaching procedure for more details). Error bars represent the standard deviation of three replicates. B) Table of the raw (k_{raw}) and relative (k_{rel}) rates of photobleaching for each dye, along with their relative stabilities to IR 676. Note that **IndaFlav4** and **BarbiFlav4** have lower photobleaching rates (k_{raw}) but comparable photostabilities (k_{rel}) to IR 676 due to their lower absorption coefficients at 660 nm.

Upon confirming that **IndaFlav4** is biocompatible and stable, we performed confocal microscopy in living A375 cells (Figure 4.14). Because of its red-shifted absorption, **IndaFlav4** is efficiently excited with far-red laser lines, enhancing its compatibility with blue, green and red commercial stains and fluorescent proteins (Figure 4.14A). Capitalizing on this advantage, we performed a four-color colocalization experiment with **IndaFlav4** (Figure 4.14B, i, false color magenta) alongside conventional markers for the nucleus (Hoechst 33342, false color blue), cell membrane (CellBrite Fix 488, false color cyan) and lysosomes (LysoTracker Red-DND-99, false color green). Gratifyingly, we observed negligible crosstalk between LysoTracker Red and **IndaFlav4** (Figure 4.14B,ii, iii), highlighting its utility for multiplexed cell labeling. Additionally, we observed minimal colocalization with each cell marker (supported by cross-section analyses and Pearson coefficients less than 0.5), suggesting that **IndaFlav4** does not target the nucleus, cell membrane or lysosomes (Figure 4.14B,iv and 4.15). Based on its small size and moderate

lipophilicity, we believe that **IndaFlav4** passively diffuses through the cell membrane, but is not lipophilic enough to be retained there.[55] Furthermore, its neutral charge is not ideal for DNA interactions in the nucleus or pH sensitivity in the lysosomes, resulting in poor localization to these organelles.[55] Lack of lysosomal staining also suggests that **IndaFlav4** is not internalized through the endosome, further supporting the notion that it is passively uptaken.[55]

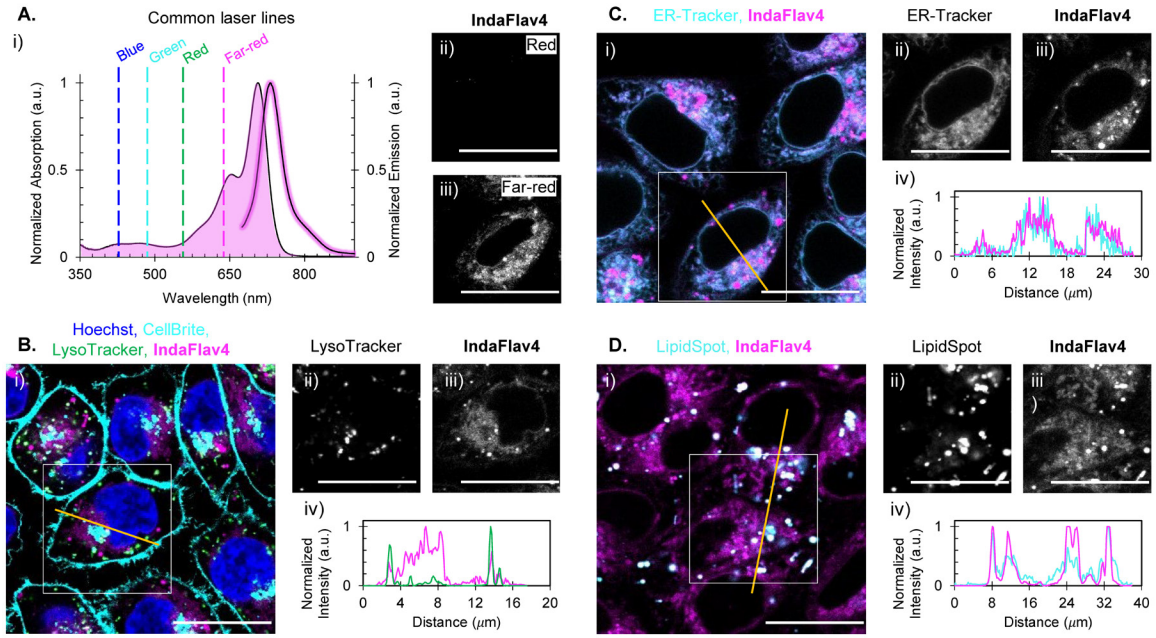

Figure 4.14. A) Absorption and fluorescence profile of **IndaFlav4** plotted against common microscopy laser lines (i). Live cell confocal microscopy of A375 cells labelled with **IndaFlav4** (25 μM) and excited by a red laser line (ii, ex. 561 nm; collect 680-850 nm) and a far-red laser line (ii, ex. 638 nm; collect 680-850 nm). B) Four-color confocal microscopy of live A375 cells labelled with Hoechst 33342 (i, blue, nucleus, ex. 405 nm; collect 420-470 nm), CellBrite Fix 488 (i, cyan, cell membrane, ex. 488 nm, 500-600 nm), LysoTracker Red DND-99 (i, green, lysosomes, ex. 561 nm; collect 575-651 nm) and **IndaFlav4** (i, magenta, 5 μM endoplasmic reticulum, ex. 638 nm; collect 680-800 nm). Zoomed inset (white box) of LysoTracker Red DND-99 (ii) and **IndaFlav4** (iii). Normalized cross-section analysis (yellow line) of LysoTracker Red DND-99 (iii, green) and **IndaFlav4** (iii, magenta). C, D) Two-color confocal microscopy of live A375 cells labelled with ER-Tracker Green (C, i, cyan, endoplasmic reticulum, ex. 488 nm; collect 500-600 nm) or LipidSpot 488 (D, i, cyan, lipid droplets, ex. 488 nm; 500-600 nm) and **IndaFlav4** (C, D, i, magenta, 25 μM, ex. 638 nm; collect 680-850 nm). Zoomed inset (white box) of ER-Tracker Green (C, ii) or LipidSpot 488 (D, ii) and **IndaFlav4** (C, D, iii). Normalized cross-section analysis (yellow line) of ER-Tracker Green (C, iv, cyan) or LipidSpot 488 (D, iv, cyan) and **IndaFlav4** (C, D, iv, magenta). Scale bars represent 20 μm. The Pearson coefficient is 0.83 for the endoplasmic reticulum and 0.66 for lipid droplets.

Noticing the strong fluorescence surrounding the nucleus, we performed additional colocalization experiments for the mitochondria and endoplasmic reticulum (ER). Furthermore, the presence of bright puncta scattered throughout the cell prompted us to investigate if **IndaFlav4** labels lipid droplets, a known feature of some merocyanine scaffolds.[56-59] We observed minimal colocalization and dissimilar staining patterns to MitoTracker Green, suggesting that **IndaFlav4** does not target the mitochondria (Figure 4.15). This is not surprising considering cationic fluorophores are best suited for mitochondrial labeling.[55] In contrast, we observed excellent colocalization and similar staining patterns for ER-Tracker Green (Figure 4.14C) and LipidSpot 488 (Figure 4.14D), with respective Pearson coefficients of 0.83 and 0.66, confirming that **IndaFlav4** has intrinsic targeting ability to the ER and lipid droplets. This colocalization was maintained at a higher confocal resolution and magnification (Figure 4.16). To determine if this selectivity is present in other cell types, we labeled RAW264.7 macrophages with **IndaFlav4**, and observed excellent localization to both organelles (Figure 4.17).

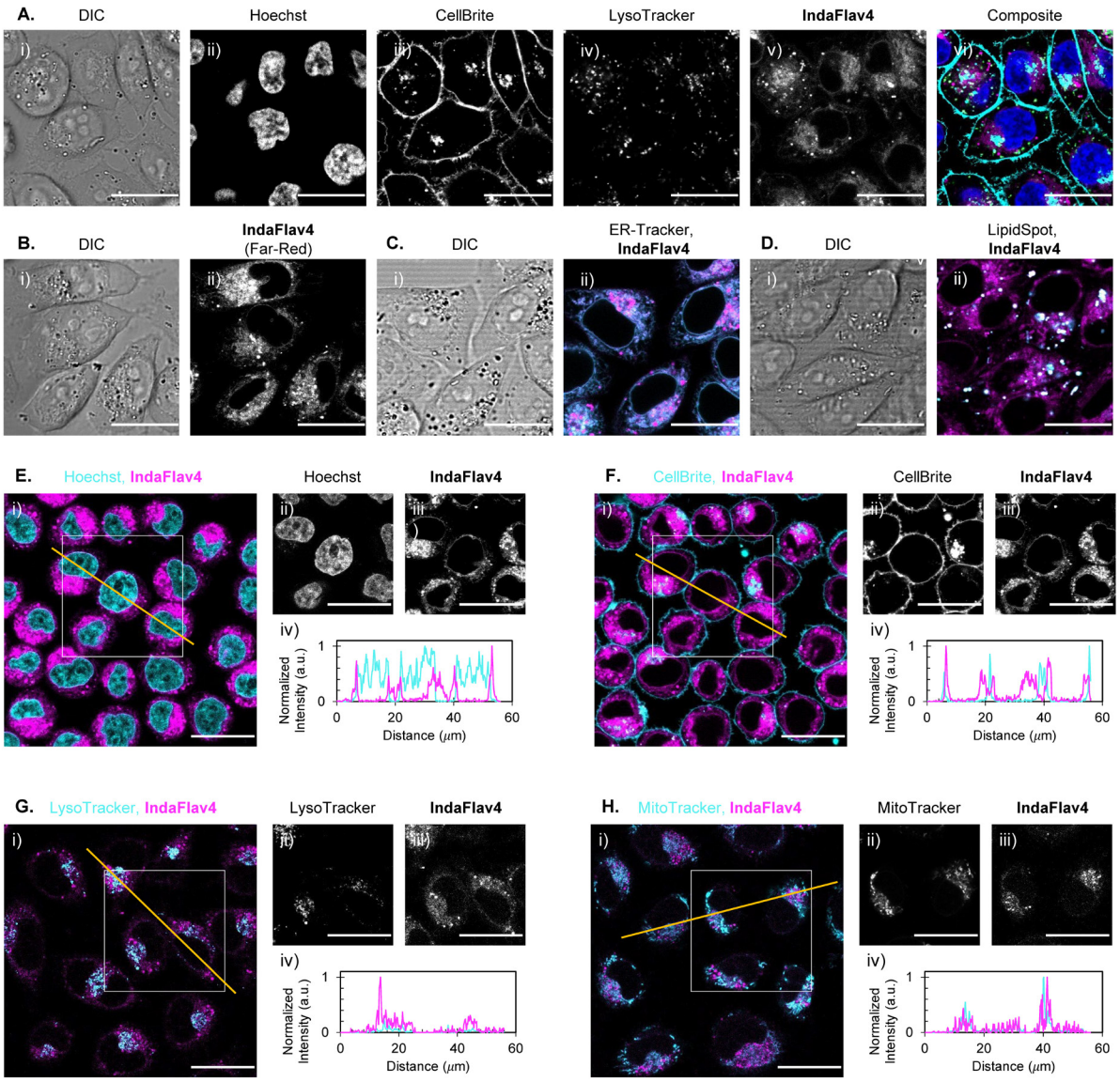

Figure 4.15. A) Direct interference contrast (DIC, i) and four-color confocal microscopy (ii-vi) of live A375 cells labelled with Hoechst 33342 (ii, vi, blue, nucleus ex. 405 nm; collect 420-500 nm), CellBrite Fix 488 (iii, vi, cyan, cell membrane, ex. 488 nm; 500-600 nm), LysoTracker Red DND-99 (iv, vi, green, lysosomes, ex. 561 nm; 575-651 nm) and **IndaFlav4** (v, vi, magenta, 5 μM, ex. 638 nm; collect 680-850 nm). B) DIC (i) and confocal microscopy (ii) of live A375 cells labelled with **IndaFlav4** (25 μM, ex. 638 nm; collect 680-850 nm). C, D) DIC (i) and confocal microscopy (ii) of live A375 cells labelled with ER-Tracker Green (C, i, cyan, endoplasmic reticulum, ex. 488 nm; collect 500-600 nm) or LipidSpot 488 (D, i, cyan, lipid droplets, ex. 488 nm; 500-600 nm) and **IndaFlav4** (C, D, i, magenta, 25 μM, ex. 638 nm; collect 680-850 nm). E-H) Two-color confocal microscopy of live A375 cells labelled with Hoechst 33342 (E, i, cyan, ex. 405 nm; collect 420-470 nm), CellBrite Fix 488 (F, i, cyan, ex. 488 nm, 500-600 nm), LysoTracker Red DND-99 (G, i, cyan, ex. 561 nm; collect 575-651 nm) or MitoTracker Green (H, i, cyan, mitochondria, ex. 488 nm; collect 500-600 nm) and **IndaFlav4** (E-H, i, magenta, 25 μM, ex. 638 nm; collect 680-850 nm). Zoomed inset (white box) of Hoechst 33342 (E, ii), CellBrite Fix 488 (F, ii), LysoTracker Red DND-99 (G, ii) or MitoTracker Green (H, ii) and **IndaFlav4** (E-H, iii). Normalized cross-section analysis (yellow line) of Hoechst 33342 (E, iv, cyan), CellBrite Fix 488 (F, iv, cyan), LysoTracker

Red DND-99 (G, iv, cyan) or MitoTracker Green (H, iv, cyan) and **IndaFlav4** (E-H, iv, magenta). Scale bars represent 20 µm. The Pearson coefficient is -0.22 for the nucleus, 0.21 for the cell membrane, 0.29 for the lysosomes and 0.43 for the mitochondria.

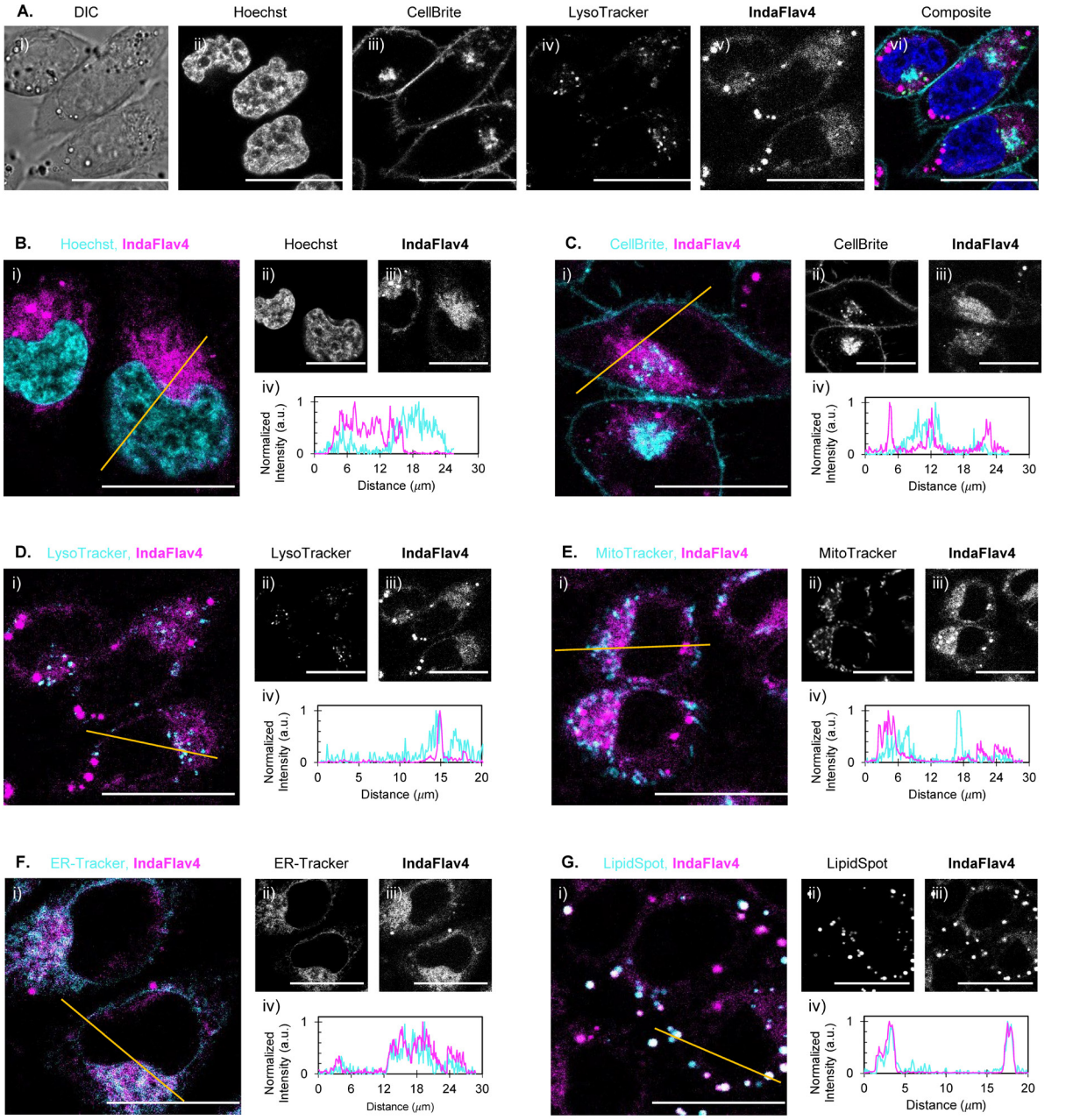

Figure 4.16. A) Direct interference contrast (DIC, i) and four-color confocal microscopy (ii-vi) of live A375 cells labelled with Hoechst 33342 (ii, vi, blue, nucleus ex. 405 nm; collect 410-480 nm), CellBrite Fix 488 (iii, vi, cyan, cell membrane, ex. 488 nm; collect 504-582 nm), LysoTracker Red DND-99 (iv, vi, green, lysosomes, ex. 577 nm; collect 582-658 nm) and **IndaFlav4** (v, vi, magenta, 5 µM, ex. 660 nm; collect 668-799 nm). B-G) Two-color confocal microscopy of live A375 cells labelled with Hoechst 33342 (B, i, cyan, ex. 405 nm; collect 410-480 nm), CellBrite Fix 488 (C, i, cyan, ex. 488 nm, collect 504-582 nm), LysoTracker Red DND-99 (D, i, cyan, ex. 577 nm; collect 582-658 nm), MitoTracker Green (E, i, cyan, mitochondria, ex. 488 nm; collect 504-582 nm), ER-

Tracker Green (F, i, cyan, endoplasmic reticulum, ex. 488 nm; collect 504-582 nm) or LipidSpot 488 (G, i, cyan, lipid droplets, ex. 488 nm; collect 504-582 nm) and **IndaFlav4** (B-G, i, magenta, 25 μM, ex. 660 nm; collect 668-799 nm). Zoomed inset (white box) of Hoechst 33342 (B, ii), CellBrite Fix 488 (C, ii), LysoTracker Red DND-99 (D, ii), MitoTracker Green (E, ii), ER-Tracker Green (F, ii) or LipidSpot 488 (G, ii) and **IndaFlav4** (B-G, iii). Normalized cross-section analysis (yellow line) of Hoechst 33342 (B, iv, cyan), CellBrite Fix 488 (C, iv, cyan), LysoTracker Red DND-99 (D, iv, cyan), MitoTracker Green (E, iv, cyan), ER-Tracker Green (F, iv, cyan) or LipidSpot 488 (G, iv, cyan) and **IndaFlav4** (B-G, iv, magenta). Scale bars represent 20 μm.

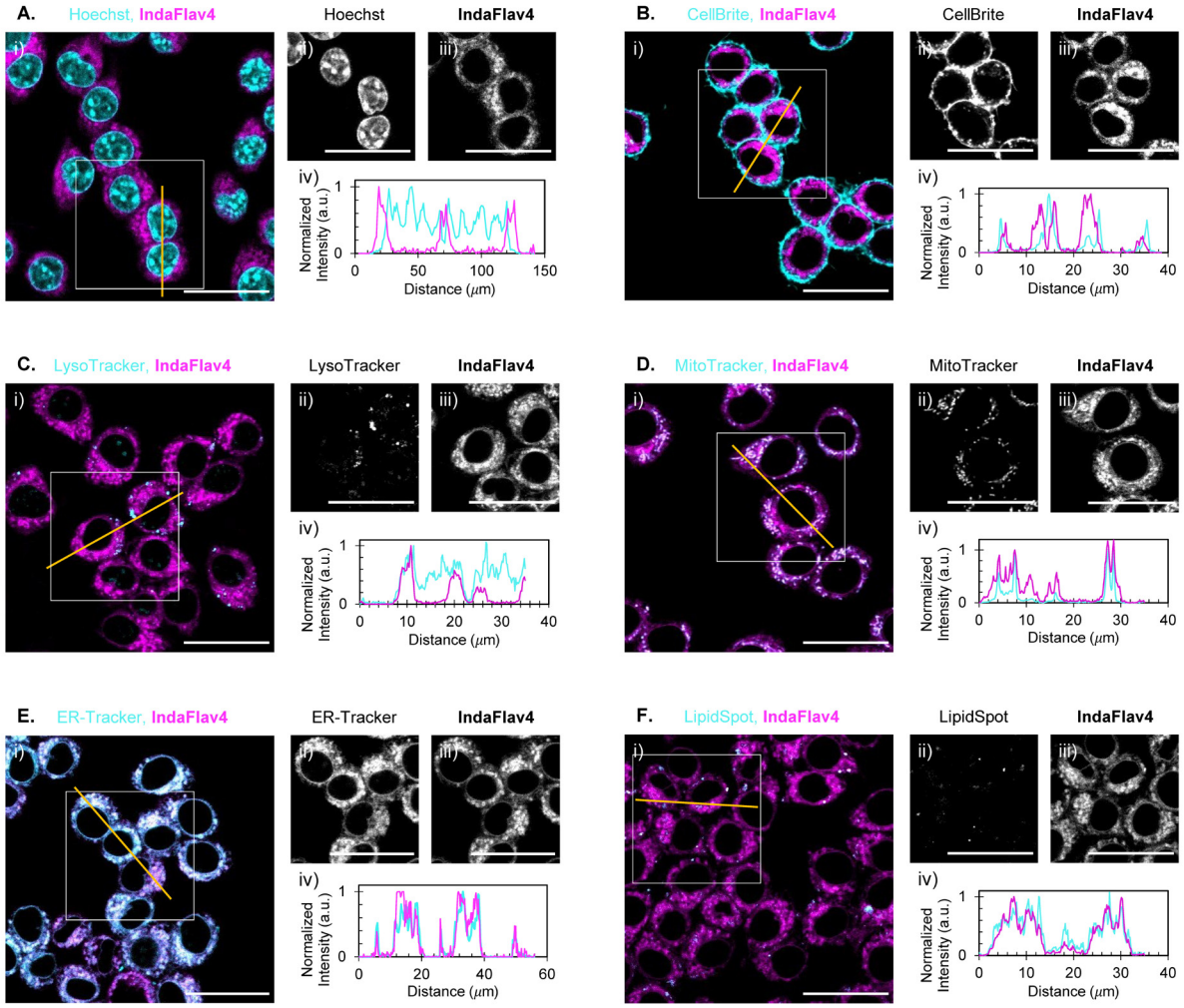

Figure 4.17. A-F) Two-color confocal microscopy of live RAW264.7 cells labelled with Hoechst 33342 (A, i, cyan, nucleus, ex. 405 nm; collect 420-500 nm), CellBrite Fix 488 (B, i, cyan, cell membrane, ex. 488 nm; collect 500-600 nm), LysoTracker Green (C, i, cyan, lysosomes, ex. 488 nm; collect 510-650 nm), MitoTracker Green (D, i, cyan, mitochondria, ex. 488 nm; collect 510-650 nm), ER-Tracker Green (E, i, cyan, endoplasmic reticulum, ex. 488 nm; collect 500-600), LipidSpot 488 (F, i, cyan, lipid droplets, ex. 488 nm; collect 500-600) and **IndaFlav4** (A-F, i, magenta, 10 μM, ex. 638 nm; collect 675-850 nm). Zoomed inset (white box) of Hoechst 33342 (A, ii), CellBrite Fix 488 (B, ii), LysoTracker Green (C, ii), MitoTracker Green (D, ii), ER-Tracker Green (E, ii) or LipidSpot 488 (F, ii) and **IndaFlav4** (A-D, iii). Normalized cross-section analysis (yellow line) of Hoechst 33342 (A, iv, cyan), CellBrite Fix 488 (B, iv, cyan), LysoTracker Green (C,

iv, cyan), MitoTracker Green (D, iv, cyan), ER-Tracker Green (E, iv, cyan) or LipidSpot 488 (F, iv, cyan) and **IndaFlav4** (A-D, iv, magenta). Scale bars represent 20 μm.

The ER labeling achieved with **IndaFlav4** is a fortuitous discovery considering there are currently no commercial ER stains for excitation above 600 nm. We believe the intrinsic ER selectivity derives from the dipolarity achieved in the cyanine state and lipophilicity of the merocyanine architecture. It is well-established that ER-targeting fluorophores should possess some amphiphilic character and sufficient lipophilicity, with calculated partition coefficients (Clog*P*) between 3.4 and 8.0.[60-64] The Clog*P* of **IndaFlav4** is 6.3, which is comfortably within this range (Table 4.4). We found that **BarbiFlav4** (Clog*P* = 5.6) and **IndaIndol4** (Clog*P* = 6.2) also localize to the ER (Pearson coefficients with ER Tracker Green = 0.82 and 0.86, respectively), supporting that this selectivity is related to the overall lipophilicity, rather than a particular structural motif (Figure 4.18). Most ER stains feature targeting groups (*e.g.*, bulky sulfonylurea ligands or ER-targeting peptides) that require additional synthetic steps and are known to disrupt cellular homeostasis.[60-65] In contrast, these merocyanine dyes are prepared in two high-yielding steps, and their simple design and low molecular weight impart excellent biocompatibility. We envision that, with careful tuning of their ground states and lipophilicity, merocyanine dyes possess unparalleled potential for future investigations of the endoplasmic reticulum.

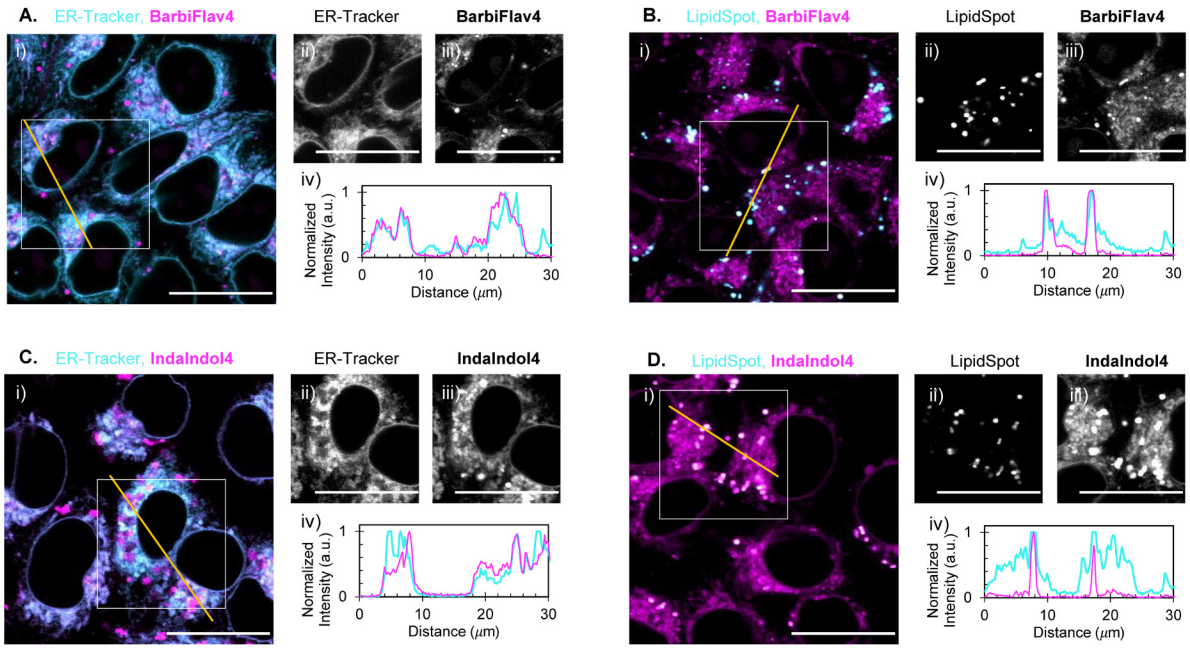

Figure 4.18. A-D) Two-color confocal microscopy of live A375 cells labelled with ER-Tracker Green (A, C, i, cyan, endoplasmic reticulum, ex. 488 nm; collect 500-600) or LipidSpot 488 (B, D, i, cyan, lipid droplets, ex. 488 nm; collect 500-600) and **BarbiFlav4** (A, B, i, magenta, 5 μM, ex. 638 nm; collect 660-850 nm) or **IndaIndol4** (C, D, i, magenta, 5 μM, ex. 561 nm; collect 566-750 nm). Zoomed inset (white box) of ER-Tracker Green (A, C, ii) or LipidSpot 488 (B, D, ii) and **IndaFlav4** (A, B, iii) or **IndaIndol4** (C, D, iii). Normalized cross-section analysis (yellow line) of ER-Tracker Green (A, C, iv, cyan) or LipidSpot 488 (B, D, iv, cyan) and **IndaFlav4** (A, B, iv, magenta) or **IndaIndol4** (C, D, iv, magenta). Scale bars represent 20 μm. The Pearson coefficient for the ER is 0.83 for **BarbiFlav4** and 0.86 for **IndaIndol4** and for lipid droplets, 0.57 for **BarbiFlav4** and 0.60 for **IndaIndol4**.

Table 4.4. Calculated partition coefficients (Clog*P*) determined by ChemDraw Professional 21.0 (PerkinElmer).

Fluorophore	Clog*P*
IndaFlav4	6.3301
BarbiFlav4	5.6247
IndaIndol4	6.1624
BarbiIndol4	4.557

4.4 Conclusion

In summary, we designed a new class of merocyanine dyes featuring a flavylium donor and a malononitrile (**MalonoFlav4**), 1,3-indandione (**IndaFlav4**) and *N*,*N*-dimethyl barbituric acid (**BarbiFlav4**) acceptor group. Capitalizing on the weak electron-donating properties of the flavylium heterocycle, all three dyes display red-shifted absorption spanning the far-red and NIR regions. Importantly, these dyes all lie between the A1─A2 ground states, depending on the acceptor strength and solvent properties.

We originally posited that these dyes favor the cyanine state with increasing polarity, as is typical with merocyanine dyes between the A1─A2 states, but ultimately discovered that the flavylium architecture imparts prominent sensitivity toward solvent viscosity. Therefore, these dyes exhibit pronounced cyanine character in high viscosity environments (*e.g.*, 1-octanol), regardless of polarity. We also found that merocyanine dyes featuring the 1,3-indandione and *N*,*N*-dimethyl barbituric acid acceptors favor the cyanine state in solvents with hydrogen bond donation, a phenomenon that has received no attention to date. This dual sensitivity toward viscosity and hydrogen bond donation allows flavylium merocyanine dyes to exhibit narrow, red-shifted absorption across a range of biologically relevant conditions, regardless of their polarity.

In addition to their unique ground state properties, we also discovered that **IndaFlav4** and **BarbiFlav4** exhibit higher ϕ_F with increasing solvent polarity and viscosity, a feature that is rarely seen in polymethine dyes. Furthermore, we demonstrate that **IndaFlav4** is more resistant to hydrogen bond-induced quenching compared to its indolenium analogue, improving the brightness of this scaffold in aqueous environments.

We exploit these properties for live cell microscopy, where we observed intrinsic targeting of both **IndaFlav4** and **BarbiFlav4** to the endoplasmic reticulum and lipid droplets. We attribute the intrinsic ER labeling to the dipolarity achieved in the cyanine state (which imbues subtle amphiphilic character) and lipophilicity ($C\log P$) of the merocyanine architecture. With access to

a far-red scaffold between the A1─A2 ground states, we readily achieved four-color labeling with **IndaFlav4** alongside commercial stains, observing minimal crosstalk between detection windows. Having realized the potential of these flavylium merocyanine dyes for labeling experiments in cell culture, future work will involve extending their beneficial properties further into the NIR and shortwave infrared (SWIR, 1000–2000 nm) regions so we can further examine their utility in more complex biological settings.

4.5 Experimental Procedures

4.5.1 General Procedures

Materials and Instrumentation

Chemical reagents were purchased from Acros Oranics, Alfa Aesar, Fisher Scientific, Sigma-Aldrich or TCI and used without purification. Anhydrous and deoxygenated THF was dispensed from a Grubb's-type Phoenix Solvent Drying System. Flash chromatography was performed with technical grade silica gel containing 60 Å pores and 40-63 μm mesh particle sizes (Sorbtech Technologies). Solvent was removed under reduced pressure using a Büchi Rotovapor with a Welch self-cleaning dry vacuum pump, and a Welch DuoSeal pump for additional evaporation. Nuclear magnetic resonance (^{1}H NMR, ^{13}C NMR and ^{19}F NMR) spectra were taken on a Bruker AV500 or AV600 spectrometer and processed with MestReNova software. All ^{1}H NMR and ^{13}C NMR peaks are referenced to their respective solvent peaks (DMSO-d_6 δH = 2.50 ppm, δC = 39.52 ppm; CD_2Cl_2 δH = 5.32 ppm, δC = 53.84 ppm; $CDCl_3$ δH = 7.26 ppm, δC = 77.16 ppm). ^{19}F NMR peaks are referenced to trifluorotoluene (δF = -63.72 ppm). High resolution mass spectrometry data were obtained on an Agilent 6545 Q-TOF mass spectrometer. Absorption spectra were collected on a JASCO V-770 or JASCO V-710 UV-Visible/NIR spectrophotometer. Excitation and emission spectra were collected on a Horiba Fluorolog-QM series fluorimeter. Excited state lifetime measurements were performed on a Horiba PTI QuantaMaster400 series

fluorimeter equipped with a delta diode setup and 529 nm excitation laser. All absorption, emission, excitation and lifetime measurements were collected using a 1 cm quartz cuvette.

Abbreviations

AcOH, acetic acid, Ac_2O, acetic anhydride, DCM, dichloromethane, DMF, dimethylformamide, DMSO, dimethyl sulfoxide, EtOH, ethanol, HBF_4, fluoroboric acid, MeCN, acetonitrile, MeOH, methanol, NaOAc, sodium acetate, Na_2SO_4, sodium sulfate, *n*-BuOH, *n*-butanol, THF, tetrahydrofuran

4.5.2. Photophysical experimental procedures

General photophysical procedures

Absorption spectra were collected between 350-900 nm, with a 2000 nm/min scan rate after blanking with the appropriate solvent. Absorption coefficients were measured using serial dilutions with volumetric glassware, and calculated according to the Beer-Lambert law. Error was calculated using the standard deviation of measurements performed in triplicate. Emission and excitation spectra were obtained with the fluorimeter parameters listed below.

			Emission spectra		Excitation spectra	
Dye	Slit widths	Integration time	Excitation	Collection	Collection	Excitation
MalonoFlav4	5-10 nm	0.1 s	590 nm	620-900 nm	660 nm	400-640 nm
IndaFlav4	5-10 nm		620 nm	650-900 nm	740 nm	400-710 nm
BarbiFlav4	5-10 nm		620 nm	650-900 nm	720 nm	400-720 nm
IndaIndol4	5 nm		510 nm	550-900 nm		
BarbiIndol4	5 nm		510 nm	550-900 nm		

Relative fluorescence quantum yields

The fluorescence quantum yield (Φ_F) of a dye is defined in equation (1), where P_E is the number of photons emitted and P_A is the number of photons absorbed.

$$\Phi_F = \frac{P_E}{P_A} \qquad (1)$$

The relative quantum yields of **IndaFlav4** and **BarbiFlav4** were determined using IR 676 (Φ_F = 16.4% in MeOH) as a reference.[66] To allow **IndaFlav4**, **BarbiFlav4** and IR 676 to be excited under identical parameters, the emission spectra for IR 676 were collected with a neutral density filter (NE20B-B) with 10 nm slit widths and corrected to account for photons removed by the filter. The relative quantum yields of **IndaIndol4** and **BarbiIndol4** were determined using HICl (Φ_F = 2.16% in EtOH) as a reference.[67]

Excited state lifetimes

Time-correlated single photon (TCSP) counting lifetime (τ) measurements of **IndaFlav4** and **IndaIndol4** were conducted in MeOH and MeCN at room temperature using a 529 nm excitation pulse laser. The decay curve was fitted using ExTime. Equations (2) and (3) were used to determine the rates of radiative (k_r) and nonradiative ($k_{n.r.}$) decay.

$$k_r = \frac{\Phi_F}{\tau} \quad (2)$$

$$k_{n.r.} = \frac{1 - \Phi_F}{\tau} \quad (3)$$

The errors for k_r and k_{nr} were determined by propagating the error of τ and Φ_F .

Photobleaching

Samples of **IndaFlav4**, **BarbiFlav4** or IR 676 were dissolved in 1-octanol and diluted to an absorption intensity less than 1 a.u. The solution was added to a screw-top cuvette and placed in a covered cardboard box 1.5 cm away from a 660 nm LED (Thorlabs M660L4), fitted with collimation adapter (Thorlabs SM2F32-B). Power was supplied using a Korad KD3005D, and the power density at this distance was measured to be 36 mW/cm^2 using a luxometer (Thorlabs PM100D). The absorption spectra for each sample were recorded every 60 min for eight hours. The absorption intensity of each timepoint was taken as a percentage of the intensity at t = 0 min.

The photobleaching data was fitted to the first-order rate decay equation (4), where A and A_0 represent the percentage of absorption intensity at time *t* and *t* = 0 min, respectively.

$$\ln[A] = -kt + \ln[A]_0 \qquad (4)$$

All R^2 values are >0.95. Each sample was photobleached in triplicate, and the error represents the standard deviation of three replicates. The rate constant (k_{raw}) was divided by the absorption coefficient of each fluorophore at 660 nm to determine their relative rates (k_{rel}) of photobleaching.

4.5.3. Cell experimental procedures

General cell culture procedures

A375 cells were purchased from ATCC (Catalog number: CRL-1619). RAW264.7 cells were purchased from ATCC (Catalog number: TIB-71). They were cultured in Dulbecco's Modified Eagle Media (DMEM, Life Technologies, Catalog number: 11995073) supplemented with 10% fetal bovine serum (FBS, Corning), sodium pyruvate (Thermo Fisher, Catalog number: 11360070) and 1% penicillin-streptomycin (Life Technologies, Catalog number: 15070063) at 37 °C and 5% CO_2 in Heracell 150i CO_2 incubators. Cells were pelleted using a Sorvall ST 40R series centrifuge. All cell work was executed in a 1300 Series A2 biosafety cabinet. Microscopy was performed with a Leica STELLARIS 5 confocal microscope using the 405 nm, 488 nm, 561 nm and 638 nm lasers and 63x oil objective lens or a Lecia SP8 LIGHTNING confocal microscope using the 405 nm, 488 nm, 577 nm and 660 nm lasers and 100x oil objective lens.

Trypan blue cytotoxicity assay

A375 cells or RAW264.7 cells were seeded onto 12-well plates with average density 2 × 10^6 cells per well. Cells were cultured for 4 h with either DMEM, DMEM containing 2.5% 1x PBS, or DMEM containing a solution of **IndaFlav4** (12.5 μM, 25 μM or 50 μM in 1% DMSO), **BarbiFlav4**

(12.5 μM, 25 μM or 50 μM in 1% DMSO) or **IndaIndol4** (5 μM, 10 μM or 20 μM in 1% DMSO), after which the media was removed and the wells were washed with 3x DMEM. Cells were suspended via trypsinization and gentle scraping, followed by mixing with trypan blue at 1:1 ratio for automated cell viability counting using the Countess 3 Automated Cell Counter (Thermo Fisher).

Live cell staining

A375 cells were plated 60,000 cells per well on an Ibidi 8-well microslide (IbiTreat, Catalog number: 80826) and allowed to adhere for 36 h. Once adherent, cells were washed with 1x Hank Balanced Salt Solution (HBSS, VWR, Catalog number: VWRL0121-0500). The cells were then incubated with **IndaFlav4**, **BarbiFlav4** or **IndaIndol4** (5-25 μM, 20 min, 37 °C). After incubation cells were washed with 1x HBSS. The cell membrane was stained with CellBrite Fix 488 (1:1000, 15 min, 37 °C, Biotium, Catalog number: 30090). The endoplasmic reticulum was stained with ER-Tracker Green BODIPY FL Glibenclamide (1 μM, 20 min, 37 °C, Invitrogen, Catalog number: E34251). Lysosomes were stained with Lysotracker Red DND-99 (10 nM, 30 min, 37 °C, Thermo Fisher, Catalog number: L7528). Mitochondria were stained with MitoTracker Green (100 nM, 30 min, 37 °C, Cell Signaling Technology, Catalog number: 9074). Lipid droplets were stained with LipidSpot 488 (1 μM, 30 min, 37 °C, Biotium, Catalog number: 70065). Nuclei were stained with Hoechst 33342 (3.24 μM, 5 min, rt, ThermoFisher, Catalog number: PI62249). Cells were washed with 1x HBSS prior to imaging.

RAW264.7 cells were plated 60,000 cells per well on an Ibidi 8-well microslide and allowed to adhere for 36 h. Once adherent, cells were washed with 1x HBSS. The cells were then incubated with **IndaFlav4** (5-10 μM, 20 min, 37 °C). After incubation cells were washed with 1x HBSS. The cell membrane was stained with CellBrite Fix 488 (1:1000, 15 min, 37 °C). The endoplasmic reticulum was stained with ER-Tracker Green BODIPY FL Glibenclamide (1 μM, 20 min, 37 °C). Lysosomes were stained with Lysotracker Green (20 nM, 30 min, 37 °C, Thermo Fisher, Catalog number: L7526). Mitochondria were stained with MitoTracker Green (100 nM, 30

min, 37 °C). Lipid droplets were stained with LipidSpot 488 (1 μM, 30 min, 37 °C). Nuclei were stained with Hoechst 33342 (3.24 μM, 5 min, rt). Cells were washed with 1x HBSS prior to imaging.

Live cell imaging

Stained cells were placed in 1x HBSS and transferred to the confocal microscope. Images were acquired within 1 h to prevent cell death. Images were acquired with a 63x or 100x oil objective at 1024 x 1024 resolution. Confocal settings are listed below.

		A375 Cells			RAW264.7 Cells		
Stain	Laser	Power Intensity	Gain	Collection (nm)	Power Intensity	Gain	Collection (nm)
Hoescht 33342	405 nm	5-18%	25-100	420-470 or 410-480	5%	50	420-500
CellBrite Fix 488	488 nm	2-60%	20-850	500-600 or 504-582	3%	8	500-600
ER-Tracker Green (BODIPY FL Glibenclamide)	488 nm	2-8%	5	500-600 or 504-582	10%	20	500-600
MitroTracker Green	488 nm	5%	10	500-600 or 504-582	2%	3	510-650
LipidSpot 488	488 nm	5-8%	30	500-600 or 504-582	10%	20	500-600
LysoTracker Green	488 nm				8%	20	510-650
LysoTracker Red DND-99	561 or 577 nm	5-50%	15-100	575-651 or 582-658			
IndaFlav4	638 or 660 nm	20-80%	50	680-850 or 668-799	5-15%	15-50	675-850
BarbiFlav4	638 nm	10-20%	10-50	660-850			
IndaIndol4	561 nm	2%	5	566-750			

4.5.4. Synthetic procedures

Synthesis of 7-(dimethylamino)-4-methyl-2-phenylchromenylium tetrafluoroborate (**4.1**)

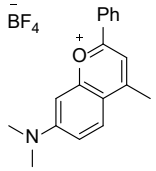

In a dry two-neck round-bottom flask equipped with a stir bar under N_2 atmosphere, 7-(dimethylamino)-2-phenyl-4*H*-chromen-4-one (652 mg, 2.46 mmol, 1.00 equiv) was dissolved in anhydrous THF (5.98 mL) and cooled to 0 °C. Methylmagnesium bromide (6.14 mL, 6.14 mmol, 2.50 equiv) was added dropwise, and the mixture was slowly warmed to rt to stir for 24 h. The mixture was quenched with an aqueous solution of 1 M HBF_4 (6.14 mL), extracted into DCM (3 × 50 mL), dried with Na_2SO_4 and evaporated down to afford **4.1** as a shiny red solid (635 mg, 1.89 mmol, 77%). ^{1}H NMR (500 MHz, DMSO-d_6) δ 8.36 (d, J = 7.8 Hz, 2H), 8.21 (t, J = 4.8 Hz, 2H), 7.81 – 7.65 (m, 3H), 7.53 – 7.47 (m, 1H), 7.40 – 7.25 (m, 1H), 3.35 (s, 6H), 2.88 (s, 3H). ^{1}H NMR is consistent with the previous report.[39]

Synthesis of 7-(dimethylamino)-2-phenyl-4-((1*E*,3*E*)-4-(*N*-phenylacetamido)buta-1,3-dien-1-yl)chromenylium tetrafluoroborate (**4.6**)

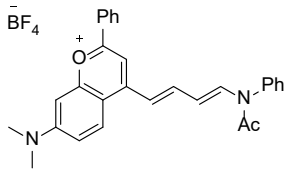

7-(dimethylamino)-4-methyl-2-phenylchromenylium tetrafluoroborate (**4.1**) (200 mg, 0.570 mmol, 1.00 equiv) and *N*-(3-(phenylamino)allylidene)benzenaminium chloride (**4.5**) (147 mg, 0.570 mmol, 1.00 equiv) were added to a two-neck round-bottom flask equipped with a stir bar and a reflux condenser. The solids were dissolved in a 1:1 mixture of AcOH:Ac_2O (5.70 mL) and the mixture was heated to 120 °C for 2 h. The mixture was cooled to rt and evaporated onto silica gel. The crude product was purified via flash chromatography, eluting with a DCM:EtOH gradient of 50:1, 25:1 and 25:2 to afford **4.6** as a dark purple solid (146 mg, 0.334 mmol, 59%). R_F = 0.36 in 10:1 DCM:MeOH. ^{1}H NMR (500 MHz, CD_2Cl_2) δ 8.44 (d, *J* = 13.4 Hz, 1H), 8.15 (d, *J* = 7.4 Hz, 2H), 8.03 (t, *J* = 13.3 Hz, 1H), 7.87 (dd, *J* = 9.8, 4.5 Hz, 1H), 7.77 (s, 1H), 7.66 – 7.57 (m, 6H), 7.28 (d, *J* = 7.4 Hz, 2H), 7.11 (d, *J* = 9.4 Hz, 1H), 6.90 – 6.79 (m, 2H), 5.54 (t, *J* = 12.6 Hz, 1H), 3.29 – 3.22 (m, 6H), 2.09 (s, 3H). ^{13}C NMR (126 MHz, CD_2Cl_2) δ 169.66, 162.88, 158.42, 156.81, 154.46, 149.18, 138.03, 133.39, 130.54, 130.05, 129.69, 129.56, 128.35, 127.19, 127.00, 118.32, 116.49, 113.55, 112.97, 102.94, 96.83, 40.68, 23.08. ^{19}F NMR (565 MHz, CD_2Cl_2) δ -152.72. HRMS (ESI): calculated for $C_{29}H_{27}N_2O_2^+$ $[M]^+$, 435.2067; found, 435.2096.

Synthesis of 2-((*E*)-4-((*E*)-7-(dimethylamino)-2-phenyl-4*H*-chromen-4-ylidene)but-2-en-1-ylidene)malononitrile (**MalonoFlav4**)

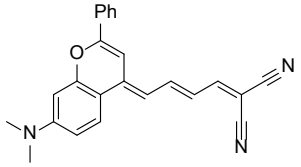

7-(dimethylamino)-2-phenyl-4-((1*E*,3*E*)-4-(*N*-phenylacetamido)buta-1,3-dien-1-yl)chromenylium tetrafluoroborate (**4.6**) (40 mg, 76 μmol, 1.0 equiv), malononitrile (**4.2**) (20 mg, 0.30 mmol, 4.0 equiv) and NaOAc (39 mg, 0.30 mmol, 4.0 equiv) were added to a dram vial equipped with a stir bar and fitted with a PTFE-lined cap. The solids were dissolved in Ac_2O (1.9 mL) and heated to 120 °C for 30 min. The mixture was cooled to rt and evaporated onto silica gel. The crude product was purified via flash chromatography, eluting with DCM. The crude product was washed with MeOH (3 × 5 mL) to afford **MalonoFlav4** as a bronze turquoise solid (19 mg, 53 μmol, 70%). R_F = 0.23 in DCM. ^{1}H NMR (500 MHz, CD_2Cl_2) δ 7.92 (s, 2H), 7.76 – 7.40 (m, 6H), 7.08 (s, 1H), 6.84 – 6.45 (m, 4H), 3.10 (s, 6H). ^{13}C NMR (126 MHz, CD_2Cl_2) δ 158.91, 155.04, 154.93, 153.71, 146.75, 141.98, 132.88, 130.98, 129.30, 125.93, 124.90, 120.63, 116.88, 114.79, 111.65, 110.16, 109.62, 100.76, 98.48, 98.42, 70.96, 40.37, 30.09. HRMS (ESI): calculated for $C_{24}H_{20}N_3O^+$ $[M]^+$, 366.1601; found, 366.1595.

Synthesis of (*E*)-*N*-(3-(1,3-dioxo-1,3-dihydro-2*H*-inden-2-ylidene)prop-1-en-1-yl)-*N*-phenylacetamide (**7**)

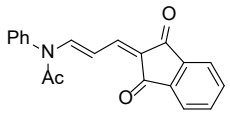

1*H*-indene-1,3(2*H*)-dione (**3**) (200 mg, 1.37 mmol, 1.00 equiv) and *N*-(3-(phenylamino)allylidene)benzenaminium chloride (**4.5**) (354 mg, 1.37 mmol, 1.00 equiv) were added to a two-neck round-bottom flask equipped with a stir bar and reflux condenser. The solids were dissolved in Ac_2O (13.7 mL) and the mixture was heated to 120 °C for 90 min. The mixture was cooled to rt, transferred to an Erlenmeyer flask and recrystallized at 4 °C for two days. The recrystallized solid was collected by vacuum filtration and washed with hexanes (3 × 10 mL) to yield **4.7** as shiny orange crystals (430 mg, 1.36 mmol, 99%). R_F = 0.47 in 10:1 DCM:MeOH. ^{1}H NMR (500 MHz, $CDCl_3$) δ 8.44 (d, *J* = 13.8 Hz, 1H), 7.91 – 7.87 (m, 1H), 7.79 – 7.75 (m, 1H), 7.69 (ddd, *J* = 6.6, 4.8, 1.5 Hz, 2H), 7.65 – 7.55 (m, 4H), 7.27 (d, *J* = 1.7 Hz, 1H), 7.25 (d, *J* = 1.3 Hz, 1H), 6.71 (dd, *J* = 13.9, 12.2 Hz, 1H), 2.01 (s, 3H). ^{13}C NMR (126 MHz, $CDCl_3$) δ 190.93, 190.09, 169.60, 147.22, 145.25, 141.77, 140.55, 138.04, 134.69, 134.58, 130.73, 130.04, 128.08, 125.32, 122.89, 122.41, 109k.04, 23.45. HRMS (ESI): calculated for $C_{20}H_{16}NO_3^+$ $[M]^+$, 318.1125; found, 318.1145.

Synthesis of 2-((*E*)-4-((*E*)-7-(dimethylamino)-2-phenyl-4*H*-chromen-4-ylidene)but-2-en-1-ylidene)-1*H*-indene-1,3(2*H*)-dione (**IndaFlav4**)

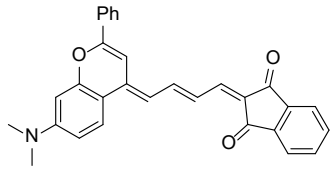

(*E*)-*N*-(3-(1,3-dioxo-1,3-dihydro-2*H*-inden-2-ylidene)prop-1-en-1-yl)-*N*-phenylacetamide (**4.7**) (30 mg, 95 μmol, 1.0 equiv), 7-(dimethylamino)-4-methyl-2-phenylchromenylium tetrafluoroborate (**4.1**) (50 mg, 0.14 mmol, 1.5 equiv) and NaOAc (23 mg, 0.28 mmol, 3.0 equiv) were added to a dram vial equipped with a stir bar and fitted with a PTFE-lined cap. The solids were dissolved in *n*-BuOH (0.95 mL) and the mixture was heated to 80 °C for 50 min. The mixture was cooled to rt and evaporated onto silica gel. The crude product was purified via flash chromatography, eluting with a DCM/EtOH gradient of 0% EtOH, 0.1% EtOH and 0.5% EtOH to afford **IndaFlav4** as a shiny turquoise solid (36 mg, 81 μmol, 85%). R_F = 0.33 in 40:1 DCM:MeOH. ^{1}H NMR (500 MHz, CD_2Cl_2) δ 7.94 (dt, *J* = 6.0, 1.8 Hz, 2H), 7.86 – 7.75 (m, 5H), 7.71 – 7.66 (m, 2H), 7.61 – 7.56 (m, 1H), 7.56 – 7.47 (m, 3H), 7.18 (s, 1H), 6.81 – 6.72 (m, 2H), 6.57 (d, *J* = 2.6 Hz, 1H), 3.10 (s, 6H). ^{13}C NMR (126 MHz, CD_2Cl_2) δ 191.03, 154.66, 153.17, 149.67, 145.10, 133.86, 133.66, 132.60, 130.43, 128.88, 125.46, 124.52, 122.86, 121.76, 121.62, 111.17, 110.10, 100.69, 98.11, 39.96, 29.68. HRMS (ESI): calculated for $C_{30}H_{24}NO_3^+$ $[M]^+$, 446.1751; found, 446.1783.

Synthesis of (*E*)-*N*-(3-(1,3-dimethyl-2,4,6-trioxotetrahydropyrimidin-5(2*H*)-ylidene)prop-1-en-1-yl)-*N*-phenylacetamide (**4.8**)

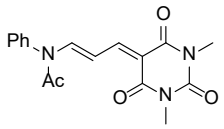

1,3-dimethylpyrimidine-2,4,6(1*H*,3*H*,5*H*)-trione (**4.4**) (200 mg, 1.28 mmol, 1.00 equiv) and *N*-(3-(phenylamino)allylidene)benzenaminium chloride (**4.5**) (331 mg, 1.28 mmol, 1.00 equiv) were added to a two-neck round-bottom flask equipped with a stir bar and reflux condenser. The solids were dissolved in Ac_2O (12.8 mL) and the mixture was heated to 120 °C for 2 h. The mixture was cooled to rt, transferred to an Erlenmeyer flask and recrystallized at 4 °C for two days. The recrystallized solid was collected by vacuum filtration and washed with hexanes (3 × 10 mL) to yield **4.8** as a fluffy yellow solid (317 mg, 97.3 μmol, 76%). R_F = 0.44 in 10:1 DCM:MeOH. ^{1}H NMR (500 MHz, $CDCl_3$) δ 8.55 – 8.48 (m, 1H), 8.18 (dd, *J* = 12.5, 0.6 Hz, 1H), 7.66 – 7.52 (m, 3H), 7.26 – 7.21 (m, 2H), 6.86 (dd, *J* = 13.6, 12.5 Hz, 1H), 3.33 (s, 3H), 3.22 (s, 3H), 2.01 (s, 3H). ^{13}C NMR (126 MHz, $CDCl_3$) δ 169.77, 162.47, 161.92, 158.11, 151.65, 150.08, 137.84, 130.81, 130.17, 127.90, 111.50, 110.30, 77.23, 28.54, 27.82, 23.45. HRMS (ESI): calculated for $C_{17}H_{18}N_3O_4^+$ $[M]^+$, 328.1292; found, 328.1295.

Synthesis of 5-((*E*)-4-((*E*)-7-(dimethylamino)-2-phenyl-4*H*-chromen-4-ylidene)but-2-en-1-ylidene)-1,3-dimethylpyrimidine-,4,6(1*H*,3*H*,5*H*)-trione (**BarbiFlav4**)

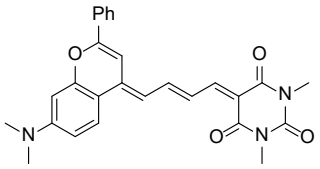

From precursor **4.8**:

(*E*)-*N*-(3-(1,3-dimethyl-2,4,6-trioxotetrahydropyrimidin-5(2*H*)-ylidene)prop-1-en-1-yl)-*N*-phenylacetamide (**4.8**) (50 mg, 0.15 mmol, 1.0 equiv) and 7-(dimethylamino)-4-methyl-2-phenylchromenylium tetrafluoroborate (**4.1**) (80 mg, 0.23 mmol, 1.5 equiv) were added to a dram vial equipped with a stir bar and fitted with a PTFE-lined cap. The solids were dissolved in pyridine (1.5 mL) and the mixture was heated to 70 °C for 50 min. The mixture was cooled to rt and evaporated onto silica gel. The crude product was purified via flash chromatography, eluting with 200:1 DCM:MeOH to afford **BarbiFlav4** as a shiny dark blue solid (50 mg, 0.11 mmol, 72%). R_F = 0.21 in 40:1 DCM:MeOH. ^{1}H NMR (500 MHz, CD_2Cl_2) δ 8.09 (d, *J* = 12.2 Hz, 1H), 7.97 – 7.87 (m, 4H), 7.74 (d, *J* = 9.2 Hz, 1H), 7.54 – 7.49 (m, 3H), 7.21 (s, 1H), 6.79 – 6.71 (m, 2H), 6.56 (d, *J* = 2.6 Hz, 1H), 3.29 (d, *J* = 1.9 Hz, 6H), 3.09 (s, 6H). ^{13}C NMR (126 MHz, CD_2Cl_2) δ 163.60, 162.74, 156.20, 155.31, 155.23, 153.81, 153.04, 152.43, 142.99, 132.75, 131.07, 129.31, 125.98, 125.14, 124.17, 111.85, 111.60, 110.54, 106.59, 101.16, 98.31, 40.37, 28.44, 28.40, 27.79. HRMS (ESI): calculated for $C_{27}H_{26}N_3O_4^+$ $[M]^+$, 456.1918; found, 456.1923.

From precursor **4.6**:

7-(dimethylamino)-2-phenyl-4-((1*E*,3*E*)-4-(*N*-phenylacetamido)buta-1,3-dien-1-yl)chromenylium tetrafluoroborate (**4.6**) (50 mg, 96 μmol, 1.0 equiv) and 1,3-dimethylpyrimidine-2,4,6(1*H*,3*H*,5*H*)-trione (**4.4**) (15 mg, 96 μmol, 1.0 equiv) were added to a dram vial equipped with a stir bar and fitted with a PTFE-lined cap. The solids were dissolved in Ac_2O (0.96 mL) and heated to 110 °C for 10 min. The mixture was cooled to rt and evaporated onto silica gel. The crude product was purified via flash chromatography, eluting with a DCM/EtOH gradient of 0.1% EtOH, 0.2% EtOH, 0.5% EtOH and 1% EtOH to afford **BarbiFlav4** as a shiny dark blue solid (24 mg, 54 μmol, 56%). R_F = 0.21 in 40:1 DCM:MeOH. ^{1}H NMR (500 MHz, CD_2Cl_2) δ 8.09 (d, *J* = 12.2 Hz, 1H), 7.97 – 7.87 (m, 4H), 7.74 (d, *J* = 9.2 Hz, 1H), 7.54 – 7.49 (m, 3H), 7.21 (s, 1H), 6.79 – 6.71 (m, 2H), 6.56 (d, *J* = 2.6 Hz, 1H), 3.29 (d, *J* = 1.9 Hz, 6H), 3.09 (s, 6H). ^{13}C NMR (126 MHz, CD_2Cl_2) δ 163.60, 162.74, 156.20, 155.31, 155.23, 153.81, 153.04, 152.43, 142.99, 132.75, 131.07, 129.31, 125.98, 125.14, 124.17, 111.85, 111.60, 110.54, 106.59, 101.16, 98.31, 40.37, 28.44, 28.40, 27.79. HRMS (ESI): calculated for $C_{27}H_{26}N_3O_4^+$ $[M]^+$, 456.1918; found, 456.1923.

Synthesis of 1,2,3,3-tetramethyl-3*H*-indol-1-ium iodide (**4.13**)

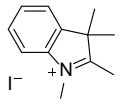

In a two-neck round-bottom flask equipped with a stir bar and fitted with a reflux condenser, 2,3,3-trimethyl-3*H*-indole (2.0 mL, 13 mmol, 1.0 equiv) and iodomethane (0.94 mL, 15 mmol, 6.4 equiv) were dissolved in anhydrous toluene (42 mL) and heated to 80 °C for 24 h. The mixture was cooled to rt and evaporated to remove the solvent. The crude solid was suspended in hexanes and filtered to yield **4.9** as a fluffy purple solid (3.4 g, 11 mmol, 85%). ^{1}H NMR (500 MHz, $CDCl_3$) δ 7.67 – 7.54 (m, 3H), 4.28 (s, 3H), 3.12 (s, 3H), 1.68 (s, 6H). ^{1}H NMR is consistent with the previous report.[68]

Synthesis of 2-((*E*)-4-((*E*)-1,3,3-trimethylindolin-2-ylidene)but-2-en-1-ylidene)-1*H*-indene-1,3(2*H*)-dione (**IndaIndol4**)

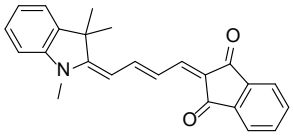

(*E*)-*N*-(3-(1,3-dioxo-1,3-dihydro-2*H*-inden-2-ylidene)prop-1-en-1-yl)-*N*-phenylacetamide (**4.7**) (44 mg, 0.14 mmol, 1.0 equiv), 1,2,3,3-tetramethyl-3*H*-indol-1-ium iodide (**4.13**) (50 mg, 0.17 mmol, 1.2 equiv) and NaOAc (34 mg, 0.42 mmol, 3.0 equiv) were added to a dram vial equipped with a stir bar and fitted with a PTFE-lined cap. The solids were dissolved in *n*-BuOH (4 mL) and the mixture was heated to 80 °C for 50 min. The mixture was cooled to rt and evaporated onto silica gel. The crude product was purified via flash chromatography, eluting with a DCM/MeOH gradient of 0% MeOH, 0.1% MeOH and 1% MeOH to afford **IndaIndol4** as a shiny purple solid (40 mg, 0.11 mmol, 81%). ^{1}H NMR (500 MHz, $CDCl_3$) δ 7.83 (ddd, *J* = 4.9, 3.4, 1.2 Hz, 2H), 7.78 – 7.71 (m, 1H), 7.66 – 7.58 (m, 4H), 7.33 – 7.26 (m, 2H), 7.25 (d, *J* = 1.3 Hz, 1H), 7.07 (td, *J* = 7.4, 1.0 Hz, 1H), 6.87 (d, *J* = 7.9 Hz, 1H), 5.88 (d, *J* = 12.6 Hz, 1H), 3.35 (s, 3H), 1.65 (s, 6H). ^{1}H NMR is consistent with the previous report.[32]

Synthesis of 1,3-dimethyl-5-((*E*)-4-((*E*)-1,3,3-trimethylindolin-2-ylidene)but-2-en-1-ylidene)pyrimidine-2,4,6(1*H*,3*H*,5*H*)-trione (**BarbIndol4**)

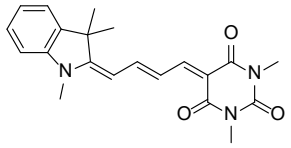

(*E*)-*N*-(3-(1,3-dimethyl-2,4,6-trioxotetrahydropyrimidin-5(2*H*)-ylidene)prop-1-en-1-yl)-*N*-phenylacetamide (**4.8**) (45 mg, 0.14 mmol, 1.0 equiv), 1,2,3,3-tetramethyl-3*H*-indol-1-ium iodide (**4.13**) (50 mg, 0.17 mmol, 1.2 equiv) and NaOAc (34 mg, 0.42 mmol, 3.0 equiv) were added to a dram vial equipped with a stir bar and fitted with a PTFE-lined cap. The solids were dissolved in *n*-BuOH (4 mL) and the mixture was heated to 80 °C for 50 min. The mixture was cooled to rt and evaporated onto silica gel. The crude product was purified via flash chromatography, eluting with a DCM/MeOH gradient of 0% MeOH, 0.01% MeOH and 0.1% MeOH to afford **BarbIndol4** as a shiny pink solid (29 mg, 78 μmol, 56%). ^{1}H NMR (500 MHz, $CDCl_3$) δ 8.18 – 8.10 (m, 1H), 7.83 (d, *J* = 12.2 Hz, 2H), 7.34 – 7.28 (m, 2H), 7.17 – 7.10 (m, 1H), 6.92 (d, *J* = 8.1 Hz, 1H), 5.91 (dd, *J* = 13.5, 7.3 Hz, 1H), 3.43 – 3.36 (m, 9H), 1.65 (s, 6H). ^{1}H NMR is consistent with the previous report.[35]

4.5.5. ^{1}H NMR Spectra

^{1}H NMR (500 MHz, CD_2Cl_2) of **4.6**

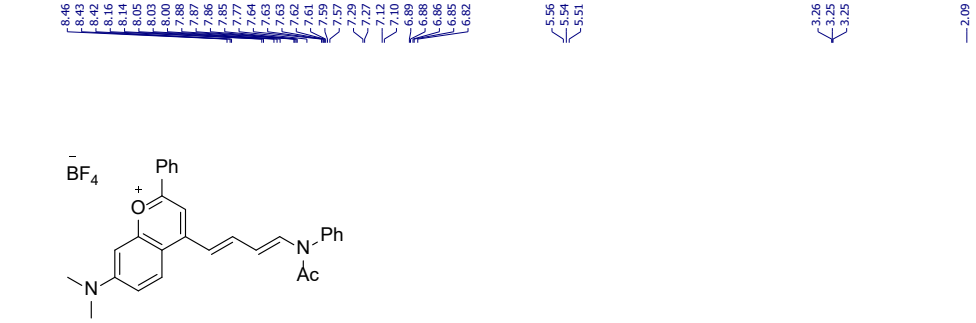

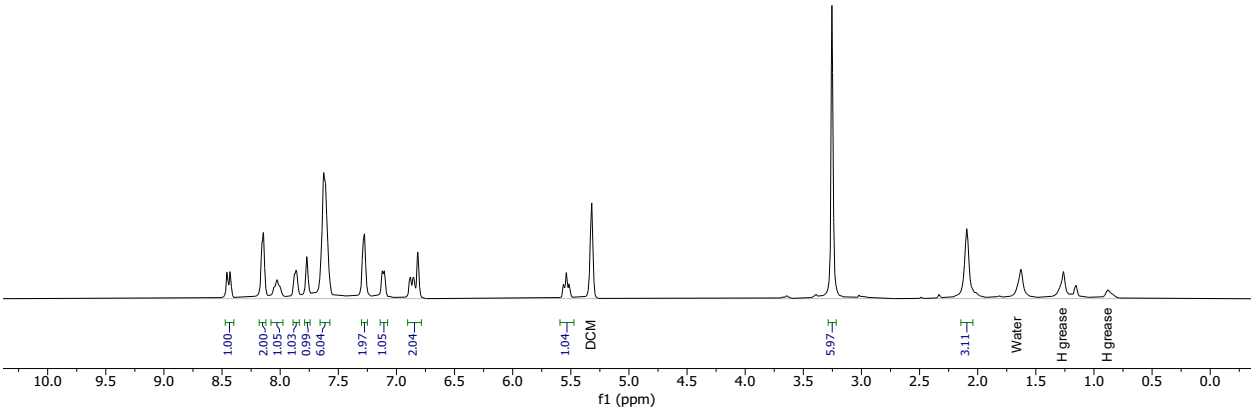

^{1}H NMR (500 MHz, CD_2Cl_2) of **MalonoFlav4**

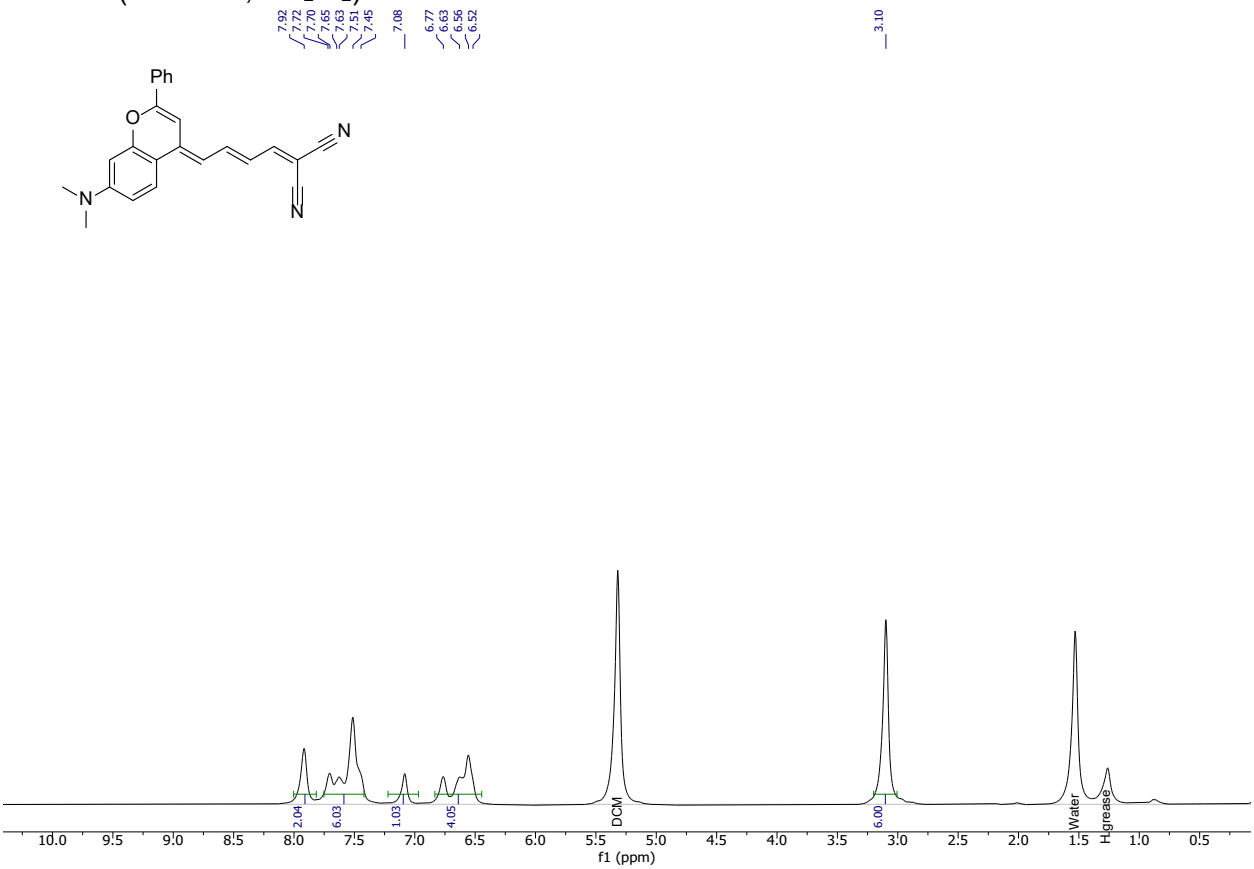

^{1}H NMR (500 MHz, $CDCl_3$) of **4.7**

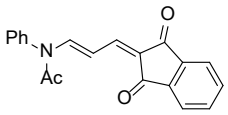

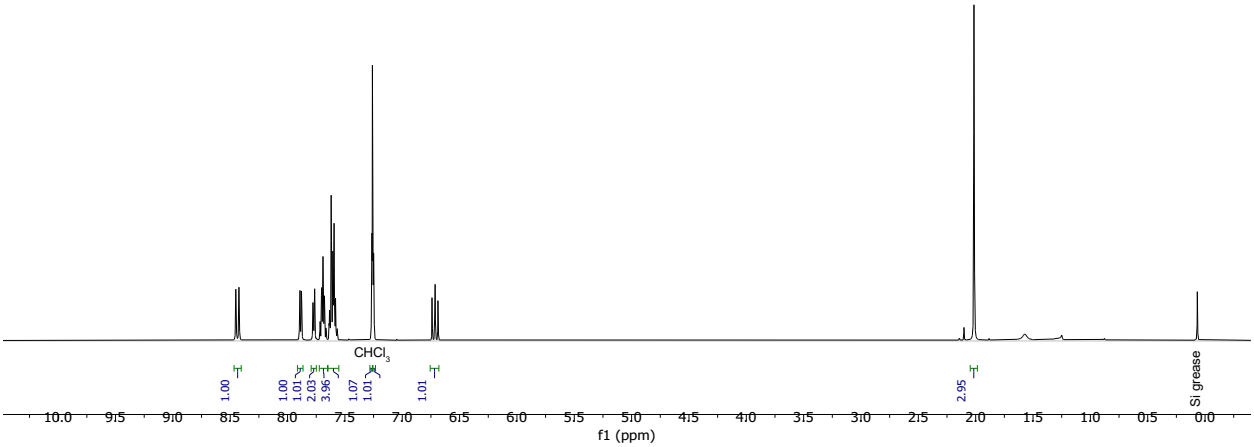

^{1}H NMR (500 MHz, CD_2Cl_2) of **IndaFlav4**

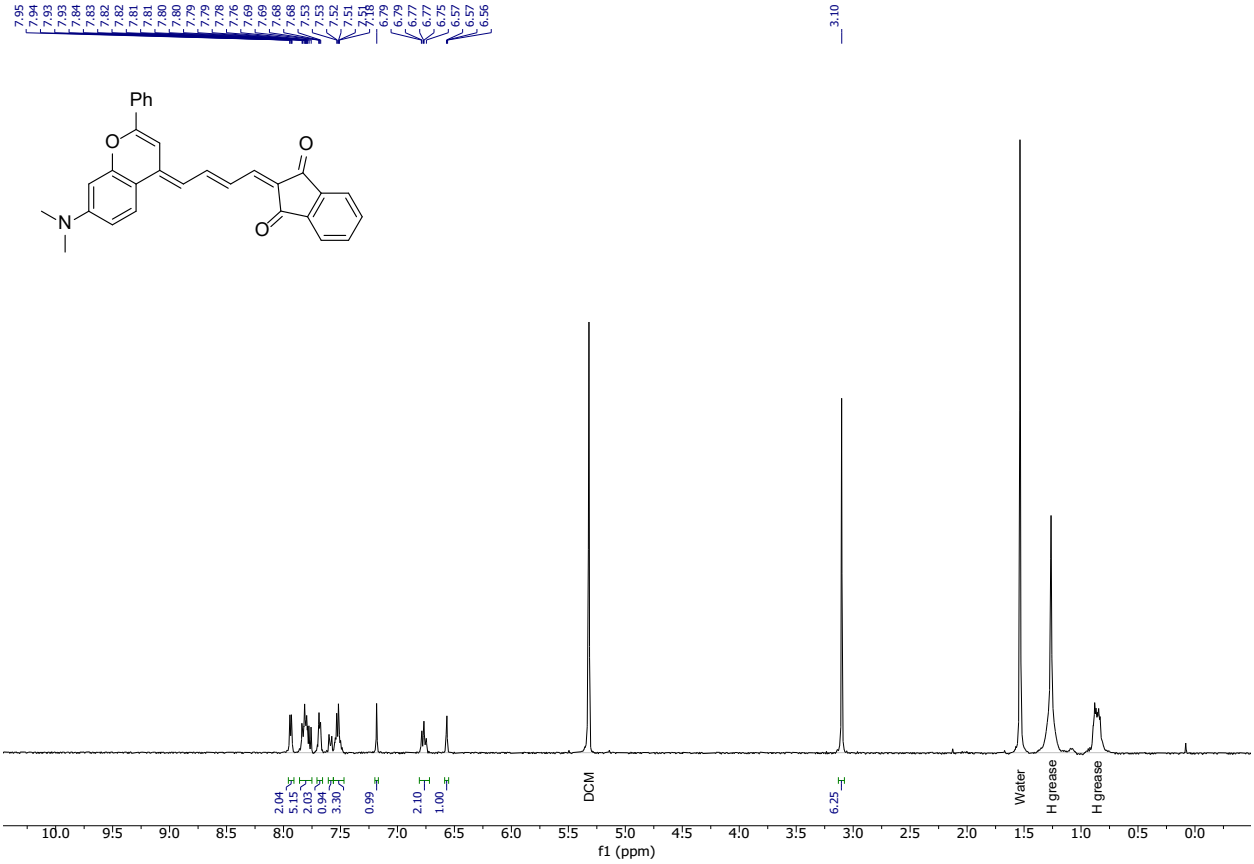

^{1}H NMR (500 MHz, $CDCl_3$) of **4.8**

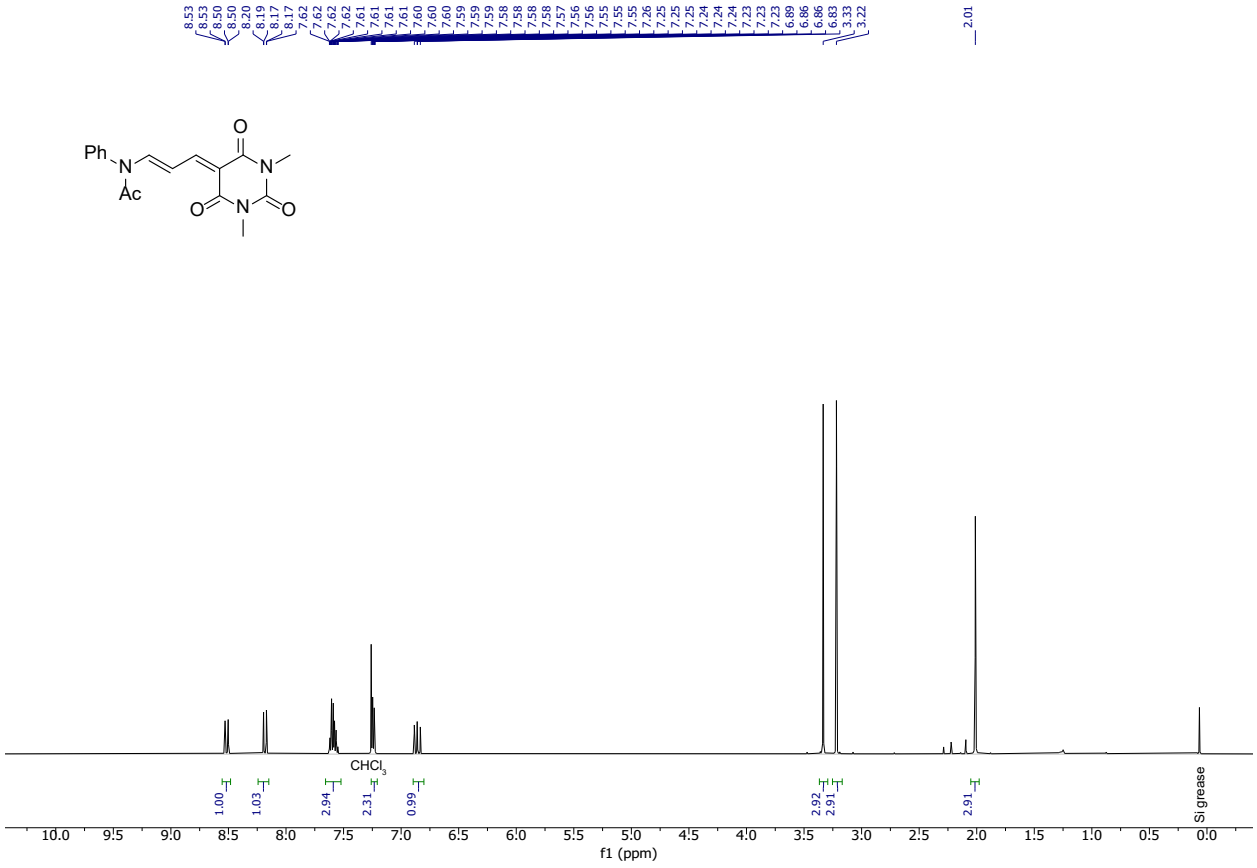

^{1}H NMR (500 MHz, CD_2Cl_2) of **BarbiFlav4**

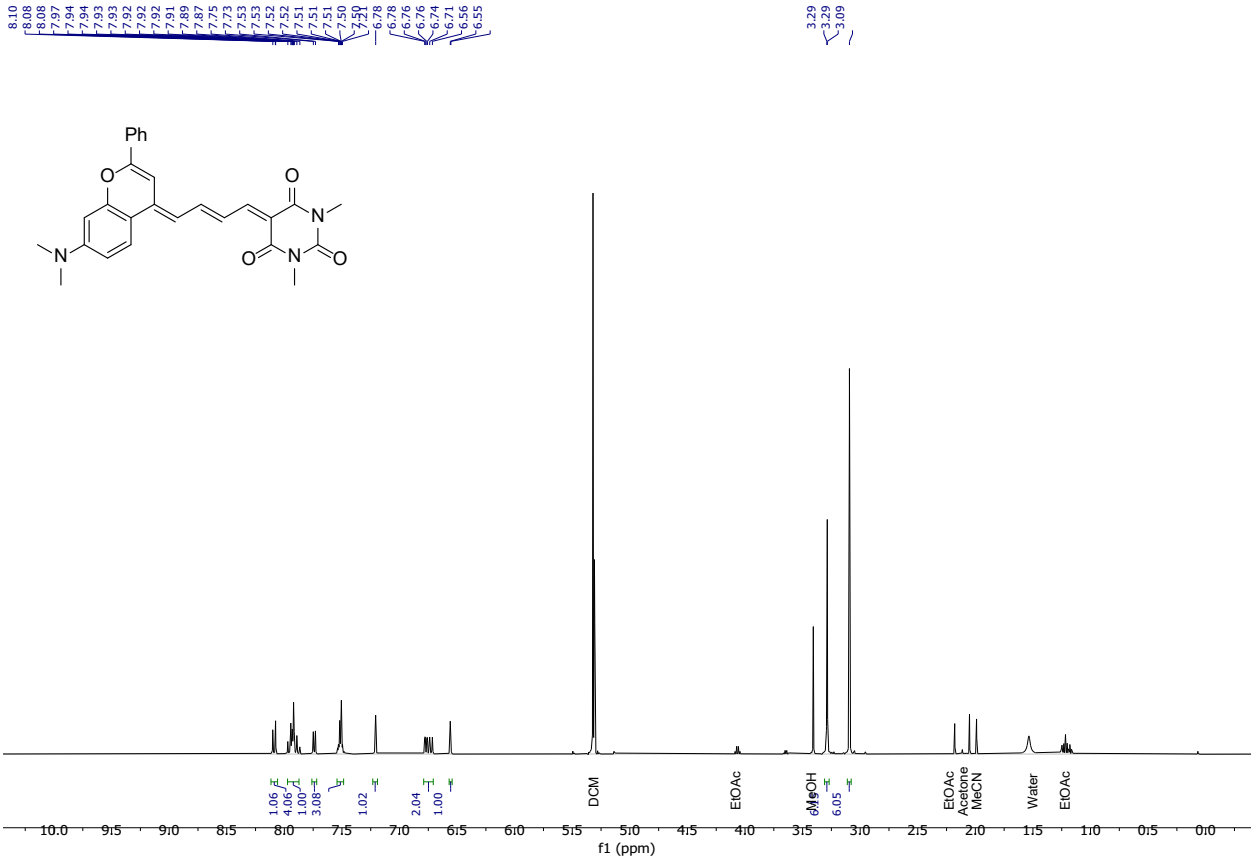

4.5.6. ^{13}C NMR Spectra

^{13}C NMR (126 MHz, CD_2Cl_2) of **4.6**

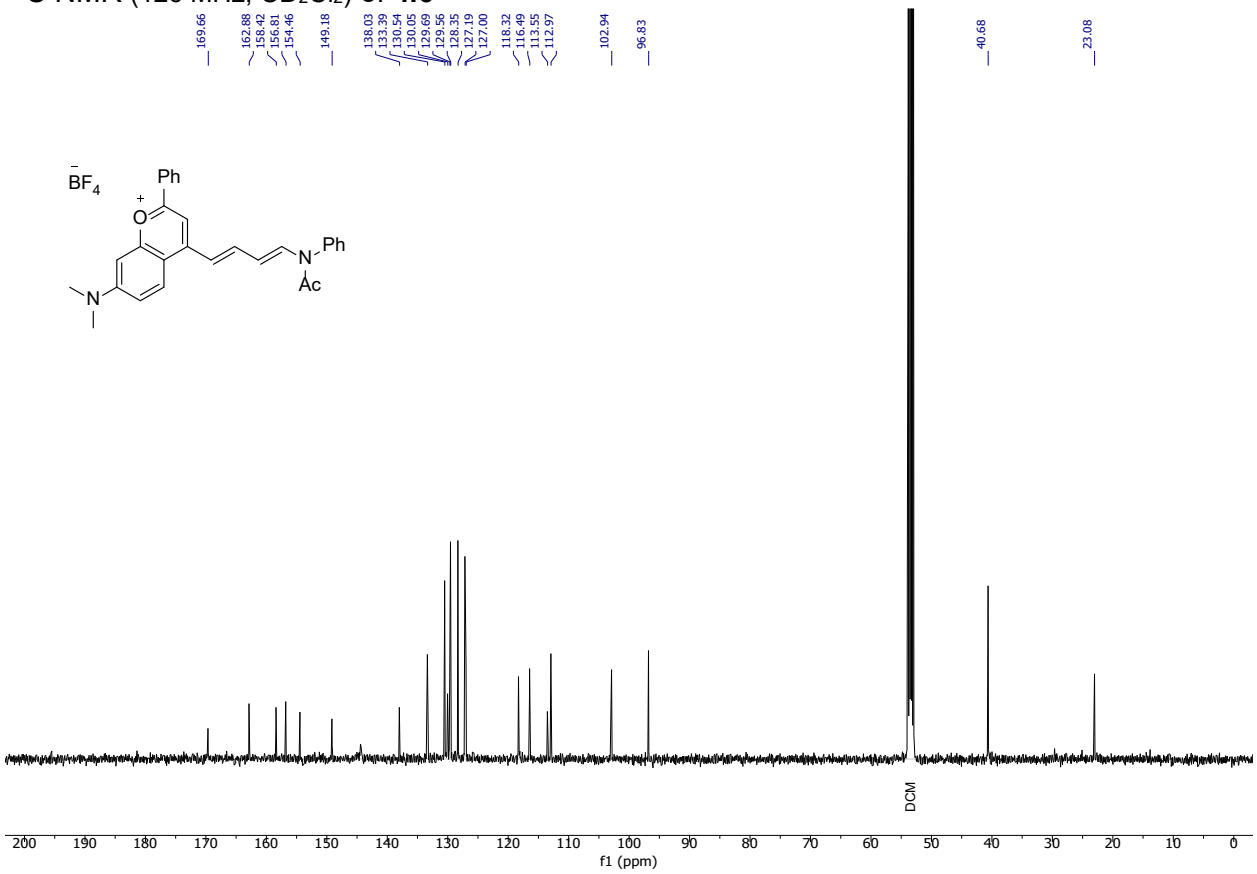

^{13}C NMR (126 MHz, CD_2Cl_2) of **MalonoFlav4**

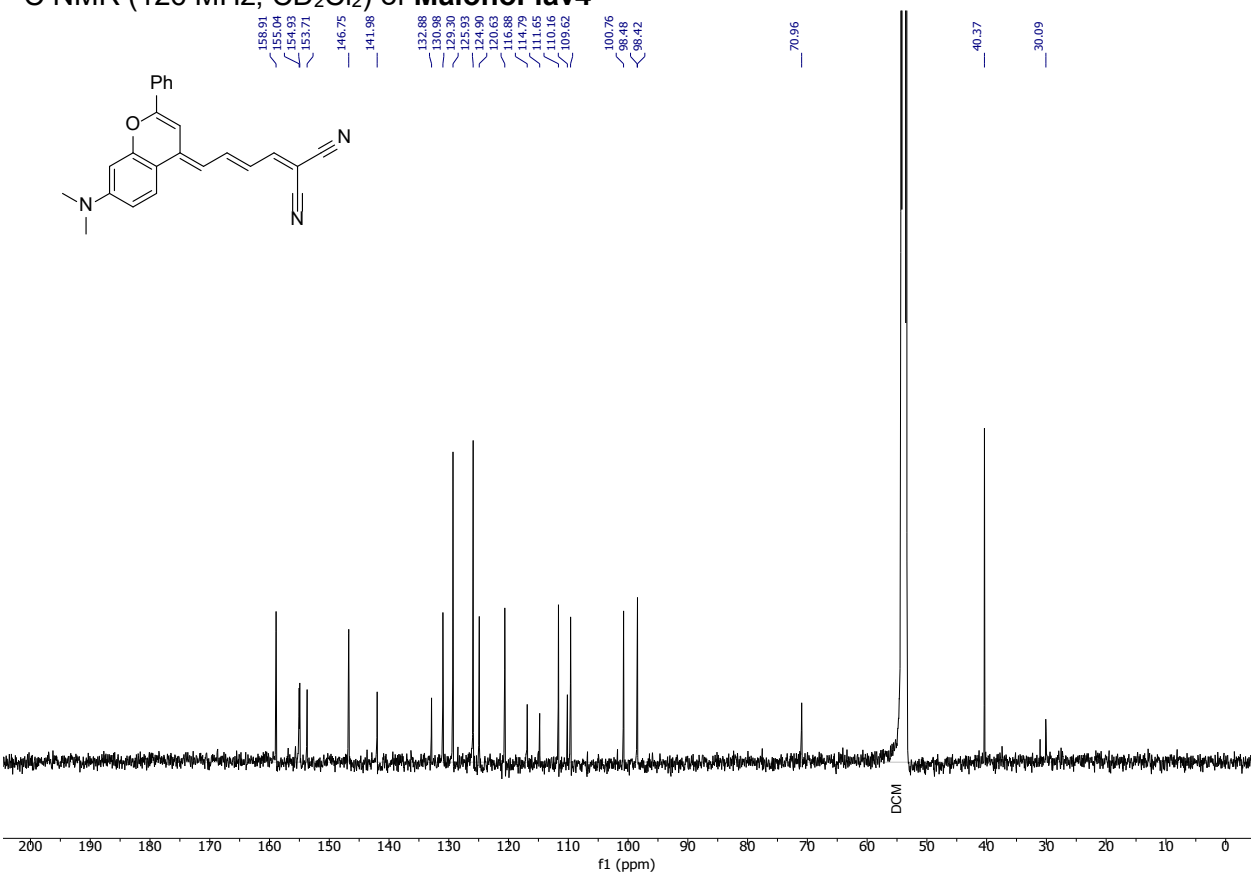

^{13}C NMR (126 MHz, $CDCl_3$) of **4.7**

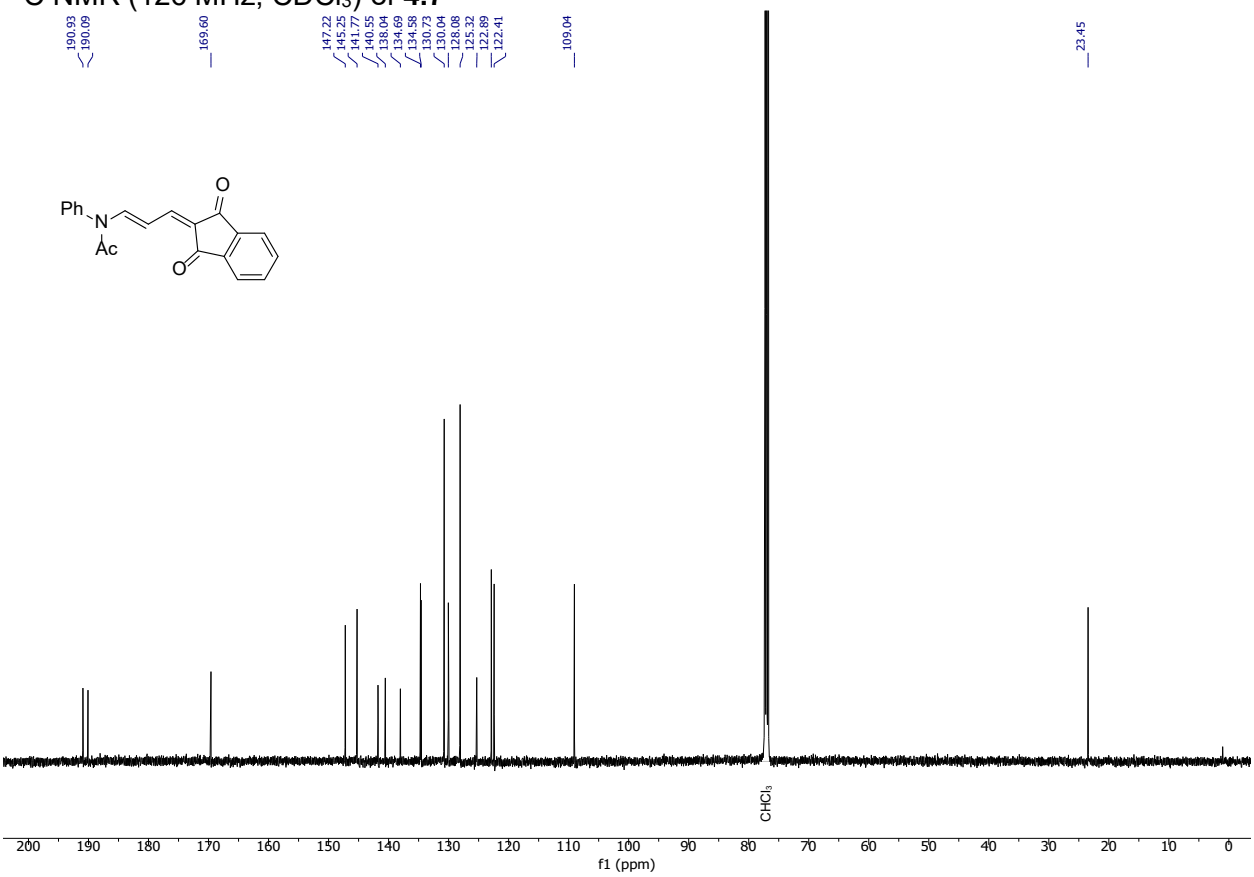

^{13}C NMR (126 MHz, CD_2Cl_2) of **IndaFlav4**

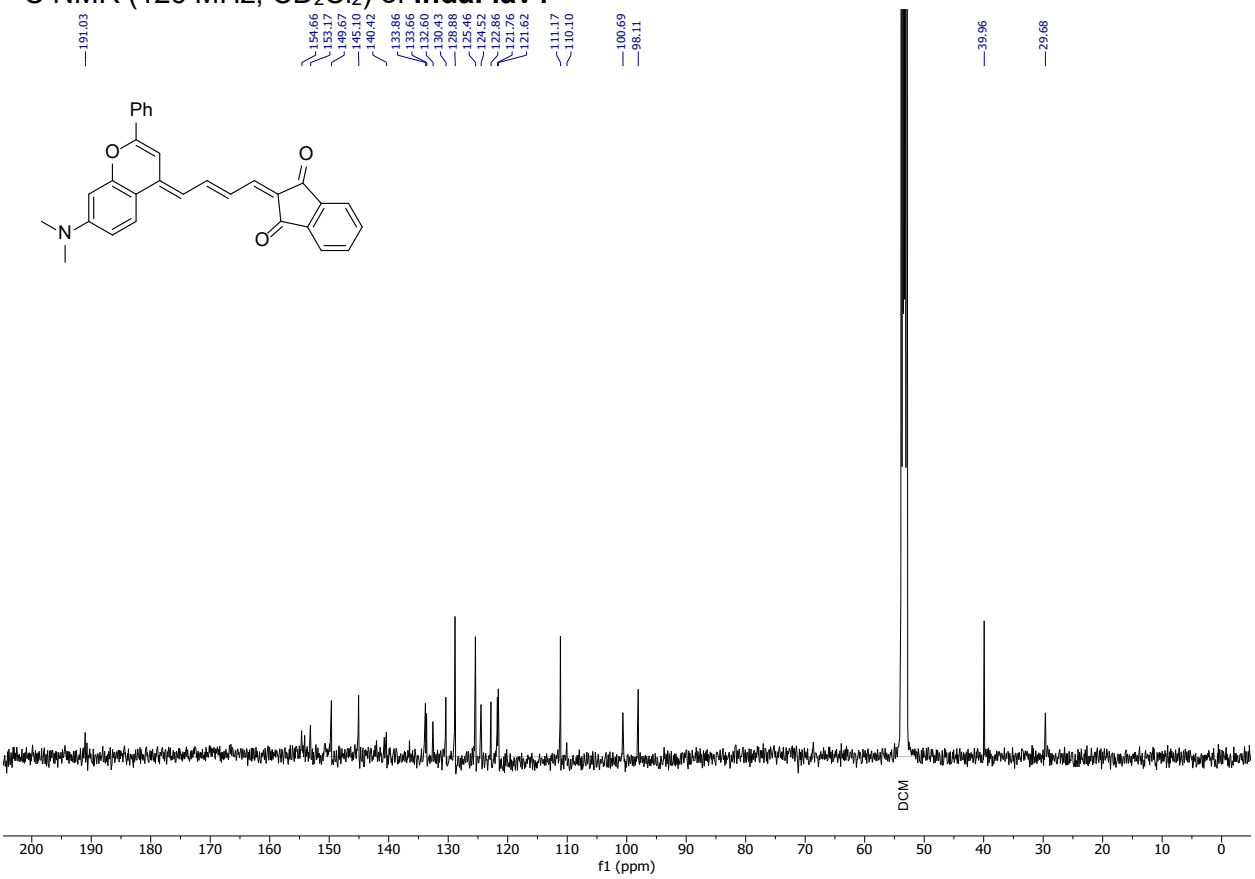

^{13}C NMR (126 MHz, $CDCl_3$) of **4.8**

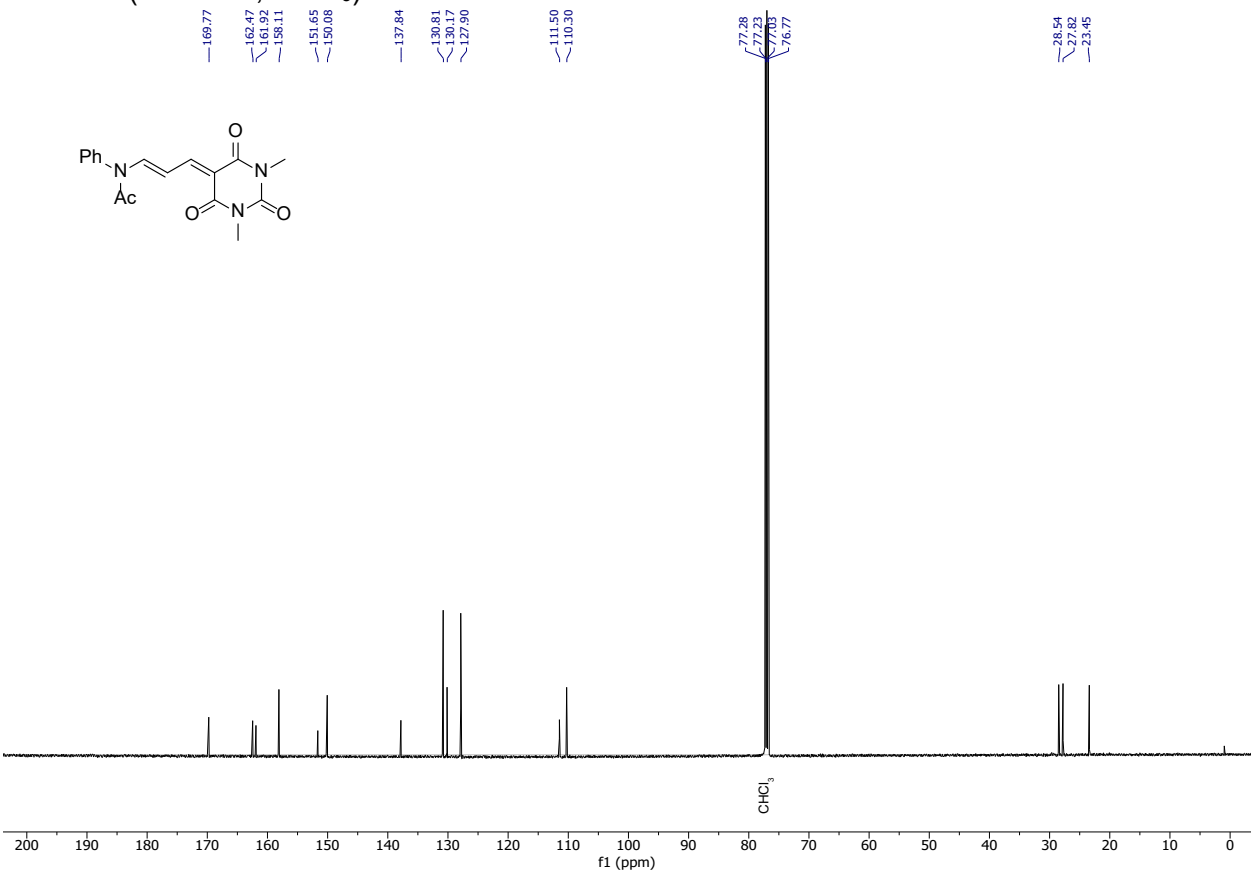

^{13}C NMR (126 MHz, CD_2Cl_2) of **BarbiFlav4**

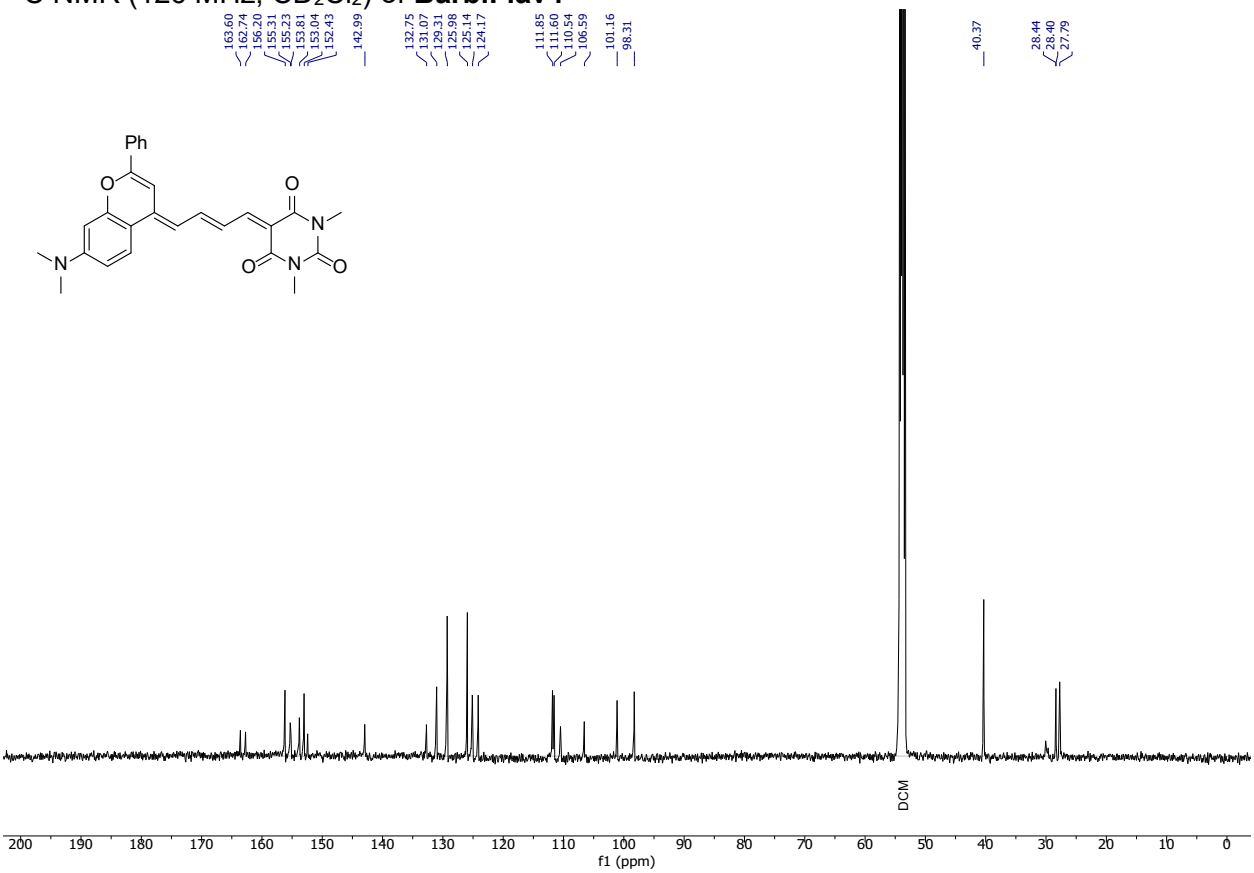

4.5.7. ^{19}F NMR Spectra

^{19}F NMR (565 MHz, CD_2Cl_2) of **4.6**

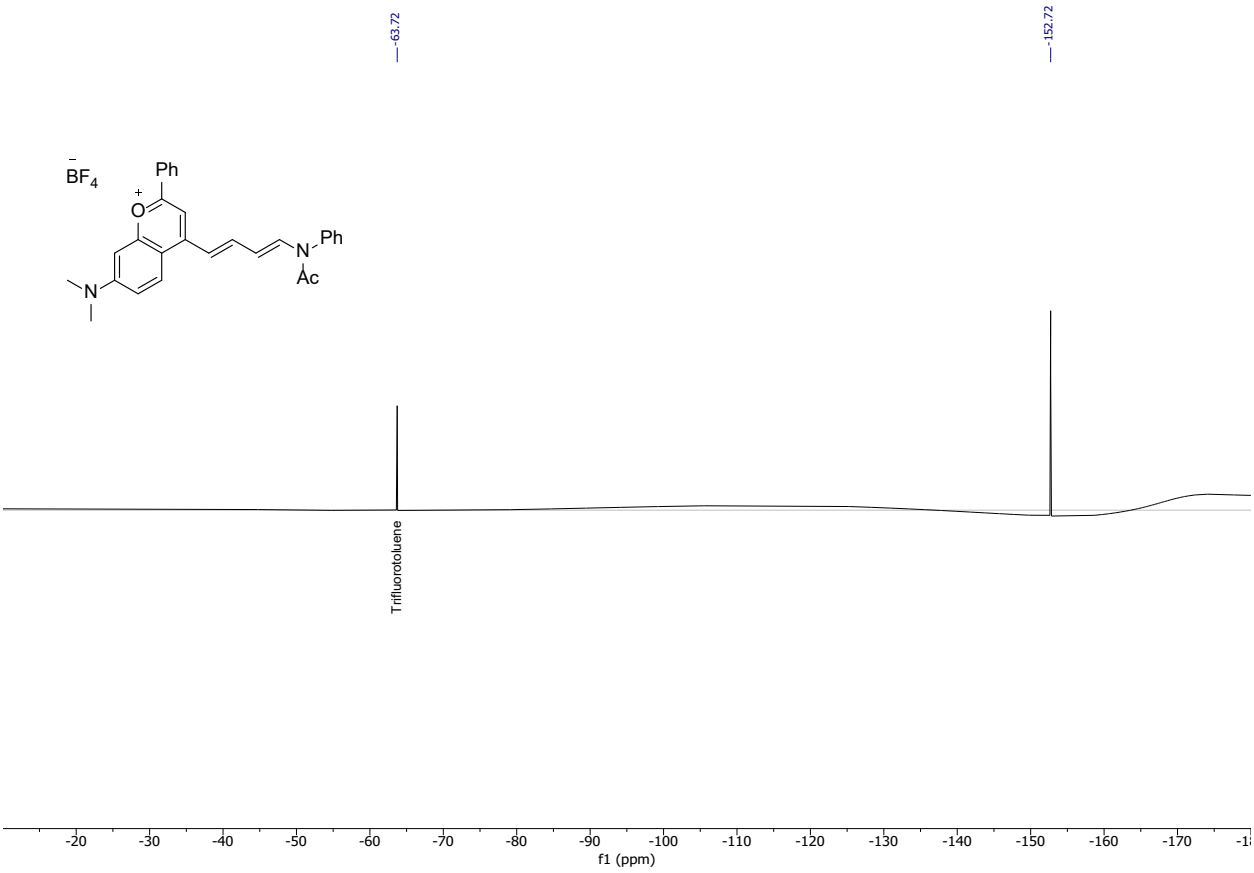

4.5.8. HRMS Spectra

HRMS of **4.6**

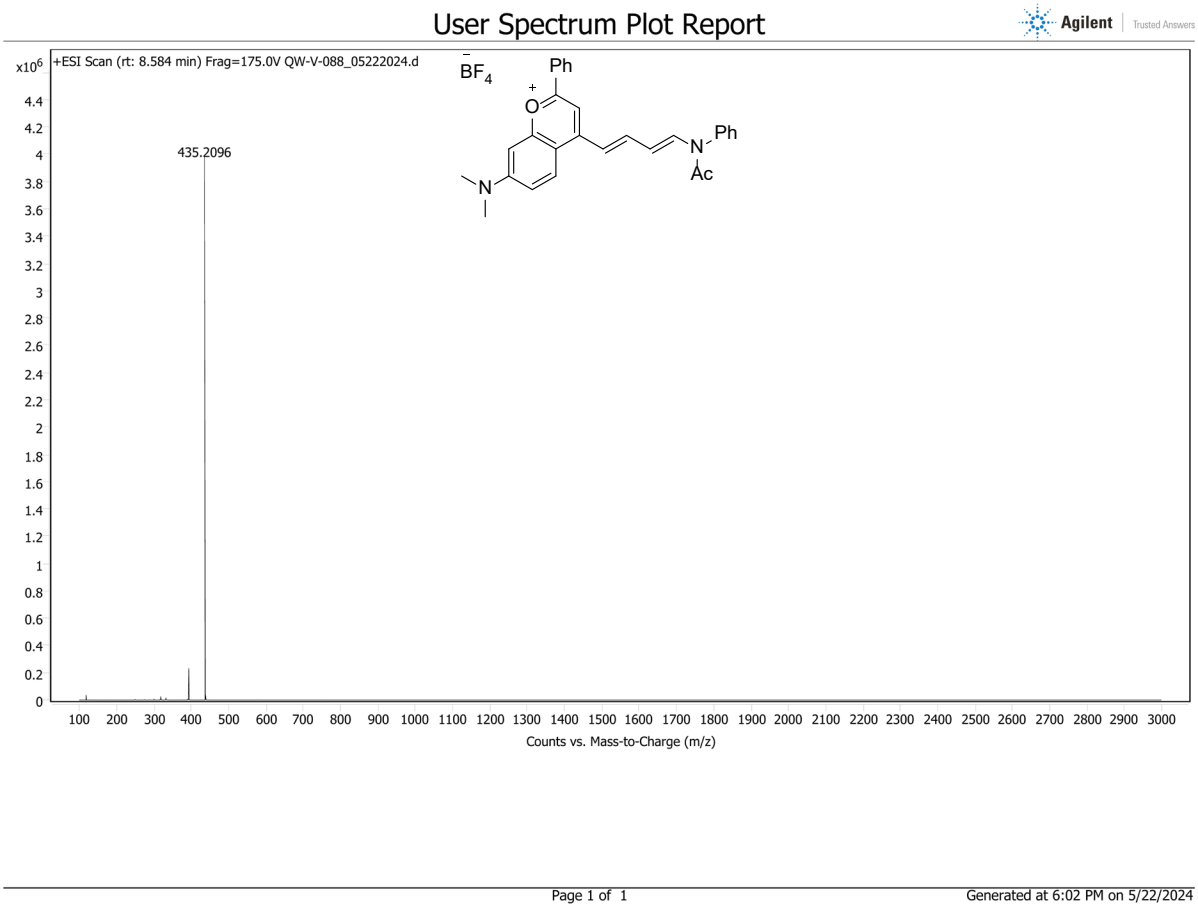

HRMS of **MalonoFlav4**

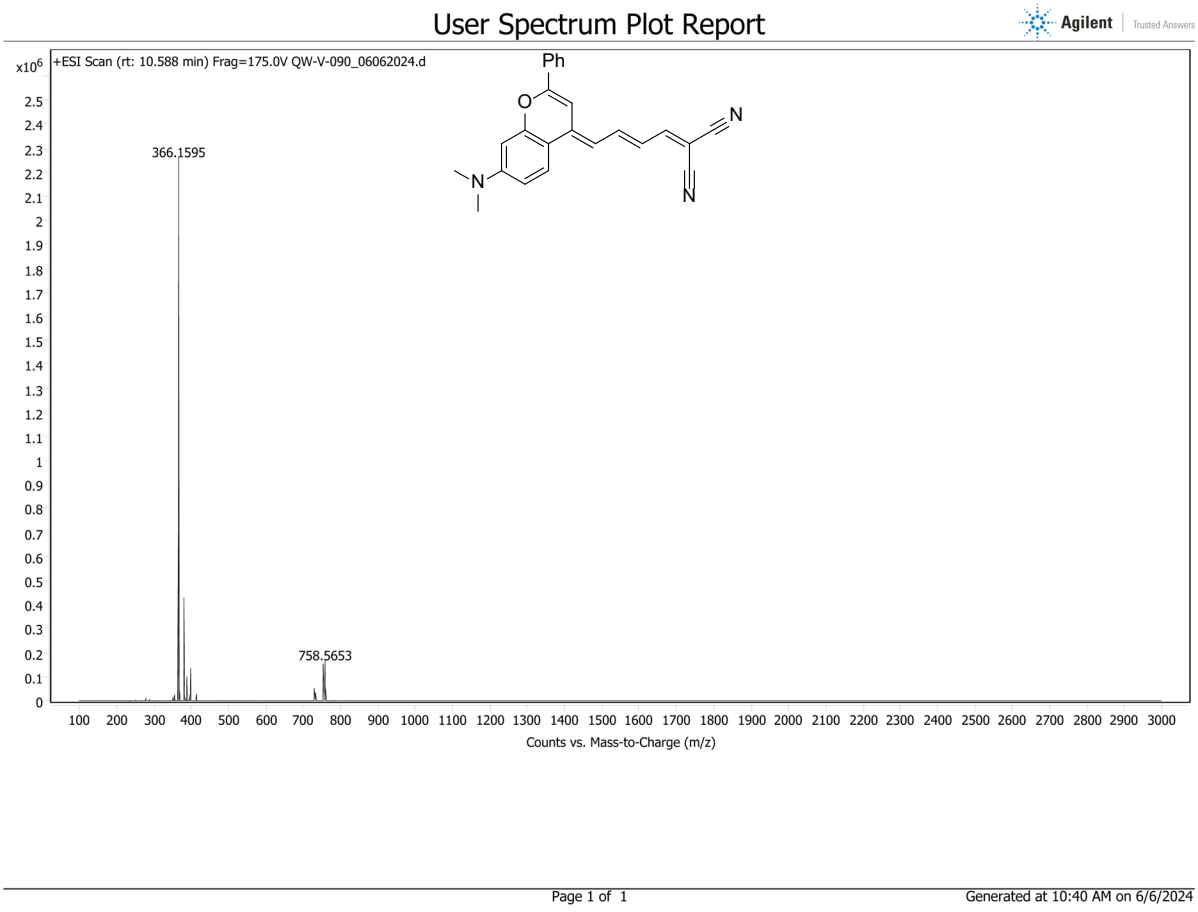

HRMS of **4.7**

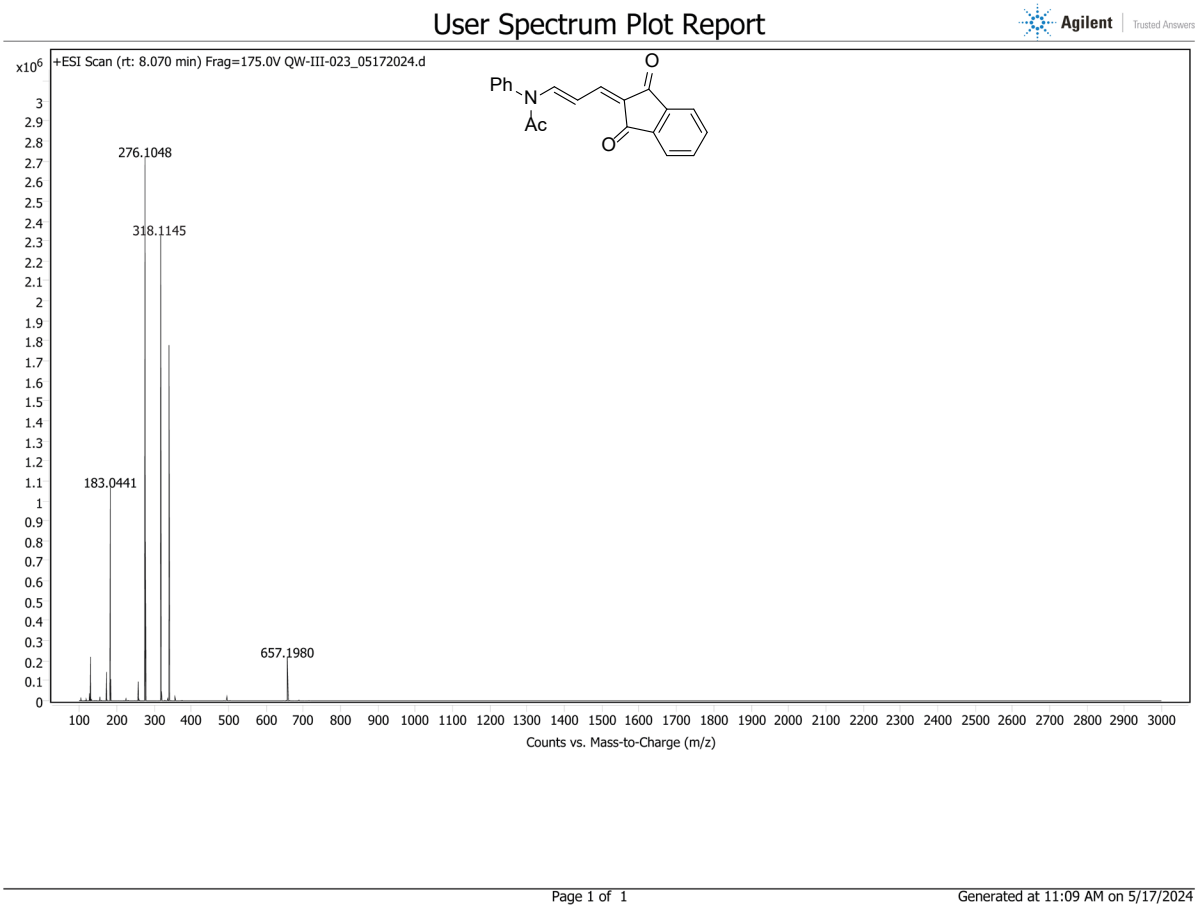
User Spectrum Plot Report
Agilent
Trusted Answers
+ESI Scan (rt: 8.070 min) Frag=175.0V QW-III-023_05172024.d
x10^6
276.1048
318.1145
183.0441
657.1980
Ph
N
Ac
O
O
Counts vs. Mass-to-Charge (m/z)
Page 1 of 1
Generated at 11:09 AM on 5/17/2024

HRMS of **IndaFlav4**

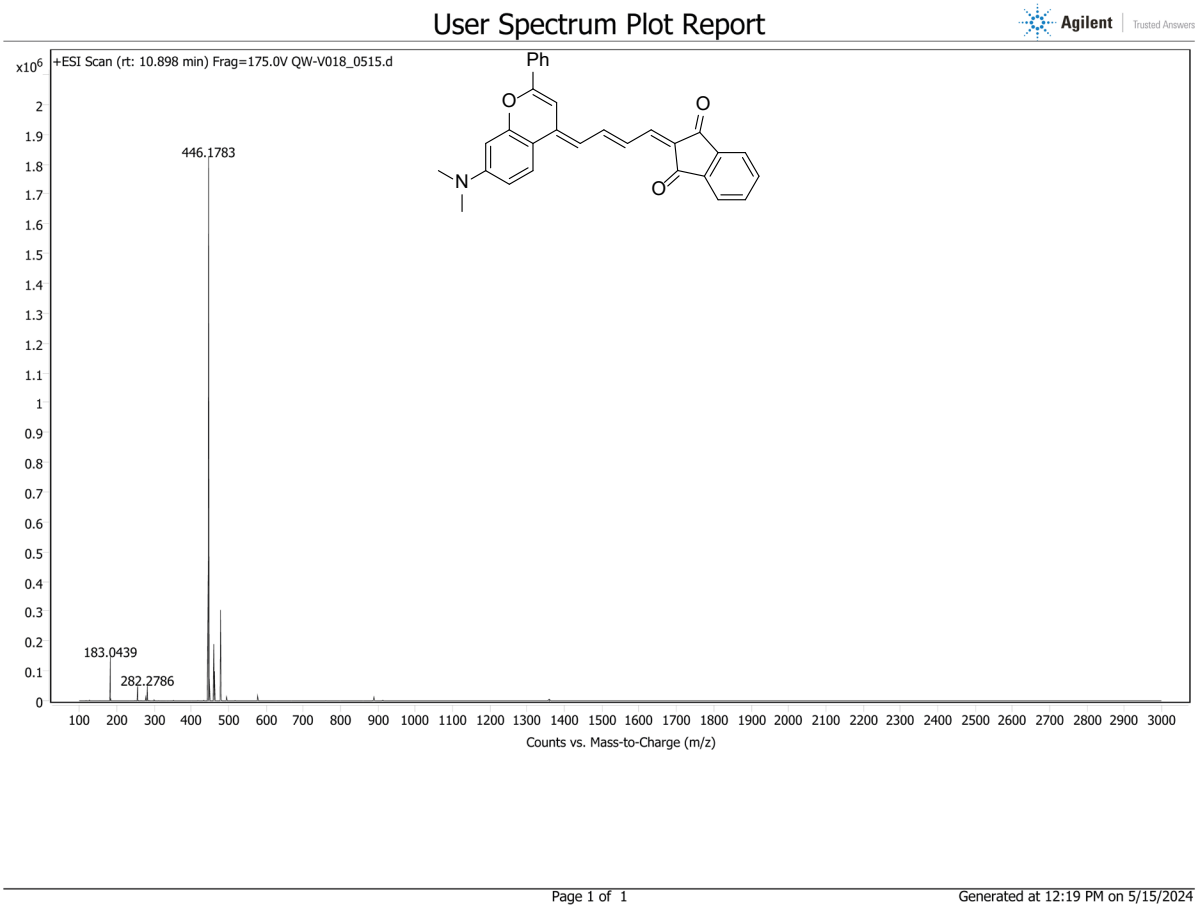

HRMS of **4.8**

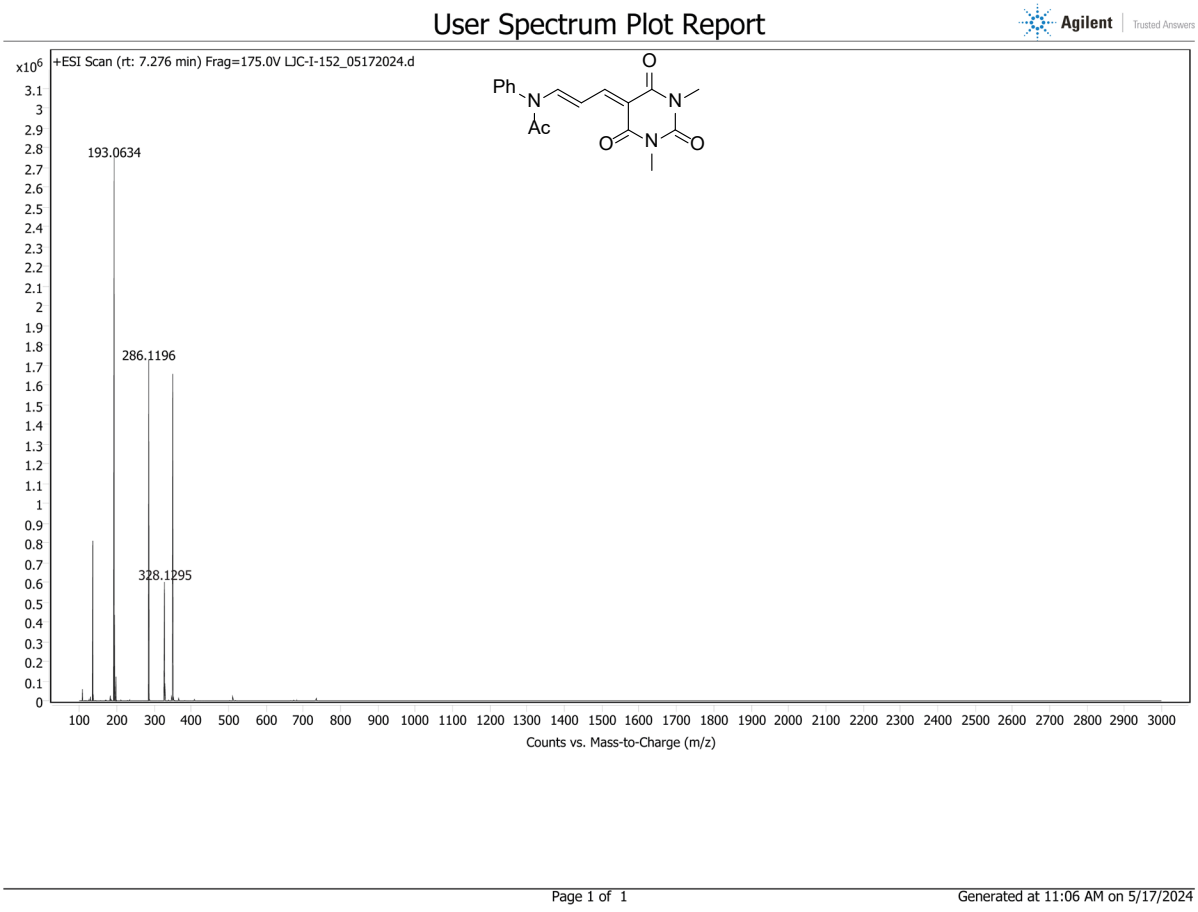
User Spectrum Plot Report
Agilent
Trusted Answers
+ESI Scan (rt: 7.276 min) Frag=175.0V LJC-I-152_05172024.d
x10^6
193.0634
286.1196
328.1295
Counts vs. Mass-to-Charge (m/z)
Page 1 of 1
Generated at 11:06 AM on 5/17/2024

HRMS of **BarbiFlav4**

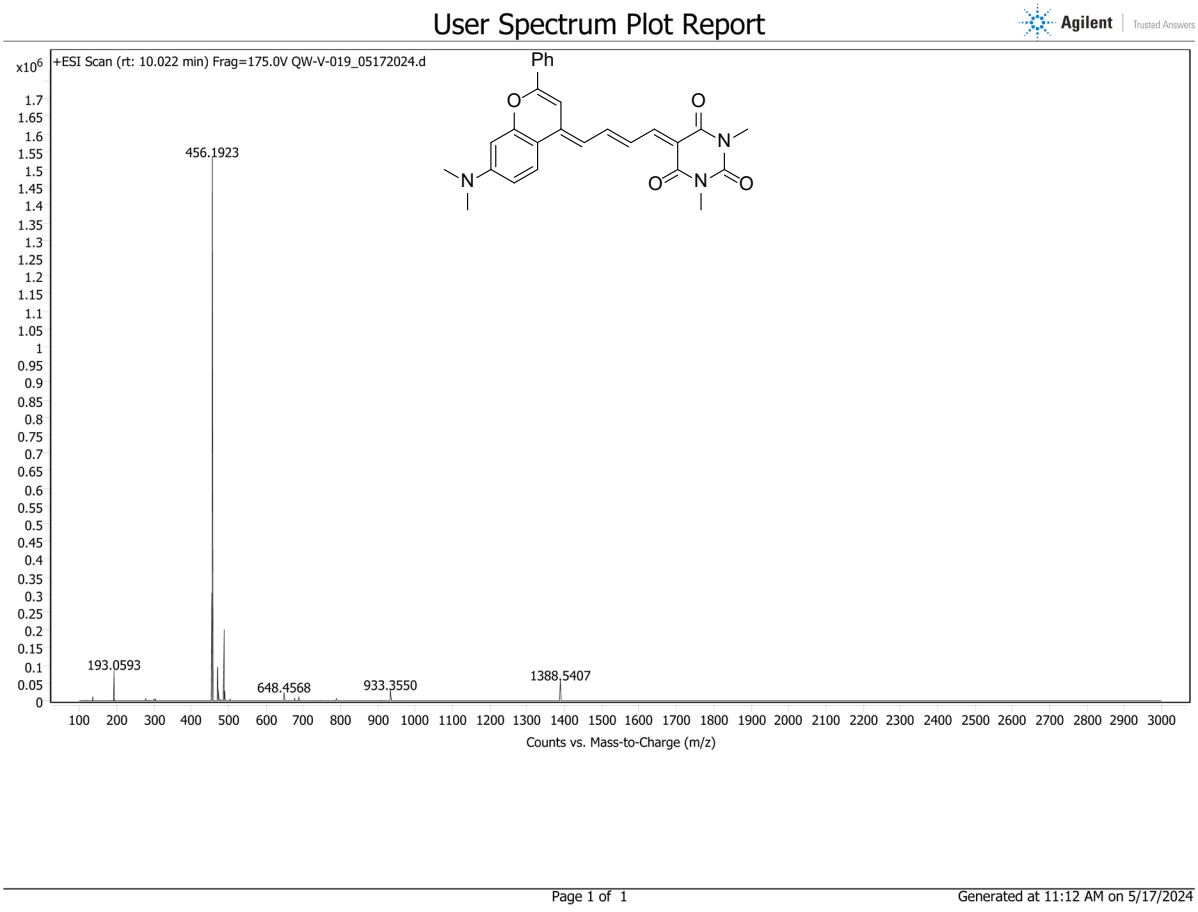

4.6 References

(1) Lichtman, J. W.; Conchello, J.-A. Fluorescence Microscopy. *Nat. Methods* **2005**, *2* (12), 910–919.

(2) Fei, K.; Zhang, J.; Yuan, J.; Xiao, P. Present Application and Perspectives of Organoid Imaging Technology. *Bioengineering* **2022**, *9* (3), 121.

(3) Lavis, L. D.; Raines, R. T. Bright Building Blocks for Chemical Biology. *ACS Chem. Biol.* **2014**, *9* (4), 855–866.

(4) Martin, A.; Rivera-Fuentes, P. A General Strategy to Develop Fluorogenic Polymethine Dyes for Bioimaging. *Nat. Chem.* **2024**, *16*, 28–35.

(5) Yuan, L.; Lin, W.; Zheng, K.; He, L.; Huang, W. Far-Red to Near Infrared Analyte-Responsive Fluorescent Probes Based on Organic Fluorophore Platforms for Fluorescence Imaging. *Chem. Soc. Rev.* **2013**, *42*, 622–661..

(6) Samanta, S.; Lai, K.; Wu, F.; Liu, Y.; Cai, S.; Yang, X.; Qu, J.; Yang, Z. Xanthene, Cyanine, Oxazine, and BODIPY: The Four Pillars of the Fluorophore Empire for Super-Resolution Bioimaging. *Chem. Soc. Rev.* **2023**, *52*, 7197–7261.

(7) Ishchenko, A. Structure and Spectral-Luminescent Properties of Polymethine Dyes. *Russ. Chem. Rev.* **1991**, *60*, 865–884.

(8) Bricks, J. L.; Kachkovskii, A. D.; Slominskii, Y. L.; Gera-sov, A. O.; Popov, S. V. Molecular Design of Near Infrared Polymethine Dyes: A Review. *Dyes Pigm.* **2015**, *121*, 238–255.

(9) Gorka, P.; Nani, R. R.; Schnermann, M. J. Cyanine Polyene Reactivity: Scope and Biomedical Applications. *Org. Biomol. Chem.* **2015**, *13*, 7584–7598.

(10) Chen, X.; Li, J.; Roy, S.; Ullah, Z.; Huang, H.; Yu, C.; Wang, X.; Wang, H.; Zhang, Y.; Guo, B. Development of Polymethine Dyes for NIR-II Fluorescence Imaging and Therapy. *Adv. Healthcare Mater.* **2024**, *2304506*.

(11) Pascal, S.; David, S.; Andraud, C.; Maury, O. Near-Infrared Dyes for Two-Photon Absorption in the Short-Wavelength Infrared: Strategies Towards Optical Power Limiting. *Chem. Soc. Rev.* **2021**, *50*, 6613–6658.

(12) Chen, W.; Liu, T.; Zou, J.; Zhang, D.; Tse, M. K.; Tsang, S.-W.; Luo, J.; Jen, A. K.-Y. Push–Pull Heptamethines Near the Cyanine Limit Exhibiting Large Quadratic Electro-Optic Effect. *Adv. Mater.* **2024**, *36*, 2306089.

(13) Bouit, P.-A.; Aronica, C.; Toupet, L.; Le Guennic, B.; Andraud, C.; Maury, O. Continuous Symmetry Breaking Induced by Ion Pairing Effect in Heptamethine Cyanine Dyes: Beyond the Cyanine Limit. *J. Am. Chem. Soc.* **2010**, *132*, 4328–4335.

(14) Pascal, S.; Haefele, A.; Monnereau, C.; Charaf-Eddin, A.; Jacquemin, D.; Le Guennic, B.; Andraud, C.; Maury, O. Expanding the Polymethine Paradigm: Evidence for the Contribution of a Bis-Dipolar Electronic Structure. *J. Phys. Chem. A* **2014**, *118*, 4038–4047.

(15) Terenziani, F.; Przhonska, O. V.; Webster, S.; Padilha, L. A.; Slominsky, Y. L.; Davydenko, I. G.; Gerasov, A. O.; Kovtun, Y. P.; Shandura, M. P.; Kachkovski, A. D.; Hagan, D. J.; Van Stryland, E. W.; Painelli, A. Essential-State Model for Polymethine Dyes: Symmetry Breaking and Optical Spectra. *J. Phys. Chem. Lett.* **2010**, *1*, 1800–1804.

(16) van der Wal, S.; Kuil, J.; Valentijn, A. R. P. M.; Van Leeuwen, F. W. B. Synthesis and Systematic Evaluation of Symmetric Sulfonated Centrally C–C Bonded Cyanine Near-Infrared Dyes for Protein Labeling. *Dyes Pigm.* **2016**, *132*, 7–19.

(17) M. P. Luciano, S. N. Crooke, S. Nourian, I. Dingle, R. R. Nani, G. Kline, N. L. Patel, C. M. Robinson, S. Difilippantonio, J. D. Kalen, M. G. Finn, M. J. Schnermann, *ACS Chem. Biol.* **2019**, *14*, 934-940.

(18) Wang, Y.; Weng, J.; Lin, J.; Ye, D.; Zhang, Y. NIR Scaffold Bearing Three Handles for Biocompatible Sequential Click Installation of Multiple Functional Arms. *J. Am. Chem. Soc.* **2020**, *142*, 2787–2794.

(19) Li, D.-H.; Schreiber, C. L.; Smith, B. D. Sterically Shielded Heptamethine Cyanine Dyes for Bioconjugation and High Performance Near-Infrared Fluorescence Imaging. *Angew. Chem. Int. Ed.* **2020**, *59*, 12154–12161.

(20) Jia, S.; Lin, E. Y.; Mobley, E. B.; Lim, I.; Guo, L.; Kallepu, S.; Low, P. S.; Sletten, E. M. Water-Soluble Chromenylium Dyes for Shortwave Infrared Imaging in Mice. *Chem.* **2023**, *9*, 3648–3665.

(21) Pascal, S.; Haefele, A.; Monnereau, C.; Charaf-Eddin, A.; Jacquemin, D.; Le Guennic, B.; Maury, O.; Andraud, C. On the Versatility of Electronic Structures in Polymethine Dyes. *Proc. SPIE* **2014**, *9253*, 92531A.

(22) Tolbert, L. M.; Zhao, X. Beyond the Cyanine Limit: Peierls Distortion and Symmetry Collapse in a Polymethine Dye. *J. Am. Chem. Soc.* **1997**, *119*, 3253–3258.

(23) Li, D.-H.; Smith, B. D. Supramolecular Mitigation of the Cyanine Limit Problem. *J. Org. Chem.* **2022**, *87*, 5893–5903.

(24) Yang, J.; Wang, K.; Zheng, Y.; Piao, Y.; Wang, J.; Tang, J.; Shen, Y.; Zhou, Z. Molecularly Precise, Bright, Photostable, and Biocompatible Cyanine Nanodots as Alternatives to Quantum Dots for Biomedical Applications. *Angew. Chem. Int. Ed.* **2022**, *61*, e202202128.

(25) Pengshung, M.; Cosco, E. D.; Zhang, Z.; Sletten, E. M. Counterion Pairing Effects on a Flavylium Heptamethine Dye. *Photochem. Photobiol.* **2022**, *98*, 303–310.

(26) Kulinich, V.; Ishchenko, A. A. Design and Photonics of Merocyanine Dyes. *Chem. Rec.* **2023**, e202300262.

(27) Mustroph, H. Merocyanine Dyes. *Phys. Sci. Rev.* **2022**, *7*, 143–158.

(28) Kulinich, V.; Ishchenko, A. A. Merocyanine Dyes: Synthesis, Structure, Properties and Applications. *Russ. Chem. Rev.* **2009**, *78*, 141–164.

(29) Parthasarathy, V.; Pandey, R.; Stolte, M.; Ghosh, S.; Castet, F.; Würthner, F.; Das, P. K.; Blanchard-Desce, M. Combination of Cyanine Behaviour and Giant Hyperpolarisability in Novel Merocyanine Dyes: Beyond the Bond Length Alternation (BLA) Paradigm. *Chem. Eur. J.* **2015**, *21*, 14211–14217.

(30) Mustroph, H.; Mistol, J.; Senns, B.; Keil, D.; Findeisen, M.; Hennig, L. Relationship between the Molecular Structure of Merocyanine Dyes and the Vibrational Fine Structure of Their Electronic Absorption Spectra. *Angew. Chem. Int. Ed.* **2009**, *48*, 8773–8775.

(31) Würthner, F.; Archetti, G.; Schmidt, R.; Kuball, H.-G. Solvent Effect on Color, Band Shape, and Charge-Density Distribution for Merocyanine Dyes Close to the Cyanine Limit. *Angew. Chem. Int. Ed.* **2008**, *47*, 4529–4532.

(32) Kulinich, V.; Derevyanko, N. A.; Ishchenko, A. A. Synthesis and Spectral Properties of Malononitrile-Based Merocyanine Dyes. *Russ. Chem. Bull.* **2005**, *54*, 2820–2830.

(33) Ishchenko, A.; Kulinich, A. V.; Bondarev, S. L.; Knyukshto, V. N. Electronic Structure and Fluorescent Properties of Malononitrile-Based Merocyanines with Positive and Negative Solvatochromism. *Opt. Spectrosc.* **2008**, *104*, 57–68.

(34) shchenko, A.; Kulinich, A. V.; Bondarev, S. L.; Knyukshto, V. N. Structure and Fluorescence Properties of Merocyanine Dyes Derived from Dimethylbarbituric Acid. *Russ. J. Gen. Chem.* **2007**, *77* (10), 1787–1798.

(35) Kulinich, V.; Derevyanko, N. A.; Mikitenko, E. K.; Ishchenko, A. A. Design and Photonics of Merocyanine Dyes. *J. Phys. Org. Chem.* **2011**, *24*, 732–742.

(36) Kulinich, V.; Mikitenko, E. K.; Ishchenko, A. A. Fluorescent Properties of Merocyanines Based on 1,3-Indandione. *Opt. Spectrosc.* **2015**, *119*, 39–48.

(37) Kulinich, V.; Derevyanko, N. A.; Ishchenko, A. A. Synthesis, Structure, and Solvatochromism of Merocyanine Dyes Based on Barbituric Acid. *Russ. J. Gen. Chem.* **2006**, *76*, 1441–1457.

(38) Cosco, E. D.; Bruns, O. T.; Franke, D.; Day, R. A.; Farr, E. P.; Bawendi, M. G.; Sletten, E. M. Flavylium Polymethine Fluorophores for Near- and Shortwave Infrared Imaging. *Angew. Chem. Int. Ed.* **2017**, *56*, 13126–13129.

(39) Cosco, E. D.; Spearman, A. L.; Ramakrishnan, S.; Lingg, J. G. P.; Saccomano, M.; Pengshung, M.; Arus, B. A.; Wong, K. C. Y.; Glasl, S.; Ntziachristos, V.; Warmer, M.; McLaughlin, R. R.; Bruns, O. T.; Sletten, E. M. Shortwave Infrared Polymethine Fluorophores Matched to Excitation Lasers Enable Non-Invasive, Multicolour In Vivo Imaging in Real Time. *Nat. Chem.* **2020**, *12*, 1123–1130.

(40) Klikar, M.; Jelínková, V.; Růžičková, Z.; Mikysek, T.; Pytela, O.; Ludwig, M.; Bureš, F. Malonic Acid Derivatives on Duty as Electron-Withdrawing Units in Push–Pull Molecules. *Eur. J. Org. Chem.* **2017**, *2017*, 2764–2779.

(41) Haenle, J. C.; Bruchlos, K.; Ludwigs, S.; Köhn, A.; Laschat, S. Rigidified Push–Pull Dyes: Using Chromophore Size, Donor, and Acceptor Units to Tune the Ground State between Neutral and the Cyanine Limit. *ChemPlusChem* **2017**, *82*, 1197–1210.

(42) Bai, Y.; Huang, Y.; Wan, W.; Jin, W.; Shen, D.; Lyu, H.; Zeng, L.; Liu, Y. Derivatizing Merocyanine Dyes to Balance Their Polarity and Viscosity Sensitivities for Protein Aggregation Detection. *Chem. Commun.* **2021**, *57*, 13313–13316.

(43) (A) A. A. Maryott, E. R. Smith, Table of Dieletric Constants of Pure Liquids, National Bureau of Standards Circular 514, 1951, p. 1-56. (B) F. Corradini, L. Marcheselli, L. Tassi, G. Tosi, Can. J. Chem. 1992, 70, 2895. (C) J. Hunger, R. Buchner, M. E. Kandil, E. F. May, K. N. Marsh, G. Hefter, J. Chem. Eng. Data 2010, 55, 2055. (D) L. G. Gagliardi, C. B. Castells, C. Rafols, M. Roses, E. Bosch, J. Chem. Eng. Data 2007, 52, 1103. (E) I. Ptowas, J. Swiergiel, J. Jadzyn, J. Chem. Eng. Data 2013, 58, 1741. (F) M. Rossberg,

Chloromethanes, Ullmann's Encyclopedia of Industrial Chemistry, 7th ed, New York, New York, 1999, p. 17. (G) W. M. Haynes, CRC Handbook of Chemistry and Physics, 95th Edition, Boca Raton, Florida, 2014, p. 6-234. (H) J. W. Thompson, T. J. Kaiser, J. W. Jorgenson, J. Chromatogr. A 2006, 1134, 201. (I) J. A. Marsella, Dimethylformamide, Kirk-Othmer Encyclopedia of Chemical Technology. New York, New York, 1999, p. 62. (J) R. G. LeBel, D. A. I. Goring, J. Chem. Eng. Data 1962, 7, 100.

(44) Gao, D.; Li, A.; Guan, L.; Zhang, X.; Wan, L. Y. Solvent-Dependent Ratiometric Fluorescent Merocyanine Dyes: Spectral Properties, Interaction with BSA as Well as Biological Applications. *Dyes Pigm.* **2016**, *129*, 163–173.

(45) Yan, J.; Zhu, J.; Zhou, K.; Wang, J.; Tan, H.; Xu, Z.; Chen, S.; Lu, Y.; Cui, M.; Zhang, L. Neutral Merocyanine Dyes: For In Vivo NIR Fluorescence Imaging of Amyloid-β Plaques. *Chem. Commun.* **2017**, *53*, 9910–9913.

(46) Toutchkine, V.; Kraynov, V.; Hahn, K. Solvent-Sensitive Dyes to Report Protein Conformational Changes in Living Cells. *J. Am. Chem. Soc.* **2003**, *125*, 4132–4145.

(47) Wu, W.-N.; Song, Y.-F.; Zhao, X.-L.; Wang, Y.; Fan, Y.-C.; Xu, Z.-H.; James, T. D. Multifunctional 1,3-Benzoxazole-Merocyanine-Based Probe for the Ratiometric Fluorescence Detection of pH/HSO3−/Viscosity in Mitochondria. *J. Chem. Eng.* **2023**, *464*, 142553.

(48) Dang, Z.; Liu, X.; Du, Y.; Wang, Y.; Zhou, D.; Zhang, Y.; Zhu, S. Ultra-Bright Heptamethine Dye Clusters Based on a Self-Adaptive Co-Assembly Strategy for NIR-IIb Biomedical Imaging. *Adv. Mater.* **2023**, *35*, 2306773.

(49) Hoche, J.; Schulz, A.; Dietrich, L. M.; Humeniuk, A.; Stolte, M.; Schmidt, D.; Brixner, T.; Würthner, F.; Mitric, R. The Origin of the Solvent Dependence of Fluorescence Quantum Yields in Dipolar Merocyanine Dyes. *Chem. Sci.* **2019**, *10*, 11013–11022.

(50) Levitus, M.; Ranjit, S. Cyanine Dyes in Biophysical Research: The Photophysics of Polymethine Fluorescent Dyes in Biomolecular Environments. *Q. Rev. Biophys.* **2011**, *44*, 123–151.

(51) Lutsyk, P.; Piryatinski, Y.; Kachkovsky, O.; Verbitsky, A.; Rozhin, A. Unsymmetrical Relaxation Paths of the Excited States in Cyanine Dyes Detected by Time-Resolved Fluorescence: Polymethinic and Polyenic Forms. *J. Phys. Chem. A* **2017**, *121*, 8236–8246.

(52) Zhong, Y.; Chen, Y.; Feng, X.; Sun, Y.; Cui, S.; Li, X.; Jin, X.; Zhao, G. Hydrogen-Bond Facilitated Intramolecular Proton Transfer in Excited State and Fluorescence Quenching Mechanism of Flavonoid Compounds in Aqueous Solution. *J. Mol. Liq.* **2020**, *302*, 112562.

(53) Hossen, T.; Sahu, K. New Insights on Hydrogen-Bond-Induced Fluorescence Quenching Mechanism of C102-Phenol Complex via Proton Coupled Electron Transfer. *J. Phys. Chem. A* **2018**, *122*, 2394–2400.

(54) Herbich, J.; Waluk, J.; Thummel, R. P.; Hung, C.-Y. Mechanisms of Fluorescence Quenching by Hydrogen Bonding in Various Aza Aromatics. *Photochem. Photobiol. A* **1994**, *80*, 157–160.

(55) Zhu, M.; Li, W.; Sun, L.; Lv, Z.; Yang, X.; Wang, Y. Advances in Fluorescent Probes for Targeting Organelles: Design Strategies, Applications and Perspectives. *Coord. Chem. Rev.* ***2024****, 512,* 215893-215917.

(56) Collot, M.; Fam, T. K.; Ashokkumar, P.; Faklaris, O.; Galli, T.; Danglot, L.; Klymchenko, A. S. Ultrabright and Fluorogenic Probes for Multicolor Imaging and Tracking of Lipid Droplets in Cells and Tissues. *J. Am. Chem. Soc.* **2018**, *140*, 5401–5411.

(57) Mukherjee, T.; Martinez-Sanchez, R. J.; Fam, K. T.; Bou, S.; Richert, L.; Garnier, D.; Mély, Y.; Kanvah, S.; Klymchenko, A. S.; Collot, M. Near Infrared Emitting Molecular

Rotor Based on Merocyanine for Probing the Viscosity of Cellular Lipid Environments. *Mater. Chem. Front.* **2021**, *5*, 2459–2469.

(58) Wu, X.; Wang, X.; Li, Y.; Kong, F.; Xu, K.; Li, L.; Tang, B. A Near-Infrared Probe for Specific Imaging of Lipid Droplets in Living Cells. *Anal. Chem.* **2022**, *94*, 4881–4888.

(59) Guo, S.; Li, C.; Lian, L.; Le, Z.; Ren, Y.; Liao, Y.-X.; Shen, J.; Hou, J.-T. Fluorescence Imaging of Diabetic Cataract-Associated Lipid Droplets in Living Cells and Patient-Derived Tissues. *ACS Sens.* **2023**, *8*, 3882–3891.

(60) Fujisawa, T.; Tamura, Y.; Yasueda, K.; Kuwata, I.; Hamachi, I. A Chemosensor for Fluorescence Detection of Lipid Droplets in Living Cells. *J. Am. Chem. Soc.* **2018**, *140*, 17060–17070.

(61) Colston, J.; Horobin, R.; Rashid-Doubell, F.; Pediani, J.; Johal, K. Why Fluorescent Probes for Endoplasmic Reticulum Are Selective: An Experimental and QSAR-Modelling Study. *Biotechnic & Histochemistry* **2003**, *78*, 323–332.

(62) Knewtson, K. E.; Rane, D.; Peterson, B. R. Targeting Fluorescent Sensors to Endoplasmic Reticulum Membranes Enables Detection of Peroxynitrite During Cellular Phagocytosis. *ACS Chem. Biol.* **2018**, *13*, 2595–2602.

(63) Phaniraj, S.; Gao, S.; Rane, D.; Peterson, B. R. Hydrophobic Resorufamine Derivatives: Potent and Selective Red Fluorescent Probes of the Endoplasmic Reticulum of Mammalian Cells. *Dyes Pigm.* **2016**, *135*, 127–133.

(64) Meinig, J. M.; Fu, L.; Peterson, B. R. Synthesis of Fluorophores that Target Small Molecules to the Endoplasmic Reticulum of Living Mammalian Cells. *Angew. Chem. Int. Ed.* **2015**, *54*, 9696–9699.

(65) Singh, D.; Rajput, D.; Kanvah, S. Fluorescent Probes for Targeting Endoplasmic Reticulum: Design Strategies and Their Applications. *Chem. Commun.* **2022**, *58*, 2413–2429.

(66) G. Chapman, G.; Henary, M.; Patonay, G. The effect of varying short-chain alkyl substitution on the molar absorptivity and quantum yield of cyanine dyes. *Anal. Chem. Insights* **2011**, *6*, 29.

(67) Lim, I.; Lin, E. Y.; Garcia, J.; Jia, S.; Sommerhalter, R. E.; Ghosh, K. S.; Gladysz, J. A.; Sletten, E. M. Shortwave infrared fluorofluorophores for multicolor *in vivo* imaging. *Angew. Chem. Int. Ed.* **2023**, *62,* 135.

(68) M. K. Burdette, M. K.; Jenkins, R.; Bandera, Y. P.; Jones, H.; Foulger, I. K.; Dickey, A.; Nieminen, A.-L.; Foulger, S. H. Click-Engineered, Bioresponsive, and Versatile Particle–Protein–Dye System. *ACS Appl. Bio Mater.* **2019**, *2*, 3183.

CHAPTER FIVE

Progress towards π-extended silicon coumarin photocages for near-infrared payload release

Quintashia Wilson, Lin-Jiun Chen, Ellen M. Sletten

5.1 Abstract

Light-responsive small molecule photocages are powerful tools for spatiotemporal drug delivery, particularly in photoactivated chemotherapy (PACT), where therapeutic agents are released upon light exposure. For clinical translation, ideal photocages must meet stringent criteria including aqueous solubility, biological stability, near-infrared (NIR) activation, and oxygen-independent bond cleavage. Coumarin-based photocages offer stability, solubility and oxygen-independent cleavage, but their limited absorption in the visible range hampers tissue penetration. To address these limitations, we propose a π-extended silicon coumarin photocage scaffold incorporating a flavylium donor to red-shift absorption into the NIR region and enable oxygen-independent cleavage. This work outlines synthetic efforts toward such photocages, highlighting a modular route beginning with a silicon coumarin core. Despite challenges in achieving the desired oxidation pattern, we identified key reactivity trends, particularly the influence of a 7-position dimethylamino substituent on oxidation outcomes. Our findings suggest that the amine group promotes non-canonical oxidation pathways, complicating synthesis of the target photocage scaffold. These insights contribute to the design of next-generation photocages and advance the development of clinically viable platforms for PACT.

5.2 Introduction

Light is a versatile trigger for controlling chemical and biological processes, offering unparalleled spatiotemporal precision in complex systems. Compared to chemical, thermal, or mechanical triggers, light is mild, efficient and non-invasive, making it an ideal stimulus for applications in medicine and biology.[1] One such application is photodynamic therapy (PDT), which combines light with exogenous photosensitizers to generate reactive oxygen species (ROS) for the targeted ablation of tumors (Figure 5.1A).[1–4] Another application is photoactivated chemotherapy (PACT), which enables spatiotemporal release of therapeutics using light-responsive photocages (Figure 1A).[5–8] Upon exposure to light, these photocages undergo covalent bond cleavage, releasing the therapeutic in a controlled manner.[9–11] PACT offers a promising alternative to PDT in environments where ROS generation is inefficient, like hypoxic tumors.[5] Despite its potential and technological transferability, PACT has yet to achieve clinical success due to the lack of photocages that meet stringent clinical requirements.

The ideal photocage should be water-soluble, biologically stable to avoid dark cleavage, responsive to near-infrared (NIR) (700-1000 nm) irradiation for deeper tissue penetration, and possess oxygen-independent cleavage to function effectively in hypoxic conditions (Figure 5.1B).[7,12] Small molecule photocages based on coumarin and xanthene scaffolds exhibit aqueous solubility, good dark stability and oxygen-independent cleavage, but their visible absorption wavelengths (VIS, 400-700 nm) limit their ability for deep tissue penetration.[13–18] This is resolved by moving to scaffolds with extended conjugation like boron-dipyrromethene (BODIPY) and cyanine fluorophores. BODPIY photocages are promising candidates for PACT, as they exhibit both NIR absorption and oxygen-independent cleavage, but their hydrophobicity and low cleavage efficiency must be addressed.[19–21] Cyanine-based photocages are another hopeful avenue for PACT translation considering the clinical uses of indocyanine green (ICG) and other

FDA-approved cyanine fluorophores.[22–24] However, most cyanine photocages exhibit oxygen-dependent cleavage, and the ones that do not exhibit low cleavage efficiency.[22,23,25,26] Altogether, the current toolbox of small molecule photocages is expanding, but still has room for improvement in order to realize the clinical potential of PACT.

Many of the design principles for enhanced fluorophores can be extended to photocages allowing for systematic optimization. Drawing on the lessons discussed in Chapters 2 and 3, we envisioned that silicon incorporation in the coumarin scaffold alongside the π-extension with a flavylium donor, would generate NIR-absorbing photocages with oxygen-independent cleavage (Figure 5.1C). Besides our work with silicon polymethine dyes and flavylium merocyanine dyes, both of these strategies have been implemented in the coumarin scaffold. There are several reports of silicon-substituted coumarin fluorophores that exhibit ~100 nm red-shift in absorption while retaining water solubility and biocompatibility.[27–29] Furthermore, π-extended coumarin photocages featuring pyridinium, indolenium and benzothiazolium donors have also been reported.[14,30] In each case, the extended photocages exhibit red-shifted absorption and better uncaging efficiencies while maintaining oxygen-dependent cleavage. By combining these two strategies, this work holds promise for producing improved photocages suitable for PACT applications, while also shedding light on how silicon and flavylium incorporation influence cleavage mechanisms. Herein, we report our synthetic efforts toward the development of π-extended silicon coumarin photocages for NIR-triggered therapeutic release.

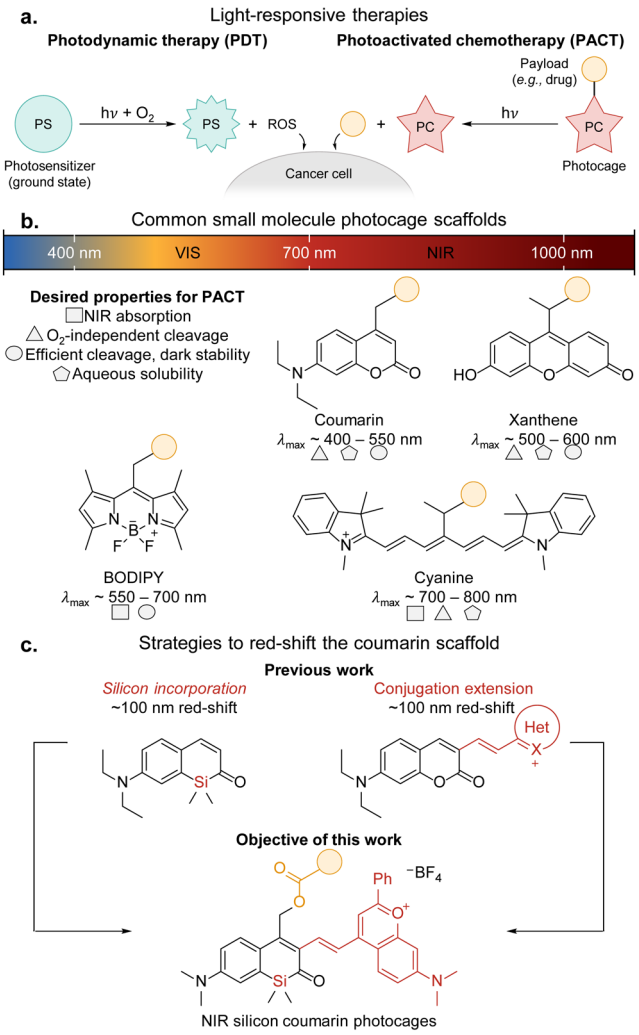

Figure 5.1. Overview of this work.

5.3 Results and discussion

To achieve a panel of π-extended silicon coumarin photocages, we envisioned a robust synthetic route featuring esterification of precursor **5.1** with various payloads (Scheme 5.1). This alcohol precursor could be derived from Heck coupling at the 3-position of **5.2** with a flavylium vinyl intermediate. Compound **5.2** could be obtained from bromination of **5.3**. To generate oxidized silicon coumarin **5.3**, we adapted the silicon coumarin route reported by Cui and coworkers[27] to append a 4-position methyl group in **5.4** that could undergo simultaneous oxidation at the 2- and 4-positions.

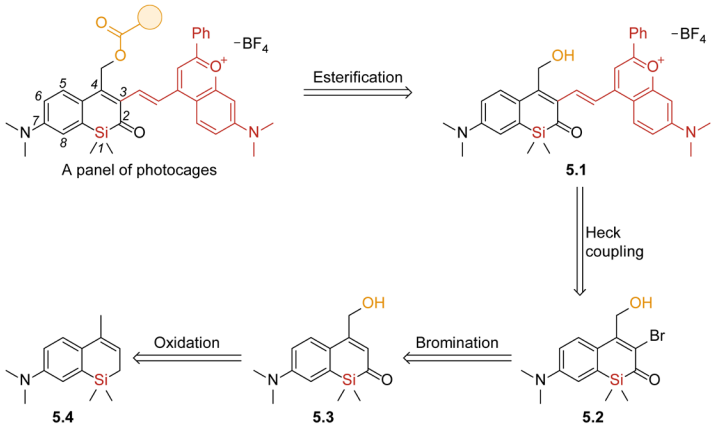

Scheme 5.1. Proposed retrosynthesis of π-extended silicon coumarin photocages.

Progress towards intermediate **5.4** began with alkylation of 2-bromo-4-(dimethylamino)benzaldehyde (Scheme 5.2A) to generate benzylic alcohol **5.5** which was subsequently oxidized to yield ketone **5.6**. We were able to generate **5.7** in trace amounts via Wittig olefination, but decided to abandon this sequence altogether as the DMP oxidation of **5.5** was low-yielding and irreproducible. Furthermore, other oxidations like PCC and Swern formed a styrene side product **5.8**, suggesting that alcohol dehydration is strongly favored at this position due to increased electron donation from the amine (Scheme 5.2B).

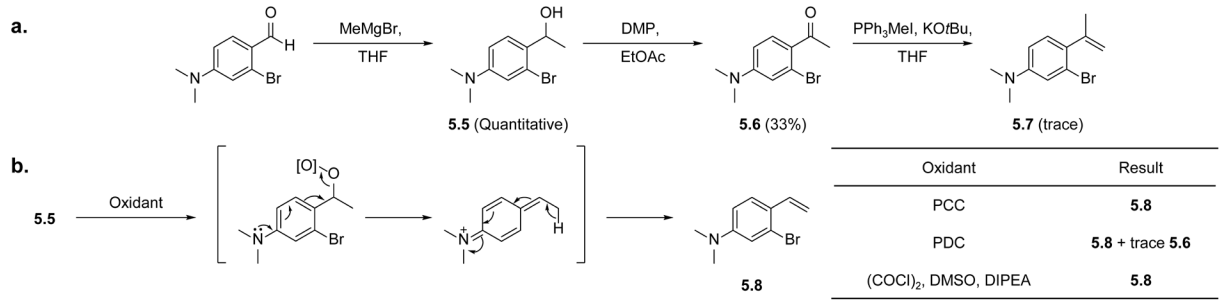

Scheme 5.2. A) Early synthetic route toward precursor **5.7** involving a low-yielding DMP oxidation. B) Proposed dehydration mechanism and oxidant screen of **5.5** to **5.8**.

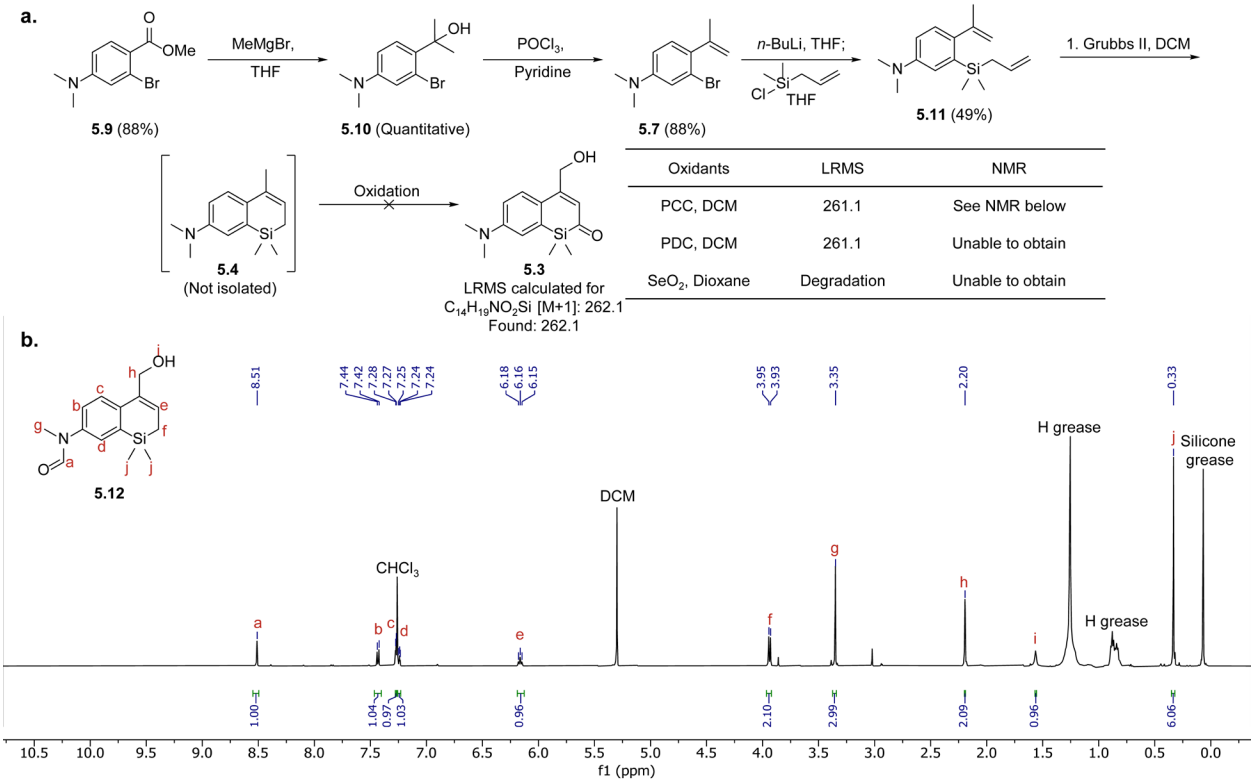

Figure 5.2. A) Improved synthetic route of **5.7** involving alcohol dehydration, followed by silylation, cyclization and oxidation to a compound consistent with the mass of **5.3**. B) ^{1}H NMR and proposed structure of unknown oxidized species.

Inspired by the dehydration of **5.5** to **5.8**, we developed a new route involving the double methylation of **5.9** to generate benzylic alcohol **5.10**, which underwent dehydration with $POCl_3$ and pyridine to produce **5.7** in excellent yield (Figure 5.2A). Next, **5.10** was subjected to lithium-halogen exchange followed by silylation with allylchlorodimethylsilane to generate **5.11**, which underwent intramolecular Grubbs metathesis to produce key intermediate **5.5.** We expected allylic oxidation at the 2- and 4-positions to proceed smoothly with selenium dioxide. Interestingly, this resulted in a complex mixture of oxidized compounds, none of which correspond to the mass of the desired coumarin. Instead, we turned to pyridinium chlorochromate (PCC) and pyridinium dichlorochromate, which have both been used for the allylic oxidations of cyclic enones.[31,32] Gratifyingly, both oxidants exclusively generated an oxidized species with a mass corresponding

to **5.3**. We were unable to confirm the identity of the crude compound by NMR due to severe spectral broadening by residual chromium salts. Attempts to remove the chromium salts using filtration, vigorous extraction and flash chromatography also proved to be largely unsuccessful. After several laborious columns, we isolated a few milligrams of the oxidized coumarin and attempted to confirm the structure by ^{1}H NMR (Figure 5.2B). Analyzing the chemical shifts and splitting patterns of various protons, we suspect that the oxidized compound is actually compound **5.12**, wherein oxidation occurred at the 4- and 7-position methyl groups. This is corroborated by the chemical shift of proton A at 8.51 ppm, which corresponds to a formamide structure, and protons H, which correspond to a sharp singlet integrating to 2H. Oxidation at the 2-position seems highly unlikely given the distinct multiplet at 6.18-6.14 ppm (proton E, 1H) that would only occur when there are adjacent methylene protons. There are no reports to our knowledge of PCC-promoted oxidations of dimethylamino substituents, but this is known to be an oxidation-sensitive site of coumarin fluorophores. It also remains unclear why the 4-position is more prone to oxidation than the 2-position.

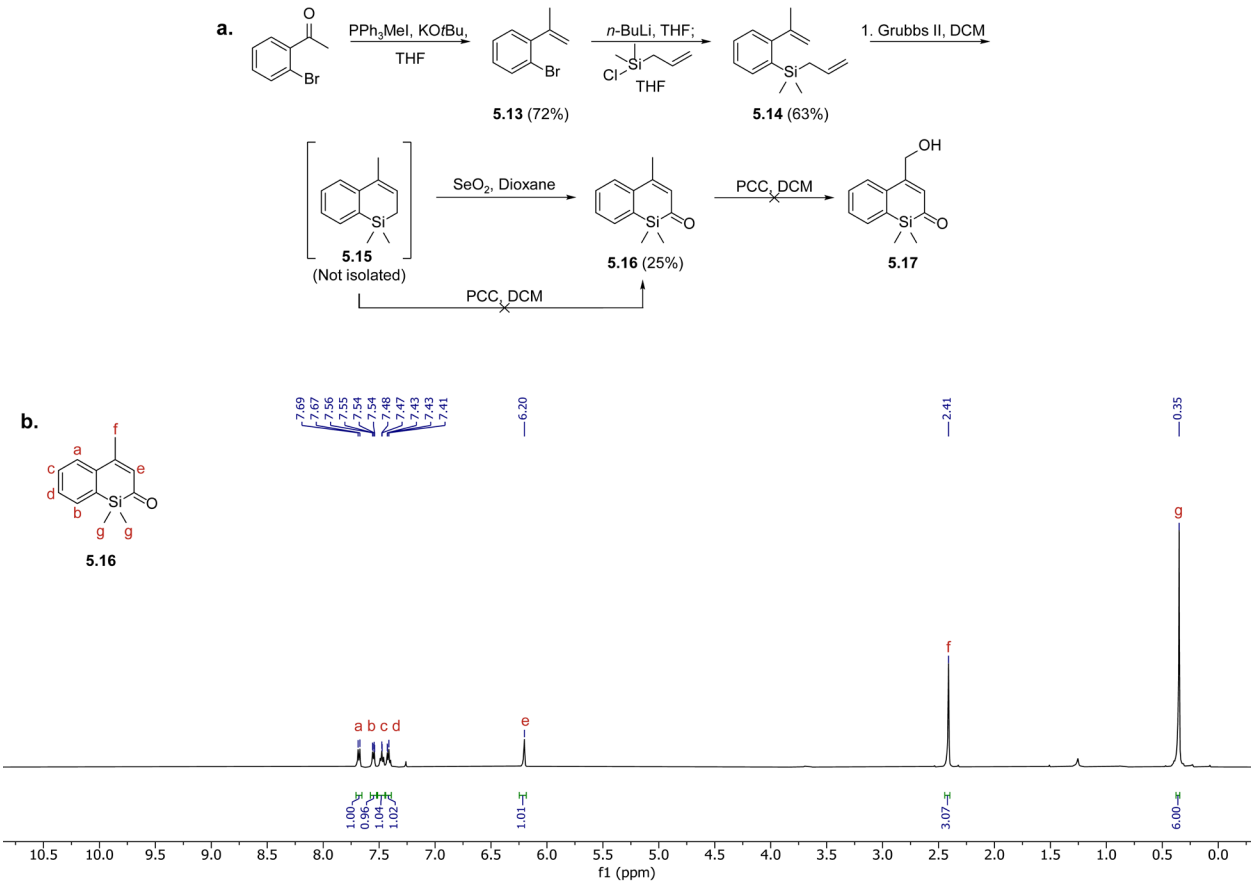

Figure 5.3. A) Synthetic route towards 7-H silicon coumarin and oxidation screen. B) ^{1}H NMR of **5.16**.

To confirm that this unusual oxidation pattern is caused by the 7-position amine, we attempted to synthesize the deaminated analog, **5.17** (Figure 5.3A). Due to the absence of the amine, we were able to perform Wittig olefination of bromoketone to **5.13** in good yield (Figure 5.3A). Silylation of **5.13** to **5.14** also proceeded smoothly. After intramolecular cyclization of **5.14** to **5.15**, the crude product was pushed forward to PCC oxidation. Contrary to the aminated precursor, oxidation with PCC resulted in degradation, while SeO_2 resulted in exclusive oxidation at the 2-position (**5.16**) (Figure 5.3A, B). Using excess SeO_2 or subjecting **5.16** to PCC did not result in oxidation at the 4-position, suggesting that oxidation at this site is affected by the amine.

Overall, these results suggest that the 7-position amine is problematic towards achieving the desired oxidation to silicon coumarin **5.5.**

5.4 Conclusions

In this study, we explored the design and synthesis of π-extended silicon coumarin photocages as promising candidates for NIR-triggered, oxygen-independent therapeutic release in PACT. By integrating silicon substitution and flavylium-based π-extension into the coumarin scaffold, we aimed to overcome the limitations of current photocage platforms, particularly in terms of absorption profile and cleavage efficiency. While synthetic access to the target oxidized silicon coumarin intermediate proved challenging, our investigations revealed a strong influence of the 7-position dimethylamino substituent on oxidation chemoselectivity, leading to unexpected oxidation at the 4- and 7-position methyl groups. Additionally, the 7-H analog exhibited exclusive oxidation at the 2-position, suggesting that the hydroxy-substituted silicon coumarin scaffold may not be a viable platform for the development of photocages. These findings emphasize the importance of scaffold reactivity in photocage design and highlight the need to explore alternative architectures better suited for controlled oxidation and therapeutic release. Future directions could include employing conventional π-extended coumarin photocages in tandem with flavylium donors to achieve NIR activation, or investigating alternative linkages at the 4-position of the silicon coumarin core (*e.g.,* such as thiols or amines) to circumvent oxidation challenges and unlock new reactivity profiles.

5.5 Experimental procedures

5.5.1 Materials and instrumentation

Materials

Chemical reagents were purchased from Acros Organics, Alfa Aesar, Fisher Scientific, Sigma-Aldrich, or TCI and used without purification.

Instrumentation

Thin layer chromatography was conducted using Silica Gel 60 F_{254} (EMD Millipore) plates. Flash chromatography was executed with technical grade silica gel with 60 Å pores and 40-63 μm mesh particle size (Sorbtech Technologies). Solvent was removed under reduced pressure with a Büchi Rotovapor with a Welch self-cleaning dry vacuum pump and further dried with a Welch DuoSeal pump. NMR spectra were taken on a Bruker AV400, AV500 or DRX500 instruments and processed with MestReNova software. NMR peaks are reported in ppm in reference to their respective solvent signals. LRMS spectra were taken on a 1260 Infinity II LC System with a G6100 Series mass spectrometer with separation on a Poroshell 120 reverse phase column (Agilent Technologies) or Agilent 6890N Quad GC/MS with EI and CI ionization capabilities.

Abbreviations

DCM = dichloromethane; DMSO = dimethyl sulfoxide; EtOAc = ethyl acetate; NH_4Cl = ammonium chloride; K_2CO_3 = potassium carbonate; KO*t*Bu = potassium *tert*-butoxide; PCC = pyridinium chlorochromate; PPh_3MeI = methyltriphenylphosphonium iodide; *sec*-BuLi = *sec*-butyllithium; TEA = triethylamine; tetrahydrofuran = THF

5.5.2 Synthetic procedures

Synthesis of 1-(2-bromo-4-(dimethylamino)phenyl)ethan-1-ol (**5.5**).

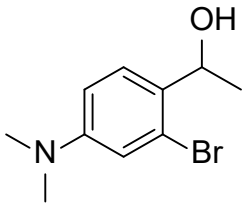

In a flame-dried two-neck round-bottom flask charged with a stir bar under N_2 atmosphere, 2-bromo-4-(dimethylamino)benzaldehyde (250 mg, 1.10 mmol, 1.00 equiv) was dissolved in anhydrous THF (11.0 mL) and cooled to 0 °C. Methylmagnesium bromide (1.4 M solution in THF, 3.91 mL, 5.48 mmol, 5.00 equiv) was added dropwise and the mixture was warmed to rt for 24 h. The mixture was quenched with NH_4Cl (6% w/v in water), extracted with DCM (50 mL x 3) and washed with water and brine. The crude product was then dried with Na_2SO_4 and concentrated *in vacuo* to give **5.5** as a yellow oil (270 mg, 1.11 mmol, Quantitative) consistent with literature reports.[2] R_F = 0.33 in 10:1 Hex:EtOAc ^{1}H NMR (400 MHz, $(CD_3)_2CO$) δ 7.46 (dd, *J* = 8.7, 0.6 Hz, 1H), 6.88 – 6.75 (m, 2H), 5.07 (qd, *J* = 6.3, 3.5 Hz, 1H), 5.13 (d, *J* = 3.8 Hz, 1H), 2.94 (s, 6H), 1.36 (d, *J* = 6.3 Hz, 3H). LRMS (ESI+): Calculated for $C_{10}H_{14}BrNO$ [M+1]: 245.0, found 245.0.

Synthesis of 1-(2-bromo-4-(dimethylamino)phenyl)ethan-1-one (**5.6**).

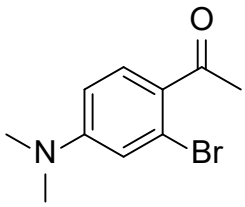

In a two-neck round-bottom flask fitted with a reflux condenser and charged with a stir bar, **5.5** (200 mg, 819 µmol, 1.00 equiv) and DMP (695 mg, 1.64 mmol, 2.00 equiv) were dissolved in EtOAc (8.19 mL) and heated to 80 °C for 4 h. The mixture was cooled to rt, filtered over celite and

evaporated onto silica. The crude product was purified via flash chromatography, eluting with 20:1 Hex:EtOAc to give **5.6** as a yellow oil (65.0 mg, 270 µmol, 33%) consistent with literature reports.[33] R_F = 0.31 in 10:1 Hex:EtOAc. ^{1}H NMR (500 MHz, $CDCl_3$) δ 7.65 (dd, *J* = 8.9, 0.8 Hz, 1H), 6.87 (d, *J* = 2.6 Hz, 1H), 6.58 (dd, *J* = 8.9, 2.6 Hz, 1H), 3.02 (d, *J* = 0.7 Hz, 6H), 2.60 (s, 3H). LRMS (ESI+): Calculated for $C_{10}H_{12}BrNO$ [M+1]: 243.0, found 243.0.

Synthesis of methyl 2-bromo-4-(dimethylamino)benzoate (**5.9**).

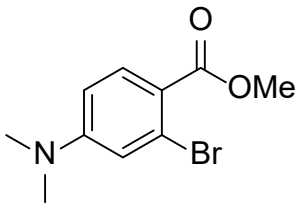

In a two-neck round-bottom flask fitted with a reflux condenser and charged with a stir bar, methyl 2-bromo-4-fluorobenzoate (6.34 mL, 42.9 mmol, 1.00 equiv) and K_2CO_3 (11.9 g, 85.8 mmol, 2.00 equiv) were dissolved in DMSO (85.8 mL). Dimethylamine (40% w/w in water, 6.7 mL, 85.8 mmol, 2.00 equiv) was added and the mixture was heated to 70 °C for 1 h. The mixture was cooled to rt, extracted with DCM (150 mL x 3) and washed with water and brine. The crude product was dried with Na_2SO_4 and concentrated *in vacuo* to give **5.9** as a white solid (9.77 g, 37.8 mmol, 88%). R_F = 0.52 in 10:1 Hex:EtOAC. ^{1}H NMR (500 MHz, $CDCl_3$) δ 7.82 (d, *J* = 8.9 Hz, 1H), 6.87 (d, *J* = 2.6 Hz, 1H), 6.54 (dd, *J* = 8.9, 2.6 Hz, 1H), 3.84 (s, 3H), 2.99 (s, 6H). ^{13}C NMR (126 MHz, $CDCl_3$) δ 166.03, 152.86, 133.34, 125.44, 116.90, 116.64, 109.72, 77.09, 51.71, 39.95. LRMS (ESI+): Calculated for $C_{10}H_{12}BrNO_2$ [M+1]: 258.0, found 258.0.

Synthesis of 2-(2-bromo-4-(dimethylamino)phenyl)propan-2-ol (**5.10**).

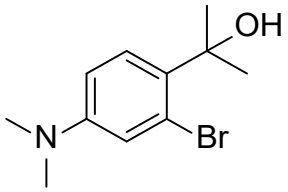

In a flame-dried two-neck round-bottom flask fitted with a reflux condenser and charged with a stir bar under N_2 atmosphere, **5.9** (1.00 g, 3.87 mmol, 1.00 equiv) was dissolved in anhydrous THF (7.75 mL) and cooled to 0 °C. Methylmagnesium bromide (1.5 M solution in THF, 7.75 mL, 11.6 mmol, 3.00 equiv) was added dropwise and the mixture was heated to 66 °C for 3 h. The mixture was quenched with saturated NH_4Cl, extracted with DCM (50 mL x 3) and washed with water and brine. The crude product was then dried with Na_2SO_4 and concentrated *in vacuo* to give **5.10** as a yellow oil (1.05 g, 5.08 mmol, Quantitative). R_F = 0.48 in 10:1 Hex:EtOAc. ^{1}H NMR (500 MHz, $CDCl_3$) δ 7.44 (d, *J* = 8.8 Hz, 1H), 6.92 (d, *J* = 2.7 Hz, 1H), 6.62 (dd, *J* = 8.8, 2.7 Hz, 1H), 2.93 (s, 6H), 1.71 (s, 6H). ^{13}C NMR (126 MHz, $CDCl_3$) δ 150.17, 133.11, 127.48, 121.40, 118.35, 111.09, 73.11, 40.32, 30.05. (ESI+): Calculated for $C_{11}H_{16}BrNO$ [M+1]: 258.2, found 258.6.

Synthesis of 3-bromo-*N,N*-dimethyl-4-(prop-1-en-2-yl)aniline (**5.7**).

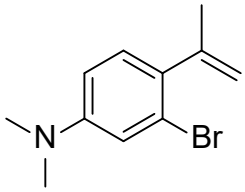

In round-bottom flask charged with a stir bar under N_2 atmosphere, **5.10** (825 mg, 3.20 mmol, 1.00 equiv) was dissolved in pyridine (3.20 mL). Phosphorous oxychloride (894 µL, 9.59 mmol, 3.00 equiv) was added dropwise and the mixture was stirred at rt for 4 h. The mixture was quenched with saturated $NaHCO_3$, extracted with EtOAc (50 mL x 3) and washed with water and brine. The crude product was dried with Na_2SO_4 and concentrated *in vacuo* to give **5.7** as a brown oil (689 mg, 2.87 mmol, 90%). R_F = 0.61 in 10:1 Hex:EtOAc. ^{1}H NMR (500 MHz, $CDCl_3$) δ 7.07

(d, *J* = 8.5 Hz, 1H), 6.90 (d, *J* = 2.7 Hz, 1H), 6.63 (dd, *J* = 8.5, 2.6 Hz, 1H), 5.18 (d, *J* = 1.8 Hz, 1H), 5.95 – 5.90 (m, 1H), 2.94 (s, 6H), 2.10 (s, 3H). ^{13}C NMR (126 MHz, $CDCl_3$) δ 150.47, 145.81, 132.51, 130.05, 122.38, 116.27, 115.72, 111.45, 40.57, 25.09. LRMS (ESI+): Calculated for $C_{11}H_{14}BrN$ [M+1]: 240.1, found 240.0.

Synthesis of 3-(allyldimethylsilyl)-*N,N*-dimethyl-4-(prop-1-en-2-yl)aniline (**5.11**).

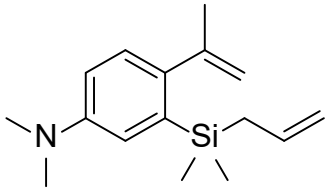

In a flame-dried two-neck round-bottom flask charged with a stir bar under N_2 atmosphere, **5.7** (450 mg, 1.87 mmol, 1.00 equiv) was dissolved in anhydrous THF (1.87 mL) and cooled to 0 °C. *Sec*-BuLi (0.9 M in hexanes, 5.16 mL, 3.75 mmol, 2.00 equiv) was added dropwise and the mixture was stirred for 1 h. Allylchlorodimethylsilane (708 µL, 5.68 mmol, 2.50 equiv) was added dropwise and the mixture was warmed to rt for 4 h. The mixture was quenched with saturated NH_4Cl, extracted with DCM (50 mL x 3) and washed with water and brine. The crude product was dried with Na_2SO_4, evaporated onto silica and purified via flash chromatography, eluting with 10:1 Hex:Toluene to give **5.11** as a brown oil (238 mg, 917 µmol, 49%) consistent with literature reports.[27] R_F = 0.56 in 10:1 Hex:EtOAc ^{1}H NMR (500 MHz, $CDCl_3$) δ 7.06 (d, *J* = 8.5 Hz, 1H), 6.94 – 6.89 (m, 1H), 6.76 – 6.72 (m, 1H), 5.81 (ddt, *J* = 16.4, 10.1, 8.1 Hz, 1H), 5.12 (dd, *J* = 2.5, 1.4 Hz, 1H), 5.91 (s, 1H), 5.88 – 5.85 (m, 1H), 5.84 (d, *J* = 1.4 Hz, 1H), 2.95 (s, 6H), 2.07 (t, *J* = 1.2 Hz, 3H), 1.84 (dd, *J* = 8.0, 1.3 Hz, 2H), 0.29 (s, 6H). ^{13}C NMR (126 MHz, $CDCl_3$) δ 147.84, 135.61, 128.36, 115.49, 113.31, 77.16, 40.91, 29.85, 26.17, 25.11, -1.18. LRMS (ESI+): Calculated for $C_{16}H_{25}NSi$ [M+1]: 259.5, found 259.9.

Synthesis of proposed compound *N*-(4-(hydroxymethyl)-1,1-dimethyl-1,2-dihydrobenzo[*b*]silin-7-yl)-*N*-methylformamide (**5.12**).

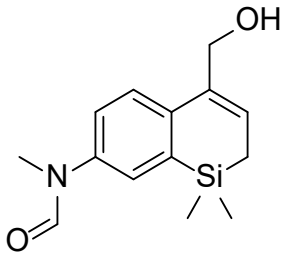

In a flame-dried two-neck round-bottom flask charged with a stir bar under N_2 atmosphere, **5.11** (238 mg, 917 µmol, 1.00 equiv) and Grubbs Catalyst ® M204 (38.9 mg, 45.9 µmol, 0.05 equiv) were dissolved in anhydrous DCM (1.83 mL) and stirred at rt for 24 h. The mixture was concentrated *in vacuo* to give a crude brown oil, which was used without further purification. The crude brown oil and PCC (394 mg, 1.83 mmol, 2.00 equiv) were dissolved in DCM (1.83 mL) and stirred at rt for 1 h. The mixture was evaporated onto silica and purified via flash chromatography, eluting with 100:1 DCM:MeOH to give **5.12** as a yellow oil (3.0 mg, 23 µmol, 3%). R_F = 0.46 in 50:1 DCM:MeOH. ^{1}H NMR (500 MHz, $CDCl_3$) δ 8.51 (s, 1H), 7.43 (d, *J* = 8.3 Hz, 1H), 7.27 (d, *J* = 2.5 Hz, 1H), 7.26 – 7.23 (m, 1H), 6.18 – 6.14 (m, 1H), 3.94 (d, *J* = 7.7 Hz, 2H), 3.35 (s, 3H), 2.19 (d, *J* = 1.5 Hz, 2H), 0.07 (s, 6H). LRMS (ESI+) $C_{14}H_{19}NO_2Si$ [M+1]: 262.1, found 261.1.

Synthesis of 1-bromo-2-(prop-1-en-2-yl)benzene (**5.13**).

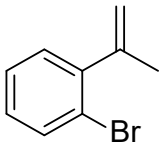

In a flame-dried two-neck round-bottom flask charged with a stir bar under N_2 atmosphere, 1-(2-bromophenyl)ethan-1-one (0.70 mL, 5.2 mmol, 1.0 equiv), KO*t*Bu (1.1 g, 10 mmol, 1.9 equiv) and PPh_3MeI (3.1 g, 7.5 mmol, 1.5 equiv) were dissolved in THF (10 mL) and stirred at rt for 24 h. The

mixture was filtered over celite, evaporated onto silica and purified via flash chromatography, eluting with hexanes to give **5.13** as a clear oil (600 mg, 3.1 mmol, 60%). R_F = 0.73 in 4:1 Hex:EtOAc. ^{1}H NMR (500 MHz, $CDCl_3$) δ 7.56 (d, *J* = 7.9 Hz, 1H), 7.29 – 7.24 (m, 1H), 7.20 (dd, *J* = 7.6, 1.8 Hz, 1H), 7.12 (td, *J* = 7.6, 1.9 Hz, 1H), 5.24 (s, 1H), 5.97 – 5.92 (m, 1H), 2.11 (s, 3H). LRMS (EI+): Calculated for $C_9H_9Br^+$: 195.9, found 195.2.

Synthesis of allyldimethyl(2-(prop-1-en-2-yl)phenyl)silane (**5.14**).

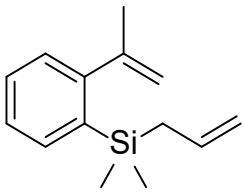

In a flame-dried two-neck round-bottom flask charged with a stir bar under N_2 atmosphere, **5.13** (400 mg, 2.03 mmol, 1.00 equiv) was dissolved in anhydrous THF (5.06 mL) and cooled to 0 °C. *Sec*-BuLi (0.9 M in hexanes, 2.70 mL, 2.44 mmol, 1.20 equiv) was added dropwise and the mixture was stirred for 1 h. Allylchlorodimethylsilane (399 µL, 2.64 mmol, 1.30 equiv) was added dropwise and the mixture was warmed to rt for 12 h. The mixture was quenched with saturated NH_4Cl, extracted with DCM (50 mL x 3) and washed with water and brine. The crude product was dried with Na_2SO_4, evaporated onto silica and purified via flash chromatography, eluting with hexanes to give **5.14** as a clear oil (286 mg, 1.32 mmol, 65%) consistent with literature reports.[27] R_F = 0.82 in 10:1 Hex:EtOAc. ^{1}H NMR (400 MHz, $CDCl_3$) δ 7.54 (ddt, *J* = 7.5, 1.5, 0.7 Hz, 1H), 7.36 – 7.31 (m, 1H), 7.28 – 7.23 (m, 1H), 7.16 (ddt, *J* = 7.6, 1.5, 0.7 Hz, 1H), 5.88 – 5.73 (m, 1H), 5.18 (ddt, *J* = 2.3, 1.5, 0.7 Hz, 1H), 5.92 – 5.84 (m, 3H), 2.11 (dd, *J* = 1.6, 0.9 Hz, 3H), 1.84 (dd,

J = 7.9, 1.3 Hz, 2H), 0.31 (d, *J* = 0.8 Hz, 6H). LRMS (EI+): Calculated for $C_{14}H_{20}Si$+: 216.1, found 216.1.

Synthesis of 1,1,4-trimethylbenzo[*b*]silin-2(1*H*)-one (**5.16**).

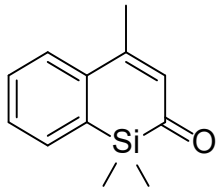

In a flame-dried two-neck round-bottom flask charged with a stir bar under N_2 atmosphere, **5.14** (189 mg, 873 µmol, 1.00 equiv) and Grubbs Catalyst ® M204 (37.0 mg, 43.7 µmol, 0.05 equiv) were dissolved in anhydrous DCM (1.83 mL) and stirred at rt for 24 h. The mixture was concentrated *in vacuo* to give a crude brown oil, which was used without further purification. The crude brown oil and SeO_2 (145 mg, 1.31 mmol, 1.50 equiv) were dissolved in 1,4-dioxane (1.75 mL) and stirred at rt for 1 h. The mixture was filtered over celite and evaporated to give **5.16** as a crude orange oil (71 mg, 350 µmol, 40%). R_F = 0.53 in 4:1 Hex:EtOAc. ^{1}H NMR (500 MHz, $CDCl_3$) δ 7.68 (d, *J* = 8.0 Hz, 1H), 7.58 – 7.52 (m, 1H), 7.47 (d, *J* = 1.7 Hz, 1H), 7.42 (d, *J* = 7.4 Hz, 1H), 6.20 (s, 1H), 2.41 (s, 3H), 0.35 (s, 6H). LRMS (ESI+): Calculated for $C_{12}H_{14}OSi$ [M+1]: 202.1, found 202.3.

5.5.3 ^{1}H NMR Spectra

^{1}H NMR of **5.5** (400 MHz, $CDCl_3$).

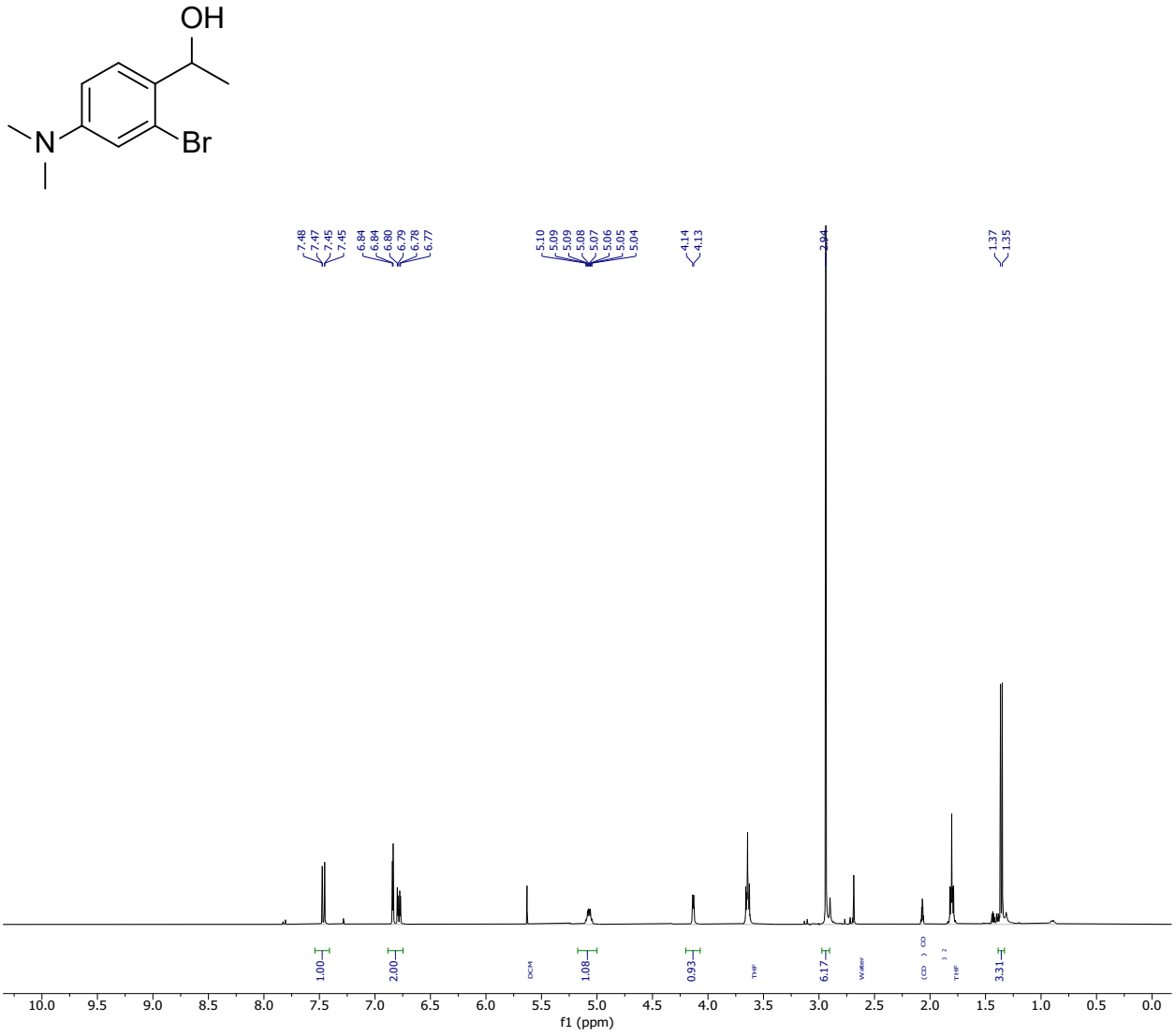

^{1}H NMR of **5.6** (500 MHz, $CDCl_3$).

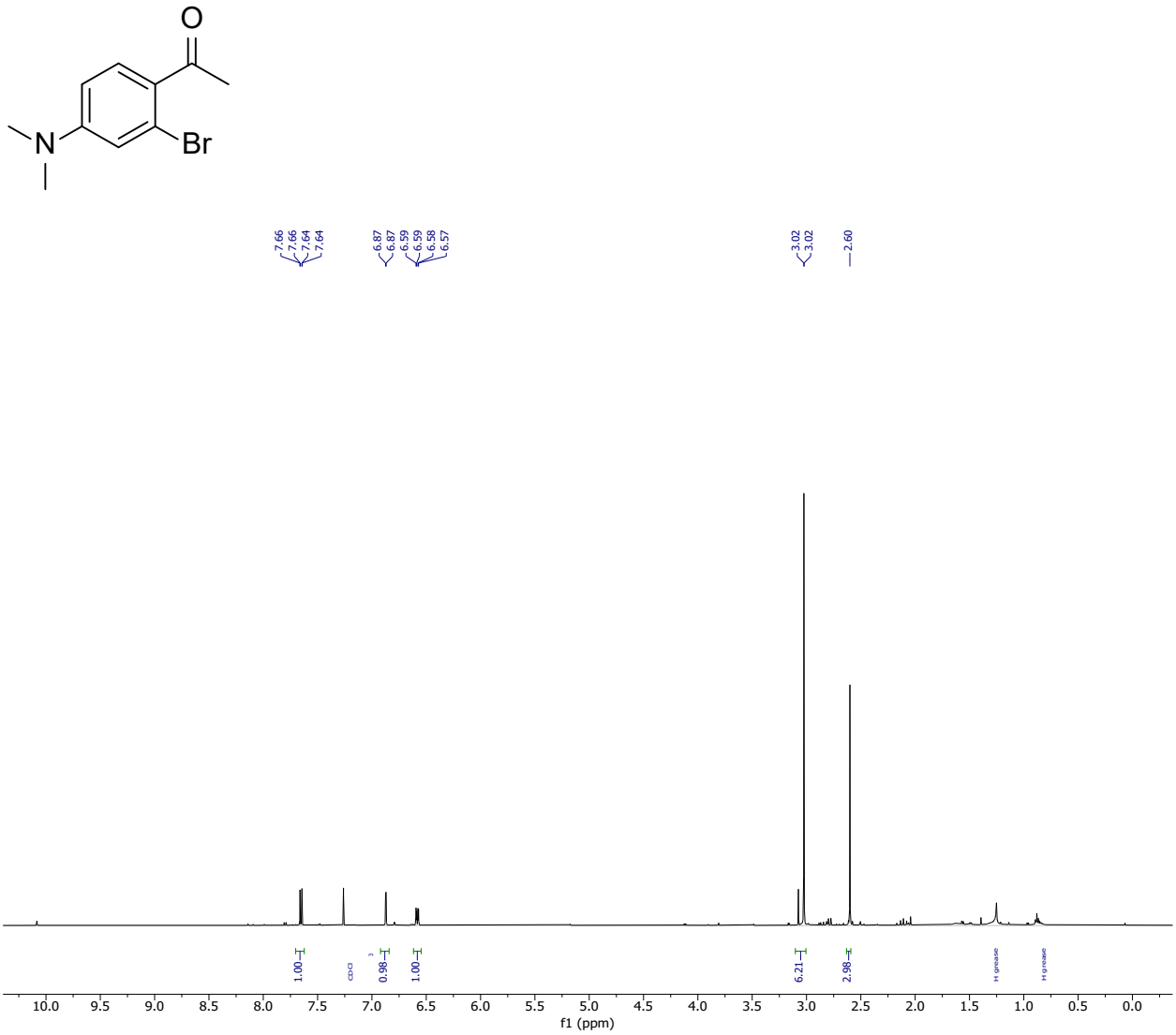

^{1}H NMR of **5.9** (500 MHz, $CDCl_3$).

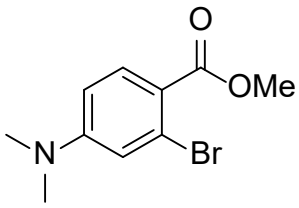

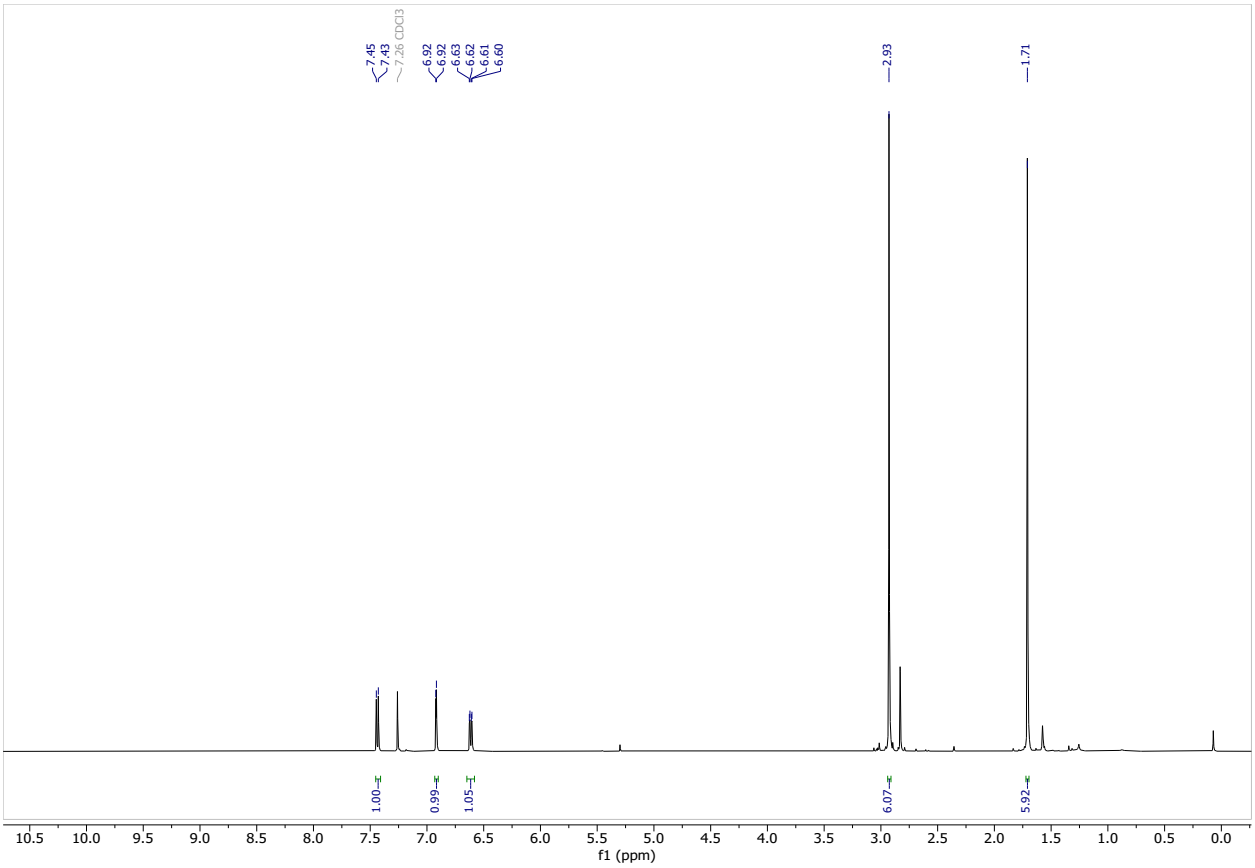

^{1}H NMR of **5.10** (500 MHz, $CDCl_3$).

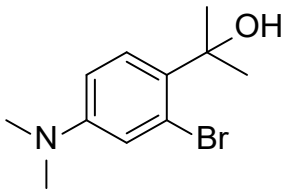

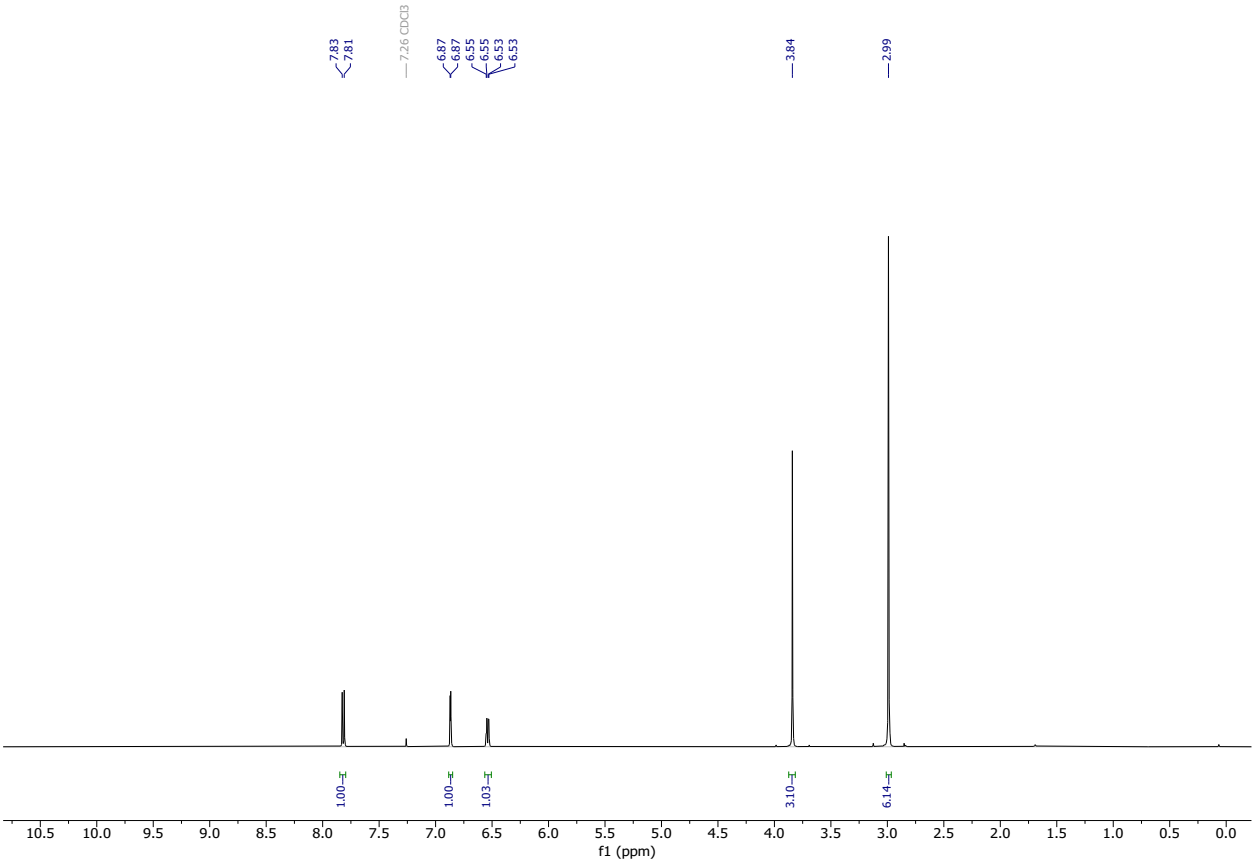

^{1}H NMR of **5.7** (500 MHz, $CDCl_3$).

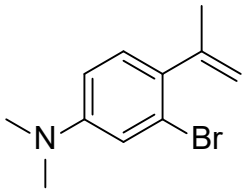

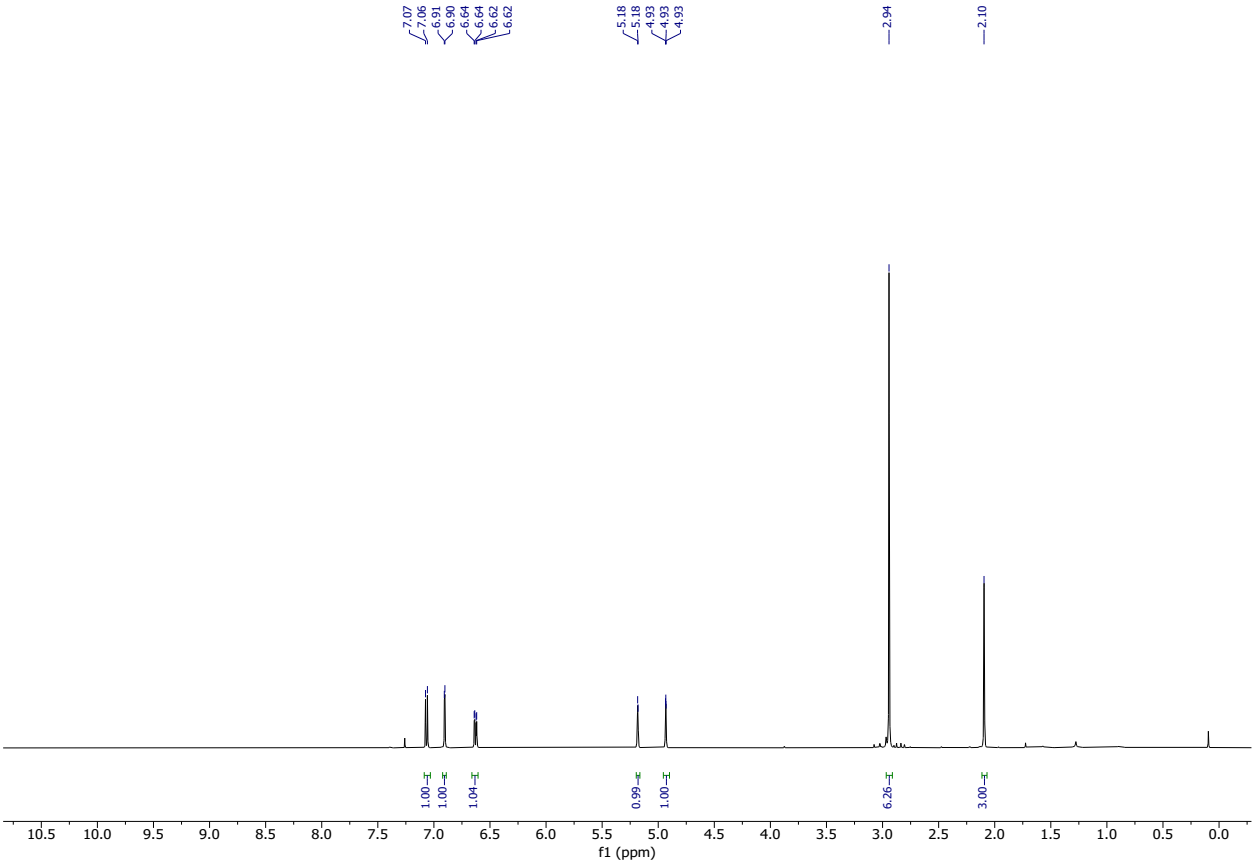

^{1}H NMR of **5.11** (500 MHz, $CDCl_3$).

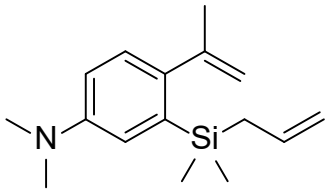

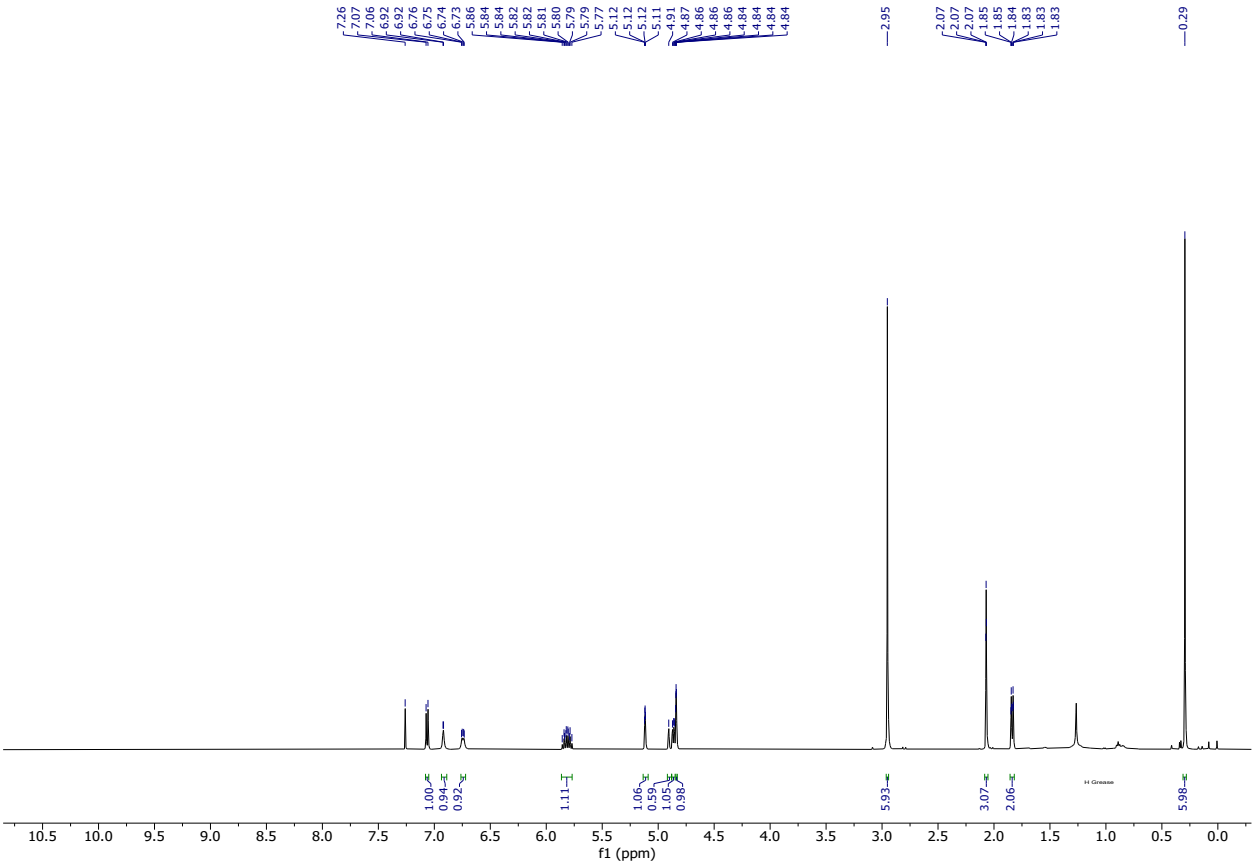

^{1}H NMR of **5.12** (500 MHz, $CDCl_3$).

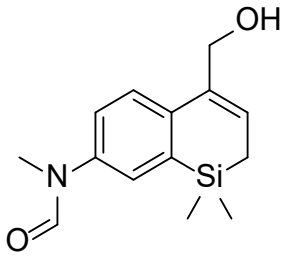

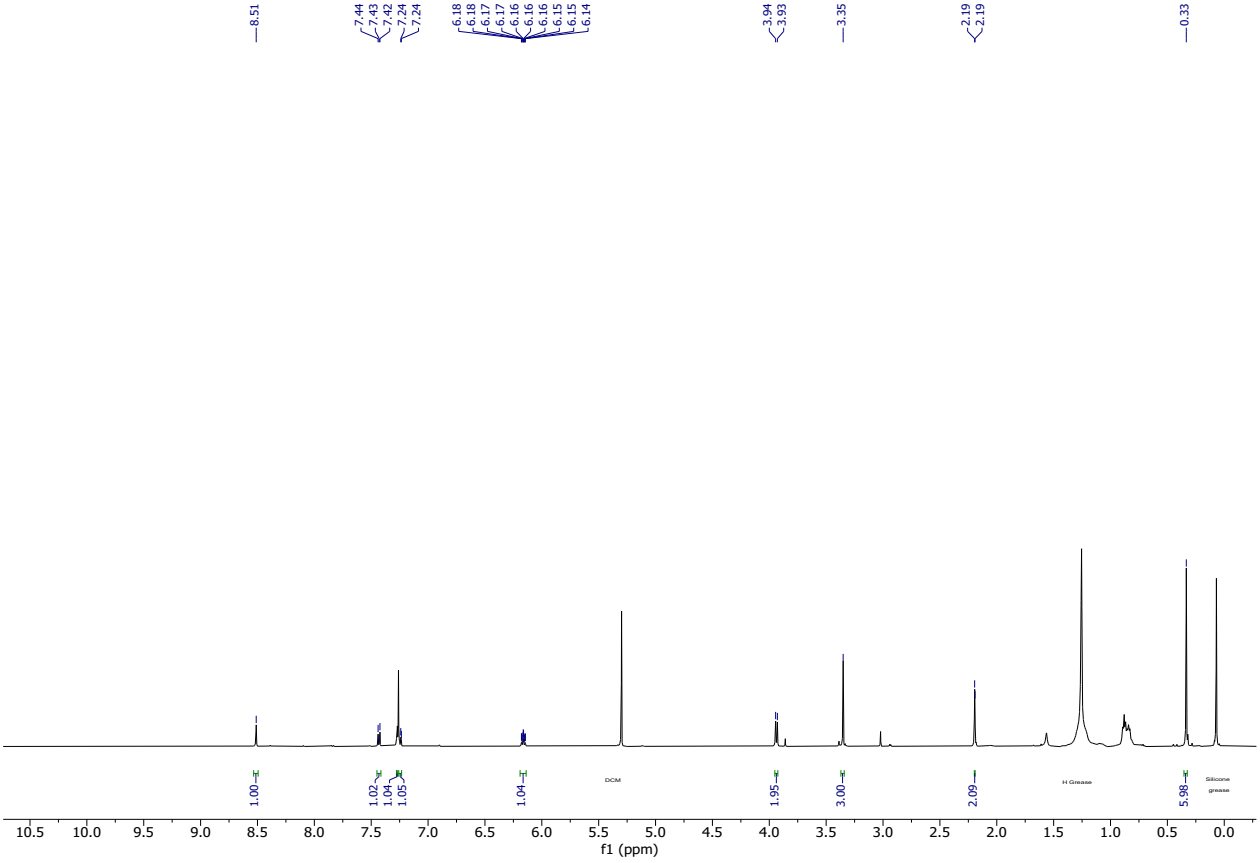

^{1}H NMR of **5.13** (500 MHz, $CDCl_3$).

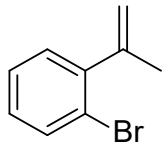

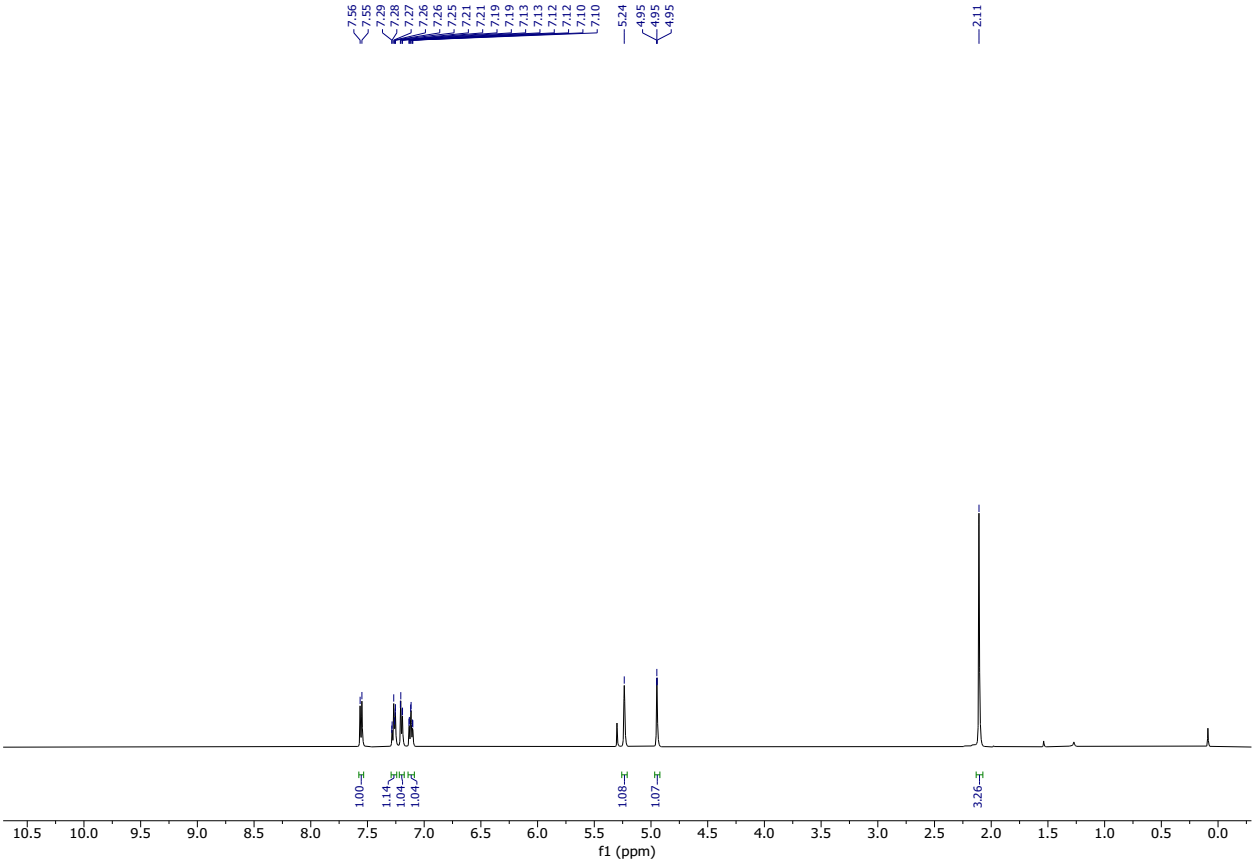

^{1}H NMR of **5.14** (400 MHz, $CDCl_3$).

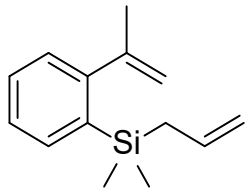

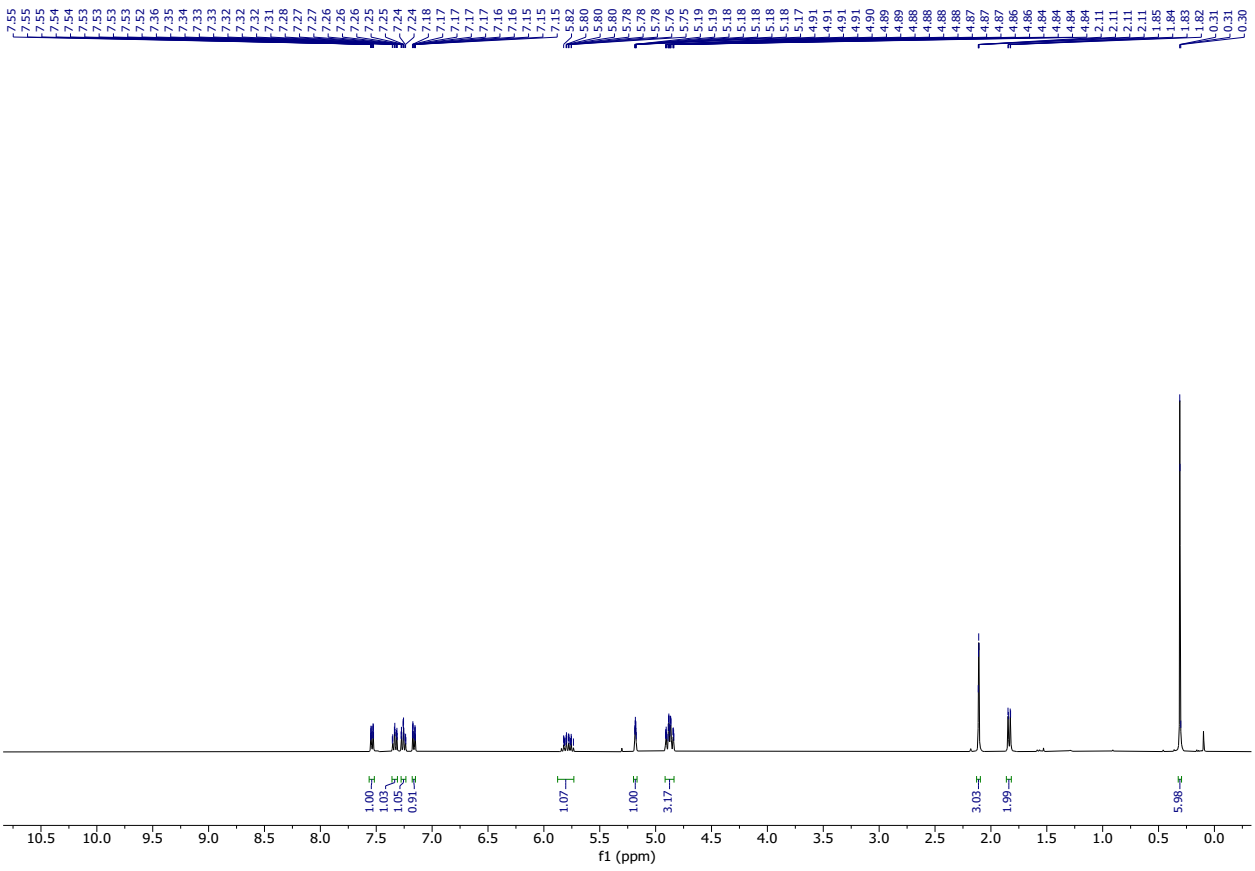

^{1}H NMR of **5.15** (500 MHz, $CDCl_3$).

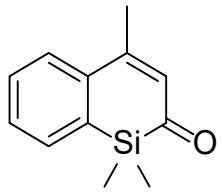

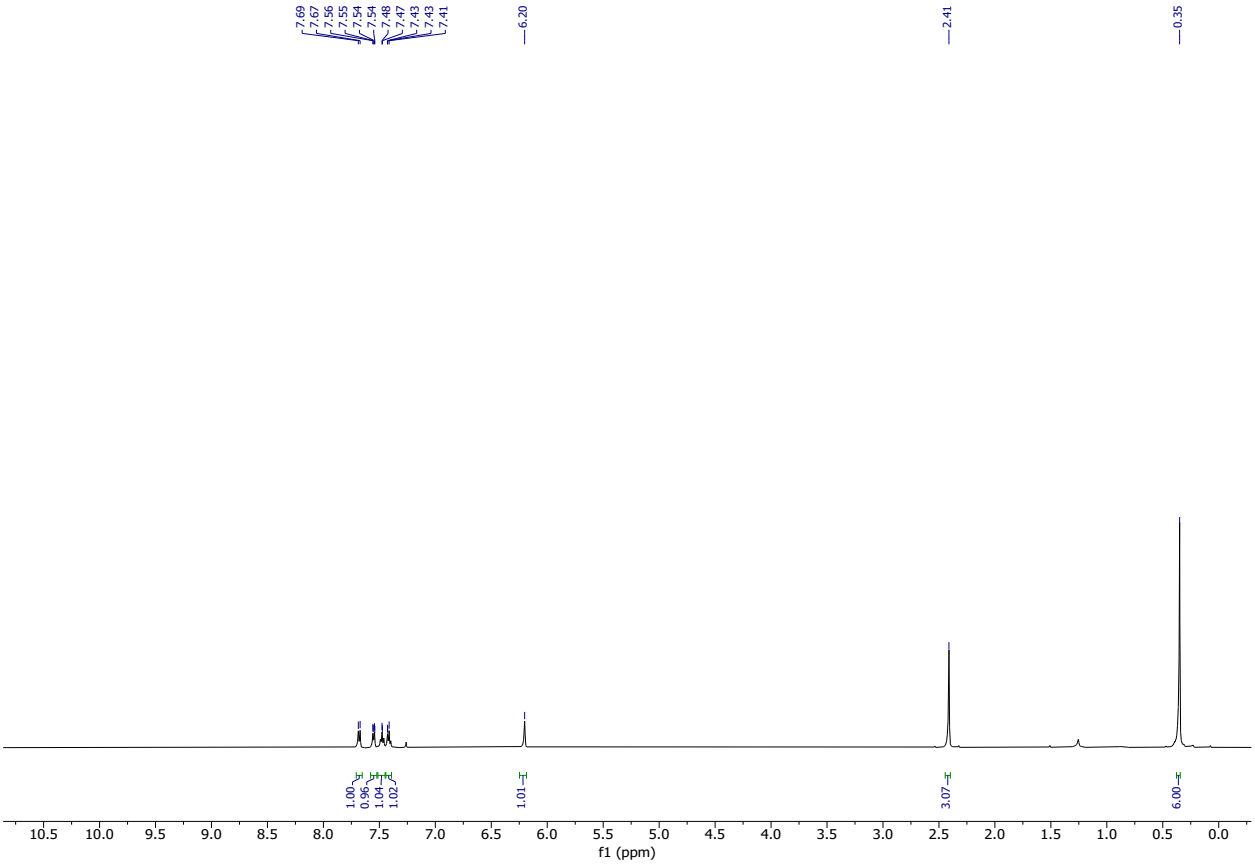

5.5.4 ^{13}C NMR Spectra

^{13}C NMR of **5.9** (500 MHz, $CDCl_3$).

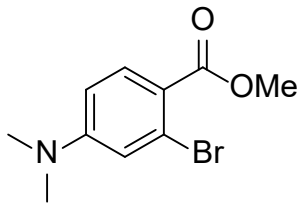

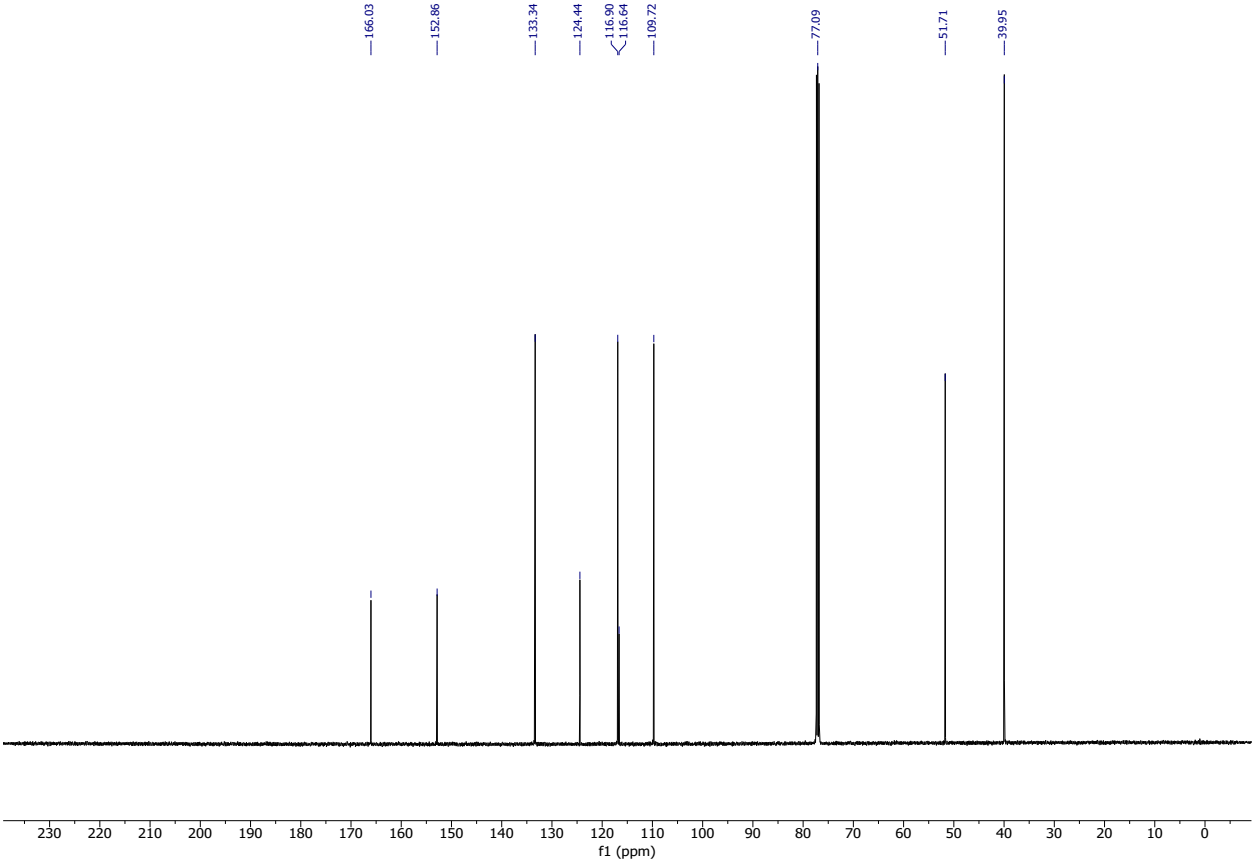

^{13}C NMR of **5.10** (500 MHz, $CDCl_3$).

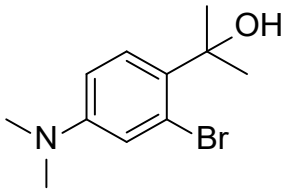

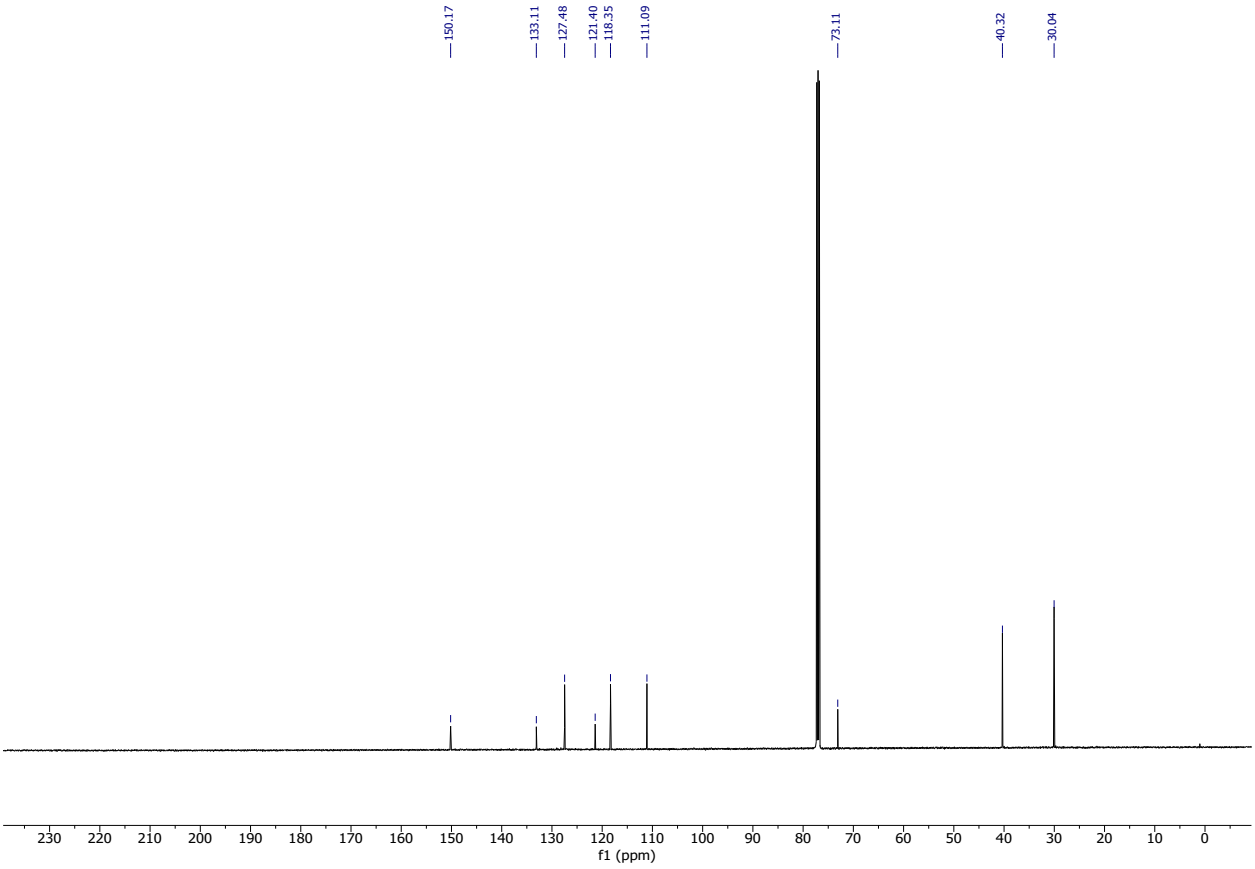

^{13}C NMR of **5.7** (500 MHz, $CDCl_3$).

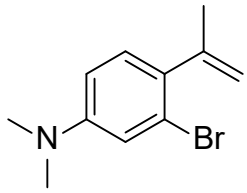

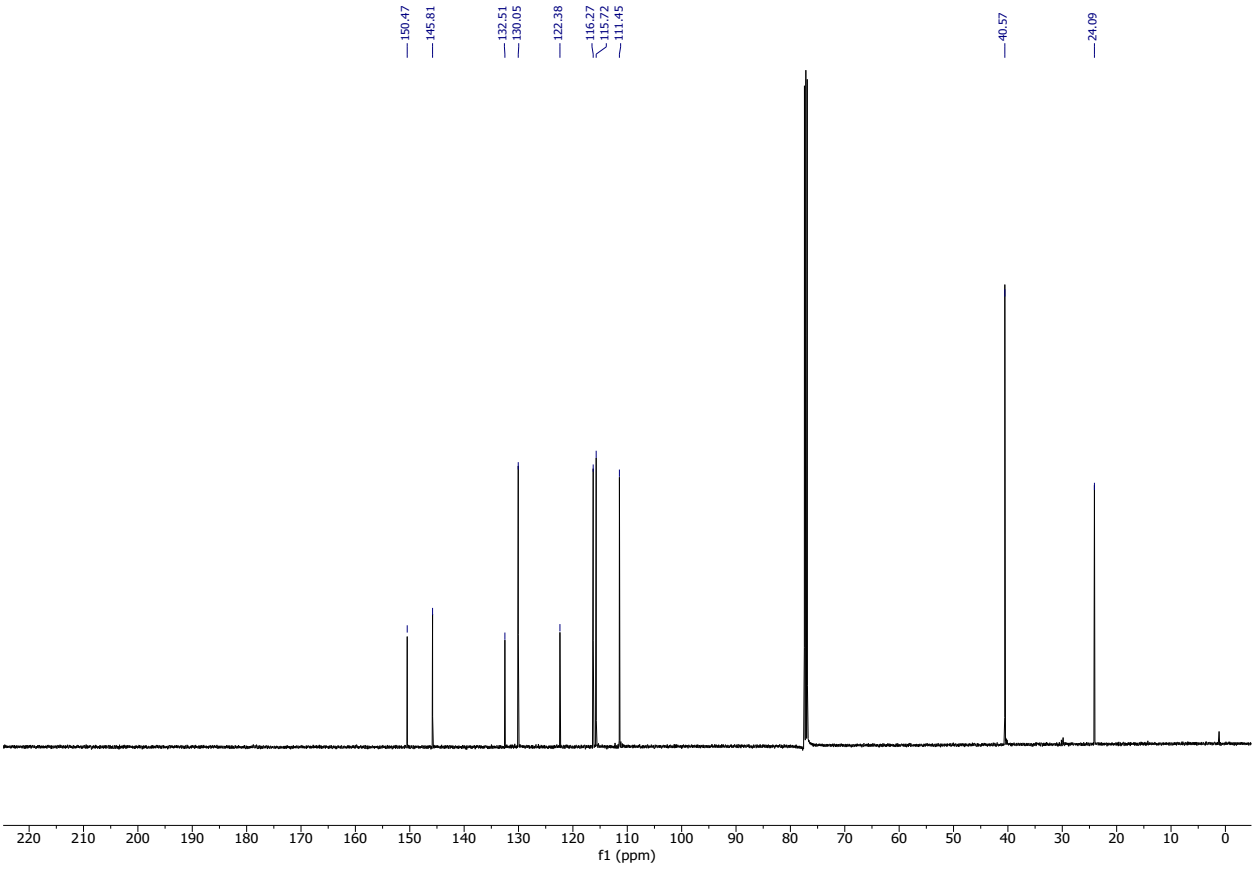

^{13}C NMR of **5.11** (500 MHz, $CDCl_3$).

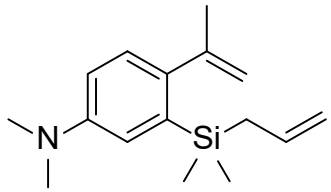

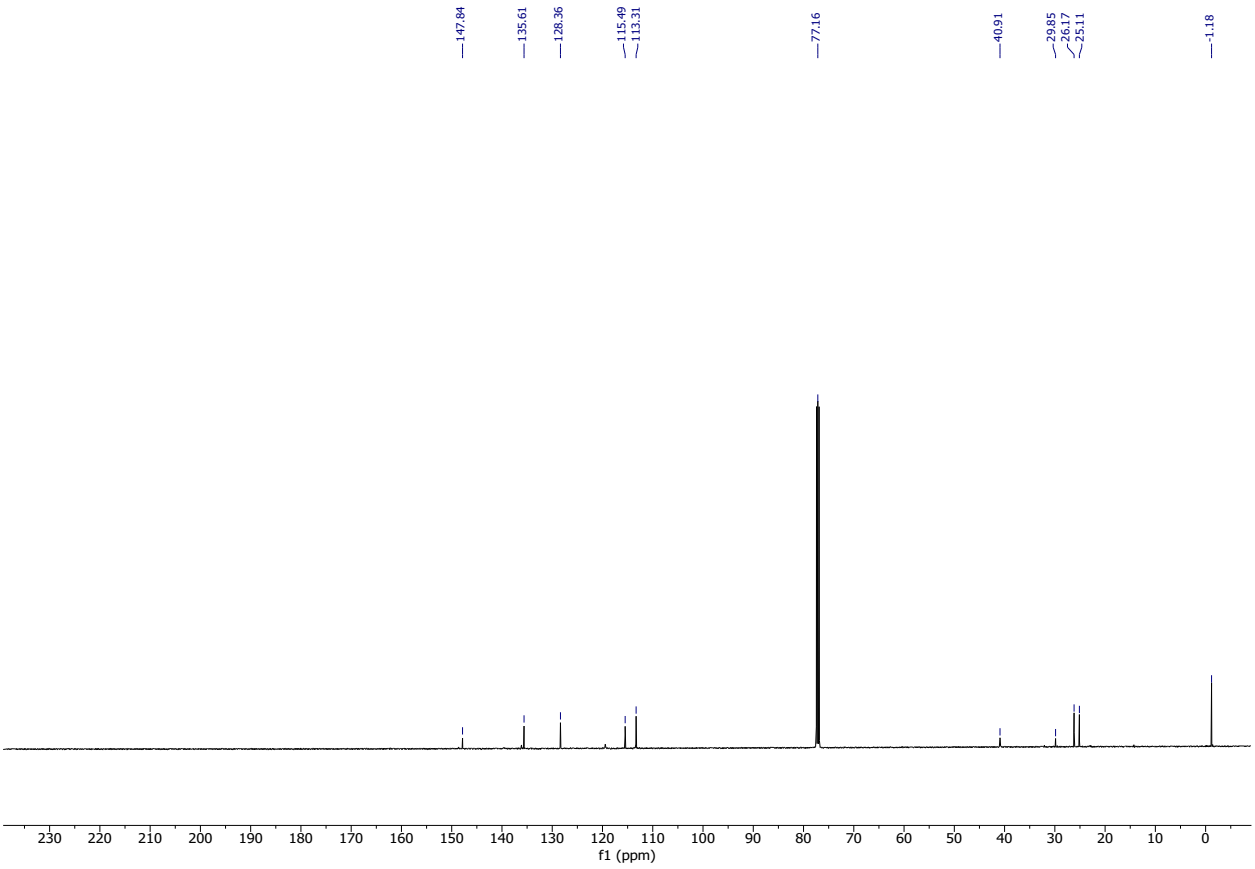

5.6 References

(1) Dolmans, D. E. J. G. J.; Fukumura, D.; Jain, R. K. Photodynamic Therapy for Cancer. *Nat Rev Cancer* **2003**, *3* (5), 380–387. https://doi.org/10.1038/nrc1071.

(2) *Light-Activated Therapy: Photodynamic Therapy - Introduction to Biophotonics - Wiley Online Library*. https://onlinelibrary.wiley.com/doi/abs/10.1002/0471465380.ch12 (accessed 2025-08-30).

(3) Correia, J. H.; Rodrigues, J. A.; Pimenta, S.; Dong, T.; Yang, Z. Photodynamic Therapy Review: Principles, Photosensitizers, Applications, and Future Directions. *Pharmaceutics* **2021**, *13* (9), 1332. https://doi.org/10.3390/pharmaceutics13091332.

(4) Cai, Y.; Chai, T.; Nguyen, W.; Liu, J.; Xiao, E.; Ran, X.; Ran, Y.; Du, D.; Chen, W.; Chen, X. Phototherapy in Cancer Treatment: Strategies and Challenges. *Sig Transduct Target Ther* **2025**, *10* (1), 115. https://doi.org/10.1038/s41392-025-02140-y.

(5) Bonnet, S. Why Develop Photoactivated Chemotherapy? *Dalton Trans.* **2018**, *47* (31), 10330–10343. https://doi.org/10.1039/C8DT01585F.

(6) Havrylyuk, D.; Hachey, A. C.; Fenton, A.; Heidary, D. K.; Glazer, E. C. Ru(II) Photocages Enable Precise Control over Enzyme Activity with Red Light. *Nat Commun* **2022**, *13* (1), 3636. https://doi.org/10.1038/s41467-022-31269-5.

(7) Welleman, I. M.; Hoorens, M. W. H.; Feringa, B. L.; Boersma, H. H.; Szymański, W. Photoresponsive Molecular Tools for Emerging Applications of Light in Medicine. *Chem. Sci.* **2020**, *11* (43), 11672–11691. https://doi.org/10.1039/D0SC04187D.

(8) Nani, R. R.; Gorka, A. P.; Nagaya, T.; Yamamoto, T.; Ivanic, J.; Kobayashi, H.; Schnermann, M. J. In Vivo Activation of Duocarmycin–Antibody Conjugates by Near-Infrared Light. *ACS Cent. Sci.* **2017**, *3* (4), 329–337. https://doi.org/10.1021/acscentsci.7b00026.

(9) Mayer, G.; Heckel, A. Biologically Active Molecules with a “Light Switch.” *Angewandte Chemie International Edition* **2006**, *45* (30), 4900–4921. https://doi.org/10.1002/anie.200600387.

(10) Klán, P.; Šolomek, T.; Bochet, C. G.; Blanc, A.; Givens, R.; Rubina, M.; Popik, V.; Kostikov, A.; Wirz, J. Photoremovable Protecting Groups in Chemistry and Biology: Reaction Mechanisms and Efficacy. *Chem. Rev.* **2013**, *113* (1), 119–191. https://doi.org/10.1021/cr300177k.

(11) Josa-Culleré, L.; Llebaria, A. In the Search for Photocages Cleavable with Visible Light: An Overview of Recent Advances and Chemical Strategies. *ChemPhotoChem* **2021**, *5* (4), 296–315. https://doi.org/10.1002/cptc.202000253.

(12) Jia, S.; Sletten, E. M. Spatiotemporal Control of Biology: Synthetic Photochemistry Toolbox with Far-Red and Near-Infrared Light. *ACS Chem. Biol.* **2022**, *17* (12), 3255–3269. https://doi.org/10.1021/acschembio.1c00518.

(13) Schulte, A. M.; Alachouzos, G.; Szymanski, W.; Feringa, B. L. The Fate of the Contact Ion Pair Determines the Photochemistry of Coumarin-Based Photocleavable Protecting Groups. *Chem. Sci.* **2025.** https://doi.org/10.1039/D3SC05725A.

(14) Bojtár, M.; Kormos, A.; Kis-Petik, K.; Kellermayer, M.; Kele, P. Green-Light Activatable, Water-Soluble Red-Shifted Coumarin Photocages. *Org. Lett.* **2019**, *21* (23), 9410–9415. https://doi.org/10.1021/acs.orglett.9b03625.

(15) Clotworthy, M. R.; Dawson, J. J. M.; Johnstone, M. D.; Fleming, C. L. Coumarin-Derived Caging Groups in the Spotlight: Tailoring Physiochemical and Photophysical Properties. *ChemPlusChem* **2024**, *89* (10), e202400377. https://doi.org/10.1002/cplu.202400377.

(16) Šebej, P.; Wintner, J.; Müller, P.; Slanina, T.; Al Anshori, J.; Antony, L. A. P.; Klán, P.; Wirz, J. Fluorescein Analogues as Photoremovable Protecting Groups Absorbing at ∼520 Nm. *J. Org. Chem.* **2013**, *78* (5), 1833–1843. https://doi.org/10.1021/jo301455n.

(17) Štacko, P.; Šebej, P.; Veetil, A. T.; Klán, P. Carbon–Carbon Bond Cleavage in Fluorescent Pyronin Analogues Induced by Yellow Light. *Org. Lett.* **2012**, *14* (18), 4918–4921. https://doi.org/10.1021/ol302244f.

(18) Egyed, A.; Németh, K.; Molnár, T. Á.; Kállay, M.; Kele, P.; Bojtár, M. Turning Red without Feeling Embarrassed─Xanthenium-Based Photocages for Red-Light-Activated Phototherapeutics. *J. Am. Chem. Soc.* **2023**, jacs.2c11499. https://doi.org/10.1021/jacs.2c11499.

(19) Palao, E.; Slanina, T.; Muchová, L.; Šolomek, T.; Vítek, L.; Klán, P. Transition-Metal-Free CO-Releasing BODIPY Derivatives Activatable by Visible to NIR Light as Promising Bioactive Molecules. *J. Am. Chem. Soc.* **2016**, *138* (1), 126–133. https://doi.org/10.1021/jacs.5b10800.

(20) Peterson, J. A.; Wijesooriya, C.; Gehrmann, E. J.; Mahoney, K. M.; Goswami, P. P.; Albright, T. R.; Syed, A.; Dutton, A. S.; Smith, E. A.; Winter, A. H. Family of BODIPY Photocages Cleaved by Single Photons of Visible/Near-Infrared Light. *J. Am. Chem. Soc.* **2018**, *140* (23), 7343–7346. https://doi.org/10.1021/jacs.8b04040.

(21) Shrestha, P.; Dissanayake, K. C.; Gehrmann, E. J.; Wijesooriya, C. S.; Mukhopadhyay, A.; Smith, E. A.; Winter, A. H. Efficient Far-Red/Near-IR Absorbing BODIPY Photocages by Blocking Unproductive Conical Intersections. *J. Am. Chem. Soc.* **2020**, *142* (36), 15505–15512. https://doi.org/10.1021/jacs.0c07139.

(22) Nani, R. R.; Gorka, A. P.; Nagaya, T.; Kobayashi, H.; Schnermann, M. J. Near-IR Light-Mediated Cleavage of Antibody–Drug Conjugates Using Cyanine Photocages. *Angewandte Chemie International Edition* **2015**, *54* (46), 13635–13638. https://doi.org/10.1002/anie.201507391.

(23) Russo, M.; Janeková, H.; Meier, D.; Generali, M.; Štacko, P. Light in a Heartbeat: Bond Scission by a Single Photon above 800 Nm. *J. Am. Chem. Soc.* **2024**, *146* (12), 8417–8425. https://doi.org/10.1021/jacs.3c14197.

(24) Russo, M.; Zielinska, D.; Hanc, K.; Ramundo, A.; Meier, D.; Szabo, A.; Štacko, P. Near-Infrared-Activated Photocages Made to Order: Late-Stage Caging Protocol. *JACS Au* **2025**, *5* (6), 2632–2640. https://doi.org/10.1021/jacsau.5c00223.

(25) Gorka, A. P.; Nani, R. R.; Zhu, J.; Mackem, S.; Schnermann, M. J. A Near-IR Uncaging Strategy Based on Cyanine Photochemistry. *J. Am. Chem. Soc.* **2014**, *136* (40), 14153–14159. https://doi.org/10.1021/ja5065203.

(26) Zhang, Y.; Yan, C.; Zheng, Q.; Jia, Q.; Wang, Z.; Shi, P.; Guo, Z. Harnessing Hypoxia-Dependent Cyanine Photocages for In Vivo Precision Drug Release. *Angewandte Chemie* **2021**, *133* (17), 9639–9647. https://doi.org/10.1002/ange.202017349.

(27) Li, C.; Wang, T.; Li, N.; Li, M.; Li, Y.; Sun, Y.; Tian, Y.; Zhu, J.; Wu, Y.; Zhang, D.; Cui, X. Hydrogen-Bonding-Induced Bathochromic Effect of Si-Coumarin and Its Use in Monitoring Adipogenic Differentiation. *Chem. Commun.* **2019**, *55* (78), 11802–11805. https://doi.org/10.1039/C9CC05895H.

(28) Sun, Y.; Li, C.; Feng, X.; Wang, C.; Wang, N.; Zhu, J.; Wang, T.; Cui, X. Si-Coumarin-Based Fluorescent Probes for Ultrafast Monitoring H2S in Vivo. *Dyes and Pigments* **2021**, *186*, 109059. https://doi.org/10.1016/j.dyepig.2020.109059.

(29) Fan, M.; Tang, Y.; Li, C.; Chen, B.; Wang, T.; Zhou, P.; Cui, X. Enhanced Fluorescence by Inter/Intramolecular Hydrogen Bonding in Si-Substituted Coumarins. *J. Phys. Chem. B* **2023**, *127* (14), 3187–3196. https://doi.org/10.1021/acs.jpcb.3c00609.

(30) Xiong, H.; Xu, Y.; Kim, B.; Rha, H.; Zhang, B.; Li, M.; Yang, G.-F.; Kim, J. S. Photo-Controllable Biochemistry: Exploiting the Photocages in Phototherapeutic Window. *Chem* **2023**, *9* (1), 29–65. https://doi.org/10.1016/j.chempr.2022.11.007.

(31) Fousteris, M. A.; Koutsourea, A. I.; Nikolaropoulos, S. S.; Riahi, A.; Muzart, J. Improved Chromium-Catalyzed Allylic Oxidation of Δ5-Steroids with t-Butyl Hydroperoxide. *Journal of*

Molecular Catalysis A: Chemical **2006**, *250* (1), 70–75. https://doi.org/10.1016/j.molcata.2006.01.031.

(32) Matsubara, S.; Oshima, K. Olefination of Carbonyl Compounds by Zinc and Chromium Reagents. In *Modern Carbonyl Olefination*; John Wiley & Sons, Ltd, 2003; pp 200–222. https://doi.org/10.1002/3527601880.ch5.

(33) Hu, G.-F.; Li, H.-J.; Zeng, C.; Wang, X.; Wang, N.; Peng, T.; Wang, S. Internal B–O Bond-Facilitated Photoisomerization of Boranes: Ring Expansion Versus Oxyborane Elimination/Intramolecular Diels–Alder Addition. *Org. Lett.* **2019**, *21* (13), 5285–5289. https://doi.org/10.1021/acs.orglett.9b01892.